Structural investigation of *Pseudomonas aeruginosa* quorum sensing receptor PqsR to aid virulence inhibition

William Richardson

Thesis submitted to The University of Nottingham for the degree of *Doctor of Philosophy*

School of Pharmacy
October 2021

Supervisors
Prof. Jonas Emsley
Prof. Miguel Cámara
Dr Michael Stocks

Abstract

Pseudomonas aeruginosa represents a significant threat to public health. *P. aeruginosa* is a ubiquitous organism and opportunistic pathogen able to infect immunologically compromised individuals and burn patients. The organism coordinates collective action, such as the release of virulence factors, through quorum sensing (QS). QS in *P. aeruginosa* is facilitate by diffusible signalling molecules from three systems: las, rhl and pqs. The latter utilises alkyl quinolones (AQ) produced by the *pqsABCDE* biosynthetic operon and PqsH. PqsR, a LysR-type transcriptional regulator (LTTRs), binds to 2-heptyl-3-hydroxy-4-quinolone (PQS) and its precursor 2-heptyl-4-quinolone (HHQ) to activate the pqs operon and virulence factors including pyocyanin and elastase. Therefore, disruption of this system represents a potential strategy to attenuate *P. aeruginosa* virulence. Prior to this thesis a large high throughput screen – as part of the SENBIOTAR research project to sensitise *P. aeruginosa* to antimicrobial therapeutics - was conducted on bioreporter strain to identify high potency antagonists.

In this thesis the binding of SENBIOTAR antagonists and derivatives were characterised by x-ray crystallography of the ligand binding domain (LBD) which has revealed relationships required for effective binding. The position of halogens within sub pocket B are considerably restricted and movement of this halogen appears to have a deleterious effect on potency observed in a bioreporter assay. It was also observed that π stacking interactions to Tyr 258, located in pocket A, could be exploited through several distinct geometries with concomitant effects of potency. Additionally, a fragment-based drug discovery campaign was launched using thermal shift (TSA) to identify compounds binders that were validated by isothermal titration calorimetry (ITC). Thus far literature studies have utilised more high cost SPR screening, but our efforts have shown an *in-silico* pre-screen and thermal shift to be effective. A benzothiazole fragment, with ligand efficiency of 0.38 was identified as a suitable starting point that could be rationally modified to increase binding affinity. However, lead-like compounds produced by growing and linking methods gave weak potency. Attempts to elucidate binding of fragments was hampered by weak resolution and difficulties outcompeting bound solvent.

To compensate for moderate-low resolution observed during crystal soaking of antagonists a crystal engineering campaign was undertaken to identify a new crystal form that diffracted to a high resolution. A total of 7 new constructs were trialled based upon 4 design different rationales: elimination of high entropy residues; disulphide locking monomer units together; improving thermostability of partially disordered loops and changing the N-terminal boundaries. Two new crystal forms were identified that elucidated previously unknown conformations of the PqsR LBD. One crystal form revealed that PqsR may have some redox sensing function via a surface exposed C108 which was confirmed by a complementation analysis to modulate protein activity. The other form revealed a canonical dimer arrangement that is adopted in most full length LTTRs structures that suggests the protein's mode of activation. Additionally, binding pocket changes were observed that will aid further medicinal chemistry development.

To gain a better understanding of PqsR functionality attempts were made to express and purify the full length receptor, reported as insoluble in the literature. Expression of the full length using standard overexpression vectors did not appear to yield soluble protein and native expression in *P. aeruginosa* failed to produce the protein that could be captured by affinity chromatography. Larger tags such as Maltose binding protein (MBP) produced aggregated material, but it was found that smaller crystal carriers developed in-house were able to effectively solubilise PqsR. Subsequent crystallisation trials identified a lithium sulphate condition that gave rise to a plate crystal habit. Despite extensive optimisation the diffraction of these crystals could not be substantially enhanced >4 Å and a suitable phase solution could not be attained by molecular replacement. Furthermore, through gel filtration, ITC and complementation experiments it was concluded the protein lacked biological activity. However, examination of truncations at positions 310 and 296 found that the disordered C-terminal was partially dispensable for function.

Finally, through a screening campaign we examined the druggability of PqsA, an anthranilate ligase required to catalyse the first step in AQ synthesis. Screening of 496 compounds yielded a single inhibitor, found to function non-competitively in the micromolar range. In *P. aeruginosa* the inhibitor reduced *pqsA* promoter activation by ~50% with an IC_{50} of 0.68 µM. Subsequent testing of pyocyanin, eDNA and AQ production

revealed a lack of significant inhibition. The attachment phenotype appeared to be altered with treated cells more prone to aggregate to plastic surfaces. Molecular docking was used to analyse molecular interactions which elucidated a probable binding event to the active site. The highest scoring docking poses showed the inhibitor to occupy the same position as the anthraniloyl – adenosine monophosphate intermediate product.

In conclusion, this thesis has broadened the structural characterisation of PqsR antagonists to drive further medicinal chemistry optimisation. The discovery that similar chemical scaffolds, such as the quinazolinone, can demonstrate subtle structural differences can aid in defining chemical space for antagonist growth. Additionally, this thesis has identified and validated a low-cost thermal shift assay for PqsR fragment discovery and elucidate new fragment starting points with high ligand efficiency. To generate superior diffracting crystals for ligand determination 2 new crystal forms have also been generated that shed light on LTTR activation and dimer interface rearrangement. Purification of the full length PqsR showed it adopted a tetrameric arrangement canonical of LTTRs but the protein failed to produce highly ordered crystals. Further optimisation of purification and crystallisation strategies will be required for structural determination.

COVID 19 statement

The latter part of my PhD was regrettably affected by the pandemic. My fragment collaboration with Ruiling Lui had been planned as a longer study with multiple attempts to acquire structural data and use ITC to drive medicinal chemistry optimisation. However, as the University chose not to extend the funding of international students this was not possible. As such I diverted my remaining time towards a SER campaign that could be useful for future antagonist development for PqsR and followed up on the biological implications of our new model. I'd like to thank Diamond Light source for continuing to provide beamline access to research groups during winter 2020.

Equipment access also had a detrimental effect on the work conducted in this PhD. For my fragment and PqsA inhibitor chapters I had planned to use the Varian CaryEclipse fluorescence spectrometer for the monitoring of intrinsic tryptophan fluorescence, to monitor fragment binding as a secondary validation measure, and for accurate monitoring of enzyme reactions. Prior to lockdown I had received training to use the instrument but upon returning to BDI access between buildings was restricted. I piloted monitoring tryptophan fluorescence using a microplate reader but found the fluorescence maxima difficult to measure accurately and as such is not reported in this thesis.

Acknowledgements

To my parents I can't say thank you enough. Your continued support throughout my PhD has been greatly appreciated and trips back to London were always a nice respite. I especially remember the help during the hard drive failure of NYE 2019.

I'd like to thank my supervisors and especially Prof Miguel Camara for the opportunity to work in the quorum sensing group.

I would like to thank Prof. Hyojung "Lori" Kim for assistance in setting up crystal trays and being a lovely lab mate for the past few years. Thank you so much for sharing a flavour of South Korean culture. Your passion for science is a joy to see and I hope you continue K-POP star Mr Kim's journey towards greater biochemical understanding. I've never seen a more determined scientist that comes in everyday with a smile and positivity. Thank you for fishing crystals throughout my PhD to avoid me butchering the drop whilst giving me practice when necessary.

A special thanks goes to Dr Ruiling Lui for a fantastic collaboration. The foray into FBDD was quite interesting and I especially enjoyed the pragmatic banter and our ritualistic beliefs regarding biophysical methods.

The PhD experience wouldn't have been complete without Dr Natalie Barrett (Dax), Dr Linzy Elton, Francis Smith and the ever-big-hearted Dr Clair Brooks. I would like to thank Maria Papaggeli for help with Pseudomonas microbiology and putting up with the occasional "why isn't this working" rant. I'd like to thank Dr Carol Paiva for plenty of "scheduled fun" including our trips to Lisbon, Prague, and the Peake District.

I'd like to thank Dr Sigrun Maurer for our wonderful conversations on all manner of sci-fi and cat related topics. You're perhaps one of the most tenacious scientists I've ever met, and I have no doubt you'll continue to impress your future colleagues! Equal appreciation goes to Dr Thomas Warwick for participating in midnight diffraction club. We've certainly seen some beautiful CBS sunrises (but hopefully no more!).

I’d like to acknowledge the people behind the CCP4 curtain for running invaluable workshops to help those new to the field. Furthermore, I’d like to thank Diamond Light source staff that work tirelessly to keep the beamlines in top notch shape and provide advice and support. I would like to thank the staff at B23 for running my samples during the pandemic and to thank Nigel Halliday and Alex Truman for technical support during my PhD.

I’d like to thank my terrific housemate Christopher “Crispy Duck” Seymour for his company through the lockdown, a steady stream of film recommendation and appreciation of the finer points of CIV 5 strategy.

Table of Contents

Abstract ..... *II*

COVID 19 statement ..... *V*

Acknowledgements ..... *VI*

Table of Contents ..... *VIII*

Figures ..... *XIV*

Tables ..... *XVIII*

Abbreviations ..... *XX*

Publications ..... *XXII*

1 Introduction *1*

1.1 The problem of antimicrobial resistance (AMR) **1**

1.2 *P. aeruginosa* as a clinical pathogen **3**

1.2.1 Intrinsic resistance 4

1.2.2 Acquired resistance 5

1.2.3 Virulence factors 5

1.2.4 Proteases 5

1.2.5 Extracellular products 6

1.2.6 Biofilms 7

1.3 Quorum sensing **9**

1.3.1 Quorum sensing in *P. aeruginosa* 10

1.3.2 QS hierarchy in *P. aeruginosa* 12

1.3.3 Las quorum sensing 13

1.3.4 Rhl system 13

1.4 Alkyl quinolone properties and function **15**

1.4.1 AQ biosynthesis 16

1.4.2 *Burkholderia* AQ synthesis 17

1.4.3 PQS associated virulence 19

1.5 LysR Type Transcriptional Regulators (LTTRs) **20**

1.5.1 DNA binding domain 21

1.5.2 Ligand/co-inducer binding domain 21

1.5.3 Multimerization 24

1.6 PqsR – function, structure, and regulation **25**

1.7 Quorum sensing inhibition in *P. aeruginosa* **29**

1.7.1 QSI by degradation and sequestration 30

1.7.2 QSI for AHL receptors 31

1.7.3 Disrupting PQS biosynthesis 32

1.7.4 PqsR antagonism 34

1.8 Use of fragments in drug discovery **37**

1.8.1 Biophysical determination of binders 37

1.8.2 Fragment to lead development 37

1.8.3 Dissecting PqsD analogue to potent fragment 39

1.8.4 PqsE fragment screen 39

1.8.5 SPR campaign on PqsR identified multiple binders 40

1.8.6 Dual targeting PqsD/R agents 42

1.9 Role of SENBIOTAR in *P. aeruginosa* drug discovery 43

1.10 Thesis aims 44

2 Materials and Methods 46

2.1 Strains 46

2.2 Plasmids 47

2.3 Media and bacterial growth 49

2.4 Cloning 50

2.5 Protein purification from *E. coli* 58

2.6 Biophysical and biochemical assays 65

2.7 Docking 71

2.8 Crystallography 72

2.9 Structural solution 76

2.10 Negative staining 76

2.11 Phenotypical assays: CTX::P_{pqsA}-*lux* 77

2.12 Phenotypical testing: Extracellular products & growth dynamics 78

3 Structural elucidation of $PqsR^{LBD}$ in complex with antagonists 81

3.1 Introduction 81

3.2 Compound used in soaking studies 82

3.3 Protein construct for crystallisation 85

3.3.1 Requirement for N-terminal cleavage 85

3.3.2 Comparison of $PqsR^{94-309}$ with other reported $PqsR^{LBD}$ structures 85

3.3.3 Purification of $PqsR^{94-309}$ for crystallisation 86

3.3.4 Purification of constructs for biophysical characterisation 87

3.3.5 Testing for co-crystallisation suitability 89

3.3.6 Crystallisation 91

3.4 Determining the binding pose of SEN66 in complex with $PqsR^{LBD}$ 92

3.4.1 LUI195-93 soaking 93

3.4.2 Comparison of binding pose between M64 and LUI195-93 97

3.4.3 SEN66 SAR analysis 98

3.4.4 Soaking failure of other SEN66 candidates 98

3.5 Determining the binding pose of SEN19 in complex with $PqsR^{LBD}$ 98

3.5.1 Binding mode of SEN19 100

3.5.2 SEN19 interactions with Tyr 258 105

3.5.3 Comparison of SEN19 & AM159-089 $PqsR^{94-309}$ complexes 105

3.5.4 Probing halogen interactions with Thr 265 106

3.5.5 Relating structural information to SAR 109

3.6 Determining the binding pose of SEN32 in complex with $PqsR^{LBD}$ 109

3.6.1 Binding mode of SEN32 series 110

3.6.2 Comparison to native AQs 116

3.6.3 Relating SEN32 structural data to SAR 117

3.7 Resolving enantiomeric differences in SEN89 benzimidazole binding to $PqsR^{LBD}$ 117

3.7.1 Crystal soaking 118

3.7.2 Racemate preference not highlighted by crystal soaking 122

3.7.3 Thermal shift analysis of both enantiomers 124
3.7.4 Further interactions between SEN89 series and the pocket 124
3.7.5 R_3 substituents optimisation for cross dimer interaction 128
3.7.6 Benzimidazole shifts to accommodate R_1 functional group 130

3.8 PqsR^{LBD} in complex with a naturally derived antagonist – 488 130
3.8.1 Difficulties in soaking 130
3.8.2 Structural solution of 488 binding to PqsR$^{94-309}$ 131
3.8.3 488 interactions with PqsR binding pocket 136

3.9 Lack of Clofoctol density 143

3.11 Discussion 147

3.12 Conclusions 149

4 Applying Fragment-based drug discovery to PqsR antagonism 150

4.1 Introduction 150

4.2 Selection of candidates by *in silico* molecular docking 151

4.3 Thermal shift analysis of PqsR$^{94-309}$ melting 154

4.4 Controls for thermal shift assay 155

4.5 Screening *in silico* selected compounds by thermal shift 156

4.6 ITC analysis on control fragments reveals different thermodynamic signatures 157

4.7 Exploration of fragments by thermal shift and ITC 159
4.7.1 Exploration of Benzothiazole fragment 1 159
4.7.2 Identifying a suitable linking partner to Fragment 1i 164
4.7.3 Finding alternative binders to pocket A 166
4.7.4 Lack of fragment 4 binding 168

4.8 *In vivo* characterisation of linked and grown fragments using PAO1-L CTX::P$_{pqsA}$-*lux* bioreporter 169

4.9 Initial soaking attempts with PqsR$^{94-309}$ 172

4.10 Re-screening library against PqsA 172

4.11 Discussion 173

4.12 Conclusions 174

5 Generating new PqsR ligand binding domain crystal forms 176

5.1 Construct design rationale 176
5.1.1 Surface entropy reduction analysis 176
5.1.2 Re-engineering loop 180-185 to reduce disorder 179
5.1.3 Engineering an intermolecular disulphide 180
5.1.4 Modification and extension of N-terminal 182
5.1.5 Constructs for purification 182

5.2 PqsR^{LBD} variant purification 183
5.2.1 SER constructs 183
5.2.2 Loop modification constructs 185
5.2.3 Interchain disulphide locking construct S123C 187
5.2.4 MBP-^{94}PqsR^{309} fusion purification 188
5.2.5 Helix extension construct 190

5.3 Crystallisation of construct variants 191
5.3.1 SER variants: K154A E278A, K154A K214Y 191

5.3.2 Loop mutants 193
5.3.3 Engineered disulphide lock variant S123C 196
5.3.4 MBP-^{94}PqsR^{309} 197
5.3.5 In-gel agarose crystallisation of wildtype ^{94}PqsR^{309} construct 197

5.4 Structural solution of engineered disulphide S123C 198
5.4.1 Effectiveness for antagonist determination 199

5.5 Structural solution for SER variants 200
5.5.1 K154A E278A 200
5.5.2 Structural determination of SER variant K154A K214Y 201

5.6 Structural solution for loop deletion DR variant 205
5.6.1 New assembly is characteristic of canonical LTTR dimer 208
5.6.2 Binding site rearrangement 209
5.6.3 In solution analysis of ^{94}PqsR^{309} DR mutant topology 211

5.7 Exploring structure-function relationships by *in vivo* complementation with *pqsA* bioreporter 212
5.7.1 PqsR mutants' response to different AQ signals 212
5.7.2 Complementation under overexpression conditions 214

5.8 Discussion 214

5.9 Conclusions 218

6 Expression, purification, and crystallisation of full length PqsR 220

6.1 Introduction 220

6.2 Disorder and hydrophobicity analysis 221

6.3 Construction and purification of His-tagged *E. coli* constructs 224
6.3.1 pET28a and pCOLD expression 224
6.3.2 Pilot expression of PqsR DNA binding domain constructs 226

6.4 Homologous expression of PqsR in *P. aeruginosa* 228
6.4.1 Expression and purification of PqsR from *P. aeruginosa* extract 228
6.4.2 Mass spectrometry and crystallisation 231

6.5 Carrier-driven solubilisation of PqsR 232
6.5.1 Expression of MBP-PqsR 233
6.5.2 Screening for additional crystallisation tags 240
6.5.3 Purification of 1BKR-PqsR 241
6.5.4 Crystal trials for full length PqsR 244

6.6 Modification to 1BKR-PqsR construct to improve crystallisation 249
6.6.1 Addition of cleavage site to remove 1BKR 249
6.6.2 Truncation of PqsR C-terminal residues to reduce disorder 251
6.6.3 Purification and crystallisation of 1BKR-PqsR^{296} 253
6.6.4 Purification and crystallisation of 1BKR-PqsR^{310} 255

6.7 1BKR-PqsR SER variants 258
6.7.1 S123C variant purification 258
6.7.2 Loop mutant (180 – 185) insolubility 260

6.8 Binding to PQS 260

6.9 1BKR-PqsR – DNA complex characterisation 261

6.10 Assessing sample folding by SAXS 262

6.11 Identification of alternative ligands for co-crystallisation 263

6.12 Stabilisation of the protein by thermal shift assays 265
6.13 Attempts to phase diffraction data 267
6.13.1 Analysis of diffraction data for 1BKR-PqsR 267
6.14 Molecular replacement trials for diffraction data 270
6.14.1 Phasing 1BKR-PqsR by molecular replacement 270
6.14.2 Phasing with *de novo* model 270
6.15 *In vivo* complementation with 1BKR-PqsR protein 272
6.16 Discussion 272
6.17 Conclusions 274
7 Disruption of the PQS system via PqsA inhibition 276
7.1 Introduction 276
7.2 Aims of this chapter 277
7.3 Results 278
7.3.1 Screening and hit compound identification 278
7.3.2 Discounting false positives through potential inhibition of the bioreporter *lux* gene products 283
7.3.3 Validation of ZN8751275 as a PqsA inhibitor 283
7.3.4 IC_{50} determination by LCMS/MS product analysis 284
7.3.5 Detecting binding by thermal shift 285
7.3.6 Crystallisation attempts for PqsA 286
7.3.7 Use of a StrepTrap for $PqsA^{1-399}$ purification 287
7.3.8 Crystallisation of $PqsA^{1-399}$Strep 288
7.3.9 Determining the binding mode of ZN8751275 in PqsA by molecular docking 289
7.3.10 Biological analysis of ZN8751275 on *P. aeruginosa* 296
7.4 Discussion 317
7.5 Conclusions 319
8 Outlook 320
9 Appendix 322
9.1 $PqsR^{LBD}$ MPD crystal screen 322
9.2 INFAC screening plates 323
9.3 Strains possessing PqsR mined from Pseudomonas Genome Database 327
9.4 Origin of each isolate from the Pseudomonas Genome Database 330
9.5 Frequency of missense, deletions, and insertions across PqsR 331
9.6 Predicted impact of missense mutations on protein stability 332
9.7 Boltzmann melting temperature analysis from change in Molar Ellipticity 333
9.8 IlvC data collection statistics and figures 334
9.9 Cleavage conditions 336
9.10 Lattice and contaminant screening of FL PqsR crystals 337
9.11 Negative stain images of PqsR 339
9.12 Surface Entropy reduction screen 340
9.13 SDS PAGE gels for SER constructs 341

9.14 Screening method for PqsA used for NCC library search 342
Preparation of Protein and Receptor Grid Generation 342
Ligand Preparation 342
Molecular Docking 342
9.15 Screening method for PqsA used for NCC library search 343
9.16 LC – MS identification of Anthraniloyl Coenzyme A: PqsA 344
9.17 Reproduction of Anthraniloyl-AMP and anthranilic acid using Autodock vina 347
9.18 Linearity test for PqsA enzymatic activity 349
9.19 Control incubations for ZN8751275 349
9.20 Disorder prediction on PqsA homolog and alignment 351
9.21 Gel filtration standards 352
10 Bibliography 353

Figures

		Page
1.1	Molecular structures of non-proteinaceous extracellular products	6
1.2	*P. aeruginosa* biofilm	8
1.3	Types of QS molecule & concept of group dependent signalling	10
1.4	QS regulatory hierarchy *P. aeruginosa*	12
1.5	Quorum sensing receptors LasR (PDB 2UV0) and homology model of RhlR	15
1.6	The most common AQ products found in *P. aeruginosa* and *Burkholderia sp*	16
1.7	PQS Biosynthesis in *P. aeruginosa*	18
1.8	Cartoon diagram of LysR-type transcription regulator	22
1.9	CrgA octamer complex	24
1.10	Comparison of tetramer structure conformation	25
1.11	Cartoon and surface representation of PqsR structure	27
1.12	Surface and stick model of AQ binding pocket	28
1.13	QSI strategies	30
1.14	Inhibitors developed against LasR and RhlR	31
1.15	Inhibitors developed towards PqsE	32
1.16	Inhibitors developed towards PqsBC and PqsD	34
1.17	Strategies for FBDD	38
1.18	PqsD fragment development from substrate analogue	39
1.19	Fragments bound to PqsE	40
1.20	Initial fragment hits for PqsR determined by SPR screening	41
1.21	Fragment merging and subsequent growth to develop favourable PqsR antagonists	42
1.22	Identification of a common scaffold applicable to PqsD and PqsR	43
1.23	Overview of $PqsR^{LBD}$ antagonist screening technique used to identify initial hit compounds	44
3.1	N-terminal residues located within the 4JVC $PqsR^{LBD}$ model	85
3.2	Comparison of $PqsR^{94-295}$ and $PqsR^{94-309}$ showing variability in loop 6	86
3.3	Purification of $PqsR^{94-309}$ for structural investigations with antagonists	87
3.4	Purification of WT $PqsR^{94-332}$ construct for ligand interaction studies	88
3.5	Purification of T265A and T265N $PqsR^{94-332}$ mutant for binding analysis	89
3.6	Piloting co-crystallisation experiments with $PqsR^{94-309}$	90
3.7	Apo-crystals of $PqsR^{94-309}$ grown in MPD conditions	91
3.8	SEN66 antagonist series	92
3.9	LUI195-93 – $PqsR^{94-309}$ complex	96
3.10	Comparison of π-π stacking between M64 and LUI195-93	97
3.11	SEN19 antagonist series	99
3.12	SEN19 – $PqsR^{94-309}$ complex	103/4
3.13	Superposition of SEN19 and 3NH2-7Cl-C9QZN complexes showing Ile236 reposition	104
3.14	Nitrile occupies the pocket A cavity formed from Ser 255 backbone	105
3.15	Effect of R_3 methoxyacetonitrile on SEN19 series binding pose	106
3.16	Binding of SEN19 to $PqsR^{94-332}$	107
3.17	Comparing binding of SEN19 to WT and T265A $PqsR^{LBD}$	108
3.18	SEN32 antagonist series	109
3.19	Electron density maps for SEN32 series $PqsR^{LBD}$ complexes	113/4
3.20	Polar interactions between SEN32 and $PqsR^{LBD}$ binding pocket residues	115/6
3.21	Variation in bicyclic position with alkyl chain	117
3.22	SEN89 compound series	118
3.23	Electron density maps for SEN89 racemate soaked into $PqsR^{94-309}$	122

3.24	Comparison of SEN89 enantiomer binding to $PqsR^{LBD}$	123
3.25	Comparing binding parameters of SEN89 enantiomers by thermal shift assay	124
3.26	Polar interactions between SEN89 and $PqsR^{LBD}$ binding pocket residues	125/6/7
3.27	Rotation of R_3 group in SEN89 and AM204-42	128
3.28	Comparison of SEN89 R_3 substituent	129
3.29	Substituent effect on benzimidazole position	130
3.30	Unmodelled ligand density from 488	134
3.31	Electron density of 488 in $PqsR^{LBD}$ binding pocket	135
3.32	Interaction between 488 and $PqsR^{LBD}$	137
3.33	488 natural product congener	138
3.34	Concentration-dependent destabilisation by 488	139
3.35	CD analysis of secondary structure content of $PqsR^{LBD}$	140
3.36	Effect of 488 on PqsR CD melting spectra	141
3.37	Near-UV acquisition for PqsR-488 host guest interaction	143
3.38	Proposed $PqsR^{LDB}$ binder Clofoctol	144
3.39	Distribution of mutations across the known PqsR structure	146
4.1	Fragment screening methodology	151
4.2	Optimisation of buffer for Thermal shift screening of $PqsR^{94-309}$	155
4.3	Thermal shift assay control ligand fQZN	156
4.4	Initial thermal shift screening of fragments from *in silico* docking	157
4.5	Comparison of SUMO-^{87}PqsR with His-^{94}PqsR binding a fragment 36	158
4.6	Binding of 7Cl-C1PQS fragment to His-^{94}PqsR	159
4.7	Binding of fragment 1 to $His^{94}PqsR$	160
4.8	Thermal shift screen of Fragment 1 derivatives	161
4.9	Binding of 1g to $His^{94}PqsR$	162
4.10	Binding of Fragment 1i to $His^{94}PqsR$	163
4.11	Binding of Fragment 10 to PqsR and effect on linking	165
4.12	Fragment 10 group exploration	166
4.13	Binding of Fragment 11 to $His^{94}PqsR$	167
4.14	Comparison of structure isomers of grown fragment 11	168
4.15	Molecular structure of fragment 4 and literature 2-naphthamide	169
4.16	Dose-dependence effect of fragment derived leads on PAO1 – L CTX::P_{pqsA}-*lux*	170/1
4.17	PqsA thermal shift to screen PqsR fragment library	173
5.1	Stick representation of $PqsR^{LBD}$ residues targeted for SER mutation	179
5.2	B-Factors of $PqsR^{LBD}$ models plotted against residue number	180
5.3	Engineered disulphide S123C in $PqsR^{LDB}$ $P6_522$ crystal form	181
5.4	Purification of SER variants K154A E278A & K154A K214Y	184
5.5	Purification of loop variant $^{94}PqsR^{309}$ constructs	186
5.6	Purification of $^{94}PqsR^{309}$ S123C	187
5.7	Coomassie stained non-reduced SDS PAGE gel showing *In vitro* disulphide bond formation of $^{94}PqsR^{309}$ S123C	188
5.8	Purification of MBP-$^{94}PqsR^{309}$	189
5.9	Purification of $^{60}PqsR^{309}$	191
5.10	SER constructs hit analysis	192
5.11	Crystal habits of $PqsR^{LBD}$ SER variants	193
5.12	Crystallisation of DR $PqsR^{94-309}$ variant hit analysis	194
5.13	Crystal habits of DR variant	195
5.14	$PqsR^{LBD}$ S123C variant hit analysis	196
5.15	Agarose-grown $^{94}PqsR^{309}$ crystals	197

5.16	*In crystallo* formation of a disulphide in S123C	199
5.17	Diffraction image of K154A E278A	200
5.18	K154A K214Y crystal structure	202
5.19	Change in tetrameric interface between $P6_522$ and $P4_322$	203/4
5.20	$^{94}PqsR^{309}$ DR crystal habit and sample electron density map	206
5.21	Cartoon diagram of $^{94}PqsR^{309}$ DR mutant dimer arrangement	208
5.22	Superposition of new dimer arrangement and CbnR (PDB 7D98)	209
5.23	Superposition of ligand binding pockets from $^{94}PqsR^{309}$ DR and WT $^{94}PqsR^{309}$	210
5.24	SAXS analysis of $^{94}PqsR^{309}$ DR mutant	211
5.25	Optimisation of IPTG induction conditions for complementation construct pME6032::*pqsR*-His	212
5.26	Activity of PqsR mutants to an excess of co-inducer molecules (40 μM) in PAO1 – N Δ*pqsAHR* CTX::P_{pqsA}-*lux*	213
5.27	Complementation of PAO1 – N Δ*pqsR* CTX::P_{pqsA}-*lux* with mutant *pqsR* under three expression conditions	214
5.28	Redox state as an activation input	217
5.29	Microarray analysis on *pqsA* and *pqsR* expression performed under oxidative conditions (1 mM H_2O_2)	218
6.1	PqsR schematic and predicted structure	221
6.2	Disorder prediction of PqsR using primary sequence	222
6.3	Secondary structure prediction based on primary sequence	223
6.4	PqsR solubility expressed with pET28a and pCOLD	225
6.5	PqsR DBD constructs expression and extraction	227
6.6	Preparation of *P. aeruginosa* lysate for protein extraction	229
6.7	Extraction and purification from *Pseudomonas* lysate	230
6.8	Elution of native *P. aeruginosa* sample from Superdex 10/300 column	231
6.9	Crystal habits displayed by *P. aeruginosa* IlvC contaminating protein	232
6.10	Effect of sorbitol media concentration on MBP-PqsR solubility	233
6.11	Effect of temperature on MBP-PqsR solubility	234
6.12	pH buffer optimisation of MBP-PqsR	235
6.13	Salt extraction optimisation of MBP-PqsR	236
6.14	MBP-PqsR purification	237
6.15	Chromatogram of MBP-PqsR elution from a Superdex 200 16/60 column	237
6.16	Re-elution of MBP-PqsR from Superdex 200 16/60	239
6.17	Solubility testing with additional carrier proteins	241
6.18	Capture and concentration of 1BKR-PqsR	242
6.19	Gel filtration of 1BKR-PqsR using a Superdex 200 16/60	243
6.20	Initial crystals observed from Nucleix suite	245
6.21	Optimisation of 1BKR-PqsR crystals	246
6.22	PqsR crystals grown in lower melting temperature agarose	247
6.23	Purification of 1BKR-TEV-PqsR	250
6.24	Trial cleavage conditions	251
6.25	Truncated PqsR constructs	252/3
6.26	1BKR – $PqsR^{296}$ purification via HisTrap HP and Heparin HP column	254/5
6.27	1BKR-$PqsR^{310}$ purification	256/7
6.28	Representative crystals produced from $PqsR^{310}$ MMS screening	257/8
6.29	Purification of PqsR S123C	259
6.30	ITC data for titration of PQS (200 μM) into 1BKR-PqsR (20 μM)	261
6.31	Analytical gel filtration with different ratios of PqsR and LysR-box	262

6.32	SAXS analysis of PqsR	263
6.33	Effect of *Burkholderia* spp. AQs on *P. aeruginosa*	265
6.34	Thermal shift melting analysis on PqsR with respect to buffer composition	266/7
6.35	Image of 1BKR-PqsR crystal in cryoloop	268
6.36	Matthews probability distribution	270
6.37	Models for phasing predicted by Robetta server	271
6.38	Complementation experiment on fusion construct	272
7.1	PqsA inhibitors described in the literature	277
7.2	Constructs for PqsA protein purification	277
7.3	Purification of PqsA Anthranilate ligase	279
7.4	Enzyme kinetic parameters from absorbance assay	280
7.5	Anthraniloyl – AMS control compound testing	281
7.6	Re-screening of *in vitro* hits against PAO1-L CTX::P_{pqsA}-*lux*	282
7.7	ZN8751275 does not influence luminescence	283
7.8	Non-competitive inhibition with respect to Anthranilate and ATP	284
7.9	IC_{50} determination for ZN8751275 on PqsA activity	284
7.10	Enzymatic reaction of PqsA with ZN8751275 quantified by LC-MS/MS	285
7.11	Thermal shift assay for PqsA in the presence of Anthranilic acid and ZN8751275	286
7.12	Expression of $PqsA^{1-399}$ and purification trial	287
7.13	Purification of $PqsA^{1-399}$strep	288
7.14	Quasi-crystals of $PqsA^{1-399}$	289
7.15	Blind docking with ZN8751275 performed with SwissDock	290
7.16	Potential binding poses at the PqsA active site determine by AutoDock Vina	293
7.17	Replacement of 3,4-dichlorophenyl with a phenyl group shifts binding pose	294
7.18	Docking poses of ZN8751275 on PqsA hinge loop	295
7.19	Impact of ZN8751275 on *P. aeruginosa* growth	296
7.20	Decrease in pqsA promoter activation in PAO1 – L upon addition of ZN8751275	297
7.21	Effects of ZN8751275 on AQ biosynthesis	298
7.22	Effect of ZN8751275 on *P. aeruginosa* aggregation	299
7.23	Synergism analysis with SEN19 and ZN8751275 on PAO1-L CTX::P_{pqsA}-*lux* bioreporter	300/1
7.24	Impact of ZN8751275 and SEN19 on pyocyanin production	302
7.25	Impact of ZN8751275 and SEN19 on eDNA release	303
7.26	Impact of ZN8751275 and SEN19 on supernatant LasB activity	304
7.27	Impact of ZN8751275 and SEN19 on Pyoverdine production in PAO1 – L	305/6
7.28	Alignment of PqsA and *Burkholderia spp.* homologs	307
7.29	Solubility assessment of HmqA and HhqA prior to protein purification	308
7.30	Purification of HmqA Anthranilate ligase	309
7.31	Purification of HhqA using StrepTrap HP column	310
7.32	Semi-quantification of methanol extracted Anthraniloyl-CoA by LC MS/MS	311
7.33	Enzymatic reaction of HmqA with ZN8751275 quantified by LC-MS/MS	312
7.34	Construct design and solubility of $HmqA^{1-430}$ and $HhqA^{1-430}$	313
7.35	Purification of $HmqA^{1-430}$ for crystallisation trials	314/5
7.37	Extraction and purification of $HhqA^{1-430}$ with and without ligand	317

Tables

		Page
1.1	LTTRs and their associated ligand	23
1.2	Literature PqsR antagonists	36
2.1	*E. coli* strains used in this study	46
2.2	*P. aeruginosa* strains used in this study	46
2.3	Table of plasmids used for complementation experiments	47
2.4	Expression constructs	48
2.5	Bacterial growth medias used in this study	49
2.6	PCR reaction components	51
2.7	PCR cycling conditions	51
2.8	Oligonucleotide primers used in this study to generate expression constructs	54
2.9	Oligonucleotide primers used in this study to generate complementation constructs	56
2.10	Oligonucleotide primers for site directed mutagenesis	56/7
2.11	Protein construct expression conditions	58
2.12	IMAC buffer conditions	60
2.13	Gel filtration buffer	61
2.14	Chromatography columns used for each construct/protein source	62
2.13	SDS PAGE composition	64
2.13	Screening conditions for $PqsR^{LBD}$	66
2.14	Screening conditions for full length PqsR – Buffers & Salts	67
2.15	Screening conditions for full length PqsR – Additives	67
2.16	Docking parameters for PqsA (PDB 5OE5)	72
2.17	Data collection information from diffraction experiments at DLS	75
3.1	Ligands complexed with $PqsR^{LBD}$	82/3
3.2	Data collection and refinement statistics for $PqsR^{LBD}$-LUI195-93 complex	94
3.3	Data collection and refinement statistics for $PqsR^{LBD}$ in complex with SEN19 and phenoxyaceonitrile (AM159-089) derivative	101
3.4	Data collection and refinement statistics for $PqsR^{LBD}$ in complex with SEN32 antagonist series	111
3.5	Crystallographic data collection and refinement statistics for $PqsR^{LBD}$ in complex with SEN89 & derivatives	119
3.6	SEN89 R isomer soaked into S123C $PqsR^{94-309}$ table of crystallographic collection and refinement	121
3.7	Optimisation of solvent washing for 488 complex determination	131
3.8	Crystallographic data collection and refinement statistics for $PqsR^{LBD}$ in complex with 488	133
4.1	Commercial libraries used for fragment screening	152
4.2	Highest scoring fragments identified from Enamine library virtual screening	153
4.3	Summary of biophysical characterisation of PqsR binding to fragments	175
5.1	SERp clusters identified for mutation to less entropic residues	177
5.2	Loop mutants determined using RosettaDesign	180
5.3	interface analysis of full length LTTRs from the PDB	182
5.4	$PqsR^{LBD}$ construct variants	183
5.5	Breakdown of precipitants giving hits for DR mutant	195
5.6	Data collection and refinement statistics for K154A K214Y	205
5.7	Data collection and refinement statistics for $^{94}PqsR^{309}$ DR	207
5.8	Summary of new crystallisation constructs	219
6.1	Data collection statistics for 1BKR-PqsR crystal diffracted on i24	269

7.1 Docking poses of ZN8751275 in the PqsA active site 291

Abbreviations

2-AA	2-aminoacetophenone
Å	Angstrom
ADME	Absorption, distribution, metabolism, and excretion
AHL	N-acyl homoserine lactones
AIPs	Autoinducing peptides
AMR	Antimicrobial resistance
APS	Ammonium persulfate
AQ	Alkyl quinolones
ASU	Asymmetric unit
AUC	Area under curve
AWARE	Access, Watch or Reserve (Antibiotics)
BL2	Biosafety level
bp	base pairs (prefix mega M, kilo K)
CD	Circular dichroism
CF	Cystic fibrosis
CIF	Crystallographic Information File
CIP	Calf-intestinal alkaline phosphatase
CoA	Coenzyme A
CV	Column volume
Da	Dalton (prefix k – kilo)
DLS	Diamond Light source
DMPK	Drug metabolism and pharmacokinetics
DMSO	Dimethyl sulfoxide
DNA	Deoxyribonucleic acid (prefix e and g for extracellular and genomic respectively)
DP	Differential power
DSF	Differential Scanning Fluorimetry
DSSP	Define Secondary Structure of Proteins
EC_{50}	Half maximal effective concentration
ECR	Elastin Congo Red
EMSA	Electrophoretic Mobility Shift assay
ESBL	Extended spectrum beta-lactamase
FBDD	Fragment-based drug discovery
FPLC	Fast protein liquid chromatography
G	Grams (prefix μ – micro & n – nano)
GF	Gel filtration
GST	Glutathione S-transferase
HHQ	2-Heptyl-4-quinolone
HMW	High molecular weight
HSL	Homoserine lactone
HTH	Helix-turn-helix
HTS	High throughput screening
IC_{50}	Half-maximal inhibitory concentration
IMAC	Immobilized metal affinity chromatography
IPTG	Isopropyl β- d-1-thiogalactopyranoside
IQS	integrated quorum sensing signal
ITC	Isothermal titration calorimetry
K_D	Dissociation constant
LBD	Ligand binding domain
LC - MS	Liquid chromatography–mass spectrometry
LE	Ligand efficiency
LLG	Log Likelihood Gain
LTTR	LysR-type transcriptional regulator
MBP	Maltose binding protein
MPD	2-Methyl-2,4-pentanediol
MR	Molecular Replacement
M_r	Molecular weight
MS/MS	Tandem mass spectrometry
MST	Microscale thermophoresis
MWCO	Molecular weight cut-off
NCC	Nottingham compound collection
NCS	Non-crystallographic symmetry
NHQ	2-nonyl-4-hydroxy-quinoline
Ni – NTA	Nickel Nitrilotriacetic acid
NICE	National Institute for Health and Care Excellence
NMR	Nuclear magnetic resonance
OD	Optical density
ORF	Open reading frame
PAGE	Polyacrylamide gel electrophoresis
PAINS	Pan-assay interference compounds
PCR	Polymerase chain reaction
PDB	Protein Data Bank
pI	Isoelectric point
PISA	Proteins, Interfaces, Structures and Assemblies
PQS	Pseudomonas Quinolone signal
QSI	Quorum-sensing inhibitors
QZN	Quinazolinone
Rg	Radius of gyration
RLU	Relative light units
RMSD	Root-mean-square deviation
Rpm	Revolutions per minute
SAR	Structure–activity relationship
SAXS	Small-angle X-ray scattering
SDCD	Synchrotron Radiation Circular Dichroism
SDM	Site directed mutagenesis
SDS	Sodium dodecyl sulfate
SEC	Size-exclusion chromatography
SER	Surface entropy reduction
SNP	Single nucleotide polymorphisms

SOE	Splicing by overlap-extension
SPR	Surface plasmon resonance
TEV	Tobacco Etch Virus
TFZ	Translation Function Z-score
Trx	Thioredoxin
TSA	Thermal shift assay
UV	Ultraviolet
VDW	Van der Waals
WT	Wildtype
ZIP	Zero interaction potency

Amino acid table:

Alanine	Ala	A
Arginine	Arg	R
Asparagine	Asn	N
Aspartate	Asp	D
Cysteine	Cys	C
Glutamate	Glu	E
Glutamine	Gln	Q
Glycine	Gly	G
Histidine	His	H
Isoleucine	Lle	I
Leucine	Leu	L
Lysine	Lys	K
Methionine	Met	M
Phenylalanine	Phe	F
Proline	Pro	P
Serine	Ser	S
Threonine	Thr	T
Tryptophan	Trp	W
Tyrosine	Tyr	Y

Publications

The following publications were produced as part of the work presented in this thesis. Specifically structural data from chapter 3 describing novel antagonist binding.

1. Soukarieh F., Mashabi, A., **Richardson, W.**, Oton E., Romero, M., Roberston, S., Grossman, S., Sou, T., Liu, R., Halliday, N., Kukavica-Ibrulj, I., Levesque, R., Bergstrom, C., Kellam, B., Emsley, J., Heeb, S., Williams, P., Stocks, M., and Cámara, M. (2021) Design and Evaluation of New Quinazolin-4(3H)-one Derived PqsR Antagonists as Quorum Sensing Quenchers in Pseudomonas aeruginosa. ACS Infectious Diseases
2. Grossman, S., Soukarieh, F., **Richardson, W.**, Liu, R., Mashabi, A., Emsley, J., Williams, P., Cámara, M., and Stocks, M. J. (2020) Novel quinazolinone inhibitors of the Pseudomonas aeruginosa quorum sensing transcriptional regulator PqsR. Eur J Med Chem
3. Soukarieh, F., Liu, R., Romero, M., Roberston, S. N., **Richardson, W.**, Lucanto, S., Oton, E. V., Qudus, N. R., Mashabi, A., Grossman, S., Ali, S., Sou, T., Kukavica-Ibrulj, I., Levesque, R. C., Bergstrom, C. A. S., Halliday, N., Mistry, S. N., Emsley, J., Heeb, S., Williams, P., Camara, M., and Stocks, M. J. (2020) Hit Identification of New Potent PqsR Antagonists as Inhibitors of Quorum Sensing in Planktonic and Biofilm Grown Pseudomonas aeruginosa. Front. Chem

1 Introduction

1.1 The problem of antimicrobial resistance (AMR)

Antimicrobial resistance poses a significant global threat to human health with wide reaching implications on other facets of society. AMR is defined as the capability of microorganisms to overcome the effect of antimicrobial treatment including antibiotics used in human healthcare. According to the independent O'Neill report published in 2016 AMR is expected to result in an increased mortality of 10 million lives per year with an expected cumulative cost 100 trillion (USD) by 2050[1]. The current predicament has led many to warn that we are entering a post-antibiotic era[2] with the previous chief Medical Officer for England, Sally Davies, conveying that some infections such as gonorrhoea already show resistance rates of up to 80%. Increasing prevalence of AMR could compromise our ability to manage infection and even complicate treatment of other conditions that require antibiotic prophylaxis[3].

The transition from the so-called "Golden era", a period of antibiotic discovery starting in the late 1920s and peaking in the 1950s with a gradual decline to present day has diminished our capacity to manage infection. Most clinically used agents are derivatives of natural products from filamentous Actinomycetes and other microbial sources. The decline in agent discovery has been attributed to exhaustion in the natural product pipeline. The lack of these 'low hanging fruit' compounds has increased development costs of effective antimicrobials and encouraged large pharmaceutical companies to exit the seemingly unprofitable market[4]. To reduce some associated costs pharmaceutical enterprises, have prioritised derivatisation of current agents. This is often advantageous as the starting compounds possess acceptable pharmacological properties and can be rationally improved. Identification of novel agents poses a greater challenge with a retrospective published by GSK[5] highlighting scientific hurdles including limited to no hit compounds identified in high throughput screening (HTS); difficulties in translating a hit compound into a broadly acting antibiotic and unexpected genomic redundancy thwarting single-enzyme inhibitor development.

Significant research efforts concerning the causes of AMR have been published with overviews clearly underpinning that both anthropogenic and biological factors play significant roles. These can broadly be divided into two classifications: volume of antimicrobial usage and the spread of resistance through contagion[6]. The usage of antibiotics has increased with a 2019 study highlighting a per capita increase of 26.2% in the usage of front-line antibiotics and a 90.9% increase in 'Watch' antibiotics (based on the commonly used AWaRe classification)[7]. Such increases have been ascribed to clinical over-prescription and a lack of historic stewardship[8]. Implementation of more effective stewardship can improve outcomes as demonstrated by a survey of 208 US programmes with 20% reporting a reduction in resistant organisms[9]. More recent studies have focused on the use of non-antibiotic chemical usage and their association with AMR. The compound triclosan, an antimicrobial and antifungal, often added to consumer healthcare products to prevent spoilage has been found to induce inherited multidrug resistance in several clinically relevant bacteria including *Pseudomonas aeruginosa*, *Escherichia coli* and *Staphylococcus aureus*[10 11]. In the case of the latter two urine model experiments showed a 100-fold reduction in ciprofloxacin efficacy[12]. Additionally, high antimicrobial usage in agriculture, with overall quantities exceeding that used in human healthcare, poses a severe risk in increasing AMR[13].

Bioinformatic analysis has allowed for effective AMR surveillance and enabled insight into the prevalence of resistance in a genomic context[14]. This has elucidated the importance of mobile genetic elements such as transposons and plasmids[15]. Furthermore, bioinformatic methods have allowed for thorough classification of resistance mechanisms summarised in Blair (2014)[16]. The interplay between antibiotic usage and resistance can be difficult to accurately determine due to "spill over" effects in which resistant and susceptible bacteria can be transmitted from person-person[17]. Therefore, an individual's risk of acquiring a resistant infection is not limited to their own antibiotic usage. Additionally, such effects emphasise a need for international cooperation regarding antibiotic usage.

Several new strategies have been researched to combat AMR which have not traditionally been applied to combat bacterial infection. An example being monoclonal antibodies binding to specific virulence factors that decorate pathogens such as O-antigen from *P.*

aeruginosa or secreted toxins[18]. Clinical trials have already shown efficacy in patients and may not be as susceptible to resistance compared to small molecule therapies. Virulence has garnered interest on the basis that disarming pathogens applies less selective pressure compared to traditional bactericidal approaches. Many agents have entered clinical trials such as small molecule inhibitors of *S. aureus* sortase that substantially decreases mortality in murine models[19]. However, the attrition rate of anti-virulence agents has yet to be determined but current progress is encouraging. Significant progress into diagnostics has been made with microfluidic technology being able to determine susceptibility without lengthy growth experiments[20]. Other methods including microcalorimetry, Raman spectroscopy and immunochromatography are being examined to provide even more rapid resistance assessment to aid patient treatment[21 22 23]. The social-economic aspect of AMR cannot be easily dismissed and coordinated changes in antimicrobial use in agricultural settings, such as the upcoming 2022 ban on reserve list antimicrobials for veterinary use in the EU, will be required.

1.2 *P. aeruginosa* as a clinical pathogen

P. aeruginosa, a gram-negative facultative anaerobe, is ubiquitous in the environment and can survive in many ecological niches. Broad adaptability such as tolerance to a wide range of temperatures and pHs have been reported[24]. Its ability to survive in very different environments can be attributed to a relatively large genome ~6.5 Mbp encoding a wide array of metabolite biosynthetic genes (5000-6000 ORFS) controlled by a complex regulatory network of around 500 response regulators [25 26]. *P. aeruginosa* is considered an opportunistic pathogen, causing infection in immunocompromised individuals. It is prevalent in hospital settings causing ventilator-associated pneumonia and poses a risk to burn ward patients. Chronic infections of *P. aeruginosa* often occurs in patients such as those with cystic fibrosis (CF). CF is caused by a defect in cystic fibrosis transmembrane conductance regulator resulting in multiple dysfunctions including a greater susceptibility to respiratory infection. Infection rates within cystic fibrosis patients vary from 60-80%[27] and correlate with increased mortality[28]. Risk of mortality is further elevated with co-infection by other pathogens including *S. aureus*[29], *Stenotrophomonas maltophilia*[30] and *Burkholderia cepacia*[31].

The ability of *P. aeruginosa* to survive in water supplies can pose a risk in hospital settings with outbreaks traceable to single outlets. Investigation into multi-drug resistant *P. aeruginosa* outbreaks have revealed that infection reservoirs are often not easily identified[32]. This organism can be transmitted via medical equipment although ventilators are a more frequent source of infection[33]. It's ability to colonise surfaces, especially those of medical equipment, makes sanitation key in controlling outbreaks.

Current NICE guidelines recommend tobramycin inhaled dry powder for treatment of CF *P. aeruginosa* infection – replacing solution inhalation methods that can be uncomfortable for patients[34]. However, this treatment has known side effects including risk of bronchospasm, chest pain and haemoptysis. Additionally, studies have questioned the effectiveness of inhaled treatments for CF patients given loss of lung function causing inherent limitations in drug distribution throughout the bronchial tree[35]. These may tie into observations showing limited clinical improvement with respect to bacterial load[36].

1.2.1 Intrinsic resistance

Multi-drug resistance in *P. aeruginosa* is common and directly worsens clinical outcome and increases the risk of mortality[37]. *P. aeruginosa* is intrinsically resistance to several antibiotics due to poor outer membrane permeability, efflux mechanisms that prevent intracellular antibiotic build up and production of inactivating enzymes such as β-lactamases. Membrane permeability is cited to be 12- to 100-fold poorer compared to *E. coli* [38] and surface porins, that facilitate uptake of small molecules, were found to selectively exclude most antibiotics[39]. Transcriptomic analysis shows that efflux pumps are overexpressed in clinical strains and strong evidence exists that this aids multidrug resistance [40] [41]. This is further reenforced by observations that efflux pump inhibitors can successfully sensitise *P. aeruginosa* to other antibiotics although toxicity prevents usage in clinical settings[42]. Many strains of *P. aeruginosa* contain inactivating enzymes that target hydrolysis liable amide or esters found in lactams and aminoglycosides class antibiotics. For lactam resistance, the inducible *ampC* gene can break lactams down by hydrolysing the amide bond of the β-lactam ring. Growing concern however lies in the increasing prevalence of strains containing Extended spectrum β-lactamases (ESBLs). These are often observed in so-called "high risk clones" that have been observed internationally[43].

1.2.2 Acquired resistance

P. aeruginosa can gain resistance by genetic mutation or by acquiring foreign genetic material. As stated above, efflux pumps can reduce antibiotic efficacy. Several studies have shown that mutations in regulatory proteins cause these systems to become overexpressed. A recent example is a R70Q MexR mutation identified in a clinical isolate from China that gained aztreonam resistance by upregulating MexAB-OprM by 15-fold[44]. Additional AMR genes can be transferred by plasmids, transposons, integrons and prophages. So called "megaplasmids", with sizes ~420 kb, poses a particular concern with the pBT2436 family often containing multiple copies of resistance genes[45].

1.2.3 Virulence factors

To establish and maintain an infection *P. aeruginosa* relies on an extensive arsenal of secreted or surface attached products. These are required for breaking down of host tissue for nutrient acquisition, eluding the host immune response and gathering of scarce resources such as free iron.

1.2.4 Proteases

P. aeruginosa possesses several clinically important proteases required for gathering resources from host cell material. In the CF lung elastase B, alkaline protease, protease IV and PasP have been detected[46]. Early studies into the prominent alkaline protease revealed degradative activity towards human gamma interferon and subsequent loss of function[47]. *In vivo* murine and *in vitro* studies have showed that both pseudolysin and protease IV are highly cytotoxic and prevented cell migration to wound sites thus inhibiting healing[48]. As such it is presumed to function similarly in human burn wounds. *P. aeruginosa* seemingly responds to the infection site with burn wound exudates prompting expression of the elastase LasB[49]. Furthermore, LasB was shown to participate in disruption of host immune factors in epithelial cells via digestion of interleukin (IL)-6 and trappin-2. Adding purified LasB to mice intranasally induced weight lose over time with higher doses significantly increasing mortality[50]. LasB stimulates inflammation through IL-1β proteolytic activation thus aiding destruction of airway structure. IL-1β proteolysis could be abated with

metalloprotease inhibitors and improved mouse pulmonary pathology[51]. Additionally, a LasB inhibitor, that binds to the Zn^{2+} active site, increased survival in *Galleria mellonella* infection models[52]. Less well studied proteases, such as the YceI-like PasP, have also been shown to digest corneal tissue and plays a key role in keratitis[53 54]. However, the activity and regulation of this protease at different infection sites is not well defined. Proteases have also been implicated in aiding cell survival during chronic infection with the intracellular FtsH preventing *in vivo* protein aggregation during growth arrest[55].

1.2.5 Extracellular products

P. aeruginosa secretes extracellular products that aids virulence. The best characterised product, pyocyanin (Figure 1.1), a tricyclic phenazine with zwitterionic properties is secreted into the medium with concentrations of up to 8.1 µM detected in wounds and significantly more observed in CF sputum (130 µM)[56]. Pyocyanin is synthesised by two identical *phzABCDEFG* (phz1 and phz2) operons which are under the control of all three quorum sensing systems[57]. A recent study into *P. aeruginosa* induced bacteraemia showed a strong correlation between high pyocyanin production and septic shock[58]. Evidence is weighted towards an oxidative stress response being responsible for host cell disruption such as stimulating the Erk/p38MAPK senescence pathway and depleting intracellular glutathione concentrations[59 60].

To enable iron acquisition under iron depleted conditions, *P. aeruginosa* releases siderophores, such as pyoverdine, to sequester low concentration iron. Pyoverdines display large structural differences but retain three key characteristics: a dihydroxyquinoline core (shown in black Figure 1.1), an amino acid chain often cyclised and ketoacid side chain. Isolation of 70 clinical strains showed a strong correlation between pyoverdine production and virulence (in *Caenorhabditis elegans* infection model). Furthermore, a deletion in *pvdF*, required for pyoverdine biosynthesis, increased survivability in murine challenge models[61]. Iron concentrations are elevated in CF patient sputum and is well correlated with *P. aeruginosa* infection underlining its importance[62].

Another key secreted molecule, rhamnolipids, a class of glycolipids, that act as surfactants aid surface motility with recent studies showing irregular swimming patterns in biosynthetic

mutants[63]. *In vitro* airway models show rhamnolipids to be important to early stage colonisation of the epithelium with exposure decreasing transepithelial resistance and disrupting epithelial cell polarity[64]. Interestingly, this model showed that protease background had little effect on early infection establishment highlighting the importance of virulence coordination. Furthermore, these lipids appear to confer protection from polymorphonuclear leukocytes with *in vivo* models showing rhamnolipid biosynthetic mutants to be more susceptible to clearance [65]. As such rhamnolipids appear to have a multifactored role in virulence as they both disable host cell defences and assisting in early colonisation.

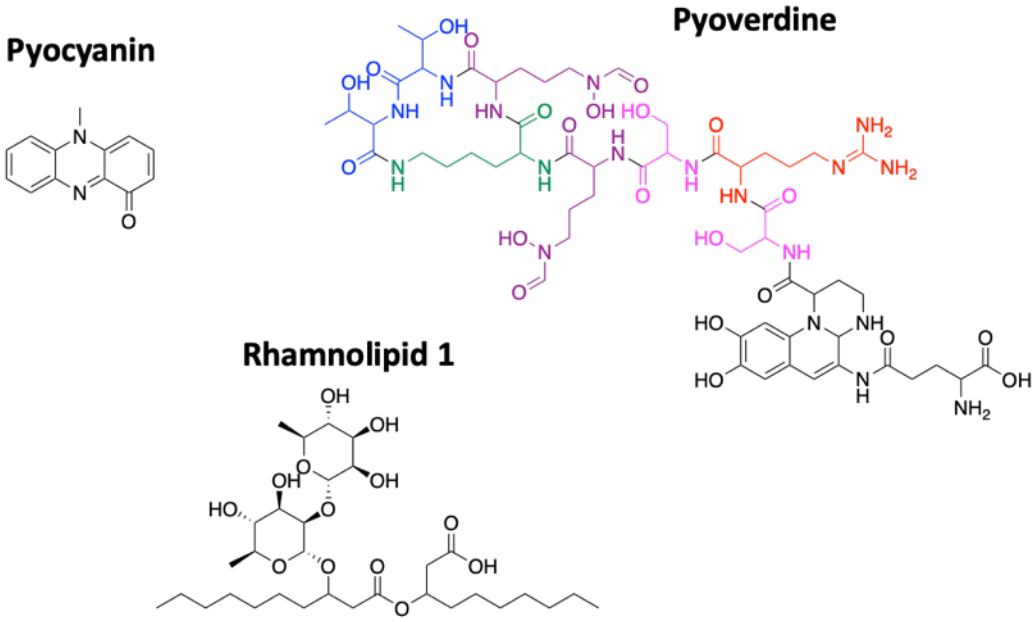

Figure 1.1. Molecular structures of non-proteinaceous extracellular products. Amino acids coloured in Pyoverdine structure.

1.2.6 Biofilms

Bacterial aggregation is a common occurrence in nature with cells associating to form biofilms supported by secreted polymers. Formation of a biofilm is typically prompted in response to a sudden change in growth conditions including temperature and resource accessibility. A transition to this lifestyle confers a significant change in gene regulation with transcriptomic analysis showing that 19.4% of genes in PAO1 being differentially expressed compared to a planktonic control[66]. Changes in gene expression were also observed at different stages of biofilm maturation showing the effect of a sophisticated genetic program. In brief, biofilm maturation is divided into 5 stages. The first stage, initial adhesion,

is characterised by bacterial surface association. Afterwards, in early attachment cells lose motility and begin producing an extracellular matrix. Microcolonies are characteristic of the third stage where the bacteria continue development of extracellular architecture to aid cell association. As these microcolonies grow they form “mushroom” shaped mature biofilms (stage 4) that due to internal cell lysis erupt, releasing sessile cells back into the extracellular environment that seed other biofilms[67].

Extracellular components of a *P. aeruginosa* biofilm are comprised of many classes of biological macromolecule including, polysaccharides, extracellular DNA (eDNA), proteinaceous and lipidic material[68]. The best studied component eDNA, released within membrane vesicles and subsequent autolysis, adopts a markedly different folding to chromosomal DNA and confers viscoelastic properties aiding in biofilm stability[69 70]. CF infections evolve over time with divergent lineages stemming from the original infection strain/s. To gain a competitive advantage in complex bacterial populations, *P. aeruginosa* use pyocins, proteinaceous structures derived from ancestral prophages, to selectively kill competitors[71].

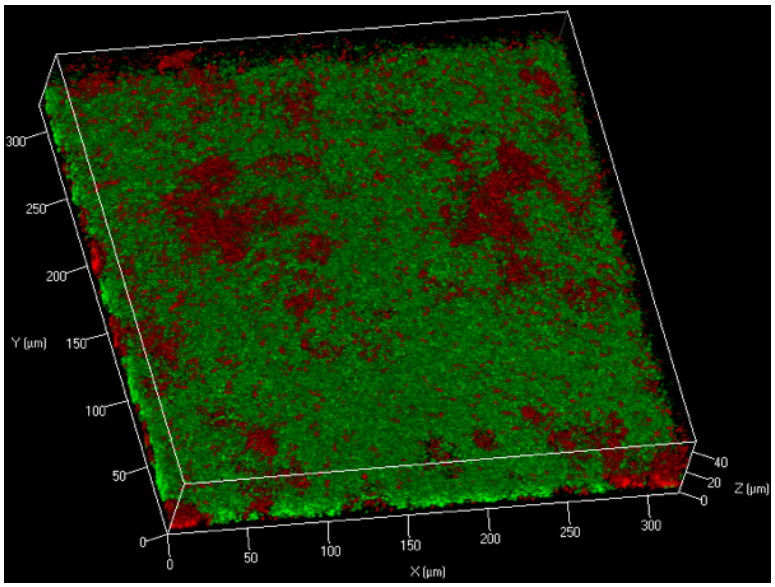

Figure 1.2. *P. aeruginosa* biofilm. 3D image of mature biofilm from strain PA14 produced by Francis Smith of the Centre for Biomolecular Sciences with green-red live dead staining.

Clinically biofilms represent a barrier to treatment with increased resistance to antibiotics compared to planktonic cells. Comparisons in clinical strains show that established biofilms can be more than 60-fold more resistant to antibiotics[72]. This increased resistance has been attributed to decreased antimicrobial penetration and prevalence of inactivating enzymes. Additionally, biofilms often harbour persister cells, baring a dormant phenotype, that display increased resistance. These cells appear only during lengthy infection and can be triggered by varying mutations[73]. The tendency to form biofilms is also well correlated with increased cytotoxicity and other virulence factors described above[74].

1.3 Quorum sensing

Quorum sensing (QS) refers to the process of microbial cell-to-cell communication mediated by small molecule diffusible signals. These signals drive coordinated behavioural changes in a population-dependent manner. Many behaviours controlled by QS have been observed and include bioluminescence, virulence factor biosynthesis and release, secondary metabolite production, DNA uptake and biofilm development. Studies have shown QS to be prevalent in several kingdoms including fungi, bacteria and even plants can be responsive to QS signals[75 76]. The first QS signalling-driven activity was first examined in the 1980s in *Vibrio fischeri*, and in particular in its ability to produce bioluminescence when reaching high population densities. Although significant progress on QS was made in the 1990s with the advent of DNA sequencing techniques enabling the discovery of QS synthase-receptor pairs[77]. These pairs, described for the *V. fischeri* bioluminescence regulatory QS switch *luxR-luxI*, had a distinct structure and many homologues of these have been found across a wide range of Gram-negative bacteria. The LuxI- homologues are responsible for the synthesis of N-acylated homoserine lactone (AHL) QS molecules that bind a specific LuxR-type protein which in turn activates/represses multiple promoters leading to a coordinated behavioural control. These systems are universal in both Gram-positive and negative bacteria and have been well characterised[78 79]. Indeed, a wide variety of AHLs have been identified in different Gram-negative bacteria that differ in acyl chain length and possess structural variation at the third carbon that can have an additional carbonyl or hydroxyl group (shown by R-group in Figure 1.3)[80]. Further research showed that these signals were not limited to AHLs but could also include small peptides as seen in Gram-positive bacteria and referred to as Autoinducing Polypeptides (AIPs). Unlike AHL signals these are produced as a gene product

– producing a precursor peptide – that is subsequently cleaved and modified prior to export into the extracellular environment [81] [82]. These peptides can be exported as linear peptides or cyclised by at the C-terminal to a serine or cysteine residue[83]. A third signal identified in both gram negative and positive bacteria is the boron based Autoinducer-2 (AI-2) molecule that has been shown to bind to chemoreceptors PctA and TlpQ in *P. aeruginosa* although the true functionality of AI-2 as a true QS molecule other than in *Vibrio spp* has been questioned[84] [85] .

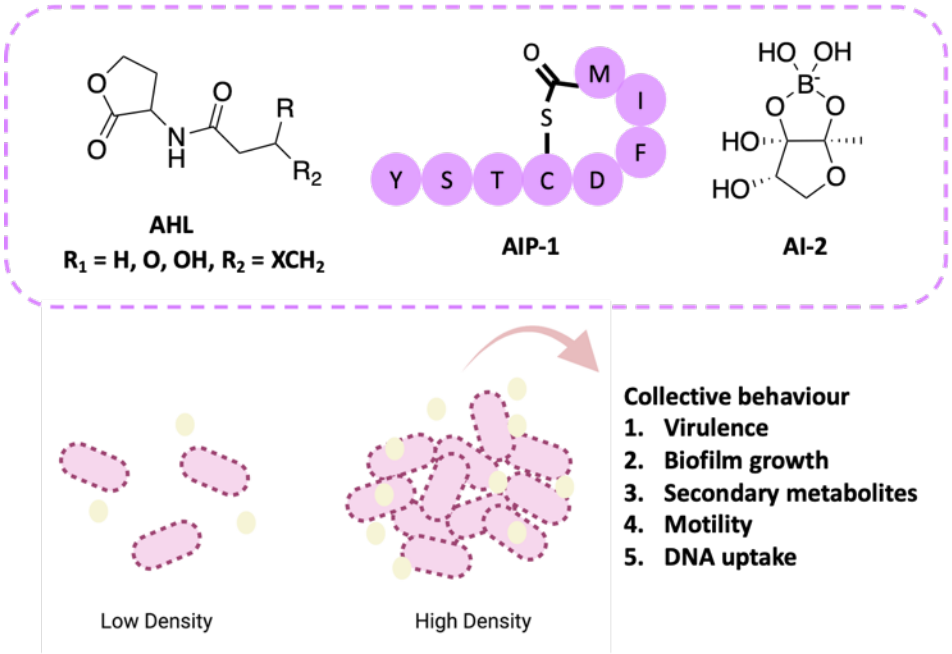

Figure 1.3. Types of QS molecule & concept of group dependent signalling. Quorum sensing signals found in bacteria. The N-acylated homoserine lactone produced and detected by luxI-LuxR synthase-receptor pairs. AIP-1 produced by *S. aureus* as a gene product from agrD and cyclised by AgrB prior to export. AI-2 signal produced by *Vibrio spp*. influenced by environmental concentrations of boron. At low cell density a proportionally low concentration of signal is present but increases with bacterial population to activate collective behaviours.

1.3.1 Quorum sensing in *P. aeruginosa*

P. aeruginosa quorum sensing has been studied since the 1990s with bioinformatic analysis identifying LasR, possessing high similarity to LuxR, and its associated protease LasB[86]. The structure of the inducer molecule was determined as *N*-(3-oxododecanoyl)-homoserine lactone (3OC12–HSL) by NMR upon purification from bacterial culture supernatant[87]. Afterwards a smaller AHL C4–HSL was discovered but was shown to not activate LasR[88]. Experiments on the regulation of rhamnolipid biosynthesis showed that it was activated by

C4–HSL upon binding to its cognate receptor RhlR. The third QS signal, PQS, was identified in 1999 when induction of lasB was observed in the absence of LasR[89]. The molecule responsible for this induction was identified as the Pseudomonas Quinolone Signal (PQS) or 2-heptyl-3-hydroxy-4-quinolone, originally studied as an antimicrobial with subsequent research showing it to activate the LysR-type regulatory protein MvfR (PqsR hereafter)[90]. A fourth signal was identified by transposon screening of a *lasR* mutant, based on the rationale that *lasR* is often inactivated in clinical isolates, that found that transposons in the *ambB* gene limited pyocyanin production. Purification of culture supernatant from a knockout and overexpressed amb pathway showed accumulation of IQS which was found to respond to phosphate concentration [91]. However, the inclusion of the molecule as a QS signal has been disputed as other studies show the amb pathway to only produce the secondary metabolite L-2-amino-4-methoxy-trans-3-butenoic acid (AMB) and attribute IQS as originating from pyochelin breakdown[92]. Recent experiments on *P. aeruginosa* highlight other environment factors are integrated into quorum sensing responses. Light intensity has been shown to control the KinB–AlgB two component system that antagonises RhlR activity [93].

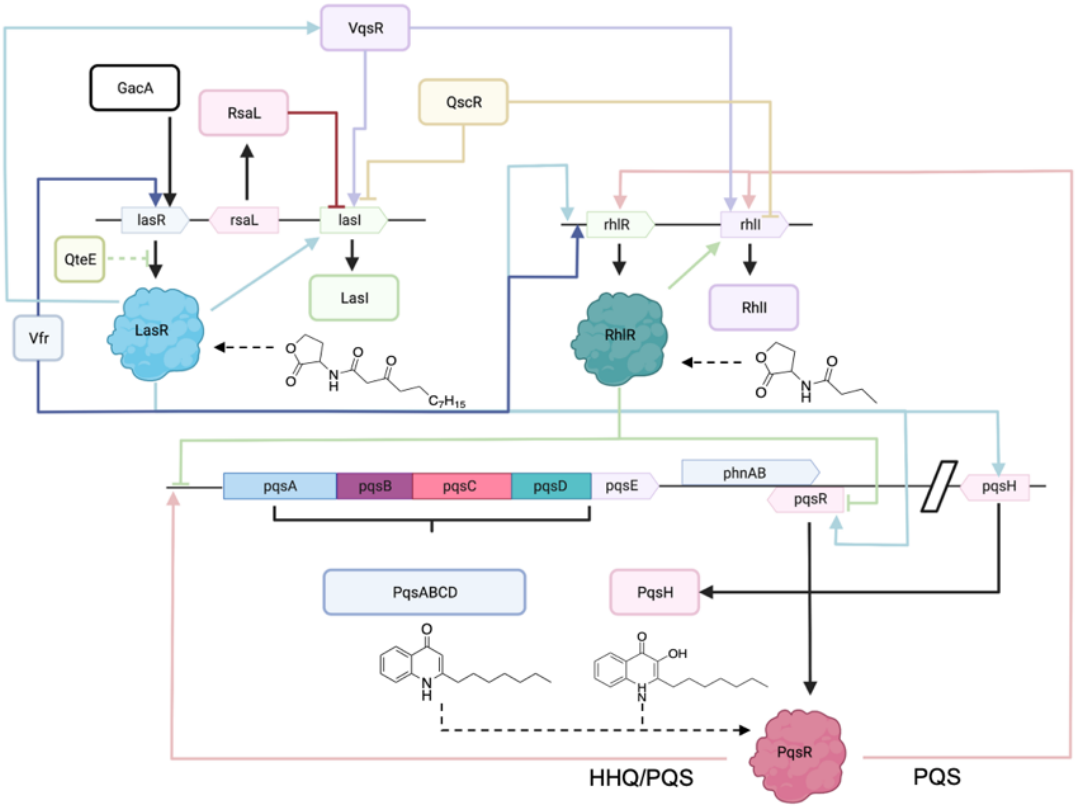

Figure 1.4. QS regulatory hierarchy *P. aeruginosa*. Positive and negative regulation shown by coloured arrows from their associated regulator. The three established *P. aeruginosa* QS signals 3OC12–HSL, C4–HSL and PQS shown next to their cognate receptor and synthase/cluster.

1.3.2 QS hierarchy in *P. aeruginosa*

The interplay between *P. aeruginosa* QS systems is highly complex to permit effective collective behaviour (Figure 1.4). The PQS system is activated by PqsR in response to either HHQ or PQS but activation of virulence promoters and *rhlR/I* are exclusively controlled by the latter signal[94]. This permits negative autoregulation as RhlR represses *pqsR*. LasR also exerts influences over the PQS system by activating both *pqsR* and *pqsH*. Both AHL systems receptors, LasR and RhlR, activate their cognate synthase creating a positive feedback loop to control regulation. Interestingly, LasR has hierarchical control over the rhl system by activating expression of *rhlR* thus promoting activation of *rhlI* by the aforementioned feedback. Furthermore, both *lasR* and *rhlR* are controlled by other virulence regulators such as Vfr, a small 24 kDa regulator that controls exotoxin production[95]. VqsR was also shown to control AHL production by activating both *lasI* and *rhlI* and is expressed in the presence of human serum and oxidative stress[96]. Additionally, another positive feedback loop is

established by LasR which activates VqsR which in turn enhances lasI expression. Conversely these synthases are both repressed by QscR, a LuxR transcriptional regulator, that when mutated causes premature AHL production[97]. Regulation is also observed at the protein level with QteE reducing LasR stability without influencing transcription or translation[98].

1.3.3 Las quorum sensing

The las system consisting of LasR and its cognate ligand 3OC12–HSL synthesised by LasI is important for virulence, with transcriptomic analysis showing that LasR controls at least 35 promoters which drive the expression of 74 genes including those that encode the secreted virulence factors AprF and LasB[99]. LasI/R control extends to several metabolism regulators including the RpoN sigma factor[100]. A lasR knockout in a murine burn infection model shows reduced lethality and less dissemination throughout the body[101]. Investigations into LasR revealed a necessity for 3OC12–HSL to be present for the expression of active and soluble protein[102] and subsequent structural biology efforts have only elucidated bound proteins with 23 PDB structures as of time of writing. Structural determination of the ligand binding domain of LasR showed an α-β-α sandwich comprised of 3 periphery helices on either side of a 5 stranded antiparallel β-sheet[103]. The binding pocket creates 5 direct hydrogen bonds with 3OC12-HSL (Figure 1.5a) and ITC measured binding affinity at 1.14 ± 0.2 μM[104]. The protein was found to bind irreversible to 3OC12–HSL and both *in vitro* and *in vivo* experimentation determined the protein to be active only as a dimer [102 105]. Unlike other LuxR type regulators promoter specificity was surprisingly broad and dyad symmetry was not required for binding, but transcriptomic analysis shows a distinct preference for a Las-box sequence (5' – ACCTGCCAGATCTGGCAGGT – 3').

1.3.4 Rhl system

The Rhl system consisting of RhlR and its cognate C4-HSL ligand (synthesised by RhlI) was initially discovered to control rhamnolipid biosynthesis[106]. The receptor protein was shown to bind to the las-box sequence in the presence and absence of its cognate ligand in difference conformations enabling differential regulation subject to the presence of signal[107]. Isolation of *P. aeruginosa* clinical strains from CF patients often show loss-of-function mutations in LasR. However, such strains including E90 still possess functional rhl

systems that act as primary drivers of cytotoxicity in lung epithelium models[108]. Furthermore, a separate study showed RhlR to possess a key role in suppressing the immune response in *Drosophila melanogaster*[109]. Thus far no structural data has been attained for RhlR with several studies reporting considerable insolubility even in the presence of the cognate C4-HSL ligand. However, some structural features can be inferred by the *E. coli* homolog SdiA that shares a high degree of similarity in the DNA binding domain (Figure 1.5b). Two papers have reported solutions including altering the binding pocket through rationale mutation[110] or optimising the expression and extraction with the latter reporting a binding affinity of 1.66 ± 0.4 μM to C4-HSL. Transposon screening in a rhlI mutant showed *pqsE* to be required for full RhlR activity and was initially hypothesised to comprise an uncharacterised QS synthase–receptor pair[111]. Further research showed PqsE to be a required effector for RhlR activity across a range of virulence promoters. A *pqsE* mutant could only be compensated for by overexpressing RhlR and not with greater concentration of C4-HSL[112]. This mechanism was further clarified in efforts to find a PqsE inhibitor. Unexpectedly, structurally characterised inhibitors that bound to the active site did not affect RhlR activity. Subsequent experiments showed that RhlR could be pulled out of *E. coli* lysates using PqsE as bait with binding abated by mutagenesis of residues distally located from the active site[113].

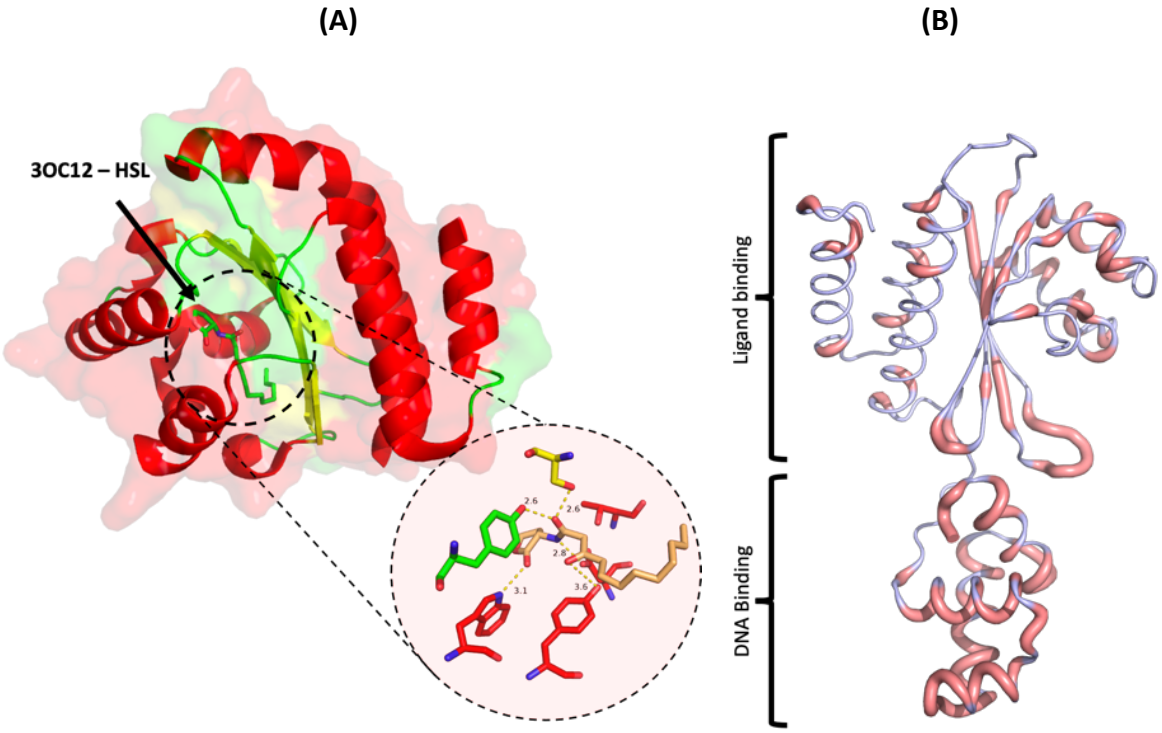

Figure 1.5. Quorum sensing receptors LasR (PDB 2UV0) and homology model of RhlR. (A) Cartoon representation of LasR with cutout showing ligand binding. Residues represented as sticks and coloured according to secondary structure element. 3OC12–HSL shown in orange. **(B)** Homology model produced with I-TASSER with template model SdiA. Areas of high conservation to SdiA shown with red tubes.

1.4 Alkyl quinolone properties and function

Naturally produced quinolones represent a structurally diverse group of molecules; early studies using electrospray ionization and LC-MS identified the production of 56 AQs from *P. aeruginosa* strain PA14 – the most common are summarised in Figure 1.6[114]. These AQs typically possess low solubility in aqueous environments with PQS soluble to ~5 µM (logP of 3.952)[115] and have a surprising number of roles in pathogenicity.

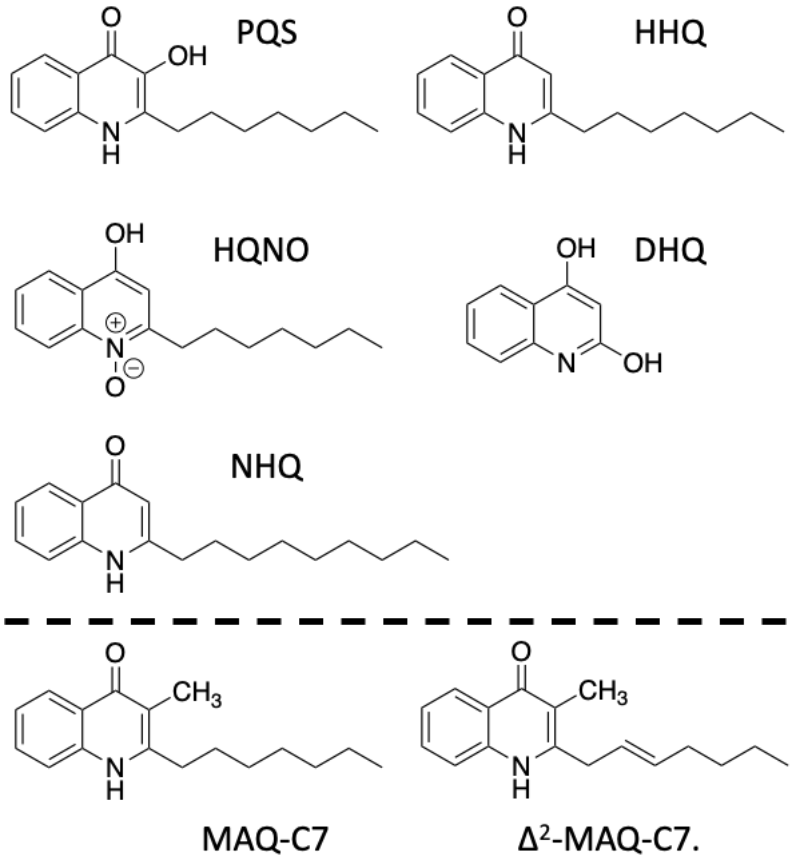

Figure 1.6. The most common AQ products found in *P. aeruginosa* and *Burkholderia sp*.. Burkholderia specific molecules are separated by a dashed line.

1.4.1 AQ biosynthesis

The pathway required for AQ synthesis was identified through transposon screening for deficient mutants[116]. Mutations in the pqs operon resulted in a lack of AQ production as well as impaired pyocyanin biosynthesis. The feed metabolite, anthranilic acid, is primarily synthesised by PhnAB although more recent studies have shown that tryptophan degradation via the kynurenine pathway can influence AQ production[117].

Anthranilic acid is activated by a two step process of adenylation and thioesterification by PqsA to form anthraniloyl – CoA. The activated thioester is transferred to the active site of PqsD which catalyses a reaction with malonyl – CoA to produce 2-aminobenzoylacetyl-CoA. The coenzyme is removed via thioesterase activity of PqsE to form 2-aminobenzoylacetate (2-ABA). Interestingly, the enzyme activity of PqsE is not required for AQ synthesis as the acyl-CoA thioesterase II TesB is able to catalyse the reaction due to promiscuous activity.

The quinolone bicyclic is formed through condensation of 2-ABA with octanoyl-CoA. The resultant molecule, HHQ, requires hydroxylation to form PQS and this reaction is catalysed by the NADH dependent PqsH. The PQS pathway has been shown to produce several additional products that influence virulence. DHQ (2,4-dihydroxyquinoline), a non-alkylated quinoline, shown to bind to PqsR in lysate driven EMSA experiments, is produced by product termination of PqsD[118]. Another derivative product HQNO (2-heptyl-4-hydroxyquinoline *N*-oxide) is formed by the FAD-dependent monooxygenase PqsL (located distally from the pqs operon) that hydroxylates the primary amine in 2-aminobenzoylacetate (2-ABA) to form the unstable 2-hydroxylaminobenzoylacetate (2-HABA)[119]. This product is accepted as a preferred substrate to PqsBC but the relatively low cellular concentration of reduced flavin may be responsible for limiting the synthesis route[120]. A non-AQ derivative product is 2-aminoacetophenone (2-AA), produced from decarboxylation of 2-ABA[121]. Higher intracellular concentrations of 2-AA have been linked to bacterial persistence making the PqsBC complex a potentially poor target for drug development as persistence phenotypes are linked to poor antibiotic efficacy[122]. The pathway is visually represented in Figure 1.7.

1.4.2 *Burkholderia* AQ synthesis

The biosynthetic operon that synthesises PQS is not unique to *P. aeruginosa* but is also found in the *Burkholderia* genus under the alternative nomenclature Hmq or Hhq. In addition to possessing homologs of PqsABCDE Burkholderia also possess HmqFG[123]. HmqF is predicted to possess two acyl-CoA dehydrogenase domains and is hypothesised to introduce an unsaturated linkage between C2 and C3 of the alkyl chain. HmqG is predicted to be a methyltransferase with function confirmed by MS/MS analysis of a *hmqG* mutant supernatant showing a lack of 3' methyl group[124]. Unusually, despite having similar operon architecture the regulation of the *hmq*/*hhq* operon is markedly different with no apparent PqsR homolog or LysR-box in the promoter. However, deletion of *hmqA* or G results in an increase in the AHL C8-HSL production suggesting quorum sensing involvement in Burkholderia AQ synthesis[123].

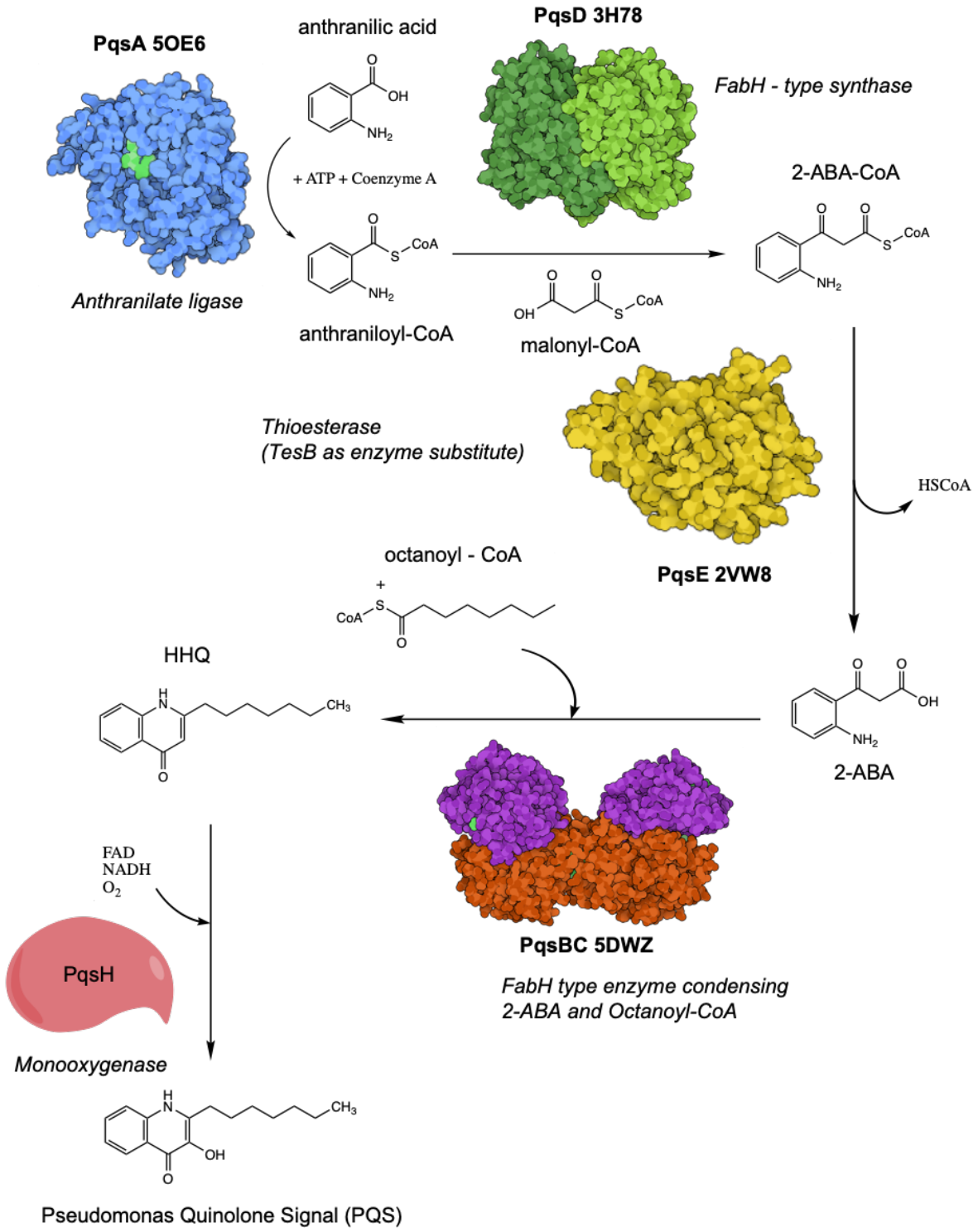

Figure 1.7. PQS Biosynthesis in *P. aeruginosa*. Current model of PQS synthesis with PDBs of relevant enzymes rendered with Illustrate. PDB codes given with each enzyme image. Anthranilic acid is activated by PqsA to form Anthraniloyl-CoA which becomes bound to the PqsD active site catalysing the addition of malonyl-CoA to form 2-ABA-CoA. The co-enzyme is removed by the thioesterase PqsE and the resultant 2-ABA is converted to HHQ by PqsBC using octanoyl-CoA. HHQ is then hydroxylated by PqsH to form PQS.

1.4.3 PQS associated virulence

Research over the last decade has highlighted that the role of PQS in virulence is multifunctional and not exclusive to PqsR mediated virulence regulation. PQS has a distinct role compared to other *P. aeruginosa* AQs in that it has ferric iron chelation properties. PQS has a high affinity for Fe^{3+} and since most PQS is membrane associated, a functionality to trap iron is further justified[125]. Growth studies have highlighted that the addition of PQS-Fe^{3+} to cells unable to produce siderophores improved growth rates suggesting that PQS acts to bypass iron acquisition and may concentrate environmental iron in membranes. Additionally, it has been theorised that the chelation properties of PQS are related to its apparently cytotoxicity[119]. Exogenously supplied PQS during lag phase of *P. aeruginosa* slows growth with additional iron supplementation countering the effect. PQS cytotoxicity has also been attributed to the generation of hydroxyl radicals. PQS addition to *P. aeruginosa* activates genes that control oxidative stress response and prompt autolysis[126]. The role PQS plays in autolysis has been theorised to provide a competitive advantage when growing in communities. Toxicity is not limited to bacterial species with PQS bestowing a lethal phenotype in *C. elegans* infection models and studies using fluorescent probes have shown ROS generation in macrophages (J774A.1 and THP-1 cells) and lung epithelial cells (A549 and NHBE)[127]. The mechanism for free radical generation has been attributed to UV exposure as PQS sensitises *P. aeruginosa* upon UV A treatment but has a significantly lesser impact on a *ΔpqsA* mutant[128]. Previously, it was thought that HQNO was the only *P. aeruginosa* AQ that directly affected cell respiration but recent studies using radical sensitive probes have highlighted that at relatively low concentrations PQS is able to inhibit mitochondrial complex I and has a weaker effect on complex III[129].

Immunomodulatory effects of PQS and HHQ have also been observed in multiple studies using both cell lines and animal models. Work using supernatant extracts of PA14 and its corresponding *ΔpqsA* mutant, unable to make these molecules, highlighted suppressed cytokine release (TNF-α and interleukin-6) by inhibition of NF-KB[130]. Interplay with AQ signals has also been observed in human regulatory systems; through microscale thermophoresis and radioactive ligand displacement experiments human AhR was shown to bind to both HHQ and weakly to PQS. Binding diminished AhR activation *in vivo* and elevated production of IL-8 in A549 alveolar cells.

Early research on PQS from *P. aeruginosa* showed that despite poor solubility supernatants from stationary phase cultures contained relatively large amounts of PQS. Interestingly, PQS has bypassed this limitation by packaging itself into membrane vesicles (MV)[131]. Further experiments with Cryo-transmission electron micrscopy showed that PQS increases membrane curvature required for MV formation. MV formation has gained interest in *P. aeruginosa* pathogenesis as it may account for transport of virulence factors other than PQS[132]. Successful MV release has been correlated with biofilm dispersal and is seemingly unique to PQS as *pqsH* mutants display an MV impaired phenotype[132]. The association of PQS to the bacterial membrane has not been fully elucidated with membrane protein components such as orphan efflux pump protein MexG shown to bind via affinity probes suggesting PQS has a role in efflux control[133].

1.5 LysR Type Transcriptional Regulators (LTTRs)

LysR Type Transcriptional Regulators are a well characterised family of transcriptional regulators found ubiquitously in bacteria with orthologs found in Archaea and Eukaryotes[134]. These response regulators have received much attention in relation to their regulatory role in many processes including metabolism, cell division, quorum sensing and virulence. Unlike some regulatory proteins this family has been shown to exhibit both repression and activation depending on the presence or absence of co-inducer molecules[135]. Several LTTRs operate on auto-regulatory feedback by activating the necessary operon/metabolic path for their co-inducers production[136]. Given their prevalence, with more than 100 structures deposited in the PDB, it is not unsurprising that this family has been the subject of significant studies. Predominantly structural studies have focused on the effector domain of the family due to notorious solubility issues and inherent flexibility of the larger protein. LTTRs slightly vary in size with most being ~300 residues but possessing relatively poor sequence identity[134]. Despite poor conservation LTTRs have remarkably well conserved structural features: an N-Terminal Helix-turn-helix (HTH) DNA binding domain; a long helical hinge region and C-terminal ligand binding domain.

1.5.1 DNA binding domain

LTTRs employ a Helix-turn-helix motif to interact with DNA. The motif, consisting of an open tri-helical bundle, are predominant in all prokaryotic and even more complex eukaryotes[137]. The third helix of the domain typically participates in binding to the DNA major groove whilst helix two rests upon the backbone. Some LTTRs, such as TsaR and BenM possess a so called winged HTH (wHTH) that contains an additional β-strand hairpin that packs against the trihelical bundle[138]. However, the functional implication of the addition is not fully understood in LTTRs.

1.5.2 Ligand/co-inducer binding domain

Starting around residue 90 the coinducer domain is divided into two smaller sub-domains connected by two antiparallel beta sheets which forms a cleft for co-inducer binding. The sub domains named RD-I and RD-II span regions 90 – 165 and 166 – 270 respectively (coloured in Figure 1.8b). The secondary structure elements of the C-terminal correspond to an alternating α helix and β sheet characteristic of a Rossmann fold. Interestingly, the domain itself, although not readily distinguished in the literature, has limited resemblance to class I substrate binding proteins although differs in that the protein subdomains are linked by single a β hairpin[139].

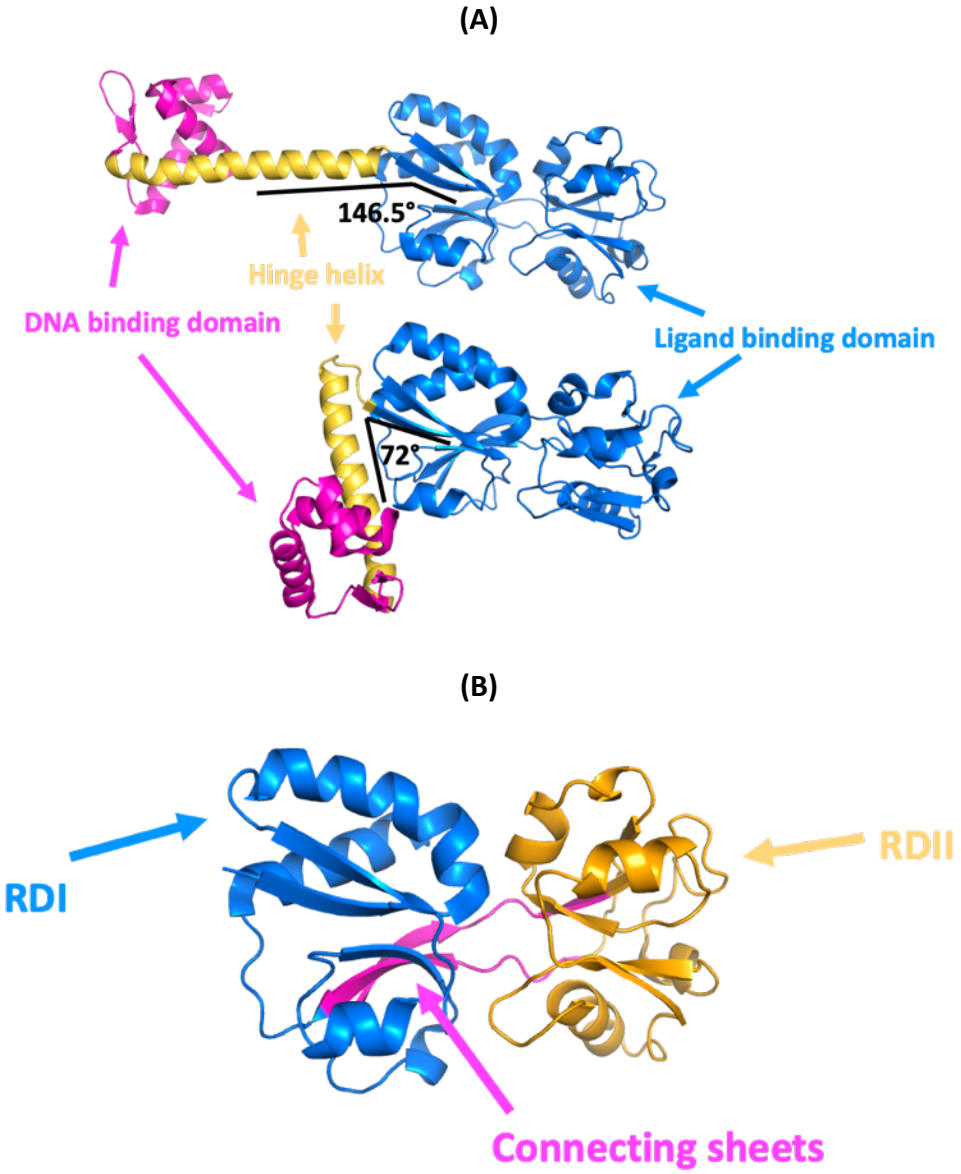

Figure 1.8. Cartoon diagram of LysR-type transcription regulator. (A) TsaR (PDB 3FXQ) showing domain architecture of a LTTR**.** Varying linker helix angle, from the crystallised tetramer, relative to LBD shown. DNA binding domain, linker helix and LBD coloured in pink, yellow and blue respectively. **(B)** Ligand binding domain structure of TsaR (PDB 3N6U) with subdomains RDI and RDII coloured in blue and yellow respectively. Connecting two stranded beta sheet is coloured in pink.

LTTRs have been shown to accept a wide range of ligands required for control over metabolism and biosynthetic clusters. A selection of structurally characterised receptors can be found in Table 1.1.

LTTR	Cognate ligand/s	Function	PDB
BenM	Benzoate & cis,cis-muconate	Regulates activation of *cat* and *ben* genes for benzoate degradation	2F78
CysB	O-acetylserine & N-acetylserine (Sulphide and thiosulphate act as anti-inducers)	Regulation of *cys* genes responsible for sulphate assimilation	4M4G
DntR	2,4-Dinitrotoluene & Salicylate	Activation of the oxidative degradation pathway of DNT	2Y7W
HinK	Histamine & Imidazole-4-acetic acid (ImAA)	Activation of PQS system, pyoverdine and histamine uptake/utilisation in *P. aeruginosa*	6M5F
LeuO	Not-determined	Pleiotropic regulator that functional in Gammaproteobacteria	6GZ0
MetR	Homocysteine	Control of methionine biosynthesis in *E. coli* and *Salmonella typhimurium*	4AB6
OccR	Octopine	Controlling transcription of the Ti plasmid octopine pathway to provide nutrients for plant pathogen *Agrobacterium tumefaciens*	5VVI
PcpR	Pentachlorophenol	Regulation of dechlorination enzymes responsible for PCP degradation in *Sphingobium chlorophenolicum*	4RPN
QuiR	Shikimate	Controls the biosynthesis of protocatechuic acid from quinate and shikimate in *Listeria monocytogenes*	5TED
TsaR	Para-toluensulfonate	Regulation of para-toluenesulfonate (TSA) degradation for carbon and energy acquisition in *Comamonas testosteroni* T-2	3N6U

Table 1.1. LTTRs and their associated ligand/s.

1.5.3 Multimerization

Most receptors have been shown to form tetramers *in vitro* by a multitude of orthogonal methods including analytical centrifugation[140], native PAGE[141] and gel filtration[142] with crystallographic evidence from over 10 full length structures revealing these to be composed of a dimer of dimers. A notable exception to the canonical arrangement is that of CrgA that forms an octamer identified through native mass spectrometry and crystallography. The latter elucidated a novel ring structure (Figure 1.9) that could form a transient duplex in combination with DNA[143].

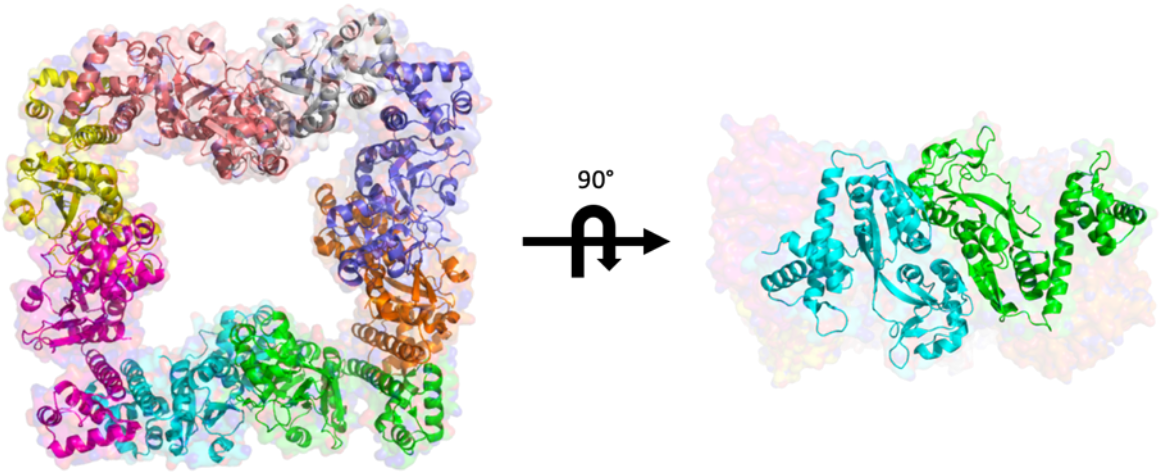

Figure 1.9. CrgA octamer complex. Each chain coloured for easier visualisation and single dimer complex visible upon 90° rotation on the x axis. Protein chains represented as cartoons and transparent surface coloured according to chain. Dimer-dimer interfaces are mostly supported by interactions between the DNA binding domain and linker helices.

The current model for LTTR activation is the "sliding-dimer" hypothesis suggesting that subtle changing in the interface between the dimer pairs confers a change in DNA binding permitting relaxation and RNAP accessibility. This was first hinted by a low-resolution structure of TsaR revealed a markedly different conformation to the other full length receptors. Comparisons of each structure showed varied interaction helices with the TsaR conformation possessing LBDs protruding at the proteins periphery conferring a large cavity between the dimer pairs[138]. This open conformation (Figure 1.10) shifts the DNA binding domains and likely permit changes in DNA binding. Separate structural studies showed other LTTRs such as ArgP and AphB adopted the open conformation even in the absence of

their cognate ligand [144] [145]. In solution SAXS revealed that one receptor, DntR, adopts the open conformation upon binding to salicylate[146]. However, it is currently not known if all LTTRs respond in the same fashion as few receptors have been reported in both states. The mechanism does appear to vary between proteins with crystallisation of the OccR LBD, an octopine binding protein, revealing a dimer subunit pivot of 70° upon binding. When modelled as a full length protein, based upon the homologous BenM, it becomes apparent that the rotation would cause a substantial change in DNA bending[147]. The prevalence of the "rotary switch" mechanism has not been fully elucidated and structural data of the full length would be required to validate this model.

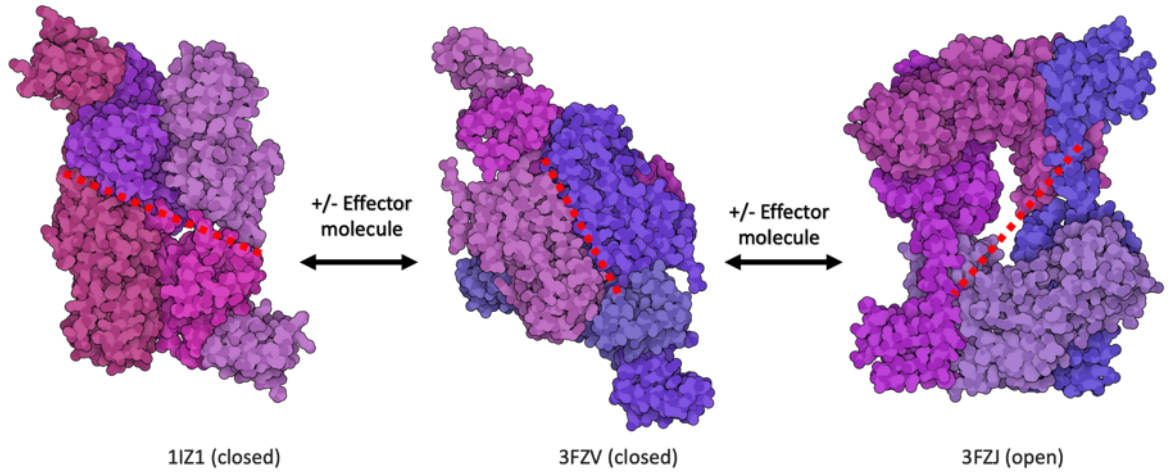

Figure 1.10. Comparison of tetramer structure conformation. Structures of closed conformations 1IZ1 and 3FZV belong to *Cupriavidus necator* CbnR and *P. aeruginosa* TR. Open conformation from *C. testosteroni* TsaR (3FZJ). Images rendered using Illustrate [148]. Interface between dimer pairs marked by a dashed red line. TsaR shows an open cavity between dimer pairs contrasting to the closed, yet distinct, structures of CbnR and TR.

1.6 PqsR – function, structure, and regulation

Implications on virulence were first identified in a transposon insertion pho34B12, containing PqsR, that displayed reduced murine virulence, lacked pyocyanin synthesis and decreased elastase production[149]. Initial characterisation indicated that PqsR had membrane binding properties determined by a GST fusion partitioning in the membrane fraction. However, this observation may be an artifact of the GST fusion[90]. This study also suggested that PqsR was actively exported into the extracellular environment which is uncharacteristic of an LTTR and may have been due to cell lysis rather than export.

PqsR was shown to control production of PQS by upregulating the *pqs* operon and anthranilate production in an autoregulatory fashion. However, transcription of the *pqs* operon was partly controlled by RhlR, inducing a less stable transcript[150]. Microarrays conducted on PA14 and isogenic *pqsR* mutant revealed that outer membrane efflux pumps such as *mexGHI-opmD* were upregulated by PqsR showing a link between PqsR and antibiotic resistance. Other virulence factors including the production of HCN, pyocyanin and lectin were also differentially regulated in the isogenic mutant[151]. ChIPseq showed that PqsR bound to 37 loci in PA14 and had a binding site that could differ from the established LysR-box (5' – TTCGGAGTCCGAA – 3')[152]. This same study found that PqsR regulated both protein secretion systems (T6SS HSI-II and T2SS) and antioxidation genes (DPS, Ahp and Trx).

Through random mutagenesis, the PqsR linker helix mutant I86F was found to confer some ligand independent activity as the presence of a potent antagonist M64 only caused a minor reduction in activity. This study found, through immunoblotting of an *in vivo* crosslinked lysate that PqsR, like most LTTRs, adopted a tetrameric arrangement[153]. It should be noted that the experiment found less intense bands corresponding to trimers, dimers, and monomers but this may be due to incomplete crosslinking. Examining PqsR protein interaction suggested possible binding to QslA, a small regulatory protein (104 residues), however this interaction could only be observed in an *in vivo* assay with PqsR peptide fragments and could not be shown *in vitro* with purified protein[154].

Structural elucidation of the full-length receptor has been inhibited by insolubility of the protein when recombinantly expressed. As such structural elucidation has been limited to the ligand binding domain. Purification of the $PqsR^{LBD}$ showed the protein to have a dimeric arrangement in solution. Determination of the binding domain structure showed a typical LTTR structure with two subdomains (CDI & CDII) connected by an antiparallel β-sheet (Figure 1.11). The binding pocket is divided into two sub-pockets A and B (Figure 1.12). Most LTTRs have a relatively small binding pocket located between CDI and CDII (pocket B), whereas the PqsR pocket extends into CDII (pocket A). Both pockets are lined with hydrophobic residues partially covered by a lid loop. The pocket was shown to be highly sensitive to mutation with replacement of most residues yielding compromised activity[155].

Compared to other LTTRs, PqsR^{LBD} adopts a unique arrangement with hinge helix observed on protein dimer's periphery instead of constituting part of the dimer interface.

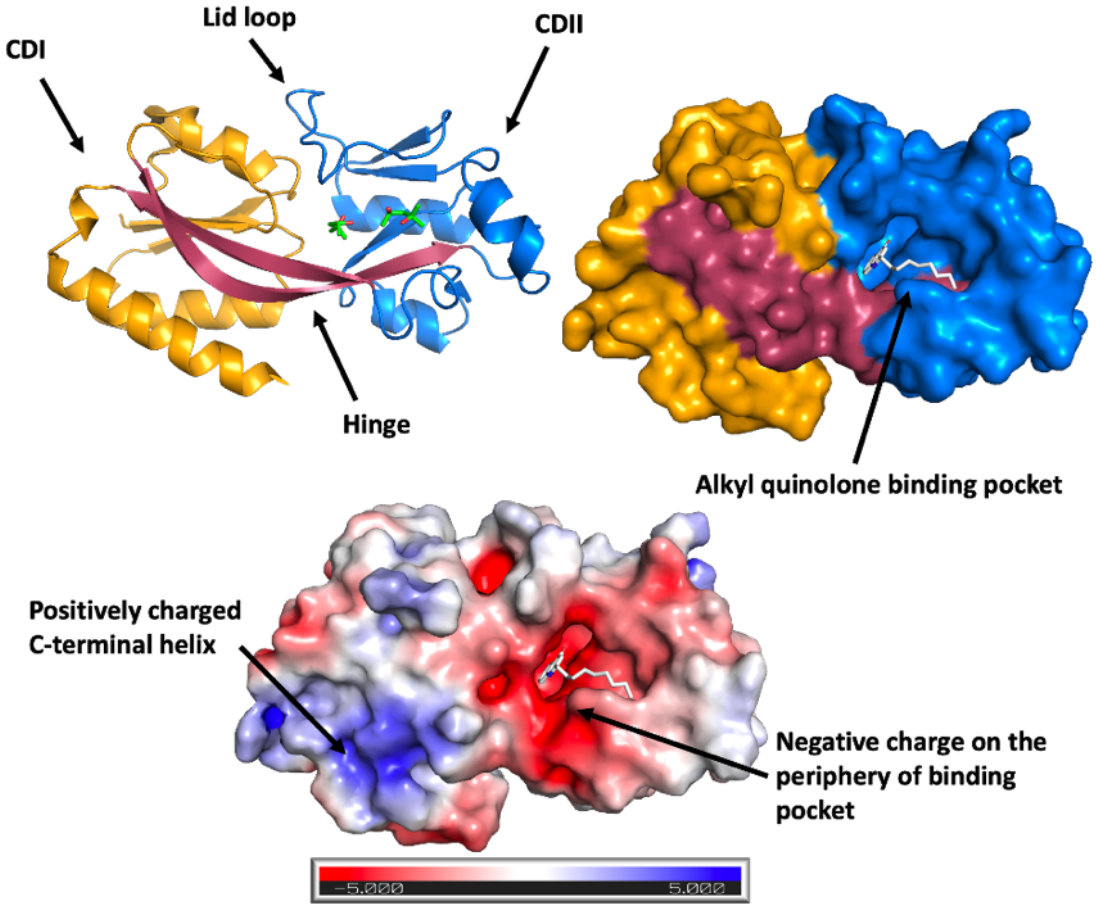

Figure 1.11 Cartoon and surface representation of PqsR structure. Cartoon structure of PqsR with colouring to match the conserved LTTR features. Two subdomains CDI and CDII are coloured in yellow and blue respectively with the yellow domain harbouring the N-terminal linker to the hinge helix and the C-terminal. The hinge between the domains is coloured in raspberry. The lid loop that partially occludes the binding site is marked. Molecular surface shown with NHQ alkyl quinolone ligand shown. The ligand is buried between the CDII domain and hinge β-sheet. Electrostatic surface is also shown that shows that the binding pocket is decorated by negatively charged residues and the C-terminal helix is largely positively charged. The opposite face possesses a weakly charged or neutral surface.

The binding pocket has a calculated volume 858.8 Å^3 (determined by CASTp) and is mostly comprised of hydrophobic residues. The first reported AQ structure of NHQ, a HHQ derivative baring a C9 alkyl chain showed the quinolone head group to occupy pocket B and was supported by interactions from Ile 149, Ala 168, Leu 207 and Thr 265. Subpocket A, which possesses a much larger cavity, accommodates the alkyl chain, and is lined by Ile 236, Val 170, Tyr 258, Leu 189, and Ile 186. Ligand analogues such as QZN have optimised

interactions with the pocket through a halogen bond to Thr 265 and by forming water mediated hydrogen bonds to the backbone.

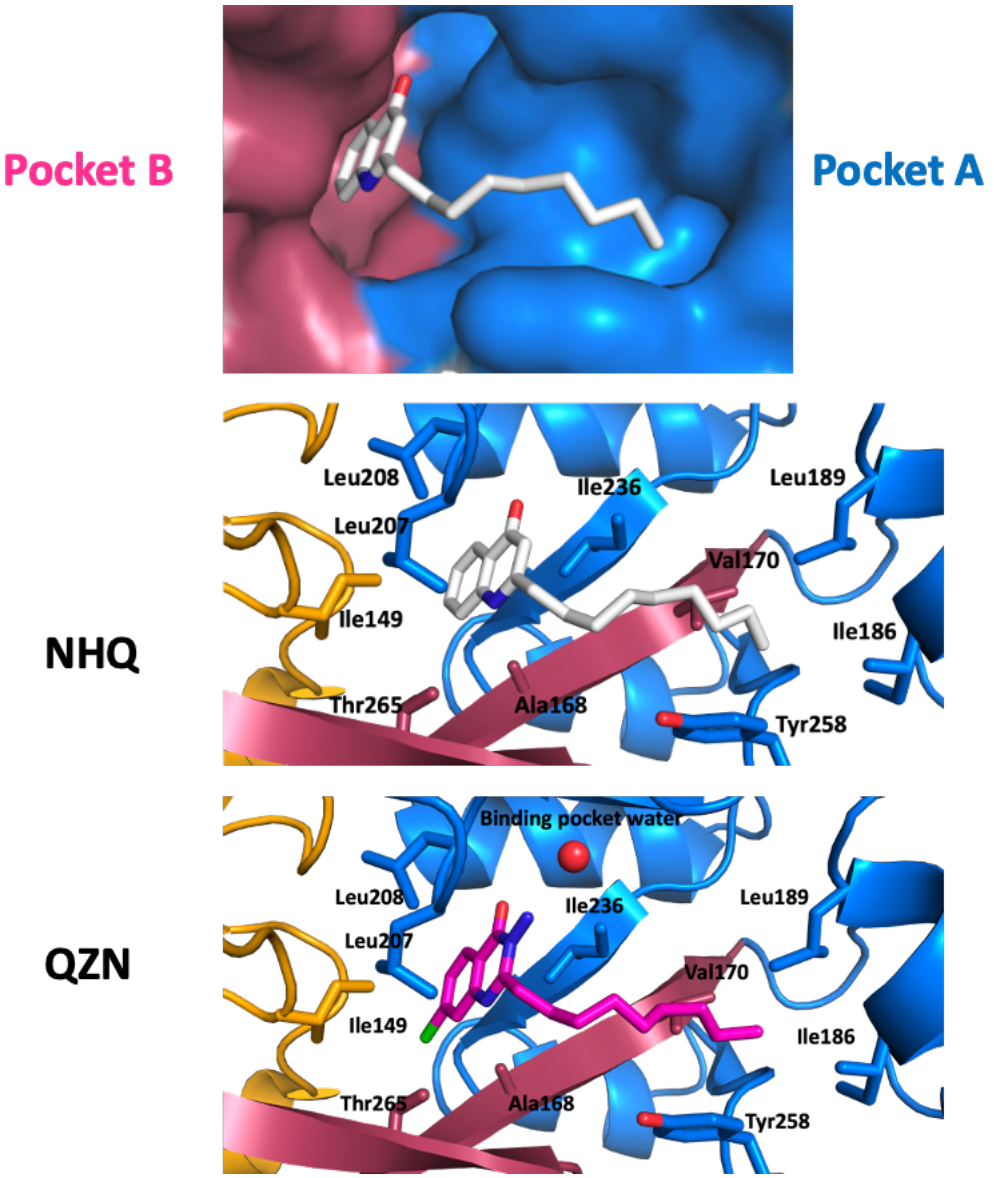

Figure 1.12 Surface and stick model of AQ binding pocket. The binding pocket of PqsR, with NHQ shown as a molecular surface with subpockets A and B coloured blue and red strawberry respectively. Cartoon representations of AQ binding showing residues as sticks from PDBs 4JVI and 4JVD. In both cases the quinolone is positioned in pocket B and the long alkyl chain is accommodated in pocket A.

Early studies in 2006 using a *pqsA-lacZ* transcriptional fusion showed PqsR to respond to multiple AQ ligands with the main activators being both PQS and HHQ[156]. This was further supported by murine burn models showing that PqsH, that converts HHQ to PQS, was dispensable for full pathogenicity whereas *pqsA* and *pqsR* mutants exhibited attenuated virulence. This study also identified a conformation change upon AQ binding when purified

PqsR^{LBD} precipitated upon incubation and this change was well correlated with *pqsA–lacZ* activation. Despite ligand-induced precipitation a FRET study reported that PQS bound to the PqsR^{LBD} (residues 91–242) with a binding affinity of 1.2 ± 0.3 μM and that the interaction between PQS and a dimer was not cooperative[157]. A later studied showed by (STD) NMR that DHQ, lacking an alkyl chain, was capable of binding with an affinity of 450 nM and could induce DNA binding using a lysate containing overexpressed PqsR[118]. This showed that the receptor was promiscuous and could accept a range of AQs.

Regulation of *pqsR* expression was found to be complex with LasR binding upstream of the *pqsR* transcriptional start site to a las/rhl box 5'- CTAACAAAAGACATAG '-3. Mutations in or truncations of the box resulted in compromised pqsR expression showing that LasR activates expression[158]. DNA-affinity chromatography on the intergenic region between *pqsR* and *nadA* showed the binding of another LTTR, CysB[159]. In-frame *cysB* mutants increased pqsR expression and acted as a pqsR repressor. Subsequent EMSA experiments showed that CysB competed with LasR for binding and *in vivo* CysB outcompeted LasR even with 3OC12-HSL supplementation. However, unexpectedly regulation was not affected by availability of cysteine, the CysB co-inducer. Furthermore, *pqsR* expression is partly controlled by the toxin-antitoxin HigAB system. A HigA binding site palindrome is 5'-TTAAC GTTAA-3' is located 382 bp upstream of *pqsR* and was shown to bind *in vitro*[160]. The antitoxin HigB was shown to destabilise the resultant complex and appears to serve to counter HigA *pqsR* repression. HigA is actively degraded by the Lon protease and only becomes abundant in late-stationary phase potentially acting to limit PqsR activity when resources become scarce.

1.7 Quorum sensing inhibition in *P. aeruginosa*

As described previously lack of efficacious antibiotics towards *P. aeruginosa* necessitates further development. As anti-virulence strategies have the noted benefit of not applying strong selective pressure that favour the emergence of resistance mechanisms, they represent an attractive strategy. The discovery that quorum sensing receptors control virulence factors and mutants retain only weak pathogenicity makes them attractive targets for anti-virulence therapeutics[161].

Quorum sensing inhibition (QSI) can be divided into three distinct strategies (Figure 1.11). 1) Disruption of signal synthesis through interference of catalytic enzymes. 2) Degradation or sequestration of the signal after export into the extracellular environment. 3) Prevention of signal binding to receptor by competition.

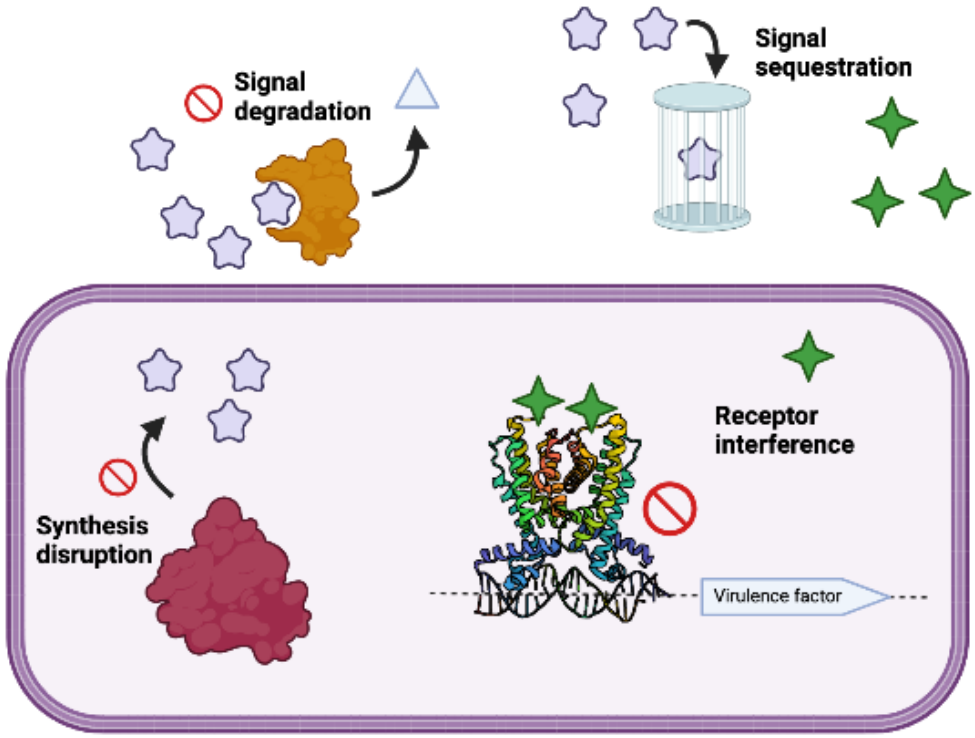

Figure 1.13. QSI strategies. Disruption of QS through multiple strategies in the cellular or extracellular environment. Prevention of signal synthesis by single enzyme or biosynthetic complex inhibition. Signals exported into the extracellular environment can be targeted by degradative enzymes or sequestered into a non-bioavailable form. Signal recognition can be disrupted by a competitive antagonist that prevents virulence factor activation and disrupts autoregulatory mechanisms.

1.7.1 QSI by degradation and sequestration

Signal degradation/sequestration has been described less frequently but examples have been characterised. Enzymes such as AHL-lactonase can hydrolyse *N*-acylhomoserine lactones with difference specificities[162]. These naturally occurring lactonases have often been the subject of enzyme engineering approaches to improve catalytical activity to make these enzymes suitable as therapeutics[163]. Functionally similar enzymes have been characterised for PQS degradation, such as Hod (1H-3-hydroxy-4-oxoquinaldine 2,4-dioxygenase), that catalyse the formation of *N*-octanoylanthranilic acid. However, biofilm growth studies showed that Hod treatment increased biofilm growth in response to loss of

"trapped iron" by PQS[164]. Sequestration strategies have been less explored with only a few characterised materials such as biosurfactants acting to limit diffusibility[165] or cationic polymers that bind QS signals[166].

1.7.2 QSI for AHL receptors

Inhibitors to the LasR and RhlR system have already been described and predominantly consist of ligand analogues. These analogues build on the lactone head group and as such are thought to bind to both AHL receptors. The inhibitor mBTL antagonised both receptors but showed greater efficacy towards RhlR with 43 ± 10% inhibition upon treatment with 1 mM. Virulence traits were also attenuated with an IC_{50} with respect to pyocyanin of 8 µM (±2)[167]. High throughput screening has elucidated other classes of antagonist such as the flavonoids, a natural product, that dual target LasR and RhlR. These could suppress both pyocyanin and swarming motility phenotypes but required relatively higher concentrations >100 µM[168]. The pitfall of relatively poor potency appears frequent with AHL targets with others classes found in HTS such as a benzimidazole series inhibiting LasB activation by 68.23% at 250 µM[169].

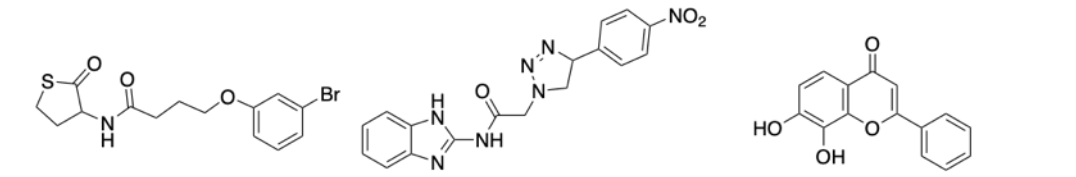

mBTL
IC_{50} 8 µM
(*S*) IC_{50} 4 µM
w.r.t. Pyocyanin inhibition

Benzimidazole – class
68.28% inhibition at 250 µM
67.10% inhibition at 125 µM
63.67% inhibition at 62.5 µM
w.r.t. GFP-LasB reporter

Docking score −8.40 kcal/mol

7,8-dihydroxyflavone
79% LasR
88% RhlR
w.r.t lasB and rhlA activation

Figure 1.14. Inhibitors developed against LasR and RhlR. Antagonists characterised for biological activity in *P. aeruginosa*. For mBTL the IC_{50} is for the racemate and for the S isomer that showed improved potency[167]. The Benzimidazole class was tested at 3 different concentrations and docked using Glide against LasR[169]. The flavonoid was tested for LasR and RhlR antagonism using luciferase bioreporters at 100 µM. At this concentration both mobility impairment and pyocyanin reduction were observed[168].

Despite development in small molecule QSI antagonist targeting of AHL-dependent systems has shown a trend in poor receptor selectivity. Given that many commensals use AHL

dependent systems developing suitable and effective agents that do not disrupt beneficial microbiota will inevitably be challenging. As such the PQS system represents a more attractive target given its occurrence is limited to *Pseudomonas* and *Burkholderia* spp.

1.7.3 Disrupting PQS biosynthesis

Apart from PqsL and PqsH inhibitor development has been carried out on all biosynthetic enzymes in the PQS pathway with several agents shown to give potent activity *in vitro*. Inhibiting PqsE has been rendered difficult due to its thioesterase activity being functionally redundant as the promiscuously acting TseB can fulfil its role[121]. Additionally, the recent discovery that PqsE acts in combination with RhlR via a protein-protein interaction complicates druggability. However, screening a large DNA-encoded small molecule library showed a 2-(phenylcarbamoyl)benzoic acid series could reduce enzyme activity significantly but did not yield a reduction of pyocyanin[170]. Although this was attributed to compound instability it cannot be discounted that the thioesterase redundancy overrides PqsE inhibition. A similar *in vivo* result was observed from a Indazole series of PqsE inhibitors discovered in a large 120 000 compound screen. These compounds bound to the active site iron cluster but failed to inhibit pyocyanin or HCN production[113]. Interestingly complementation experiments using non-catalytic residues mutants that mimicked inhibitor binding could disrupt these phenotypes suggesting a lack of efficacy was due to low permeability.

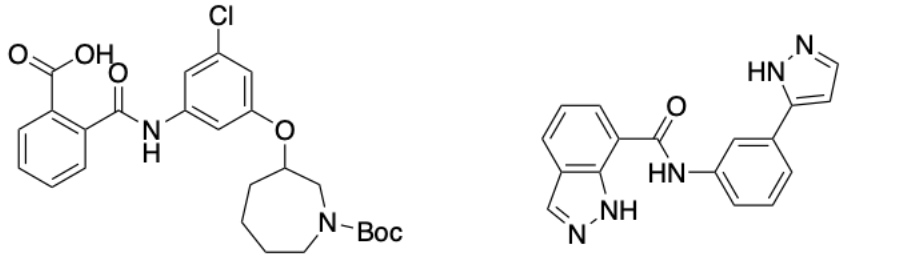

2-(phenylcarbamoyl)benzoic acid series
PqsE IC_{50} 5.6 ± 1 µM
na on pyocyanin

Indazole-class PqsE inhibitor
K_{app} = 175 nM
ΔT_m = 3.4°C

Figure 1.15. Inhibitors developed towards PqsE. Both inhibitor series could reduce PqsE thioesterase activity but failed to reduce virulence traits *in vivo*. Most potent series from each paper shown in the figure. The 2-(phenylcarbamoyl)benzoic acid series displayed a strong IC_{50} *in vitro* towards PqsE but failed to reduced pyocyanin. The indazole series was found to bind in the nanomolar range using fluorescence polarization and induced stabilisation on thermal shift assay but also failed to reduce pyocyanin, hydrogen cyanide production and pyoverdine.

PqsD inhibitor development benefited from insight gathered from FabH (β-ketoacyl-ACP synthase) that possessed structural similarity. Several of these inhibitors were anthranilic acid derivatives and were shown by SPR and enzyme assays to also bind PqsD. The most potent 2-benzamidobenzoic (Figure 1.16) possessed an K_D of 5.2 μM and inhibited enzyme activity dose dependently with an IC_{50} of 3 ± 0.7 μM[171]. A similar approach was adopted for a 5-aryl-ureidothiophene-2-carboxylic acid series, that was originally designated as a weak RNAP inhibitor[172]. The series was optimised to confer greater selectively and could be modified with an electrophilic warhead to attack Cys 112. However, despite strong *in vitro* potency none of the inhibitors from this series displayed activity against *P. aeruginosa* HHQ production[173]. Furthermore, "me-too" design strategies that identify chemically similar compounds have been employed. This entailed screening substrates of *Alfalfa* chalcone synthase, that also possessed a similar active site and therefore would accommodate ligands with similar properties. This revealed that Catechol based substrates could act as micromolar inhibitors towards purified PqsD and reduced HHQ production *in vivo*[174].

The breakdown product of 2-ABA, 2-aminoacetophenone (2-AA) was first identified as a PqsBC competitive inhibitor with a K_i of 54.5 μM[175]. However, *in vivo* this compound stimulates antibiotic tolerance by reducing ribosomal protein gene expression. Furthermore, treatment of 2-AA can induce a persistence phenotype in clinical pathogens *A. baumannii* and *B. thailandensis*[122]. Other PqsBC inhibitors, which were discovered by re-assessing 2-AA output from a library of PqsR antagonists, could reduce virulence and increase lung cell survival[176]. However, as expected these inhibitors were later found to induce persistence to meropenem due to increased 2-AA production[177]. Increased DHQ production was also observed with treatment which can act as a PqsR agonist. Given 2-AA production is an inevitable consequence of PqsBC inhibition the enzyme complex is unlikely to be useful target.

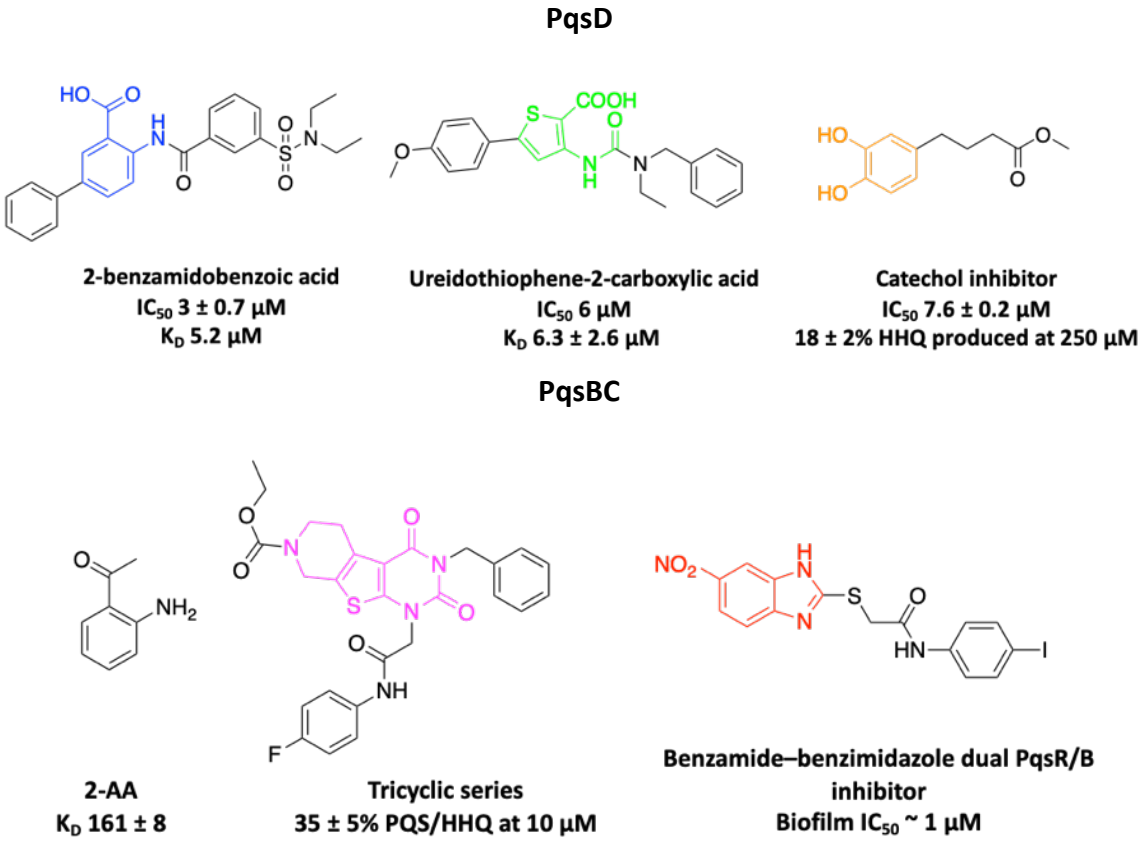

Figure 1.16 Inhibitors developed towards PqsBC and PqsD. Key function group coloured for easy visualisation. Anthranilic acid shown in blue, thiophene-2-carboxylic acid in green, catechol in orange, benzamide-benzimidazole in red and tricyclic core in pink. 2-benzamidobenzoic acid and ureidothiophene-2-carboxylic tested *in vitro* on purified PqsD with binding affinity determined with ITC[171 172]. Catechol was tested on purified PqsD and tested for HHQ reduction in PA14 *ΔpqsH*[174]. 2-AA was tested on the PqsBC complex using a spectrofluorimetric assay to determine affinity[175]. The tricylic series and benzamide-benzimidazole were tested for reduction in HHQ/PQS and biofilm formation respectively in PA14[178].

1.7.4 PqsR antagonism

Antagonists towards PqsR were first observed by examining the extracellular products produced by competing organisms such as *Candida albicans.* Farnesol, a sesquiterpene, was found to directly bind to PqsR and diminished *P. aeruginosa* virulence production. However, oils represent a significant challenge for medicinal chemistry optimisation. Additionally, further studies showed that the oil inhibited bacterial growth making it undesirable as an anti-virulence agent[179]. Other natural products such as vanillin have also been reported as PqsR antagonists but require very high concentrations to decrease virulence (>1 mM). Molecular evidence for binding is also limited with vanillin and other reported natural products[180 181].

Quinolone and quinazolinone scaffolds have proven effective antagonists, likely to due to shape complementarity with the binding pocket. Initial development focuses on ligand analogues of HHQ and PQS (shown in Table 1.2). Initial SAR conducted on HHQ examined the addition of electron withdrawing and donating groups to the benzene moiety and sought to ascertain the importance of alkyl chain length. This revealed a heptyl chain to produce optimal activity. The introduction of strong electron withdrawing groups such as nitrile, trifluoromethyl, or nitro gave rise to strong antagonists such as compound 19, shown in Table 1.2, that exhibited strong potency and reduced virulence traits[182]. Further work on PQS analogues showed a bioisoteric replacement of the hydroxyl group with amine gave improved potency and addition of an electron withdrawing group conferred strong antagonism. The resultant compound, QZN, reduced biofilm formation and attenuated pyocyanin production[155]. These observations were capitalised on in the development of a related 7-chloro-4-aminoquinoline series identified by re-screening antiprotozoal agents that yielded compound Ia that displayed improved potency owing to a surmised π-stacking to Tyr 258[183].

High throughput screening revealed a potent benzamide-benzimidazole series that reduced AQ production and pyocyanin[184]. This compound, M64, was shown by ITC to bind with tight affinity (5.4 nM) and co-crystal structure confirmed a phenoxy group could π-stack to Tyr 258. Interestingly, slight structural modification, such as replacement of the phenoxy group with an iodine atom, could confer PqsBC inhibition. The utility of the π-stack was recently reported in a new series that grew a previously linked fragment yielding a compound 4 that possessed a high IC_{50} 11 nM and acted synergistically with tobromycin[185] (Table 1.2).

Table 1.2. Literature PqsR antagonists

Name	Structure	*In vivo* effect	Molecular Target Validation	Ref
QZN	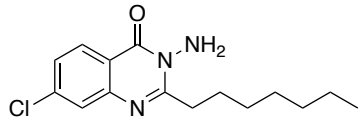	Dose-dependent reduction in P_{pqsA} promoter activity with an IC_{50} of 5 ± 1.6 µM. Reduction in lectin, pyocyanin and biofilm formation.	Co-crystal structure	155
Cmp 19	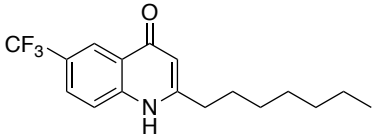	Reduction in P_{pqsA} promoter activity IC_{50} of 54 ± 23 nM in PA14. Reduces pyocyanin production by 74% at 3 µM.	SPR on immobilised $PqsR^{LBD}$ (K_D 57 nM)	182
Cmp Ia	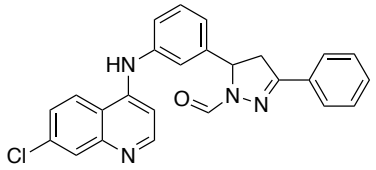	Dose-dependent reduction in P_{pqsA} promoter activity with an IC_{50} of 2.3 ± 0.51 & 12.4 ± 1.79 µM for PAO1 and PA14 respectively. Reduction in pyocyanin, HAQ production and biofilm thickness	Molecular docking	183
Vanillin	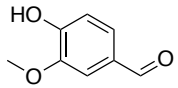	IC_{50} in P_{pqsA}-*gfp* biosensor of 0.81 mM, diminished virulence traits at ~1 mM	Molecular docking	180
Farnesol	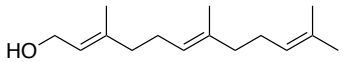	Dose-dependent reduction in PQS & pyocyanin	EMSA with lysate on labelled pqsA promoter	186
M64	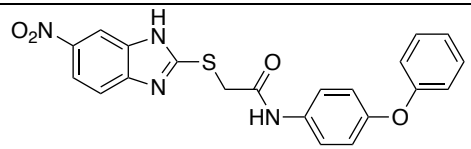	Reduces PQS, HHQ and pyocyanin with IC_{50}s of 200, 350 and 300 nM respectively. Reduction in 2-AA and persister cell formation.	ITC (K_D 5.4 nM) & Co-crystal structure	184 153
Cmp 4	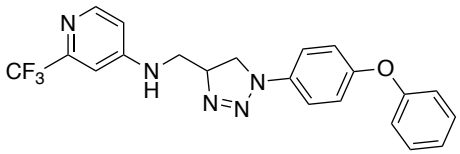	IC_{50} of 11 nM in *E. coli* P_{pqsA}-*lacZ* bioreporter and pyocyanin IC_{50} of 0.2 µM. Reduction in AQ production and synergistic with tobramycin.	Co-crystal structure	185

1.8 Use of fragments in drug discovery

Fragment-based drug discovery (FBDD) is an appealing alternative for hard to drug targets. Fragments are classed as low molecular weight compounds of up to 300 Da with limited molecular complexity[187]. FBDD contrasts to traditional HTS in that a much smaller library of fragments is used for initial screening with often a high degree of re-usability between targets. Additionally, fragments typically achieve binding through a small number of hydrogen bonds allowing for enthalpically driven binding[188]. Reduced extraneous complexity lowers the risk of unintended steric hindrance and ideally prevents the final lead being unfavourably lipophilic. FBDD requires small screening campaigns, in the range of 100-1000 congeners compared to traditional methods and often fragment libraries can be customised with respect to the target protein.

1.8.1 Biophysical determination of binders

Prior to screening, a fragment library can be docked to the protein of interest to enrich the screening library with potential binders. Experimental screening can be performed using several biophysical techniques including Surface Plasmon Resonance (SPR), Thermal Shift assay (TSA), microscale thermophoresis (MST), Ligand/protein-observed NMR and X-Ray crystallography[189]. Depending upon library size a secondary screen may be implemented to identify non-specific binders or aggregators[190]. The choice of screening procedure is influenced by availability of equipment and expertise. In academia, a common strategy is to screen for binders by at least two methods and characterise binding further with structural studies.

1.8.2 Fragment to lead development

Hit fragments will often be subject to further modification to make them suitable for growth or will be explored by a biophysically guided SAR. Identified fragments can be developed into lead-like compounds through 3 strategies[191]. If reliable structural information is known through either NMR or X-ray data fragments can be linked together if occupying different areas within the binding pocket. Although optimisation is required to ensure the chosen linker does not adversely affect binding of either fragment. If successful, the linked

compound will exhibit much improved binding due to the chelate effect[192]. The second approach is to grow the fragment by extending the molecule, typically informed with structural data, to gain additional interactions inside the pocket and improve upon entropic binding contributions with the addition of bulkier constiutents[193]. The last strategy, fragment merging, works on the basis that two or more fragments will overlap within the binding pocket. Common scaffolding requirements can be extrapolated to synthesise a new compound with potentially better binding and additional optimisation to create a more drug-like compound. In all cases of fragment optimisation structural information in the form of protein-observed NMR or X-Ray crystallography is usually needed for rational design[194].

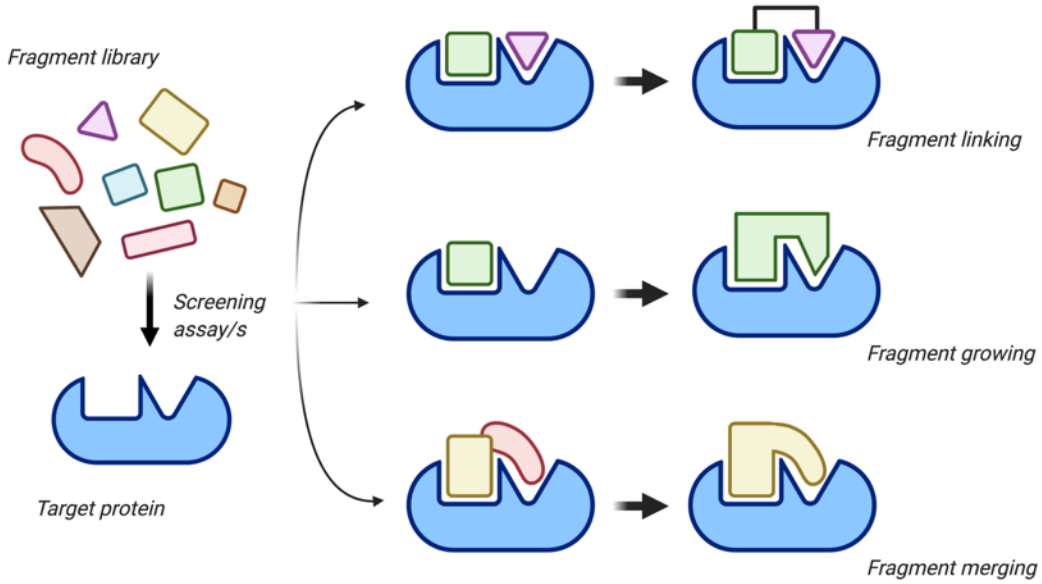

Figure. 1.17 Strategies for FBDD. Representation of a theoretical target with two binding pockets possessing different topologies. These pockets can be screened for fragment binding by an assay or biophysical methods. Three strategies can be used to derive a lead from validated fragments. In fragment linking two separate fragments binding at separate locations are combined by a linker which increases binding affinity by avidity. In fragment growing a single hit is expanded upon by rational design to exploit more interactions within the pocket. Fragment merging requires two or more fragments that overlap within the binding site/s. These are combined into a single scaffold that exploits interactions from both fragments.

Several proteins in the pqs pathway have been the subject of FBDD projects including PqsE, PqsD and PqsR. All campaigns have yielded small molecule products that bound *in vitro* but translating hit fragments into QSI has proven difficult. This has primarily been due to poor chemistry starting points or high affinity fragments failing to translate into *in vivo* activity.

1.8.3 Dissecting PqsD analogue to potent fragment

PqsD fragments were developed using a non-traditional methodology; substrate analogue based inhibitors were designed based upon the anthraniloyl-CoA substrate produced by PqsA. The analogue was shortened, rigidified and cyclised to produce a fragment that maintained similar biological activity compared to the substrate analogue (Figure 1.18)[195]. Subsequent evaluation highlighted that the two enantiomers derived from the chiral-centre displayed different binding thermodynamic parameters with the *R*-isomer binding more favourably[196]. The fragment was able to reduce the production of PQS & HHQ as well as decrease biofilm formation, although these experiments required a high concentration of inhibitor (250 µM and 500 µM). Further chemical optimisation of this fragment series has not occurred suggesting that poor *in vivo* efficacy has proven intractable.

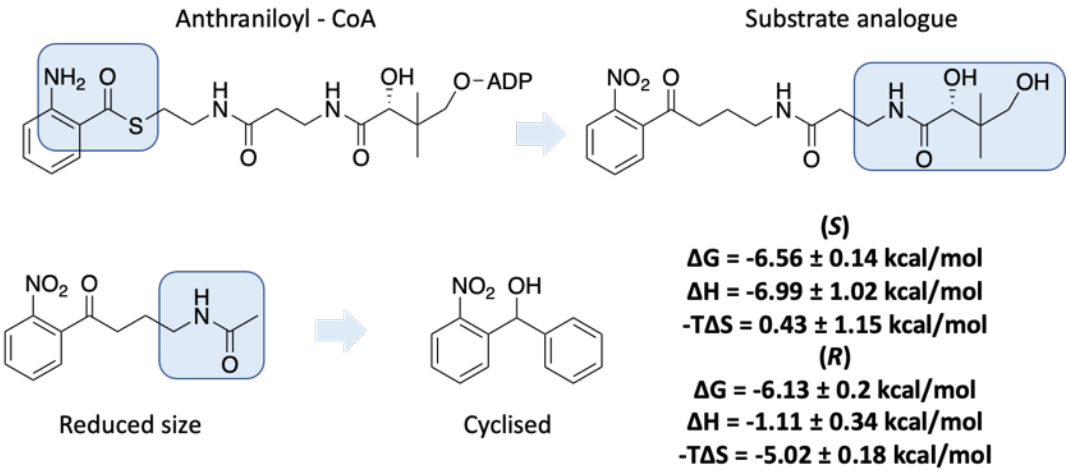

Figure. 1.18 PqsD fragment development from substrate analogue. A non-hydrolysable substrate mimetic, lacking the sulphur bond, was synthesised that did not contain the adenosine moiety. This inhibitor was reduced in size but remained potent. The subsequent small inhibitor was further modified by cyclisation of the amide bond to create a small chiral fragment. Thermodynamic binding parameters given for the two isomers of the fragments as determined by ITC[196].

1.8.4 PqsE fragment screen

Using a thermal shift assay screening method, a series of PqsE fragments were identified from a library of 500 fragments. Thermodynamics of binding and validation was achieved by ITC and X-ray crystallography. Structural determination revealed the carboxylic acid groups of the fragments occupies a distinct configuration around the bi-Fe^{2+} centre compared to natural 2-ABA product (Figure 1.19). Interestingly, despite the fragments inhibiting thioesterase activity no corresponding effect on virulence factors such as pyocyanin was

observed[197]. A similar observation was noted in the compound series described in 1.7.3 suggesting that PqsE enzymatic activity is dispensable for virulence. The druggability of the now characterised PqsE-RhlR interaction has yet to be assessed although fragment-based methods have been successfully used to disrupt PPI such as the CK2β dimer[198].

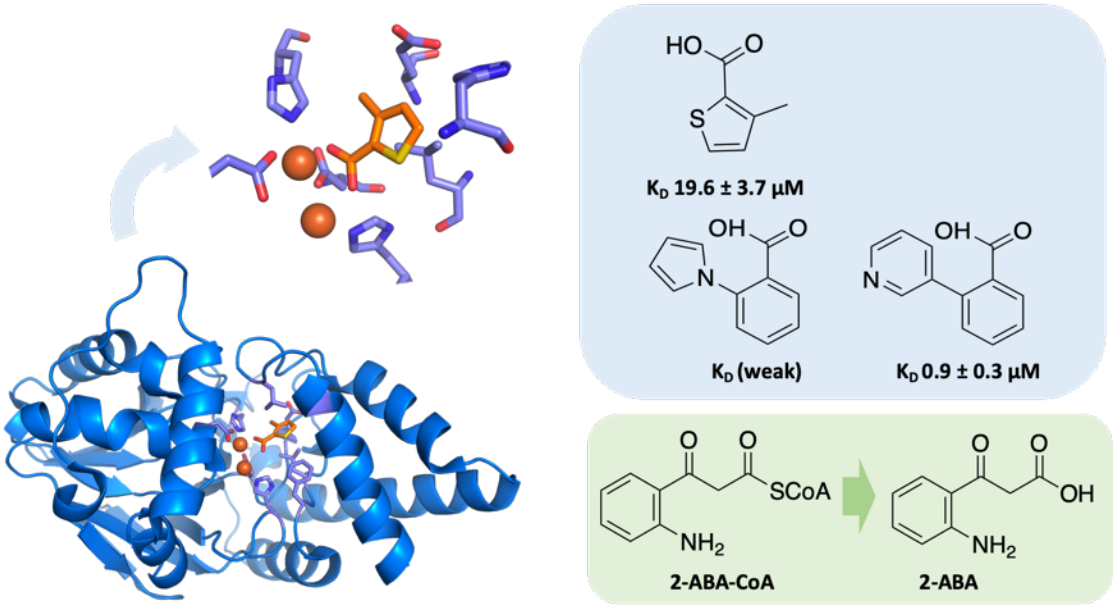

Figure. 1.19 Fragments bound to PqsE. PqsE co-crystal structure with thiophene fragment displacing a bidentate interaction with Fe^{2+} (PDB code 5HIS)[197]. Fragments detected by DSF and validated by ITC in blue pane. Binding constants from ITC (or qualitative evaluation) given with the fragment. 2-ABA-CoA substrate and 2-ABA product shown in green pane.

1.8.5 SPR campaign on PqsR identified multiple binders

Development of antagonists towards PqsR has received greater attention compared to the other enzymes in the pathway. An initial SPR screening project revealed a small series of promising fragments from a library of 106 compounds. The four hits identified had good ligand efficiency >0.45 (defined by binding energy contribution per heavy atom)[199]. However, the lead fragment containing a hydroxamic acid lead displayed low aqueous solubility and were predicted to be mutagen. As a result, the same group screened (via SPR) a broader library of 720 compounds to identify a second generation of fragments with broader chemical diversity. Several binders, shown to compete with PQS, were characterised by SPR and ITC. Mutagenesis suggested the binding of the lead oxadiazole fragment was mediated by π-π stacking from Phe221 but unlike the secondary lead 2-

naphthamide was not hydrogen bonded to Gln194. Through SPR the fragments were shown to be competing but clearly differently positioned within the pocket. Strangely further optimisation did not lead to a potent lead-like compound suggesting the fragments, although good binders, were not promising for further antagonist development[200].

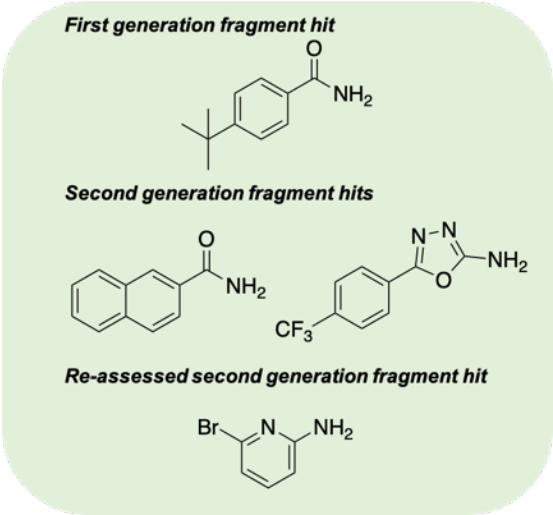

Figure. 1.20 Initial fragment hits for PqsR determined by SPR screening. First generation PqsR fragment with hydroxamic acid displayed high affinity by ITC but poor aqueous solubility and was toxic. This fragment was judged by ITC to have a binding affinity of 0.9 μM mostly driven by a strong enthalpic contribution (-9.7 ± 0.3 kcal/mol)[199]. Second generation were shown to have high affinity by gave poor *in vivo* activity. The binding affinity, determined by ITC, of the fragments shown are 1.8 ± 0.2 and 3.7 ± 0.1 μM respectively[200]. Re-assessment of the library, by enthalpic contributions, revealed a fragment with high ligand efficiency that could be further optimised. This fragment possessed a binding affinity of 10 ± 1.3 μM and enthalpic efficiency of 1.17[201].

As the previous three hit fragments failed to yield activity in *P. aeruginosa* a new pyridine fragment was selected for modification and growth based upon strong enthalpic binding properties relative to size. This parameter was considered as hydrogen bond placement in a predominantly lipophilic pocket would be a significant barrier to binding. The pyridine fragment was optimised into a lead like compound by attaching another aromatic moiety through a flexible linker to partially mimic the natural ligands PQS and HHQ. Replacement with less flexible linkers entirely abolished antagonist activity. Soaking studies highlighted that the flexibility was required to angle the second aromatic moiety towards the region normally occupied by the alkyl-chain (pocket A). Additionally, potency was granted by extending the linker further to exploit π-π stacking with Tyr258 (Figure 1.21). The final

compound displayed *P. aeruginosa* virulence reduction comparable to ligand based analogues[201].

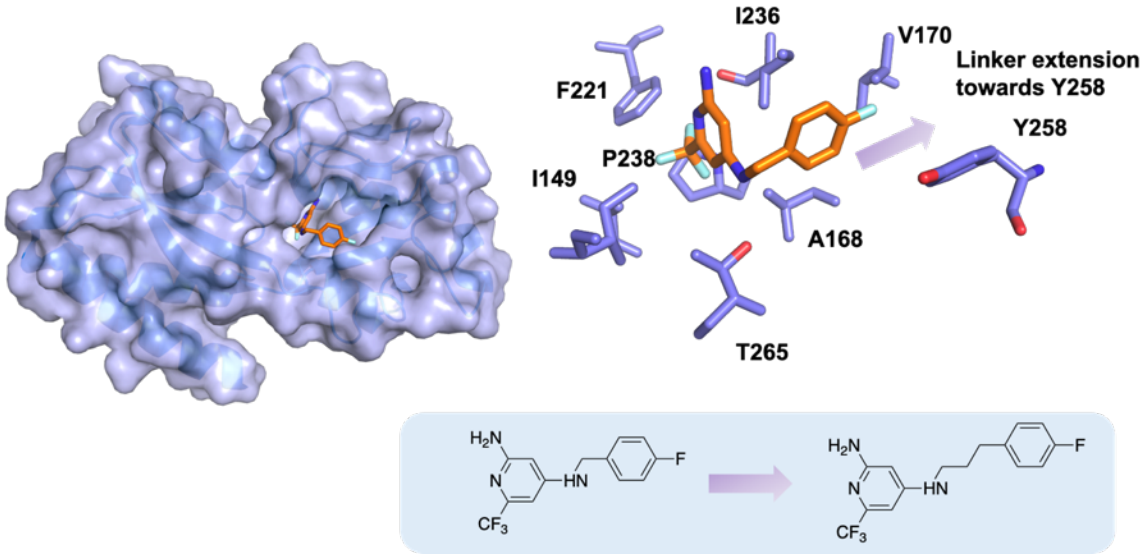

Figure. 1.21 Fragment merging and subsequent growth to develop favourable PqsR antagonists. Lead like compound is grown to increase entropic binding contributions and to extend fluorobenzyl group further into pocket A to enable π-π stacking with Y258 (PDB code 6Q7V)[201].

1.8.6 Dual targeting PqsD/R agents

Interesting work has been conducted to create a dual antagonist/inhibitor for PqsR/D. By SPR screening a PqsD inhibitor was identified with serendipitous similarity to a PqsR antagonist. Each shared a pyrimidine core linked to a triazole ring decorated with a sulfonyl group (Figure 1.22). The two structures were combined and additionally modified to create a fragment-like molecule (M_r 225.23) with good solubility and inhibition of both proteins as determined by biological assay. Despite its size the fragment could inhibit virulence factors including pyocyanin and pyoverdine and was surprisingly found to inhibit biofilm formation and reduced virulence in a similar animal model[202]. Unusually, further SAR proved challenging with respect to maintaining activity against both proteins. The study concluded that difficulties in improving activity may be due to limited cell penetration. It should be noted that the binding assessments for these compounds were performed in bioreporter assays and so target binding validation is not yet available. Structural information would be required to explain the SAR data, yet it does highlight that multi-target pharmacology is possible for the PQS system and provides a strong effect on virulence markers.

.

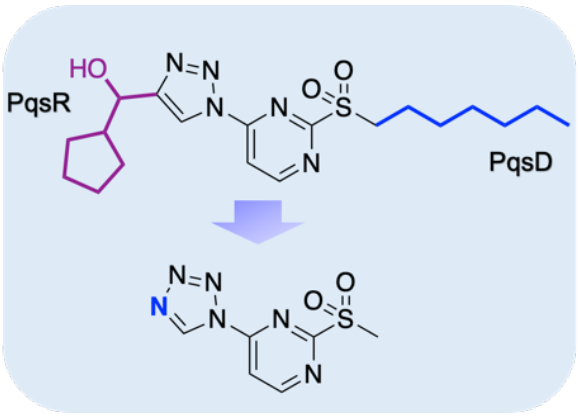

Figure. 1.22 Identification of a common scaffold applicable to PqsD and PqsR. Original hit decoration of PqsR antagonist and PqsD inhibitor coloured in purple and blue respectively. Resultant fragment inhibited virulence traits but subsequent optimisation failed to improve potency. The fragment had a potency (IC_{50}) of 15 and 21 µM towards PqsR and PqsD respectively and inhibited pyocyanin production by 72% at 400 µM.

1.9 Role of SENBIOTAR in *P. aeruginosa* drug discovery

As detailed above QSI for las, rhl and pqs have been elucidated in multiple studies. However, the clinical relevance of targets such as LasR have been questioned in recent years due to prominence of inactive las systems in chronic cystic fibrosis. Additionally, individual knockouts of both *lasR* and *rhlR* do not fully suppress virulence[203]. Furthermore, biochemical intractability of RhlR has hindered structural characterisation and early-stage drug discovery. Contrastingly, multiple studies have showed pqs to have a strong association with virulence and has been shown to increase survivability against antimicrobials and phages in the lung[204]. Currently no QSI has been approved for clinical use and the outcomes of most campaigns appear to stall in early drug development due to unsuitability of the chemistry such as Farnesol or due to poor target validation.

The sensitising *Pseudomonas aeruginosa* biofilms to antibiotics and reducing virulence through novel target inhibition MRC research project (SENBIOTAR) is an international collaboration investigating pqs inhibition strategies using biophysical, microbiological, and medicinal chemistry efforts to develop both small molecules and peptide nucleic acids. The project is coordinated by Prof. Miguel Camara and chiefly based at the Biodiscovery institute at the University of Nottingham. PqsR was chosen for as an target for medicinal chemistry efforts due to the reported mutant phenotype, partially structural

characterisation (as shown in subsection 1.6) and encouraging early fragment and substrate analogues efforts. Full elucidation of compound discovery is detailed in Soukarieh *et al.*, 2018[183 205]. Briefly, molecular docking was utilised using PDB 4JVI as an input model (with bound ligand QZN removed). The model was hydrogenated, waters removed and residue rotamers optimised using Schrödinger suite[206]. Glide docking was conducted using the extra precision (XP) functionality around a 20 Å box and ranked by score. Compounds with favourable scores were retrieved from Nottingham Compound collection (NCC) and validated using an *in vivo* promoter fusion assay. Compounds were screened at 10 µM in PAO1 – L CTX::P_{pqsA}-*lux* (bioreporter) with hit threshold defined as a reduction of 50% compared with a DMSO solvent control. Further medicinal chemistry optimisation was guided by IC_{50} measurements conducted in the same strain. A general schematic of the screening methodology is represented below in Figure 1.23:

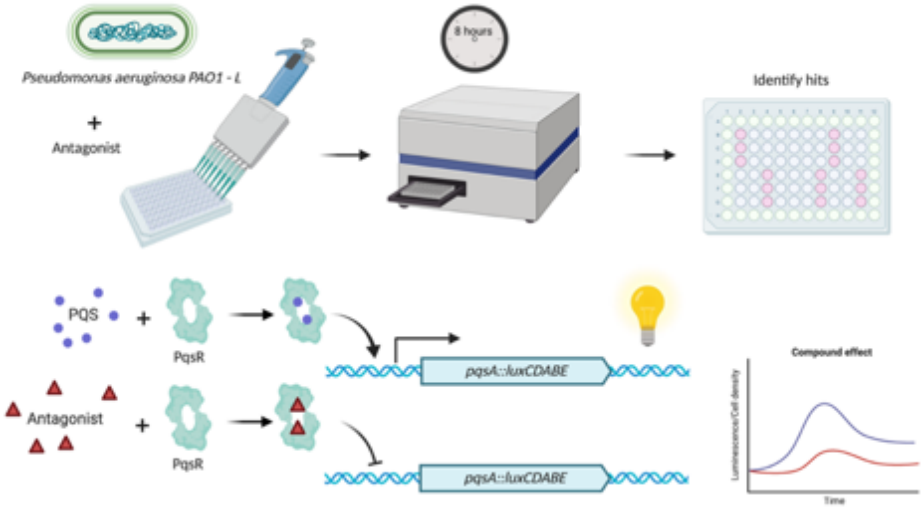

Figure 1.23 Overview of PqsR^{LBD} antagonist screening technique used to identify initial hit compounds. Potential antagonists were tested in triplicate on a 96 well plate and antagonist activity determined after 8 hours representing the expression maxima. Promoter activation is inhibited by antagonist binding resulting in reduced luminescence represented by the red line in the diagram.

1.10 Thesis aims

PqsR plays a clear role in the virulence of *P. aeruginosa* and through the SENBIOTAR program (MRC MR/N501852/1) several new agents have been identified from the Nottingham compound library. Understanding their modes of binding will aid further SAR and elucidate key interactions in the PqsR ligand binding pocket. Other modes of medicinal chemistry development could be undertaken such as how FBDD can be applied to PqsR with

similar success as described in the literature. In addition, successful purification of the full-length receptor would aid in determining the mechanism of action behind LTTRs and how the AQ signals can induce conformation change.

The aims of this thesis therefore are to:

- Solve structural complexes of PqsR and SENBIOTAR derived antagonists to enable molecular interactions to be resolved and equated to potency.
- Gather biophysical data that describes the binding events and key residues involved in attaining high affinity.
- Assess whether an *in silico* method can successful enrich a fragment library for PqsR
- Find a suitable method to express and solubilise the full length receptor to allow biophysical studies and crystallisation.
- Identify if dual targeting another PQS biosynthetic target would complement a PqsR antagonist.

2 Materials and Methods

2.1 Strains

2.1.1 E. *coli* strains

Table 2.1 *E. coli* strains used in this study

Strain name	Genotype	Reference
DH5α	F^{-} *endA1 glnV44 thi-1 recA1 relA1 gyrA96 deoR nupG purB20 φ80dlacZΔM15 Δ(lacZYA-argF)U169, hsdR17(rK^{-}mK^{+}), λ^{-}*	207
TOP10	F^{-} *mcrA Δ(mrr-hsdRMS-mcrBC) φ80lacZΔM15 ΔlacX74 nupG recA1 araD139 Δ(ara-leu)7697 galE15 galK16 rpsL(Str^{R}) endA1 λ^{-}*	Invitrogen
BL21 (DE3) CodonPlus RIL	F^{-} *ompT gal dcm lon hsdSB(rB^{-}mB^{-}) λ(DE3 [lacI lacUV5-T7p07 ind1 sam7 nin5]) [malB^{+}]$_{K-12}$(λ^{S})* [argU ileY leuW Cam^{R}]	Aligent 208
S-17	RP4 2-Tc::Mu-Km::Tn7, *recA, thi, pro, hsdR^{-}, hsdM^{+}*	209

2.1.2 *P. aeruginosa* strains

Table 2.2 *P. aeruginosa* strains used in this study

Strain name	Genotype	Reference
PAO1-L	PAO1 Lausanne subline (wild type)	210
PAO1-N	PAO1 Nottingham subline (wild type)	Nottingham lab collection
PAO1-L Δ*pqsA*	*pqsA* chromosomal deletion mutant derived from PAO1-L	211
PAO1-L Δ*pqsR*	*pqsR* chromosomal deletion mutant derived from PAO1-L	205
PAO1-L Δ*lasR*	lasR chromosomal deletion mutant derived from PAO1-L	Nottingham lab collection
PAO1-N Δ*pqsR*	*pqsA* chromosomal deletion mutant derived from PAO1-N	155

PAO1-N Δ*pqsAHR*	*pqsAHR* chromosomal deletion mutant derived from PAO1-N	[155]

2.2 Plasmids

2.2.1 Complementation plasmids

Table 2.3 Table of plasmids used for complementation experiments

Plasmid	Description	Ref
pME6032	Complementation vector containing $lacI^{Q}$- P_{tac} and Tc^{R}	[212]
pME6032::*pqsR*-His	ORF of *pqsR* cloned into pME6032 with C-termini his-tag	Recreated from [155]
pME6032::*pqsR*-His C108S	pME6032::*pqsR*-His harbouring a C108S mutation	This study
pME6032::*pqsR*-His Y258A	pME6032::*pqsR*-His harbouring a Y258A mutation	[155]
pME6032:*pqsR*-His Y258F	pME6032::*pqsR*-His harbouring a Y258F mutation	This study
pME6032:*pqsR*-His Y258Q	pME6032::*pqsR*-His harbouring a Y258Q mutation	This study
pME6032:*pqsR*-His Loop$^{180\text{-}185}$	pME6032::*pqsR*-His harbouring a double deletion and mutation at residues 180 – 185 to YSSA	This study
pMiniCTX- lux(Gm^{R})::*pqsA*	Transcriptional reporter fusion of *pqsA* promoter region to luciferase (*pqsA*::*luxCDABE*)	[213]

2.2.2 Expression constructs

Table 2.4 Expression constructs. Molecular weight and pI calculated with Protparam[214].

Construct	No. of residues	Molecular weight (kDa)	pI	Ref
pET28a::*pqsR*$^{94-309}$	239	26.7	6.16	Recreated from [155]
pET28a::*pqsR*$^{94-309}$ S123C	239	26.7	6.16	This study
pET28a::*pqsR*$^{94-309}$ K154A K214Y	239	26.7	5.91	‘’
pET28a::*pqsR*$^{94-309}$ K154A E278A	239	26.6	6.16	‘’
pET28a::*pqsR*$^{94-309}$ SR Loop deletion	238	26.7	6.11	‘’
pET28a::*pqsR*$^{94-309}$ DR Loop deletion	237	26.5	6.11	‘’
pET28a::*pqsR*$^{60-309}$	272	30.5	6.45	‘’
pET28a::*pqsR*$^{94-332}$	262	29.27	6.63	‘’
pET28a::*pqsR*$^{94-332}$ T265A	262	29.27	6.63	‘’
pET28a::*pqsR*$^{94-332}$ T265N	262	29.27	6.63	‘’
pMAL(X)E::*pqsR*$^{94-309}$	589	64.8	5.20	‘’
pMAL(X)E::*pqsR* (AAA linker)	703	77.5	5.81	‘’
pMAL(X)E::*pqsR* (AAAAS linker)	705	77.6	5.81	‘’
pTRX::*pqsR* (GSAM linker)	452	50.2	6.32	‘’
pSC1::*pqsR*	449	50.7	6.87	‘’
pSC2::*pqsR*	465	51.4	6.47	‘’
pSC2::TEV_*pqsR*	471	52.2	6.36	‘’
pSC2::*pqsR*^{310}	443	49.0	6.15	‘’
pSC2::*pqsR*^{296}	429	47.3	6.15	‘’
pSC2::*pqsR* S123C	465	51.5	6.47	‘’
pSC2::*pqsR* DR Loop deletion	463	51.3	6.44	‘’
pUCP18::*pqsR*_His	338	38.0	7.25	‘’
pET24b::*pqsA*$^{1-399}$	407	44.3	6.01	‘’

pET24b::*pqsA*$^{1-399}$_strep	409	44.5	5.81	‘’
pET24b::*pqsA*_strep	527	57.8	5.86	‘’
pET24b::*hmqA*$^{1-430}$	437	47.7	6	‘’
pET24b::*hmqA*_strep	561	61.1	6.08	‘’
pET24b::*hhqA*$^{1-430}$	437	59.5	6.83	‘’
pET24b::*hhqA*_strep	437	47.4	6.55	‘’

2.3 Media and bacterial growth

Small cultures (5-10 mL) of bacteria were routinely grown in 50 mL falcon tubes with a loose cap at 37°C with shaking at 180-200 rpm. Large cultures >100 mL were grown in 1L flasks under the same conditions. The list of medias used in experimentation is given below:

Table 2.5 Bacterial growth medias used in this study. *Supplemented with 500 mM sorbitol for PqsR. (1) Casamino acids defined as the hydrolysis of Bovine Casein and as such contains all naturally occurring amino acids with respective concentrations related to the αS1, αS2, β, κ phosphoproteins (2) M9 Salts defined as 15 g/L KH_2PO_4, 2.5 g/L NaCl, 33.9 g/L Na_2HPO_4, 5 g/L NH_4Cl.

Media	Composition
Lysogeny broth	10 g/L Tryptone, 5 g/L Yeast Extract, 5 g/L NaCl
2YT	16 g/L Tryptone, 10 g/L Yeast Extract, 5 g/L NaCl
NZYCM	10 g/L Tryptone, 5 g/L Yeast Extract, 5 g/L NaCl, 1 g/L Casamino acids, 1 g/L $MgSO_4$
TB*	12 g/L Tryptone, 24 g/L Yeast Extract, 5 g/L Glycerol supplemented with 1/10 TB salts (23.1 g/L KH_2PO_4 125.4 g/L K_2HPO_4)
Pseudomonas isolation agar (PIA)	20 g/L Peptone, 1.4 g/L $MgCl_2$, 10 g/L K_2SO_4, 0.025 g/L Triclosan, 13.6 g/L Agar
CAA	10 g/L Casamino acids[1], 10 g/L M9 Salts[2], 1 mM $MgSO_4$, 1 mM $CaCl_2$
RPMI	RPMI 1640 as detailed by Gibco Thermofisher (not supplemented with L-Glutamine or Phenol Red). RPMI contains all naturally occurring amino acids (excluding alanine), vitamins, inorganic salts and glucose.

2.4 Cloning

2.4.1 gDNA extraction from *P. aeruginosa* and plasmid extraction

Genomic DNA from *P. aeruginosa* strain PAO1 – N was extracted from a 5 mL culture grown overnight using the Wizard Genomic DNA Purification Kit (Promega). Changes in sequences of *pqsR* and *pqsA* are negligible across common lab strains. Plasmids were extracted from 5 mL DH5α or TOP10 cultures grown for 18 hours supplemented with appropriate antibiotic.

2.4.2 Conjugation

5 mL cultures of donor S-17 *E. coli* and recipient *P. aeruginosa* were prepared in LB at 37 and 42°C respectively as overnight cultures. Cultures were combined in a 1:1 ratio in 1 mL and washed by centrifugation at 7,000 *x g* for 5 minutes and resuspended in the same volume of fresh media. This procedure was repeated twice and upon final resuspension the volume was reduced to 30 µL and plated on LB agar and dried under a flame. After 6 hours of mating at 30°C cells were homogenised in 1 mL LB and 50 µL plated onto PIA with relevant antibiotic. Resultant colonies were patch plated twice and used for further experimentation.

2.4.3 Polymerase chain reaction (PCR)

Several PCR reactions were subject to variation depending upon template and application. Typically, Velocity Polymerase (Bioline) was used to make most PCR products, unless otherwise stated the PCR reaction and cycling conditions are given below. Annealing temperatures were determined using the NEB Tm calculator. After PCR, all products were visualised on a 0.8-1% Agarose gel stained with SyberSafe dye (x1) and gel extracted using the Wizard Clean up kit (Promega). Components for PCR amplification are given in Table 2.6 and conditions in Table 2.7.

Component	Volume/ Target Concentration
5 x Hi-Fi Reaction Buffer	10 µL
10 mM dNTP (each)	1.5 µL
gDNA	1 – 50 ng
10 µM Primers (each)	2.5 µL
Enzyme*	1 µL
DMSO	1.5 µL
Water	Up to 50 µL

Table 2.6 PCR reaction components. *Enzymes used in this work include Velocity polymerase (bioline), Q5 Polymerase (NEB), Phusion (NEB) and OneTaq (NEB) with reactions varied according to manufacturer's guidance.

Step	Temperature	Duration (mins)	Repeat
Initial denaturation	98°C	2	1
Denaturation	98°C	0.5	30
Annealing	40-70°C [1]	0.5	
Extension	72°C	0.5/kb	
Extension	72°C	10	1

Table 2.7 PCR cycling conditions. (1) temperature determined by composition and calculated using annealed primer sequence by NEB Tm calculator.

2.4.4 Splice overlap extension (SOEing) PCR

To create a Thioredoxin fusion protein an overlapping PCR was formed using PCR products derived from pTRX containing the thioredoxin gene (a generous gift from Dr Warwick, University of Nottingham) and gDNA from *P. aeruginosa*. After gel extraction and purification 100 ng of each PCR product was added to a PCR mixture that excluded forward and reverse primers. After 7 cycles of denaturation, annealing and extension the forward and reverse primers were added for the remaining 30 cycles. The PCR product was further purified by gel extraction and used for downstream cloning into pET24b.

2.4.5 Restriction digests

Purified PCR products and isolated plasmids were digested using Restriction enzymes from NEB performed in CutSmart buffer. Reactions for cloning were set up with approximately 1 µg of material and incubated at 37°C in a thermocycler for 2 hours. Additional enzyme was added, and the vector dephosphorylated using CIP for a further hour. The reaction was heat inactivated at 65°C for 15 minutes. Products were separated on an agarose gel and extracted as above.

2.4.6 DNA product ligation

Digested vector and PCR products were quantified by Nanodrop (A_{260}) and ligated using T4 Ligase (NEB) in a reaction mixture of 10 or 20 µL. Approximately 20-50 ng of vector was used and different ratios of inserts were added. The reaction was incubated under alternating temperature conditions 10 – 18°C for 16 hours. Reactions were transformed into chemically or electrocompetent cells.

2.4.7 Chemically competent cells preparation

Chemically competent cells were prepared by using $CaCl_2$ method. Briefly an overnight culture was prepared from a single colony of the desired strain. The following day the culture was diluted 1/1000 in fresh media, typically 50 – 100 mL. The culture was incubated until an OD_{600} of 0.5 - 0.7 had been reached. The culture was chilled on ice, cells collected by centrifugation and resuspended in 50 mM $CaCl_2$. The suspension was incubated on ice for 1 hour and washed again in 1/10 volume with 100 mM $CaCl_2$ supplemented with 15% glycerol.

The suspension was incubated overnight and the next day the cells were given a final wash prior to storage at -80°C.

For transformation, 100 µL of cells were thawed and incubated with 1 – 5 µL of purified DNA or ligation mixture. After 20 minutes of incubation the cells were subjected to a heat shock at 42°C for 40 seconds. The cells were recovered with 0.75 mL of LB and incubated with shaking for 1 hour. Cells were concentrated by centrifugation and plated onto antibiotic selective agar.

2.4.8 Electrocompetent cells

Cells were incubated as described above but were washed with 10% glycerol 3 times. Cells were resuspended in a final volume of 1 mL and flash frozen at -80°C. After incubation with 1 µL DNA cells were transformed by transferring 50 µL into a 2 mm cuvette and electroporated with a BioRad MicroPulser using a voltage of 2.5 kV (setting 2). Cells were recovered with addition of 1 mL of LB for 1 hour followed by plating on selective agar.

2.4.9 Site directed mutagenesis (SDM)

Mutagenesis was performed on the pET28a::*pqsR*$^{94\text{-}309}$ construct for Surface Entropy Reduction (SER) optimisation. These were generated using a modified method from Agilent. PCR using PfU Turbo (Aligent) was performed with 10 ng of vector and 0.5 µM forward and reverse primers. The reaction parameters began with a 1 minute denaturation at 95°C followed by 18 cycles of 95°C for 1 minute; 55°C for 1 minute and 68°C for 7 minutes. Unmodified DNA was digested by the addition of 1U DpnI (New England Biolabs) for 3 hours at 37°C. 2 µL of reaction was transformed into DH5α and colonies screened for mutation by Sanger sequencing. Desired mutations that proved recalcitrant to this method were carried out under modified parameters using a 20 cycle PCR supplemented with 2% DMSO.

Mutants that could not be successfully generated through this method were instead prepared by Splice Overhang extension PCR in which the internal primers originally designed for the method above were used to create fragments with appropriate external primers. This was the case for pME6032::*pqsR*-His T265A and Q160A.

2.4.10 Primers used in PCR

Table 2.8 Oligonucleotide primers used in this study to generate expression constructs

Identifier	Sequence (5' -3')	Description
PqsR-MBP_AAA_F	ATCGGCGGCCGCAATGCCTAT TCATAACCTGAATC	Primers for cloning *pqsR* into pMAL and pSC vectors. NotI and BamHI sites underlined.
PqsR-MB_AAA_R	ATCGGGATCCCTACTCTGGTG CGGCGCGCTG	
PqsR-MBP_AAAAS_F	ATCGGCTAGCATGCCTATTCATA ACCTGAATC	Primers for cloning *pqsR* into pMAL(X) with extended linker NheI site underlined.
Thio_F	ACTGACCATATGGCACATC ATCACCACC	Primers for SOEing PCR of Thioredoxin (*Txn*) and *pqsR*. NdeI site underlined. GSAM linker sequence highlighted in bold.
Thio R	ATGAATAGG**CATCGCGCTACC**TGCCA GGTTCGCGTCC	
GSAM_PqsR_F	GGTAGCGCGATGCCTATTCATA ACCTGAATC	Forward primer for amplifying *pqsR* to include linker sequence
PqsRDBD_F	AGTCAGCATATGCCTATTCATAA CCTGAATCAC	Forward primer for making DNA binding domain constructs. NdeI site is underlined.
PqsRDBD_R69	AGTCGAATTCCTATTA**GTGGTGATGGT GATGATGCCA**AGGGATCAGGCGAAGCG	Reverse primer for *pqsR* terminating at residues 69, 85, 106 with WHHHHHH C –terminal (bold)
PqsRDBD_R85	AGTCGAATTCCTATTA**GTGGTGATGG TGATGATGCCA**GGCGATGTCGCCGATCAG	
PqsRDBD_R106	AGTCGAATTCCTATTA**GTGGTGATGGT GATGATGCCA**CGACGGCGGGATGG	
TEV_pqsR_F	ATCGGCGGCCGCA**GAGAATCTGTACTTTCAG AGC**CCTATTCATAACCTGAATC	Primers for amplifying *pqsR* to include TEV cleavage site
TEV_pqsR_R	ATCGCTCGAGTTACTACTCTGGTGCGGCGCG	

	CTGG	
pqsR310_R	ATCGCTCGAGTTATTAGATGCTCGGTTGC CAGG	Reverse primers for amplifying *pqsR* terminating at residues 310 & 298
PqsR298_R	ATCGCTCGAGTTATTAGCCGAGTTCGCGC AGGC	
pqsR_pUCP19_F	TATGAATTCATGCCTATTCATAACCTGAATC	Primers for *P. aeruginosa* homologous expression of *pqsR*. EcoRI and HindIII siteS underlined and his tag in bold.
pqsR_pUCP19_R	ATCGAAGCTTCTATTA**GTGGTGATGGT GATGATG**CTCTGGTGCGGCGCGCTGG	
60pqsR_F	ACTGGCTAGCACCGAGCAGGCGCTTCGCCTG	Primer designed to extend construct boundary to residue 60.
PqsA_F	CTATCGCATATGTCCACATTGGCCAACCTG	Forward primer amplifying *pqsA* gene for cloning into pET28A. NdeI site underlined
PqsA399_R	ATCGCTCGAGGTCTTCCCGCCCACAGTG	Reverse primer amplifying *pqsA* gene terminating at residue 399. XhoI site underlined
PqsA399_strep	AGTCGGATCCCTATTA**CTTTTCGAACTG CGGGTGGCTCCA**CGCGCTGTCTTCCCGCC CACAGTG	Reverse primer amplifying *pqsA* gene terminating at residue 399 with the addition of a Strep – II –tag (bold). BamHI site underlined.
PqsA_strep	AGTCGGATCCCTATTA**CTTTTCGAA CTGCGGGTGGCTCCA**CGCGCTACATGC CCGTTCCTCCGGAAGGTTGTC	Reverse primer amplifying *pqsA* with the addition of a Strep – II –tag (bold). BamHI site underlined.
HmqA_F	ATCGCATATGGATGACTTTTGCCGCGCG	Primers for inserting *hmqA* truncated variant into pET24b. NdeI and XhoI sites underlined. HisTag sequence in bold.
HmqA430_R	ATCGGGATCCTTACTA**GTGGTGATGGTG ATGATG**GCTCGCGCGCGCCTGATAGAAC	
HhqA_F	ATCGCATATGGACAACTTTTGCCGCACG	Primers for inserting *hhqA* truncated variant into pET24b. NdeI and XhoI sites underlined. HisTag sequence in bold.
HhqA430_R	ATCGGGATCCTTACTA**GTGGTGATGGTG ATGATG**GCTGGCGCGCGACTGGTAGAAC	

Primers: Complementation constructs

Table 2.9 Oligonucleotide primers used in this study to generate complementation constructs

Identifier	Sequence (5’ -3’)	Description
PqsR_C_His_F	TATGAATTCATGCCTATTCATAACCTGAATC	Amplification of *pqsR* for insertion into pME6032 with a C – terminal Histag (bold). EcoRI and XhoI sites underlined.
PqsR_C_His_R	TATCTCGAGTCA**GTGGTGATGGTGATGATG**C TCTGGTGCGGCGCGCTGG	

Primer: Site directed mutagenesis (SDM)

Table 2.10 Oligonucleotide primers for site directed mutagenesis. Mutagenesised sequence highlighted in bold text. Primers ordered with HPLC preparations from Sigma. Tms for each reaction were calculated assuming full annealing to target site.

Identifier	Sequence (5’ -3’)
T265A	GCGGCATCGAC**GCG**AAGGTGTATTGC GCAATACACCTT**CGC**GTCGATGCCGC
T265N	GCGGCATCGACA**AT**AAGGTGTATTGC GCAATACACCTT**AT**TGTCGATGCCGC
S123C	GAGGTGCGTATCAGGC**A**GACCATGTTGAAATCG CGATTTCAACATGGTC**T**GCCTGATACGCACCTC
K154A	CCATCGACGAGGAACTG**GC**GATCTCCCGCTTCAACC GGTTGAAGCGGGAGATC**GC**CAGTTCCTCGTCGATGG

K214Y	GGCCGGTCAGCGAC**TAT**GTGCTCTTCGTGGAA TTCCACGAAGAGCAC**ATA**GTCGCTGACCGGCC
E278A	CAGGAAGCTGCGC**G**CGGATTCCAGCGC GCGCTGGAATCCG**C**GCGCAGCTTCCTG
Single residue loop deletion	GCACCCGTTGTGCAGTGCATC**GTATTAT**ATCGCGAGCC GGCTCGCGAT**ATAATACGAT**GCACTGCACAACGGGTGC
Double residue loop deletion	GCACCCGTTGTGC**TATAGCAGCGC**CATCGCGAGCC GGCTCGCGATG**GCGCTGCTATA**GCACAACGGGTGC
Y258F	GTCCTCAGCGAACTCT**T**CGAACCGGGCGGCATCG CGATGCCGCCCGGTTCG**A**AGAGTTCGCTGAGGAC
Y258Q	GTCCTCAGCGAACTC**CAG**GAACCGGGCGGCATCG CGATGCCGCCCGGTTC**CTG**GAGTTCGCTGAGGAC
Q160A	GATCTCCCGCTTCAAC**GCC**TGCGTGCTCGGCTACACC GGTGTAGCCGAGCACGCA**GGC**GTTGAAGCGGGAGATC
C108S	CCATCCCGCCGTCGTTC**A**GCGATACGGTGAGCAG CTGCTCACCGTATCGC**T**GAACGACGGCGGGATGG

2.5 Protein purification from *E. coli*

2.5.1 Protein expression

Expression in *E. coli* was conducted in 2 L Erlenmeyer Flasks with 250 mL of media. For expression, starter cultures were inoculated from single colonies and incubated overnight at 30 - 37°C with 180 – 200 rpm shaking. The following day, cell density was monitored and in the case of Amp^R expression the culture was washed with an equivalent volume of fresh media to remove excreted lactamase. In all cases cultures were diluted to a range between 0.005 – 0.02 OD_{600} and incubated at 37°C. Induction parameters including cell density, inducer concentration, temperature and duration are given in Table 2.11 below. After induction, cells were harvested by centrifugation at ~4000 *x g* for 0.5 – 1 hour and cell paste washed with either PBS or fresh media. Cell paste was flash frozen in liquid nitrogen and stored at -80°C until required.

Table 2.11 Protein construct expression conditions. Culture growth and induction parameters used for protein expression in *E. coli.* *2YT for PqsR C-terminal constructs supplemented with 5% glycerol

Construct	*E. coli* cell line	Media	Induction OD_{600}	IPTG (mM)	Temperature (°C)	Expression Duration (Hours)
MBP fusion proteins (full length and C-terminal)	BL21 codon plus RIL	TB	0.7	0.5	16	20-24
Full length PqsR fusions	BL21 codon plus RIL	TB	0.6-0.8	0.1	17	20
PqsR C-terminal domain constructs (94 – 309 and 94 – 332)	BL21 codon plus RIL	LB & 2YT*	0.6-0.9	0.4	16-18	18
PqsR DNA binding domains	BL21 codon plus RIL	TB	0.6-0.8	0.1	17	20
PqsA and HmqA/HhqA homologs	BL21 codon plus RIL	TB	0.6-0.7	0.1	18	16
TEV protease	BL21	2YT	0.5	1	30	5

2.5.2 Cell lysis

Flash frozen cell paste was resuspended in buffer with a ratio of 5 – 10 mL per gram. Resuspension buffer was supplemented with a cOmplete™ EDTA-free tablet (cOmplete™ for Streptavidin or MBP constructs), ~1 – 2 mg/mL Lysozyme and 1U/mL DNase I. After incubation on ice with gentle agitation for 30 minutes the suspension was sonicated on ice using 18 µm pulses of 15 seconds with 15 second breaks using a 705 Sonic Dismembrator (overall energy input was 15 – 20 kJs per 50 mL tube). Afterwards, supernatant was clarified by centrifugation at 13,000 *x g* or 20,000 *x g* for 1 hour. The material was further clarified by passing through a 0.22 µm syringe filter. The lysate was kept chilled on ice until subjected to chromatography procedures.

2.5.3 Ni – NTA

Immobilised metal chromatography (IMAC) was achieved using a HisTrap HP or Crude FF column (GE healthcare) with buffers listed in Table 2.12. Before loading lysate, the columns were blank run with 5 column volumes (CV) of Buffer B containing 500 mM imidazole (to dissociate unbound Ni^{2+}) followed by 10 CV of Buffer A. The lysate was loaded at 2.5 mL/min and unbound material washed off with at least 15 CV of Buffer A. For FL PqsR a 3 CV wash of 1.5 M NaCl was performed prior to elution. Elution was achieved by linear gradient on an AKTA FLPC system (PURE or Prime) using 10-15 CVs to 100% Buffer B. Fractions were evaluated by SDS PAGE and fractions containing material of the correct size compared to the induced control sample were pooled for further purification.

Constructs	Buffer A	Buffer B
Full length PqsR constructs	50 mM Tris-HCl (pH = 8), 500 mM NaCl, 50 mM Imidazole	+ 500 mM Imidazole
$PqsR^{94-309}$ (Wildtype and mutants)	50 mM HEPES (pH = 8.5), 500 mM NaCl, 5% Glycerol, 20 mM Imidazole	,,
$PqsR^{94-332}$ (Wildtype and mutants)	50 mM HEPES (pH = 8.5), 500 mM NaCl, 5% Glycerol, 20 mM Imidazole	,,
$PqsA^{1-399}$, $HmqA^{1-430}$ and $HhqA^{1-430}$	50 mM Tris-HCl (pH = 8), 300 mM NaCl, 10 mM Imidazole, 1 mM DTT	,,

Table 2.12 IMAC buffer conditions

2.5.4 StrepTactin

Lysate containing Strep(II) tagged constructs were loaded onto a StrepTrap HP column at a flowrate of 1 ml/min. The column was washed with 10 CV of 100 mM Tris-HCl (pH = 8), 300 mM NaCl, 1 mM EDTA, 2 mM $MgCl_2$ & 1 mM DTT. Elution was achieved using 6 CV of buffer supplemented with 2.5 mM desthiobiotin. The 5 mL fractions were run on SDS PAGE to evaluate purity and pooled for preparative dialysis.

2.5.5 MBP Affinity chromatography

Lysate containing N-terminal MBP fusions[215] was prepared in 50 mM Tris – HCl (pH = 7.5), 500 mM NaCl, 1 mM EDTA, 1 mM DTT and 50 mM L -arginine/L – glutamate. The column was washed with 10 CV of buffer and eluted with 5 CV of Buffer supplemented with 10 mM D-maltose.

2.5.6 Anionic exchange (HiTrap Q)

Material containing the protein of interest was dialysed in low salt buffer consisting of 50 mM Tris – HCl, 0-50 mM NaCl and supplemented with 1 mM $MgCl_2$. The following day the dialysate was further diluted with the same buffer. The protein was loaded onto a HiTrap Q and washed with 5 CV of buffer. The column was eluted using a 60 mL linear gradient (0 – 1 M NaCl) on an AKTA FPLC system with a flow rate of 2.5 mL/min.

2.5.7 Heparin chromatography

DNA binding proteins were further purified using Heparin chromatography, fractions containing PqsR were dialysed as stated above with the exception that a higher salt concentration of 175 mM was used. The material was loaded onto a HiTrap Heparin HP and eluted on a linear gradient from 0.15 M to 1.5 M NaCl.

2.5.8 Gel filtration

Separation of protein by hydrodynamic radius was performed using either a 16/60 Superdex 75 or 16/60 Superdex 200 column. Sample was concentrated using a Vivaspin 20 (3/5/10K MWCO) to ≤ 5% of the column volume and clarified by centrifugation at 13,000 *x g* for 10 minutes. The material was loaded onto the column using an ATKA FLPC system with a flow rate of 0.8 mL/min. Isocratic elution was carried out collecting 2 – 5 mL fractions after the void volume had passed. Analytical gel filtration was carried out on a Superdex 200 10/300 GL using a flowrate of 0.75 mL/min with a sample injection volume between 100-500 µL. Elution buffer for each protein construct is listed below in Table 2.13.

Constructs	**Buffer**
Full length PqsR constructs	20 mM Tris-HCl (pH = 8), 200 mM NaCl, 0.5 mM TCEP*
MBP - PqsR	50 mM Tris-HCl (pH = 7.5), 500 mM NaCl, 50 mM L-Arginine/L-Glutamate, 10 mM D-Maltose
$PqsR^{94-309}$ (Wildtype and mutants)	20 mM Tris-HCl (pH = 7.4), 150 mM NaCl
$PqsR^{94-332}$ (Wildtype and mutants)	50 mM Tricine-NaOH (pH = 8), 250 mM NaCl, 2.5% Glycerol
$PqsA^{1-399}$, $HmqA^{1-430}$ and $HhqA^{1-430}$	20 mM HEPES (pH = 8), 150 mM NaCl, 1 mM TCEP
$PqsA^{Strep}$, $HmqA^{Strep}$ and $HhqA^{Strep}$	50 mM HEPES (pH = 8), 150 mM NaCl, 1 mM DTT

Table 2.13 Gel filtration buffers *TCEP was substituted for DTT in some instances. No effect on column retention time was observed.

2.5.9 Protein cleavage

Thrombin cleavage was performed during sample dialysis with 0.25 mM $CaCl_2$ and 1 U of recombinant Thrombin (BioUltra Sigma T9326) added per mg of target protein. TEV protease was purified from an *in vivo* self-cleaving MBP construct kindly provided by Prof. Hyojung Kim (Woosuk University) using Ni – NTA followed by dialysis. Prepared TEV was flash frozen at 1 mg/mL aliquots.

2.5.10 Chromatography performed on each construct

Constructs	**Columns used**
MBP tagged constructs	MBPTrap, Superdex 200 16/60
Full length PqsR constructs	HisTrap, Heparin, Superdex 200 16/60
PqsR ligand binding domain constructs	HisTrap, Superdex 75 16/60
PqsA, HmqA and HhqA constructs	StrepTrap, HiTrap Q, Superdex 75 16/60
P. aeruginosa extract	HisTrap Crude, Heparin HP, Superdex 200 10/300

Table 2.11 Chromatography columns used for each construct/protein source

2.5.11 *P. aeruginosa* protein expression

The ORF for *pqsR* was inserted into the medium-high copy number plasmid pUCP18 by restriction cloning with the addition of a C-terminal His tag introduced on the reverse primer. The shuttle vector was transformed into *P. aeruginosa* strain PAO1-L Δ*pqsR*. Colonies from the transformation were re-streaked onto fresh agar plates supplemented with 400 μg/mL carbenicillin. Presence of the plasmid was confirmed by colony PCR. A single colony was used to inoculate 50 mL of LB and incubated overnight at 30°C.

The following day the culture was washed to remove excess beta-lactamase generated by the carbenicillin resistance cassette to promote plasmid retention. The resuspended culture

was diluted by 1/100 in NZYCM media supplemented with 5 g/L glycerol and incubated at 37°C with continuous shaking at 200 rpm. To limit potential spillage of pathogenic material culture volume was limited to 200 mL in 1 L flasks. At an OD_{600} of 0.4-0.5 the cultures were induced with 1 mM IPTG and incubated for a further 4 hours at 30°C. Cells were harvested by centrifugation at 4000 *x g* for 1 hour. To aid lysis cells were washed with PBS (137 mM NaCl, 2.7 mM KCl, 10 mM Na_2HPO_4 and 1.8 mM KH_2PO_4) supplemented with 1 mM EDTA and 10% glycerol. The cell paste was washed again in PBS without supplements and pellets frozen in liquid N_2.

2.5.11.1 *P. aeruginosa* protein extraction

Pellets weighing ~ 5 g were thawed and resuspended in 30 mL lysis buffer consisting of 50 mM sodium phosphate (pH = 7.4), 250 mM NaCl and 1 mg/mL lysozyme. The suspension was incubated by gentle agitation for 30 minutes and proteases abated with Roche cOmplete™ protease inhibitor. Cell suspensions were decanted into Lyse Matrix B BigPrep tubes and lysed by 5 cycles of 30 seconds at 6 m/s in a FastPrep 24 system. Lysate was centrifuged twice at 10,000 *x g* for 30 minutes. Viscosity was further reduced by passing the lysate through a syringe needle several times and lysate filtered with a 0.45 μm syringe filter.

2.5.12 SDS Polyacrylamide gel electrophoresis (PAGE)

Discontinuous SDS PAGE gels were prepared for analysis of protein composition and relative abundance during recombinant protein purification. Depending on the M_r of the target protein a range of acrylamide concentrations in the resolving gel was utilised. The stacking gel was consistently prepared at 6%. The composition of each percentage gel is given in Table 2.12.

	Stacking	Resolving		
Component	6%	12%	14%	16%
SDW	2.6	2.6	2.1	1.6
Acrylamide (30%)	1	3.2	3.73	4.27
0.5 M Tris – HCl pH 6.8	1.25	-	-	-
1.5 M Tris – HCl pH 8.8	-	2	2	2
10% SDS	0.05	0.08	0.08	0.08
10% APS	0.05	0.08	0.08	0.08
TEMED	5	0.008	0.008	0.008
Total	5	8	8	8

Table 2.12 SDS PAGE composition. Stated volumes given in millilitres. SDW = Sterile distilled water.

Sample were prepared for SDS PAGE by adding 20 µL 5x SDS PAGE buffer to 80 µL sample. These samples were heated to 90°C for 10 minutes in a PCR thermocycler and loaded immediately after. Prestained Protein Marker Broad Range (11-250 kDa) NEB or Spectra™ Multicolor Broad Range Protein Ladder (Thermofisher) was loaded for size comparison. Electrophoresis was conducted in BioRad Mini-Protean tank; gels were initially run at 100 V for 10 minutes to allow for samples to stack followed by 180 V until the bromophenol blue dye front had reached the bottom of the gel.

2.5.13 Gel Staining

Gels were removed from the tank and washed with water to remove excess SDS. The gels were stained either with Coomassie R (in Methanol/Acetic acid) or with Quick Coomassie Stain from ProteinArk according to manufacturer's instructions and imaged with a mobile camera or BioRad Gel Doc.

2.5.14 Protein identification

Proteins were separated by SDS PAGE, stained with Coomassie and bands of interest excised and stored in 1.5 mL tubes. Protein identification was conducted by the Metabolomics &

Proteomics Laboratory, University of York with trypsin digestion followed by MALDI-TOF/TOF.

2.5.15 Protein quantification

Sample quantification was achieved using the Nanodrop 1000 (Thermofisher) by measuring absorbance at 280 nm. In each case the buffer was used as a blank and molecular extinction coefficient and molecular weight were provided to the software to produce a corrected mg/ml value. Values were calculated using the Expasy server with primary sequence input.

2.6 Biophysical and biochemical assays

2.6.1 Thermal shift assay (TSA)

TSA experiments were conducted in a 96 well plate format using an Applied Biosystems 7500 instrument. For $PqsR^{LBD}$ a master mix consisting of 500 μL of 1.5 mg/ml protein and 500 μL 40x sypro orange was prepared. 10 μL was dispensed into each well of a MIcroAmp qPCR plate with the except of two (No protein controls). For buffer screening 40 μL of 1.25x buffer/salt solution was added to each well. The plate was sealed with MicroAmp Optical Adhesive Film and briefly centrifuged at 300 *x g* for 3 minutes to enable thoroughly mixing of assay components. In the instrument the plate was incubated for 5 minutes at 30°C prior to 1°C/min ramping to 95°C. At each increment the fluorescence activity of the dye was measured using the SYBR Green filter set. Each condition was assessed in duplicate. The screening conditions are shown below in Table 2.13.

	1	2	3	4	5	6	7	8	9	10	11	12
A	Citrate 150 NaCl	Citrate 150 NaCl	MES 150 NaCl	MES 150 NaCl	PIPES 150 NaCl	PIPES 150 NaCl	MOPS 150 NaCl	MOPS 150 NaCl	TRIS 150 NaCl	TRIS 150 NaCl	HEPES 150 NaCl	HEPES 150 NaCl
B	Citrate 250 NaCl	Citrate 250 NaCl	MES 250 NaCl	MES 250 NaCl	PIPES 250 NaCl	PIPES 250 NaCl	MOPS 250 NaCl	MOPS 250 NaCl	TRIS 250 NaCl	TRIS 250 NaCl	HEPES 250 NaCl	HEPES 250 NaCl
C	Imidazole 150 NaCl	Imidazole 150 NaCl	Tricine 150 NaCl	Tricine 150 NaCl	Bicine 150 NaCl	Bicine 150 NaCl	Glycine 150 NaCl	Glycine 150 NaCl	No protein	No protein	Protein	Protein
D	Imidazole 250 NaCl	Imidazole 250 NaCl	Tricine 250 NaCl	Tricine 250 NaCl	Bicine 250 NaCl	Bicine 250 NaCl	Glycine 250 NaCl	Glycine 250 NaCl	UREA 250 mM	UREA 250 mM	MPD (5%)	MPD (5%)
E	NaCl 50 mM	NaCl 250 mM	NaCl 500 mM	KCl 10 mM	KCl 50 mM	KCl 150 mM	$MgCl_2$ 5 mM	$MgCl_2$ 20 mM	$MgCl_2$ 50 mM	$AmSO_4$ 10 mM	$AmSO_4$ 50 mM	$AmSO_4$ 150 mM
F	NaCl 50 mM	NaCl 250 mM	NaCl 500 mM	KCl 10 mM	KCl 50 mM	KCl 150 mM	$MgCl_2$ 5 mM	$MgCl_2$ 20 mM	$MgCl_2$ 50 mM	$AmSO_4$ 10 mM	$AmSO_4$ 50 mM	$AmSO_4$ 150 mM
G	Glycerol 2.5%	Glycerol 5%	Glycerol 10%	Glycerol 20%	EG 2.5%	EG 5%	EG 10%	EG 20%	DMSO 1%	DMSO 2%	DMSO 5%	DMSO 10%
H	Glycerol 2.5%	Glycerol 5%	Glycerol 10%	Glycerol 20%	EG 2.5%	EG 5%	EG 10%	EG 20%	DMSO 1%	DMSO 2%	DMSO 5%	DMSO 10%

Table 2.13 Screening conditions for $PqsR^{LBD}$. Buffers coloured in green with pH chosen in accordance to the pKa. Salts and organics coloured in blue and yellow respectively. (MES = 2-morpholin-4-ylethanesulfonic acid, PIPES = piperazine-N,N'-bis(2-ethanesulfonic acid, MOPS = 3-(N-morpholino)propanesulfonic acid, MPD = 2-Methyl-2,4-pentanediol, EG = Ethylene glycol, AmSO4 = Ammonium sulphate and DMSO = Dimethylsulfoxide).

For fragment screening using this method the assay was altered to include 5 μL of compound from a concentrated DMSO stock to a final concentration of 250 μM or 500 μM. The concentration of the buffer remained the same as the dye was diluted into 1.25 buffer prior to use.

TSA on full length PqsR

The full length PqsR was assessed by this method with a few modifications. The concentration of the protein was lowered to 1 mg/ml and buffers and salts were tested more exhaustively by two independent experiments. The screening conditions are shown in Tables 2.14 & 2.15.

	1	2	3	4	5	6	7	8	9	10	11	12
A	Citrate 150	Citrate 150	Cacodylate 150	Cacodylate 150	MES 150	MES 150	PIPES 150	PIPES 150	MOPS 150	MOPS 150	PO_3 150	PO_3 150
B	Citrate 250	Citrate 250	Cacodylate 250	Cacodylate 250	MES 250	MES 250	PIPES 250	PIPES 250	MOPS 250	MOPS 250	PO_3 250	PO_3 250
C	Tris 150	Tris 150	HEPES 150	HEPES 150	Imidazole 150	Imidazole 150	Tricine 150	Tricine 150	Bicine 150	Bicine 150	Glycine 100	Glycine 100
D	Tris 250	Tris 250	HEPES 250	HEPES 250	Imidazole 250	Imidazole 250	Tricine 250	Tricine 250	Bicine 250	Bicine 250	Glycine 250	Glycine 250
E	NaCl 100	NaCl 100	NaCl 150	NaCl 150	NaCl 250	NaCl 250	NaCl 500	NaCl 500	KCl 50	KCl 50	KCl 150	KCl 150
F	KCl 250	KCl 250	KCl 500	KCl 500	$AmSO_4$ 50	$AmSO_4$ 50	$AmSO_4$ 100	$AmSO_4$ 100	$AmSO_4$ 200	$AmSO_4$ 200	$AmSO_4$ 250	$AmSO_4$ 250
G	$MgCl_2$ 10	$MgCl_2$ 10	$MgCl_2$ 50	$MgCl_2$ 50	$LiSO_4$ 500	$LiSO_4$ 500	$LiSO_4$ 1000	$LiSO_4$ 1000	$LiSO_4$ 1500	$LiSO_4$ 1500	$MgSO_4$ 10	$MgSO_4$ 10
H	$MgSO_4$ 50	$MgSO_4$ 50	$CaCl_2$ 20	$CaCl_2$ 20	$CaCl_2$ 50	$CaCl_2$ 50	MPD 1%	MPD 1%	No protein		Protein (No additive)	

Table 2.14 Screening conditions for full length PqsR – Buffers and Salts. Buffers coloured in green and salts in yellow. Abbreviations are the same as stated in Table 2.13 with the addition of PO_3 = Sodium phosphate buffer.

	1	2	3	4	5	6	7	8	9	10	11	12
A	5% Glycerol	5% Glycerol	10% Glycerol	10% Glycerol	20% Glycerol	20% Glycerol	5% EG	5% EG	10% EG	10% EG	20% EG	20% EG
B	50 mM Glucose	50 mM Glucose	100 mM Glucose	100 mM Glucose	250 mM Glucose	250 mM Glucose	100 mM Trehalose	100 mM Trehalose	200 mM Trehalose	200 mM Trehalose	500 mM Trehalose	500 mM Trehalose
C	50 mM NaAc	50 mM NaAc	150 mM NaAc	150 mM NaAc	50 mM KAc	50 mM KAc	150 mM KAc	150 mM KAc	50 mM AmAc	50 mM AmAc	150 mM AmAc	150 mM AmAc
D	50 mM $NaSO_4$	50 mM $NaSO_4$	150 mM $NaSO_4$	150 mM $NaSO_4$	250 mM $NaSO_4$	250 mM $NaSO_4$	1% Ethanol	1% Ethanol	2% Ethanol	2% Ethanol	5% Ethanol	5% Ethanol
E	50 mM Urea	50 mM Urea	250 mM Urea	250 mM Urea	500 mM Urea	500 mM Urea	1% DMSO	1% DMSO	2% DMSO	2% DMSO	5% DMSO	5% DMSO
F	50 mM Gua-HCl	50 mM Gua-HCl	250 mM Gua-HCl	250 mM Gua-HCl	500 mM Gua-HCl	500 mM Gua-HCl	50 µM 488	50 µM 488	250 µM 488	250 µM 488	500 µM 488	500 µM 488
G	50 µM fQZN	50 µM fQZN	250 µM fQZN	250 µM fQZN	500 µM fQZN	500 µM fQZN	50 µM Frag 15	50 µM Frag 15	250 µM Frag 15	250 µM Frag 15	500 µM Frag 15	500 µM Frag 15
H	Me-HHQ	Me-HHQ	5 mM DTT	5 mM DTT	1 mM TCEP	1 mM TCEP	Tween 0.05%	Tween 0.05%	Tween 0.1%	Tween 0.1%	Protein (No additive)	

Table 2.15 Screening conditions for full length PqsR – Additives. Colour key: Small organics and sugars coloured in yellow, salts in blue, solvents in grey, chaotropic denaturants in purple, ligands in green and reducing agents and detergents in white (compound 488 is characterised in chapter 3 and fragments fQZN and 15 shown in chapter 5). Acetate is abbreviated to Ac in salts and guanidinium to Gua.

Data analysis

Data was exported as an .xls file from the Applied Biosystems 7500 control software and analysed by NAMI as distributed by the following GitHub repository: “grofte/NAMI”. Waterfall plots were generated using NAMI with the addition of a .sol file giving buffer condition and concentration.

2.6.2 Isothermal titration calorimetry (ITC)

Fragment and lead-like compound binding to the $PqsR^{94-332}$ was characterised by ITC. Flash frozen protein was thawed and clarified by centrifugation. The sample was dialysed overnight against 250 mL of buffer with constant stirring and a change after 2 hours. The sample was further clarified and quantified by triplicate readings using A280 accounting for an ε of 22920 M^{-1} cm^{-1}. The sample was diluted to a value between 25 – 200 µM with ITC buffer compensating for additional dilution by co-solvent DMSO. The ligand of interest was dissolved in DMSO and diluted as appropriate in dialysis buffer such that the final concentration of DMSO matched that of the protein solution. ITC measurements were conducted on a Malvern MicroCal PEAQ by first rinsing the sample cell with 280 µL buffer followed by protein sample. Ligand was injected into the sample with 19 injections of 2 µL. To observe saturation of weak binders higher concentration in the syringe was used such as x20 or x40 compared to [sample]. Titrations were conducted at 25°C using syringe mediated stirring of 750 rpm with a reference power set to 6 DP. Ligand injection spacing was set to 180 seconds to allow for baseline stabilisation between injections. Ligand to buffer titrations were used as controls to ensure heats of dilution were weak. Data was analysed using the Malvern ITC analysis software. To account for weak binding of fragments N values were often fixed to 1.

2.6.3 SAXS analysis

Samples of FL-PqsR and $PqsR^{LBD}$ were subjected to SAXS on DLS beamline B23. In the case of FL-PqsR the protein was thawed from the frozen aliquot and gel filtrated using an analytical Superdex 200 10/300 column in a mobile phase consisting of 50 mM Tris – HCl (pH = 8), 200 mM NaCl and 1 mM TCEP to remove HMW material. The sample was centrifuged to remove aggregates and provided with matched buffer for SAXS analysis. Data collection was kindly performed by Dr Alice Goode. For $PqsR^{LBD}$ the protein was dialysed against a buffer of 20

mM Tris-HCl, 150 mM NaCl and 1 mM TCEP (crystallisation buffer supplemented with reducing agent). The sample was centrifuged and collected at a concentration series starting with 3.1 mg/mL (125.8 µM). Data collection was kindly performed by Prof. Boyan Bonev and Sara Zandomeneghi. Data was analysed using the PRIMUS (part of the ATSAS suite, EMBL[216]) to determine scattering parameters and the program DAMMIF was used for shape determination. Fitting of experimental structures to SAXS data was performed using Crysol.

2.6.4 Circular Dichroism (CD)

Samples for CD analysis were buffer exchanged using a PD-10 de-salting column followed by further dialysis into a low chloride buffer (replaced by NaF) with 10 mM sodium phosphate buffer. CD experiments were performed at B23 (DLS proposal 29624-1). Due to restrictions CD experiments were performed by Dr Rohanah Hussain and Dr Tiberiu-Marius Gianga on a Chiroscan instrument (AppliedPhotophysics) and SRCD custom instrument. To aid sample solubility, that favoured chloride anion, concentrated HCl was added to samples just prior to experimentation.

2.6.5 Gel filtration complex experiments

LysR box DNA (sequence shown below), was annealed by mixing DNA to 100 µM concentration (equimolar) and heated to 90°C for 10 minutes followed by a decrease of 1°C per minute until room temperature and considered to be a 100 µM of annealed duplex product hereafter. Fusion protein and duplex DNA were combined, at different molar ratios, and incubated for 1 hour at room temperature prior to loading 200 µL of sample onto a Superdex 200 10/30 column equilibrated with 25 mM Tris-HCl, 200 mM NaCl, 0.1 mM EDTA and 0.5 mM TCEP with a flow rate of 0.5 ml/min.

Sequence (5’ – 3’)
TTCGGA**G**TCCGAA
TTCGGA**C**TCCGAA

2.6.6 PqsA enzyme assays - absorbance

Determination of anthraniloyl – CoA activity was assessed by measuring product formation at 365 nm. Substrate concentrations were determined based upon dissolved mass with the

exception of ATP which was reconstituted from a heterogenous hydrate and quantified by absorbance at 259 nm using the known molar extinction coefficient of E = 15,400 M^{-1} cm^{-1}. A master mix consisting of 100 mM HEPES – NaOH (pH = 8), 1 mM ATP (disodium salt), 0.5 mM coenzyme A (trilithium salt), 0.5 mM DTT, 2 mM $MgCl_2$ and 100 nM PqsA was assembled and prewarmed at 37°C in a heat block for 3 minutes. The master mix was dispensed into a UV-Star® 96 well plate containing 17.5 µL inhibitor diluted from a 50 mM stock solution (5% final DMSO). Inhibitor concentrations were pre-selected based on prior experimentation using a gradient of concentrations and observed solubility in reaction buffer. The reaction was allowed to incubate for a further 5 minutes at 37°C and reaction initiated by addition of 17.5 µL anthranilic acid (1 mM). Readings were taken on a TECAN SPARK at 5 second intervals for 5 minutes. Each reaction was repeated at least once. Determining mode of inhibition with respect to anthranilate was difficult due to a high K_M that could not be accurately determined. Linear rates were determined using Graphpad PRISM version 7 and plotted with Michaelis-Menton kinetics to elucidate inhibition mode.

2.6.7 LC – MS

Analysis of enzyme reaction products were evaluated using Liquid Chromatography coupled to Mass Spectrometry (LC -MS). Reactions were prepared as stated above but with a reduced reaction volume of 200 µL. Reactions were initiated with the addition of anthranilic acid and incubated at 37°C for 5 minutes. 20 µL of each reaction mixture was added to 200 µL of methanol and thoroughly vortexed. The sample was centrifuged at 10 minutes at 13,000 *x g* to remove precipitated protein material. 100 µL from the top of the solution was taken for further analysis. Semi-quantification with was performed by Dr Nigel Halliday using a Qtrap 6500 hybrid triple-quadrupole linear ion trap mass spectrometer in tandem with an Exion LC system (Sciex) with Phenomenex Synergi Hydro RP column (150 x 2 mm, 4µm.

In the absence of an authentic synthetic standard of anthraniloyl-CoA, a surrogate Co-A compound was used to assist in tuning the mass spectrometer for selected reaction monitoring (SRM). Under positive electrospray conditions, collision induced dissociation of CoA-derivatives leads to a prominent fragmented ion due to the neutral loss of m/z=507[217].

Therefore, an infusion of acetyl-CoA solution was used to set appropriate MS parameters that induce this characteristic fragmentation.

Under positive electrospray conditions, the singly charged protonated precursor ion of anthraniloyl-CoA, m/z=887.2, was fragmented to a product ion of m/z=380.1 using a collision energy of 49, de-clustering potential of 56 and collision cell exit potential of 15.

Samples were injected and migrated with a gradient elution consisting of 100% mobile phase A (50 mM NH_4OAc) for 1 minute followed by an increase to 5% B (100& MeCN) at 1.4 minutes, 25% B at 7 min and 40% B at 8 min. After a further 3 minutes the gradient was returned to 0% B (total elution volume 15 minutes). Using these conditions, detected anthraniloyl-CoA gave a chromatographic peak with a retention time of 6.31 minutes.

For IC_{50} determination a gradient of inhibitor was incubated with reaction without anthranilic acid for 10 minutes. 5 minutes after addition of anthranilic acid (optimised for linearity based on absorbance assay – Appendix 9.17) samples were removed and quantified. A slope was plotted using 4 variables in Prism 8 with no constraints.

2.7 Docking

PqsA docking of inhibitor ZN8751275 was performed with AutoDock vina[218] using PDB model 5OE5[219]. The protein was prepared by deleting water except for 1081/A which bridges the amine of the anthranilic acid and Glu 162 and 1184/A that forms multiple contacts to the ribose ring and carbonyl preceding the phosphoester bond. Polar hydrogens were added, and grid of suitable size drawn using Autodock Tools[220].

Exhaustiveness was optimised using the co-crystal ligand of anthraniloyl – AMP requiring a value of 24 to find a pose in good agreement with experimental data. Grid parameters are stated in Table 2.17.

Table 2.16 Docking parameters for PqsA (PDB 5OE5). (Stated values in Å)

Parameters	Active site	Hinge site
Centre *x*	-20	-32
Centre *y*	18	7
Centre *z*	-14	-18
Size x	18	14
Size y	12	30
Size z	14	18

2.8 Crystallography

2.8.1 Condition screening in nanolitre volumes

Crystallisation conditions were screened using Swissci 96-Well 2-Drop Plates. 80 µL of precipitant solution were dispensed into the reservoir well. Protein solution, pre-centrifuged to remove aggregated material, of two different concentrations were dispensed using a Mosquito liquid handling system (SPT Labtech). Typically, 200 nL of protein material was dispensed into wells 1 & 2 with the same volume of precipitant solution added. The plate was sealed using either tape (HD Clear) or EasySeal sheets (Molecular dimensions). Plates were monitored for crystal growth after set-up and at regular intervals thereafter.

2.8.2 Additive screening

Additive screening was attempted using two Additive screens: Additive Screen HT (Hampton) and ANGSTROM Additive Screen™ (Molecular dimension). For testing in a 96 well set up using the Mosquito 150 nL of reservoir was combined with 50 nL of additive solution. For 48 well plate preparation a 4 µL drop was prepared with the ratio 1:0.8:0.2 of protein sample, reservoir, and additive.

2.8.3 InFactorial Sceening

InFactorial screening matrices were calculated using MIMER[221] and formulated by stock dilution into 2 mL blocks with a total volume > 1 mL. Composition of the two INFAC screens are detailed in Appendix 9.2 and are based on lithium sulphate as the primary precipitant

set to concentrations between 1.2-1.7M with 50 mM cacodylate or MES buffering agent (pH 6 – 6.5) and additional salt concentration of 10 – 20 mM magnesium or potassium acetate. Additives used in the broader INFAC included ethylene glycol, 2-Methyl-2,4-pentanediol, ammonium acetate or imidazole.

2.8.4 Preparation of seed stock

Seed stocks were created using MicroSeed Beads (Molecular Dimensions) according to the manufacturer's instructions such that crystals were crushed using a microtool and transferred into a 1.5 mL tube in 10 µL volumes of reservoir solution until a solution of 50 µL had been attained. The tube was vortexed for three minutes and an additional 450 µL of reservoir added. The stock was aliquoted into PCR tubes at 50 µL volumes and frozen at -80°C.

2.8.4.1 Microseed matrix seeding (MMS)

For MMS a 600 nL drop was set up using the Mosquito using 300 nL of protein sample, 200 nL precipitant and 100 nL seed stock. Reservoir volume remained the same (80 µL).

2.8.4.2 Manual seeding

For manual seeding experiments using a seed stock 10% of the final drop volume was added. Streak seeding was performed by dipping a hair (beard) into the seed stock and streaking it through the drop or by moving the hair through an undisturbed drop prior to moving it through the recipient drop.

2.8.5 In gel crystallisation

Gel crystallisation was adapted from a published protocol in *Lorber, et al* (2009)[222]. Briefly, a 2% (w/v) stock solution of Low Melting point Agarose (UltraPure™ Thermofisher) was prepared with milli-Q water and thoroughly dissolved by heating and filtered to remove particulates. Crystallisation drops were prepared by adding agarose, equilibrated to above gelation temperature in a heat block, to the drop at a final concentration of 0.2-0.5%. All experiments were conducted in sitting drop format in either 48 well MRC or 24 well Crychem plates.

2.8.6 Soaking experiments: $PqsR^{94-309}$ with antagonists

For PqsR antagonist structural determination Ligand Binding domain (LBD) crystals were grown in either 24 well hanging drop Cryschem Plate or sitting drops with the precipitant solution containing 100 mM trisodium citrate, 200 mM ammonium acetate and 2-Methyl-2,4-pentanediol (MPD). Both citrate pH (5.5 – 6.5) and MPD (3%-10%) concentration was varied along the plate's X and Y axis respectively (shown in Appendix 9.1). Soaking was conducted in wells with large single crystals. For soaking the compounds were dissolved in a multi-component solution consisting of MPD, ethylene glycol, water and DMSO and added directly to the drop at ten times the initial protein concentration. After 16 hours of soaking the crystal was cryocooled in a solution of artificial reservoir supplemented with 25% MPD or 25% glycerol/ethylene glycol.

2.8.7 Data collection parameters

All diffraction experiments were conducted at Diamond Light Source (DLS) using the following data collection parameters listed below in Table 2.17.

Sample name (Protein_Ligand)	Beamline	Resolution (Å)	Wavelength (Å)	Transmission (%)	Images (no.)	Total Oscillation (°)
$PqsR^{94-309}$_SEN89 (mixed isomer)	I24	2.7	0.9686	20	1800	180
$PqsR^{94-309}$_SEN19	I04	2.45	0.9795	100	1000	100
$PqsR^{94-309}$_AM159-089	I04-I	2.5	0.9159	75	900	90
$PqsR^{94-309}$_LUI195-93	I24	2.5	0.9686	5.09	1800	180
$PqsR^{94-309}$_AM204-004	I04	2.71	0.9795	100	1000	100
$PqsR^{94-309}$_AM204-25	I04	2.5	0.9795	100	600	90
$PqsR^{94-309}$_AM204-42	I04	2.5	0.9795	100	600	90
$PqsR^{94-309}$_AM204-21	I04	2.5	0.9795	100	600	90
$PqsR^{94-309}$_SG129-192	I24	2.5	0.9686	20	900	90
$PqsR^{94-309}$_SG192-173	I04	2.2	0.9795	100	900	90
$PqsR^{94-309}$_ SG192-177	I04	2.2	0.9795	100	1800	180
$PqsR^{94-309}$_ SG192-183	I04	2.2	0.9795	100	900	90
$PqsR^{94-309}$_SG192-127	I04	2.2	0.9795	100	900	90
$PqsR^{94-309}$_488* (two datasets)	I24	2.5	0.9687	50.46	360	180
$PqsR^{94-309}$ S123C_SEN89 (R isomer)	I24	2.5	0.9998	26.57	900	180
$PqsR^{94-309}$ K154A K214Y	I24	2	0.9999	49.3	900	180
$PqsR^{94-309}$ DR	I24	1.9	0.999	31.69	900	180

Table 2.17 Data collection information from diffraction experiments at DLS

2.9 Structural solution

2.9.1 Antagonist determination

As the $PqsR^{LBD}$ crystals were isomorphous to the apo-crystals previous reported for the $PqsR^{94-309}$ construct[155] the ligands were identified by rigid body refinement with REFMAC[223] using 4JVC with MPD solvent removed from the binding pocket. Ligand restraints (CIF format) were generated using AceDRG[224] and ligand fitting was performed using COOT[225]. Using COOT's find ligand function the ligand was fitted into difference density (assessed at 3 σ). The structure was further refined iteratively using REFMAC and coot with model quality assessed using MOLPROBITY. Fitting of the ligand generally decreased R/R_{free} in each model.

2.9.2 Solving PqsR construct derivatives

The K154A K214Y mutant was initially processed into space group $P4_122$ but molecular replacement using PHASER with the 4JVC input model showed the enantiomeric space group $P4_322$ to be the correct solution giving a very high Log-likelihood gain (LLG) of 1162.29 and packing score of 36.86 (TFZ). Further refinement was carried out in REFMAC and COOT with the latter used to modify the mutated residues. Final refinement was carried out with PBD-REDO.

The loop mutant DR was processed into $P12_11$ but phasing by molecular replacement initially failed. Phasing with MrBump found a marginal solution that yielded excellent and interpretable electron density. Further building was carried out in Buccaneer and repeated COOT and REFMAC cycles. Non-crystallographic symmetry (NCS) was accounted for in refinement with chains A and B aligned. However, due to the NCS higher than expected R factors are observed with the R_{free} at 10% above resolution.

2.10 Negative staining

Negative stain of PqsR was conducted by Dr Sigrun Maurer using the following method. A solution of PqsR was centrifuged at 16,000 *x g* for 10 minutes and diluted to ~0.001-2 mg/mL. Carbon coated copper grids (R1.2/1.3, 400 mesh – Quantifoil Microtools GmbH) were prepared by glow discharge for 60 seconds at 15 mA on Agar using a Turbo Carbon Coater glow discharge unit. A protein drop size of 3 - 8 µL was pipetted onto a grid and

blotted with 8 µL of 2% uranyl acetate and incubated for 1 minute prior to further blotting. Observations were made on a JEOL 2100plus TEM LaB6 with Gatan Ultrascan camera, operated at 200 kV. Images were viewed and contrast optimised with ImageJ.

2.11 Phenotypical assays: CTX::P_{pqsA}-*lux*

2.11.1 IC_{50} determination: Luminescence bioreporter

IC_{50} measurements were conducted on a Greiner black bottom 96 well plate. A concentration series of antagonist was prepared in DMSO and diluted in LB such that the final concentration progressed in a half logarithmic scale from 100 µM to 0.01 µM with a final DMSO concentration of 0.1%. Overnight cultures of PAO1 – L mCTX::*PpqsA*-lux were diluted to 0.01 OD_{600} in fresh LB. Volumes of 200 µL were dispensed and incubated at 37°C statically with cell density and relative light unit (RLU) readings being taken every 15 minutes for 16 hours. The maximum RLU/OD_{600} reading was taken and IC_{50} calculated using GraphPad PRISM fitting to log(inhibitor) vs. response (three parameters) model. In the case of weak antagonists when solubility impeded the analysis of sufficiently high concentrations necessary to invoke a convincing bottom plateau a constraint was applied to the of remaining activity after treatment with 10 µM SEN19. This model assumes that increasing concentration of the antagonist/inhibitor of interest would reach this value.

2.11.2 EC_{50} determination

To determine compound activation of the P_{pqsA} promoter. A Δ*pqsA* mutant (non-AQ producing) with the chromosomal mCTX::P_{pqsA}-*lux* insertion was incubated with concentrations of agonist from 10 µM to 0.001 µM in half-logarithmic intervals. Maximum RLU (observed between 6 - 7.5 hours) were normalised to cell density. EC_{50} was calculated using PRISM 9 using a four-parameter dose-response curve.

2.11.3 Synergy determination

To determine the pharmacological effect of 2 lead compounds both were trialled together in a concentration matrix on PAO1 – L mCTX::P_{pqsA}-*lux.* 8 Half log concentrations of both agents were used to generate an activity matrix based on remaining luminescence activity observed between 6 – 7.5 hours. The matrix was prepared in Microsoft Excel and uploaded to SynergyFinder web server[226]. Dose-activity relationships were fitted to the LL4 setting and

Zero Interaction potency (ZIP) was chosen as the synergy model characterised by the assumption that non-interacting drug partners produce negligible changes in one another's dose-response and deviation from this expected result is indicative of a synergistic or antagonistic relationship[227].

2.11.4 Complementation experiments

Complementation experiments were conducted using two methodologies. To determine mutant functionality pME6032::*pqsR*-His and mutant derivatives were transformed into a Δ*pqsR* strain with mCTX::P_{pqsA}-*lux*. Expression was induced with either varying concentrations of IPTG or IPTG was fixed at 50 µM. RLU and cell density was monitored as described above. To determine agonist binding expression was induced with 50 µM IPTG and 40 µM AQs (representing excess compared to physiological concentration).

2.12 Phenotypical testing: Extracellular products & growth dynamics

2.12.1 Growth profile

Overnight PAO1 - L cultures were re-diluted to 0.01 OD_{600} in biological triplicate and added to microtitre plates. Cells were grown at 37°C with agitation every 15 minutes lasting 3 seconds. Growth was measured every 15 minutes at OD_{600} and data plotted in PRISM using a logistical growth model to evaluate rate and peak growth (with data truncated prior to culture decline).

2.12.2 Pyocyanin

Biological triplicate 10 mL cultures of PAO1 and Δ*pqsA* control mutant were prepared in 100 mL flasks by dilution of overnight cultures to 0.01 OD_{600}. Test compounds were added to 3 times IC_{50} value (determined by transcriptional fusion) with a final DMSO concentration of 0.2%. Cultures were incubated at 37°C for 16 hours. Supernatant was prepared by centrifugation at 10,000 *x g* for 10 minutes followed by syringe filtering (0.22 µm). Organic extraction of pyocyanin was formed by adding 4.5 mL of chloroform to 7.5 mL of supernatant. After vigorous mixing the phases were settled by centrifugation and organic layer removed. The organic layer was collected and acidified with 1.5 mL of 0.2 M HCl. The resultant solution was thoroughly mixed and separated. The acid layer was removed and

read in a spectrophotometer at OD_{520}. Readings were normalised to the untreated control cultures.

2.12.3 Elastase

Cultures were prepared as stated above and 100 µL of supernatant was collected for elastase quantification. A solution of 20 mg/mL Elastin-Congo Red was prepared in ECR buffer consisting of 100 mM Tris – HCl, 1 mM $CaCl_2$ (pH 7.4). Using frequent mixing to keep solid substrate in a homogenous suspension 900 µL of Elastin-Congo Red was added to the collected supernatant and incubated at 37°C with shaking at 200 rpm. The enzymatic reaction was carried out for 4 hours and stopped by removal of physical substrate by centrifugation and reading the absorbance of the supernatant at OD_{494}. Readings were normalised to account for cell density. A Δ*lasR* mutant was used as a low producing control.

2.12.4 eDNA

DNA precipitation was conducted on supernatants to assess the impact of compounds on eDNA release. Briefly, 50 µL of 3 M sodium acetate was added to 450 µL of supernatant followed by 1.5 mL of ice-cold 100% ethanol. The sample was thoroughly mixed and DNA allowed to precipitate during an overnight incubation at -20°C. Precipitated DNA was collected by centrifugation and pellet washed twice with 70% ethanol. After decanting the final wash, the pellets were dried on a heat block set to 50°C. The pellets were resuspended in dH_2O and measured on a Nanodrop 1000.

2.12.5 Pyoverdine

Pyoverdine release in the presence of PqsA inhibitor was assessed by fluorescence assay. To increase siderophore release experiments were conducted in iron deficient CAA and RPMI medias. Overnight cultures of *P. aeruginosa* were washed three times in PBS and diluted to 0.002 OD_{600} in CAA media or RPMI. PqsA inhibitor and PqsR antagonist was added at 3 times the IC_{50} respectively with a final DMSO concentration of 0.2%. A low pyoverdine control was added in the form of iron ($FeCl_3.6H_2O$) supplementation to 40 µM. Fluorescence and cell density measurements were performed on an Infinite 200 Pro TECAN plate reader with fluorescence monochromator. Every 15 minutes fluorescence was measured using an

excitation wavelength of 405 nm and emission measured at 460 nm with a gain of either 50 or 75 and cell density monitored as previously stated.

2.12.6 AQ extraction procedure and quantification

To quantify AQ content of *P. aeruginosa* supernatant triplicate 5 mL cultures were prepared from single colonies in the presence of DMSO or inhibitor. After 16 hours, 1 mL of sample was centrifuged at 10,000 *x g* for 10 minutes followed by filtering through a 0.2 µm syringe filter. 100 µL of supernatant was diluted with 390 µL of fresh media and 10 µL of 7Cl-7C-PQS (internal standard) to a final concentration of 200 nM. 500 µL of acidified ethyl acetate was added to the supernatant dilution and samples shaken for 3 minutes at 200 rpm. Samples were left to stand for 5 minutes and organic layer was transferred into a new tube. This procedure was repeated twice more until the final volume of organic extract reached 1.5 mL.

Quantification with respect to synthetic standard 7Cl-7C-PQS was performed by Nigel Halliday, experimental officer at the University of Nottingham.

2.12.7 Statistical testing

Unless otherwise stated statistical testing was conducted using one way ANOVA with Tukey post-hoc multiple comparisons testing with Graphpad PRISM 9. P values are denoted as stars: P *≤ 0.5; *, P ≤ 0.01; ***, P ≤ 0.001 and ****, P≤ 0.0001.*

3 Structural elucidation of $PqsR^{LBD}$ in complex with antagonists

3.1 Introduction

As described in 1.6 PqsR has a large binding pocket (calculated volume of 858.8 $Å^3$) and is subdivided into two subpockets. These subpockets A and B host the hydrophobic alkyl chain and quinolone moiety from the native AQ ligands[155]. In terms of lead development, PqsR presents an interesting challenge due to a high degree of hydrophobicity that limits the potential for hydrogen bonding. This necessitates the need for bulky constituents to gain potency whilst balancing chemical properties to allow for cell and biofilm penetration. Ligand analogues of native AQs and previous HTS has yielded compounds possessing biological potency with effects on virulence and pathogenicity suggesting that the target is readily druggable[115 184 177] (described in Chapter 1.7.4).

As described in Chapter 1.9 a HTS campaign using a *P. aeruginosa* bioreporter was conducted that elucidated several high potency hits against PqsR. These were subsequently taken for medicinal chemistry optimisation. The compounds shown in Table 3.1 are the initial hits and derivatives from this HTS and are grouped into 5 distinct series based upon their initial hit reference: SEN66, SEN32, SEN19 and SEN89. The last series – 488 – was not discovered in the SENBIOTAR HTS campaign but was produced as part of a collaboration with Unilever. It was initially derived from a secondary metabolite screen from a natural library bank conducted by Unilever. Prior to this study each compound series had been subjected to molecular docking to build a model of binding.

3.2 Compound used in soaking studies

To further aid optimisation of each compound series soaking into PqsR crystals was conducted to elucidate the binding pose of each ligand and identify interactions within the binding pocket. The ligands successfully elucidated are summarised in Table 3.1 below with associated antagonist series noted.

Table 3.1: Ligands complexed with PqsR^{LBD}

Name	Structure	Series / Head group	Molecular weight	Reported IC_{50} (μM)[1]	Lipophilicity (LogP)[2]
LUI195-93	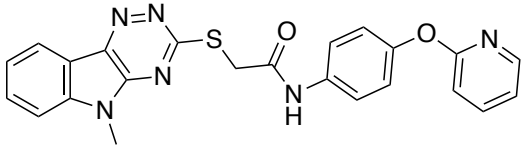	SEN66 1-((5-methyl-5*H*-[1,2,4]triazino[5,6-*b*]indol-3-yl)thio)propan-2-one	442.5	0.25 ± 0.12 0.34 ± 0.03	3.67
SG192-183	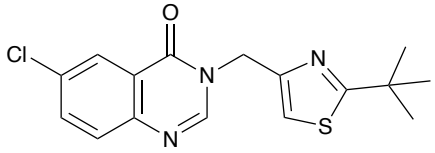	SEN32 6-chloro-3-(thiazol-4-ylmethyl)quinazolin-4(3H)-one	333.83	0.397 ± 0.14 0.65 ± 0.04	4.07
SG192-127	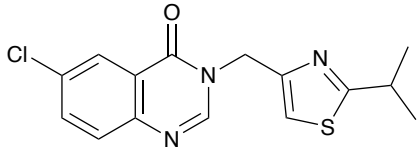	SEN32 6-chloro-3-(thiazol-4-ylmethyl)quinazolin-4(3H)-one	319.81	1.05 ± 0.42 1.58 ± 0.36	3.46
SG192-173	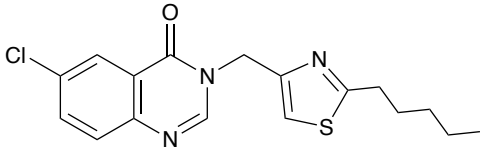	SEN32 6-chloro-3-(thiazol-4-ylmethyl)quinazolin-4(3H)-one	347.86	0.31 ± 0.16 0.34 ± 0.04	4.55

SG192-177	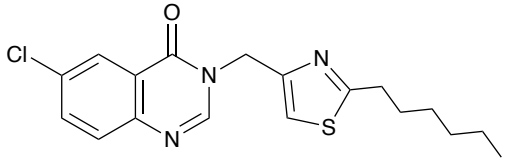	SEN32 6-chloro-3-(thiazol-4-ylmethyl)quinazolin-4(3H)-one	361.1	0.3 ± 0.18 0.27	4.81
SEN19	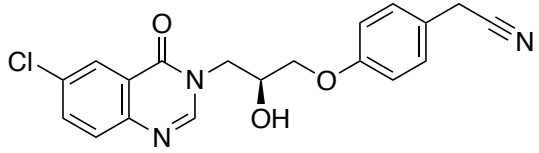	SEN19 (*S*)-6-chloro-3-(2,3-dihydroxypropyl)quinazolin-4(3*H*)-one	369.81	11.0 ± 0.8 1.1± 0.35	2.33
AM159-089	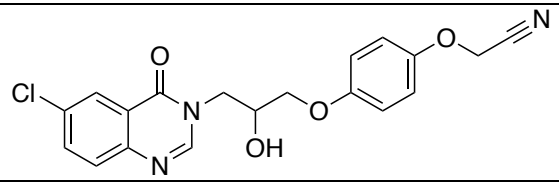	SEN19 (*S*)-6-chloro-3-(2,3-dihydroxypropyl)quinazolin-4(3*H*)-one	385.80	27.6 ± 1.3	2.21
SEN89	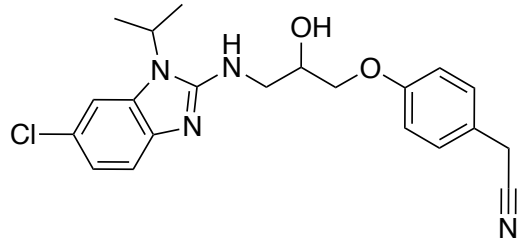	SEN89 6-chloro-1-isopropyl-*N*-methyl-1*H*-benzo[*d*]imidazol-2-amine	398.89	0.14 ± 0.05 0.09 ± 0.01	4.34
AM204-004	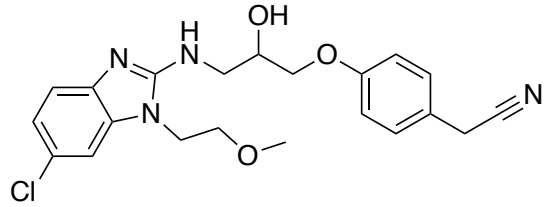	SEN89 6-chloro-N-methyl-1H-benzo[d]imidazol-2-amine	414.89	0.18 ± 0.04 0.12 ± 0.04	3.63

AM204-025	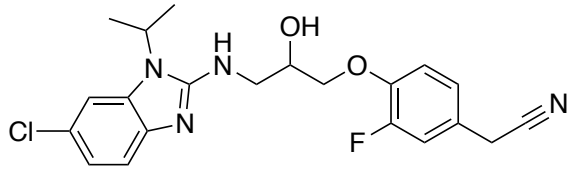	SEN89 6-chloro-1-isopropyl-N-methyl-1H-benzo[d]imidazol-2-amine	416.88	0.05 ± 0.02 0.12 ± 0.02	4.34
AM204-42	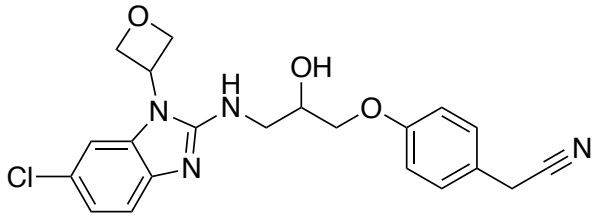	SEN89 6-chloro-N-methyl-1-(oxetan-3-yl)-1H-benzo[d]imidazol-2-amine	412.87	0.15 ± 0.01 0.32 ± 0.08	3.60
488[3]	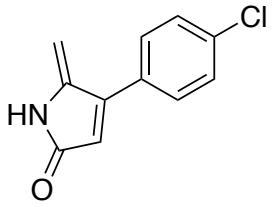	Lactam series 4-(4-chlorophenyl)-5-methylene-1,5-dihydro-2*H*-pyrrol-2-one	205.64	21.72 ± 0.71 19.84 ± 3.2	2.85

1. IC_{50} determinations conducted by or under the supervision of Dr Pantalone, Ruiling Ru, Scott Grossman and Alaa Mushabi using CTX::P_{pqsA}-*lux* bioreporter assay performed in technical and/or biological triplicate . Values given with respect to strains PAO1 – L (top) and PA14 (bottom).
2. cLogP (Lipophilicity) calculated with ALOGPS 2.1 server
3. 488 from Unilever lactam collection supplied by Dr Pantalone

3.3 Protein construct for crystallisation

For structural elucidation of antagonist complexes the construct developed in *Ilangovan, A.* (2011) containing the *pqsR* coding sequence for residues 94 – 309 was cloned into pET28a such that the N-terminal contained a hexahistidine tag and thrombin cleavage site[228].

3.3.1 Requirement for N-terminal cleavage

For PqsR^{LBD} crystallisation, other studies removed the his-tag prior to crystallisation, likely to reduce the deleterious effects of additional disordered components. However, as Figure 3.1 shows the His-tag protrudes into the solvent channel and would therefore be unlikely to impact robust crystallisation. Additionally, diffraction experiments on crystals grown from un-cleaved protein did not have any additional residues at the N-terminal except for weak density that likely corresponds with a serine residue from the cleavage site.

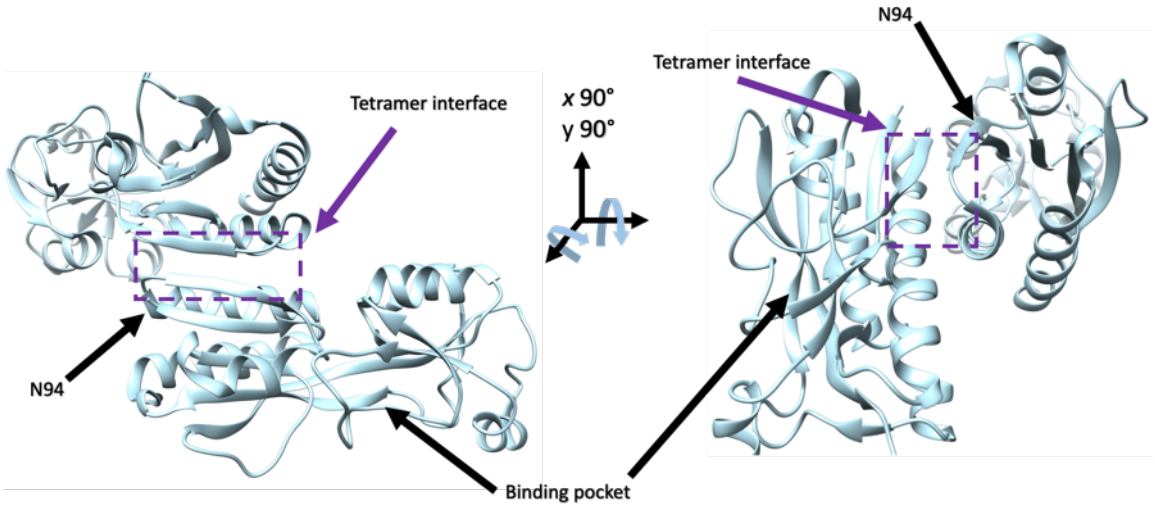

Figure 3.1. **N-terminal residues located within the 4JVC PqsR^{LBD} model**. Cartoon representation of the 4JVC model in light blue with an arrow showing the un-cleaved N-terminal. Additional residues will not impede crystallisation as they are not located at crystallisation interfaces, nor will the additional residues protrude into the binding pocket. The binding pocket between CDI and CDII is marked with an arrow and the tetramer interface between two sets of crystallographic dimers is marked in purple and is comprised of a β-sheet 2 and α helix 1.

3.3.2 Comparison of PqsR$^{94\text{-}309}$ with other reported PqsR^{LBD} structures

PqsR^{LBD} has been previously crystallised to assess ligand binding. Yet, only three crystal forms have been observed and only two successfully solved and reported. The first form reported in *Ilangovan, A.* (2011) $P6_522$[229], and a slightly smaller construct PqsR$^{94\text{-}295}$ giving

rise to an orthorhombic crystal system $C222_1$[153]. The former was observed exclusively in this study and may be due to shifting domain boundaries. Model alignment revealed good agreement with an average RMSD (of the total alignment) of 0.52 Å. The only region of disparity lies between residues 180 – 185 which in the $P6_522$ model forms the end of loop 6 and α3-helix. However, in the $C222_1$ model this helix was shortened. And loop extended suggesting the secondary structure had become destabilised. Additionally, Leu183 has flipped orientation by 180° and is buried with other hydrophobic residues. This local change in secondary structure has been attributed to the use of co-crystallisation and a smaller construct size.

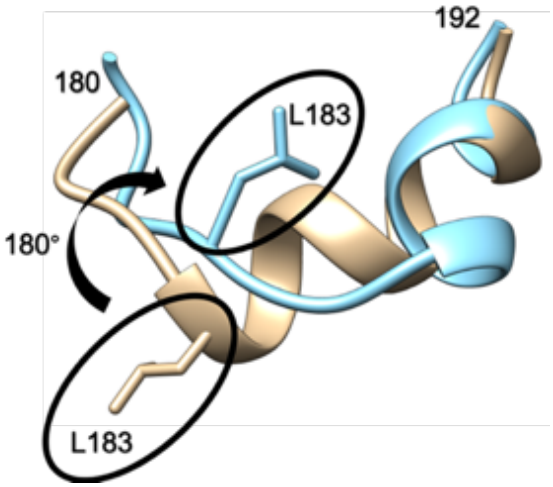

Figure 3.2. Comparison of PqsR$^{94-295}$ and PqsR$^{94-309}$ showing variability in loop 6. Cartoon representation of 4JVC and 6B8A coloured in gold and blue respectively. Leu183, with 180° flipped orientation labelled and circled.

3.3.3 Purification of PqsR$^{94-309}$ for crystallisation

The PqsR$^{94-309}$ truncate, chosen as it removes the flexible C-terminal region, was purified via a two-step chromatography procedure shown in Figure 3.3. A gradient elution on a HisTrap HP, produced a relatively pure product with some low molecular weight (LMW) contaminants (~11 kDa) in the earlier fractions. These contaminants were subsequently removed by gel filtration on a Superdex 75 16/60 column (preparative for purification of larger volumes and protein quantity). The elution volume of 60 mL corresponded to an M_r of 36.8 kDa in agreement with the expected homodimer. Yield from 1 L of culture was >20 mg.

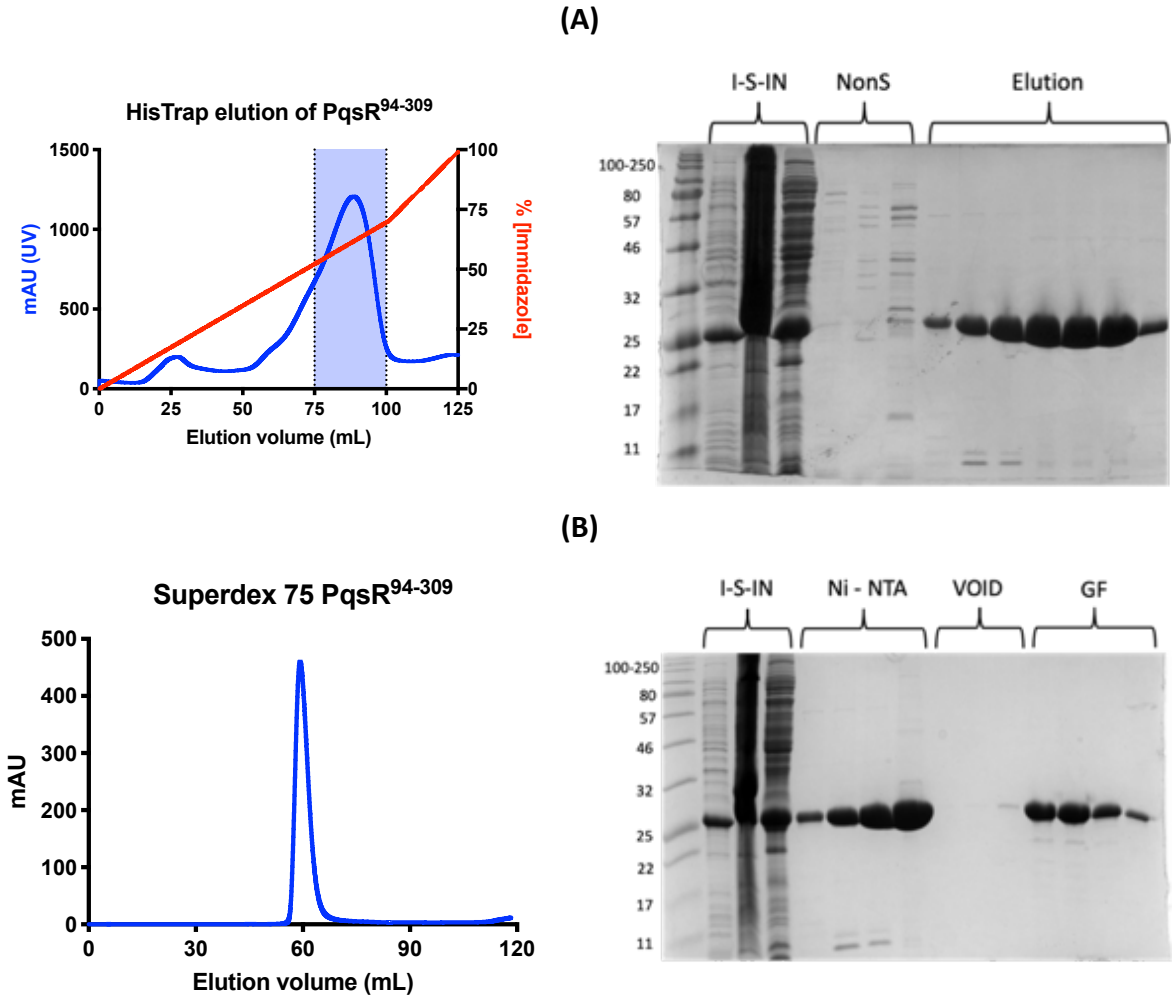

Figure 3.3. Purification of PqsR$^{94-309}$ for structural investigations with antagonists. (A) Imidazole gradient (0 – 500 mM) with PqsR$^{94-309}$ eluting at an imidazole concentration of >350 mM. 16% SDS PAGE gel showing cell pellet, soluble and Insoluble fractions (I-S-IN), Non-specific fractions eluting before the main peak and primary elution (75 – 100 mL). A small degree of LWM contaminant is observed in the first two fractions of HisTrap HP elution. **(B)** Isocratic elution of pooled material producing a single peak ~60 mL with SDS PAGE showing removal of LMW contaminants. Purity, as judged by SDS PAGE, is over 95%.

3.3.4 Purification of constructs for biophysical characterisation

For interaction studies the entire C-terminal was utilised as the flexible region may participate in ligand interaction in a manner non accounted for in a crystallographic model. The mutations at Thr 265 were designed to assess the impact of halogen bonding previously described for halogen derivates of native AQs[155]. Purification of PqsR$^{94-332}$ and T265A/N mutants were purified using the same protocol as for PqsR$^{94-309}$ with the exception that NaCl concentration was increased to 500 mM during Ni-NTA and gel filtration was carried out in

an optimised buffer consisting of 50 mM Tricine-NaOH (pH = 8), 250 mM NaCl and 2.5% glycerol. Salt concentration was lowered in consideration of binding experiments whereby the high concentration may disrupt hydrogen bonding to the pocket. Yield for $PqsR^{94-332}$ from 1 L (~5 g) was 27.4 mg with most sample loss occurring during overnight dialysis into gel filtration buffer and subsequent concentration. As expected, the elution volume was slightly reduced corresponding to the extra residues at the C-terminal with a M_r of 44 kDa which agrees with the expected dimer mass of 58.54 kDa. Purification is shown in Figure 3.4 with overall final product purity >95%.

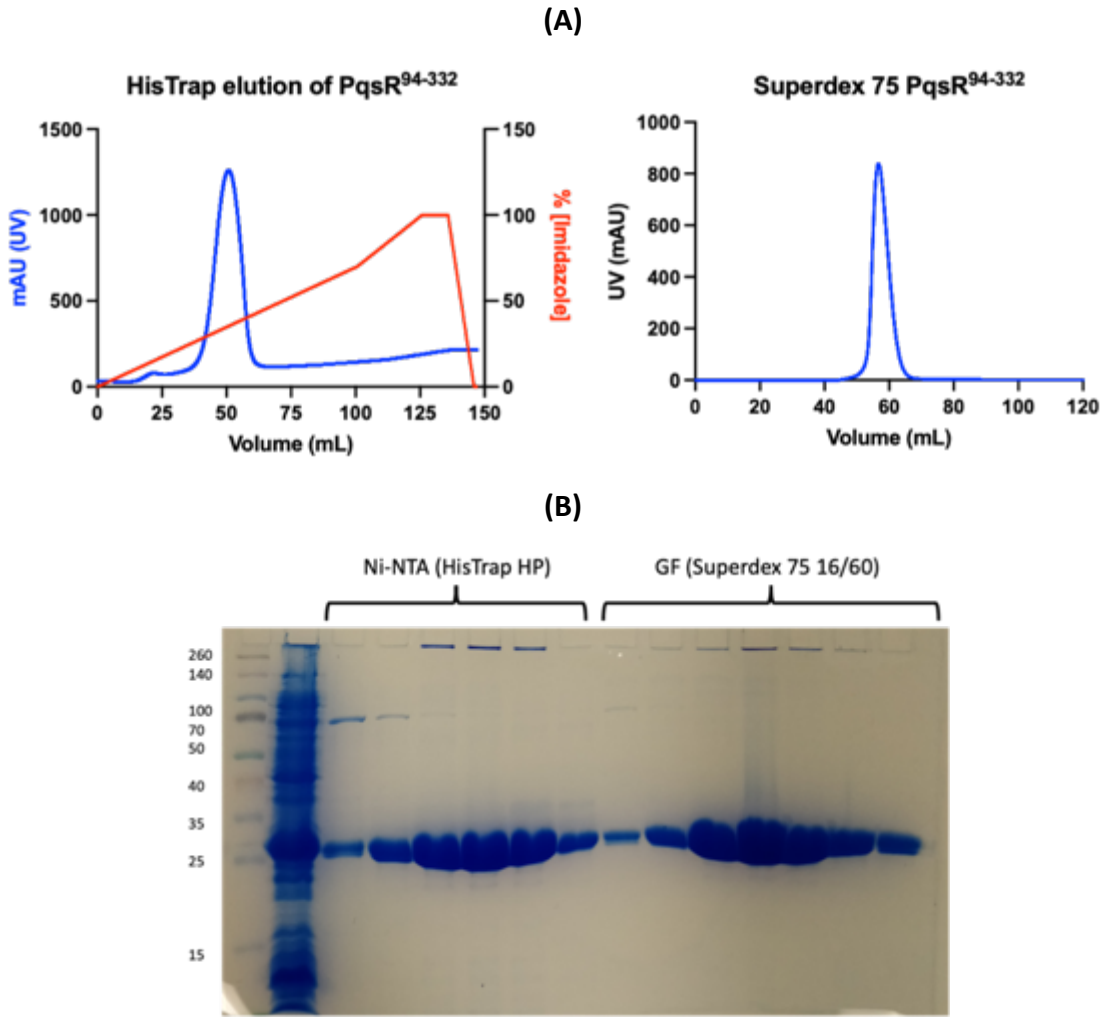

Figure 3.4. Purification of WT $PqsR^{94-332}$ construct for ligand interaction studies. (A) Elution profile of $PqsR^{94-332}$ by imidazole gradient on a HisTrap HP column (left) and isocratic elution through a Superdex 75 16/60 column (right). The elution shows that the material is only contains a negligible proportion of aggregate. **(B)** SDS PAGE gel showing minimal contamination in the preparation with slight smearing due to high concentration. The gel shows that a contaminating band of ~70 kDa has been removed by gel filtration.

T265A and T265N mutants gave slightly poorer yield of 10.2 mg from 1 L of culture suggesting the proteins were less stable. This is further supported by observations that the

T265N mutant precipitated after Ni-NTA suggesting that hydrophobicity in the pocket must be preserved for stability. Both proteins eluted at the same volume on gel filtration showing that the mutants did not impact quaternary structure (Figure 3.5).

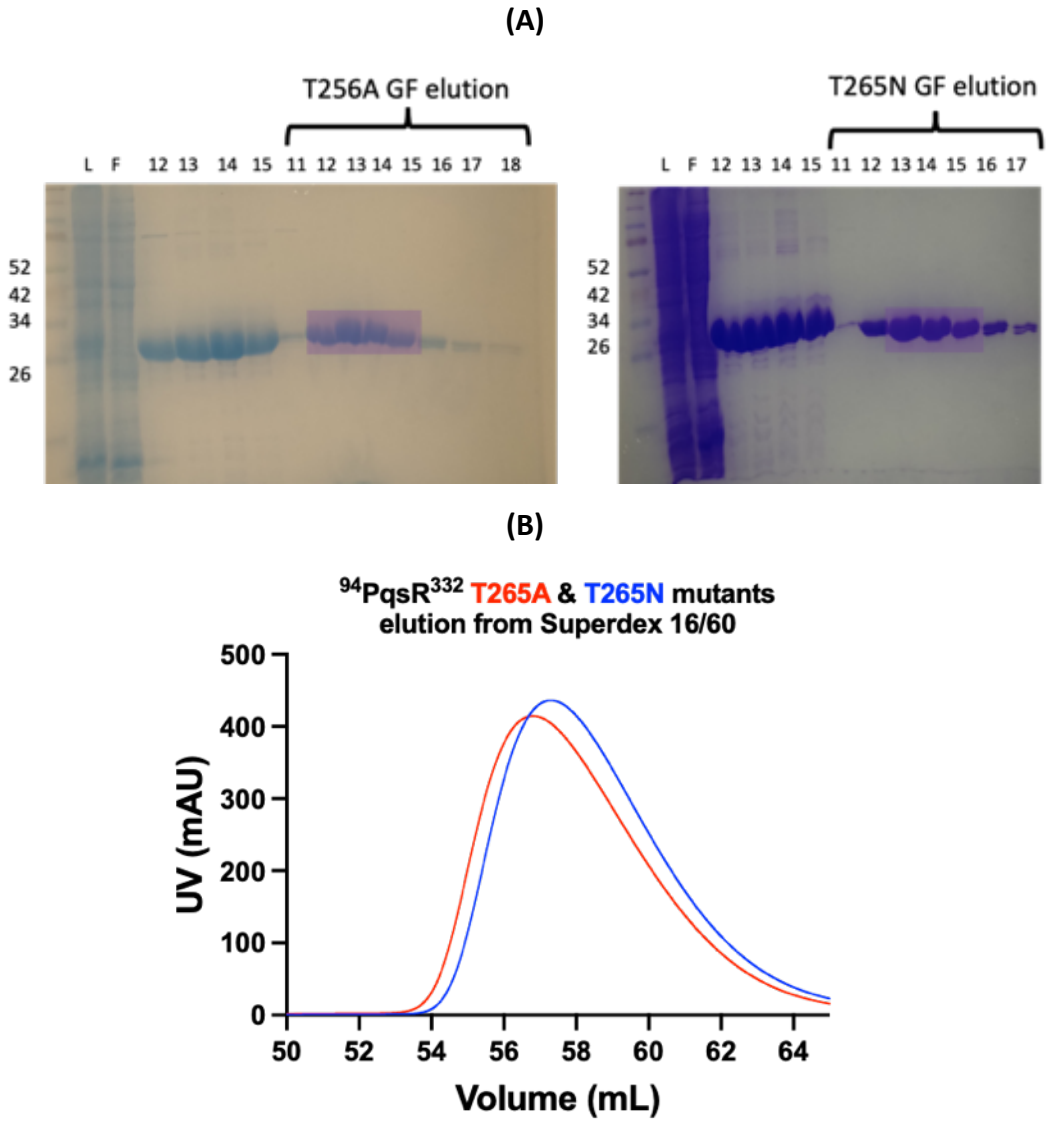

Figure 3.5 Purification of T265A and T265N PqsR$^{94-332}$ mutant for binding analysis. (A) Representative SDS PAGE gel showing purity of both mutant constructs. Material pooled for use after gel filtration highlighted in purple. **(B)** Overlayed elution chromatograms for each mutant with a consistent elution peak between 56-58 mL showing mutants were non-disruptive to stable dimer formation. UV traces are coloured red and blue for T265A and T265N respectively.

3.3.5 Testing for co-crystallisation suitability

Formation of protein-ligand complexes can be achieved by two experimental designs: co-crystallisation of the ligand with the protein and soaking ligand into apo grown crystals. Co-crystallisation is often considered a more desirable route for structural determination as it

allows for a greater degree of conformational change as highlighted previously with the orthorhombic $C222_1$ space group. To test the suitability of $PqsR^{94-309}$ for co-crystallisation the protein was incubated with different antagonist series for a limited time (10 minutes). As shown by Figure 3.6a quantifying the remaining material by UV absorption at A280 was complicated by strong compound absorbance which is most apparent with the lactam 488 that is higher than the DMSO control. Visual inspection, shown in Figure 3.6b of sample after centrifugation highlighted a pellet after each incubation suggesting that substantial protein material can aggregated upon ligand addition which would disfavour co-crystallisation.

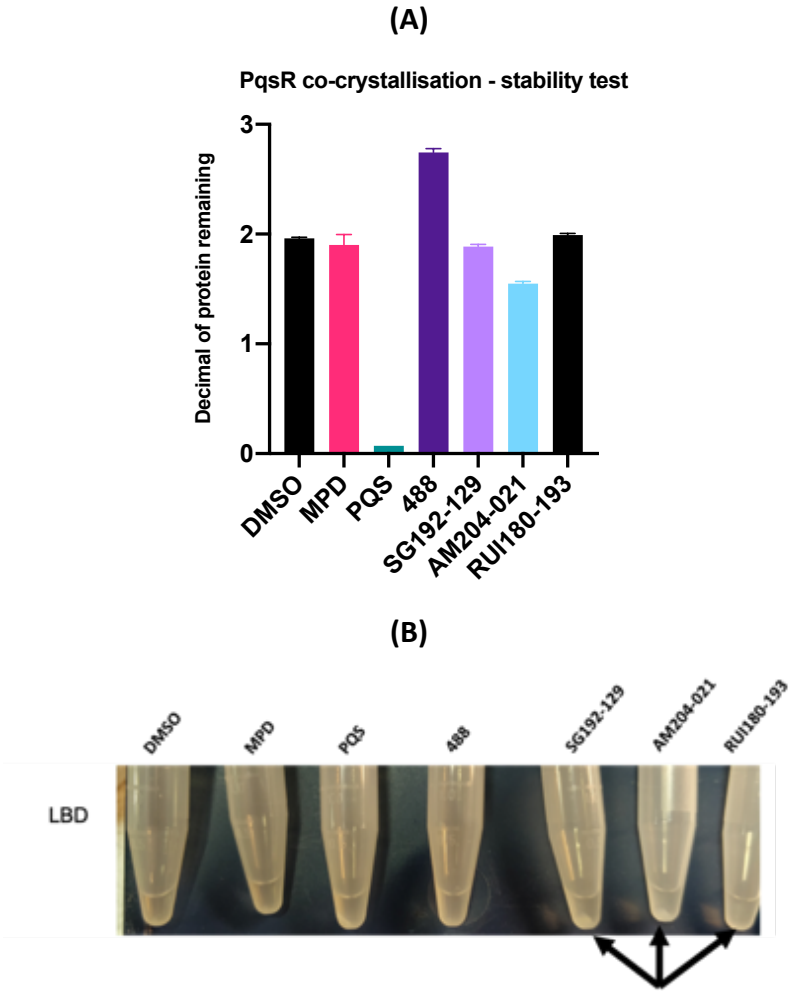

Figure 3.6. Piloting co-crystallisation experiments with $PqsR^{94-309}$. Antagonists added to protein sample in a 1:1 molar ratio for a 10 minute incubation. **(A)** Quantification of PqsR concentration by absorbance at 280 nm after centrifugation expressed as a proportion of the DMSO only control. Spectral properties of the antagonists impeded accurate quantification of the remaining material. **(B)** Precipitated protein observed after centrifugation for 10 minutes at 13,000 *x g*. Arrow denoting large pellets after treatment that could not be re-dissolved in a larger amount of buffer.

3.3.6 Crystallisation

Crystallisation conditions were adapted from *Ilangovan, A.* 2011[228] with 4 – 8 mg/mL PqsR$^{94-309}$, prepared freshly or thawed and clarified by centrifugation, crystallised in a 3 - 8% 2-Methyl-2,4-pentanediol (MPD) in the presence of ammonium acetate (200 mM) buffered with sodium citrate (100 mM, pH 5 – 6.5). Crystals grew within 7 days as either a shower of small crystals (unsuitable for soaking), larger (> 50 µm) crystals clumped together or larger single isolated crystals (Figure 3.7) with the latter habit appearing at lower protein concentration and being the most suitable for soaking.

(A)

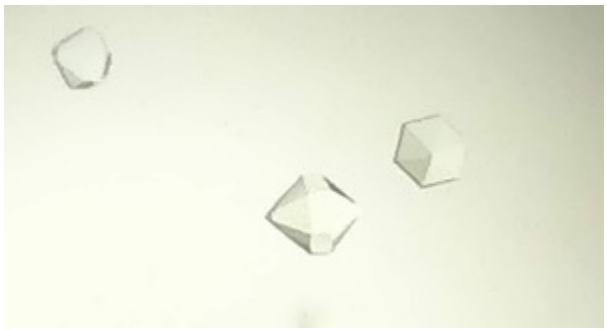

(B)

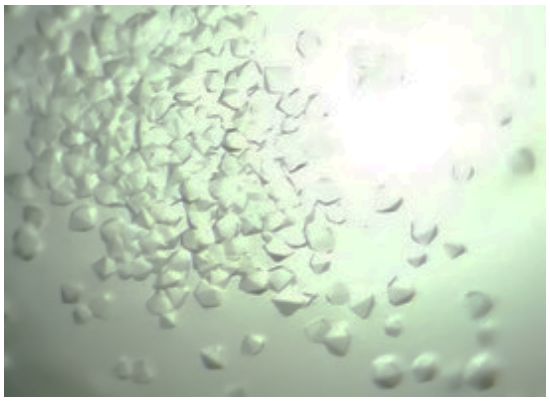

Figure 3.7. Apo-crystals of PqsR$^{94-309}$ grown in MPD conditions. **(A)** Large, well isolated dihexagonal crystal habit suitable for soaking **(B)** Well sized crystals aggregated together making soaking unsuitable. All crystals were grown in either 48 or 24 well plates (hanging or sitting drops) and incubated at 20°C.

3.4 Determining the binding pose of SEN66 in complex with PqsR^{LBD}

The SENBIOTAR hit SEN66 was originally identified as having a strong IC_{50} of 0.98 µM in PAO1 – L but unusually was inactive in the more commonly used PA14 strain. As shown in Figure 3.8 the SAR strategy involved modification of the tricyclic ring to include bulkier halogens substituents, alteration of the linking groups (R_3-R_5) and growth from the 4-chlorophenyl group (R_2).

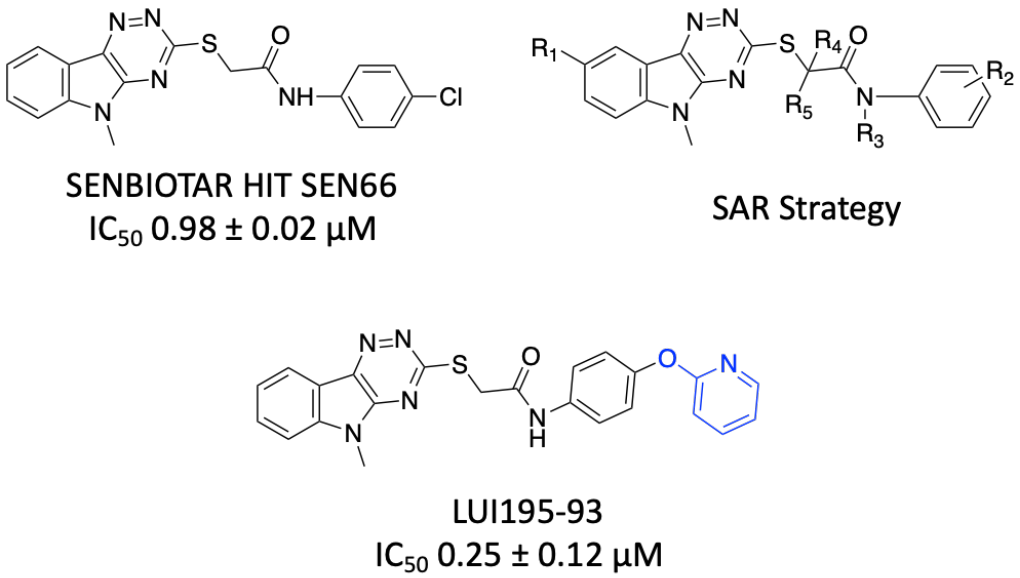

Figure 3.8. **SEN66 antagonist series**. Three molecular structures showing initial hit compound from HTS (top, left), SAR strategy employed (top, right) and optimised compound for crystal soaking with pyridine-2-yloxy (R_2) group highlighted in blue. Potency values from PAO1 – L CTX::P_{pqsA}-*lux* given.

Addition of a bromine atom to R_1 enabled activity in both PAO1 and PA14 with only a slight loss in potency towards PAO1-L. Removal of the chlorine atom from the chlorophenyl group reduced activity in both strains and moving the group to *meta* positions retained only weak antagonist activity. A disubstituted R_3 with 3, 4 dichloro retained only weak activity when the bulkier bromine was present at R_1. Substitution of R_2 with methyl and 4-trifluoromethoxy yielded inactive and weakly active compounds respectively. Addition of larger aromatics including phenoxy and pyridin-2-yloxy improved activity significantly with compound LUI195-93 possessing improved IC_{50} towards PAO1 (0.25 µM) and PA14 (0.34 µM). The resultant compound reduced pyocyanin production to less than 25% compared to untreated cultures and reduced AQ production significantly. Unusually, the compound was not shown to reduce biofilm formation and even increased biofilm viability. Interestingly,

ITC was previously conducted with the initial hit SEN66, however, no direct binding could be determined perhaps due to the instability of the protein-ligand complex as observed in 3.3.5 with the LUI180-193 analogue.

3.4.1 LUI195-93 soaking

Due to poor solubility LUI195-93 could not be easily soaked into apo crystals, with a multicomponent solvent system consisting of MPD, ethylene glycol, water and DMSO used to introduce the compound into the drop. Diffraction data resolution was determined to 3.2 Å with collection and refinement statistics summarised below in Table 3.2. The crystal was isomorphous to previously characterised 4JVC model and could be phased using Refmac5[223] with 4JVC to adjust for minor changes to unit cell dimensions.

Table 3.2: Data collection and refinement statistics for $PqsR^{LBD}$-LUI195-93 complex

Data collection	$PqsR^{94-309}$ – LUI195-93 Complex
Wavelength (Å)/beamline	0.9686
Space group	P 6_5 2 2
a, b, c (Å)	118.75, 118.75, 115.24
α, β, γ (°)	90.0, 90.0, 120.0
Resolution (Å)	76.85 – 3.2
No. of unique reflections	8390 (1466)
Rmerge (%)	23.4 (139)
Mean I/Sig(I)	6.6 (1.6)
Completeness (%)	99.9 (99.7)
Redundancy	13.5 (14)
CC½	0.988 (0.982)
Refinement	
Resolution range (Å)	76.85-3.20
R/Rfree (%)	0.207 / 0.242
Mean B-factor (Å)	126.16
r.m.s.d. bond lengths (Å)	0.0040
r.m.s.d. bond angles (°)	1.289
Ramachandran plot statistics (%)	
Preferred regions	96.02
Outliers	1.99
PDB ID	6TPR

Clear difference density was observed in the pocket which was substantially larger than MPD density and continuous across pockets A and B. The ligand was modelled into the pocket using coot. As shown in Figure 3.9 the ligand adopts an “L” conformation to fit into the pocket with the tricyclic 5-methyl-5H-[1,2,4]triazino[5,6-b]indole buried in pocket B making hydrophobic interactions with Ile149 and Leu207. The curvature is permitted by the thioacetamide linker that adopts an acute angle of 72.6° between the tricyclic head group and 2-phenoxypyridine. As shown in Figure 3.9c LUI195-93 possesses a close contact between the thioacetamide sulphur atom and the carbonyl oxygen of Leu208 (2.9 Å distance with a C=O to S angle of 121.2°). Additionally, a single hydrogen bond is present between the linker amide nitrogen and Leu207 peptide carbonyl (3.5 Å). The key interaction to the protein appears to be conferred by π-π stacking between the pyridinyl group and Tyr258.

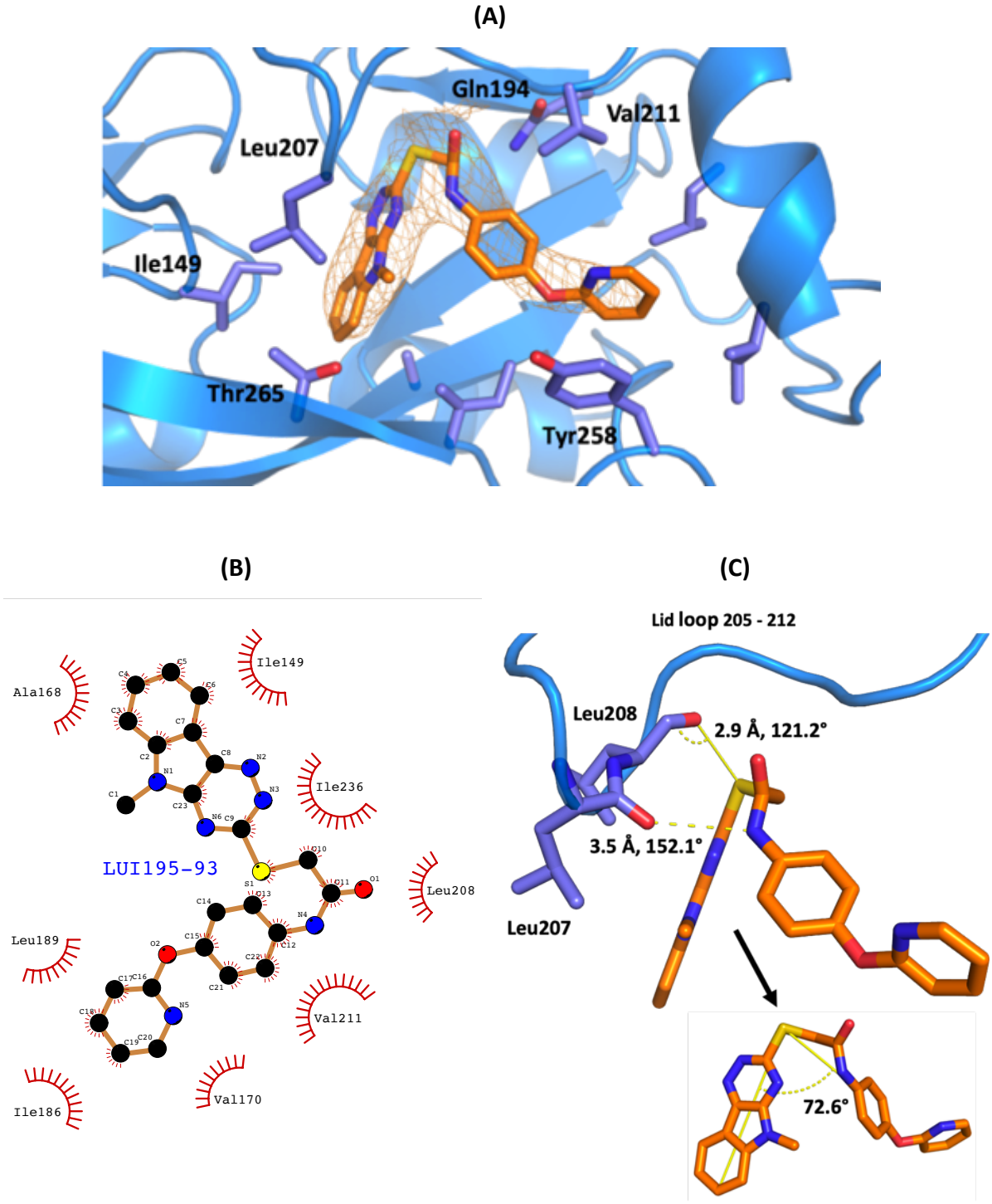

Figure 3.9. LUI195-93 – PqsR$^{94-309}$ complex (A) LUI195-93 ligand (coloured orange) modelled into PqsR$^{94-309}$(marine ribbon with interacting residues coloured in slate blue) with 2Fo-2Fc map, contoured at 1 σ, coloured in light orange. **(B)** LigPlot representation of LUI195-93 occupying the pocket. The tricyclic ring shares hydrophobic interactions to Ala 168, Ile149 and Ile 236. π-π interaction not accounted for due to distance cutoffs for hydrophobic interactions. **(C)** Electrostatic Interactions between LUI195-93 and peptide backbone residues Leu207 and 208. Angles formed between donor, acceptor and hydrogen stated. Hydrogen's atoms added to structure in PyMOL using the h_add function. Exert showing rotated ligand with angle between tricyclic ring and 2-phenoxypyridine marked.

3.4.2 Comparison of binding pose between M64 and LUI195-93

Previous antagonist development towards PqsR highlighted the importance of π-π with Tyr 258 to gain potency[153 201]. Analysis of M64, a benzimidazole based compound possessing a phenyl group as an alternative to pyridinyl as seen in LUI195-93, adopts a similar curved arrangement to fit into the binding pocket (PDB 6B8A). Examination of the π-π stacking interactions shows the pyridinyl group from LUI195-93 has a significantly more favourable overlap with the tyrosyl with a shift – averaged by ring member – of 2.1 Å towards the binding pocket perimeter (Figure 3.10b). The overall distance between aromatics do not show significant deviation (4.3 Å) yet the dihedral angle between the aromatic centroids differing by 14° with M64 possessing a more favourable angle of 8.5° compared to 22.8° for LUI195-95. This data highlights that exploiting interactions with Tyr 258 can be achieved by sandwich or parallel displaced stacking. Bioreporter data suggested that M64 has a slightly poorer IC_{50} compared to LUI195-93 which may be accounted for by the difference in π-π stacking.

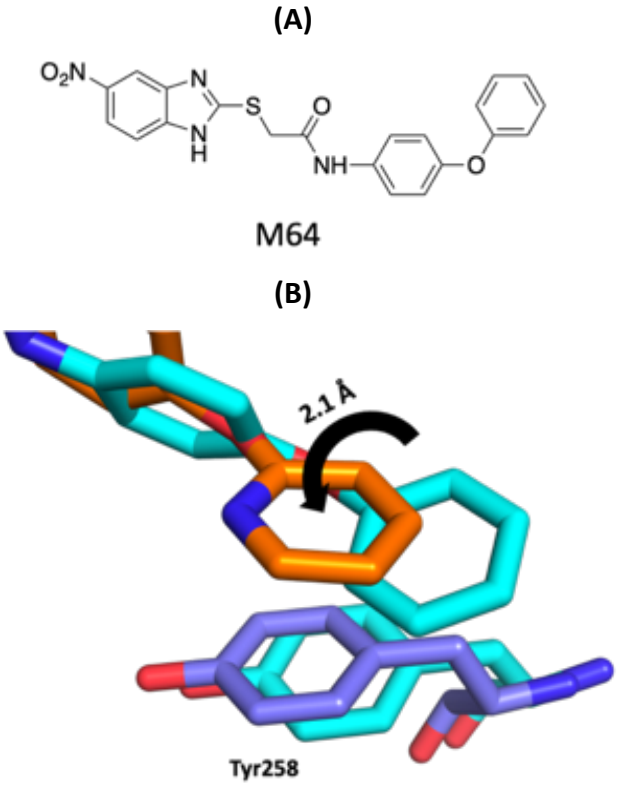

Figure 3.10. Comparison of π-π stacking between M64 and LUI195-93 (A) Structure of M64 possessing the same thioacetamide linker as LUI195-93 **(B)** Superposition of the LUI195-93 structure (orange and slate blue) and M64 (68BA, light blue) showing a relative shift of 2.1 Å. This permits the pyridinyl group to share a sandwich interaction with Tyr258 whereas M64 adopts a parallel-displaced π stack.

3.4.3 SEN66 SAR analysis

Gaining potency in the SEN66 series was most successful by optimising the R_2 position. Removal of the chlorine atom at position R_2 from the initial hit resulted in a lack of potency. Assuming the ligand position does not vary with respect to the solved structure it is likely the 4-chloro group participates in a halogen- π interaction with Tyr258. This also explains the weaker potency exhibited when the chlorine atom is added at the *meta* and *ortho* positions as the increased distance to Tyr258 will weaken interaction. A similar SAR relationship was observed in the development of M64 with loss of potency observed upon removal of the phenoxy or substitution with a chlorine atom abolishing and weakening activity respectively.

3.4.4 Soaking failure of other SEN66 candidates

Soaking was attempted with R_1 bromine and R_2 phenoxy which shows activity towards both PAO1 and PA14. However, no additional density was observed in the binding pocket after phasing. This was attempted multiple times using different solubilisation mixtures and even addition of solid ligand (as a powder) to the drop. This was likely due to either very limited solubility in the well condition consisting of 3-8% MPD or inability to access the binding pocket due to bulky substituents, especially true for the bromine addition. The poor solubility would also preclude co-crystallisation as significant co-solvent would be required for complex formation.

3.5 Determining the binding pose of SEN19 in complex with $PqsR^{LBD}$

The SEN19 hit, which possesses a quinazolinone head group bearing resemblance to the native AQ ligands, was found to reduce *pqsA* expression significantly with an IC_{50} of 13.1 µM. To begin SAR analysis a commercial library was purchased for exploration of positions R_1, R_2 and importance of linker amine (Figure 3.11). All these compounds were determined to be inactive when tested at 10 µM. These observations suggested difficulty in the optimisation of this series and requirement for structural information to inform further work.

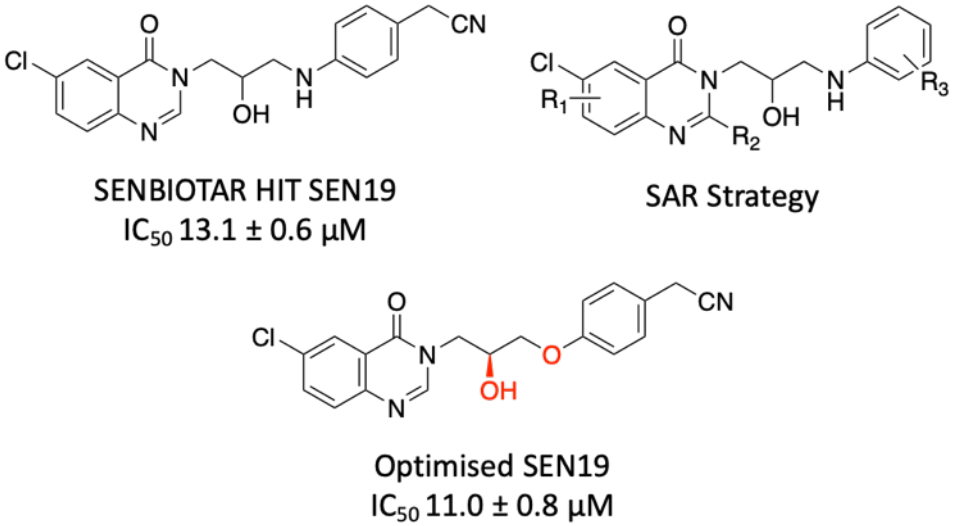

Figure 3.11 SEN19 antagonist series. Three molecular structures showing initial SENBIOTAR hit possessing an amine linker to the phenylacetonitrile group (left) and (right) scheme for antagonist optimisation. Highest affinity compound shown below with optimisation compared to original hit highlighted in red. Potency values from PAO1 – L CTX::P_{pqsA}-*lux* given.

Optimisation of the antagonist at R_1 by replacement with different small substituents highlighted that only the 6 and 7 positions were suitable for substitution but were not able to tolerate bi-substitution, likely due to spatial constraints. Substitution of a larger halogen improved both efficacy (percentage remaining activity) and potency with highly electronegative groups (NO_2 and CF_3) possessing improved activity. This was reminiscent of SAR conducted for QZN (described in 1.7.4). Addition of a methyl group to the R_2 (position 2 on the quinazoline) disrupted activity. Given that this position is exploited in QZN with alkyl chain length effecting IC_{50} or EC_{50} significantly the binding mode of the quinazoline was presumed to be different. Manipulation of R_3 highlighted the acetonitrile group to be important for biological activity and when repositioned to the *meta* position impaired activity and shortening to a benzonitrile (in either *para* or *meta*) also abolished activity. Replacement of the nitrile at R_3 with a fluorine atom also weakened activity. Unlike LUI195-93 and M64 an addition of a phenoxy group did not improve activity but addition of a smaller oxadiazole retained activity and potency. Explorational of the chiral linker highlighted that an amine bioisostere was able to replace the alcohol. Interestingly oxidation of the alcohol to a ketone retains activity highlighting that chirality can be dispensable which is also observed in the thioacetamide linker of LUI195-93.

3.5.1 Binding mode of SEN19

Apo crystals were soaked for 16 hours with SEN19 and AM159-089 (with a methoxylacetonitrile at position R_3) dissolved in a mixed solvent system consisting of MPD, ethylene glycol, water and DMSO before cryocooling and data collected on DLS I04. Complexes were determined to resolutions of 2.65 and 3 Å respectively with additional density adopting a 'L' shape, similar to LUI195-93, observed in both datasets larger than the apo – bound MPD molecules. Data collection and refinement statistics are given in Table 3.3.

Table 3.3 Data collection and refinement statistics for $PqsR^{LBD}$ in complex SEN19 and AM159-089 derivative

Data collection	$PqsR^{94-309}$ – SEN19 Complex	$PqsR^{94-309}$ – AM159-089 Complex
Beamline	I04	I04
Wavelength (Å)	0.9159	0.9159
Space group	P 6_5 2 2	P 6_5 2 2
a ,b, c (Å)	119.79, 119.79, 116.5	120.43, 120.43 115.78
α, β, γ (°)	90, 90, 120	90, 90, 120
Resolution	77.47 – 2.65	104.3 – 3.00
No. of unique reflections	14874	10259
R_{merge} (%)	8.9 (99)	11.1 (225.2)
Mean I/Sig(I)	10.7 (2)	17.3 (1.2)
Completeness	99.9 (100)	99.1 (99.5)
Redundancy	9.3 (9.9)	18.6 (18)
CC½	0.806 (0.676)	1.000 (0.887)
Refinement		
Resolution range (Å)	77.59 – 2.65	77.61 - 3.00
R/Rfree	0.23 / 0.26	0.22 / 0.27
Mean B-Factor (Å)	108.3	120.8
r.m.s.d bond lengths (Å)	0.0038	0.0034
r.m.s.d bond angles (°)	1.32	1.300
Ramachandran plot statistics (%)		
Preferred regions	95.52	97.51
Outliers	0	0.5
PDB ID	-	-

Difference density inside the pocket clearly showed that the 6-chloroquinazolinone from SEN19 was positioned within pocket B and the phenylacetonitrile group extended into pocket A (Figure 3.12a). Ligand curvature was observed at the secondary alcohol which permits the quinazolinone ring to adopt a previously unobserved conformation within the pocket. Other halogenated quinazolinone ligands, such as 3NH2-7Cl-C9QZN (Table 1.2) have been previously reported (4JVI)[155]. Superposition of 4JVI and SEN19 highlights that despite the chlorine atoms being substituted at different positions the relative spatial position of the chlorine atoms was not hugely deviated – 1.4 Å suggesting that spatial constraints in pocket B limits the freedom of moment of large halogens (Figure 3.12c). Additionally, in the case of 4JVI it was observed the rotamer of Thr 265 changed to accommodate the halogen. Furthermore, superposition shows that the alcohol in SEN19 occupies the position of bound water in 4JVI that forms a hydrogen bond with 3' amino group in 3NH2-7Cl-C9QZN which mediates a hydrogen bond with Gln 194. With SEN19 the alcohol forms a direct hydrogen bond with Gln 194 (2.7 Å) which, in combination with water displacement would increase binding affinity to the pocket. The superposition further shows that the nitrile group of SEN19 aligns with the end of the nonyl tail of 3NH2-7Cl-C9QZN.

(A)

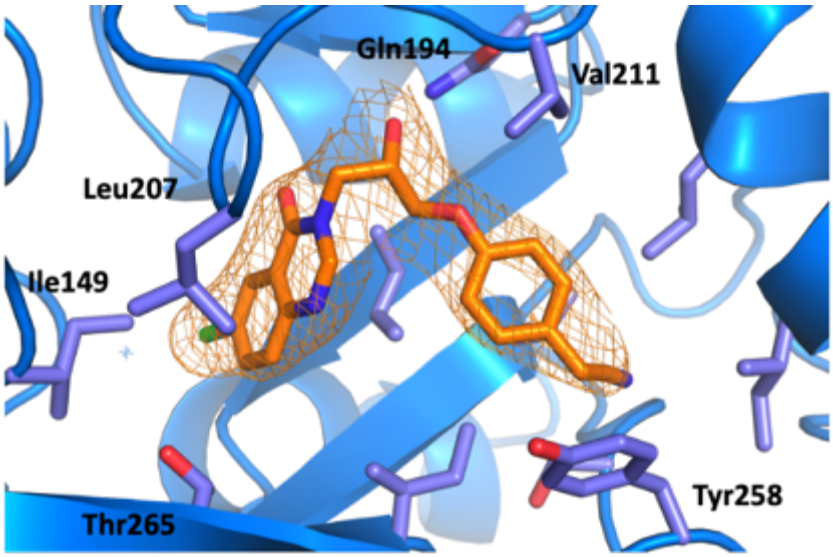
Gln194
Val211
Leu207
Ile149
Tyr258
Thr265

(B)

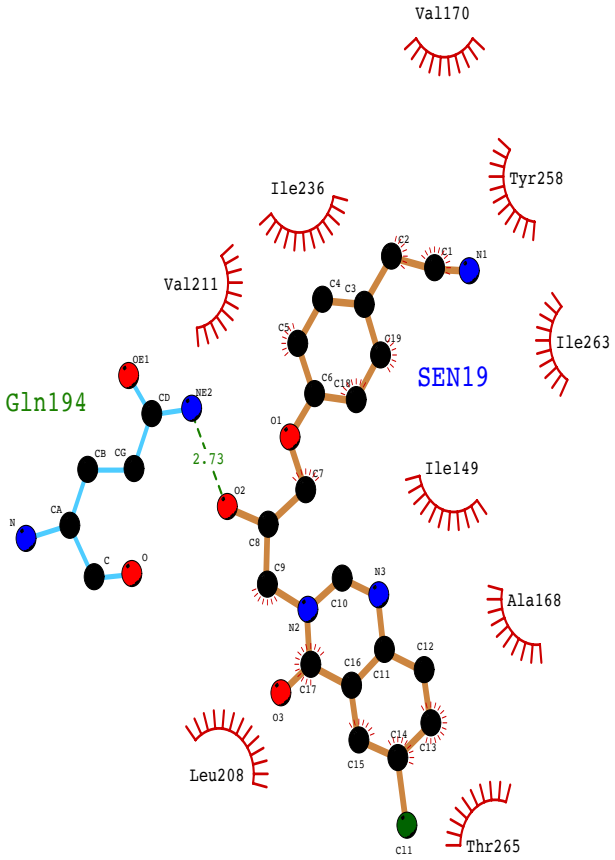
Val170
Tyr258
Ile236
Val211
Ile263
SEN19
Gln194
2.73
Ile149
Ala168
Leu208
Thr265

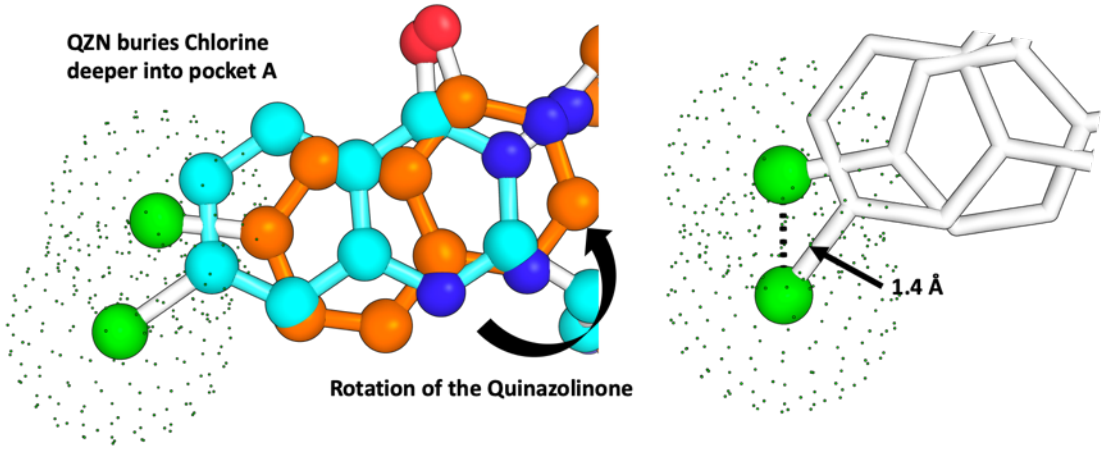

Figure 3.12 SEN19 – PqsR$^{94-309}$ complex (A) SEN19 ligand (coloured orange) modelled into PqsR$^{94-309}$(marine ribbon with slate blue residues). 2Fo-Fc represented as a mesh set to 1 σ with carve of 1.6 coloured in light orange **(B)** LigPlot 2D representation of binding showing a hydrogen bond between SEN19 alcohol and Gln 194. **(C)** Superposition of the quinazolinone bicyclic of SEN19 (orange) and 3NH2-7Cl-C9QZN (blue) showing relative rotation of the bicyclic within pocket B (right) and distance between chloro groups given left.

Soaking does not always show ligand induced structural changes however, the soaking of SEN19 has altered the rotamer at Ile 236 such that the longer chain of the *sec*-butyl fits underneath the alcohol rather than being pointed at the chiral centre. This change in conformation avoids an unfavourable atomic clash and highlights how the pocket can subtly alter to permit antagonist binding.

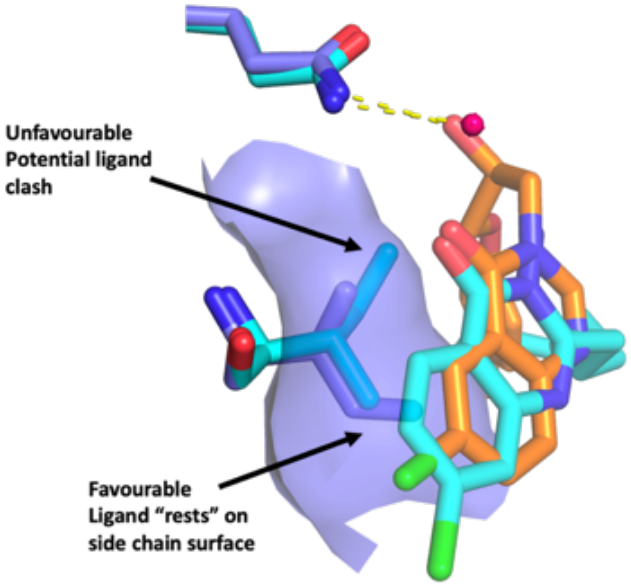

Figure 3.13. Superposition of SEN19 and 3NH2-7Cl-C9QZN complexes showing Ile236 reposition. Local rearrangement of Ile236 side chain to accommodate SEN19 more aptly and avoids a clash. SEN19 Ile 236 surface modelled, coloured slate. Hydrogen bond between Gln 194 and SEN19 mimics the water mediated bonding observed with 3NH2-7Cl-C9QZN.

3.5.2 SEN19 interactions with Tyr 258

As with LUI195-93, SEN19 also forms a π stack with Tyr258. However, this takes the form of a T-shaped interaction with a centroid distance of 5.6 Å. Interestingly, the nitrile group, which might be expected to form a polar interaction with the hydroxyl of Tyr 258 is directed away, but parallel with the aromatic ring and as such shares hydrophobic interaction that could be characterised as an unconventional π stack (Figure 3.14). Additionally, the nitrile group is supported by the hydrophobicity cavity created by the backbone of Ser 255 (multipolar interaction with H – C(α)).

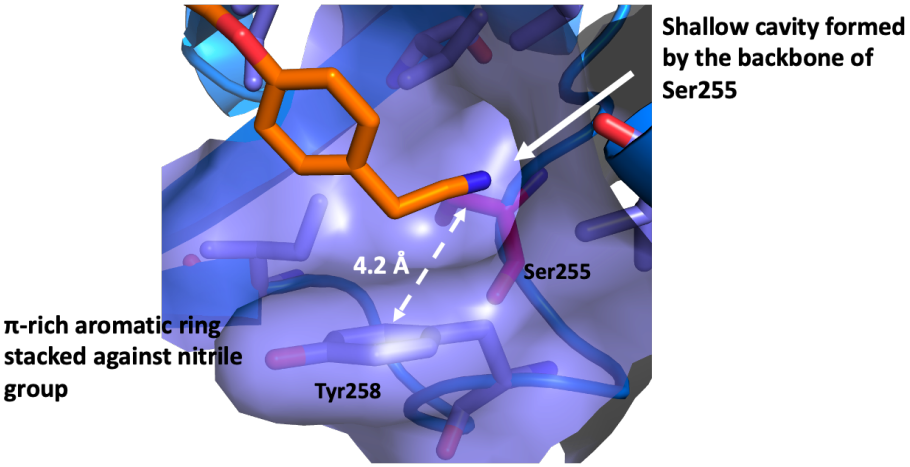

Figure 3.14 Nitrile occupies the pocket A cavity formed from Ser 255 backbone. An unconventional π stack is formed between the nitrile group of SEN19 and Tyr 258 (measured distance of 4.2 Å between carbon atom in CN bond and tyrosyl centroid).

3.5.3 Comparison of SEN19 & AM159-089 $PqsR^{94-309}$ complexes

Modification of R_3 with an methoxylacetonitrile, expected to increase the mobility of the nitrile group within pocket A, caused distortion in the binding pose of AM159-089 compared to SEN19. The deformation in binding pose may be responsible for the 2-fold loss in potency exhibited by AM159-089. To assess whether the group did granted additional mobility molecule B Factors were examined which did not show a significant increase compared to the rest of the molecule, although relative mobility appeared to increase towards the end of the nitrile, suggesting limited flexibility (Figure 3.15a).

(A)

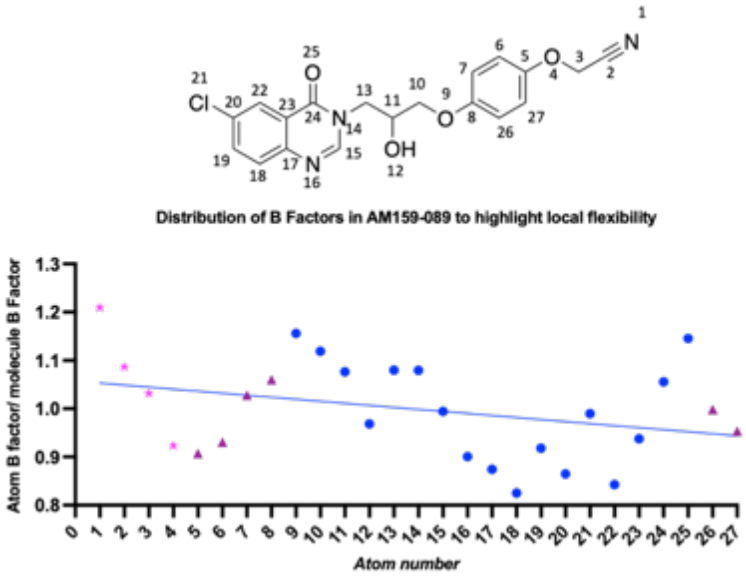

(B)

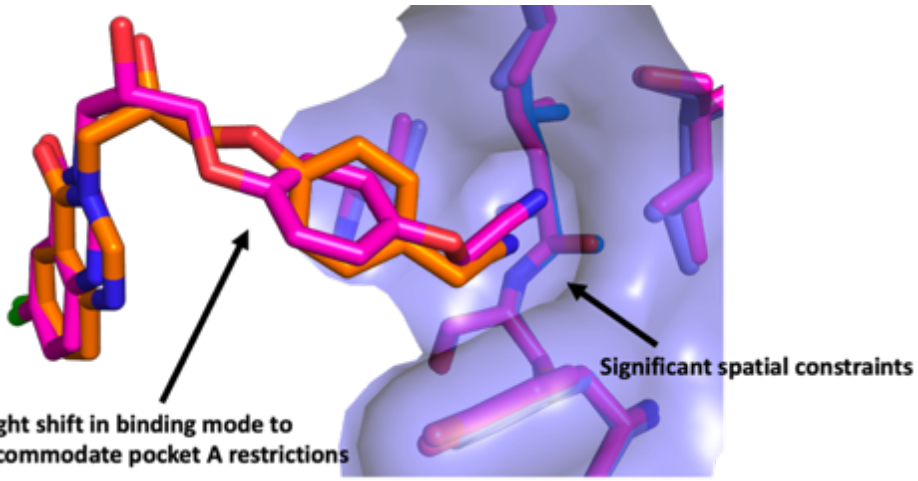

Figure 3.15. Effect of R_3 methoxyacetonitrile on SEN19 series binding pose (A) AM159-089 antagonist bearing the methoxyacetonitrile group with labelled atoms from the molecule and B factor relative to the molecule's overall B – Factor. No significant relationship across the molecule was observed but the nitrile has some relative mobility compared to methoxy oxygen atom. The methoxylacetonitrile group is marked as pink stars, and phenyl group denoted as triangles. **(B)** Superposition of SEN19 (orange) and AM159-089 (pink) with the surface of pocket A shown in slate. No conformational change is apparent within pocket A suggesting the nitrile groups's position is limited and in the case of AM159-089 the spatial restriction has caused a slight deformation in binding pose.

3.5.4 Probing halogen interactions with Thr 265

As different positions had been observed for Thr 265 it was hypothesised that the rotamer differed depending on bound ligand and that in solution a more favourable interaction could be present. Operating under the hypothesis that halogen substitutions may affect

binding by halogen bond formation with the hydroxyl oxygen of Thr 265 binding analysis was conducted using ITC with PqsR$^{94-332}$ in an optimised buffer consisting of 20 mM Tricine – NaOH (pH = 8), 250 mM NaCl and 2.5% glycerol. Given limited ligand solubility 5% DMSO co-solvent was required to ensure solubilisation. Strong binding between SEN19 and PqsR$^{94-332}$ was observed upon titration with an observed dissociation constant (K_D) of 16.6 ± 6.7 nM (n = 3), a representative isotherm is given below in Figure 3.16. This is significantly higher than the established IC_{50} of 1.1 ± 0.35 µM showing that other factors play a role in the *in vivo* assay such as cell permeability. Stoichiometry was determined to be less than 1 (0.789) suggesting a portion of the protein was not actively binding sample or due to errors in plotting a tight binding interaction.

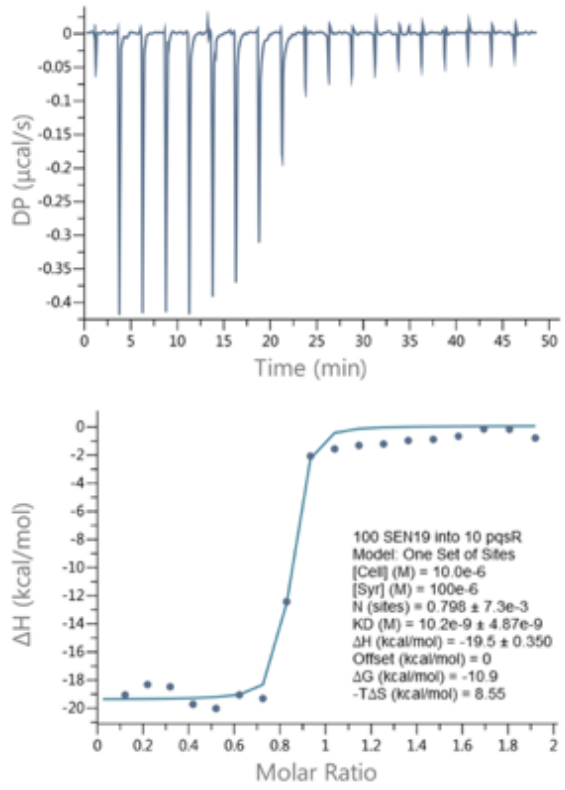

Figure 3.16. Binding of SEN19 to PqsR$^{94-332}$. Representative Isotherm (n = 3) of 100 µM SEN19 titrated into 10 µM PqsR$^{94-332}$. Heats generated from ligand into buffer were subtracted from each datapoint. C value calculated as 980 based upon C = [PqsR^{LBD}]/K_D which falls within a reasonable range for the instrument. Strong binding with K_D of 10.2 nM determined. Enthalpic interactions contribute significantly to binding with a ΔH of -19.5 kcal/mol.

The binding of SEN19 to PqsR$^{94-332}$ was driven by favourable enthalpic relationships suggesting the presence of favourable hydrogen bonding. To test the role of Thr 265 in

binding a T265A mutant was titrated with SEN19 under the same experimental conditions. Given the expected electrostatic interaction between 7 chloro and Thr 265 it was surprisingly that binding was unaffected by the mutation. The only apparent change appeared to be a minor increase in entropy (~1 Kcal/mol) suggesting that without the additional constraints imposed by Thr 265 SEN19 adopts a less favourable conformation (Figure 3.17).

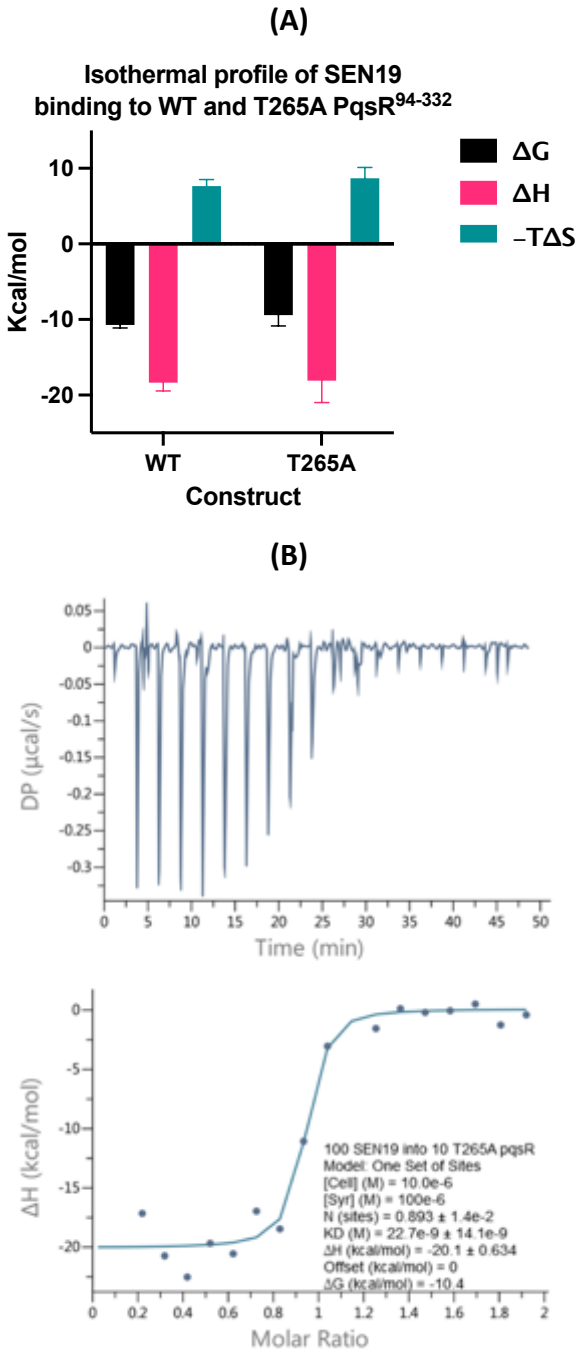

Figure 3.17. Comparing binding of SEN19 to WT and T265A PqsR^{LBD} (A) Thermodynamic profile of SEN19 binding to PqsR$^{94-332}$ WT and T265A mutant **(B)** Representative isotherm of SEN19 100 µM SEN19 titrated into 10 µM T265A PqsR$^{94-332}$ (n = 2) performed under the same conditions as above.

3.5.5 Relating structural information to SAR

From the structural data it is apparent that substituents building on the *para* nitrile group are spatially constrained which explains the weaker activity observed with an additional methylene group (-CH_2**CH_2**CN). The slight shift in binding pose caused by the addition of the methoxy group at R_3 reduced activity as well suggesting the manipulation of this position can influence binding across the pocket. Attempts to modify the alcohol reduced activity emphasising the importance of hydrogen bonding to Gln 194. Structural analysis showed the position of the R_1 halogen is restrictive which explains the weakened activity when chloro group is added to the 7th position. Abrogation in activity upon addition of a methyl group at R_2 may be explainable as apparent steric hindrance from Leu 207 or by flexibility in the lid loop residues.

3.6 Determining the binding pose of SEN32 in complex with PqsR^{LBD}

The SEN32 hit, possessed an IC_{50} of 13.2 ± 2.73 towards PAO1 – L with the SAR strategy focusing on manipulation of the halogen substituent and thiazole ring to yield more interactions in pocket A (Figure 3.18).

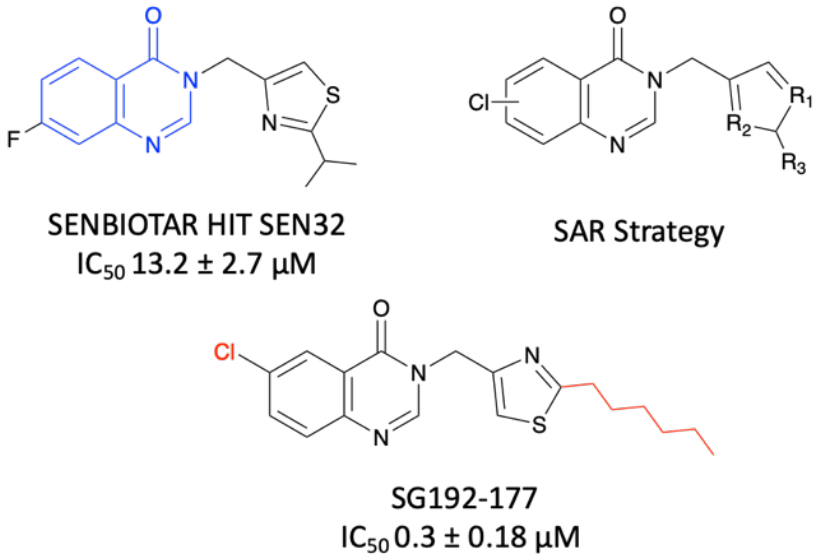

Figure 3.18. **SEN32 antagonist series.** (Left) Initial hit compound, SEN32 with quinazolinone moiety coloured in blue and (right) schematic showing areas of SAR optimisation and the most potent compound from the SAR bearing a 6-chloro group and hexyl chain coloured red. Potency values from PAO1 – L CTX::P_{pqsA}-*lux* given.

Initial investigation to the halogen position showed that addition of a chlorine atom to position 6 gave better potency compared to fluorine at position 7 which contrasted with the SAR conducted around 3NH2-7Cl-C9QZN. Replacement of the thiazole ring with an oxadiazole bioisostere abated activity entirely and inversion of the nitrogen and sulphur atoms reduced activity highlighting the position of the sulphur atom to be important. Removing or shortening the isopropyl from the initial hit resulted in a loss of activity whereas increasing the alkyl chain length increased activity proportionally with branched chains giving better activity likely due to improved entropic contributions. Adding a phenyl to R_3 improved activity significantly most likely by exploiting the π-π interactions first observed in LUI195-93. Addition of a secondary or tertiary amine linker to an alkyl group at R_3 impaired activity suggesting that rigidity in the tail is disfavoured. Differences in activity between strains (PAO1 and PA14) were attributed to bacterial uptake and efflux as the PqsR binding pocket is unchanged between strains.

3.6.1 Binding mode of SEN32 series

Multiple attempts to soak compounds from this series deteriorated crystal quality and impaired diffraction. This could be attributed to the compound's increased lipophilicity (higher logP values) compared to the other series. To improve resolution of these complexes, dehydration methods were attempted in which drop volume was replaced with higher MPD concentrations. However, the resultant diffraction was extremely poor with most datasets having resolution poorer than 3.5 Å and therefore being unsuitable for structural solution. To improve soaking result a variant of the multisolvent mixture was employed consisting of 12.5% dioxane, DMSO, ethylene glycol, 1,2 propanadiol and MPD combined with citrate buffer and ammonium acetate (37.5% Aqueous). Upon addition crystals were observed to crack, likely from the osmotic shock from the high organic content compared to the mother liquor. Resolution of the complexes were determined between 2.95-3.2 Å with a conservative cut off applied to limit the effect of anisotropy. After phasing, each dataset showed difference density in the pocket consistent with a large ligand which adopted a similar position to the native AQs. Refinement statistics after ligand fitting are shown in Table 3.4:

Table 3.4 Data collection and refinement statistics for $PqsR^{LBD}$ in complex with SEN32 antagonist series

Data collection	$PqsR^{94-309}$ – SG192-127	$PqsR^{94-309}$ – SG192-183	$PqsR^{94-309}$ – SG192-173	$PqsR^{94-309}$ – SG192-177
Beamline	I04	I04	I04	I04
Wavelength (Å)	0.9795	0.9795	0.9795	0.9795
Space group	$P6_522$	$P6_522$	$P6_522$	$P6_522$
a ,b, c (Å)	120.27, 120.27 115.04	120.79, 120.79, 114.39	119.32, 119.32, 114.76	118.91, 118.91, 115.46
α, β, γ (°)	90. 90. 120	90, 90, 120	90, 90, 120	90, 90, 120
Resolution	60.13 – 3.15	60.39 - 2.95	59.66 – 3.00	115.46 – 3.2
No. of unique reflections	8476 (1514)	10879 (1704)	10169 (1599)	7628 (1370)
R_{merge} (%)	8.1 (80.3)	8.5 (107)	9.7 (170)	6.1 (39.8)
Mean I/Sig(I)	13.9 (2.9)	12.6 (1.7)	17.1 (1.7)	16.6 (3.1)
Completeness (%)	95.7 (96.6)	100 (100)	100 (100)	92.4 (93.7)
Redundancy	10.1 (10.4)	9.6 (10.2)	19.2 (20.2)	9 (9)
CC½	0.970 (0.966)	0.998 (0.917)	0.999 (0.932)	0.997 (0.972)
Refinement				
Resolution range (Å)	60.20-3.15	60.47 - 2.95	59.73 – 3.00	76.97 – 3.2
R/Rfree	0.195 / 0.241	0.20/0.257	0.193/0.255	0.204/0.261
Mean B-Factor ($Å^2$)	143.6	131.6	139	146.2
r.m.s.d bond lengths (Å)	0.0077	0.0081	0.0076	0.0025
r.m.s.d bond angles (°)	1.653	1.671	1.364	1.236
Ramachandran plot statistics (%)				
Preferred regions	97.51	95.52	94.53	96.52
Outliers	0	0	0	0
PDB ID	6Z17	6Z07	6YZ3	6Z5K

The different density after phasing showed an unexpected pose for each ligand. Clear density for the electron rich chlorine atom was observed in the same area as 3NH2-7Cl-C9QZN. This suggested the quinazolinone group had flipped within the pocket. To further examine this observation the model was run through POLDER (phenix) to produce an omit map[230]. By excluding bulk solvent correction the omit map can improve weak features typically obscured by masking. These maps, shown in Figure 3.19, also indicated strong density of the chloro group and highlighted the bicyclic ring had indeed flipped.

(A)

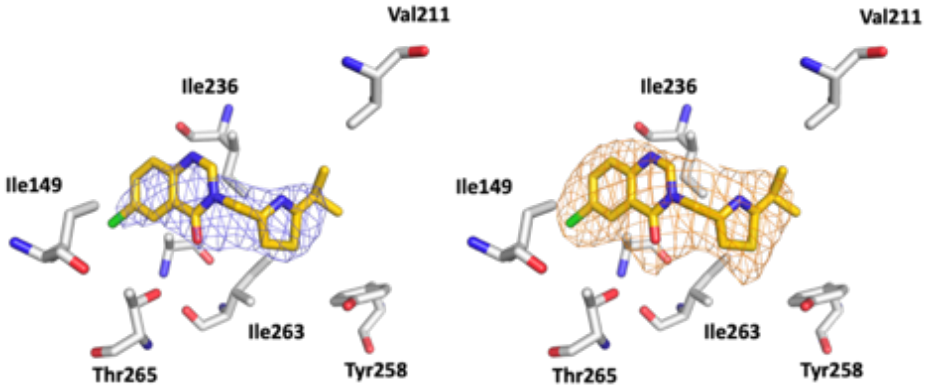
Val211
Ile236
Ile149
Ile263
Thr265
Tyr258
Val211
Ile236
Ile149
Ile263
Thr265
Tyr258

(B)

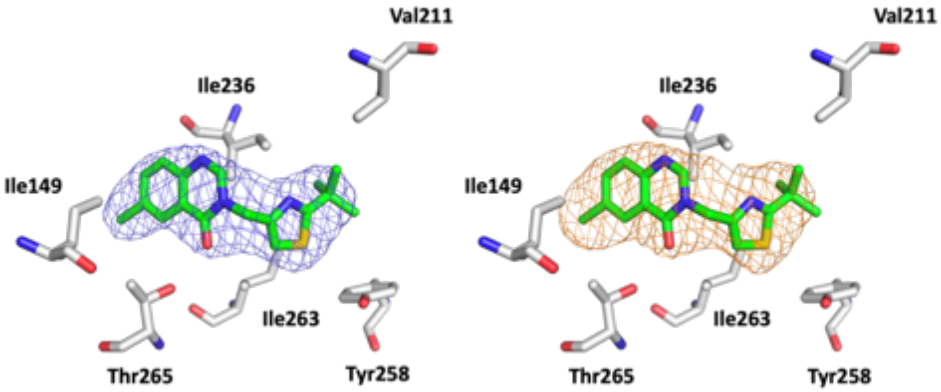
Val211
Ile236
Ile149
Ile263
Thr265
Tyr258
Val211
Ile236
Ile149
Ile263
Thr265
Tyr258

(C)

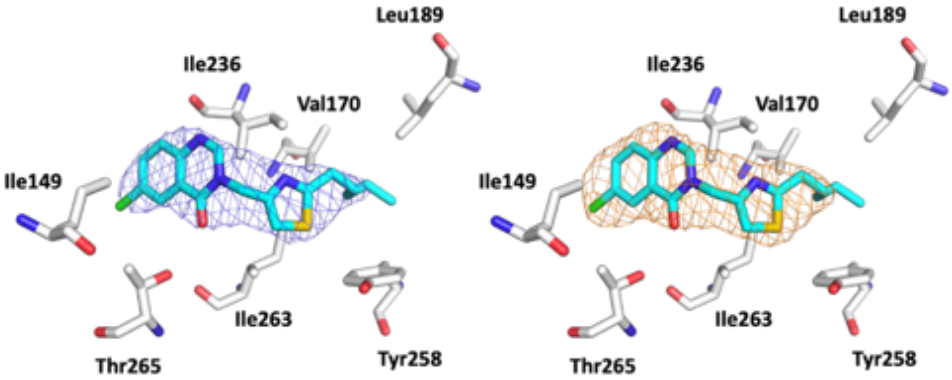
Leu189
Ile236
Val170
Ile149
Ile263
Thr265
Tyr258
Leu189
Ile236
Val170
Ile149
Ile263
Thr265
Tyr258

(D)

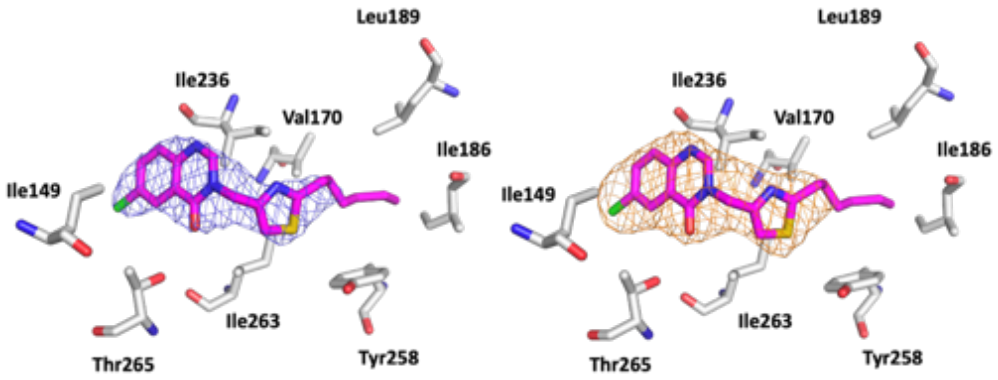

Figure 3.19 Electron density maps for SEN32 series PqsR^{LBD} complexes (Left) 2Fo-Fc Electron density from Refmac[223] (contoured to σ = 1) and (right) Omit map generated from Phenix.polder[230] (contoured to σ = 3). Ligands represented as sticks: SG192-127 in yellow **(A)**, SG192-183 in green **(B)**, SG192-173 in light blue **(C)** and SG192-177 in pink **(D)**. Clear electron density is observed for the chlorine atom in each antagonist showing a flip in quinazolinone ring compared to other models.

Given that native AQs and derivatives (NHQ, HHQ and QZN) all adopt the same position the apparent flipping of the quinazolinone ring is quite interesting and suggests the position of the large halogen is more privileged in the pocket which links to previous observation in the SEN19 series and previous studies with the ligand analogue QZN[155]. The new position of the quinazolinone permits a different range of interaction, specifically with Thr 265. As shown Figure 3.20, Thr265 can form an electrostatic interaction with the ketone carbonyl (3.3 – 3.8 Å). This may compensate for any penalties associated with the new conformation of the quinazolinone. Interestingly, this is not the only change in the quinazolinone position observed through soaking. Soaking of $3C_2NH_2$-7Cl-C9QZN yielded electron density showing the bicyclic occupying pocket A instead being buried in pocket B[228]. Although the change observed in the SEN32 series is not as substantial it shows that binding pose of the bicyclic is not necessarily conserved.

Electrostatic interaction is further observed between the thiazole sulphur atom and the hydroxyl group on Tyr 258. The sulphur atom acts as a hydrogen bond acceptor from the hydroxyl group with distances within accepted geometric parameter observed in higher resolution models[231]. Interestingly, the electron density around the alkyl chain is poorer with SG192-173 and SG192-177 compared to the rest of the molecule suggesting the pentyl and hexyl chains have greater flexibility within pocket A. However, despite apparent

flexibility these longer alkyl chains permit greater hydrophobic interaction as the ligands can stretch further into pocket A and contact the α3 helix.

SG192-127

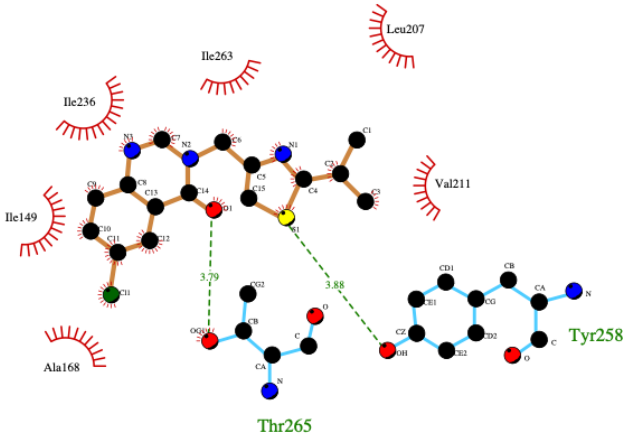

SG192-183

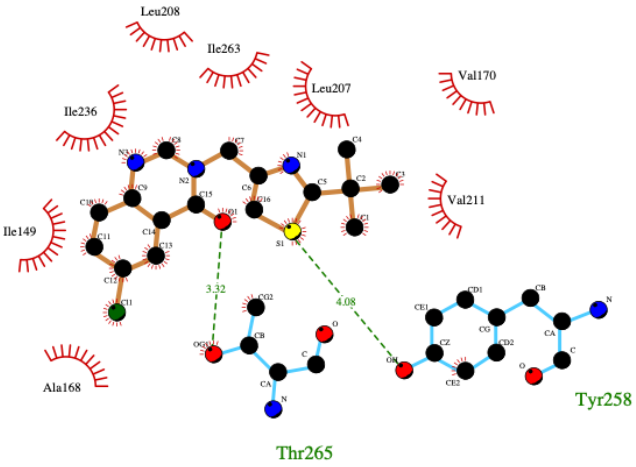

SG192-177

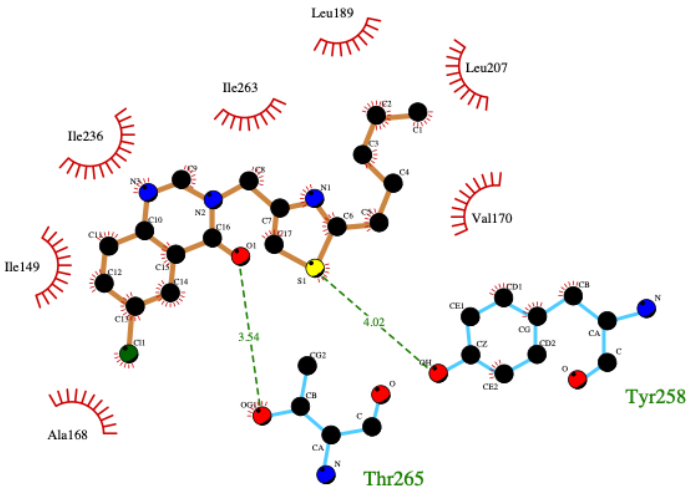

SG192-177

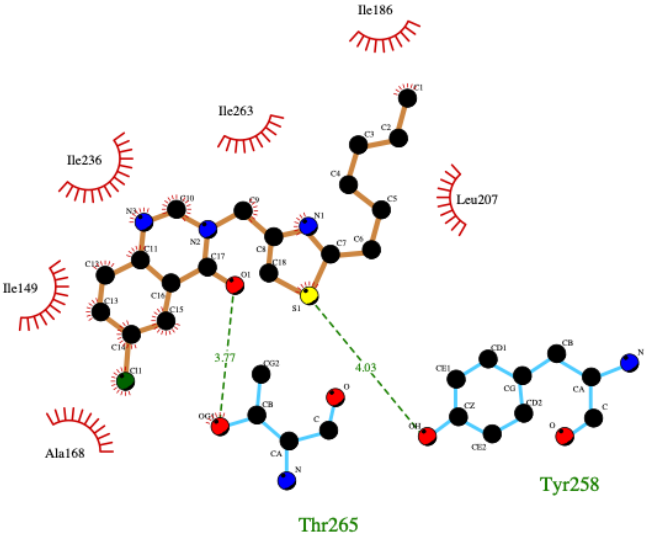

Figure 3.20. Polar interactions between SEN32 series and PqsR^{LBD} binding pocket residues. LigPlot 2D representation of SEN32 series antagonist binding. Electrostatic interactions observed between each antagonist carbonyl and Thr 265 & the sulphur atom of the thiazole with Tyr 258 hydroxyl group.

3.6.2 Comparison to native AQs

Superimposing the SEN32 series structures highlights a minor shift in the position of the bicyclic ring correlated with the presence of a long alkyl chain (Figure 3.21). Although limitations in resolution make subtle shifts hard to interpret the observation appears to be consistent with previous HHQ, NHQ and QZN structures, that possess long alkyl chains. The difference may be explainable by greater conformational freedom in the pocket without a large alkyl chain taking up the majority of pocket A. The SEN32 series, despite having a thiazole ring, occupies the same area as native AQs HHQ and NHQ highlighting that long alkyl chains are dispensable to adopt this binding mode.

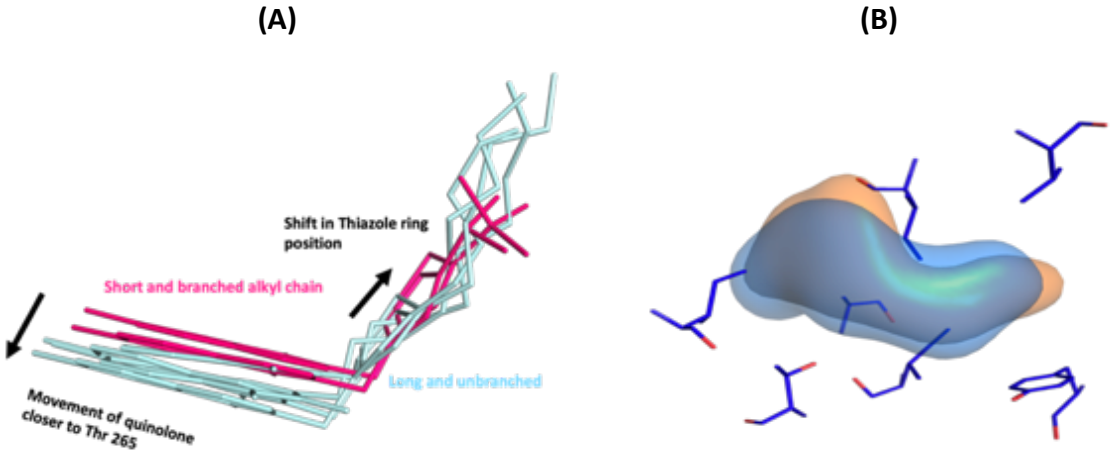

Figure 3.21. Variation in bicyclic position with alkyl chain (A) Superposition of SEN32 series antagonists with HHQ, NHQ and QZN (PDBs 6Q7U, 4JVD, 4JVI respectively). Ligands with long unbranched alkyl chains coloured in pink and short and branched coloured in blue. Shift in bicyclic position due to lessened restrains from a large alkyl chain and shift in thiazole ring (distance between most diverged sulphur atoms 1.9 Å). **(B)** Averaged gaussian maps of SEN32 series (blue) and native AQs (orange) further demonstrate congruent binding position.

3.6.3 Relating SEN32 structural data to SAR

Structural data has shown that the SEN32 series, much like SEN19 has constricted halogen placement on the quinazolinone further supporting the notion that spatial constrains within pocket B are strict. The electrostatic interaction between the thiazole sulphur atom and Tyr258 suggests the reason for poorer activity in oxadiazole isostere was due to increased bond length due to the smaller atom size. Additionally, the improved potency observed with longer alkyl chains is clearly due to greater hydrophobic interactions, especially to the back of pocket A.

3.7 Resolving enantiomeric differences in SEN89 benzimidazole binding to PqsR^{LBD}

The SEN89 series of antagonists has demonstrated the greatest potency compared to the other series characterised in the SENBIOTAR project. The structure bears some resemblance to M64 in the possession of a benzimidazole core but unlike M64 has substituents branching off the N1 atom in the imidazole ring. As with the previous series, the position of the halogen is important with only a chlorine atom at the 6th position (R_1) showing activity which is not fully restored in the presence of a trifluormethyl group. Moreover, activity was arrogated with a 5,6- dichorobenzimidazole suggesting that even a smaller bicyclic is

confined by the same spatial constraints as observed with the quinazolinone based antagonists. Exploration of the R_3 position revealed improvement upon addition of bulkier functional groups in which an ethyl and isopropyl had almost a 2-fold increase in potency. Addition of cyclised groups at R_3 were similarly effective but potency suffered with increasing size however, this was not the case with unbranched groups. Interestingly, composition of the distal function group on R_3 affected function significantly with tertiary amines giving poorer activity compared to hydroxyl or ethers. Attempts to change the electronegativity of the phenoxy with the addition of fluoro groups to R_4 and R_5 improved potency.

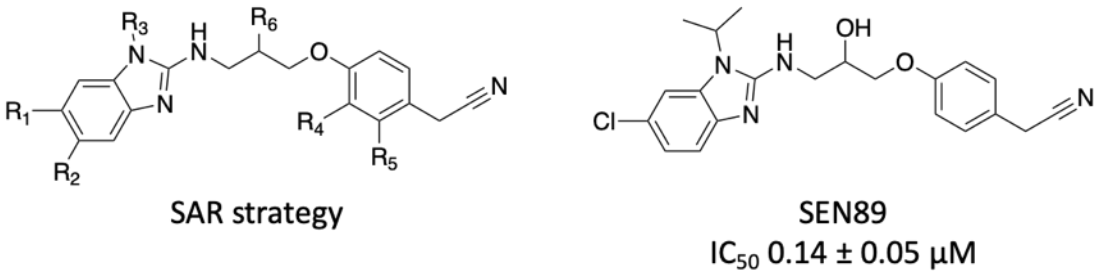

Figure 3.22 SEN89 compound series. SAR scheme given left and highest potency hit (right). Potency values from PAO1 – L CTX::P_{pqsA}-*lux* given.

3.7.1 Crystal soaking

For soaking experiments, each antagonist (except AM204-25 and SEN89-R) was provided as solid racemates around the secondary alcohol. Soaking success rate was relatively high, despite low solubility of the antagonists. Data for each soak was taken from Xia2 implementing DIALS and phased using the apo-4JVC model by REFMAC5[223]. Data collection and refinement statistics are given in Table 3.5:

Table 3.5: Crystallographic data collection and refinement statistics for $PqsR^{LBD}$ in complex with SEN89 & derivatives

Data collection	$PqsR^{94-309}$ – SEN89	$PqsR^{94-309}$ – AM204-004	$PqsR^{94-309}$ – AM204-25	$PqsR^{94-309}$ – AM204-42	$PqsR^{94-309}$ – AM204-21
Beamline	I24	I04	I04	I04	I04
Wavelength (Å)	0.9686	0.9795	0.9795	0.9795	0.9795Å
Space group	P 6_5 2 2	P 6_5 2 2	P 6_5 2 2	P 6_5 2 2	P 6_5 2 2
a ,b, c (Å)	121.12	119.03,	119.23,	119.69	120.27
	121.121	119.03,	119.23,	119.69	120.27
	115.53	115.92	115.80	115.44	115.44
α, β, γ (°)	90, 90, 120	90, 90, 120	90, 90, 120	90, 90, 120	90, 90, 120
Resolution	104.89 - 2.90	115.92 – 2.75	59.61 - 2.88	59.84 – 2.75	60.13 - 3.16
No. of unique reflections	11410 (1602)	13152 (1704)	11260 (1625)	12919 (1873)	8281 (1469)
R_{merge} (%)	18.7 (134.1)	10.7 (133.2)	5.9 (125.6)	6.9 (126.2)	12.8 (124.3)
Mean I/Sig(I)	10.1 (2.2)	10.5 (1.2)	14.5 (1.6)	16.1 (1.9)	11.2 (1.7)
Completeness (%)	98.1 (88.4)	99.9 (100)	98.2 (98.9)	98.4 (99.2)	94.3 (95.0)
Redundancy	16.1 (15.2)	10.2 (10.8)	9.8 (10.1)	9.8 (9.6)	10 (10)
CC½	0.998 (0.653)	0.988 (0.816)	0.998 (0.935)	0.999 (0.939)	0.843 (0.923)
Refinement					
Resolution range (Å)	105.11 - 2.90	103.30 - 2.80	59.68 - 2.88	59.91 - 2.75	53.39 - 3.16
R/Rfree	0.219 / 0.247	0.223 / 0.285	0.201 / 0.251	0.233 / 0.263	0.208 / 0.245
Mean B-Factor (Å)	98.5	109.5	120.6	107.9	124.5
r.m.s.d bond lengths (Å)	0.0057	0.0034	0.0046	0.0027	0.0043
r.m.s.d bond angles (°)	1.377	1.267	1.416	1.284	1.437
Ramachandran plot statistics (%)					
Preferred regions	93.03	93.03	93.53	97.01	89.05
Outliers	0.5	0	1.00	0	0.5
PDB ID	-	-	-	-	-

The *R* isomer of SEN89 was soaked into a modified crystal system designed to attain higher resolution (Chapter 6.1.3 & 6.4). Diffraction quality was not substantially different and crystal characteristics such as space group and unit cell were not significantly different. Diffraction had moderate anisotropy so the data was reprocessed using Xia2 DIALS and the subsequent unmerged data was anisotropically corrected using the STARANISO server to establish diffraction model based on ellipsoidal cut offs. This permits weak and incomplete resolution shells to contribute to map calculation. Data collection and refinement statistics are given in Table 3.6.

Table 3.6: SEN89 *R* isomer soaked into S123C PqsR$^{94-309}$ table of crystallographic collection and refinement

Data collection	PqsR$^{94-309}$ S123C SEN89 *R* isomer soak
Beamline	I24
Wavelength (Å)	0.9998
Space group	P 6_5 2 2
a ,b, c (Å)	118.493 118.493 117.079
α, β, γ (°)	90.0 90.0 120.0
Resolution (Å)	102.62 - 2.54
Ellipsoidal resolution (Å) (direction)	3.306 (a*)
	3.306 (b*)
	2.536 (a*)
No. of reflections (ellipsoidal)	162127 (7841)
No. of unique reflections (ellipsoidal)	8795 (441)
R_{merge} (%)	8.9 (171)
Mean I/Sig(I)	23.6 (1.8)
Completeness spherical (%)	52.9 (8.8)
Completeness ellipsoidal (%)	87.5 (77.5)
Redundancy	18.4 (17.8)
CC½	1.000 (0.63)
Refinement	
Resolution range (Å)	102.83 - 2.54
R/Rfree	0.247 / 0.299
Mean B-Factor (Å)	76.7
r.m.s.d bond lengths (Å)	0.003
r.m.s.d bond angles (°)	1.272
Ramachandran plot statistics (%)	
Preferred regions	92.54
Outliers	0.50
PDB ID	

3.7.2 Racemate preference not highlighted by crystal soaking

Soaking of the racemate SEN89 had clear electron density in the binding pocket with distinct structural features showing that the benzimidazole group was buried in pocket B and the phenyl extended into pocket A adopting a similar position to that observed in SEN19. However, the enantiomer identity around the secondary alcohol was difficult to determine. Both *R* and *S* isomers could be modelled into the positive Fo-Fc density and examination of each isomer after refinement showed negligible differences. This suggested that either *S* or *R* isomer was able to bind to the pocket. Higher resolution may have been sufficient to resolve enantiomeric preference but at 2.9 Å this was not possible.

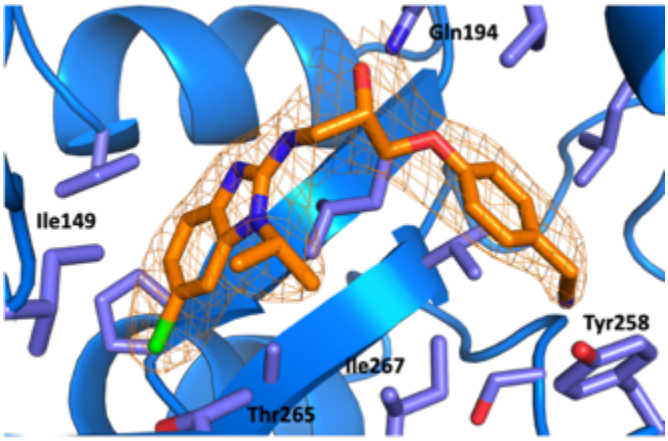

Figure 3.23. Electron density maps for SEN89 racemate soaked into PqsR$^{94-309}$. SEN89 is coloured in orange (*S* is modelled) Residues within 4 Å of SEN89 are coloured slate. 2Fo-Fc map is shown in orange contoured at 1 σ with carve set to 1.6 around the ligand. SEN89 adopts a similar pose to SEN19. SEN89 binds across both subpockets A and B with the benzimidazole group occupying the smaller subpocket B and phenyl extending into pocket A.

To determine if both enantiomers can bind independently, the racemate was separated by chiral chromatography and provided as single enantiomer solids. These were independently soaked and both yielded difference density in the pocket confirming that both enantiomers were able to bind. Superposition of the two isomer structures showed variation in hydrogen bonding distance to the alcohol. As shown in Figure 3.24 the *R* isomer possesses a more favourable hydrogen bond with Gln194 with the distance between the amine and alcohol being 2.9 Å whereas the *S* isomer has 3.3 Å distance. Additionally, the amine linker connecting the benzimidazole has a more favourable interaction with the backbone carbonyl of Leu207 permitting a stronger hydrogen bond interaction. The interaction with

Tyr258 is deleteriously affected by the enantiomer change as the *R* isomer has a greater centroid distance (6.3 Å) compared to the *S* isomer (5.6 Å). The phenyl ring has shifted position slightly such that the interaction is more parallel in the *R* isomer. These small structural changes most likely account for more potent IC_{50} with the *R* isomer reported by Alaa Mashabi (Division of Biomolecular Science & Medicinal Chemistry, University of Nottingham).

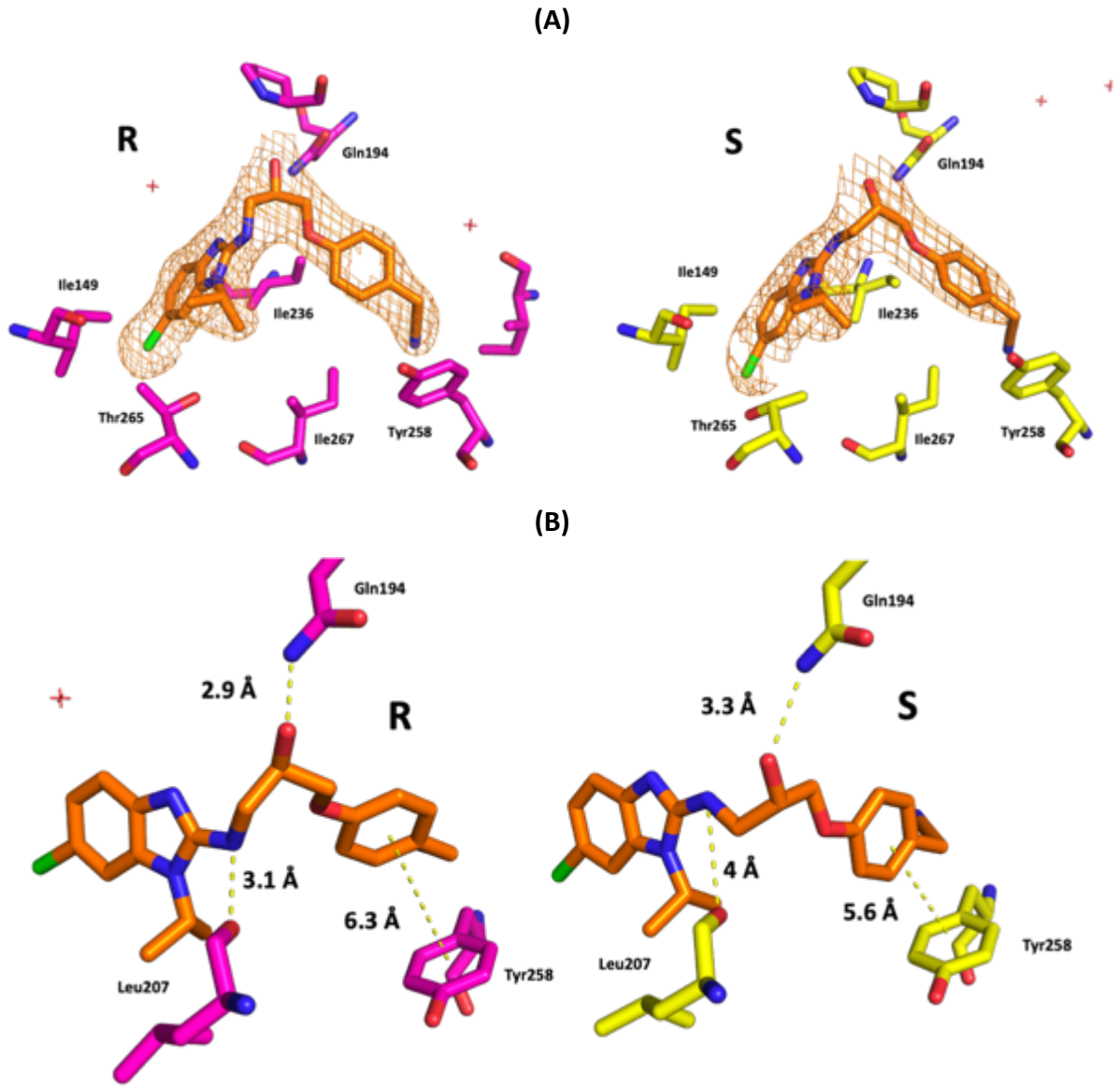

Figure 3.24. Comparison of SEN89 enantiomer binding to PqsR^{LBD} (A) Independently solved *S* & *R* enantiomers of SEN89 highlighting that both can bind with negligible change in position of the benzimidazole core in pocket B. Structures represented as stick models with antagonists coloured in orange and protein residues coloured in pink and yellow for *R* and *S* respectively. **(B)** The *R* isomer of SEN89 has more favourable hydrogen bonding to Gln194 and the backbone carbonyl of leu207. The π-π stacking with Tyr258 is weakened by a greater bond distance with a more parallel interaction adopted compared to the *S* isomer.

3.7.3 Thermal shift analysis of both enantiomers

Although ITC was not possible due to the insolubility of both isomers, we attempted thermal shift analysis at a relatively high concentration of DMSO (10%) with increased amounts of glycerol to abate antagonist driven aggregation. Some studies have shown that binding data can be attained from such experiments[232]. Testing the sample at varying concentrations of *S* and *R* isomers generated data that could be fitted to a one site binding model as shown in Figure 3.25. This showed that the *R* isomer had greater apparent affinity compared to the *S* (6.6 µM vs 14.7 µM). This is further supported by biosensor data (produced by Alaa Mashabi) showing that the *R* isomer has greater potency.

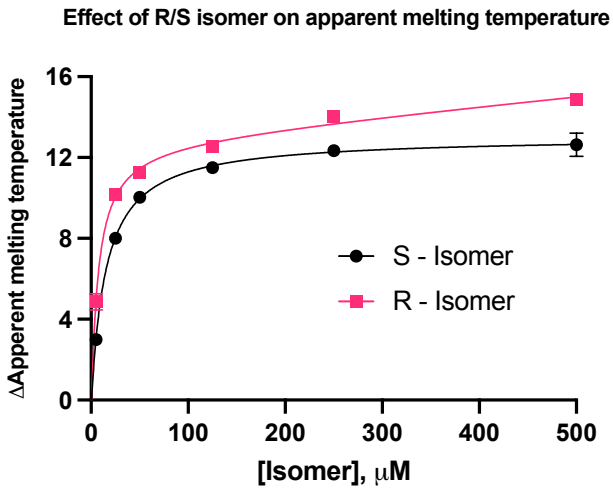

	S	R
B_{MAX} (ΔT_M)	**13.4**	**14.05**
K_D (µM)	**14.71**	**6.616**
(95% CI) (µM)	**10.92-19.15**	**2.6 – 11.59**
R^2	**0.9950**	**0.9926**

Figure 3.25. Comparing binding parameters of SEN89 enantiomers by thermal shift assay. Binding parameters attained from a melt of $PqsR^{94-309}$ with varying concentrations of R and S isomer of SEN89. Curve fitting performed in PRISM using a One-site model without constraints. Apparent binding parameters given in the table (right). (n = 3).

3.7.4 Further interactions between SEN89 series and the pocket

Analysis of hydrophobic interactions show that the benzimidazole is sandwiched between a series of hydrophobic residues including Ile149, Ala169, Phe221 and the polar residue Thr265. The phenoxylacetonitrile group maintains a π-π stack with Tyr258 and the nitrile adopts a similar position as observed in the SEN19 series buried in a cavity consisting of Val 170 and Leu189. As shown in Figure 3.26 by LigPlot the R_3 substituents do not interact via hydrogen bonding to other residues in the pocket. Furthermore, the fluorine atom on R_4

does not appear to directly interact with a carbonyl so it's apparent gain in potency cannot be explained with structural information. Presumably the atoms assists with compound penetration or binding is benefitted from inductive effects on the phenyl group.

(A)

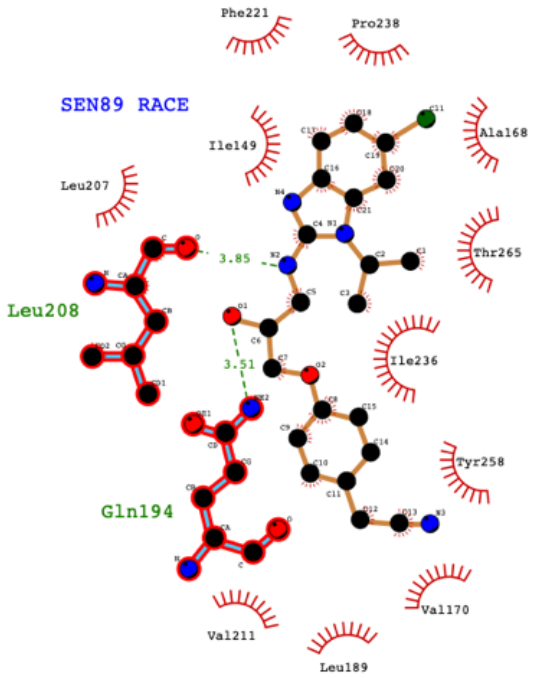

(B)

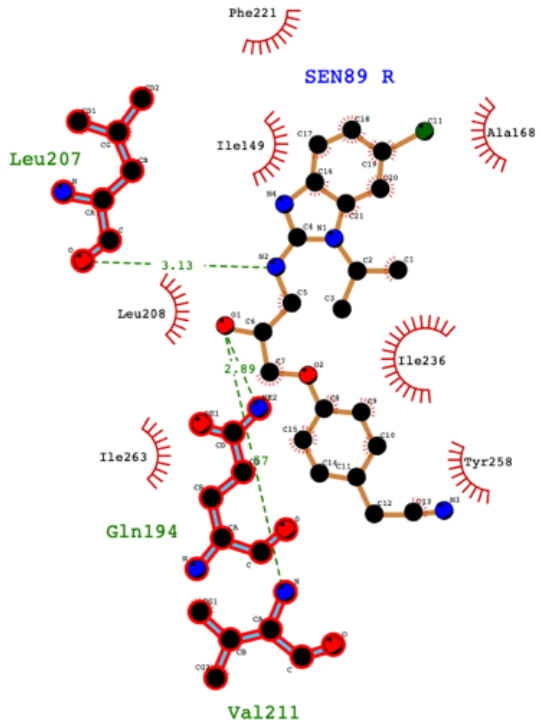

(C)

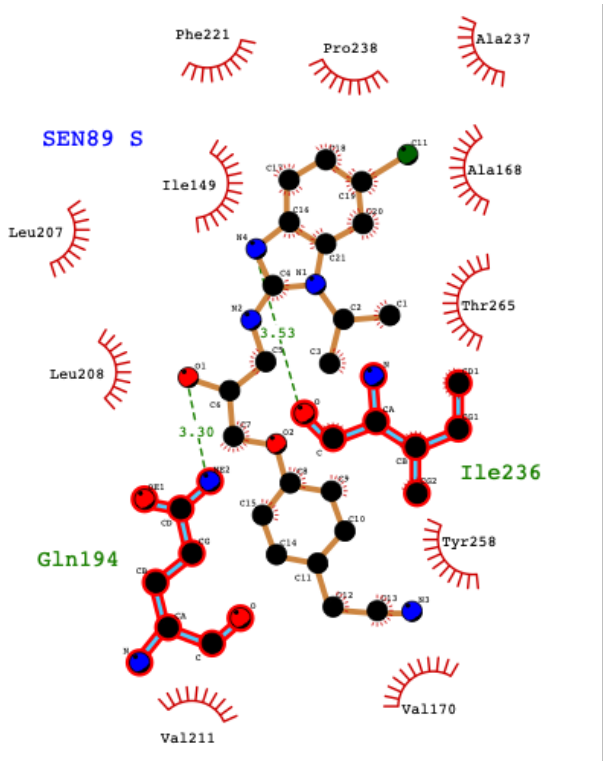

(D)

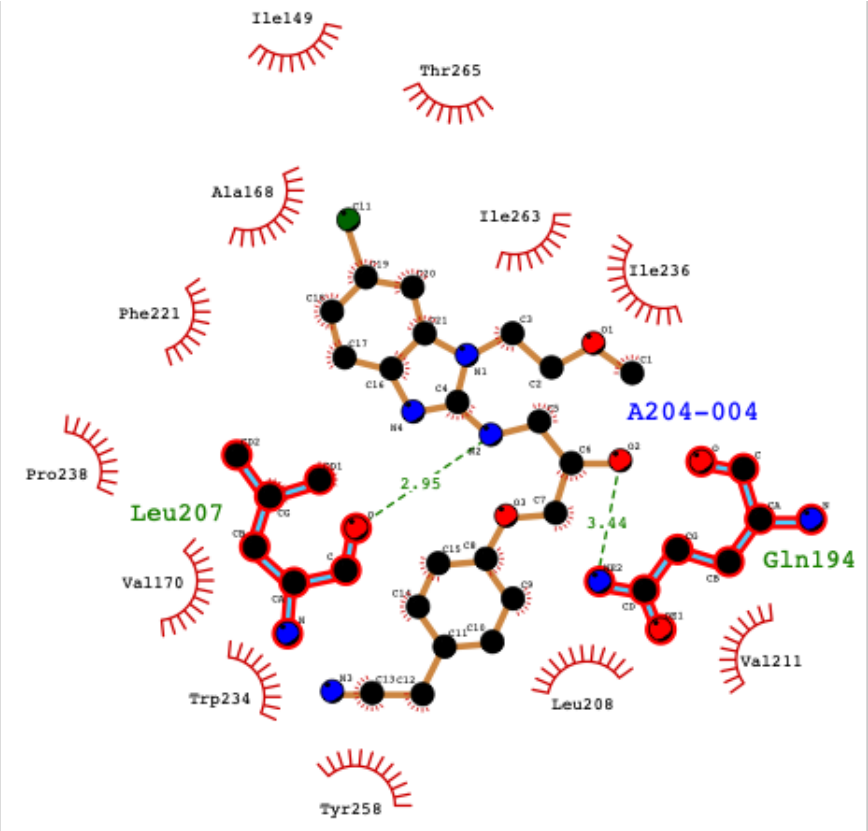
Ile149
Thr265
Ala168
Ile263
Ile236
Phe221
A204-004
Pro238
2.95
Leu207
3.44
Gln194
Val170
Val211
Trp234
Leu208
Tyr258

(E)

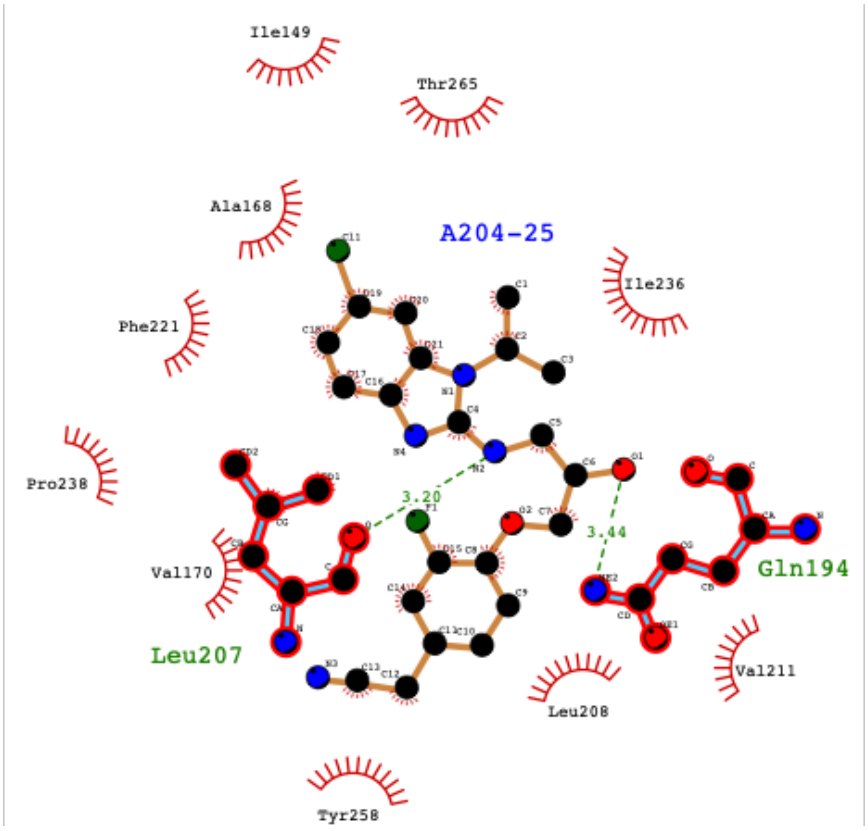
Ile149
Thr265
Ala168
A204-25
Ile236
Phe221
Pro238
3.20
3.44
Gln194
Val170
Leu207
Val211
Leu208
Tyr258

(F)

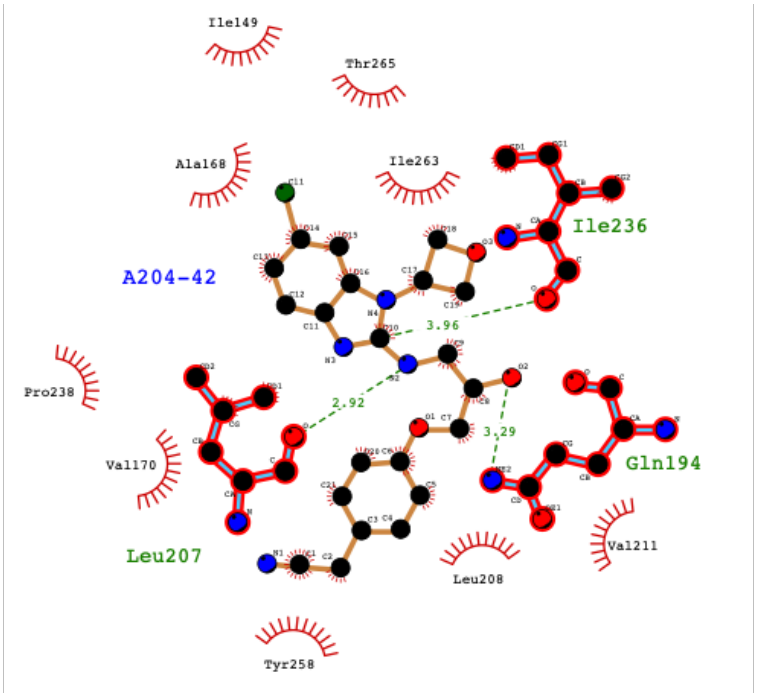

Figure 3.26. Polar interactions between SEN89 and PqsR^{LBD} binding pocket residues. LigPlot^{+} rendering of binding poses of SEN89 Racemate and independent isomer models (**A,B,C**) and derivatives (**D,E,F**). Benzimidazole head group is sandwiched by the same hydrophobic residues (Ala 168 and Ile263) and interaction between Gln194 to the chiral alcohol is observed in each structure. No hydrogen bond interaction is observed with the R_3 substituents in the pocket. Ligands coloured in light orange and interacting ligands with polar interaction in sky blue with red border. Hydrophobic residues are marked by a red dashed wedge. Ligand and residues named in blue and green font respectively.

Superimposing the SEN89 series shows that the position of the R_3 group changes in an unanticipated fashion between SEN89 and AM204-42 (Figure 3.27). The expectation would be that the isopropyl atoms should have the same coordinates as found in the oxetanyl group but in the AM204-42 model the group has rotated by 90° such that it adopts a more parallel position to the bicyclic ring. Interestingly, as the LigPlot analysis (above) showed the oxetanyl does not form hydrogen bonding with surrounding residues so the reason for this movement is unclear.

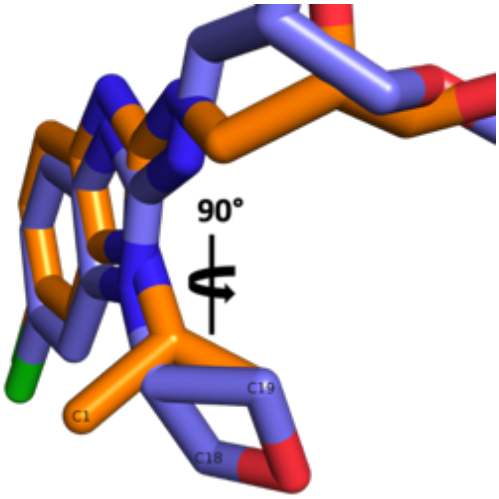

Figure 3.27. Rotation of R_3 group in SEN89 and AM204-42. Ligands represented as sticks with SEN89 (race) antagonist and AM204-42 superimposed showing the rotation of the oxetanyl group relative to the isopropyl. SEN89 and AM204-42 coloured in orange and purple respectively. Carbon atoms C1 from SEN89 & (C3 obscured by oxetanyl) C18 and C19 from oxetanyl labelled.

3.7.5 R_3 substituents optimisation for cross dimer interaction

R_3 substituents were shown in the SAR to have a significant effect on potency. Structural data suggests that two mechanisms explain this relationship. Extension of the R_3 substituent increases the number of hydrophobic interactions between the lid loop Leu 207 and the β-sheet Ile 263 (Figure 3.28). As such the R_3 substituent is sandwiched between the residues which would increase entropic contributions. The second is a function of the R_3 group protruding outside of the pocket, potentially being exposed to solvent that occupies the dimer interface. Although not observable in the crystallographic model one would expect the oxygen atom in the 2-methoxyethyl and oxetanyl group to act as a hydrogen bond acceptor with water. This interaction may stabilise or destabilise the interface which increases the observed potency of the compounds. This however does not explain SAR observed with tertiary amines at R_3 which also should be able to act as acceptors. As a route to additional optimisation the size of the substituent could be increased further to form a hydrogen bond with dimer Lys266 (Figure 3.28b). As the distance from the oxygen atoms to lysine is 6.2 and 5.2 Å for AM204-004 and AM204-42 respectively the addition of 1 or 2 methylene groups would produce an ideal bond length for interaction.

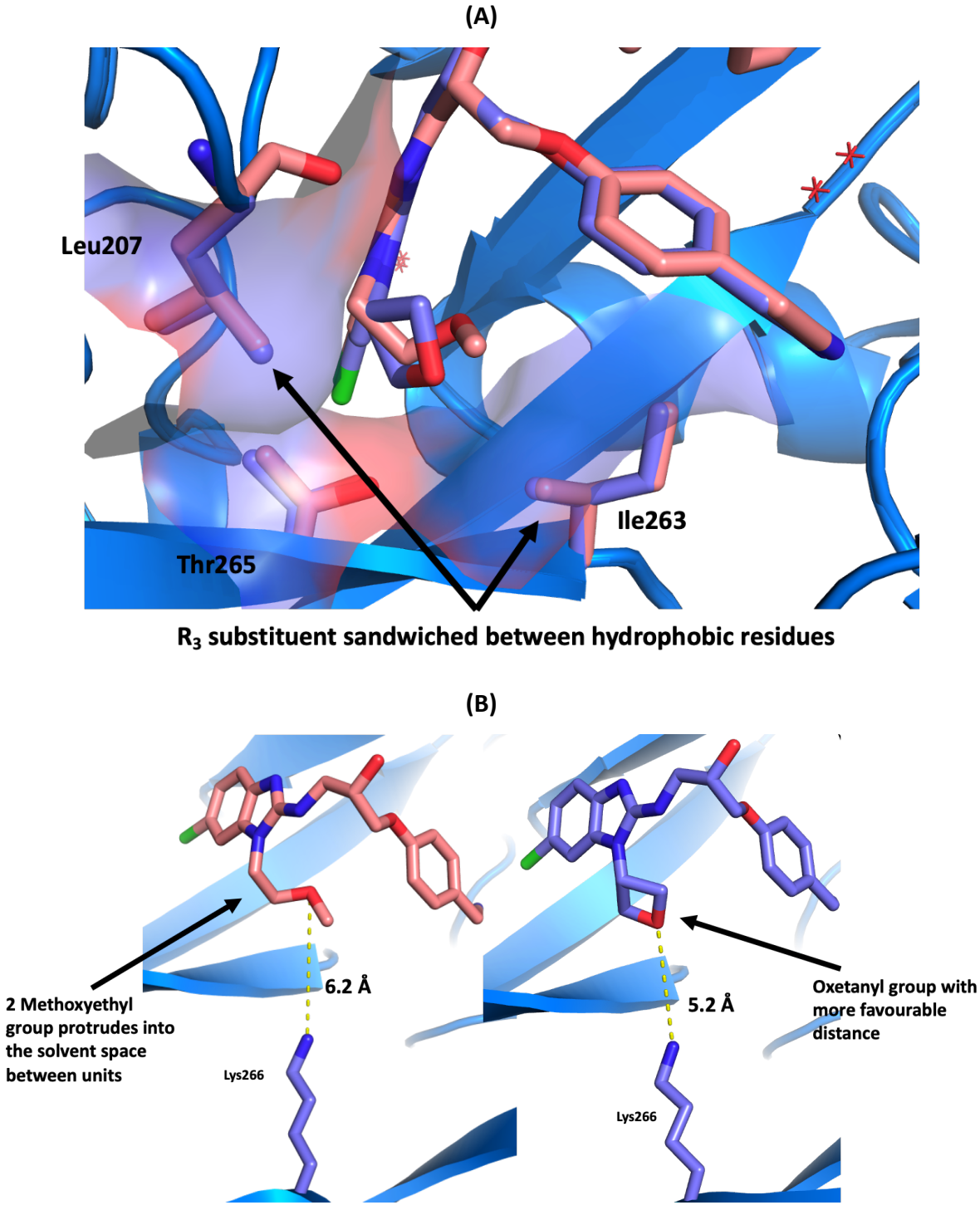

Figure 3.28. Comparison of SEN89 R_3 substituent (A) R_3 groups sandwiched between Leu207 and Ile263 **(B)** R_3 substituent protruding outside of the pocket potentially interacting with solvent or influence dimer stability. This presents an attractive opportunity to produce a new hydrogen bond by extending the R_3 substituent size.

3.7.6 Benzimidazole shifts to accommodate R_1 functional group

Superposition of SEN89 with M64, that also contains a benzimidazole moiety buried in pocket B shows the chlorine atom from SEN89 occupies the same position as the nitro group oxygen lending credence to the idea that this part of the pocket is spatially constricted (Figure 3.29). The position of the benzimidazole has been shifted as the result of having a larger nitro group, however, it may also be due to the greater rigidity caused by the thioacetamide linker that the SEN89 series does not possess.

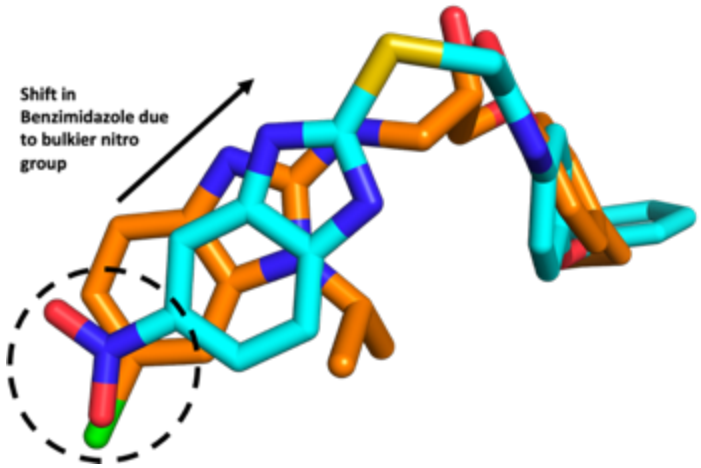

Figure 3.29. Substituent effect on benzimidazole position. Superposition of M64 (light blue) and SEN89 (orange) showing the positional conservation of the function group coming from the benzimidazole and subsequent shift in position of the bicyclic to accommodate the larger functional group.

3.8 $PqsR^{LBD}$ in complex with a naturally derived antagonist – 488

3.8.1 Difficulties in soaking

The smallest PqsR antagonist characterised, 488, is a semi-synthetic natural product analogue shown to have micromolar affinity using the CTX::P_{pqsA}-*lux* system – operating with apparent less affinity compared to molecules in the SENBIOTAR project[233]. Several attempts to soak the ligand failed to produce expected electron density suggesting that the small molecule either bound elsewhere or had especially weak affinity. In several cases the ligand stained the crystals yellow, suggesting that the ligand had entered the lattice. Despite no visual defects observed upon soaking crystals soaked with 488 showed compromised diffraction >3.5 Å suggesting the ligand had damaged the crystal packing. To promote complex formation co-crystallisation was attempted by incubating $PqsR^{94-309}$ with excess

ligand (1:5) prior to crystallisation (using MPD conditions) but this only yielded dark brown precipitate with crystal nucleation entirely abated.

It was surmised that the binding affinity may be too weak to compete out the pseudo-ligand MPD which based on the known density (0.92 g/mL) and concentration range used for crystallisation 3 - 8% represents an effective molar concentration > 0.234 M. As such the soaking methodology was adjusted to titrate out the MPD using different cryo-protectants that would increase binding pocket accessibility. Several were screened using the Hampton cryo kit supplemented with 488 (adding around ¼ volume to the drop) to determine the optimal agent. The impact on diffraction is shown below in Table 3.7.

Table 3.7: Optimisation of solvent washing for 488 complex determination

Cryo-protectant	Concentration[A] (% v/v)	Diffracting power[B] (Å)
PEG 200	25	3.26
PEG 400	25	4.83
PEG 500	25	3.5
Sucrose	35	5.14
Ethylene Glycol	50	2.93
Al's oil	25	3.32

A. Concentration (calculated by accounting for ½ or ¼ dilution of the CryoPro stock solution) **B.** Resolution as determined by Xia2 DIALS. Diffraction on DLS beamline i24 set to 50% transmission.

As shown above most cryoprotecting agents except for ethylene glycol, Al's oil, and PEG 200 negatively affected diffraction. Al's oil is not as favoured for ligand determination as it comprised of components with varying molecular weight which could bind non-specifically to different areas, especially true for a protein with hydrophobic patches. PEG 200 was not too detrimental but its resolution was clearly weaker compared to ethylene glycol.

3.8.2 Structural solution of 488 binding to PqsR$^{94-309}$

488's relatively small size presents a challenge to accurate structural determination given resolution limitations. Additionally, the predicted position of the ligand overlaps with the modelled position of MPD solvent. Modelling of the ligand therefore required *in priori* knowledge of solvent binding to prevent mismodelling. Map calculation with apo-PqsR$^{94-309}$ and subsequent refinement showed a large, cylindrical patch of unmodelled density which

was larger than that of MPD. Additionally, contouring the difference map at σ = 3 showed MPD is partially excluded from the density which adopts a perpendicular position relative to MPD. As shown in Figure 3.30 the electron density was asymmetrically proportioned with a larger patch observed towards the centre of pocket B. This agreed with the expected shape of 488 with a heavier chlorophenyl group and smaller pyrrolone. Previous investigation validated MPD's position by omit map at a higher resolution (2.5 Å), therefore its positioning should be reliable for comparison. To improve structural feature determination the data was further processed using STARANISO which extended the resolution to 2.6 Å. STARANISO functions by performing anisotropic cut-offs of merged intensity data to estimate structure amplitudes based upon an ellipsoidal model.

Table 3.8: Crystallographic data collection and refinement statistics for $PqsR^{LBD}$ in complex with 488

Data collection	$PqsR^{94-309}$-488	Data collection	$PqsR^{94-309}$ 488 complex
Beamline	I24	Beamline	i24
Wavelength (Å)	0.9687	Wavelength (Å)	0.96872
Space group	$P6_522$	Space group	P 6_5 2 2
a ,b, c (Å)	121.207, 121.207, 115.274	a ,b, c (Å)	121.403, 121.403, 115.506
α, β, γ (°)	90, 90, 120	α, β, γ (°)	90.0 90.0 120.0
Resolution	41.76 - 2.95	Resolution (Å)	105.138 – 2.594
No. of unique reflections	11068 (1739)	Ellipsoidal resolution	3.219 (a*)
R_{merge} (%)	9.4 (139.6)	(Å) (direction)	3.219 (b*)
Mean I/Sig(I)	17 (1.7)		2.473 (a*)
Completeness (%)	99.9 (99.8)	No. of reflections (ellipsoidal)	374572 (18996)
Redundancy	19.3 (18.4)	No. of unique reflections (ellipsoidal)	10563 (528)
CC½	0.999 (0.89)	R_{merge} (%)	10.5 (164)
Refinement		Mean I/Sig(I)	15.8 (1.7)
Resolution range (Å)	39.71-2.95	Completeness spherical (%)	65.6 (14.9)
R/Rfree	0.218 / 0.264	Completeness ellipsoidal (%)	95.4 (86.4)
Mean B-Factor (Å)	132.0	Redundancy	35.5 (36)
r.m.s.d bond lengths (Å)	0.0033	CC½	1.000 (0.891)
r.m.s.d bond angles (°)	1.270		
Ramachandran plot statistics (%)			
Preferred regions	95.02 %		
Outliers	0		
PDB ID			

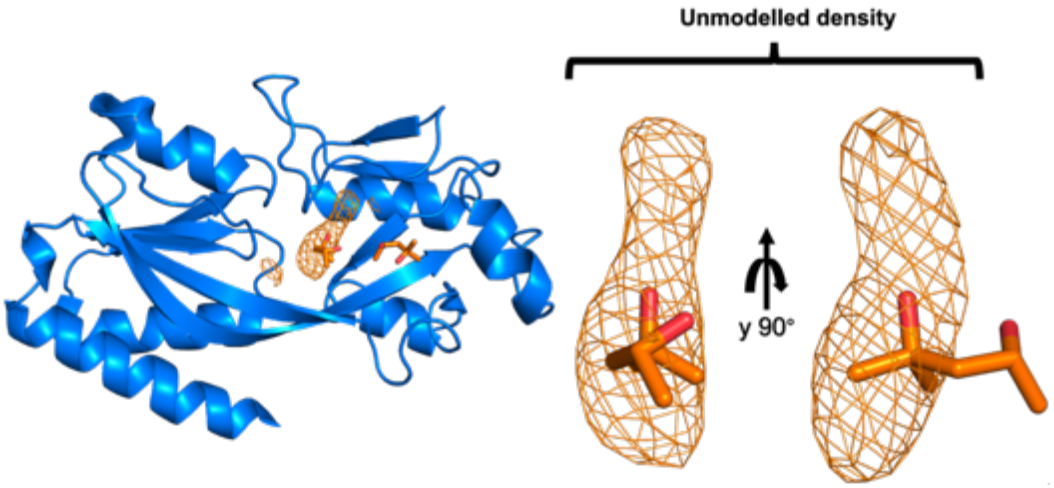

Figure 3.30. Unmodelled ligand density from 488. Positive density (coloured in orange) from Fo-Fc map contoured to 3 σ in binding pocket with the previously established position for MPD shown as orange sticks. The positive density extends into sub-pocket designated B1.

Ligand fitting into the density was successful as electron density matched the expected size of the ligand however, the alkene group was not covered in electron density at 3 *σ*. Interestingly, after refinement positive density peaks appeared around the ligand suggesting the ligand's position within the binding site may be slightly mobile or that low occupancy water was present. Using higher resolution data from 4JVC two waters were added in agreement to their previously observed positions. The positive density close to the ligand reduced, but not entirely suggesting the remaining difference is likely due to noise. This noise was reduced when STARANISO corrected data was applied suggested the elevated noise was due to anisotropy. Analysis with POLDER confirmed ligand presence as the correlation between the synthetically generated data (assuming presence) and the experimental data is higher than that produced by bulk solvent. POLDER functions by excluding bulk solvent that may obscure weak electron density[230]. Inspection of the omit map and polder map, shown in Figure 3.31, showed good density coverage on the omit map and reasonable fit to the POLDER map which had a larger size than expected. This could be due to bulk solvent protrusion into the binding site that has not been fully accounted for combined with the relatively weak resolution. In the ellipsoidally cut data, with higher resolution (2.5 Å), density surrounding the 488 ligand is better defined. In all cases the electron density for the second MPD molecule remained presence after refinement.

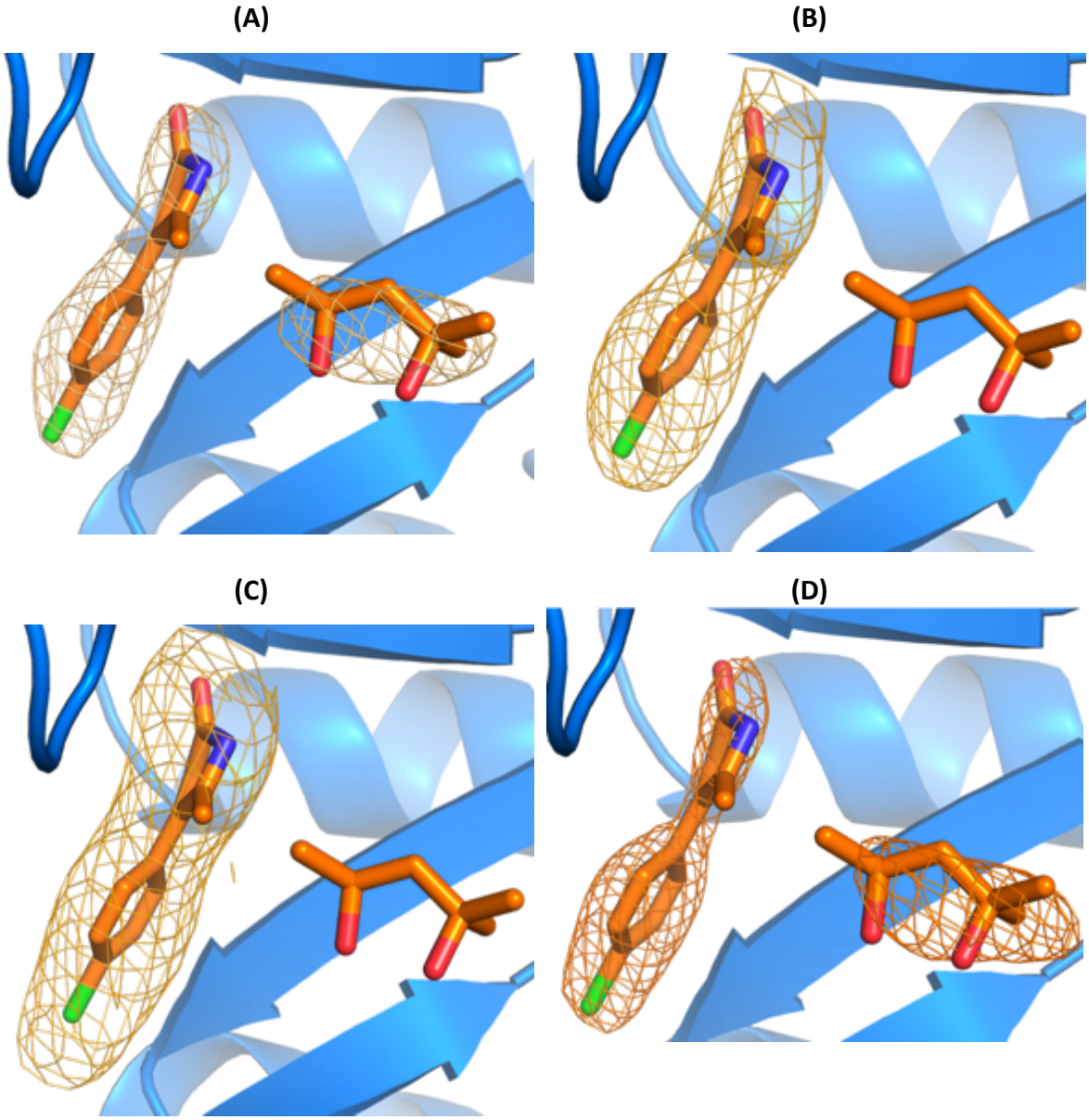

Figure 3.31. Electron density of 488 in PqsR^{LBD} binding pocket (A) 488 2Fo-Fc map generated by REFMAC5[223] (1 σ) **(B)** 488 simple omit map created by Phenix (3 σ) **(C)** 488 POLDER map (5 σ) **(D**) Fo-Fc density (3 σ) surrounding the ligand from STARANISO corrected data. 488 ligand and MPD depicted as orange sticks.

3.8.3 488 interactions with PqsR binding pocket

488 possesses a unique binding pose within pocket B. It adopts an elevated position taking it closer to the loop lid rather than towards pocket A (shown in Figure 3.32) in a subpocket designated B1. 488 binding is mediated by three key interactions. The first being a halogen bond between the chlorine atom and Thr265. The second is a weak electrostatic interaction between the NH from the pyrrolone and hydroxyl oxygen of Ser196 (bond distance 4.5 Å). Lastly, a hydrogen bond was observed between the ketone and the backbone amide nitrogen of Leu197 (3.2 Å) with the latter serving as a hydrogen bond donor. It is likely this bond is responsible for orientating the ligand. As shown by LigPlot 488 is further supported by hydrophobic interactions clustered around the chlorophenyl head group and include interactions from Ile149, Ala168, Pro238, Phe221 and Ile236.

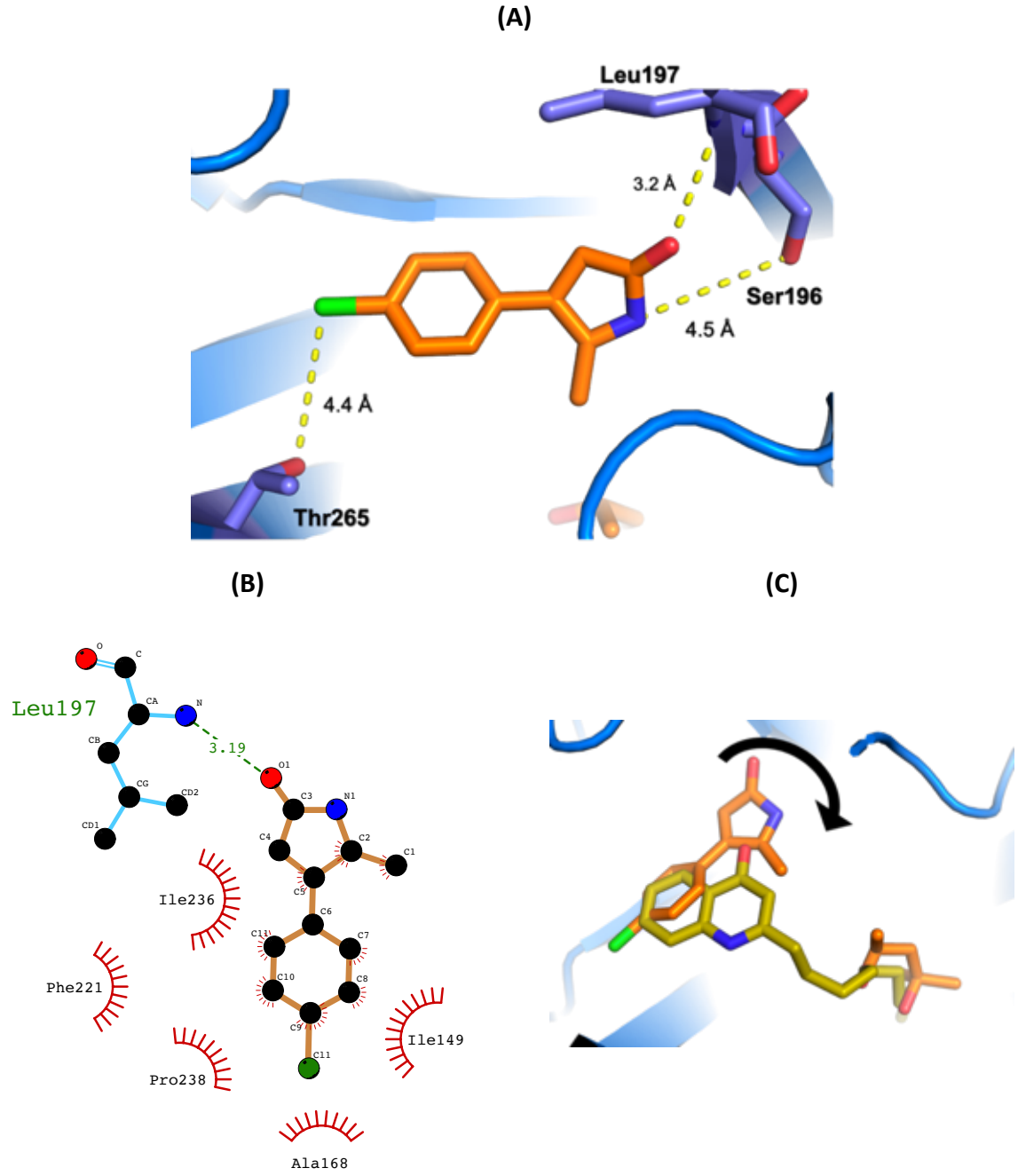

Figure 3.32. Interaction between 488 and PqsR^{LBD} (A) Model of 488 binding to PqsR^{LBD} highlighting three key electrostatic interactions. Halogen bond between the chlorine atom and Thr 265; hydrogen bond between pyrrolone and Leu197 backbone and electrostatic interaction with Ser196. **(B)** Interaction map of 488 generated using LigPlot^{+} showing a hydrogen bond between the pyrrolone and peptide backbone of Leu197. Ligplot also shows the chlorophenyl group to be supported by hydrophobic interactions from pocket B residues. **(C)** Superposition of 488 and NHQ showing the unique orientation of 488 with pyrrolone occupying pocket B1.

Although not disclosed the progenitor of 488 by chemical similarity is likely cladodionen (shown below, abv. Clad) isolated from the marine fungus *Cladosporium sp*. Z148. A

previous docking study with Clad suggested a different binding pose to 488 in which the antagonist caressed the lid loop rather than occupying pocket B[181]. The different orientation may be explainable by the chlorine atom forming a halogen bond with Thr 265 thus stabilising 488's different binding pose. Additionally, a recent series showed that the activity of 488 could be optimised further by extending the alkene with a 2-mercaptopyridine group[234]. Assuming the ligand adopts a similar position to 488 the group could penetrate pocket A to make a π-π stacking interactions with Tyr 258 (Figure 3.33).

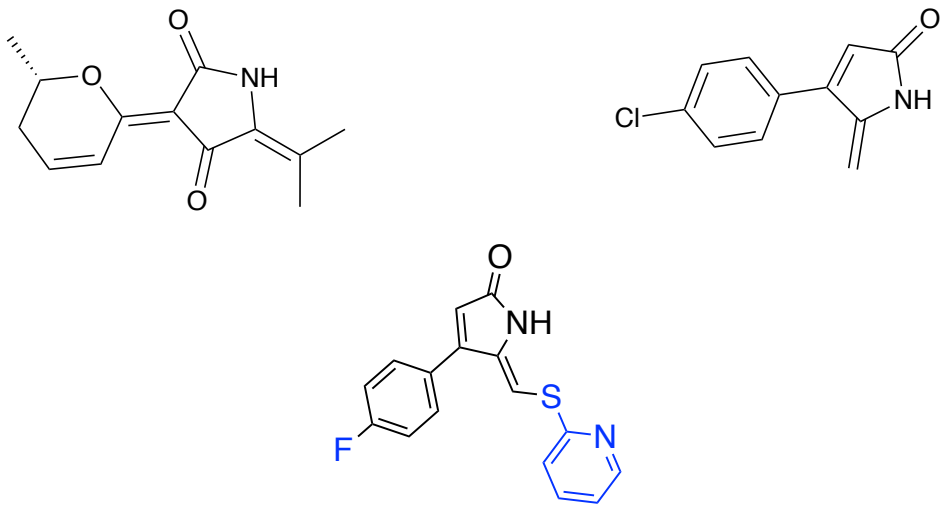

Figure 3.33. 488 natural product congener. Cladodionen (left) natural product isolated from Marine flora and semi-synthetic analogue 488 right. Newly reported series baring a 2-mercaptopyridine surmised to interact with Tyr 258 in pocket A. Varied substituents are marked in blue.

3.8.4 488 is a destabilising fragment

Binding was initially validated by Dr Pantalone (University of Nottingham) using ITC giving a dissociation constant of 1.74 μM[235]. To further validate the interaction a thermal shift experiment was carried out which highlighted the compound destabilised the protein in a concentration dependent manner (Figure 3.34). Interestingly, destabilising fragments have been characterised in the literature as difficult to optimise as the compound is presumed to bind to both the folded and denatured states with some notable exceptions[236 237 238].

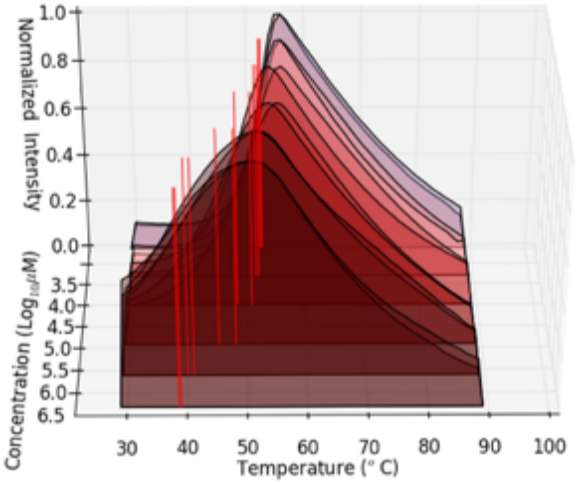

Figure 3.34. Concentration-dependent destabilisation by 488. Waterfall plot showing 488 induced destabilisation in a concentration dependent manner. Melting temperature marked at each concentration with a red line. Experiment conducted on $PqsR^{94-309}$ (n = 2 for each concentration tested).

3.8.5 Circular dichroism to measure 488's impact on $PqsR^{LBD}$ secondary structure

To further explore the nature of the halogen bond to Thr 265 and the preservation of chlorine atom position in SEN19 and SEN89 we decided to use 488 as a chemical probe to explore this interaction more comprehensively. We hypothesised that replacement of the threonine residue with asparagine would shorten the interaction distance thus increasing bond strength whilst the alanine mutant would limit interaction. Circular dichroism, although not often used for ligand binding interrogation, can provide key information regarding in solution structural changes that are not apparent in static crystal soaking or described in the thermodynamic parameters outputted from ITC. Samples were dialysed into a CD compatible, low chloride buffer, in which the ion content was replaced with NaF and buffering system changed to phosphate. At the beamline, the samples were further adjusted with small quantities of concentrated HCl to abate sample aggregation. Melting curves, as shown in Figure 3.35, performed on the mutants in the absence of 488 compound highlighted that secondary structure remained largely similar with respect to Beta strand and Turn components. However, T265N showed an increase in helix content at the expense of disordered components. This effect was more prominent with the T265A mutant showing a change of 9.4% compared to the wildtype. Comparing the wildtype protein to the theoretical values from DSSP analysis of PDB 4JVC showed good agreement[239]. The largest area of discrepancy lies with the helical content (11.6%). Thermal melts with all samples revealed similar secondary structure changes with an increase in helical and beta sheet

components at the expense of turns and disordered content. Whilst the transition for beta sheet was smooth the change in alpha content could not be fully described by a Boltzmann melt curve likely due to sample aggregation at high temperatures.

(A)

PqsR^{LBD}	Alpha (%)	Beta (%)	Turn (%)	Other (%)
Wildtype	17.64	28.79	13.97	39.61
T265A	27.03	24.88	12.66	35.43
T265N	23.79	26.4	13.11	36.7
DSSP 4JVC	29.2	25.5	14.8	30.6

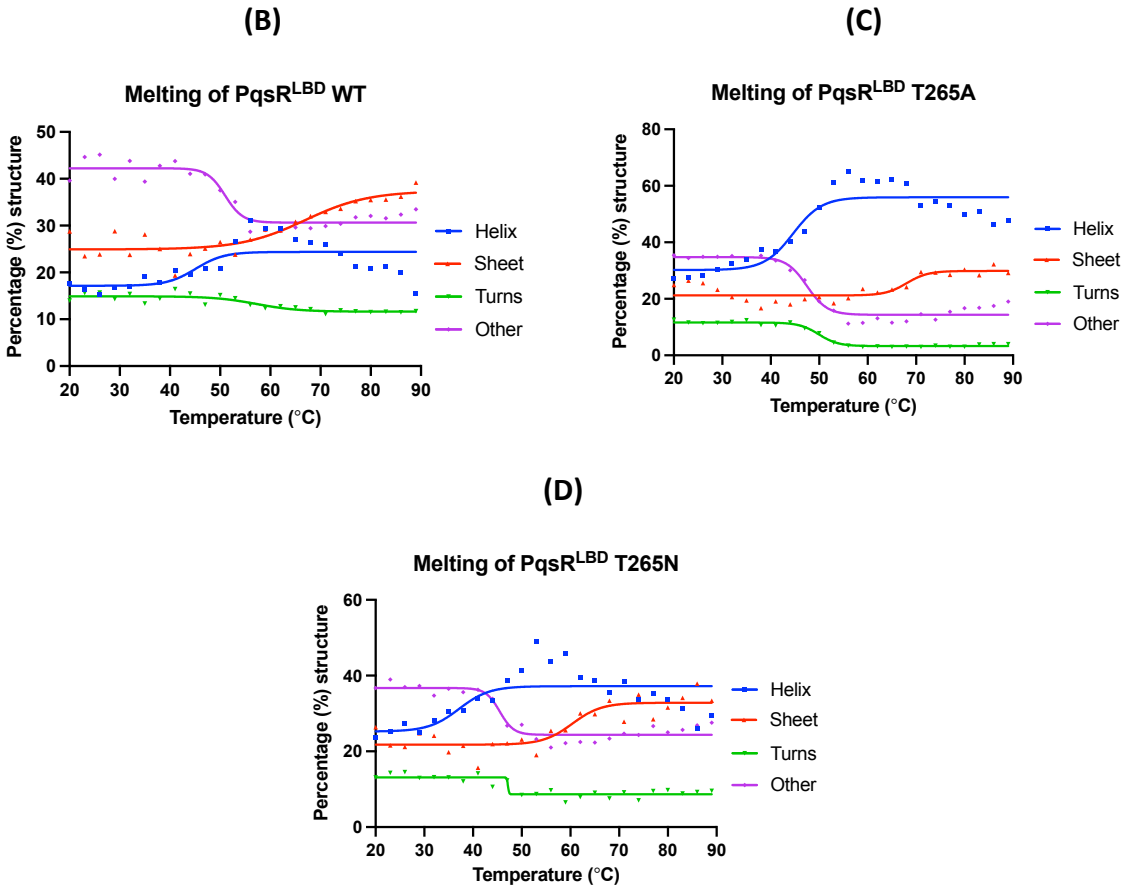

Figure 3.35. CD analysis of secondary structure content of PqsR^{LBD} (A) Secondary structure content at 20°C with respect to alpha, beta, turn and unassigned content. Assignment is based upon characteristics defined by DSSP[240]. **Changes in secondary structure as a function of temperature (B)** Wildtype, **(C)** T265A and **(D)** T265N PqsR$^{94-332}$ as determined by monitoring Far-UV (200 – 250 nm) as a function of temperature. Measurements taken on a Chirascan instrument at Diamond Light Source (B23).

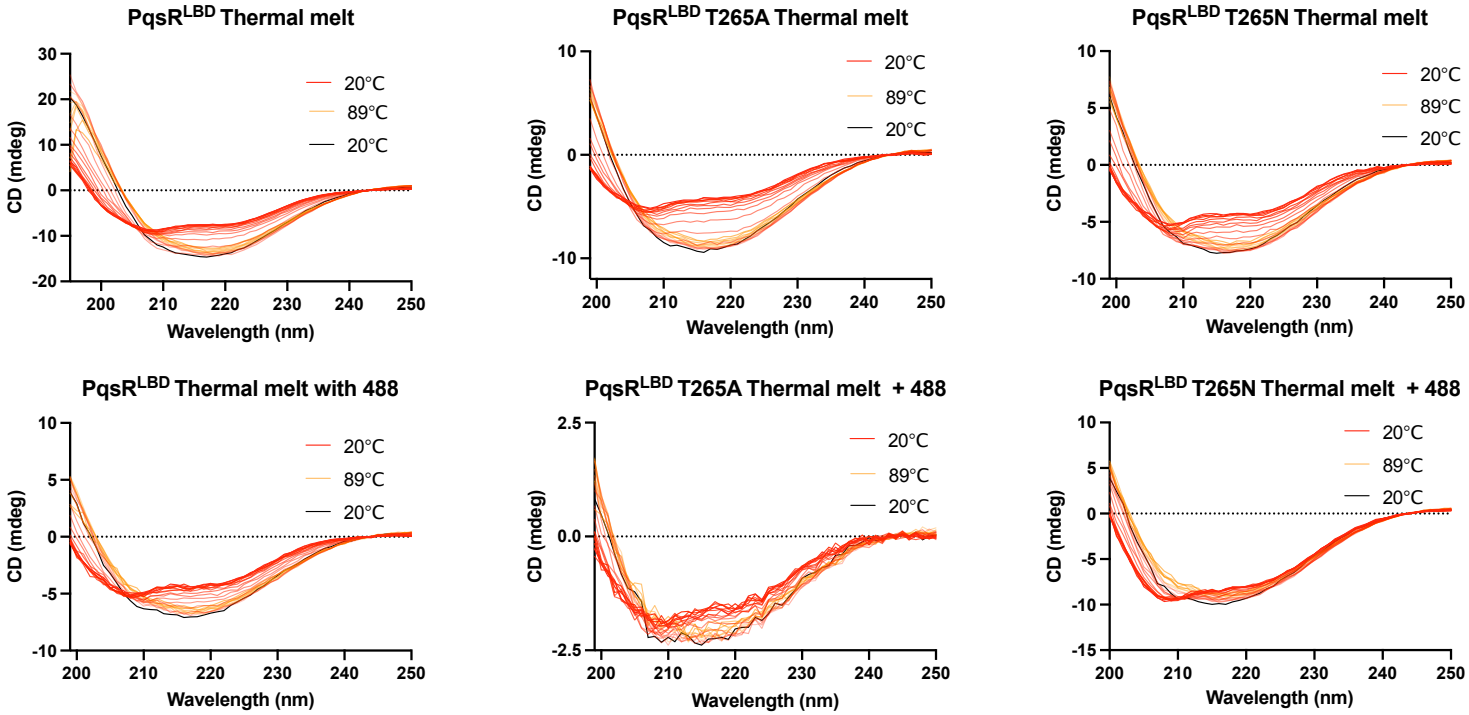

	Wildtype T_m (°C)	T265A T_m (°C)	T265N T_m (°C)
Apo	**49.28**	**46.85**	**43.01**
PqsR:488 (1:3)	**49.99**	**50.06**	**62.52**

Figure 3.36. Effect of 488 on PqsR CD melting spectra. Far-UV CD spectra as a function of temperature. Spectra is colour coded with respect to temperature with lower temperature represented as red and higher temperature shown with light orange. Black line shows a return to 20°C after the melt highlighting an irreversible change. Sample data attained on a Chiroscan instrument at concentrations of 32.98, 12.61 and 14.9 µM for wildtype, T265A and T265N respectively with 488 ligand added at a 3 molar ratio. Melting temperatures were determined by fitting a Boltzmann curve to Molar circular dichroism (Δε) (219 nm) plotted against temperature (fits can be found in Appendix 9.7).

Calculation of the apparent melting temperature of the apo protein was 49.3°C which was in good agreement with the temperature determined by thermal shift (52.9°C). Differences between melting temperature determination are due to methodological differences in data collection. A CD experiment monitors secondary structure elements as a function of denaturant (wavelength 170 – 260 nm) whilst a TSA experiment monitors the unfolding of the tertiary structure through the subsequent exposure of hydrophobic residues. Differences have been reported in the literature with often DSC showing greater agreement with CD but relatively little investigation has been performed to explain discrepancies between these two methods[241 242]. Based on the apo melt curves the wildtype protein had the greatest stability followed by T265A and T265N. This shows the inclusion of more polar residues into the binding pocket is disfavoured. Unlike thermal shift CD showed that 488 stabilised secondary structure slightly in the wildtype protein (+0.7°C). Unexpectantly, this stabilisation effect was increased in both mutant samples with the largest increase in stabilisation observed in the T265N mutant (19.5°C). This large increase could be due to the ligand compensating for the destabilising T265N mutation. Contrary to our hypothesis T265A did appear to bind to 488 with a shift of 3.23°C observed.

Near UV measurements describe the chromophore environments of aromatic residues including tryptophan and to a weaker extent tyrosine and phenylalanine. This permits limited analysis of tertiary structure from CD data but unlike far UV cannot be assigned to specific structural features. Near UV experiments conducted on $PqsR^{LBD}$ showed only a weak near UV signal whilst the ligand expectedly possessed no CD signal (achiral). As shown in Figure 3.37 monitoring of near UV (240 - 320 nm) regions in response to ligand addition highlighted that for wildtype, T265A and T265N mutants an induced CD (ICD) signal is observed[243]. As ICD only occurs upon the restriction of conformational freedom arising from intermolecular interaction, we can infer that 488 binds to all three constructs.

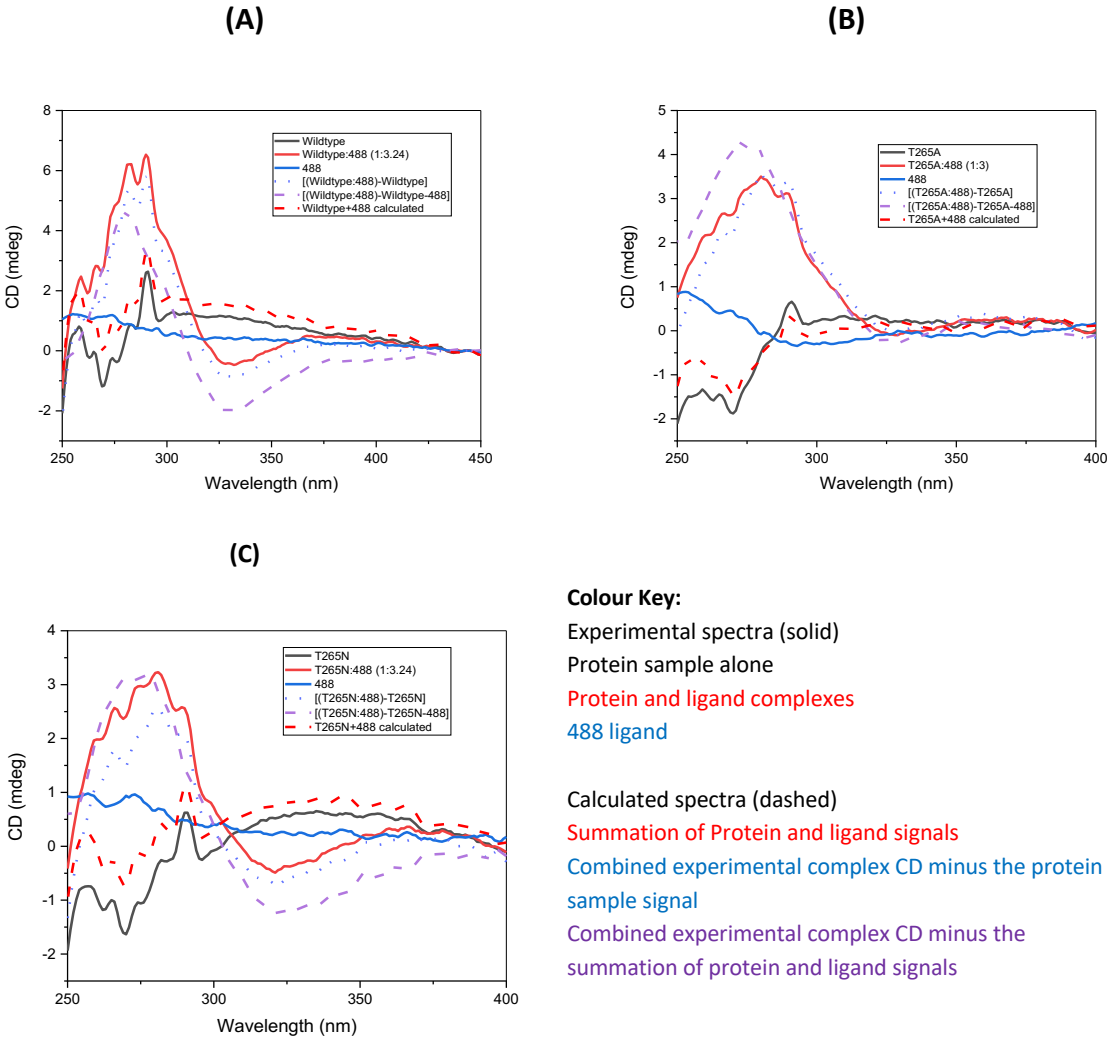

Figure 3.37. Near-UV acquisition for PqsR-488 host guest interaction. (A) Wildtype **(B)** T265A **(C)** T265N. Ellipticity is given as millidegrees (mdeg). Each sample was scanned 4 times at 20°C with averaged signal plotted. 488 ligand added to protein sample in a 1:3 or 1:3.24 ratio (specified in graph key). CD from achiral 488 ligand shown in blue possesses no significant signal. Apo samples (black) all show weak signal. Signals from 488-$^{94}PqsR^{332}$ complexes are shown in red and are significantly higher than the theoretical summation of 488 + $^{94}PqsR^{332}$ signals (dashed red line) highlighting the occurrence of induced CD. High residuals observed in the dashed blue and purple lines further indicate that the induced CD cannot be accounted for by $^{94}PqsR^{332}$ alone or by the summed signal from $^{94}PqsR^{332}$ + 488. A colour key indicating spectra origin is given on the bottom right.

3.9 Lack of Clofoctol density

Determination of binding pose for the novel antagonists shown above represents a significant step in lead development and can aid subsequent SAR to find more potent agents. However, typical pharmaceutical drug development is handicapped by significant time investments. The associated costs and time to optimise a new agent and risks

associated with toxicity and unfavourable ADME characteristics can complicate development[244]. An alternative strategy involves screening approved therapeutics against different targets to identify agents with favourable "drug-like" features[245]. A popular screening tool is the PHARMAKON FDA approved library (currently consisting of 7,538 compounds). A screen conducted previously[246], using a similar luciferase biosensor, identified clofoctol to be a promising agent with IC_{50} of 20 µM towards *pqsA* promoter inhibition. To determine its binding mode to PqsR, soaking was conducted as above but subsequent examination of electron density maps produced by both DIMPLE[247] and phased independently with PHASER[248] and REFMAC[223] on multiple crystal soaks (n = 7) revealed no additional electron density. Clofoctol, unlike other antagonists tested was highly soluble (reflected by a high predicted LogP), suggesting that a lack of density was due to weak/limited binding rather than solubility limitations. Interestingly, the study conducted by D'Angelo *et al.*,[246] suggested clofoctol binds with the 2,4,4-trimethylpentyl group occupying pocket B and extending into pocket A. This conflicts with the binding dynamics favoured by AQs in which the more hydrophobic functional group occupies pocket A. Given, that ITC conducted by Dr Pantolone (personal communication) on the binding domain ($PqsR^{94-309}$) showed no significant heat upon titration it is likely that the compound either binds to the DNA binding domain or to a different component of the PQS system.

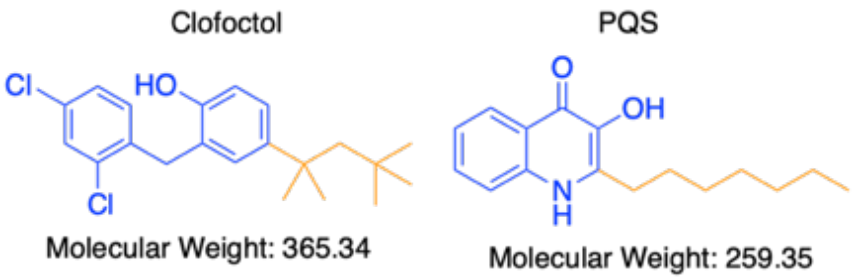

Figure 3.38. Proposed $PqsR^{LDB}$ binder clofoctol. Clofoctol and PQS structures with chemical commonalities highlighted. Hydrophilic head groups shown in blue and lipophilic substituents in orange. Compound lipophilicity is highly divergent with a LogP of 8.19 and 2.03 respectively.

3.10 Analysing PqsR sequence conservation

As with any bacterial target, the prospect of resistant mutations accruing represents a risk in therapeutic development. Fortunately, many clinical and environmental isolates have been sequenced and can aid in prediction of unfavourable target changes.

3.10.1 Database Analysis

Coding sequences of PqsR were attained on May 2020 from the Pseudomonas Genome Database (PGD) [249]- filtering for Complete genomes only - and BACTOME (Helmholtz Centre for Infection Research)[250]. Strains from PGD originate from clinical and environment isolates and from different locations. Most isolates were attained from clinical settings and are listed in Appendix 9.3 with breakdown shown in 9.4. Isolate sequences from BACTOME were taken using their SNP extraction tool filtering for the highest confidence score - 222. The number of strains from each source are listed below:

Data source	Number of strains
Pseudomonas Databank	190
BACTOME	417

Sequences mined from the PGD were trimmed to only include the residues present within the 4JVC model and aligned using CLUSTALW[251]. The corresponding clustal file was analysed using ProtSkin[252] outputting a PDB file with B-factors replaced to represent sequence conservation with PAO1 as a reference. These were further altered to be expressed as a percentage using PDB Editor[253]. Sequence conservation scores from BACTOME were manually calculated and applied to the model in the same manner.

3.10.2 Comparisons between datasets

Both datasets showed a greater proportion of mutations in the ligand binding domain compared to the DBD and hinge helix (Appendix 9.5). As shown in the Figure 3.39 some commonality in the distribution of mutations were apparent between the two datasets. Mutations in Loop 1 (binding pocket lid) were relatively common with missense mutations of R200H and S201F commonly observed. Substitution at residue 200 to histidine is relatively conservative and only a hydrogen bond to Asp 161 would be altered. S201F would be a more significant change as it would create a clash with Ala 134 and likely induce a conformation change in loop 1 to compensate. Additionally, both datasets possess mutations affecting the loop length between β strands 3 and 4 with a deletion of 5 residues

observed in the PGD set. Such a deletion would cause a substantial strain on the loop and affect binding pocket topology. Less prevalent shared mutations include V215A which would give residues in the lid loop greater conformation freedom and V162E that creates a salt bridge to Lys 266 on the opposing antiparallel β strand likely to increase the stability of secondary structure.

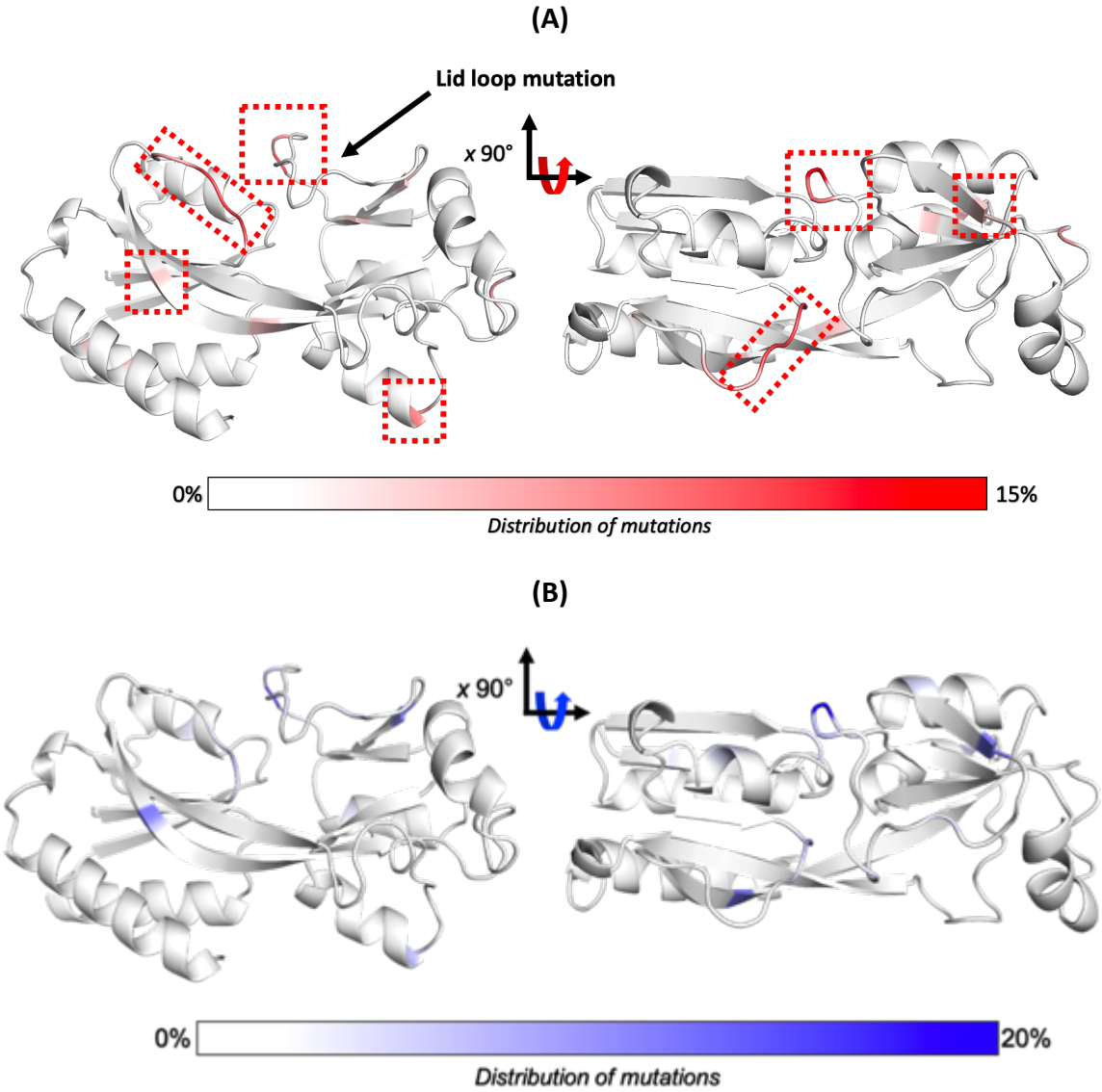

Figure. 3.39. Distribution of mutations across the known PqsR structure. (A) Mutant pool mined from the PGD with gradient colour marking frequency from White (0%) to Red (15%). Lid loop mutation influencing binding pocket topology marked. **(B)** Mutant pool of clinical isolates from Bactome with White (0%) to Blue (20%) gradient. Commonalities between datasets are marked with dashed boxes on the PGD dataset.

3.10.3 Binding pocket mutations

Surprisingly, only a handful of mutations in the binding pocket are observed, the most significant being I149insSTF. Substitution of isoleucine to serine could decrease pocket

hydrophobicity and reduce spatial constraints in pocket B. The two additional residues would increase the length of the corresponding loop potentially perturbing secondary structure and altering the pocket size. Located deeper into pocket B a T166P mutation is also observed which may disrupt the two antiparallel beta sheets connecting subdomains RD1 & RDII. However, as shown in LigPlot analysis - Figures 3.9b, 3.12b, 3.20, 3.26, 3.32b – no antagonist makes direct hydrophobic or polar interactions this deep into the pocket.

3.10.4 Conservation of dimer interface and predicted impact on protein stability

No mutations across the large dimer interface were observed in either dataset showing the interface maintained by Q160, E259, H184, E276, R289 and K266 was highly conserved. Using PremPS[254] the effect of missense mutations on protein stability was examined. This showed that most mutations were not predicted to be deleterious to stability (listed in Appendix 9.6).

3.11 Discussion

Structural elucidation of PqsR antagonists has enabled a more in depth understanding of SAR attained using an *in vivo* bioreporter. Structural data has demonstrated that pocket B can bind a variety of different moieties including bicyclic (SEN19, SEN32 and SEN89) and tricyclic aromatics (SEN66) and data from other groups show single disubstituted aromatics to be suitable binders[201]. However, it should be noted that these head groups do not penetrate the narrow channel proceeding off from pocket B. It may be possible to penetrate this region further whilst simultaneously improving solubility by introducing head groups with a greater number of chiral centres. Additionally, none of the antagonists tested exploit the shallow surface adjacent to pocket B comprised of Tyr 268 and the backbones of Ile 149 and 266. SEN89 antagonists could be further modified to exploit this region as the R_3 substituents are orientated outside of the pocket and could be extended further.

For the SEN32 series it was observed that the position of the halogen significantly influenced binding leading to an unexpected flipping of the quinazolinone. Interestingly, similar SAR were observed in a 4-aminoquinoline series that demonstrated the dispensability of the carbonyl for interaction with the lid loop[255]. In this series, the most potent antagonist possessed a 12-aminododecyl alkyl chain which given its size is likely to

protrude from the pocket suggesting that SEN32 could be further modified to include longer chains and possibly be conjugated. The same study showed a CF_3 group at the 7^{th} position on the quinoline gave weaker activity compared to a chlorine atom. As our data shows the position of the halogen is restricted, we can surmise that the bulkier CF_3 group is even more disfavoured and wouldn't be a suitable isostere for the quinazolinone antagonists reported here. Further SAR should be conducted relating halogen substituent to potency using the bioreporter assay. From our soaking studies on the SEN66 series we were unable to ascertain whether a bromine atom was tolerated within pocket B but this may have been due to the larger tricyclic head. As such halogen investigation should be carried out with smaller head groups such as the benzimidazole or phenyl from SEN89 and 488 respectively.

Our data showed that the two isomers (R and S) of SEN89 can bind to PqsR independently with bioreporter and thermal shift data suggesting the R isomer has slightly improved affinity. Our structural data suggests this is due to more favourable hydrogen bonding compared to the S isomer. However, the question remains as to whether each derivative has the same binding preference and if substituents can change the preference enantiomer. Given the instability of the protein when combined with antagonist this could be further studied by an immobilised method such as SPR. Given the expected nanomolar potency competitive assays with the native ligand PQS would be required to differentiated binding affinity. In the case of the R isomer the hydrogen on the chiral centre could be exploited further as it points into the pocket and as such growth from this position could increase the number of ligand-protein interactions and improve binding.

Due to the methodology chosen, co-crystal via soaking, potential structural rearrangements may have been unobserved. Although this is an accepted limitation of soaking studies it does make it harder to ascertain whether secondary structure changes are taking place and in some instances comparison of soaked and co-crystallised structures have revealed differences[256]. Our CD study with 488 revealed secondary structure stabilisation suggesting that some conformational changes are occurring upon binding. A viable strategy would be to attempt NMR in solution studies with labelled protein to assess whether considerable chemical shifts are occurring. However, given the propensity of ligand induced aggregation further attempts to stabilise the protein would be required.

3.12 Conclusions

- Most antagonists binding to PqsR adopt an L-shaped conformational pose with the longer and short sides resting in pockets A and B respectively.
- Tyr285 can be exploited by several modalities including hydrogen bonding to the hydroxyl or π-π stacking with distinct geometries conferring changes to antagonist potency.
- Position of halogen groups within pocket B appear to be conserved with little spatial deviation suggesting the position of large halogens are restricted and represents a bottleneck to further optimisation in pocket B.
- Weak binders can be characterised by crystallography using a washing technique to dispel weakly bound solvent molecules.
- Bioinformatic analysis of two databases of strains show the PqsR protein is well conserved, especially in the binding pocket.

4 Applying Fragment-based drug discovery to PqsR antagonism

4.1 Introduction

Exploration of PqsR antagonism through ligand analogues and high throughput screens has been performed in several studies[302 184]. Both approaches have successfully identified potent PqsR antagonists but often have undesirable chemistries such as a high degree of hydrophobicity or nitro groups that lead to toxicity risks[303 184]. This would complicate later development of the lead-like compound into a therapeutic. As discussed in chapter 1, fragment based methodologies can produce compounds with enthalpically favourable target binding and high ligand efficiency. This approach has previously been attempted on PqsR and recently produced a compound (4 in Table 1.2) possessing not only potent activity but favourable drug metabolism and pharmacokinetics (DMPK)[185]. However, this successful compound is the product of only a single FBDD campaign clearly underpinning that additional work will identify similarly or more favourable starting points. We also anticipated the discovery of fragments that may bind to more than one target as was the case for a PqsD/R inhibitor/antagonist that shared a single triazole core (detailed in Introduction 1.8.6 and Figure 1.22).

Our investigation utilised a different methodology compared to the FBDD screen undertaken in previous studies and is shown in the schematic in Figure 4.1[200]. Initial hits were filtered using *in silico* docking to identify suitable binders, these were screened using a thermal shift assay – ideal for low cost and fast screening. Fragments that produced a shift (albeit positive or negative) were analysed further by isothermal titration calorimetry to determine binding parameters. Fragments that performed well in biophysical assays were analysed further by x-ray crystallography and subjected to linking or growth strategies. The subsequent hits were analysed for biological activity using a PAO1 – L bioreporter strain to elucidate potency and efficacy.

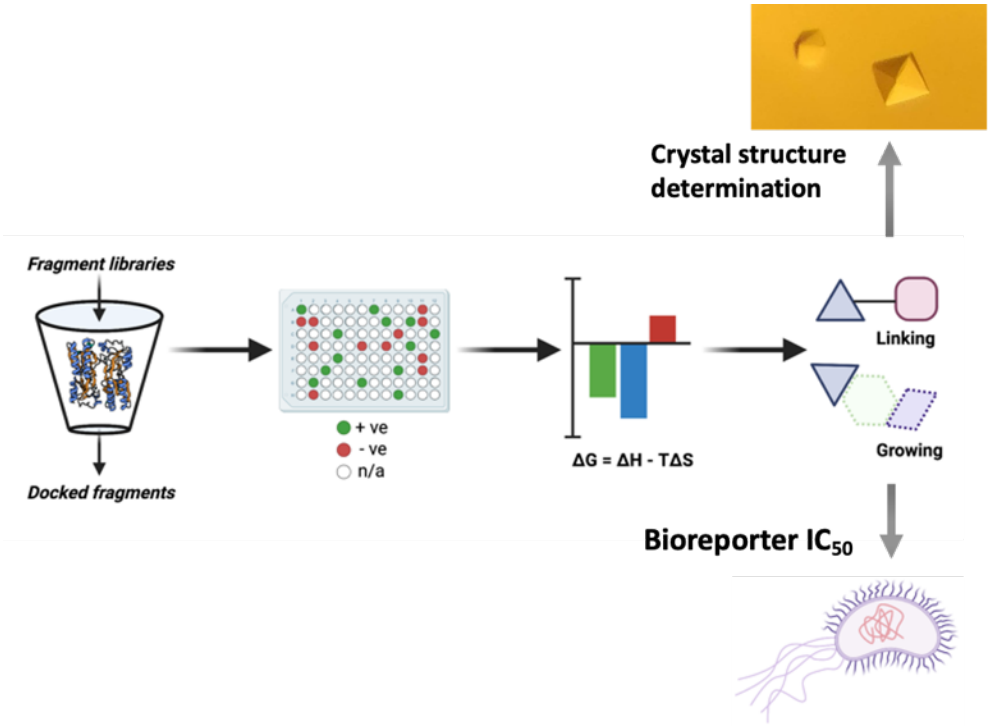

Figure 4.1. Fragment screening methodology. Fragments assessed by molecular docking prior to selection by biophysical methods. Thermal shift assay acts as a primary screen that is orthogonally validated by ITC. Selected fragments can be transitioned to leads by growing or linking strategies.

4.2 Selection of candidates by *in silico* molecular docking

Fragment selection by *in silico* molecular docking was performed by Ruiling Lui (Computational chemistry cluster, University of Nottingham) on the basis that docking would enrich the initial library[304]. However, it should be noted that docking of fragments can be fraught with difficulty as binding energy differences between different poses can be small. This is supported by comparative studies showing that high scoring docked and crystallographic models often differ by > 1 Å RMSD[305]. Consensus as to the level of agreement between computational and biophysical methods vary substantially with some studies reporting agreement of ~20% (NMR validated) whereas others show upwards of ~48% (enzyme activity validated)[306]. Although both hit rates are much higher than the typically cited 3-10% (FBDD)[307] and substantially so for traditional high throughput screening (HTS) <1%.

Chemical libraries were screened using Maestro[206] in high throughput virtual screening mode implementing the OPLS3e forcefield[308]. After docking Ruiling Lui manually curated hits

based upon medicinal chemistry consideration including chemical complexity with respect to future modification (presence of chemical handles in the form of functional groups that could be modified) and commercial availability including price. Fragment libraries originated from Enamine and are detailed in the table below:

Library name	Features	No. of entities
3D Shape Diverse Fragment library	Structures possess a high degree of diversity and have an Fsp^3 cutoff of 0.35 conferring significant shapeliness.	1200
Essential fragment library	Structures based on frequently reported fragments with supporting structural elucidation. High degree of solubility with concentrations of up to 2 mM in aqueous buffer.	320
Single Pharmacophore library	Fragments carrying only a single pharmacophore (often polar group) that can interact with the target. Due to their sparse functionality interactions can be easily deconvoluted and optimised.	1500
sp^3 rich fragment library	Higher prominence of chiral centres with an Fsp^3 cut-off criteria of 0.47. Increasing evidence has shown that sp^3 rich fragments possess features more favourable to development including greater access to chemical space and solubility[309].	50272

Table 4.1. Commercial libraries used for fragment screening. Libraries can be accessed and downloaded from the Enamine website[310]. Ruiling Lui accessed these libraries through 2018-2021.

Given the considerations detailed above Ruiling Lui selected 9 hits mined from the top scoring poses with selections 3 and 9 derived from fragmentation of already characterised binders LUI195-93 (chapter 3) and M64 literature compound (PDB 6B8A)[184]. Both

compounds, based on crystallographic studies, should bind to pocket B in the receptor. The 9 selected 'initial' compounds are detailed in Table 4.2 below:

No.	Structure	MW[A]	LogP[B]	Score[C]
1.	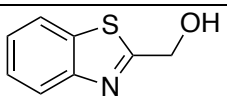	165.21	1.57	-6.68
2.	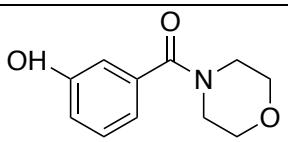	207.23	0.62	-7.82
3.	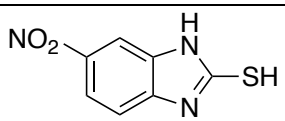	195.2	1.75	-6.27
4.	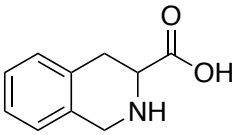	177.2	1.14	(R) -7.17 (S) -6.85
5.	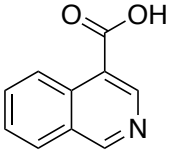	173.17	1.25	-6.89
6.	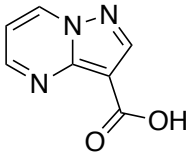	163.14	-0.65	-7.01
7.	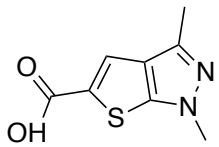	196.22	-0.32	-7.00
8.	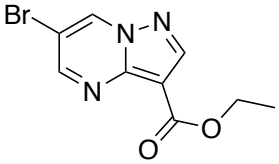	270.09	0.26	-6.57
9.	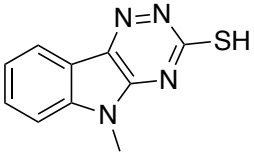	216.26	2.88	-7.16

Table 4.2. Highest scoring fragments identified from Enamine library virtual screening. (A) Molecular weight described in Dalton (Da) **(B)** LogP calculated using ChemDraw **(C)** Glide docking score with units of kcal/mol. Selections performed by Ruiling Lui.

4.3 Thermal shift analysis of $PqsR^{94-309}$ melting

Prior to fragment screening using thermal shift analysis the protein's melting was optimised according to recommendations in the literature[311]. Variables including pH, salt and additive were tested to determine the most appropriate buffer for analysis (Figure 4.2). Analysis showed that $PqsR^{94-309}$ favoured an alkaline buffer with a pH of 8.5 (optimal for Tricine based on pK_a). To ensure this effect was not correlated with excess ions using for buffering (NaOH) the buffer screen was run at two NaCl concentrations of 150 and 250 mM. The screen included MPD solvent, used for protein crystallisation (at concentrations between 3 – 8%), which showed a strong destabilising effect at 5% (v/v) or 389 mM. A positive linear relationship was observed with increasing concentrations of NaCl and $AmSO_4$ indicating that their presence is favourable to protein stability. The favourability of sulphate is not entirely surprisingly given that it was shown to aid the full length receptor (chapter 4). Examination of co-solvent favourability showed a distinct preference for glycerol with a strongly positive correlation observed. Negative relationships were observed with respect to ethylene glycol and DMSO suggesting that solvent required for fragment solubilisation would impact the melting temperature. As such the thermal shift buffer was changed to 50 mM Tricine-NaOH (pH = 8.5), 500 mM NaCl and 5% glycerol with 10% DMSO for complete ligand solubilisation. The amount of glycerol was kept low to ensure the non-aqueous content did not exceed 15%.

(A)

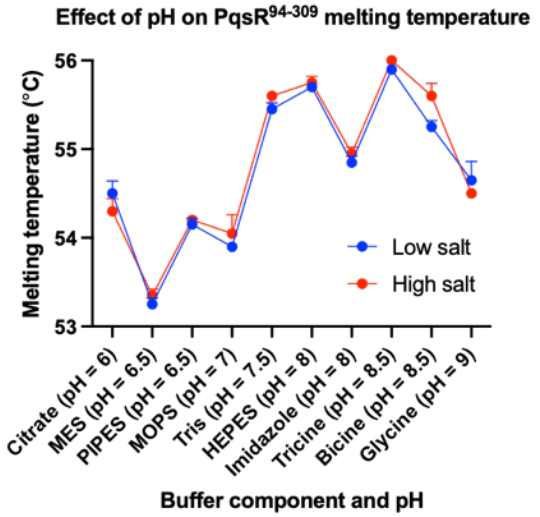

(B)

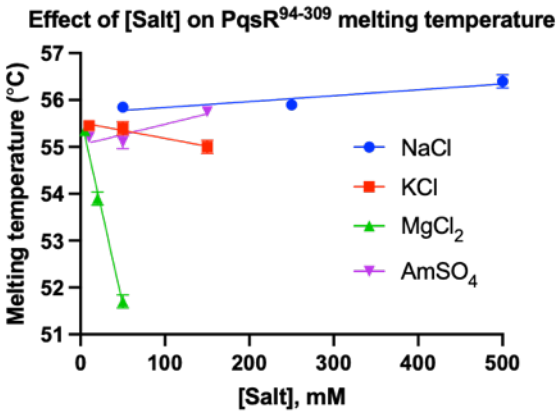

(C)

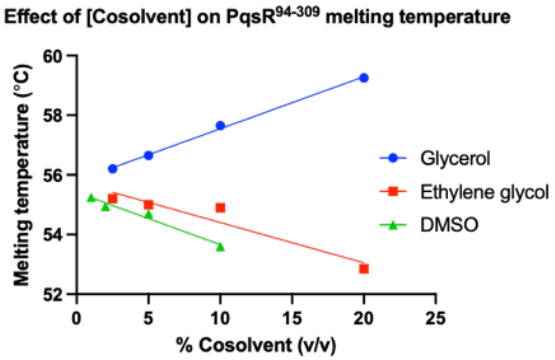

(D)

Component	Relationship °C/[conc.][1]	R^2
NaCl	0.0013	0.810
KCl	-0.0034	0.817
$MgCl_2$	-0.08	0.992
$AmSO_4$	0.0044	0.790
Glycerol	0.1744	0.996
Ethylene glycol	-0.1351	0.903
DMSO	-0.1755	0.969

(1) concentration as mM for salts and % (v/v) for solvents.

Figure 4.2. Optimisation of buffer for Thermal shift screening of PqsR$^{94-309}$. (A-C) Melting temperature with respect to reagent condition or concentration. **(D)** Table summarising relationships of tested components fitted to a linear relationship in PRISM 9. Melting performed on a Biosystems 7500 instrument with a ramping rate of 1°C/minute. Melting temperatures calculated using NAMI. Each condition represents N = 2 sample wells.

4.4 Controls for thermal shift assay

Each thermal screen plate needed suitable binding controls for both stabilising and destabilising fragments. As shown in chapter 3, 488 shows a concentration dependent destabilising relationship and can be used for the latter. To find a fragment for the former the larger SEN19 ligand was fragmented to use its 6-chloroquinazolin-4(1H)-one head group (fQZN hereafter). As shown in Figure 4.3, concentration testing showed the compound to

have a concentration dependent relationship that could be fitted to a Hill plot to derive an apparent dissociation constant of 323.1 µM representing a significant loss in binding affinity compared to SEN19 (10.2 nM ITC). However, for a fragment this represents a reasonable binding affinity and highlights that a thermal shift assay can be used to approximate binding parameters.

(A)

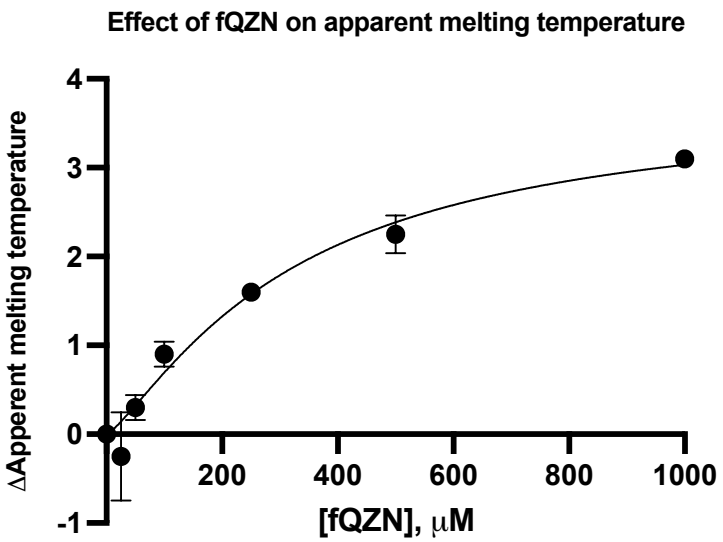

(B)

B_{MAX} (°C)	3.757
K_D (µM)	323.1
(95% CI)	172.4 - 3491
R^2	0.9593

(C)

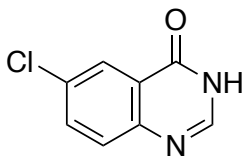

Figure 4.3. Thermal shift assay for control ligand fQZN (A) Binding parameters attained from a melt of $PqsR^{94-309}$ with varying concentrations of fQZN. Curve fitting performed in PRISM to a Hill slope. **(B)** Binding parameters as determined by PRISM 9. Each concentration data point represents the mean of two samples. **(C)** The structure of fQZN – 6-chloroquinazolin-4(1H)-one head group.

4.5 Screening *in silico* selected compounds by thermal shift

Fragments were screened at two concentrations (to observe concentration-dependency) of 250 and 500 µM. Out of the 8 fragments tested by thermal shift assay only fragments 1 and 9 displayed a large shift with 1 being weakly stabilising at 500 µM (+ 0.5°C) and 9 being significantly destabilising. Fragment 2 exhibited an unusual concentration relationship as the effect at 500 µM was weakly destabilising but at a lower concentration became weakly stabilising.

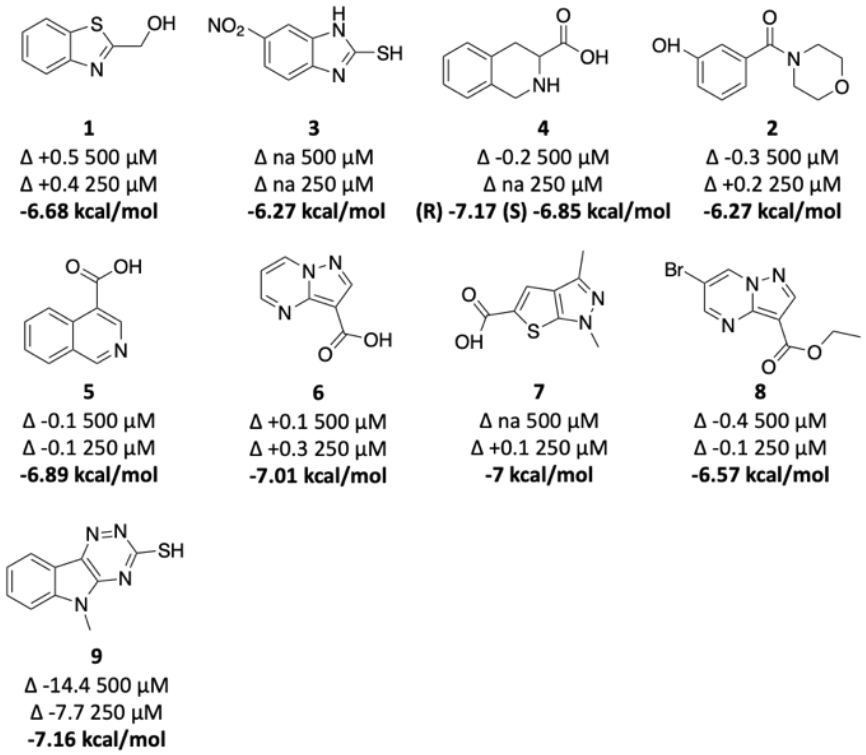

Figure 4.4. Initial thermal shift screening of fragments from *in silico* docking. Thermal shift results determined using NAMI and remaining activity (RA%) determined by Dr Fadi Soukarieh or Ruiling Lui at 50 µM using the PAO1 – L CTX::P*pqsA-lux* bioreporter. Shifts at 250 and 500 µM fragment compared to the DMSO control given ($\Delta T_m = T_m^{DMSO} – T_m^{fragment}$). Fragment numbers and docking score from Table 4.2.

4.6 ITC analysis on control fragments reveals different thermodynamic signatures

As a secondary validation method and to determine binding parameters ITC was employed. Additionally, PqsR fragment campaigns described in the literature have used ITC thereby allowing for hit comparisons. As previous studies utilised a SUMO tagged protein (HisSUMO-^{87}PqsR) for binding studies we initially sought to compare binding parameters of an already characterised fragment. We surmised that the SUMO fusion could be potentially obstructive to some binding events or that shallow pockets on the SUMO tag may harbour some fragment affinity and hinder successful deconvolution of binding events. Ruiling Lui synthesised a hydroxamic acid fragment (36) from the literature. As shown in Figure 4.5b the affinity was 2-fold higher with the fusion construct compared to the His-tagged construct (His^{94}PqsR) used in this study, but the Gibbs free energy remained in good agreement. The change in entropy and enthalpy appeared to have the biggest discrepancy with the entropy being substantially less favourable in the untagged construct. This may be attributable to the fusion or assay conditions as the literature study used less NaCl (150 mM) which would reduce hydrophobic interactions contributing to entropy change.

However, in lieu of a solubility tag maintaining a higher salt concentration was an acceptable compromise. Additionally, the high binding affinity correlated well with a significant thermal shift of 4.5°C at 500 µM (Figure 4.5c).

(A)

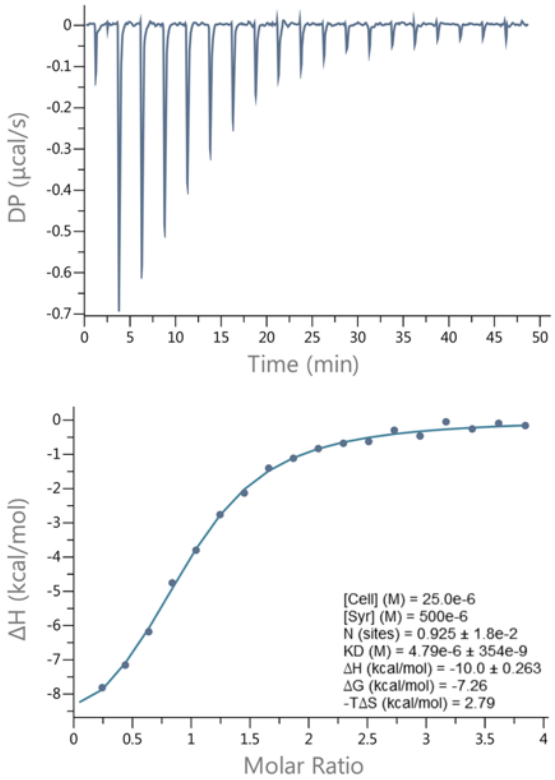

(B)

	SUMO-^{87}PqsR *	^{94}PqsR
K_D (µM)	4.1 ± 0.6	8.86 ± 3.5
ΔH	-8.9 ± 0.2	-13.7 ± 3.2
ΔG	-7.4 ± 0.1	-6.9 ± 0.3
-TΔS	1.5 ± 0.3	6.8 ± 3.5
LE	0.53	0.49

*Values as described in *Klein et al* 2012[199]

(C)

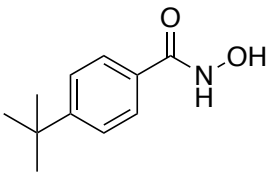

Δ +4.5°C 500 µM
Δ +3.7°C 250 µM

Figure 4.5. Comparison of SUMO-^{87}PqsR with His-^{94}PqsR binding fragment 36. (A) Representative isotherm of 500 µM of fragment 36 injected into 25 µM His-^{94}PqsR after ligand into buffer subtraction. **(B)** Table showing thermodynamic parameters from literature and this study. Standard deviation is representative of n = 3 titrations. Ligand efficiency (LE) defined as – ΔG/N, N are non-hydrogen atoms. Parameters from the equation ΔG = ΔH – TΔS are in kcal/mol. **(C)** Structure of the hydroxamic acid control fragment 36.

To allow for comparison to larger ligands, such as the native AQ or antagonist analogues we fragmented an AQ derivative 7-chloro-2-heptyl-3-hydroxyquinolin-4(1H)-one, characterised as a strong agonist in a *pqsA-lacZ* transcriptional fusion[115], to truncate the alkyl chain to a single methyl group (7Cl-C1PQS). This was advantageous as initial tests with the shortened AQ did not induce precipitation as observed with AQs possessing C7 alkyl chains. As shown in Figure 4.5, titration revealed a similar binding affinity and ligand efficiency to fragment 36 but possessed a different thermodynamic signature. The binding enthalpy was less favourable than 36 but was not inhibited by unfavourable entropy showing distinct binding

modes. Unfavourable entropy is attributed to a conformation change therefore our ITC data suggests that 36 induces such a change whereas 7ClC1-PQS does not.

(A)

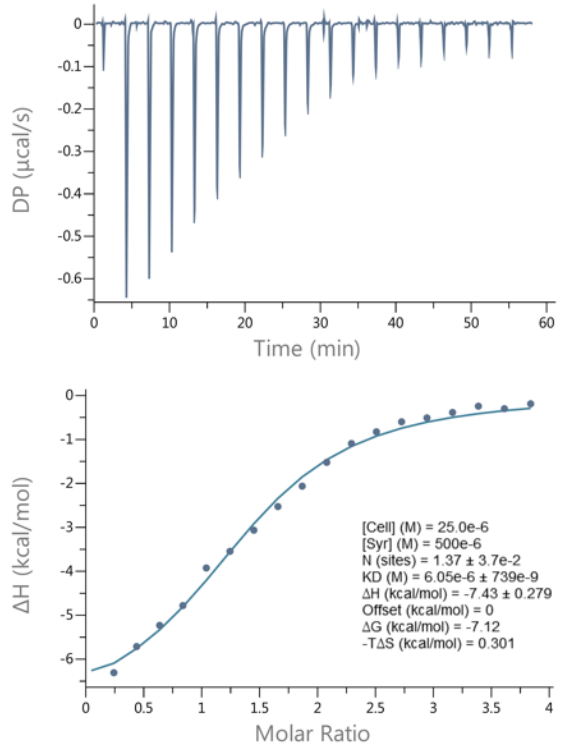

(B)

	Cl-C1PQS
K_D (µM)	5.42 ± 0.9
ΔH	-7.14 ± 0.4
ΔG	-7.19 ± 0.1
-TΔS	-0.06 ± 0.5
LE	0.51

(C)

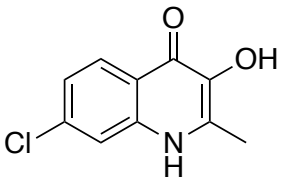

Figure 4.6. Binding of 7Cl-C1PQS fragment to His-^{94}PqsR. (A) Representative isotherm of 500 µM 7Cl-C1PQS injected into 25 µM His-^{94}PqsR after ligand into buffer subtraction. **(B)** Table indicating thermodynamic parameters derived from two independent experiments. Thermodynamic parameters given in kcal/mol. **(C)** Structure of 7Cl-C1PQS with single methyl group at position 2.

4.7 Exploration of fragments by thermal shift and ITC

4.7.1 Exploration of Benzothiazole fragment 1

Initially fragment 1 binding to His^{94}PqsR performed under the same parameters as the control fragments showed a lack of saturation. Signal was optimised by increasing protein cell concentration to 207 µM and injecting a high concentration of fragment 1 (5 mM). A binding affinity of 864.5 µM was attained from two experiments with a LE of 0.38 showing it was a poorer binder compared to both control fragments (Figure 4.7). Fragment 1 binding was dominated by enthalpic contributions but possessed poorer entropy than 7Cl-C1PQS.

(A)

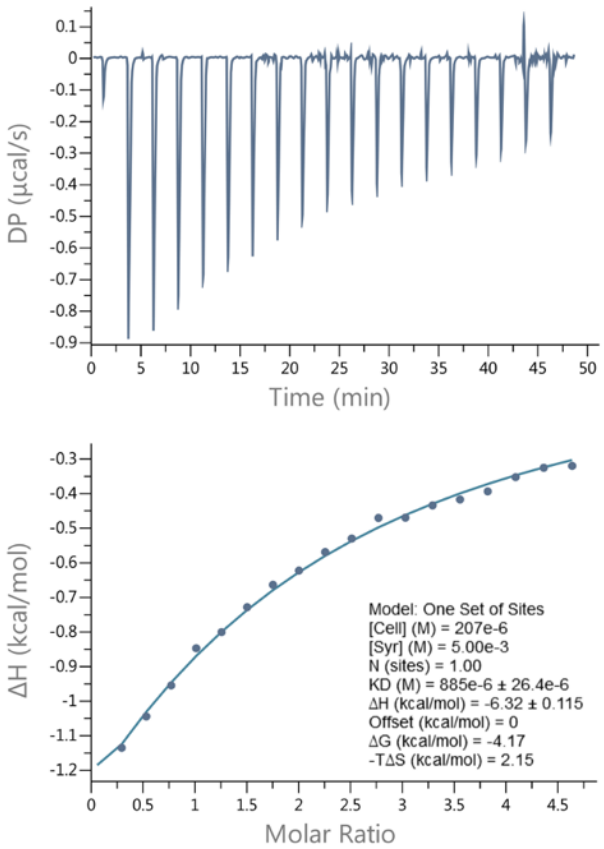

(B)

	Frag 1
K_D (µM)	864.5 ± 29.0
ΔH	-6.13 ± 0.1
ΔG	-4.19 ± 0
-TΔS	2.0 ± 0.2
LE	0.38

(C)

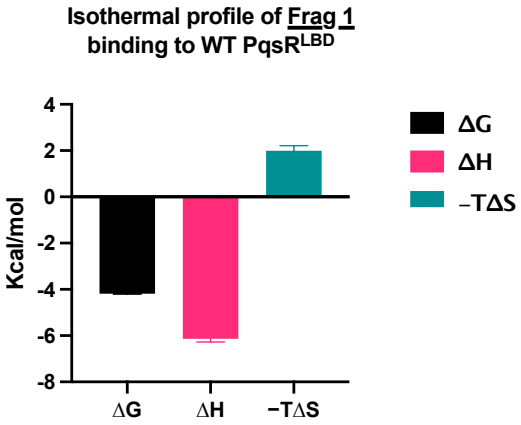

Figure 4.7. Binding of fragment 1 to His^{94}PqsR. (A) Representative isotherm of 5 mM fragment 1 injected into 207 µM His-^{94}PqsR after ligand into buffer subtraction. **(B)** Table indicating thermodynamic parameters derived from two independent experiments. Thermodynamic parameters given in kcal/mol. **(C)** Table represented as a graph for convenient visualisation. The stoichiometry has been fixed to one based upon observations from control ligands.

The alcohol group on fragment 1 was subsequently modified to facilitate linking and growing strategies. As the fragment was surmised to bind in the same position as the benzimidazole group in M64 (PDB 68BA) the phenyl ring was further modified to include halogens to gain additional hydrophobic interactions and exploit halogen bonding with Thr 265. Nine derivatives were synthesised and tested by thermal shift (Figure 4.8). Preliminary growth of the methanol group to an ethan-1-ol gave no thermal shift compared to the DMSO control suggesting that binding had become impaired. This may be due to a loss in orientational entropy from the additional methyl that prevents the alcohol from freely adopting a favourable position[312]. Further extension with 3 more methylene groups gave a

slight destabilisation implying that the entropic penalty had been overcome by an increasing number of hydrophobic interactions. This trend is further observed with growth to a heptyl chain giving a larger stabilising shift than smaller groups. Replacement of the alcohol group with a weaker hydrogen bonding amine appears to negate any shift implying that a strong hydrogen bond was required for binding. Conversion of the fragment to an acetamide (for the purpose of linking) gave a larger shift showing that the amide was favourable to binding. The carbonyl may be able to adopt a similar position to the alcohol group and act as a hydrogen bond acceptor. The addition of a bulky bromine to positions 5 and 6 on the Benzothiazole appeared to have varying effect. Both displayed atypical concentration-dependency and gave a higher melting temperature at a lower concentration of fragment. A likely explanation is that at higher concentrations less favourable positions are adopted.

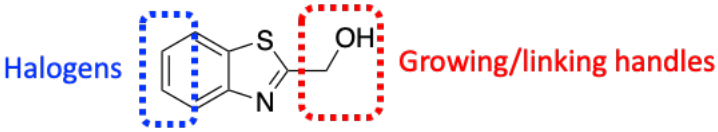

ID	Halogen	Growing	ΔTm (°C) 500 µM	ΔTm (°C) 250 µM	logP(*)
1	-	Methanol	+ 0.5	+ 0.4	1.57
1b	-	Ethan-1-ol	0	+ 0.05	2.07
1c	-	Butan-1-ol	- 0.37	- 0.15	2.97
1d	-	Heptan-1-ol	+ 0.9	+ 1.1	4.22
1e	-	5-Benzylpentan-1-ol	- 0.3	0	4.57
1f	-	Methanamine	- 0.23	0	1.19
1g	-	Acetamide	+ 1.15	+ 0.5	1.89
1h	6-Br	Acetamide	+ 1.1	+ 1.4	2.72
1i	5-Br	Acetamide	+ 0.6	+ 1.2	2.72

Figure 4.8. Thermal shift screen of Fragment 1 derivatives. (A) Fragment 1 structure with areas of modification marked. **(B)** Table with modification followed by change in melting temperature compared to solvent only sample. (*) LogP analysis conducted with ChemDraw.

As the thermal shift with fragment 1g (acetamide modified) gave a greater degree of change it was further characterised by ITC. Due to limited solubility the fragment could only be

titrated at 2 mM. As shown in Figure 4.9 ITC showed a 2-fold tighter binding to the protein but the resultant LE was less favourable suggesting the amide did not contribute as efficiently to binding compared to the original alcohol (1).

(A)

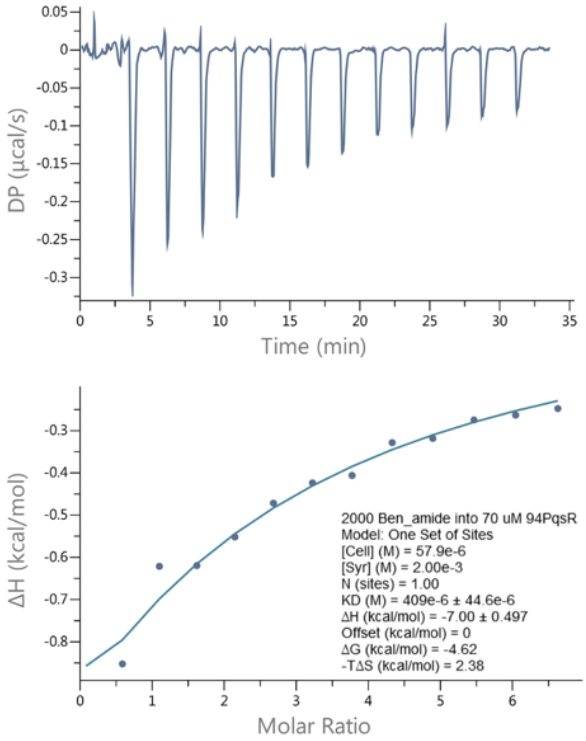

(B)

	Frag 1g
K_D (µM)	382.5 ± 37.5
ΔH	-6.6 ± 0.5
ΔG	-4.4 ± 0.3
-TΔS	1.9 ± 0.5
LE	0.34

(C)

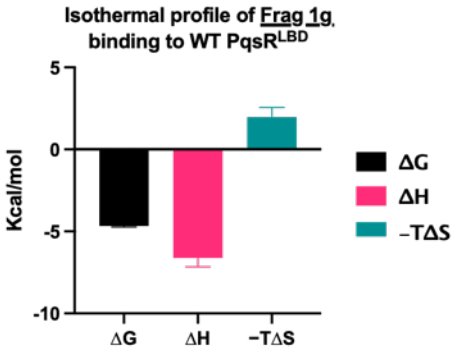

Figure 4.9. Binding of 1g to His^{94}PqsR. (A) Representative isotherm of 2 mM 1g injected into 57 µM His-^{94}PqsR after ligand into buffer subtraction. **(B)** Table indicating thermodynamic parameters derived from two independent experiments. **(C)** Table represented as a graph for convenient visualisation. The stoichiometry has been set to one based upon observations from control ligands.

Binding analysis of the 5-bromo substituent (1i) showed a higher K_D of 94.7 µM by ITC (Figure 4.10). However, it should be noted that the solubility was even poorer than 1g. This observation somewhat conflicts with the SAR reported in the SEN66 series (chapter 3) in which addition of a bulky bromine atom in pocket B resulted in poorer activity, which we had attributed to strict spatial constraints. However, as the benzothiazole is smaller than the tricyclic core the same constraints may not apply. Additionally, the bromine atom provides a significant enthalpic gain in binding with a corresponding deterioration in

unfavourable entropy. This unfavourable entropy exceeds that of 36 suggesting an even larger disruption in protein conformation. The enthalpic efficiency (defined by -ΔH/n, n = non-hydrogen atoms) of 0.5 and 1.3 kcal/mol for 1g and 1i shows a significant increase granted by the bromine suggesting the bromine contributes more through polar interactions rather than hydrophobic.

(A)

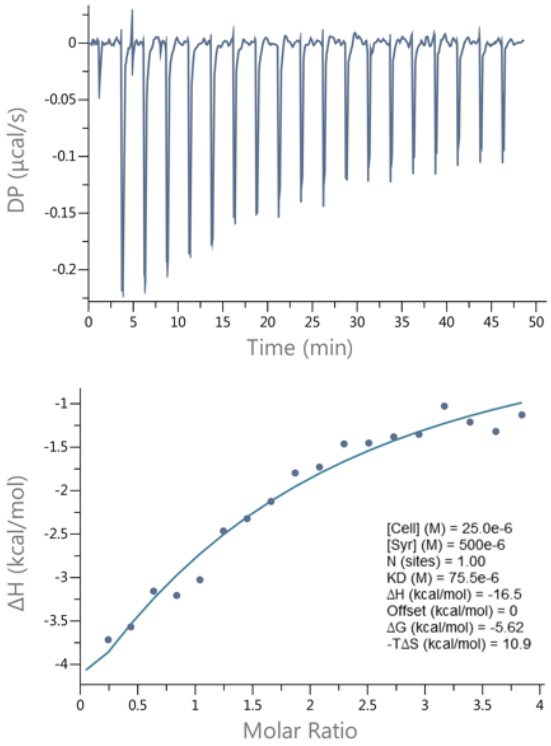

(B)

	Frag 1i
K_D (µM)	94.7 ± 41.2
ΔH	-18.5 ± 4.9
ΔG	-5.52 ± 0.2
-TΔS	13.1 ± 5.4
LE	0.39

(C)

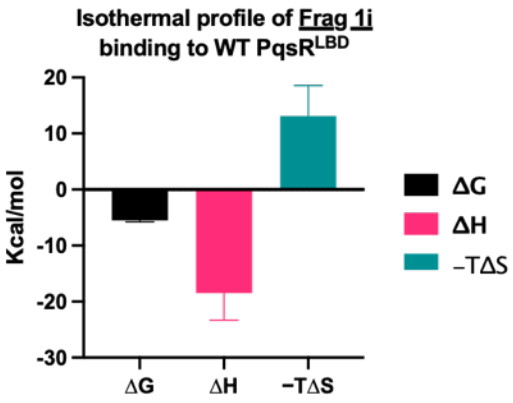

Figure 4.10. Binding of Fragment 1i to His^{94}PqsR. (A) Representative isotherm of 500 µM 1i injected into 25 µM His-^{94}PqsR after ligand into buffer subtraction. **(B)** Table indicating thermodynamic parameters derived from three independent experiments. **(C)** Table represented as a graph for convenient visualisation. The stoichiometry has been set to one based upon observations from control ligands.

Fragment 1h, a structural isomer with the bromine atom at position 6, could not be assessed by ITC as the same titration parameters as used above did not approach saturation. As such binding parameters could not be determined. We could surmise that an

apparent lack of binding under these parameters suggests this position is disfavoured and should not be pursued further.

4.7.2 Identifying a suitable linking partner to Fragment 1i

Without structural information linking of fragments can be challenging however, our ITC results gave some evidence that fragment 1i binds to pocket B. As such Ruiling Lui split SEN66 (chapter 3.4) to give N-(4-chlorophenyl) acetamide (fragment 10 hereafter) which based upon the LUI 195-93 – $PqsR^{LBD}$ complex structure would occupy pocket A and π-π stack with Tyr 258. Given that an amide group on fragment 1 increased ligand efficiency this presented a convenient linking strategy. As shown in 5.11c when used in combination the fragments gave an increased shift compared to when used independently suggesting that they could bind together unobtrusively. The linked compound (26) was further tested showing a weaker shift likely due to a loss in each fragment's rotational freedom and consequent entropic penalty. Independent analysis on 10 showed it to have a high ligand efficiency of 0.55 with interaction dominated by enthalpic contributions making it an ideal fragment for linking. Additionally, the fragment possessed only weak unfavourable entropy similar to 7Cl-C1PQS.

(A)

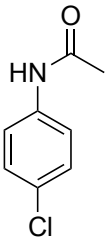

(B)

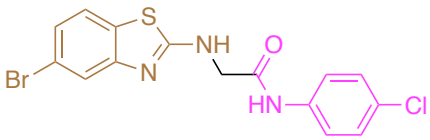

(C)

Fragment/s	ΔTm (°C) 500 µM	ΔTm (°C) 250 µM
1i	+ 1.9	-
10	+ 1.1	+ 1.1
10 + 1i	+ 2.5	+ 2.23
26	+ 1.9	+ 2.17

(D)

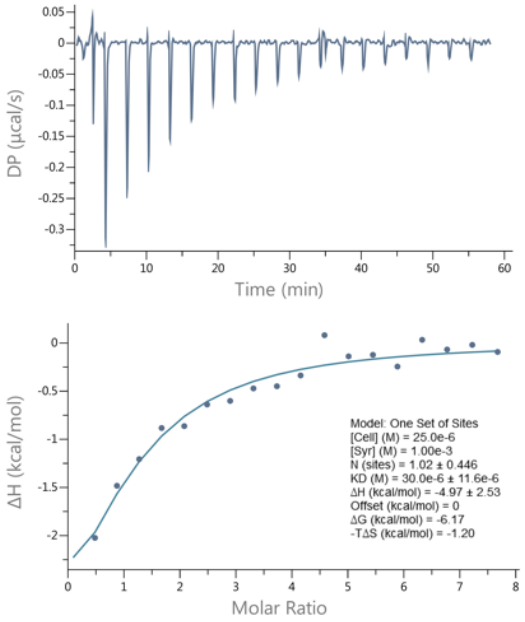

(E)

	Frag 10
K_D (µM)	**35.3 ± 7.4**
ΔH	**-6.3 ± 1.9**
ΔG	**-6.1 ± 0.1**
-TΔS	**0.22 ± 2**
LE	**0.55**

(F)

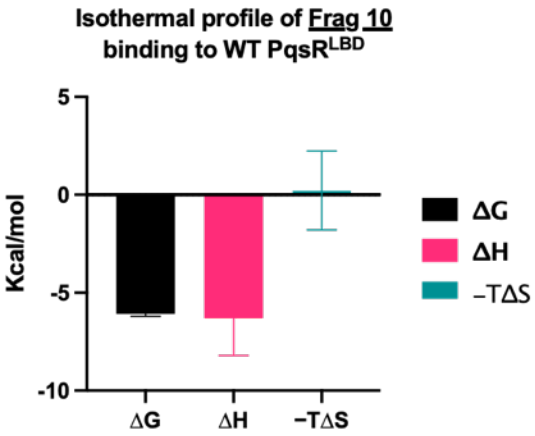

Figure 4.11. Binding of Fragment 10 to His^{94}PqsR and effect on linking. (A) Structure of Fragment 10 **(B)** Structure of linked compound 26 coloured to show individual fragments (1i & 10) **(C)** Thermal shift results of compounds in isolation, together and covalently linked. **(D)** Representative isotherm of 1 mM Fragment 10 injected into 25 µM His-^{94}PqsR after ligand into buffer subtraction. **(E)** Table indicating thermodynamic parameters derived from two independent experiments. Thermodynamic parameters given in kcal/mol. **(F)** Table represented as a graph for convenient visualisation.

4.7.3 Finding alternative binders to pocket A

Based on our crystallographic observations in chapter 3 and Ruiling Lui's docking we surmised that 10 bound to pocket A. Ruiling Lui synthesised related compounds based upon three strategies: group exploration to find stronger functional groups; additional ring placement and the inclusion of nitrile groups that improved potency in the SEN19 series (chapter 3). Group exploration revealed a strong preference for a nitro group as determined by greater thermal shifts although these carry the potential for future toxicity[303]. Nitro containing compounds were able to both stabilise and destabilise the protein with no apparent determining factor. Removal of the nitro group or chlorine atom reduced the observed shift considerably and replacement with a similarly electronegative nitrile failed to compensate. Placement of a piperazine ring appeared to reduce the magnitude of shift and addition of a phenoxy group favoured a destabilising effect.

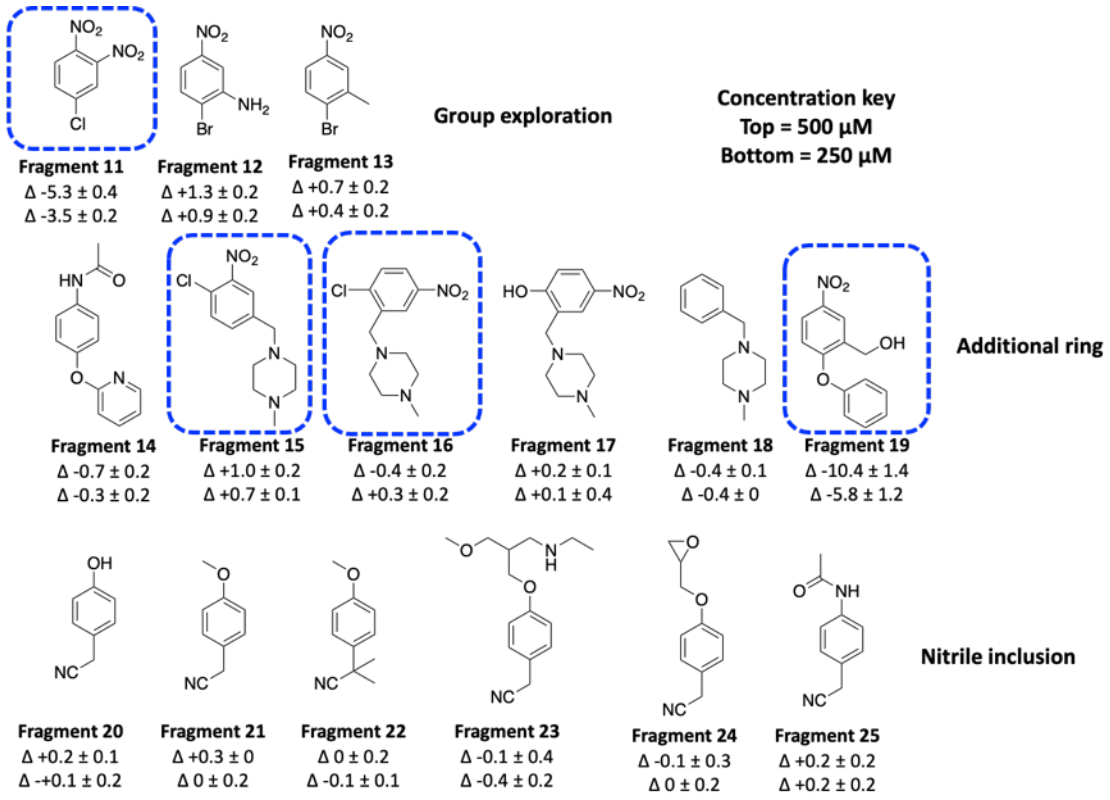

Figure 4.12. Fragment 10 group exploration. Groups surmised to bind to pocket A on PqsR^{LBD}. Thermal shift given in °C and are the mean of three or four replicates with standard deviation provided (to 1 dp). Compounds marked in blue were taken for further analysis by ITC. Melting performed on a Biosystems 7500 instrument and temperatures calculated with NAMI.

As nitro containing compounds gave a greater shift these were further examined by ITC to compare their binding to 10. Fragment 11 (4-chloro-1,2-dinitrobenzene) bound with a 2-fold weaker K_D and possessed a poorer ligand efficiency of 0.45 compared to 10 (Figure 4.13).

(A)

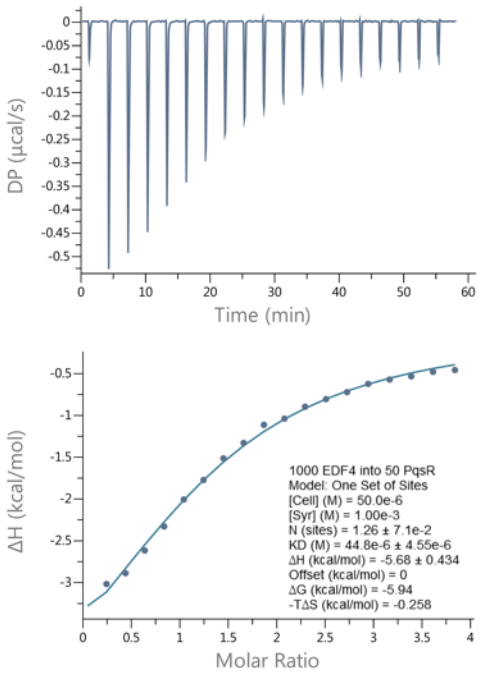

(B)

	Frag 11
K_D (µM)	62.5 ± 25.0
ΔH	-7 ± 2.1
ΔG	-5.8 ± 0.2
-TΔS	1.3 ± 2.2
LE	0.45

(C)

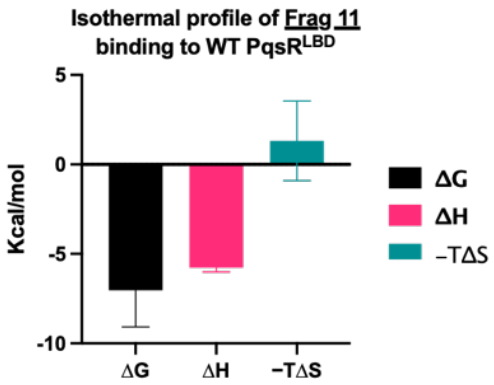

Figure 4.13. Binding of Fragment 11 to His^{94}PqsR. (A) Representative isotherm of 1 mM 11 injected into 50 µM His-^{94}PqsR after ligand into buffer subtraction. **(B)** Table indicating thermodynamic parameters derived from two independent experiments. Thermodynamic parameters given as kcal/mol. **(C)** Table represented as a graph for convenient visualisation.

Further exploration of the N-methyl piperazine structural isomers showed good agreement with the thermal shift data as fragment 15 (3-nitro 4-chloro) bound with an affinity of 217 µM whereas 16 (2-chloro 5-nitro) gave no binding under the same conditions (Figure 4.14). Replacement of the nitro group from fragment 11 with piperazine reduced ligand efficiency from 0.45 to 0.28 suggesting that a N-methyl piperazine would be an unfavourable fragment linker. This apparent loss of binding appears to be due to an increase in unfavourable entropy from 1.3 to 5.78 kcal/mol.

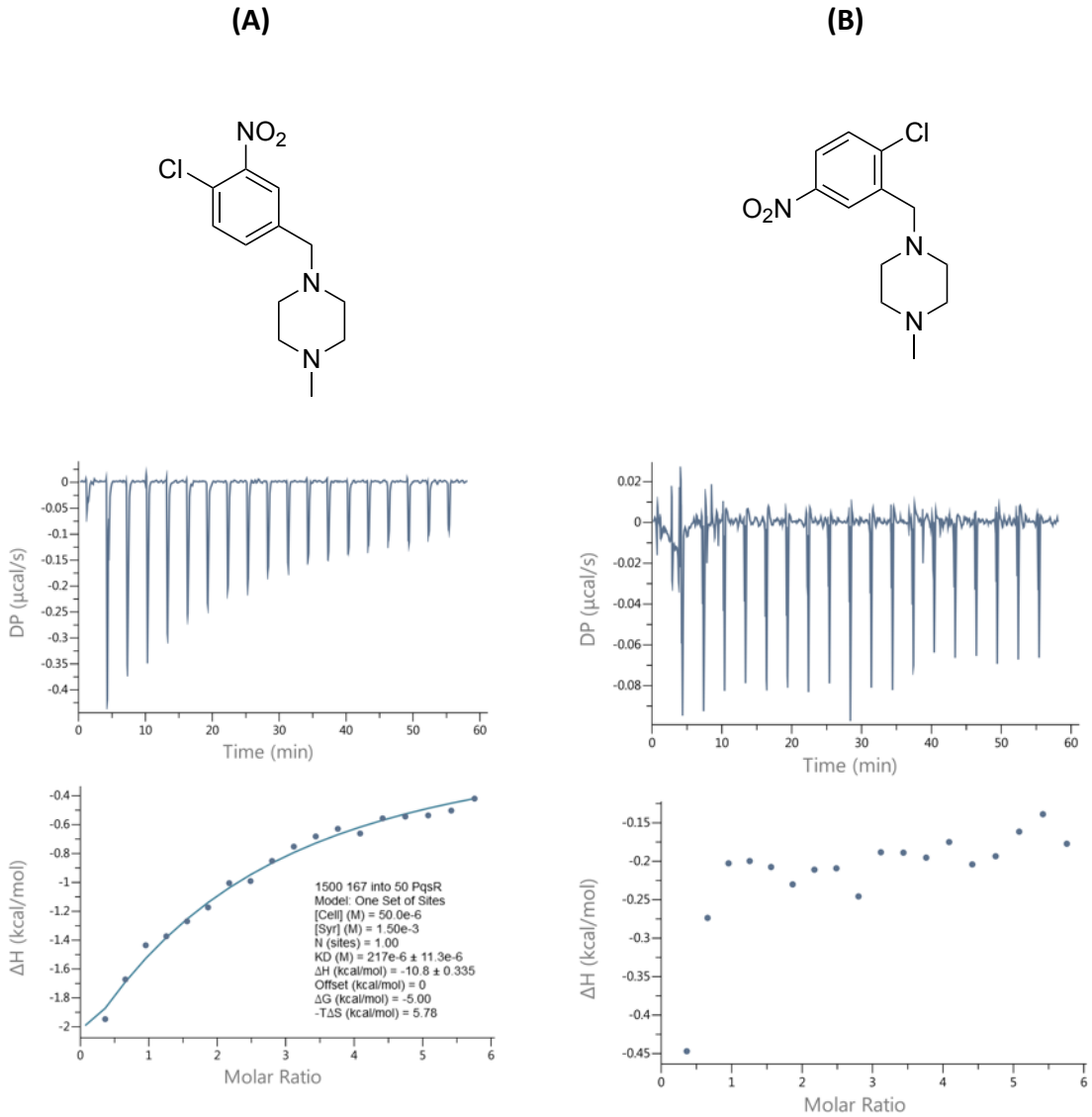

Figure 4.14. Comparison of structure isomers of grown fragment 11 (A) 1.5 mM fragment 15 titrated into 50 µM His^{94}PqsR showing a K_D of 217 µM. **(B)** 1.5 mM fragment 16 titrated under the same conditions with no apparent binding.

Attempts to examine fragment 19, that gave a strong destabilising effect on thermal shift, by ITC was unsuccessful. Examining the material from the sample cell after titration revealed the compound induced aggregation in the protein.

4.7.4 Lack of fragment 4 binding

Our initial thermal shift results with fragment 4 was disappointing as a previous fragment campaign identified a 2-naphthamide fragment with K_D (ITC) determined as 1.8 ± 0.2 µM [200]. In agreement with our thermal shift data no binding could be detected by ITC upon ligand

injection at 1 or 2 mM into 50 µM His^{94}PqsR. This suggests that aromaticity must be preserved for fragment binding.

Figure 4.15. Molecular structure of fragment 4 and literature 2-naphthamide (A) Fragment 4 as shown in Table 4.2 with a calculated ΔG of -7.17 & -6.85 kcal/mol (XP score) for R and S respectively. **(B)** Literature 2-naphthamide fragment with a ΔG of –7.9 ± 0.1 (ITC)[200].

4.8 *In vivo* characterisation of linked and grown fragments using PAO1-L CTX::P$_{pqsA}$-*lux* bioreporter

To elucidate the functional relationships between fragments *in vivo* characterisation was performed on linked and grown fragments. None of the resultant linked compound exhibited strong potency at the tested concentration range (up to 100 µM). As such potencies were extrapolated by constraining the bottom plateau to the remaining activity after treatment with a characterised binder SEN19 (chapter 3). With this analysis we could see that the fragment 1 series possessed the greatest potency with compound 26 (linked 1i & 10) giving the highest IC$_{50}$ of 23 µM. Growth of fragment 1 with an alkyl chain gave a similar SAR to the SEN32 series with longer chains yielding greater potency. Fragment 4, which was identified as a poor binder by ITC and thermal shift, expectedly yielded poorly active compounds. However, linking to the strong binder 10 could rescue activity but only if linked at the carboxylic acid to yield an amide (31). As expected by a lack of binding from ITC compounds derived from fragment 16 were unable to rescue activity (compounds 27 and 28). IC$_{50}$ determinations are shown in Figure 4.16 with goodness of fit shown. Compounds containing fragment 4 were assessed as racemates.

27

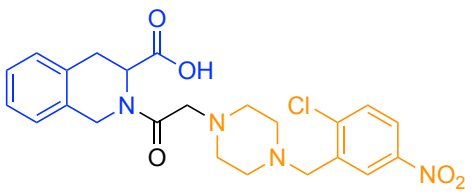

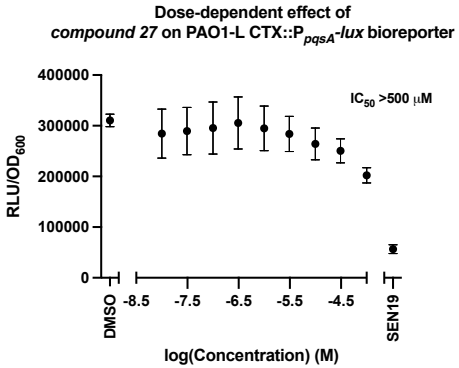

28

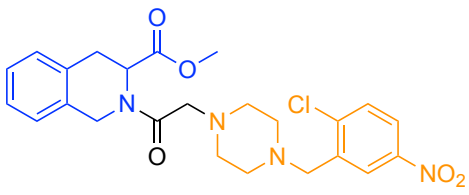

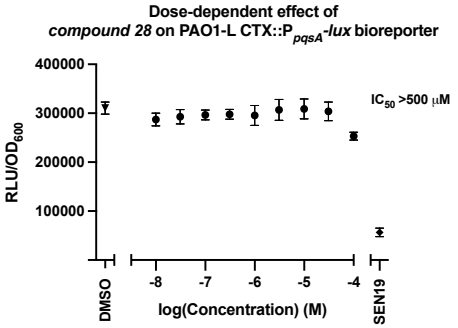

29

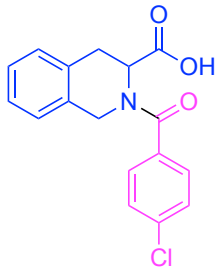

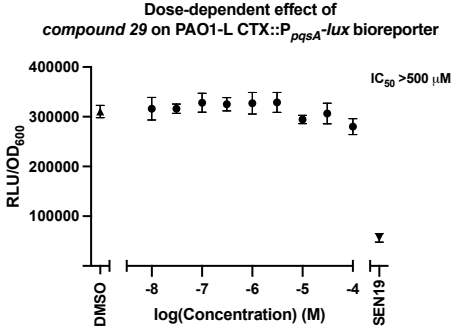

30

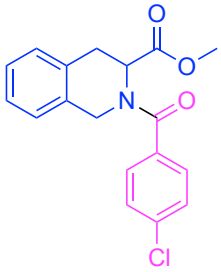

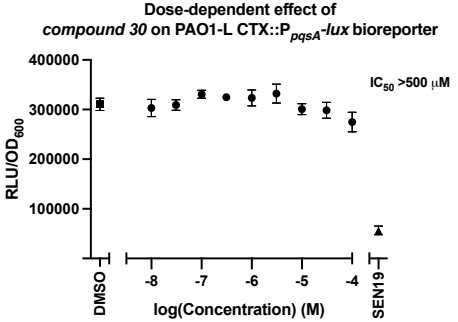

31

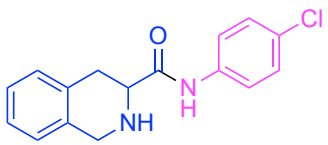

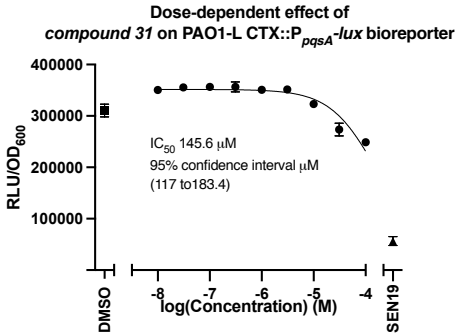

26

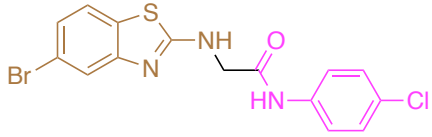

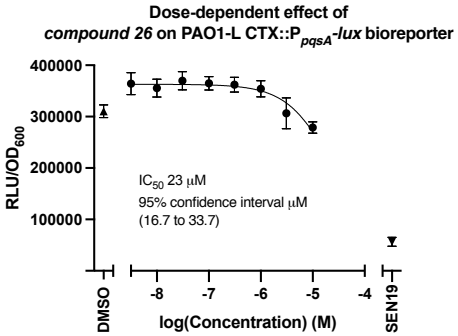

32

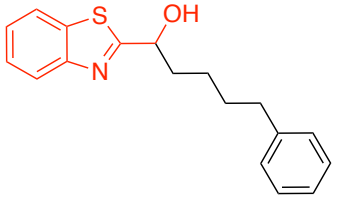

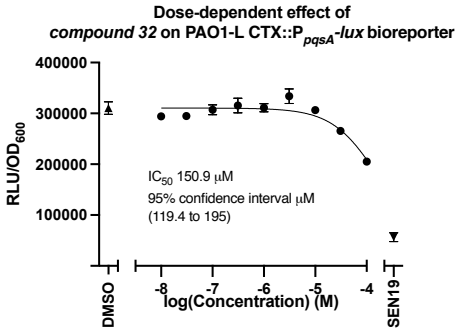

33

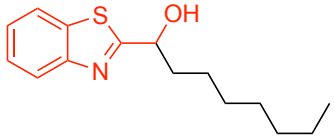

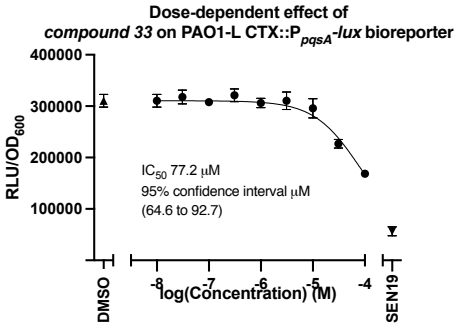

34

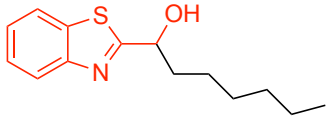

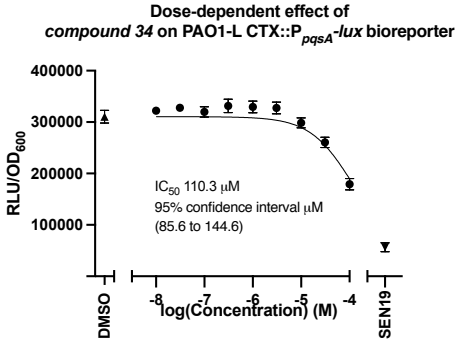

Compound	Parent Fragment/s	Parent K_D (µM)*	IC_{50} (µM)	CI 95% (µM)	R^2
27	4 & 16	NB & NB	109.2	62 - 210.5	0.30
28	4 & 16	‘’	387.8	252.3 – 704.9	0.17
29	4 & 10	NB & 35.3	787.1	408.2 - 3582	0.20
30	4 & 10	‘’	620	367.3 - 1502	0.35
31	4 & 10	‘’	145.6	117.8 – 183.4	0.89
26	1i & 10	94.7 & 35.3	23	16.7 – 33.8	0.74
32	1	864.5	150.9	119.4 - 195	0.83
33	1	‘’	77.2	64.6 – 92.7	0.93
34	1	‘’	110.3	85.6 – 144.6	0.86

Figure. 4.16. Dose-dependence effect of fragment derived leads on PAO1 – L CTX::P*pqsA*-*lux*. Progenitor fragments coloured as Fragment 1, Fragment 4, Fragment 10, Fragment 16 & Fragment 1i. IC_{50} determinations calculated in PRISM with a bottom constraint fitted to the remaining activity upon treatment with SEN19 (characterised tight binder, refer to chapter 3). Fitting achieved using a three-variable dose-dependency model in PRISM. IC_{50} and 95% confidence intervals summarised in table with goodness of fit shown as R^2. *K_D stated from parent fragment or fragments from ITC experimentation and is given in the order stated in the “Parent Fragment/s” column.

4.9 Initial soaking attempts with PqsR$^{94-309}$

To gain insight into fragment binding fragments 1 and the S and R isomers of fragment 4 were soaked into PqsR^{LBD} crystals. These were selected based upon direct evidence of binding in the case of fragment 1 and weak biological activity from linked fragment 4 (tested as racemates. Despite a prominent destabilising effect fragment 9 was not prioritised as it shares the same head group as SEN66 which was elucidated in chapter 3. The same soaking methodology (employed in chapter 3) was used but examination of difference density after molecular replacement with Phaser or viewing a DIMPLE map gave no indication of ligand binding and in the case of fragment 1 salt crystals readily formed.

4.10 Re-screening library against PqsA

Reusing the same fragment library to screen multiple targets has been shown to be successful in other FBDD campaigns. An example being the screening campaign against the *M. tuberculosis* L-arginine synthesis pathway – composed of 4 enzymes. Using thermal shift with a library of 960 fragment yielded 27 fragments hits that were all validated by at least one orthogonal method and could be structurally elucidated[313]. Although no common fragment was identified it showed that multiple targets can increase the utility of a modest library. As described in chapter 7 PqsA was readily purified and a *pqsA* knockout displays an attenuated virulence with respect to pyocyanin production.

An optimal buffer pH of 8.5 identified in the initial characterisation of PqsA[314] was used for the shift supplemented with 1 mM $MgCl_2$, 150 mM NaCl and 2.5% glycerol added for stability. A subset of the fragment library consisting of 27 fragments were initially screened at 250 and 500 µM. Control fragments, substrates for PqsA, anthranilic acid and ATP were both stabilising with ATP producing a greater shift compared to anthranilic acid. A lack of hits identified at lower concentration prompted a repeat at 1 mM. Most fragments, at this concentration, were destabilising with the strongest shown in Figure 4.17. Unexpectantly some common hits were observed including the literature fragment 36 which already has a high LE for PqsR. Both 11 and 15 were destabilising with the former giving a more pronounced shift. The only stabilising fragment tested was 17 giving a shift of +0.8°C at 1 mM. Known PqsR pocket B binders were also destabilising including the head group of

SEN66 (fragment 9) and fragment 1 derivates 1h & 1g. Unfortunately, due to time restrictions these fragments could not be examined further.

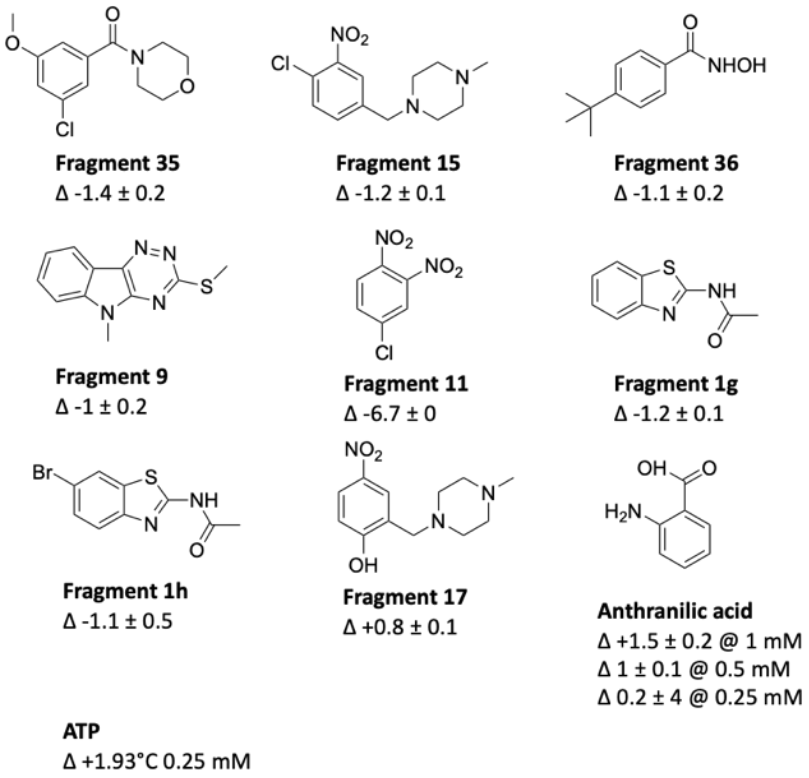

Figure 4.17. PqsA thermal shift to screen PqsR fragment library. Best performing fragments (at 1 mM) with melting temperature shift compared to DMSO solvent only given in °C and are representative of an average of three samples with SD given to 1 dp. Melting performed on a Biosystems 7500 instrument and temperatures calculated with NAMI.

4.11 Discussion

Previous FBDD campaigns with PqsR have utilised relatively expensive screening platforms including SPR to screen libraries. Thermal shift represents a more cost-effective screening procedure, and our study has found that a fragment identified in the SPR screen was strongly stabilising in thermal shift. Furthermore, our study has shown that both stabilising and destabilising fragments could bind to PqsR with high affinity. Negative shifting fragments have often been considered as poor leads as they have been hypothesised to bind preferentially to a denatured state[307]. However, the literature shows that despite this many fragments with negative shifts can be examined with other biophysical methods and co-crystals can be attained [237 236 238 315]. In some instances the change between stabilising and destabilising has been inferred to show difference in binding mechanisms to explain SAR[316]. Our study demonstrates similar relationships as known binders such as the head

group of SEN66 produces a significant negative shift whereas the fQZN, the headgroup from SEN19, provides a strong positive shift. Further analysis comparing the constituent head groups and potency of the resultant compounds would be useful to elucidate mechanistic differences. Furthermore, as the binding pocket is located on the dimer axis it would be of interest to explore whether the integrity of the dimer is preserved. This could be examined by gel filtration experiments, dynamic light scattering (DLS) or analytical ultracentrifugation. Furthermore, as shown with DntR inclusion of a the cognate ligand to concentrations >0.1 mM triggers conformation change[146]. As shown in the previous chapter the full length can be readily purified as a fusion. SAXS could be employed with range of fragments to identify similar transitions.

Due to time limitations a greater number of linked fragments could not be generated however, our ITC data shows that the inclusion of fragment 16 was a poor choice due to an apparent lack of binding. The structural isomer, 15, should yield stronger binding and further work should explore whether this restores activity in the linked compounds. Additionally, as observed in 21 masking the carboxylic acid, from fragment 4, improved potency therefore one would expect a linkage from the carboxylic acid to 15 to improve binding further. As discussed in chapter 3 the inclusion of chiral centres into pocket B binders was surmised as a potential optimisation route under the premise that deeper areas of the pocket could be reached. However, our observation that fragment 4 failed to bind suggests that addition chirality in this region is disfavoured.

Additionally, our thermal shift screen potentially identified a series of fragments that could destabilise PqsA including a literature fragment reported to have biological activity (36). This should be assessed further with the goal to produce a compound capable of acting as a dual inhibitor/antagonist. Structural data would be required to determine the mode of binding to aid optimisation.

4.12 Conclusions

- Thermal shift shows a good concentration-dependent relationship that can be fitted to a hill slope for binding affinity determination although this disagreed with the more reliable ITC methodology.

- Benzothiazole is a good scaffold for further medicinal chemistry development with bioreporter assay showing grown fragments to possess dose-dependent activity. ITC demonstrated the fragment can be further modified without significant detriment to ligand efficiency.
- Fragment 11 was identified as another potent binder but growth with a piperazine was found to have a stringent isomer preference with only the 3-nitro 4-chloro (*ortho*) fragment 15 being able to bind. However, the inclusion of a piperazine also reduced binding affinity.
- Fragmenting compounds identified through HTS into fragments was successful in finding fragment 10 that possessed high ligand efficiency and suggests a strategy to further enrich a PqsR fragment library.

Interactions described in this chapter are summarised below in Table 4.3:

Fragment	K_D (ITC)	ΔH	ΔG	-TΔS	LE
36	8.86 ± 3.5	-13.7 ± 3.2	-6.9 ± 0.3	6.8 ± 3.5	0.49
Cl-C1PQS	5.42 ± 0.9	5.42 ± 0.9	-7.19 ± 0.1	-0.06 ± 0.5	0.51
1	864.5 ± 29.0	-6.13 ± 0.1	-4.19 ± 0	2.0 ± 0.2	0.38
1g	382.5 ± 37.5	-6.6 ± 0.5	-4.4 ± 0.3	1.9 ± 0.5	0.34
1i	94.7 ± 41.2	-18.5 ± 4.9	-5.52 ± 0.2	13.1 ± 5.4	0.39
10	35.3 ± 7.4	-6.3 ± 1.9	-6.1 ± 0.1	0.22 ± 2	0.55
11	62.5 ± 25.0	-7 ± 2.1	-5.8 ± 0.2	1.3 ± 2.2	0.45
15	217 ± 11.3	-10.8 ± 0.3	-5	5.78	0.28

Table 4.3 Summary of biophysical characterisation of PqsR binding to fragments. Data imported from tables across the chapter. Thermodynamic parameters are given as kcal/mol.

5 Generating new PqsR ligand binding domain crystal forms

5.1 Construct design rationale

As described in chapters 3 and 5 the $PqsR^{LBD}$ construct exhibited only moderate resolution >2.5 Å and as such structural features including enantiomeric preference could not be easily determined. Additionally, the presence of the pseudo-ligand MPD seemingly hindered binding of smaller, less potent ligands such as 488 that required ethylene glycol washing to enable ligand density to become evident. Surface entropy reduction (SER) and other strategies to decrease disorder can result in new crystal forms with higher diffraction compared to the wildtype sequence with an improvement of up to 1.5 Å described in the literature[317]. SER has been integral in generating crystals for many structural projects with RhoGDI being the classically cited example[318]. Furthermore, SER has been successfully utilised in improving ligand determination by removing flexible regions[319]. A higher resolution crystal system would also enable newer fragment screening methodologies such as PanDDA[320] that enables high throughput screening and elucidation of weak binders. To improve the chances of finding a suitable crystal system several strategies were employed and are detailed in this chapter.

5.1.1 Surface entropy reduction analysis

Sequence analysis with the **S**urface **E**ntropy **R**eduction prediction (SERp) server[321] was run twice with strict alanine replacement and then broadened to low entropy residues (Ser, Thr, His, Tyr). This revealed two common clusters 1 and 3 shown in Table 5.1.

Cluster	Residues identified	Proposed mutation	SERp score
1 EELK (151-154)	E151 E152 K154	A A A	4.89
2 KQDNAE (137-142)	K137 Q138	A A	3.25
3 EE (243-244)	E243 E244	A A	2.97
4 TALESERS (273-280)	E276 E278	S S	3.55

Table 5.1 SERp clusters identified for mutation to less entropic residues. Clusters 1 and 3 commonly identified in two runs using different replacement parameters.

Cluster 1 highlighted Lys 154 that in multiple crystal structures lacks electron density suggesting high disorder and does not closely interact with other residues (>7 Å). As such truncating the residue to an alanine would be unlikely to be detrimental to protein folding. The adjacent Glu 151 Glu 152 were poor choices for mutagenesis as the former was situated close to the symmetry mate binding site and shared a polar interaction with Tyr 268 whilst the latter shares a salt bridge to Lys 137. Cluster 2 was also a poor choice as it contained the aforementioned Lys 137 and Gln 138 lies on a packing interface. Cluster 3 containing Glu 243 Glu 244 would be unfavourable as both residues' form intra-helix hydrogen bonds that stabilise the secondary structure of helix 5. The last cluster indicated that Glu 267 Glu 278 would be suitable choices. However, Glu 267 is hydrogen bonded to His 184 (2.63 Å) which should be preserved to avoid secondary structure change. Glu 278 has a much weaker association with Ser 280 (3.7 Å) indicating that this residue is suitable for mutagenesis.

Optimisation of crystal contacts would also aid crystallisation; using PISA[322] to analysis the 4JVC model assembly Lys 214 was found to occupy a crystal contact. The opposing residue, on the adjacent chain, His 173, does not possess complementary charge therefore disfavouring interaction. Replacement with a similarly large residue that could interact would enhance the interaction. A replacement with tyrosine, shown to be prominent in

protein-protein interfaces[323,324], would permit a polar interaction with His 173. Additionally, an increase in hydrophobicity would improve the low ΔG (solvation free energy gain) of the interface.

Despite the literature suggesting that mutating local clusters is the most effect strategy in protein SER, local clusters could not be identified without a high risk of affecting local protein fold and increasing instability. As such a more conservative approach of mutating distally located single residues was devised. Analysis showed three favourable mutations in the construct which would improve crystal contacts and reduce surface entropy including K154A, K214Y & E278A. These mutations were implemented as pairs with the most conservative mutation K154A (shown in Figure 5.1).

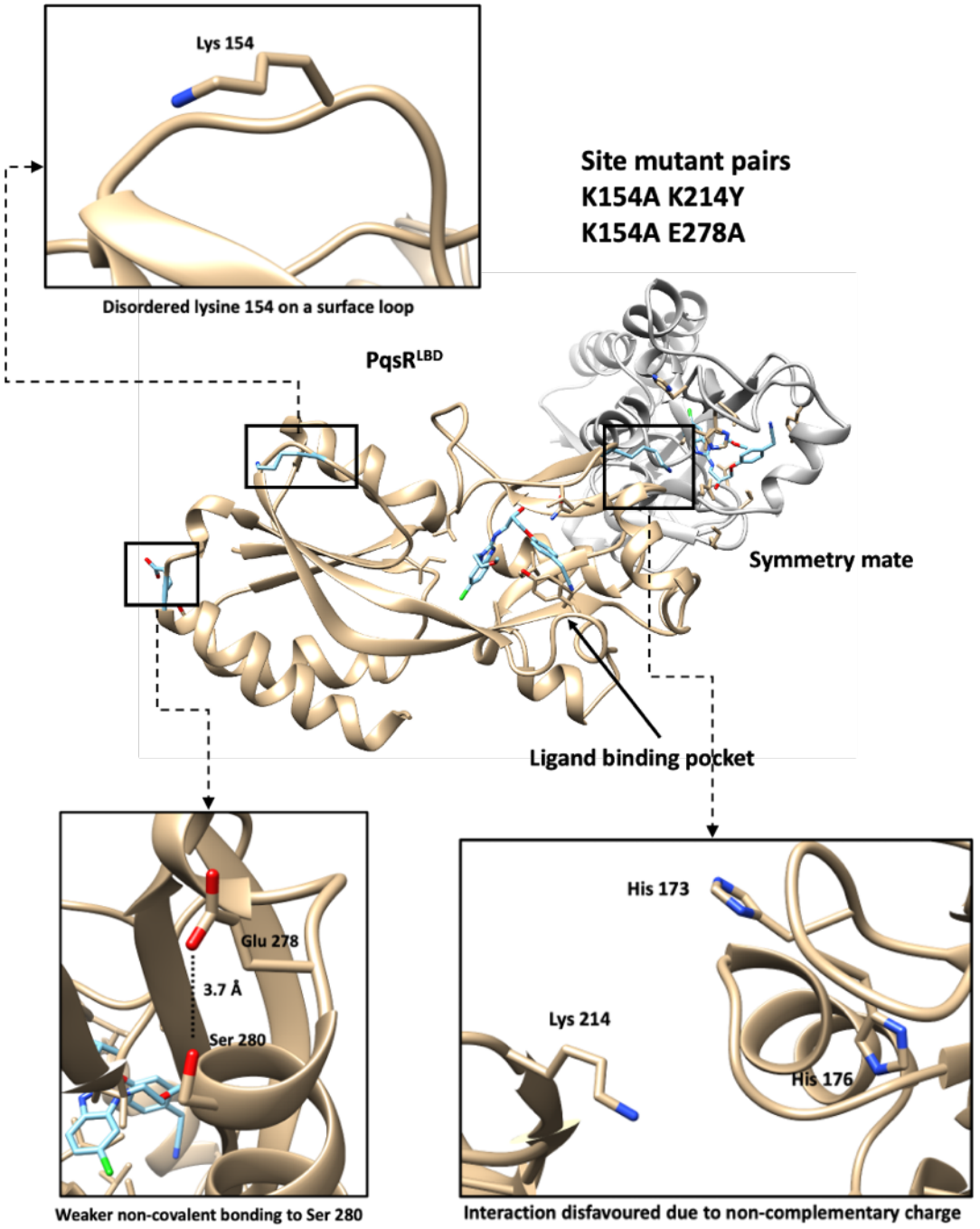

Figure 5.1. Stick representation of PqsR^{LBD} residues targeted for SER mutation. Cartoon representation of PqsR LBD with AM204-004 bound (SEN89 series) coloured in tan and light blue respectively. Proposed target residues are coloured blue with black squares drawn around. The symmetry mate is coloured grey to make it visually distinct and is pointed behind the plane.

5.1.2 Re-engineering loop 180-185 to reduce disorder

B factors, that describe the motion of individual atoms and their deviation from the modelled position, can be good indicators of disorder. High average B factors are a symptom of poor crystal quality yet localised B factors can highlight areas of partial disorder

or flexible loops. Plotting B-factors against residue from several models showed residues 177-190 to have elevated B-Factors compared to the overall structure (Figure 5.2).

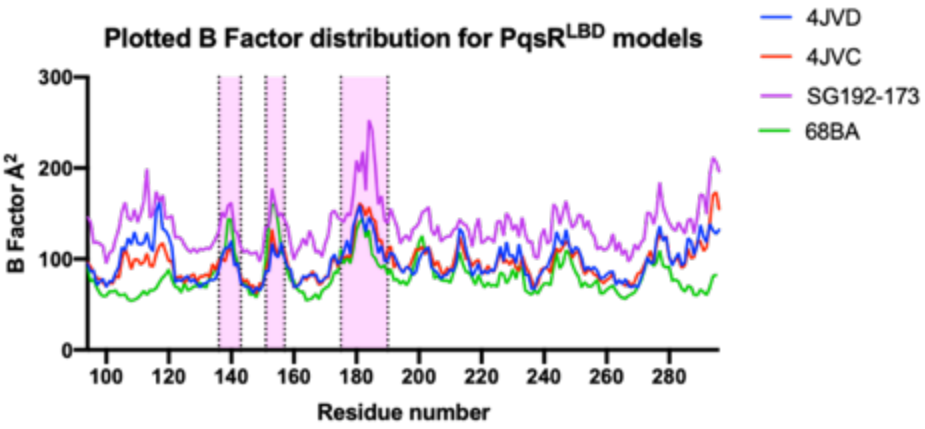

Figure 5.2. B-Factors of PqsR^{LBD} models plotted against residue number. Non-termini areas of elevated B-Factors marked in pink.

These residues, contained in helix 3 and loop 4, were selected for optimisation by computational design. To reduce inherent flexibility the size of this region was reduced by one and two residues using COOT. The models were submitted to the RosettaDesign[325] server with parameters to optimise thermostability of residues 180-185 and suggest substitution with low entropy residues (Tyr, Ala, Ser and Thr). The outputs are summarised in the table below:

Replacement	Native sequence	Mutated sequence
Double residue deletion (DR)	NASLHS	YSSA
Single residue deletion (SR)	NASLHS	SSSYY

Table 5.2 Loop mutants determined using RosettaDesign

Examining RosettaDesign's output of the single residue (SR) deletion model identified a triple serine sequence which may have been translationally disfavoured. As such the second serine was substituted for an alanine in the final construct.

5.1.3 Engineering an intermolecular disulphide

A lesser-known technique for improving protein crystallisation is the introduction of disulphide bonds to "lock" a flexible protein into a single conformation[326]. Non-engineered linkages have also been observed at crystal interfaces such as in the SARS papain-like

protease (PDB 7D7K). Adding disulphide linkages to already established crystal contacts was surmised to reduce interchain movement and subsequently improve resolution. To design inter-chain disulphide bonds symmetry mates were generated in Chimera and saved as separate chains. This model was analysed with Disulfide by Design 2 (DbD2)[327] to identify suitable candidates for mutation that possessed appropriate geometry for bond formation. This identified a single substitution at position 123 that would introduce a disulphide with its own symmetry mate. As shown in Figure 5.3 this would introduce two linkages per dimer unit. The only drawback of this mutant was that an exposed surface cysteine could be deleterious to protein stability from aberrant oxidation. Further analysis with DbD2 and SSBOND[328] failed to identify a single mutation that would form a disulphide with a pre-existing cysteine.

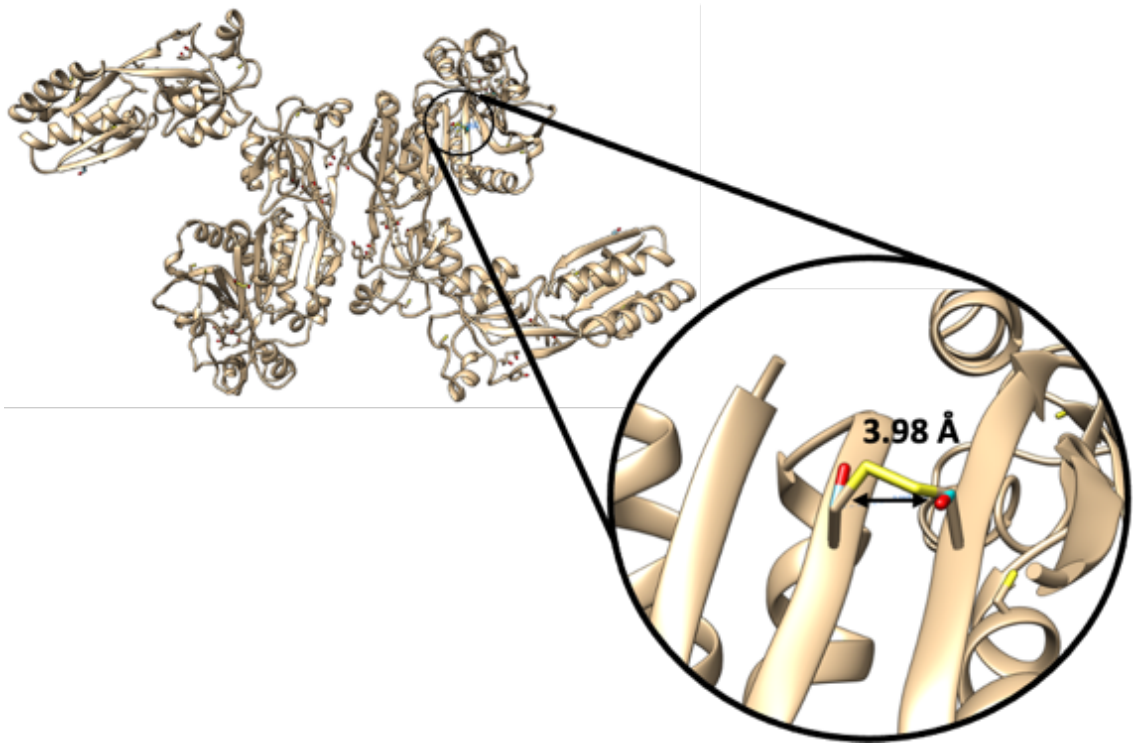

Figure 5.3. Engineered disulphide S123C in PqsR^{LDB} P6$_5$22 crystal form. PqsR^{LBD} dimer (PDB 4JVC) with symmetry mates generated with Chimera. Exert showing Ser 123 residues represented as sticks with a Cβ – Cβ distance of 3.98 Å. Proposed disulphide linkage overlayed with yellow sticks forming an interchain covalent bond.

5.1.4 Modification and extension of N-terminal

Another method to increase the diffraction of $PqsR^{LBD}$ may be to change the construct boundaries that can introduce additional packing interfaces. Examination of full-length receptors in the PDB shows that the linker helix bridging the LBD and DBD usually forms a large interface. As shown in the table below analysis of several full-length receptors shows the interface areas to be comparatively large and, in some instances, have a greater contact area compared to the dimeric interface with similar binding energies (ΔG). As such a construct extending the terminal boundary to residue 60 could exploit these interactions.

PDB	Interface area (Å^2)		ΔG (kcal/mol)[1]		Total bonds[2]	
	Helix	**Dimer**	**Helix**	**Dimer**	**Helix**	**Dimer**
4X6G	1330.9	1251.1	-18.2	-20.2	16	7
5AE5	759.5	1467.2	-12.2	-20.0	4	20
6G1D	1569.7	1186.8	-18.7	-10.1	14	23
1IZ1	1203.3	1271.2	-18.3	-15.9	14	14
3FXU	1440.7	1389.0	-26.1	-22.9	17	16
2ESN	1748.9	2134.7	-23.5	-11.9	14	25

Table 5.3. interface analysis of full length LTTRs from the PDB. (1) Calculated using PISA and rounded to 1 dp. **(2)** Bonds defined in the PDB as polar contacts and salt bridges (at physiological pH).

Additionally, the N-terminal was further modified with a MBP fusion to facilitate crystallisation by providing large surfaces to enable crystal contact formation[329]. A rigid -AAAAS - linker, predicted to form an α helix, was selected to mimic the linker helix described above.

5.1.5 Constructs for purification

From the analysis conducted above the following variants were constructed for crystal trials and expressed in BL21(DE3) CP. Construct characteristics, based upon primary sequence, are listen in Table 5.4. All constructs were successfully expressed with induced bands detected on SDS PAGE (image not shown).

No.	Name	pI	M_r (kDa)
1.	^{94}PqsR^{309} K154A K214Y	5.91	26.7
2.	^{94}PqsR^{309} K154A E278A	6.16	26.6
3.	^{94}PqsR^{309} SR	6.11	26.7
4.	^{94}PqsR^{309} DR	6.11	26.5
5.	^{94}PqsR^{309} S123C	6.16	26.7
6.	MBP-^{94}PqsR^{309}	5.20	64.8
7.	^{60}PqsR^{309}	6.45	30.5

Table 5.4. PqsR^{LBD} construct variants. pI and molecular weight calculated with Protparam.

5.2 PqsR^{LBD} variant purification

5.2.1 SER constructs

Both K154A K214Y and K154A E278A variants were purified by Ni-NTA eluting at 120- and 155-mM imidazole respectively. A HMW contaminant was detected in both preparations but was subsequently removed by gel filtration. Both constructs eluted at 61 mL corresponding to a M_r of 35.5 kDa which would suggest a compact dimer (Figure 5.4c). This shows that neither combination of surface mutations impacted oligomeric state. Gel filtration of K154A K214Y showed a greater amount of material eluting in the void suggesting it was more prone to aggregation. Yields for the constructs were 1.2 mg/g and 0.9 mg/g for K214Y and E278A respectively (purification chromatograms and PAGE shown in Figure 5.4).

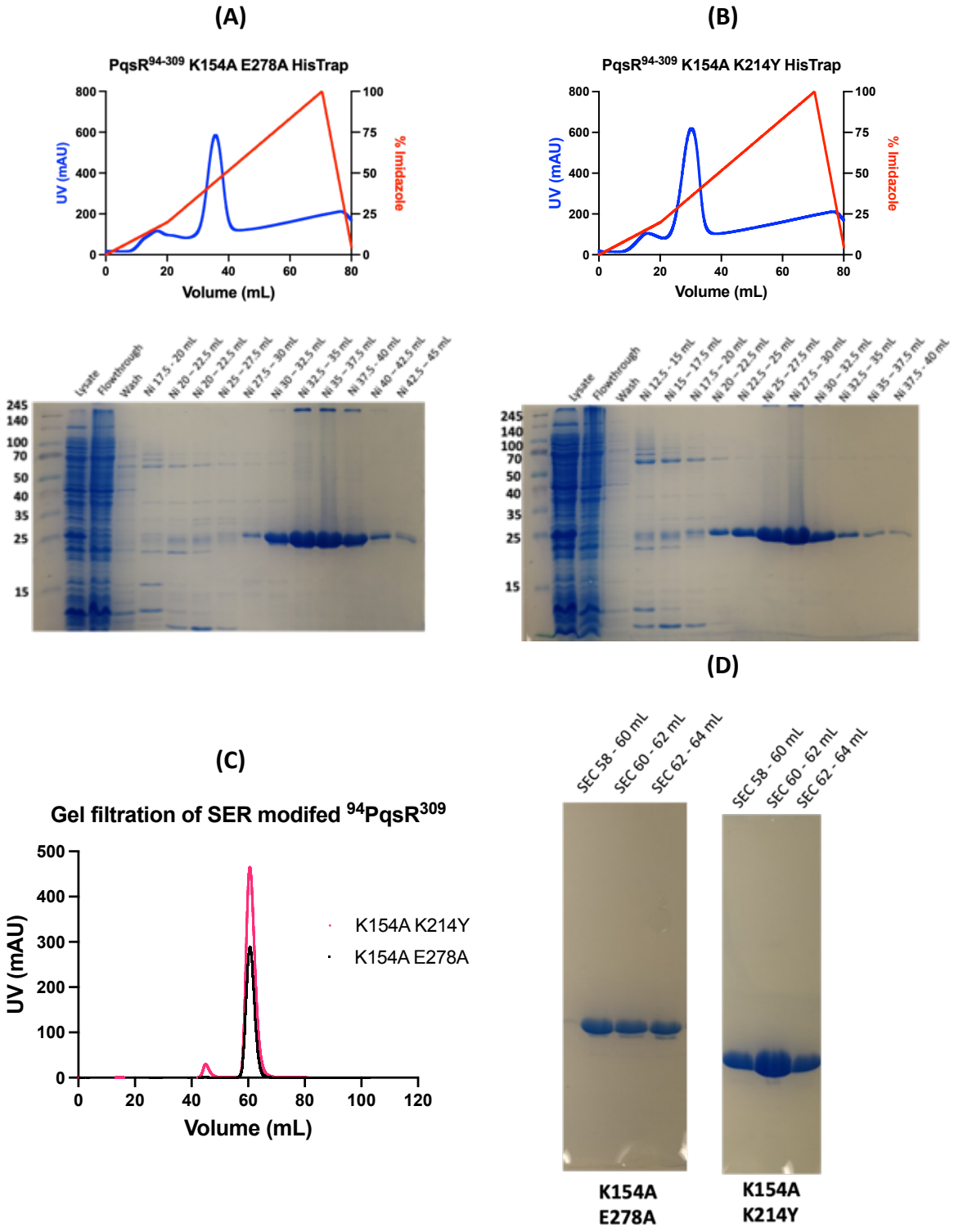

Figure 5.4. Purification of SER variants K154A E278A & K154A K214Y. (A) HisTrap HP elution of K154A E278A and SDS PAGE gel showing high purity. **(B)** HisTrap HP elution of K154A K214Y and associated page with similarly high purity. **(C)** Chromatogram overlay of both mutants eluting from a Superdex 75 16/60 column as a single peak at 61 mL. **(D)** SDS PAGE of both mutant proteins after gel filtration. Estimated purity >95%. Uncropped gels can be found in Appendix 9.13.

5.2.2 Loop modification constructs

Both loop mutants with a single (SR) and double (DR) deletion were successfully expressed in BL21(DE3)CP giving an induced and soluble band on SDS PAGE (not shown). Both constructs were successfully captured on HisTrap HP columns and eluted with high purity at 170- and 185-mM Imidazole respectively (Figure 5.5ab). However, despite the apparent high solubility of the SR mutant dialysis and subsequent cleavage with thrombin appeared to severely destabilise the protein with a significant amount (>95%) precipitating in the dialysis bag. As the optimised loop sequence did not contain a thrombin cleavage site this was not due to off-target cleavage. Subsequent loading of the resultant material onto a Superdex 75 column showed substantial aggregation with a single peak being observed within the trailing material from the void (Figure 5.5c). This peak at 64.3 mL corresponds to a M_r of 28.2 kDa suggesting the protein has adopted a monomeric arrangement. The DR mutant remained stable during dialysis and cleavage & elution from the same column gave a volume of 62.7 mL which was more consistent with the wildtype construct (chapter 3). This mutant gave the highest yield of 3.8 mg per gram cell paste.

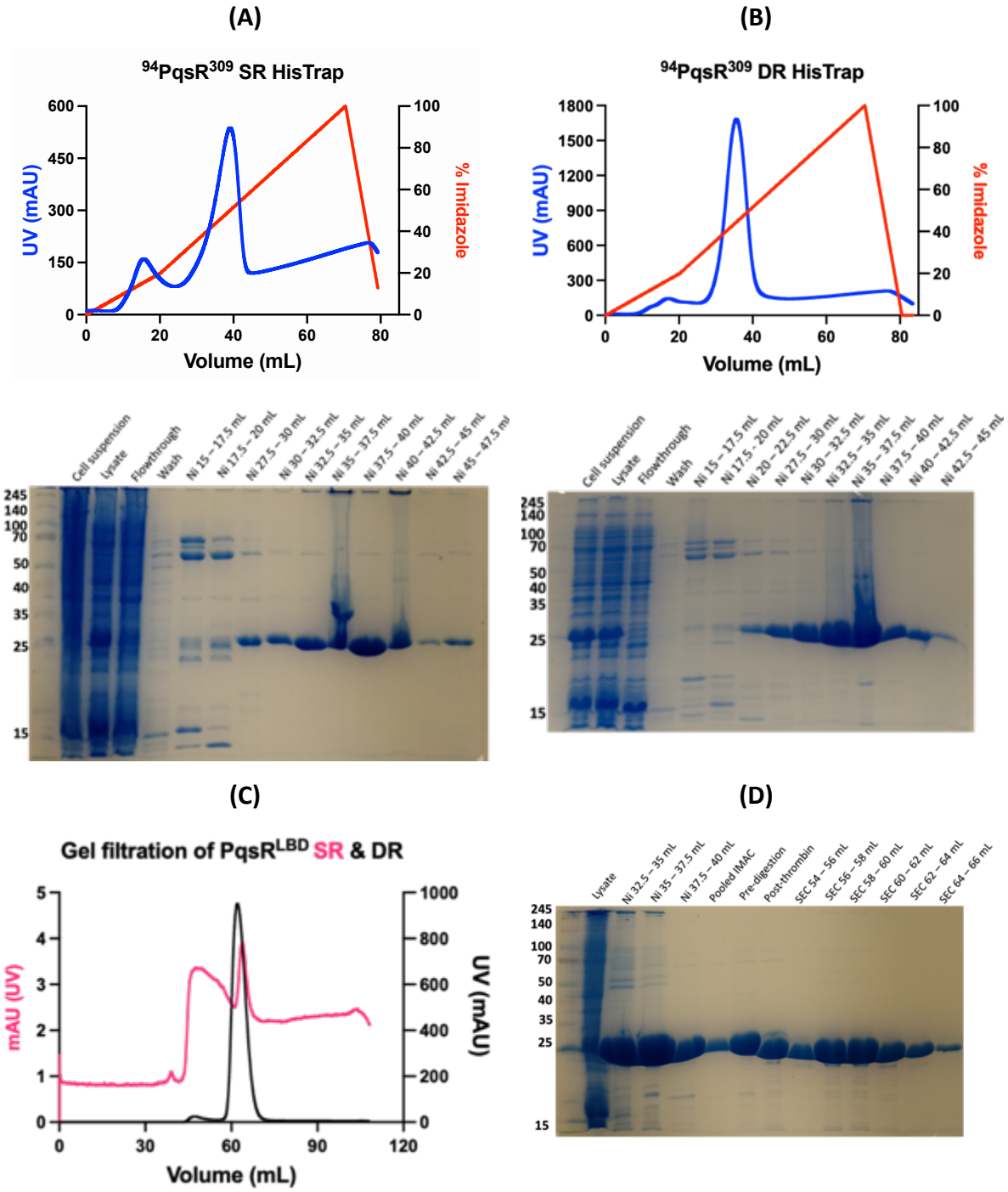

Figure 5.5. Purification of loop variant $^{94}PqsR^{309}$ constructs. (A) HisTrap elution of SR loop mutant with associated SDS PAGE showing purity. **(B)** Purification of DR mutant as with (A). **(C)** Gel filtration of SR and DR constructs on a Superdex 75 16/60. Chromatograms are coloured pink and black respectively with axis coloured appropriately. SR mutant elutes primarily in the void with a small amount of material eluting at 64.3 mL. **(D)** SDS PAGE of DR mutant after cleavage and gel filtration showing >95% purity. Fractions 56 – 64 were taken for concentrations and crystallisation trials.

5.2.3 Interchain disulphide locking construct S123C

Although disulphide containing proteins are often expressed in specialised strains the ^{94}PqsR^{309} S123C construct was expressed in BL21(DE3) CP as *in vivo* disulphide formation would have been undesirable as linkages between dimers may lead to aggregation. The construct was enriched with a HisTrap HP column and cleaved with thrombin overnight. The only contaminant observable was at ~70 kDa and could be removed by gel filtration, eluting in the void volume. The sample eluted from the column at 60.8 mL corresponding to 35.2 kDa which would fit a compact dimeric arrangement. A slight trailing void volume was observed that might be an indication of tetramers – formed by disulphide linked dimer pairs. Yield from 8.5 grams of cell paste was 6 mg of material (0.7 mg/g) which was >95% pure (as judged by SDS PAGE).

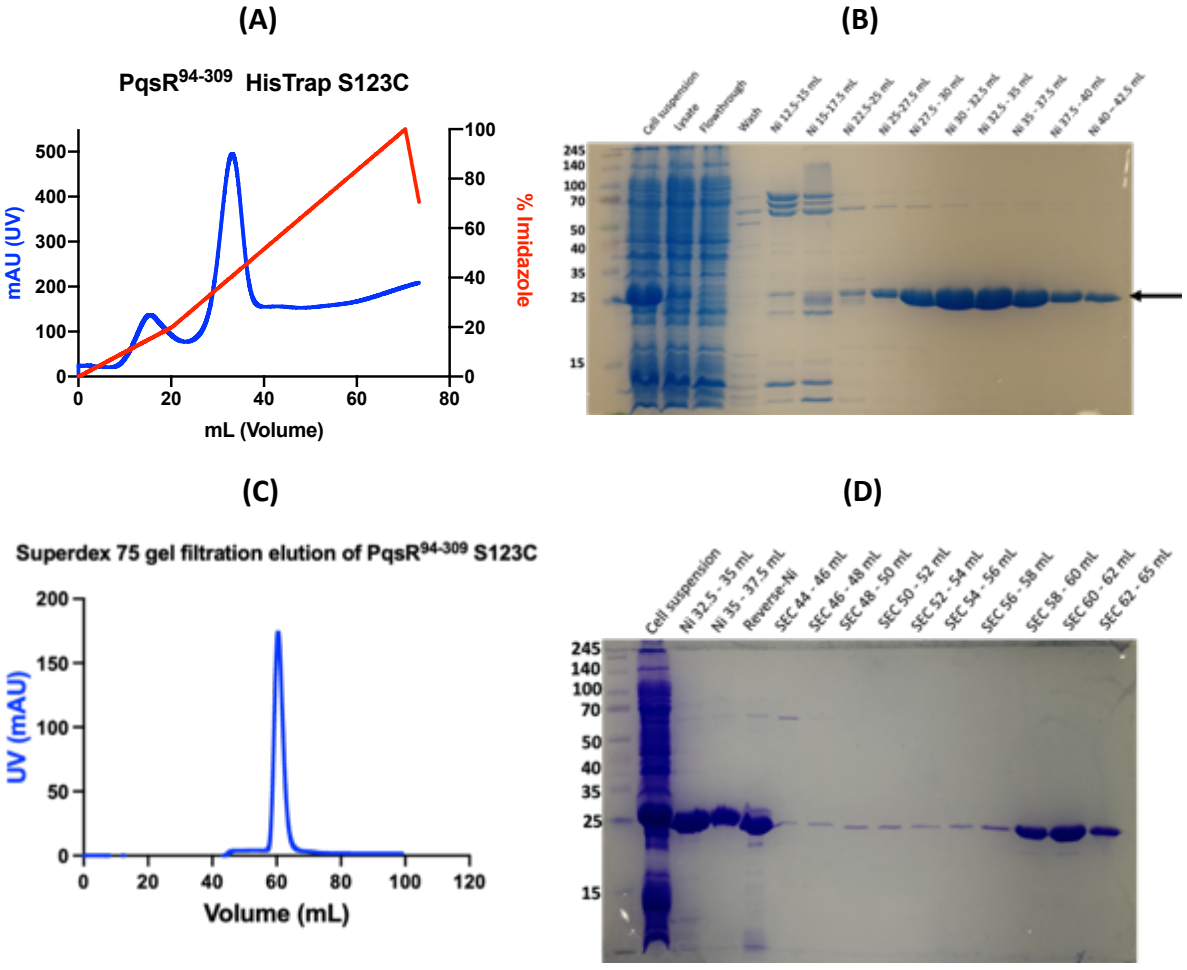

Figure 5.6. Purification of ^{94}PqsR^{309} S123C. (A) Chromatogram showing elution from a HisTrap HP column. Most material eluted between 25 – 40 mL with an imidazole concentration over 170 mM. **(B)** SDS PAGE of HisTrap elution showing the product (marked by arrow) with >95% purity except for a small contaminant ~70 kDa. **(C)** Gel filtration of sample with single peak at 60.8 mL and **(D)** SDS PAGE gel showing high purity of the cleaved protein.

To determine if disulphide linkages were occurring *in vitro* purified sample was incubated at room temperature overnight and subjected to unreduced SDS PAGE. As shown in Figure 5.7 this revealed the presence of an additional band at ~50 kDa that would correspond with the expected 53.4 kDa of a disulphide formed between two LBD monomers.

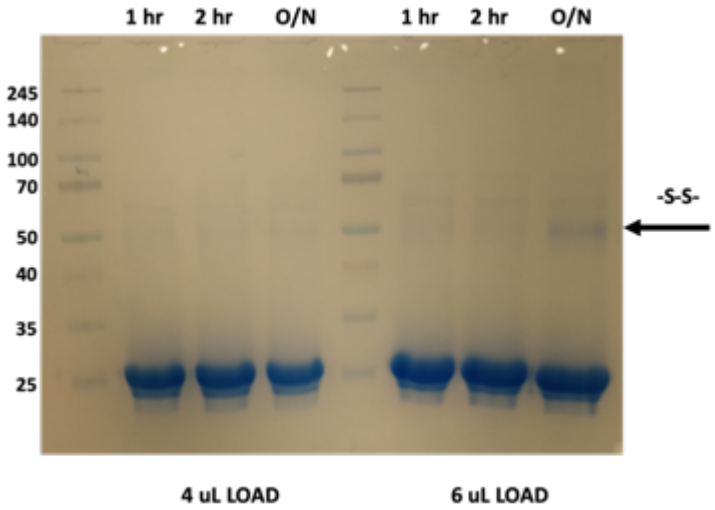

Figure 5.7. Coomassie stained non-reduced SDS PAGE gel showing *In vitro* disulphide bond formation of ^{94}PqsR^{309} S123C. Non-reducing SDS PAGE showing the appearance of a band at ~50 kDa corresponding to monomer-monomer disulphide bond formation. This represents a small fraction of the material and shows formation is time dependent.

5.2.4 MBP-^{94}PqsR^{309} fusion purification

The MBP fusion to ^{94}PqsR^{309} was successfully expressed in BL21(DE3)CP and was subsequently captured on an MBPTrap HP column. Most of the material eluted from the column in the first two fractions (2 CV) but contained several contaminating bands with a lower apparent M_r. Most of these contaminants eluted in the void volume during gel filtration as well as a proportion of MBP-^{94}PqsR^{309} suggesting it was prone to aggregation. The elution volume of 76.6 mL corresponds to an apparent size of 57.3 kDa. As the theoretical mass of the fusion is 64.8 kDa the peak would correspond to a monomer. This is unexpected given that ligand binding domains of LTTRs are canonically dimers. The unexpected elution could be due to the MBP-tag having disrupted the dimeric interface through steric effects or that the protein's elution has been retarded due to hydrophobic interactions with the column media. SDS PAGE also showed a small degree of breakdown as bands corresponding to the individual proteins are visible. Whether this breakdown was

heat induced from SDS PAGE protocol or spontaneously formed could not be determined. The overall yield was 9.4 mg per litre of culture.

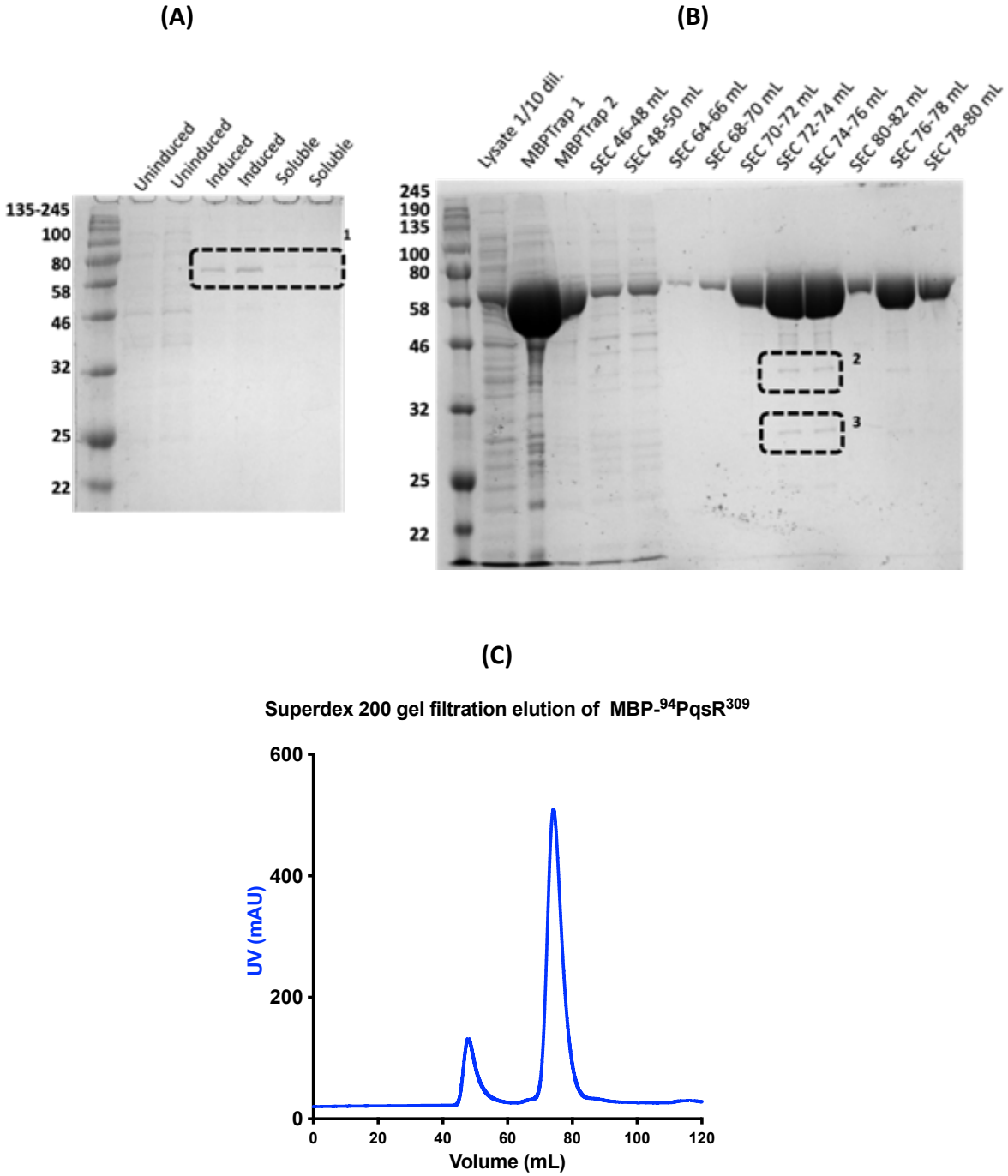

Figure 5.8. Purification of MBP-^{94}PqsR^{309}. (A) SDS PAGE samples of uninduced and induced culture (16°C O/N with 0.4 mM IPTG) and micro-sonicated 'soluble' samples. Box marked 1 highlights the induced and soluble band of correct size (58-80 kDa) **(B)** SDS PAGE gel showing purification of construct by Maltose elution of an MBPTrap HP column followed by gel filtration. Breakdown products are marked with boxes labelled two and three and correspond to MBP and ^{94}PqsR^{309} respectively based on size. **(C)** Chromatogram of MBP-^{94}PqsR^{309} elution from Superdex 200 16/60 column. Peak is monodispersed and well resolved from aggregation at 45 mL.

5.2.5 Helix extension construct

The ^{60}PqsR^{309} construct was successfully expressed with an induced band observed in the cell suspension but appeared to be poorly soluble with no band observed in sonication prepared lysate (Figure 5.9b). However, a small amount of protein was detected in the flowthrough. Earlier eluting fractions between 10 – 20 mL contained the band of interest between 25 - 35 kDa. As shown on the chromatogram in Figure 5.9 a shallower peak was observed after 30 mL that contained cleaner protein except for a small contaminant around 15 kDa. Material was lost through concentration and subsequent elution from a Superdex 200 column only revealed a very small peak at 92.5 mL corresponding to an apparent M_r of 16.6 kDa. As this was smaller than expected for the monomer it is likely the sample is interacting non-specifically to the column media. Due to the relatively low yield the construct was not used further.

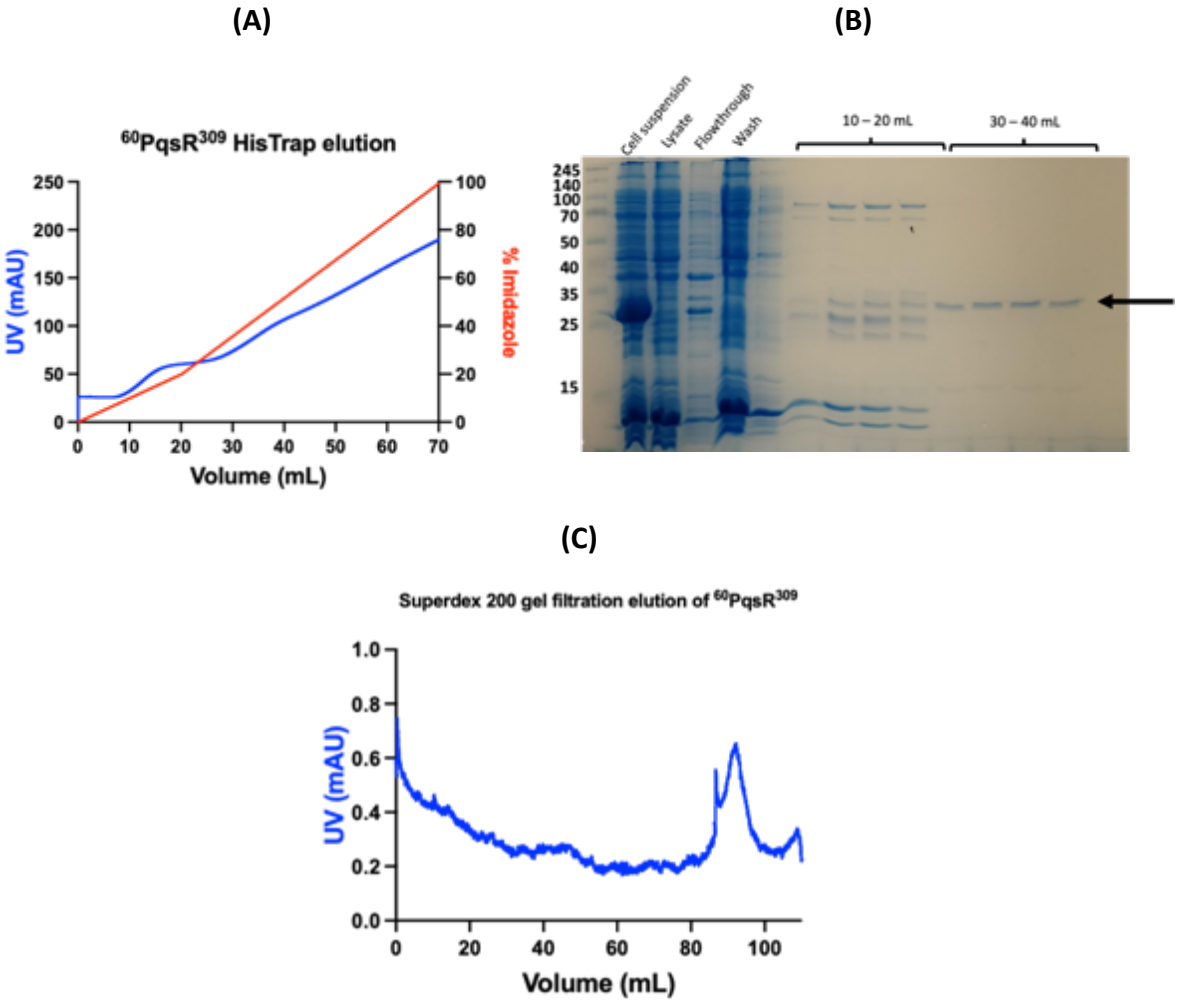

Figure 5.9. Purification of $^{60}PqsR^{309}$. (A) HisTrap HP elution of $^{60}PqsR^{309}$ with two shallow peaks at 10-20 mL and 30-40 mL. **(B)** SDS PAGE gel showing the composition of the two peaks with purer material contained in the second peak. **(C)** Elution from Superdex 200 16/60 showing a single peak at 92.6 mL (~0.4 mAU) unsuitable for further work.

5.3 Crystallisation of construct variants

From the construct variants purified only $^{60}PqsR^{309}$ could not be progressed to crystallisation trials. To bias the crystallisation experiments a custom 96 condition screen was created, based on other studies reporting $PqsR^{LBD}$ structures and crystals, utilising MPD, ethylene glycol, ethanol and NaCl as primary precipitants The screen composition is further detailed in the Appendix 9.12. Crystallisation trials of successful mutants are described below:

5.3.1 SER variants: K154A E278A, K154A K214Y

SER variants were concentrated successfully to 4 and 8 mg/mL and screened using the custom SER screen, Morpheus, MIDAS, and the Ligand Friendly screen (LFS). Many

conditions gave rise to crystals of both variants with the K154A E278A variant forming a greater number of hits. As shown in 6.10a, most hits were derived from the Morpheus screen which was dominated by needle and spherulite habits. The K154A E278A variant gave most hits in the custom screen, with a hexagonal bipyramidal habit, suggesting its crystal form was similar to wildtype.

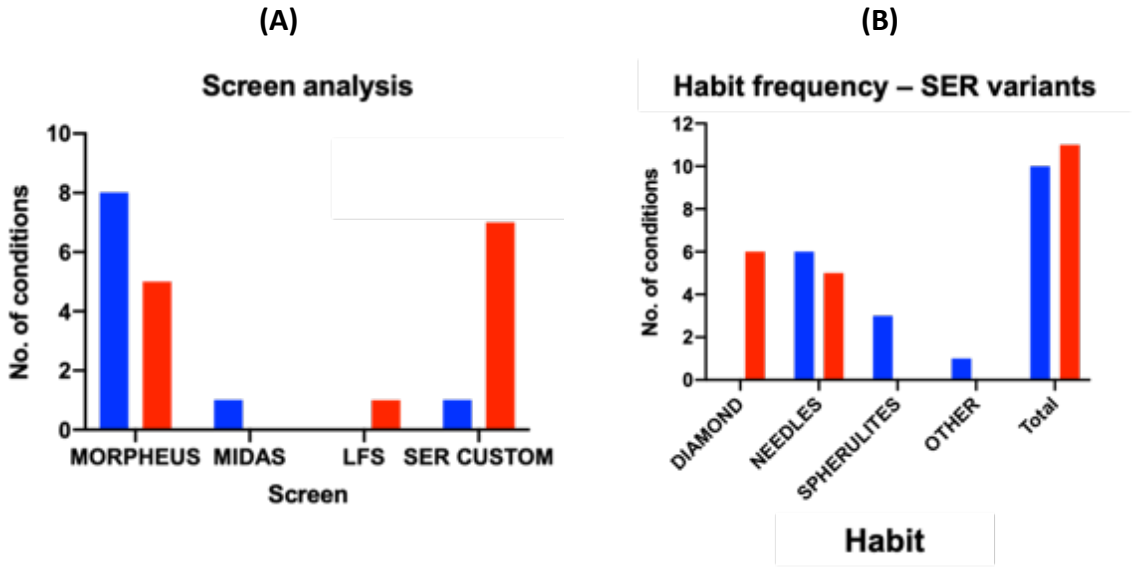

Figure 5.10. SER constructs hit analysis. (A) Number of conditions yielding crystalline material with respect to screen. **(B)** Crystal habits observed for both constructs in all tested screens. Red and blue colouring representing K154A E278A and K154A K214Y respectively. Diamond refer to the hexagonal bipyramidal habit observed in the wildtype construct (chapter 3).

Only a few conditions, not containing MPD, gave rise to crystals. Diamond, needle and spherulite habits, pictured in Figure 5.11, grew in MPD based conditions after a few days. Although crystals grown from the Morpheus suite, containing multi-solvent systems, show that PEGS are tolerated in the crystallisation mixture. The MIDAS suite produced crystalline material in several conditions including 35 % v/v Polypropylene glycol 400 & 20 % w/v SOKALAN® CP 45 but these were qualitatively poor compared to other hits. However, extended incubation in the MIDAS suite gave rise to a prismatic habit grown from PPGBA 400 (Jeffamine) and could be reproduced using commercial solution by exploiting varying protein:precipitant ratios to increase speed of formation (6.11b).

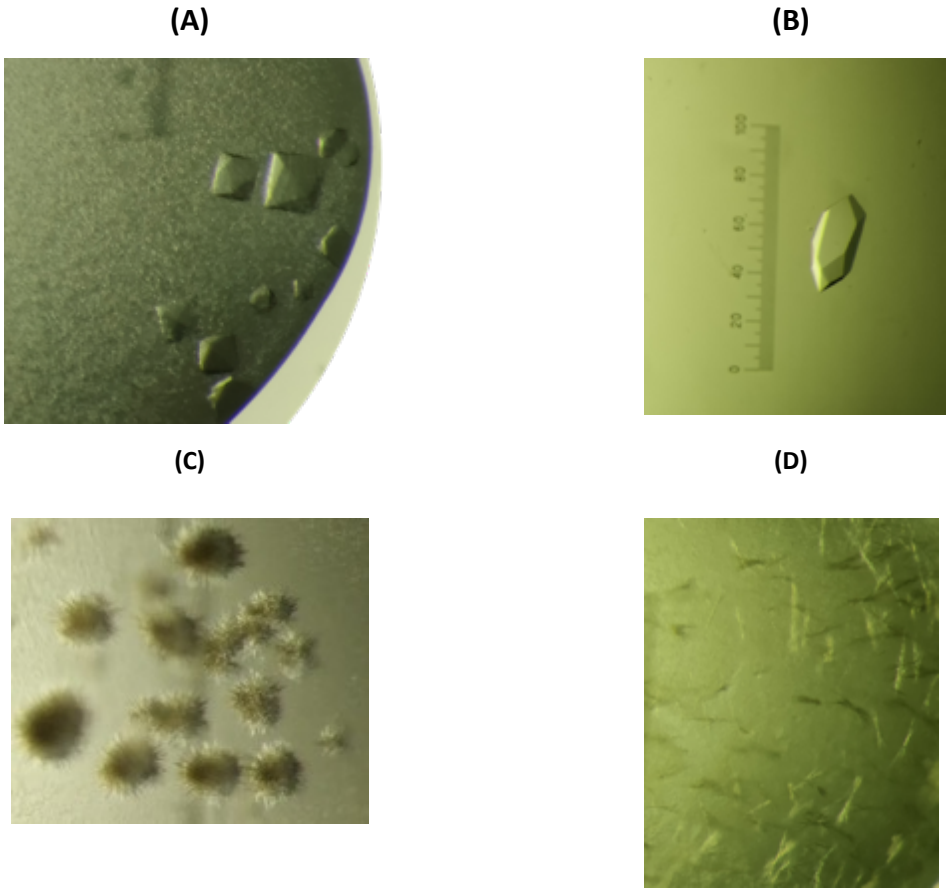

Figure 5.11 Crystal habits of PqsR^{LBD} SER variants. (A) Hexagonal bipyramidal habit adopted by K154A E278A with 0.1 M sodium citrate tribasic dihydrate (pH = 5.5), 0.2 M ammonium acetate, 10% MPD & 10% glycerol **(B)** 20 µm length crystal with prismatic habit adopted by K154A K214Y at 10 mg/mL with 0.1 M lithium citrate tribasic tetrahydrate 0.1 M Tris (pH = 8.5) & 15% v/v PPGBA 400. **(C)** Spherulite habit observed with K154A K214Y grown using 0.1 M Sodium HEPES - MOPS (pH = 7.5), 0.1 M carboxylic acids mix, 12.5% v/v MPD; 12.5% PEG 1000; 12.5% w/v PEG 3350. **(D)** Needles observed from both mutants - E278A shown – with conditions grown from 0.1 M Tris - BICINE (pH = 8.5), 0.1 M carboxylic acids, 12.5% v/v MPD; 12.5% PEG 1000 & 12.5% w/v PEG 3350.

5.3.2 Loop mutants

Concentrating the SR mutant failed as the remaining sample was lost to sample adsorption on the ultrafiltration membrane. The DR mutant was successfully concentrated to 10 mg/mL and set up at 4 and 10 mg/mL. As shown in Figure 5.12 a high number of hits were observed in all screens except for Morpheus with the predominant crystal habit being microcrystals or needle clusters.

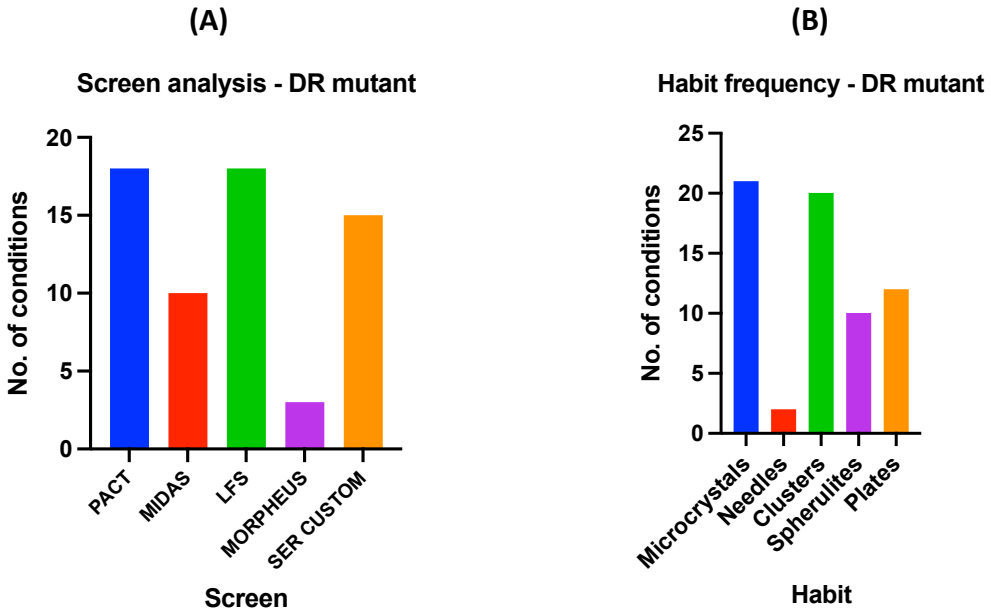

Figure 5.12. Crystallisation of DR PqsR$^{94-309}$ variant hit analysis (A) Number of conditions yielding crystalline material with respect to screen. **(B)** Crystal morphologies observed in 96 well plate formats across all screens.

A wider variety of precipitants were observed compared to the wildtype and other variants tested. These are listed in Table 5.5. PEG conditions were most frequently observed but the morphology differed substantially with PEG 1500 mostly yielding microcrystals and needle clusters. Larger polymers gave rise to larger crystals but were less abundant. As pictured in Figure 5.13, plate habits were observed with ethanol and glycerol ethoxylate as the precipitant. This habit could be reproduced by streak seeding into hanging drops containing the non-volatile glycerol ethoxylate. Streak seeding also improve crystal size and quality (Figure 5.13c).

Precipitant	No. of hits
PEG 1500	8
PEG 3350	8
MPD	7
Ethanol	4
PEG 1000	3
Poly(acrylic acid sodium salt) 2100	3
Glycerol Ethoxylate	3
PEG 6000	2
NaCl	2
Polyvinylpyrrolidone & PEG 4000	1
Jeffamine ED-2003	1
SOKALAN CP 5	1
Polyvinylpyrrolidone & PEG 5000	1
Ethylene Glycol	1
Glycerol & PEG 4000	1
MPD, PEG 1000 & PEG 3350	1
PEG 500 MME & PEG 20000	1

Table 5.5 Breakdown of precipitants giving hits for DR mutant. Table is sorted by frequency of hits.

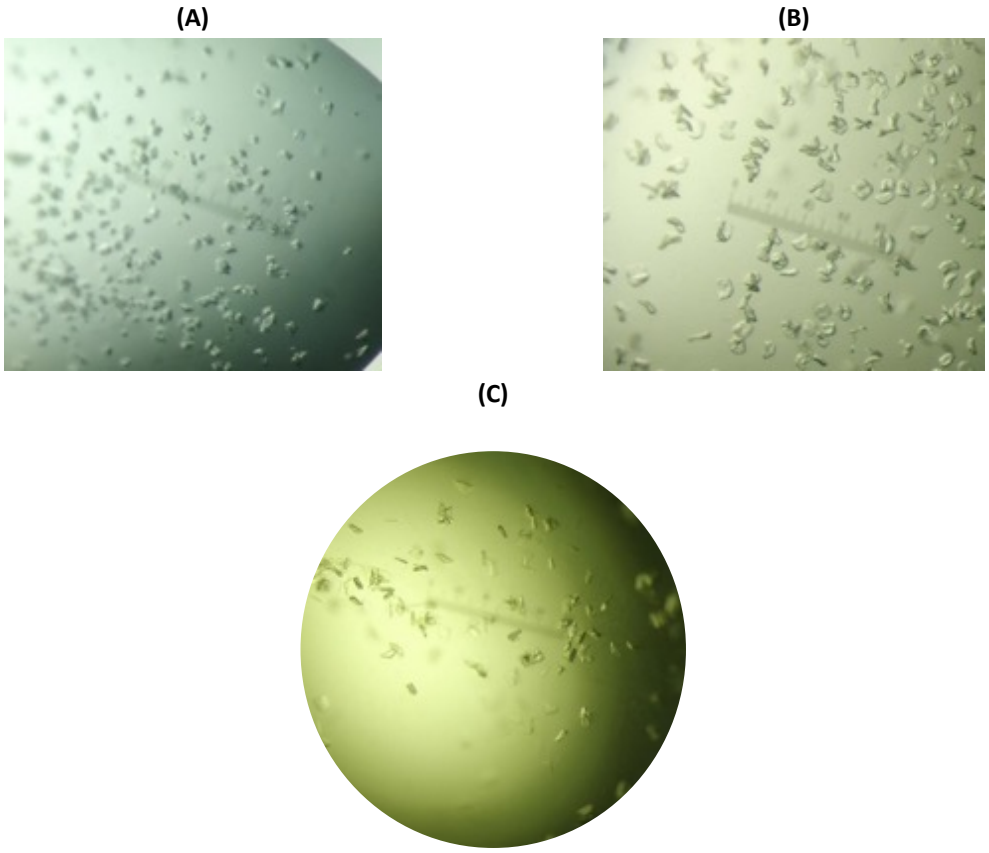

Figure 5.13. Crystal habits of DR variant. (A) Plates/shards habit grown in a 400 nL drop from 0.2 M ammonium chloride, 0.1 M HEPES (pH 7.5) & 25 % v/v glycerol ethoxylate. **(B)** Stacked plates observed in 0.2 M lithium chloride, 0.1 M citrate (pH 6) & 10% ethanol. **(C)** Superior quality crystals grown by streak seeding into glycerol ethoxylate.

5.3.3 Engineered disulphide lock variant S123C

Although some reducing agent had been used using dialysis and cleavage (50 µM TCEP) to abate aberrant disulphide formation this was omitted in the final gel filtration and subsequent concentration. As shown in Figure 5.14 most hits were attained in the custom screen and predominantly in ethylene glycol and MPD conditions. Most hits displayed the hexagonal bipyramidal habit exhibited with the wildtype construct. An elongated crystal form was also observed that grew exclusively in ethylene glycol (Figure 5.14d).

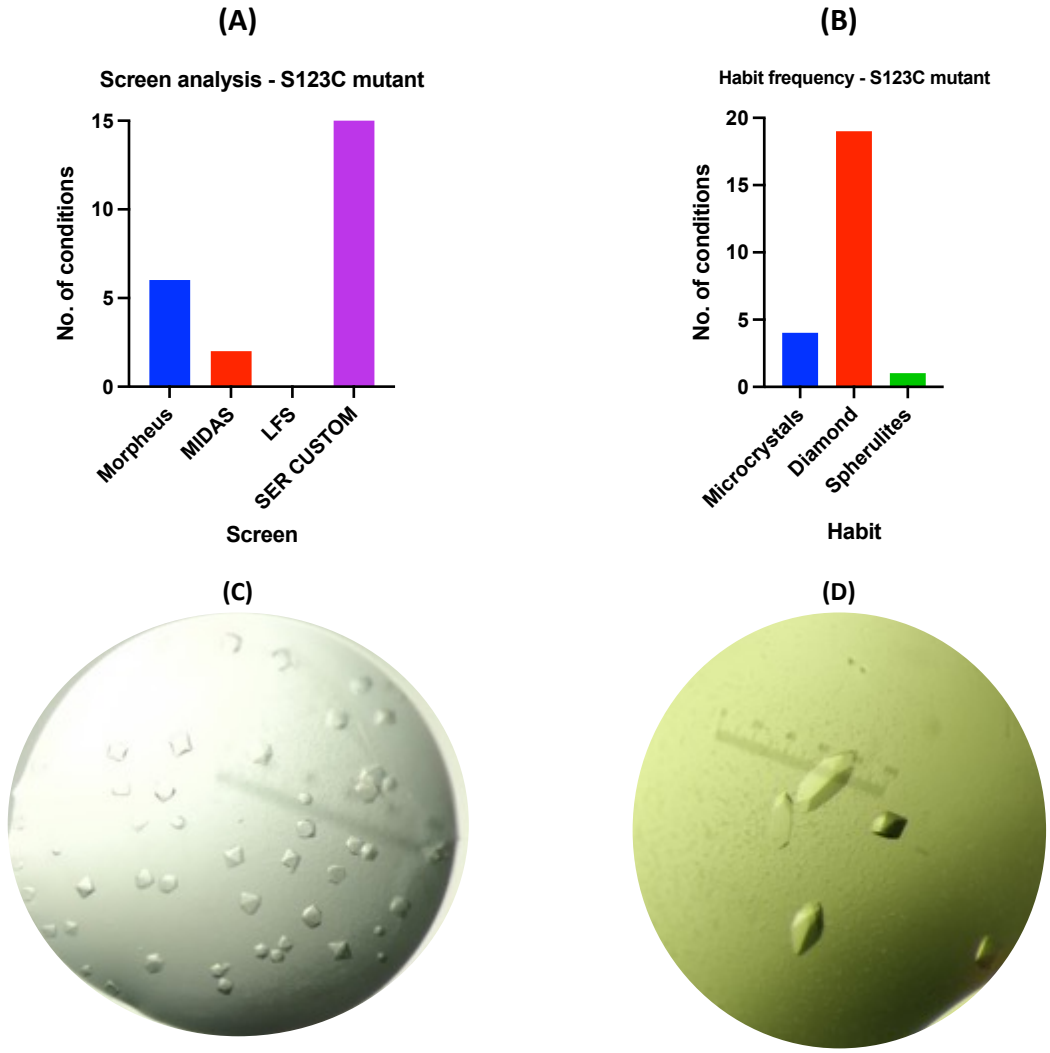

Figure 5.14. PqsR^{LBD} S123C variant hit analysis (A) Number of conditions yielding crystalline material with respect to screen. **(B)** Crystal habits observed in 96 well plate formats across all screens. **(C)** Hexagonal bipyramidal habit grown from 0.2 M potassium acetate & 35 % v/v pentaerythritol propoxylate (5/4 PO/OH) **(D)** Elongated habit grown in a 400 nL drop from 0.1 M Tris (pH 8.25), 0.2 M magnesium chloride & 30% ethylene glycol.

5.3.4 MBP-^{94}PqsR^{309}

Fractions after gel filtration were concentrated to 4 and 10 mg/mL for crystal trials. Precipitation was observed in the Vivaspin device during concentration, leaving a film on ultrafiltration membrane. Crystal trays were set up with Nucleix and the MPD suite. No crystals were observed after 1 month, but some light precipitation was observed in many wells. At higher concentrations of MPD, darker amorphous precipitate was observed.

5.3.5 In-gel agarose crystallisation of wildtype ^{94}PqsR^{309} construct

As an alternative strategy to gaining higher resolution, in-gel crystallisation was attempted using the same methodology as used for full length PqsR in chapter 4 with the same MPD condition reported for crystallisation in chapter 3. This has been effective in the literature to generate ligand complexes that normally deteriorate crystal quality[330 331]. Crystals grew with a dipyramid prismatic habit that differed to the hexagonal bipyramid habit normally observed in the absence of agarose. However, the crystals remained quite small and due to difficulties observed in retrieving the full length receptor were not optimised further.

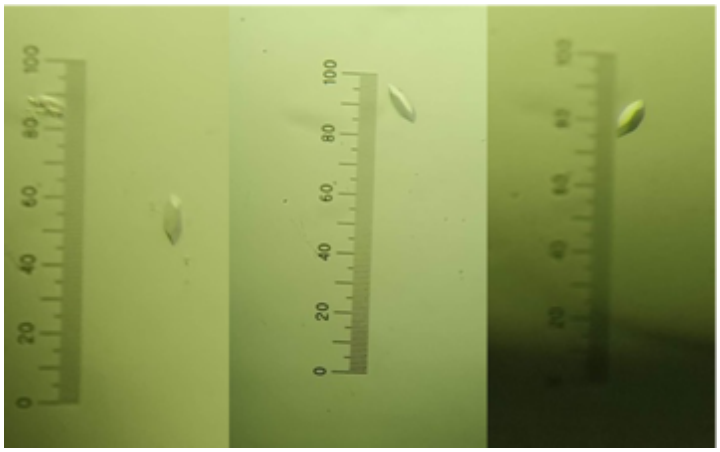

Figure 5.15. Agarose-grown ^{94}PqsR^{309} crystals. 4 mg/mL protein in a 4 µL sitting drop supplemented with 0.1-0.2% low melting agarose. Small dipyramid prismatic crystals grew within days that differed from the expected habit observed in chapter 3.

5.4 Structural solution of engineered disulphide S123C

The S123C crystals adopted the same unit cell dimensions and space group as observed in the wildtype 4JVC model. As such phasing could be carried out by using 4JVC as a starting model (Data collection and refinement statistics refer to SEN89 R isomer determination detailed in Table 3.6). Refinement using REFMAC showed $2F_o$-F_c density across the crystallographic interface that would be consistent with a disulphide bond. Refinement with a single conformer, generating a disulphide was insufficient and positive F_o-F_c density was observed from the original modelled hydroxyl position from Ser 123. As such the cysteine conformer was split, to equal occupancy, to satisfy both density pockets (Figure 5.16b). Deformation of the beta sheet containing Cys 123 was observed suggesting that bond formation had pulled the residues closer together. The new crystal form also contained a bound ethylene glycol molecule from the crystallisation mother liquor bound at the dimer interface (Figure 5.16c). This molecule was sandwiched between Tyr 165 and Asp 264 and is supported by hydrogen bonding to the carboxylate of the latter (3.5 Å). To account for symmetry a single molecule with occupancy of 0.5 was used such that each ASU contained a single molecule that could occupy the same position (to prevent VDW repulsion).

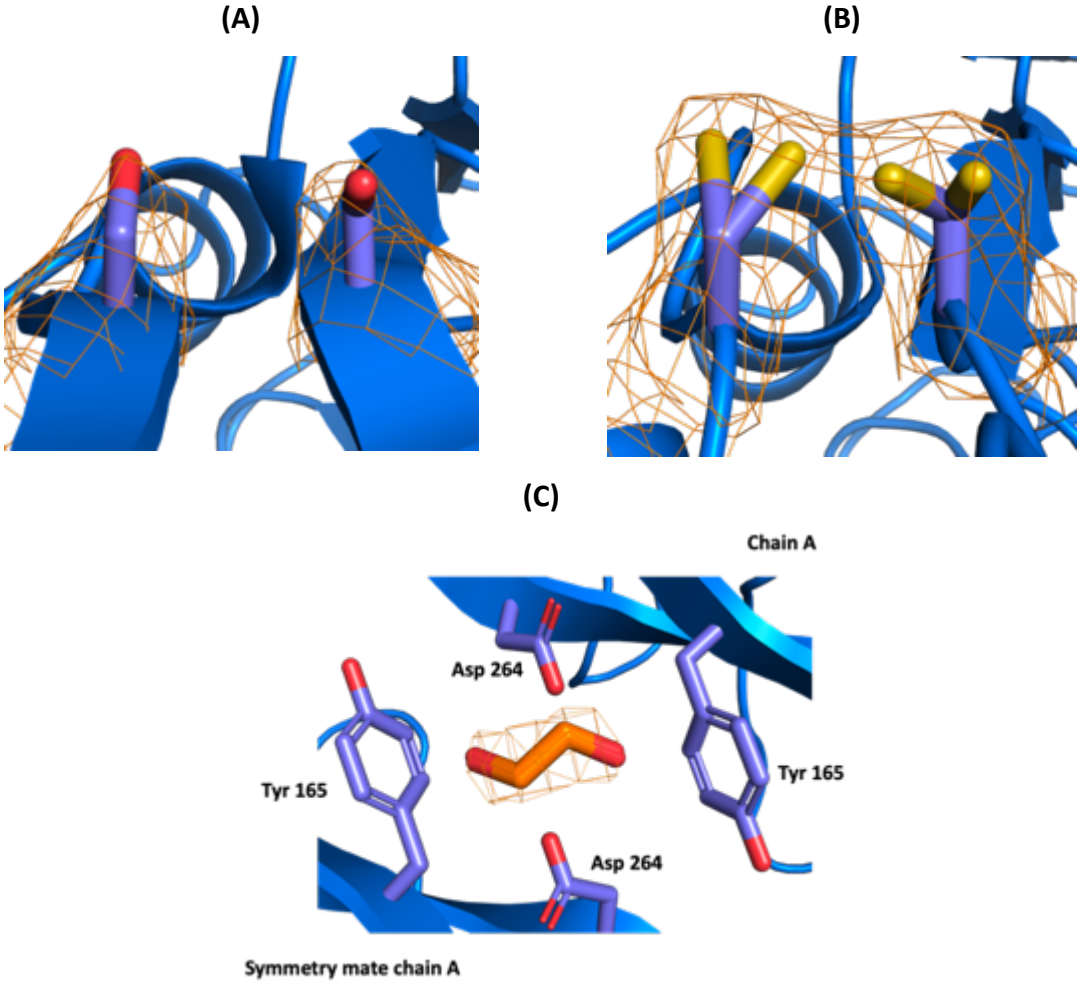

Figure 5.16. *In crystallo* formation of a disulphide in S123C. (A) $2F_o$-F_c electron density map calculated from wildtype crystal from PDB entry 4JVC **(B)** $2F_o$-F_c electron density map calculated from S123C crystal. Density accounted for by Cys 123 adopting two conformations. **(C)** Ethylene glycol molecules (two at 0.5 occupancy) bound at the dimer interface with $2F_o$-F_c electron density map. Individual residues shown as sticks in slate blue and bound ligand as orange. Density maps contoured to 1 σ with a carve of 1.6 Å.

5.4.1 Effectiveness for antagonist determination

As the S123C crystal form gave the largest crystal habit and best appearance they were chosen for antagonist determination giving a resolution of 2.54 Å. However, most soaked crystals gave similar or worse resolution than that reported in chapter 3 with an average limit, determined by Xia2 DIALS, calculated to 3.29 Å (± 0.49). A select group of linked fragments were chosen for soaking that gave reasonable IC_{50}s, as determined in chapter 5, but only compound 26 gave contiguous density within the pocket. As MPD was not present in the crystallisation conditions any density within the pocket would belong to the ligand. However, ligand features were ambiguous and could not be modelled (data not shown).

5.5 Structural solution for SER variants

5.5.1 K154A E278A

Diffraction of K154A E278A, performed on i24, was poorer than 3 Å and not continued further. However, as ice rings were observed (pictured below in Figure 5.17a) it is conceivable that ice formation during cryoprotection impaired diffraction. Initial space group and unit cell parameter determination with Mosflm[332] and EDNA[333] suggested an orthorhombic space group P 2 2 2. Cell content analysis highlighted that a Matthews coefficient of 3 molecules in the asymmetric unit was most likely (probability. 0.74) with a calculated solvent content of 48.33%.

(A) **(B)**

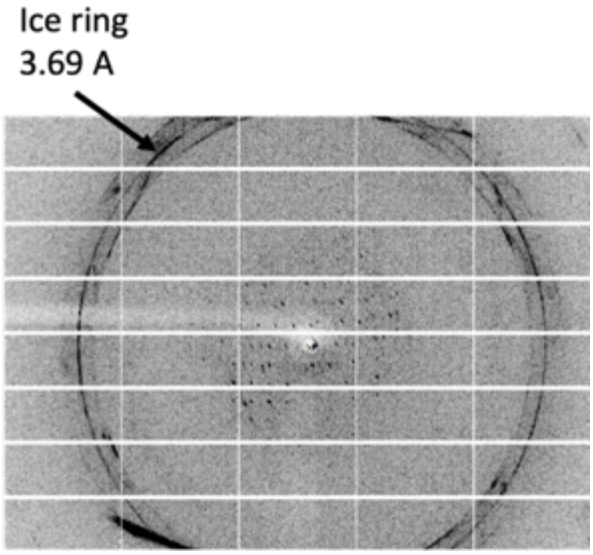

Space group	P 2 2 2
a ,b, c (Å)	77.8, 79.2, 114.6
α, β, γ (°)	90, 90, 90

(C)

N(mol)	Prob(N)	Vm Å^3/Da	% Solvent content	Mw (kDa)
1	0.01	7.14	82.8	24.7
2	0.21	3.57	65.6	49.4
3	0.73	2.38	48.3	74.2
4	0.04	1.79	31.1	98.9
5	0	1.43	13.9	123.6

Figure 5.17. Diffraction image of K154A E278A. (A) Image taken on i24 with 20.37% transmission with an exposure time of 50 milliseconds. Low resolution reflections observed with ice ring marked. **(B)** Table of crystal parameters determined by Mosflm ISPyB plug-in. **(C)** Crystal content calculated by Rupp server[290] with inputted cell parameters and molecular weight. Resolution was set to 5 Å (maximum allowed for server).

5.5.2 Structural determination of SER variant K154A K214Y

Diffraction conducted on K154A K214Y crystals gave similar resolution to the wildtype with the limit determined with DIALS to be 2.7 Å. Phasing by molecular replacement using PHASER achieved a high confidence solution with LLG of 984.17 and TFZ score of 34.99 (collection and refinement statistics listed in Table 5.6). After refinement the RMSD from alignment to the wildtype 4JVC model was 1.66 Å. The most substantial change appeared in helix 1 with a clockwise rotation observed. This rotation affected the positions of Phe 107 and Cys 108 substantially. As shown by Figure 5.18a the side chain of Phe 107 has moved 4.6 Å and Cys 108 has shifted 2.4 Å. In the latter's case the movement has changed the residue's environment from hydrophobic to solvent exposed. This has resulted in an apparent disulphide formation with its symmetry partner. Although examination of electron density shows a dual conformation with the previous orientation still present.

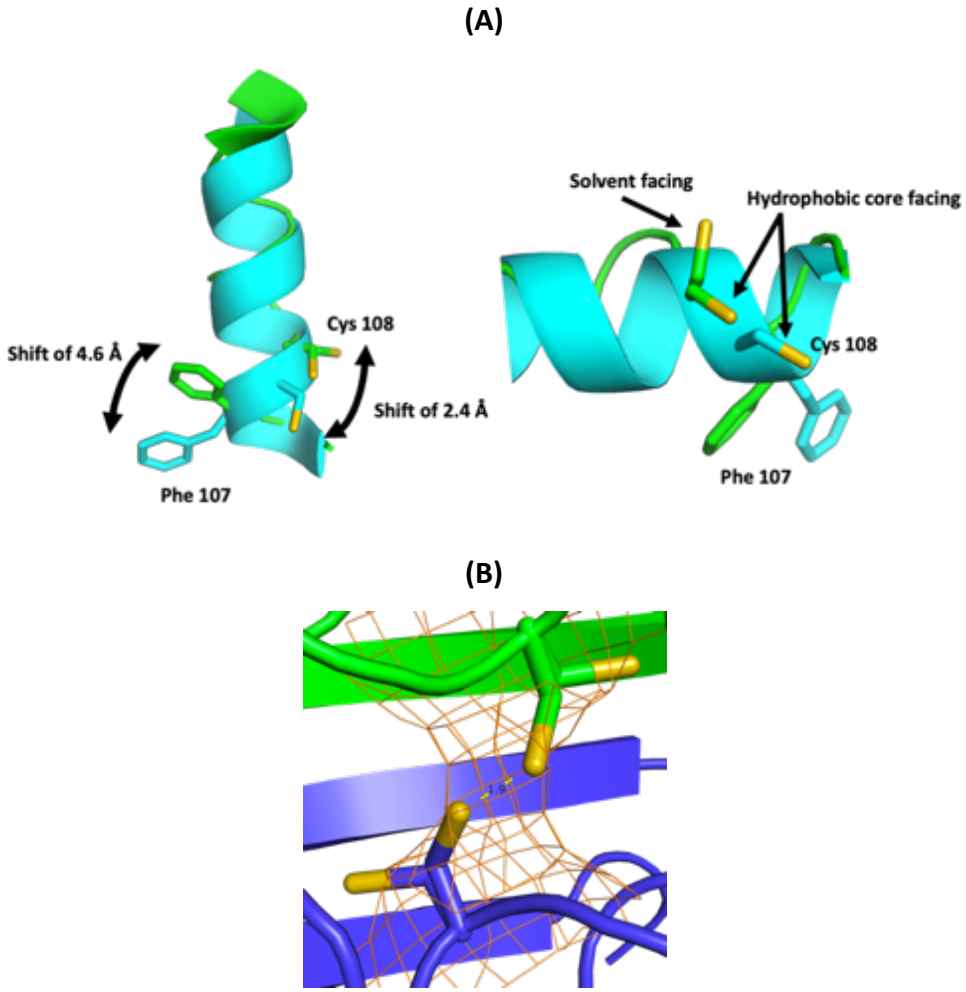

Figure 5.18. K154A K214Y crystal structure (A) Rotation of helix 1 showing re-positioning of Phe 107 and Cys 108. Dual conformation of Cys 108 with one rotamer solvent exposed whilst the other is directed into the protein's hydrophobic cavity. **(B)** $2F_o$-F_c electron density map calculated from K154A K214Y crystal and contoured 1 σ with a carve of 1.6 Å. Measured distance measured in PyMOL between sulphur atoms is 1.9Å.

Examination of the crystal packing, canonically considered to be the tetrameric interface, shows that the dimer has been rotated vertically by 92.2° in the new structure compared to the wildtype arrangement (Figure 5.19a). Consequently, this has subtly changed the interface with Arg 126 forming a bidentate interaction to the carboxylate group of Asp 117 which would be stronger than the wildtype interaction with the backbone carbonyl of Asn 120. As shown by Figure 5.19b most of the hydrophobic interactions are preserved in the interface but the inclusion of strong salt bridges would make it more stable compared to the wildtype arrangement.

Alignment of the binding site from each structure does not reveal any significant changes showing that the pseudo-ligand MPD in the wildtype structure does not have any impact on the binding pocket's topology. From a whole-structure alignment the only area showing significant backbone deviation are residues 153-155. The loop's backbone has shifted by >3 Å and is most likely attributed to the K154A mutation (data not shown).

(A)

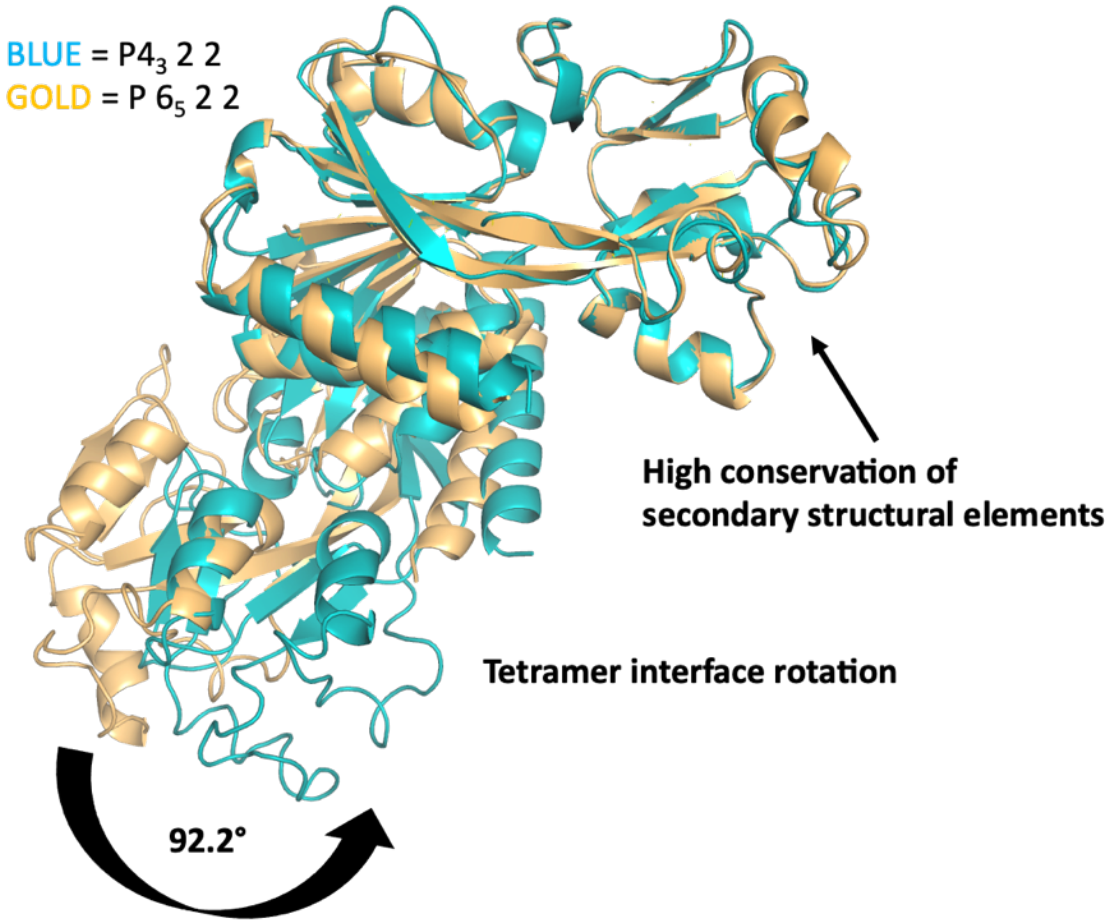

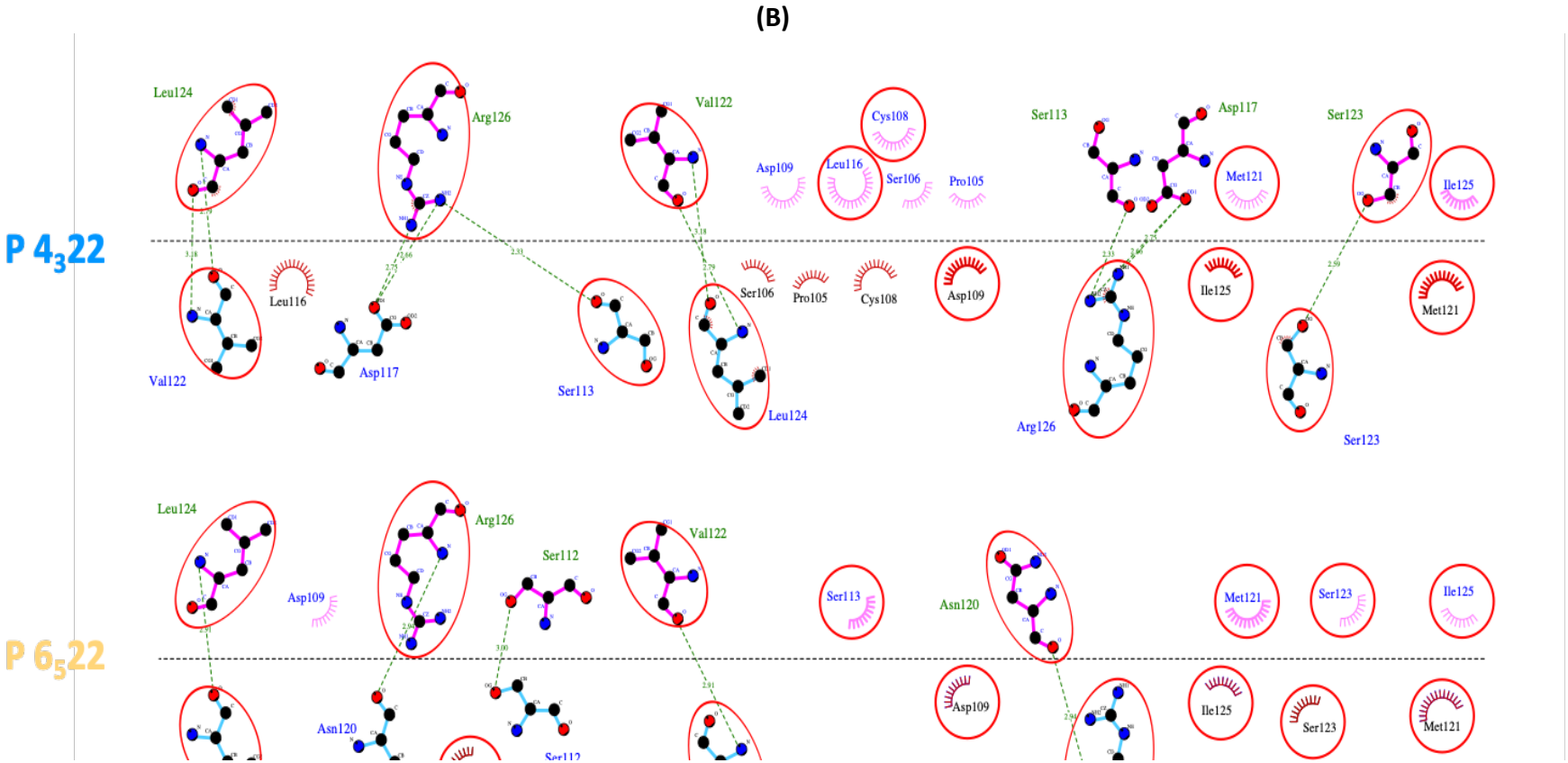

Figure 5.19. Change in tetrameric interface between P6$_5$22 and P4$_3$22. (A) Superimposition of monomers from each crystal form's ASU with tetrameric interface shown. Rotation calculated by measuring a commonly aligned residue (Arg 126) and Leu 186 from each symmetry mate. Structural elements from the ASU are well conserved apart from the rotation in helix 1 **(B)** 2D representation of the interface constructed by DIMPLOT. Common residues are marked with red circles showing overall preservation of hydrophobic interactions. Hydrogen bonds and salt bridge interactions are denoted by dashed green lines. Asn 120 no longer participates in the interface within in new arrangement.

Table 5.6: Data collection and refinement statistics for K154A K214Y

Data collection	K154A K214Y*
Beamline	i24
Wavelength (Å)	0.9999Å
Space group	P 4_3 2 2
a ,b, c (Å)	79.1, 79.1, 114.3
α, β, γ (°)	90, 90, 90
Resolution	114.27 – 2.7
No. of unique reflections	10520 (489)
R_{merge} (%)	0.194 (3.6)
Mean I/Sig(I)	10.3 (0.3)
Completeness (%)	100 (94)
Redundancy	23.9 (22.8)
CC½	1 (0.7)
Refinement	
Resolution range (Å)	79.19-2.70
R/Rfree	0.253/0.296
Mean B-Factor (Å)	100.1
r.m.s.d bond lengths (Å)	0.0064
r.m.s.d bond angles (°)	1.346
Ramachandran plot statistics (%)	
Preferred regions	88.73
Outliers	2.45
PDB ID	-

*Dataset processing through multixtal DIALS merging of two datasets. Statistics have been produced by ISPyB.

5.6 Structural solution for loop deletion DR variant

Diffraction conducted on I24 showed the DR variant to diffract to a high resolution <2 Å. Determination of the Matthews coefficient from unit cell parameters suggested 3 molecules were present in the asymmetric unit with a solvent content of 61.1%. Initial phasing

attempts with PHASER and MOLREP failed to identify a suitable solution due to a high degree of non-crystallographic symmetry. Using MrBUMP, implementing the ENSEMBL function, a suitable solution was identified with 4 molecules in the asymmetric unit and a lower solvent content of 48.1%. Further model building, including alteration of the modified loop 140-146 was performed using Buccaneer. Iterative refinement with COOT and REFMAC gave a final R/R_{free} of 0.23/0.27. The elevated R_{free} is attributed to the NCS but resultant electron density maps were of excellent quality (Figure 5.20b). An image of the *in situ* crystal after diffraction and table of crystallographic data and refinement statistics can be found in Figure 5.20a and Table 5.7 respectively.

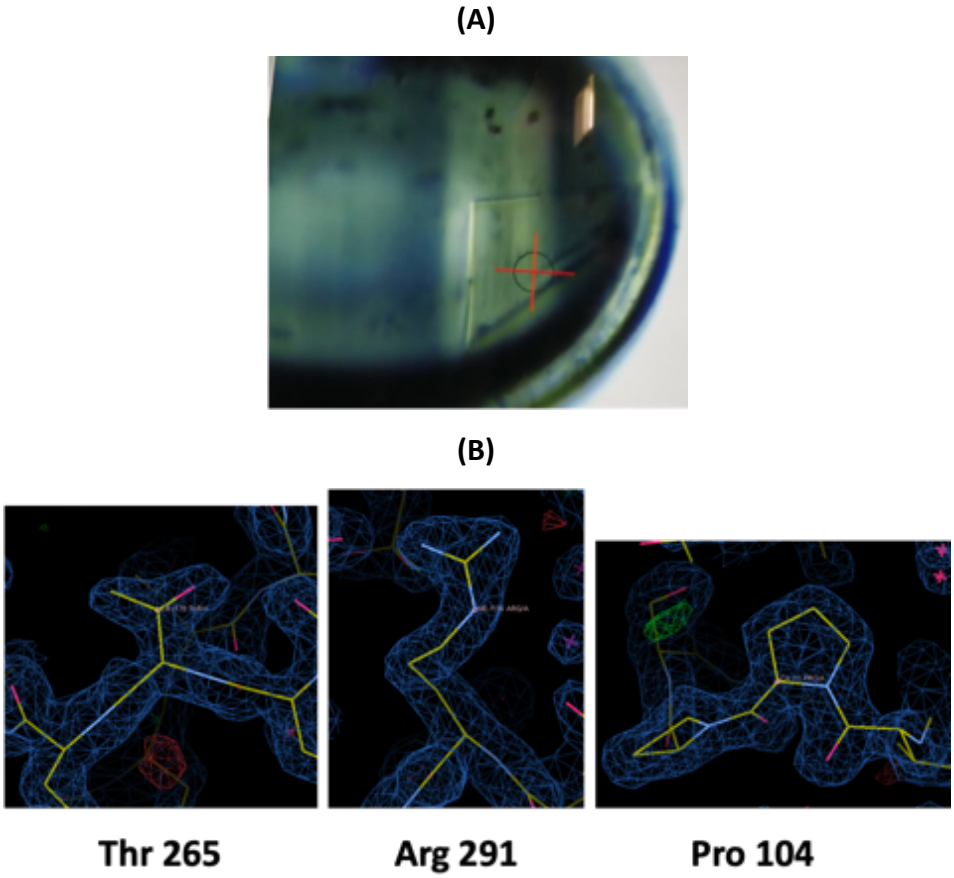

Figure 5.20. ^{94}PqsR^{309} DR crystal habit and sample electron density map (A) ^{94}PqsR^{309} DR crystal, grown from glycerol ethoxylate, within a CrystalCap™ SPINE. Image taken on DLS beamline i24. **(B)** Representative electron density map ($2F_o$-F_c) of residues in chain A of ^{94}PqsR^{309} DR variant model. Images taken from COOT model building software. Map is contoured 1 σ with a carve of 1.6 Å.

Table 5.7: Data collection and refinement statistics for ^{94}PqsR^{309} DR:

Data collection	Loop mutant (DR)*
Beamline	i24
Wavelength (Å)	0.9999Å
Space group	P 1 2_1 1
a ,b, c (Å)	72.6, 64.5, 79.95
α, β, γ (°)	90, 93.11, 90
Resolution	79.84 – 1.77
No. of unique reflections	70254 (2919)
R_{meas} (%)	0.16 (1.27)
Mean I/Sig(I)	5.6 (0.5)
Completeness (%)	97.5 (81.5)
Redundancy	3.2 (2.5)
CC½	1 (0.3)
Refinement	
Resolution range (Å)	79.83 - 1.77
R/Rfree	0.23/0.27
Mean B-Factor (Å)	A: 22.9
	B: 25.2
	C: 26.2
	D: 27.1
	Avg. (protein) 25.54
r.m.s.d bond lengths (Å)	0.0070
r.m.s.d bond angles (°)	1.511
Ramachandran plot statistics (%)	
Preferred regions	95.70
Outliers	0.95
PDB ID	-

*processed by DIALS

5.6.1 New assembly is characteristic of canonical LTTR dimer

Examination of the new dimer packing showed a significant change compared to the wildtype arrangement. The new arrangement has the binding pocket exposed to solvent whereas the binding pocket in the wildtype arrangement is buried in the dimer interface. An increase in binding site accessibility would suggest the new arrangement was 'poised' to receive ligand. Consequently, the hinge region, constructed from two β-strands between the RDI and RDII subdomains, is now located on the protein's periphery (Figure 5.21). Additionally, the offset angle between the dimer was increased from 17.6° to 97.3° and as such adopted a crossed topology (perpendicular interface).

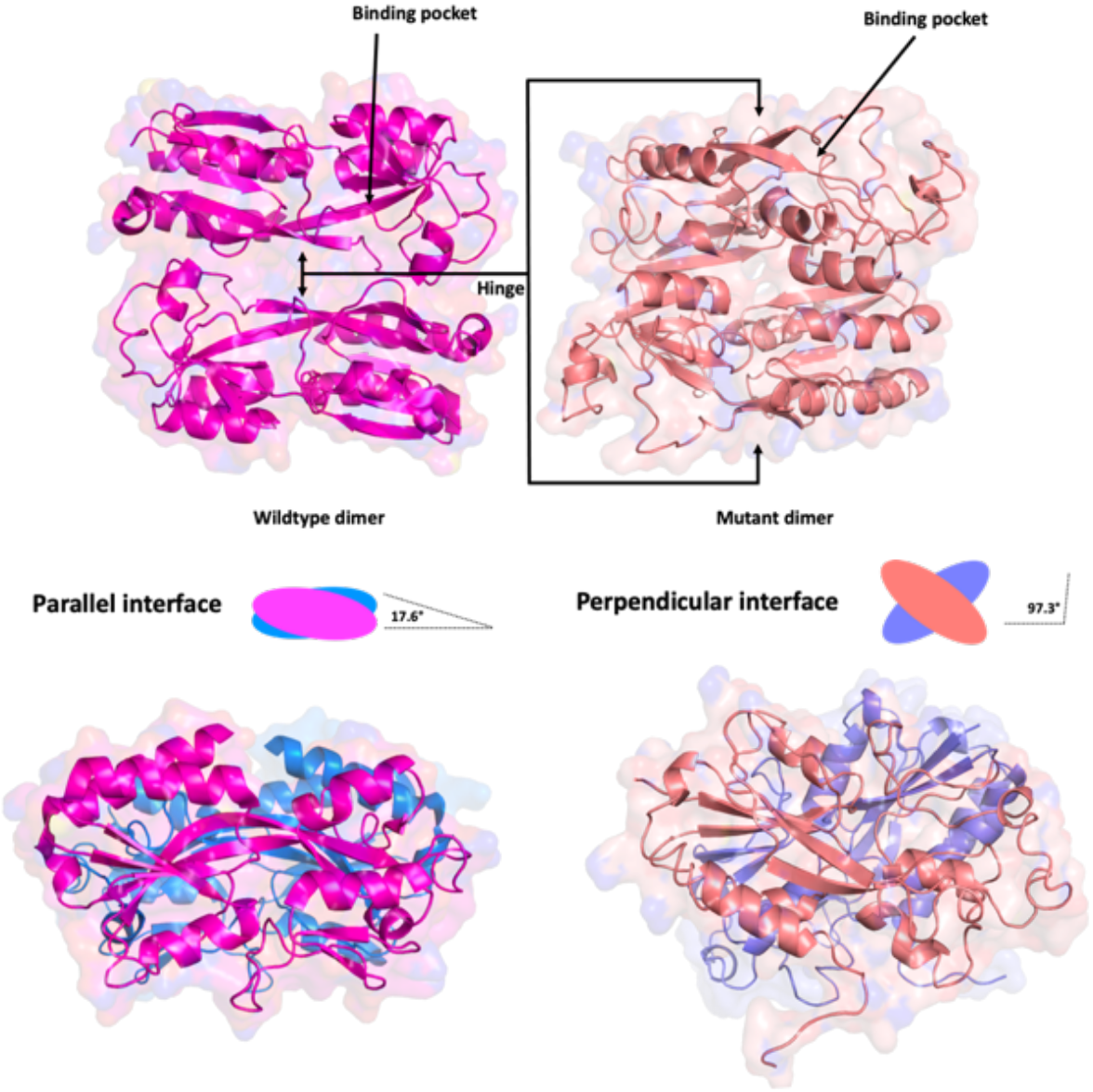

Figure 5.21. Cartoon diagram of ^{94}PqsR^{309} DR mutant dimer arrangement. Comparison of dimer interface between WT and DR variant dimer. Dihedral angle calculated in Chimera between monomers by creating a plane between residues 94 and 235. Wildtype and mutant coloured in hot pink and salmon respectively.

Comparing the new arrangement to a wide range of LTTRs shows that it is adopts a similar configuration. This arrangement is observed in crystallised full-length receptors and superposition with a protein-DNA complex – CbnR – reveals good agreement suggesting that the full length protein would be in an conformation capable of DNA binding (Figure 5.22).

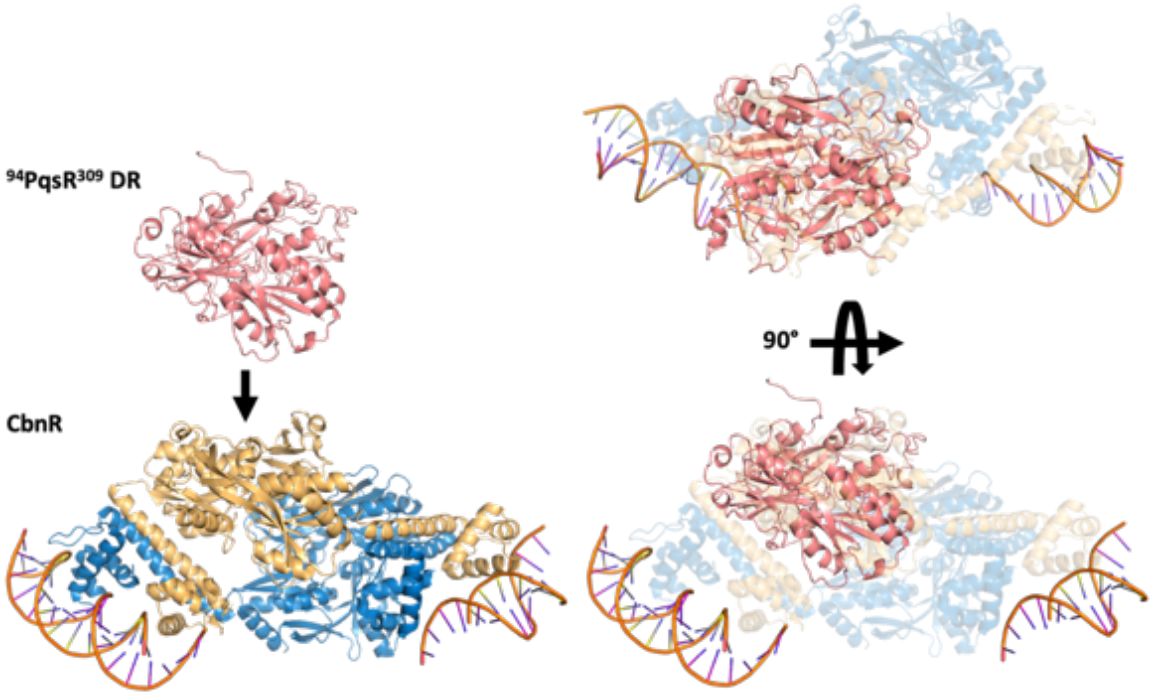

Figure 5.22. Superposition of new dimer arrangement and CbnR (PDB 7D98). RMSD determined as 4.4 Å using PYMOL. Proteins represented as cartoons with the new dimer structure coloured red. The CbnR dimer pairs are coloured yellow and blue respectively. Superposition shows the dimer structure aligned to yellow CbnR dimer. DNA shown as cartoon coloured in orange.

5.6.2 Binding site rearrangement

Examination of the binding pocket gave good agreement with the wildtype conformation with a single exception. Tyr 258, often targeted for π-π stacking in antagonist discovery efforts, was flipped outside of the pocket. As shown in Figure 5.23 the Tyr centroid has been shifted by 6.6 Å and rotated out the pocket by 106.9°. The wildtype conformation partially appears to have been stabilised by a hydrogen bond to Gln 160 on the opposing monomer therefore a change in interface has lessened the restraints on the tyrosine. This appears to have also enabled Ile 186 to adopt a new rotamer pointing away from the pocket. We surmise this was universally weaken ligand binding to the receptor due diminished

interactions with the tyrosyl group that includes both hydrophobic interactions and hydrogen bonding.

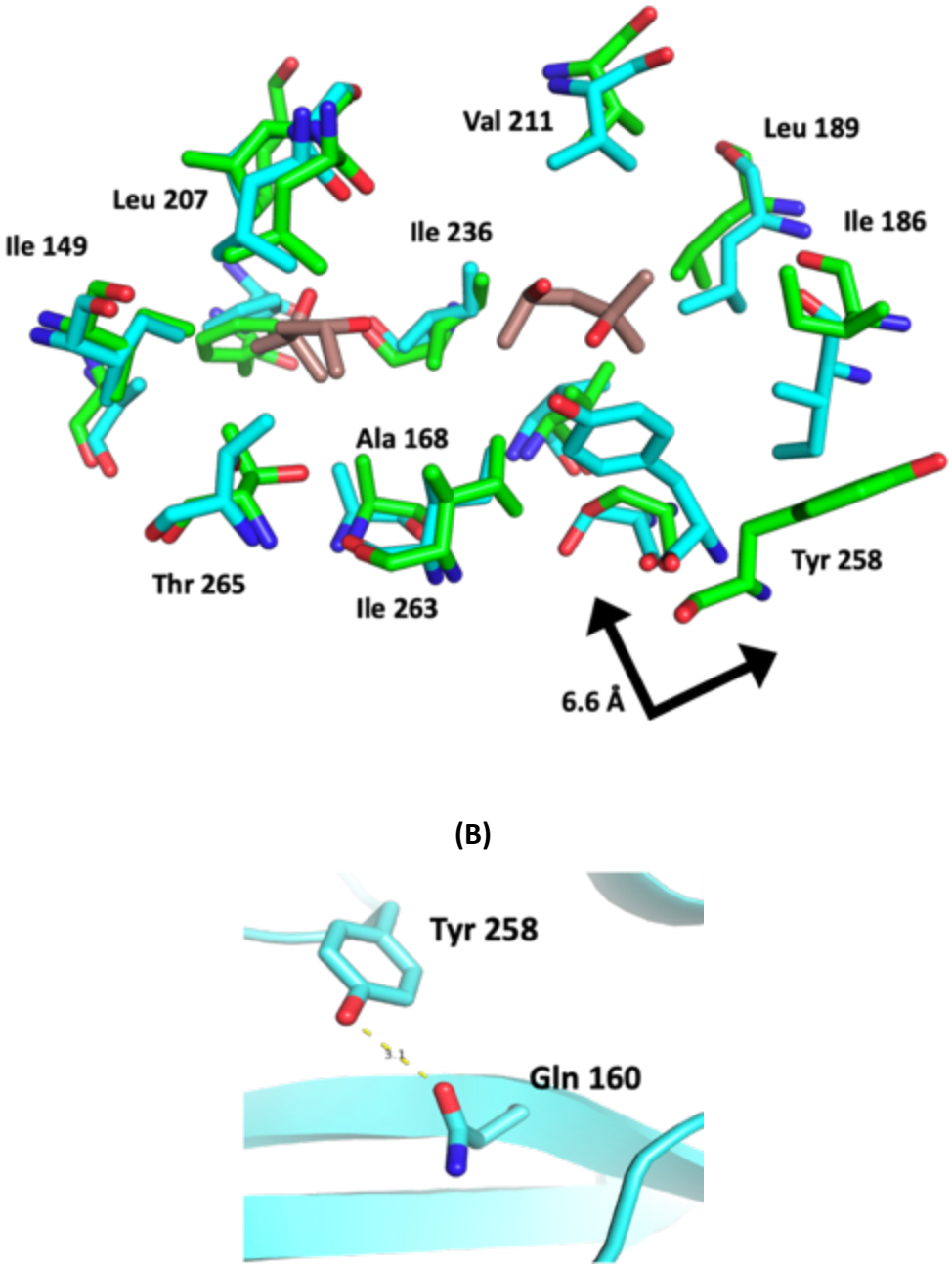

Figure 5.23. Superposition of ligand binding pockets from ^{94}PqsR^{309} DR and WT ^{94}PqsR^{309}. Colouring in blue and green respectively. Pseudo-ligand MPD shown as sticks in brown. **(B)** Stabilising hydrogen bond between Tyr 258 and Gln 160 with a bond distance of 3.1 Å.

5.6.3 In solution analysis of ^{94}PqsR^{309} DR mutant topology

To determine if the protein adopts the same interface in solution SAXS was performed on the DR variant. Sample aggregation was noted at low q values (characterised by a steep rise) – Figure 5.24a – and was excluded from further analysis. The Rg was calculated at 26.43 Å and molecular weight determined as 50.9 kDa which was in good agreement with the theoretical 49.3 kDa for a dimeric species. Theoretical Rg's calculated in CRYSOL for both crystallographic models suggested they were both more compact compared to the in-solution state. Fitting showed that the wildtype model gave better agreement with the experimental data than variant dimer with greater discontinuity observed at high q. This disagreement may be due to the structure occupying a 'hybrid' state between the two models but weighted more strongly towards the wildtype arrangement.

(A) **(B)**

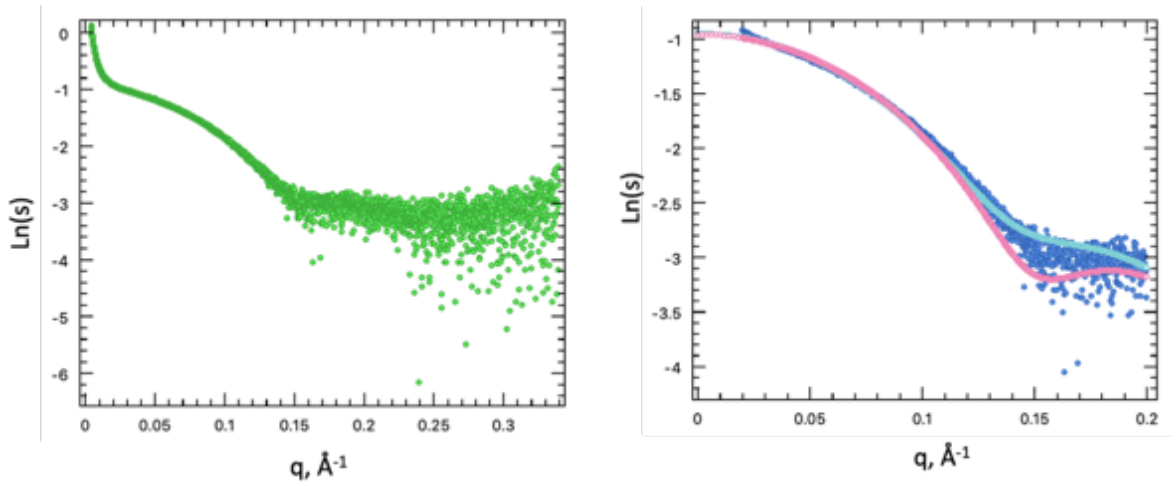

(C)

	WT	DR mutant
X^2	1.495	2.062
Rg*	23.91	23.33

Figure 5.24. SAXS analysis of ^{94}PqsR^{309} DR mutant. (A) Logarithmic plot of the scattering intensity I(s) vs angle (in Å^{-1}). Error bars have been removed for simplicity. **(B)** The same plot with low q data truncated to 0.02 to and high q to 0.2. Plots from wildtype dimer (4JVC) and new interface shown in light blue and pink respectively. **(C)** Fitting statistics against the SAXS profile. Data processing (determination of high and low q) and fitting with CRYSOL[334] performed by Dr James Doutch (Diamond Light source). Data acquisition performed on beamtime B21 with a 3.1 mg/mL sample in 20 mM Tris-HCl, 150 mM NaCl and 1 mM TCEP. *Theoretical Rg calculated from atomic model with CRYSOL and given in Å.

5.7 Exploring structure-function relationships by *in vivo* complementation with *pqsA* bioreporter

To further validate the new models a series of complementation experiments were performed, similar to those used to probe binding pocket residues in *Ilangovan et al,.* (2013)[155]. For comparison with this study, we generated a dose-response analysis to determine suitable inducer concentrations to permit P*tac* promoter activation. To replicate the results of this study, which showed residual activity in the absence of co-inducer to be ~30%, we found that 50 µM IPTG was sufficient (Figure 5.25).

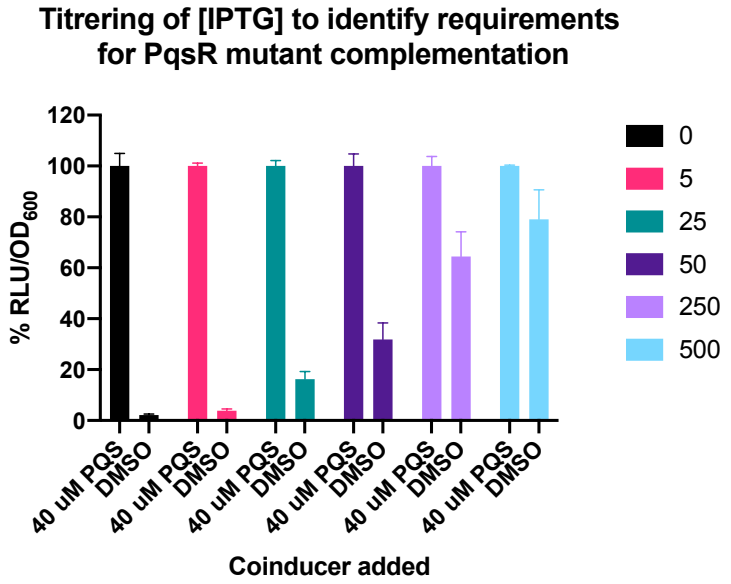

Figure 5.25. Optimisation of IPTG induction conditions for complementation construct pME6032::*pqsR*-His. Plasmid transformed into PAO1 – N CTX::P_{pqsA}-*lux*. Data is normalised to the peak attained at 7 hours when co-inducer PQS is present in the culture. Key showing concentration, in µM, of IPTG differentiated by colour.

5.7.1 PqsR mutants' response to different AQ signals

Given the observation in chapter 4 that a methylated HHQ ligand (bioisostere of the 3-hydroxy with 3-methyl) can act as an activator it was included alongside the *P. aeruginosa* PQS and HHQ AQs. As expected PQS gave the highest activation of the P*pqsA* promoter followed by HHQ (~75%) and Me-HHQ (~56%). A lack of AQ supplement gave a weaker residual response of 27% consistent with the previous study[155].

Examination Tyr 258 mutants highlighted that aromaticity and polarity were required for promoter engagement. Removal of the hydroxyl group (Y258F) showed weaker activity (~80%) in the presence of PQS and severely compromised activity with respect to HHQ and HHQ-CH_3. Residual activity without co-inducer was almost entirely absence. Complete loss of aromaticity with glutamine or alanine showed a significant loss in promoter activation but still responded more strongly to PQS compared to other AQs. However, it should be noted that preservation of polarity with Y258Q retained higher activity than Y258A. Both were unable to effectively discriminate between weaker activating ligands HHQ and HHQ-CH_3 (Figure 5.26).

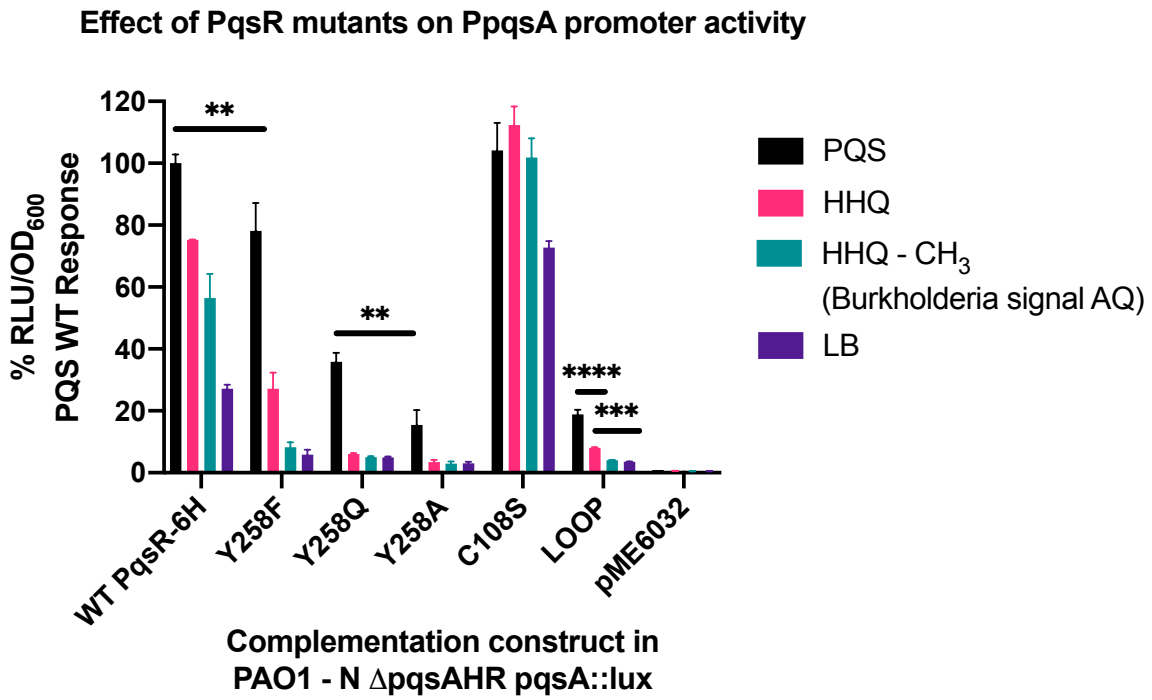

Figure 5.26. Activity of PqsR mutants to an excess of co-inducer molecules (40 µM) in PAO1 – N *ΔpqsAHR* CTX::P_{pqsA}-*lux*. Peak taken at maxima (9 hours) of WT PqsR response to PQS. Statistical testing performed using Prism One-way Anova with significance displayed as follows **, P ≤ 0.01; ***, P ≤0.001, ****, P≤0.0001.

As shown above the loop mutant DR could be activated by PQS and HHQ albeit weakly with the mutant capable of discriminating between both AQs. Mutation of Cys 108, shown to form an interchain disulphide, displayed increased activity compared to the wildtype with a much higher residual activity in the absence of co-inducer suggesting that the protein was operating in a more ligand-independent fashion. Given the reducing environment of

Cytoplasm it is unlikely that the cysteine promotes aggregation, especially as the wildtype 4JVC structural data showed it to be buried.

5.7.2 Complementation under overexpression conditions

Complementation experiments in the absence of AQ supplementation was examined using a Δ*pqsR* mutant. In agreement with the previous experiment the C108S mutant shows stronger activity compared to the wildtype. At residue 258, only a Y258F mutant can restore function when overexpressed whereas the Y258A and T258Q mutants remain functionally impaired. This reinforces the observations made in the triple mutant but highlights that excess ligand can act to restore function. The loop mutant is similarly weakly active but overexpression appears to restore some functionality. (Figure 5.27).

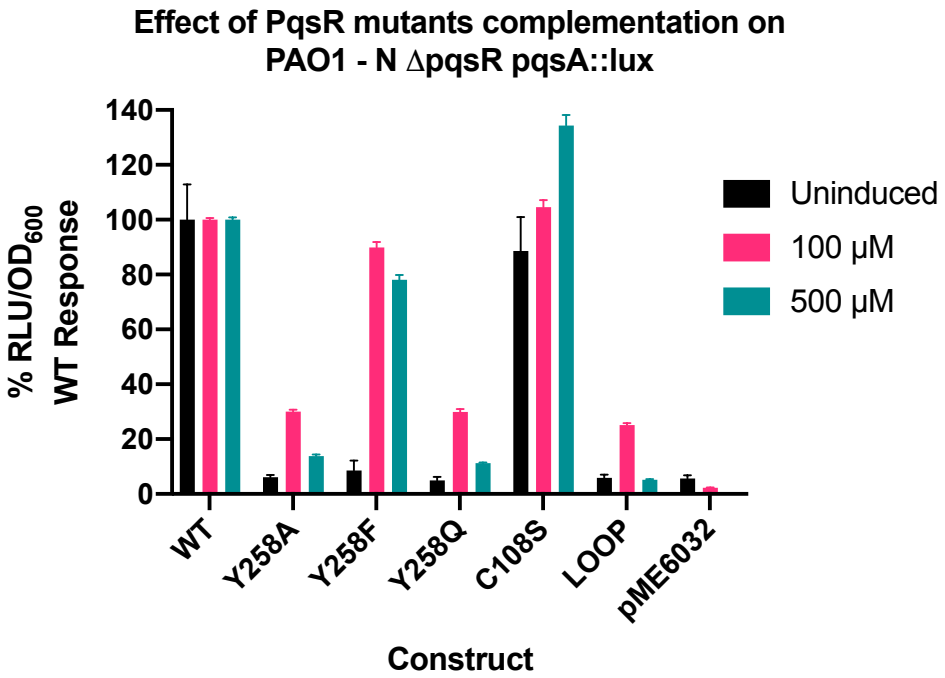

Figure 5.27. Complementation of PAO1 – N *ΔpqsR* CTX::P_{pqsA}-*lux* with mutant *pqsR* under three expression conditions. Experiments performed in LB without additional AQ supplementation. Figure key showing concentration of IPTG differentially coloured. Maximum RLU/OD_{600} taken and normalised to WT *pqsR* construct. The wildtype sequence in pME6032::*pqsR*-His and pME6032 empty vector are used as a positive and negative controls.

5.8 Discussion

Overall, 3 of 7 crystal variants successfully produced diffracting crystals with only a single variant giving a substantial improvement in terms of resolution. However, additional

optimisation can be implemented to improve diffraction properties further. A campaign to improve HIV reverse transcriptase used an iterative process combining successful mutants together to identify crystal forms that were both resistant to solvent and highly ordered[319]. Combining the engineered disulphide mutant S123C, that gave robust crystallisation, with a series of SER mutants may prove equally effective. The DR mutant, although giving high resolution diffraction, has not been tested for solvent resistance. Further experiments to test the feasibility of co-crystals and soaking should be performed to determine the utility of this mutant in antagonist/fragment binding. The only crystal form to not yield good quality diffraction, K154A E278A, should reproduced and cryoprotection optimised. Initial diffraction analysis suggested the protein crystallised into a new orthorhombic form that may provide further information on changes in dimer arrangement and mechanism.

Analysing the DR variant structure showed a unique packing arrangement for PqsR that is adopted by most LTTRs. The mechanism behind LTTR function has been hypothesised as the 'sliding dimer' permitting subtle contractions and expansions that influence DNA binding. The new structure may suggest that, for PqsR, this mechanism is facilitated by dimer rotation. However, subsequent SAXS analysis showed this to not be the predominant form in solution, yet complementation experimentation showed this mutant to only possess weak activity and attempts to introduce the mutant into the full-length receptor produced insoluble protein (chapter 4). As it stands, these observations are difficult to reconcile into an activation model. Additional SAXS experiments with both the wildtype and DR variant would prove fruitful to compare protein topologies. Our observations in chapter 5 also suggest that small fragment-like ligands can be introduced without inducing severe aggregation, to determine if the protein undergoes a structural shift upon binding. In our SAXS experiment discrepancy at high q between experimental and modelled dimers suggest that in solution an intermediate state is predominant. This state/s could be elucidated through Molecular dynamic simulations to reveal the physiological apo dimer[335]. Additionally, as the loop mutant gave relatively weak activity compared to the wildtype further experiments to understand the loop length and compositional penalties should be carried out. Given that a single residue deletion led to unstable protein in ^{94}PqsR^{309} and a double deletion had a similar effect in the fusion construct it is likely that the area plays a key role in multimerization.

The DR crystal form also showed positional changes of Tyr 258 with complementation data revealing that both aromaticity and polarity are important to activity. Disruption of hydrogen bonding by removing the hydroxyl showed a reduction in activity and preservation of polarity with a glutamine mutant responded to co-inducer more effectively than alanine. These observations suggest that Tyr258 has functional duality. The tyrosine may function to not only maintain dimer stability but without restraint adopts a less productive position which is deleterious to co-inducer binding through changes in pocket topography. This should have some bearing on future SAR campaigns to exploit both positions and may already explain why some antagonists, expected to form strong π-π interactions, fail to show potency[201].

In the K154A K214Y variant a rotation in helix 1 was observed, seemingly mediated by an interchain disulphide. A similar rotation was observed in MetR, a regulator from *Neisseria meningitidis*, aided by an intrachain disulphide between Cys 103 and 106[336]. This was speculated to act as a redox sensor and through the movement of Glu 102 could alter the shape of the binding pocket. Furthermore, oxidative stress has been shown to directly influence the activity of other LTTRs, including OxyR, OxyS and HypT[337 338 339]. In the case of OxyR and HypT examination of the same helix does not reveal substantial changes suggesting that the mechanism for redox sensing is varied within the family. In the case of OxyR the mechanism for redox activation is still debated with *in vitro* and *in vivo* data supporting a consensus that multiple activation mechanisms are possible[340]. Based on our data we propose that the interchain disulphide formed through Cys 108 plays a role in stabilising a tetrameric complex.

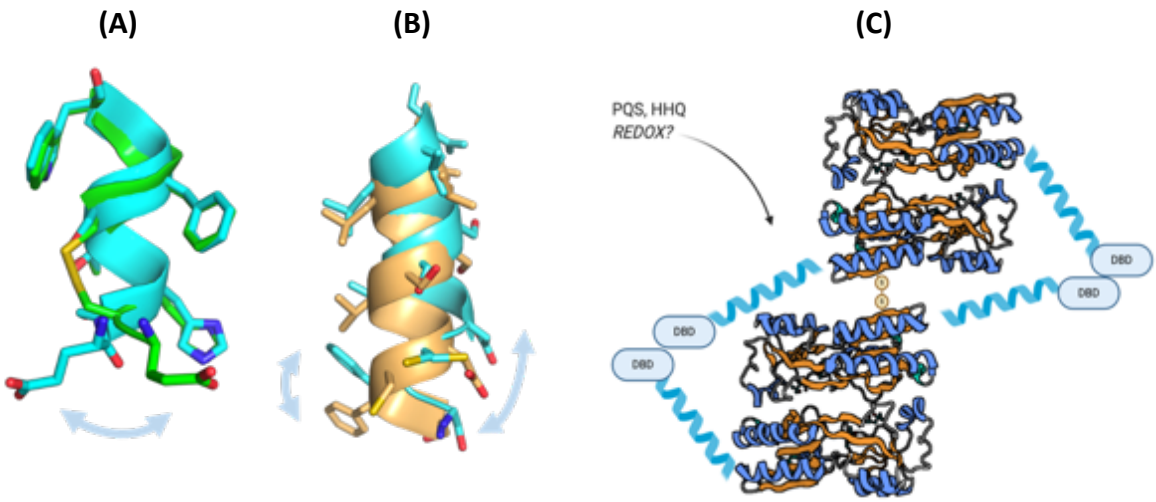

Figure 5.28. Redox state as an activation input. (A) MetR helix 1 in a reduced and oxidised state coloured blue and green respectively. Intrachain disulphide formed by Cys 103 and 106 affecting a rotation to Glu 102. **(B)** A similar rotation observed from the P 4_3 22 crystal form. **(C)** Proposed model for PqsR activation in which an interchain disulphide can aid in tetramer stabilisation.

Interestingly, a microarray dataset examining pyocyanin genes in response to oxidative stress showed that both *pqsA* and *pqsR* expression is reduced under oxidative conditions supporting the hypothesis that redox influences PqsR activation (Figure 5.29)[341]. Additionally, PQS, the system's cognate ligand, plays a role in oxidative stress so a link to PQS regulation would serve as feedback. Under oxidative conditions any interchain disulphide would be stabilised which would be consistent with our observations that a C108S mutant retains higher activity. However, it should also be noted that oxidative pressure will undoubtedly affect additional components, such as the PQS biosynthetic enzymes, so conclusions cannot easily be drawn. Further experiments on the effect of redox conditions, with AQ supplementation, should be conducted to evaluate the contributing factors.

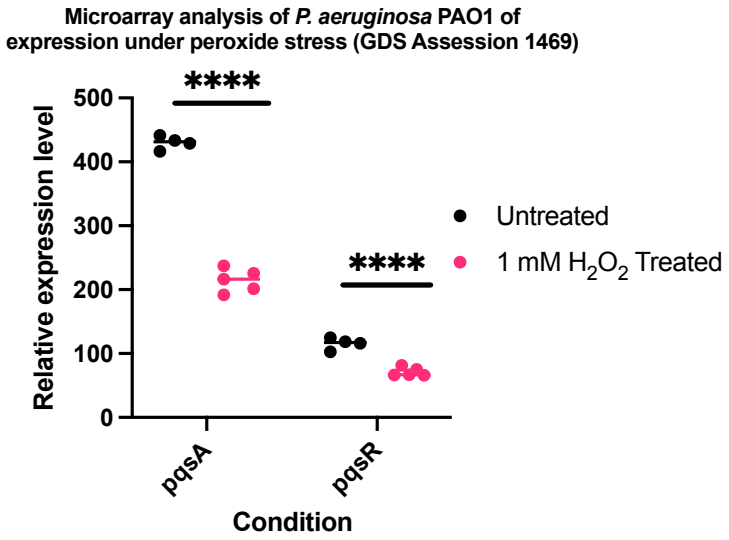

Figure 5.29. Microarray analysis on *pqsA* and *pqsR* expression performed under oxidative conditions (1 mM H_2O_2). Expression of *pqsA* and *pqsR* is reduced under oxidative conditions highlighting that redox plays a role in control of the PQS system. Microarray data listed publicly under GDS 1469 originating from Chang et al,. (2005)[341]. Statistical analysis conducted with an unpaired t-test in PRISM. ****, P≤0.0001.

5.9 Conclusions

- 7 mutants were designed based upon varied rationales including high entropy residue mutation, loop optimisation, construct boundary change and fusion to crystallisation chaperone. 6 were successfully purified but only 4 formed crystals readily.
- 3 crystal variants diffracted sufficiently for structural determination with a single variant diffracting better than 2 Å.
- An engineered disulphide robustly formed crystals in a wide range of conditions that did not require MPD as the primary precipitant. However, they did not exhibit markedly better diffraction.
- The SER K154A K214Y combination revealed unique crystal packing that indicated that an interchain disulphide could form via Cys 108. Complementation experiments showed this residue was important for activity.
- The DR mutant produced a dimer interface reminiscent of other LTTRs structures, but the form was not predominant in solution. Complementation with the mutant gave only weakly active protein.

Summary of SER constructs can be found in Table 5.8:

Construct	Rationale	Purification	Crystals	Diffraction
^{94}PqsR^{309} K154A K214Y	Eliminate high entropy surface residues	Monodispersed and good yield	Yes	2.7 Å
^{94}PqsR^{309} K154A E278A	‘’	‘’	Yes	Poorer than 5 Å
^{94}PqsR^{309} SR	Re-engineering partially flexible surface loops	Good enrichment by Ni-NTA but prone to aggregation	NA	NA
^{94}PqsR^{309} DR	‘’	Monodispersed and good yield	Yes	1.77 Å
^{94}PqsR^{309} S123C	Introduce disulphide to interlock monomers	Monodispersed protein but lower yield than the SER mutants and wildtype construct	Yes	2.54 Å
MBP-^{94}PqsR^{309}	Crystallisation carrier to alter crystallisation contacts	Successful purification but a portion of the material was aggregated and eluted within the void. Breakdown MBP and ^{94}PqsR^{309} observed	No	NA
^{60}PqsR^{309}	Extending the construct boundary to include the linker region	Extremely poor yield with a low amount of soluble material and subsequent weak enrichment.	NA	NA

Table 5.8 Summary of new crystallisation constructs.

6 Expression, purification, and crystallisation of full length PqsR

6.1 Introduction

All LysR-type proteins consist of two domains including a N-terminal DNA binding domain containing a helix-turn-helix motif coupled to a long alpha helix linker. The C-terminal domain, responsible for co-effector binding, is larger and is composed of two subdomains linked by a long beta sheet. As shown in Figure 6.1 PqsR has been predicted to follow this canonical structure. Purification of full length receptor has been attempted by several groups previously[157 229]. In all instances insoluble product was reported but no rescue strategies were employed. LysR-type proteins are notorious for solubility issues[257], which through crystallographic analysis of dimeric and tetrameric arrangements, that are currently thought to be due to unsatisfied but weaker interaction interfaces. At low concentrations, such as in a cellular environment, aberrant interaction is not favoured but upon high protein concentration (typically reached during overexpression) these interfaces are adopted prompting higher level oligomerisation and aggregation[258]. These effects have made full length LTTRs recalcitrant to crystallisation which explains the relatively few reported in the literature compared to studies of their respective ligand binding domains. In some cases, LTTR protein production has been improved by lowering expression temperature in conjunction with supplying the endogenous ligand such as with HsdR[136]. In some cases, LTTRs have proven so unstable that a large carrier protein has been required for soluble expression. This strategy proved successful for LcrX, a LTTR from *Xanthomonas axonopodis*, that solubly expressed in the presence of MBP and retained DNA binding affinity for its promoter[259]. Other LysR regulators, like CatM displayed improved solubility with increasing the salt concentration and supplementation with high concentrations of osmolytic agents[260]. Alternative strategies used with other DNA binders has been to increase the osmolarity of the expression media using sugars or amino acids. This approach has been used successfully in the author's lab for the solubilisation of AgrA, a quorum sensing regulator, from *S. aureus*[261].

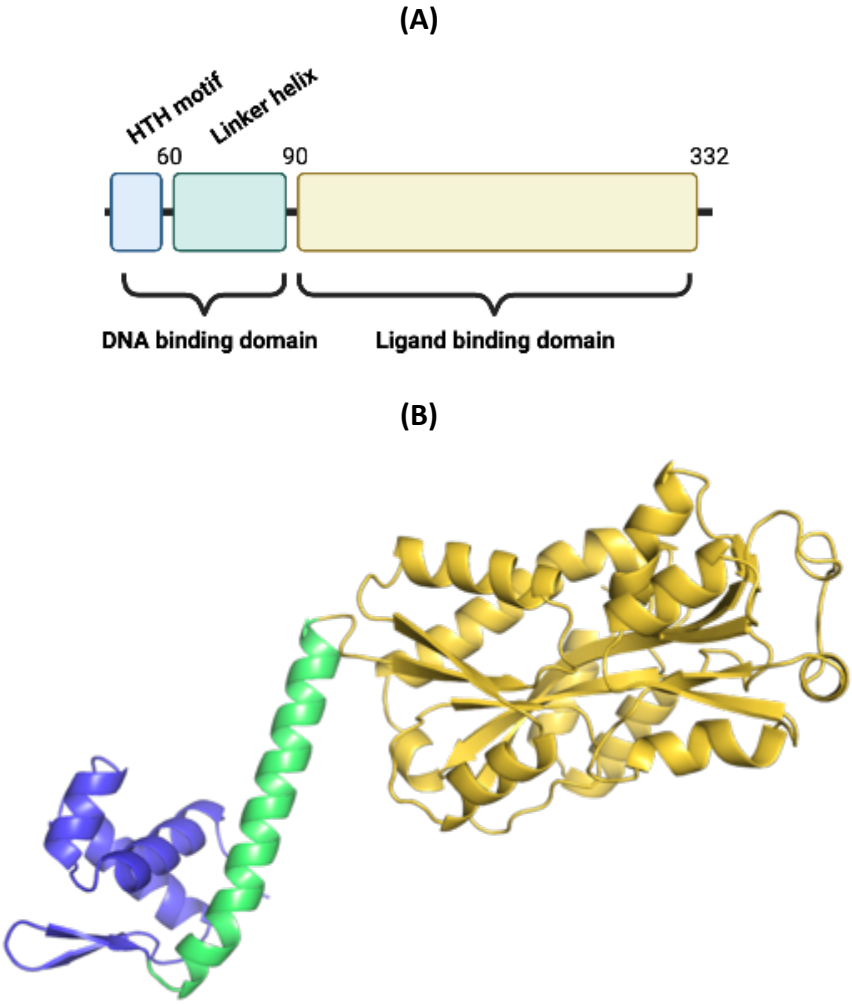

Figure 6.1 PqsR schematic and predicted structure. (A) PqsR schematic showing the full length receptor with domain boundaries assigned in previous investigations[153]. Protein encoded by gene locus PA1003 in PAO1 reference strain. **(B)** trRosetta predicted model of PqsR generated using the Yang-lab server[262]. Domains are coloured blue/green and yellow to distinguish the DNA binding domain and ligand binding domain respectively.

6.2 Disorder and hydrophobicity analysis

Protein disorder is usually unfavourable for crystallisation as disordered loops and residues will not readily pack into a crystal. Analysis of disorder can also suggest regions involved in protein-protein interactions or require stabilisation by a ligand. As shown in Figure 6.2 disorder prediction for PqsR shows only substantial disorder towards the end of the C-terminal. This is in agreement with previous observations in the truncated LBD construct where residues beyond 296 are unobservable in the electron density[155]. A small degree of disorder was also detected at the N-terminal but spans a much smaller region of ~10 residues with a lower probability score 0.6-0.8 compared to >0.85 for the C-terminal.

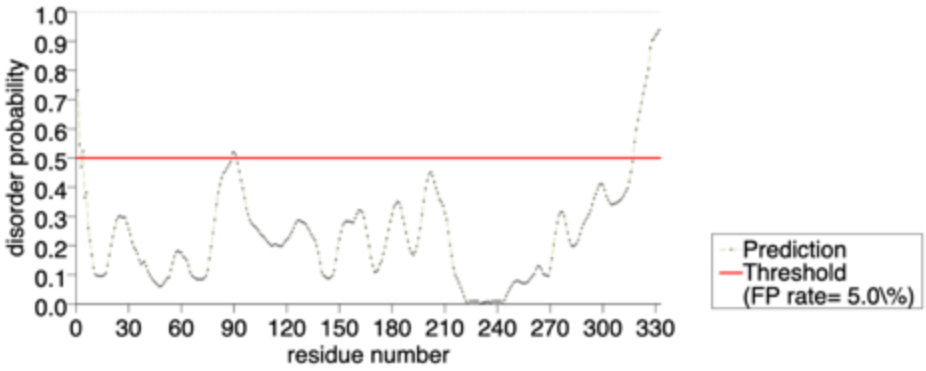

Figure 6.2. Disorder prediction of PqsR using primary sequence. Significant disorder, above the calculated threshold of 0.5 is located at the C – terminal. Analysis performed using the PrDOS server[263].

Secondary structure prediction from the primary sequence using PsiPRED[264] shows the expected LTTR characteristics with a series of three helices constituting the Helix-turn-helix domain of a typical LysR (Figure 6.3). A large linker helix was detected from residue 62 to 87 (26 residues in length) which is capped at the N-terminal by a proline. Boundary prediction suggests that residue 60 marks the end of the HTH motif. In agreement with the disorder prediction the C-terminal 300-332 region has limited secondary structure elements. Composition analysis also suggests that the C-terminal has membrane binding properties despite most residues being small aliphatic residues or polar. Despite a positive value on the Kyte and Doolittle scale the N-terminal DNA binding domain is not significantly more hydrophobic compared to other DNA binding proteins. For example, the Lac repressor DNA binding domain (UniProt B8LFD5_ECOLI) has a greater hydrophobic content of 49% compared to that of PqsR with 45%.

(A)

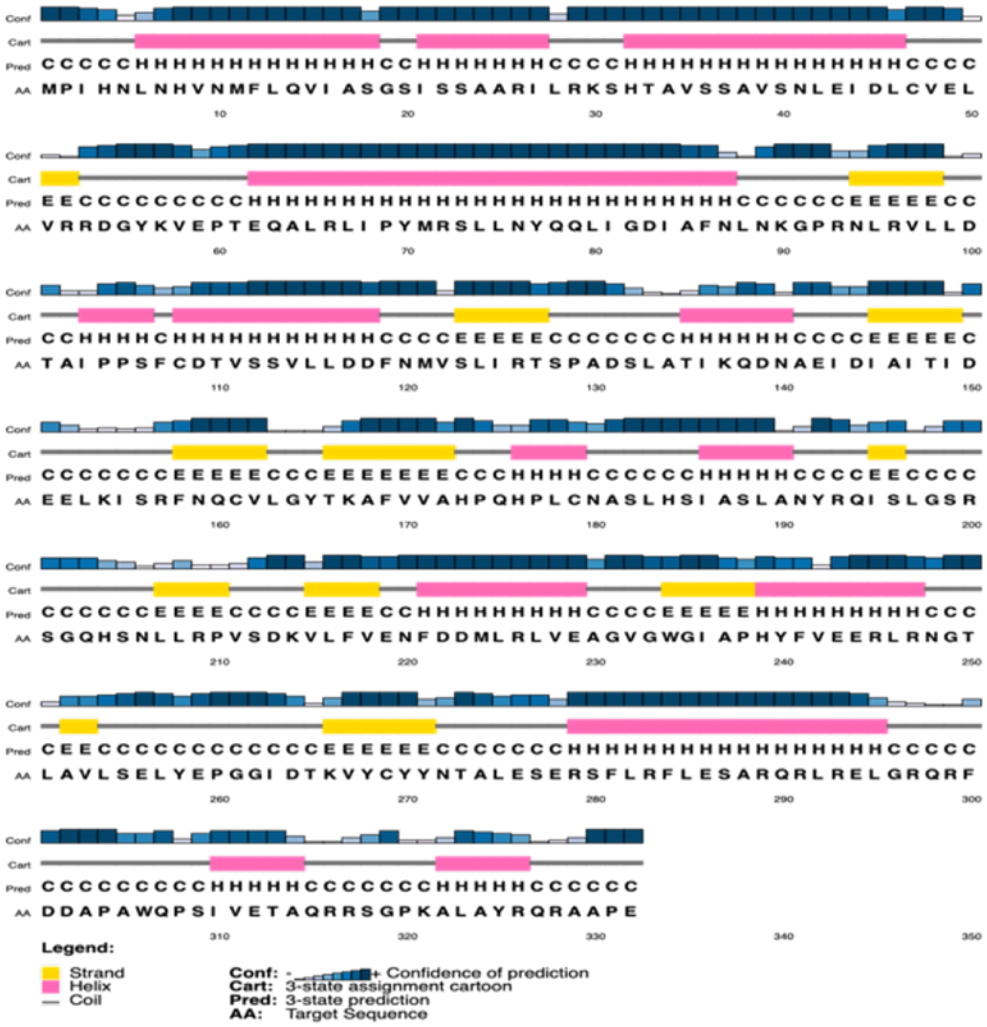
Conf
Cart
Pred
AA
Legend:
Strand
Helix
Coil
Conf: - + Confidence of prediction
Cart: 3-state assignment cartoon
Pred: 3-state prediction
AA: Target Sequence

(B)

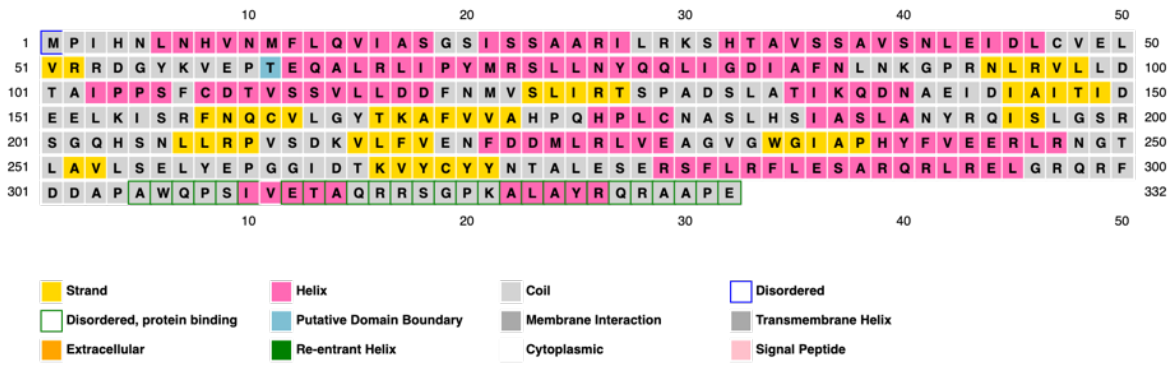
Strand
Helix
Coil
Disordered
Disordered, protein binding
Putative Domain Boundary
Membrane Interaction
Transmembrane Helix
Extracellular
Re-entrant Helix
Cytoplasmic
Signal Peptide

(C)

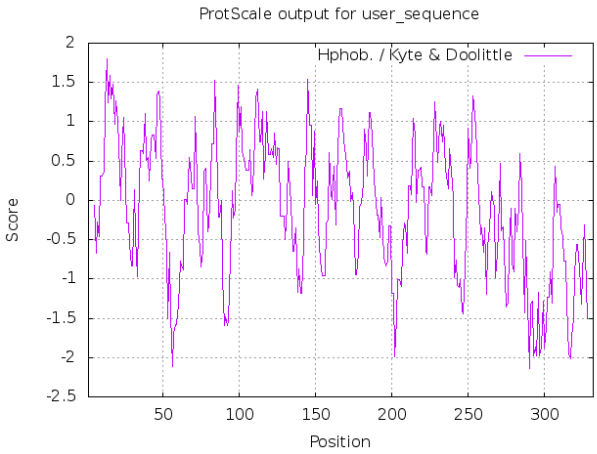

Figure 6.3. Secondary structure prediction based on primary sequence. (A) Secondary structure prediction and respective confidence scores. **(B)** Secondary structure prediction with additional annotations showing predicted disorder and membrane binding **(C)** Hydrophobicity analysis using Expasy following the Kyte & Doolittle scale showing most of the protein to be polar with negative scores across the C-terminal domain. A slightly higher degree of hydrophobicity is observed towards the N-terminal.

6.3 Construction and purification of His-tagged *E. coli* constructs

6.3.1 pET28a and pCOLD expression

To confirm previous observations that the protein, expressed alone, is insoluble the full length *pqsR* gene was cloned into pET28a vector and pCOLD-I both encoding N-terminal His tags[265]. pCOLD is optimised for low temperature expression due to the presence of the *cspA* promoter which only stabilises at temperatures below 15°C[266 267]. Given that low temperatures have successfully solubilised other LysR proteins it was reasonable it may be appropriate for PqsR. Cultures containing either a pCOLD or pET28a *pqsR* construct were induced under a low (16°C) or very low (12°C) temperature. Lysing the cultures by micro-sonication showed that only insoluble material was produced using pET28a and no material was made when expressed at 12°C suggesting expression was compromised (Figure 6.4a). This is consistent with observations made in other studies attempting to produce the full length protein. pCOLD failed to produce any material even when expressed at lower temperature. To further investigate if expression failure in pCOLD was due to a lack of induction a small concentration series of 0.1 mM, 0.5 mM, and 1 mM IPTG was used to induce cultures for 24 hours. However, no band with the expected size ~37.5 kDa was observed in either the induced or soluble lanes on SDS PAGE (Figure 6.4b).

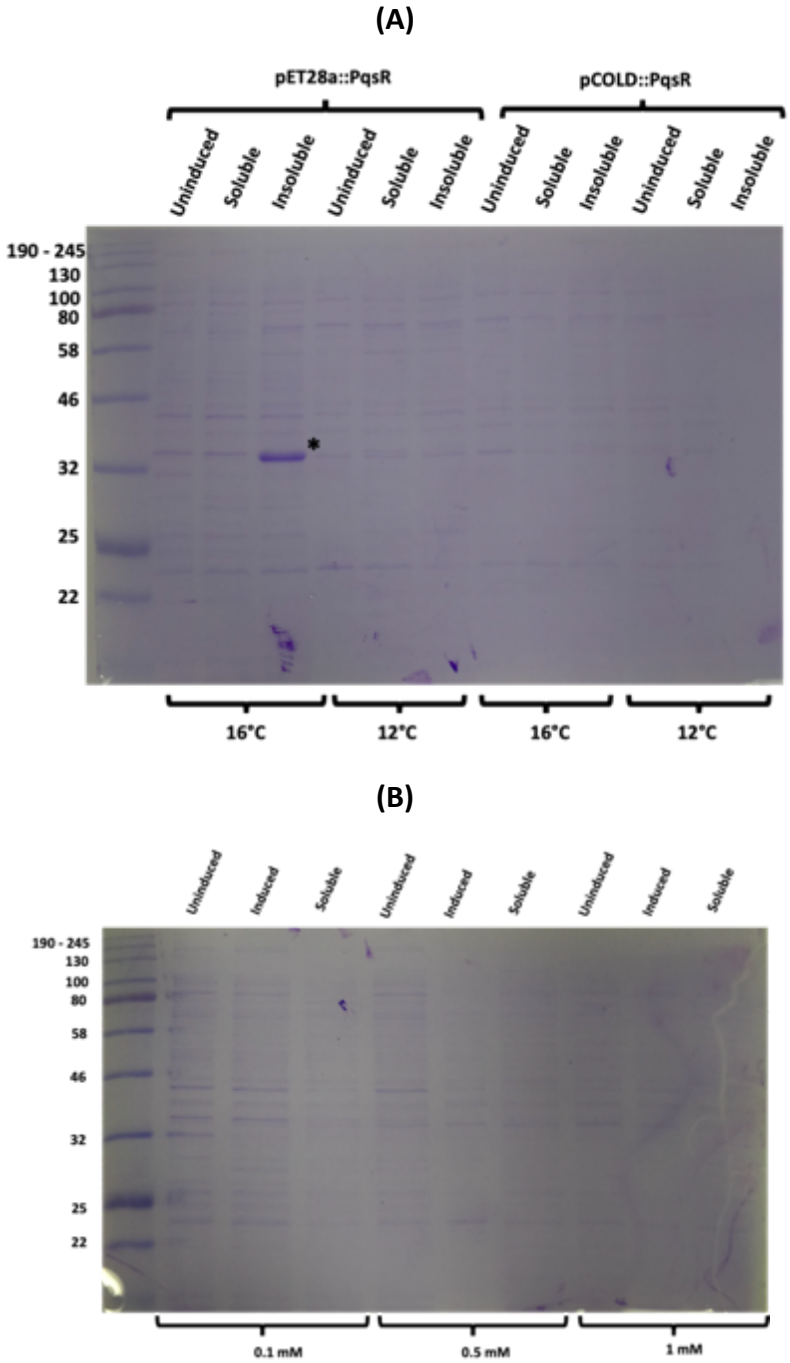

Figure 6.4. PqsR solubility expressed with pET28a and pCOLD (A) SDS-PAGE analysis of PqsR solubility upon induction of BL21(DE3) CP transformed with pET28a::*pqsR* and pCOLD::*pqsR* and incubated at 16 and 12°C. Protein induced using 0.1 mM IPTG overnight (>16 hours) lysed using micro-sonication (300 J energy) normalised to pre-induction cell density (0.7 OD_{600}). Band at approximately 37 kDa is consistent with the theoretical size of PqsR. **(B)** Expression of pCOLD::*pqsR* performed under different inducer concentrations . Culture growth for 24 hours at 12°C and lysed as for (A). No material of the same size was observed in any tested condition.

6.3.2 Pilot expression of PqsR DNA binding domain constructs

Some studies that found full length LTTRs to be recalcitrant to crystallisation have used truncations to facilitate structural studies such as using the effector binding domains (e.g. LeuO from *E. coli*[268]). However, success has also been found in purification and crystallisation of DNA binding domains such as with *P. aeruginosa* CysB[269]. Three constructs, shown in Figure 6.5, were designed to investigate different regions of the DNA binding domain. This included just the core binding motif (1-69), the motif and part of the linker helix (1-85) and the motif and the entire linker helix (1-106). Each was C-terminally tagged with a **W**HHHHHH to permit detection on UV (as the DBD has no tryptophan residues) and His tag for purification. Induction and solubility testing was performed which showed that $PqsR^{1-69}$ failed to express. Both $PqsR^{1-85}$ and $PqsR^{1-106}$ showed bands of approximately the correct size but were not significantly observable in the soluble fraction. To compensate for the apparent lack of solubility high salt buffers (500 mM NaCl) were employed for extraction however attempts to enrich the material by affinity chromatography (HisTrap) failed to produce a significant amount of either construct as shown by poor UV intensity measured at 280 nm (Figure 6.5). $PqsR^{1-106}$ despite yielding more product was heavily contaminated and further purification by Heparin chromatography further failed to enrich the material (data not shown). As such these constructs were deemed unsuitable for further work given that crystallographic investigation would require milligrams of material.

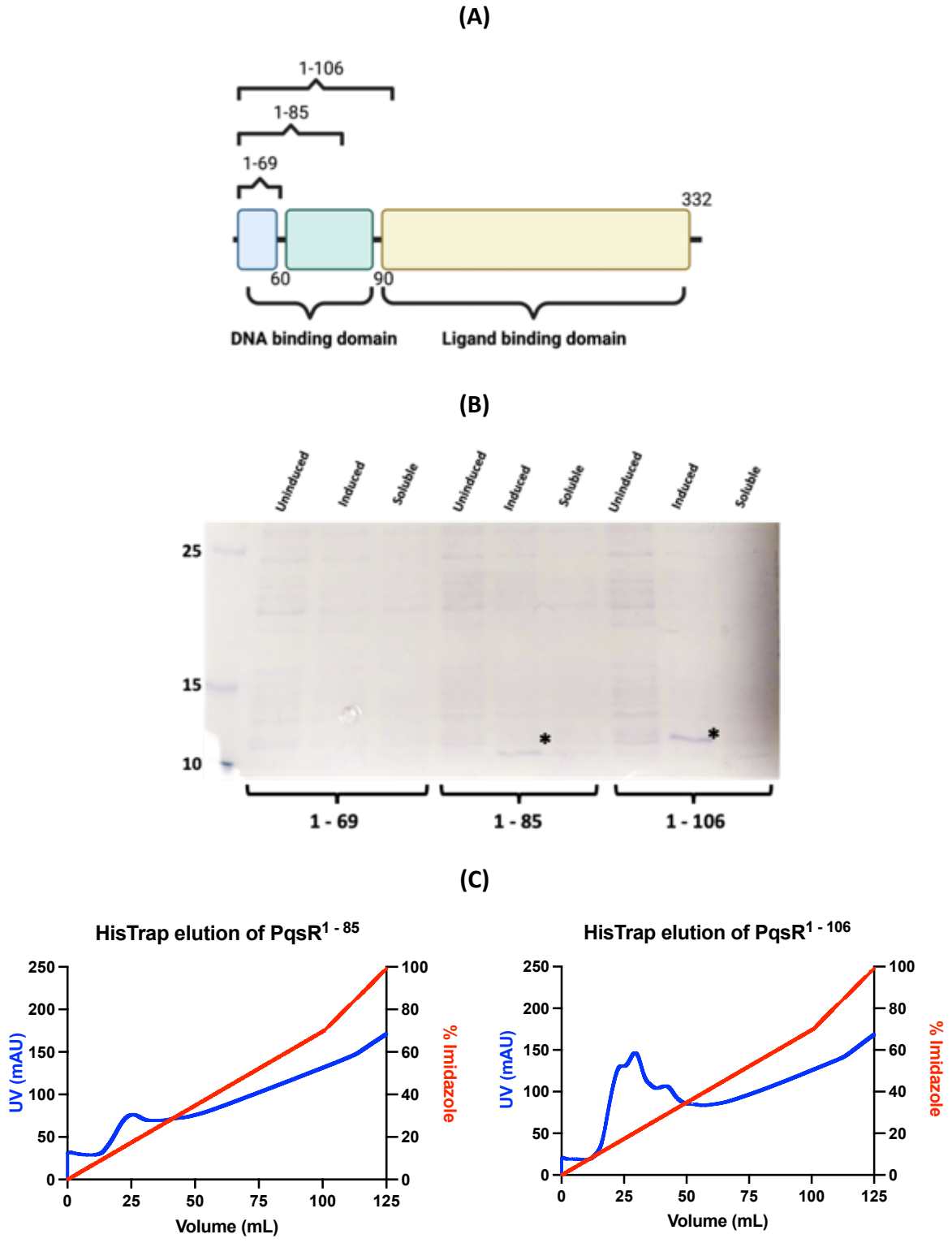

Figure 6.5. PqsR DBD constructs expression and extraction. (A) N-terminal constructs cloned into pET24b for purification **(B)** Induction and solubility gel (16% acrylamide) for DNA binding domain constructs showing protein expression in $PqsR^{1-85}$ and $PqsR^{1-106}$ marked by asterisk. **(C)** Elution chromatograms from HisTrap HP loaded with lysate overexpressing $PqsR^{1-85}$ and $PqsR^{1-106}$. UV measurements are taken at 280 nm using an AKTA Pure instrument. Weak enrichment by NTA of constructs 1-85 and 1-106 using higher salt buffer. Both constructs were unstable after purification with multiple contaminants.

6.4 Homologous expression of PqsR in *P. aeruginosa*

A rescue strategy employed in several literature studies utilises *P. aeruginosa* to express the protein of interest such that the protein is exposed to its native environment with optimal folding conditions[270 271 272]. However, this has mostly been used for membrane and extracellular proteins that may require specific lipid components or export mechanisms absent in "workhorse" *E. coli* BL21(DE3)[273]. The *pqsR* gene was cloned into an intermediate-to-high copy number vector pUCP19 harbouring a *P. aeruginosa* ori[274]. For growth, modified NZCYM media, a rich media containing casamino acids was used, as it allows for rapid growth of *P. aeruginosa*[275]. The media was further supplemented with glycerol as described for protein production protocols from *P. fluorescens*[276].

6.4.1 Expression and purification of PqsR from *P. aeruginosa* extract

To comply with BL2 safety regulations, small 250 mL cultures were chosen for growth. Analysis on an induction gel showed a faint band below 40 kDa suggesting successful induction of the protein although it was partly visible in the uninduced culture too but this was likely due to the leakiness of the *lac* promoter (Figure 6.6b). Furthermore, PCR testing on cultures confirmed the presence of the *pqsR* gene highlighting the plasmid was not lost during induction. For purification, 11.15 g cell paste was disrupted using 0.1 mm silica sphere mediated homogenisation in a FastPrep instrument (Figure 6.6a). The resultant suspension was highly viscous and required mechanic disruption with a syringe and further centrifugation prior to loading.

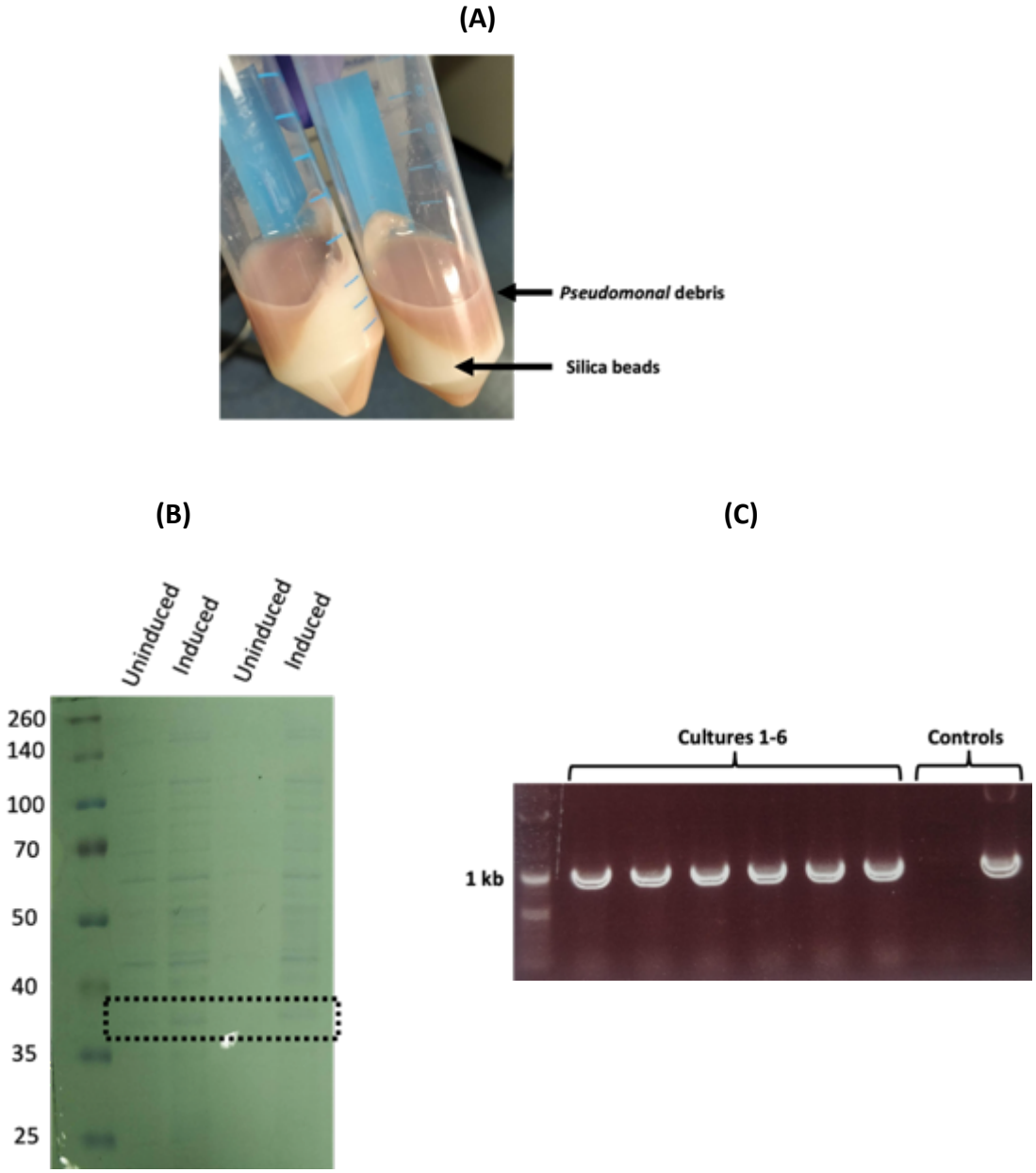

Figure 6.6. Preparation of *P. aeruginosa* lysate for protein extraction. (A) Cell paste after lysis, distinctive red colour is purportedly iron complexes within membrane and cell debris. **(B)** 14% SDS PAGE of two independent pre and post induction cultures lysed by SDS PAGE protocol **(C)** PCR on cell paste after induction showing plasmid retention. Negative control is an untransformed PAO1 - N Δ*pqsR* colony and positive control is isolated pUCP19::*pqsR*-His plasmid.

Apparent enrichment of material from the HisTrap Crude column was remarkably poor with most of the material eluting between 10 – 20 mL corresponding to an imidazole concentration of 50 – 100 mM suggestive of poor tag accessibility and weak binding to the column (Figure 6.7a). The material was readily separated further by Heparin affinity eluting at >400 mM NaCl in a sharp asymmetric peak with back-tailing (Figure 6.7b). The observed

band at 40 kDa was contaminated with a higher molecular weight (HMW) species not sufficiently removed by HisTrap or Heparin chromatography. As chaperone contamination is frequently observed in recombinant protein production it is presumed this band may represent the *P. aeruginosa* homolog of GroEL PA4385 (~57.1 kDa).

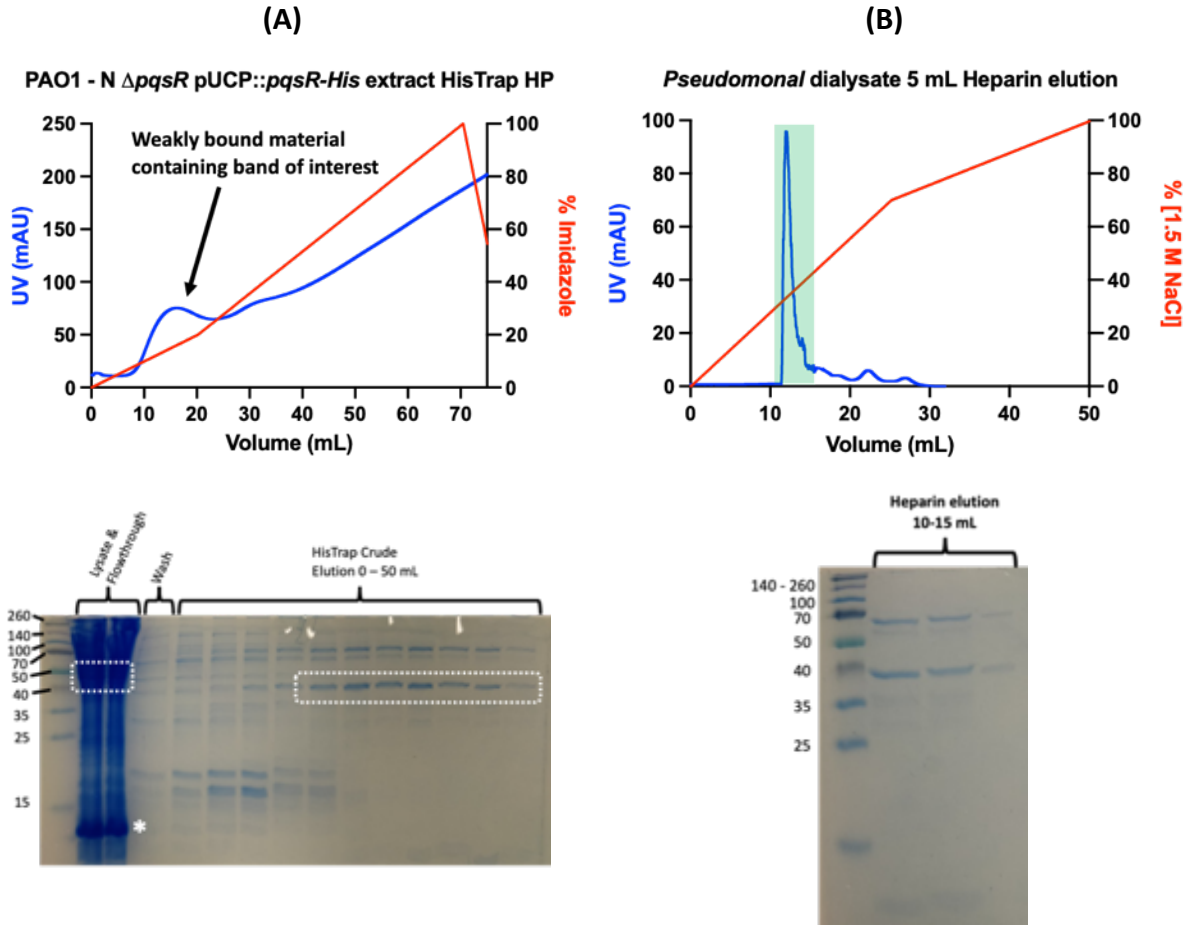

Figure 6.7. Extraction and purification from *Pseudomonas* lysate (A) HisTrap Crude elution with imidazole with a peak eluting between 10 and 20 mL. Resultant SDS PAGE shows the presence of HMW contaminants. Protein of interest marked with white boxes and star shows presence of lysozyme used to digest cell wall during lysis. **(B)** Sharp elution from Heparin 5 mL resin but HMW contaminant between 50-70 kDa on SDS PAGE was not separated.

To further purify the product the collected material was concentrated and loaded onto a Superdex 10/300 column and eluted at 10.95 mL corresponding to a large apparent M_r of 354 kDa (Figure 6.8a). This was unexpected given the typical tetrameric arrangement of most LysR-type proteins but it should be noted that some LTTRs have been known to adopt substantially higher level oligomers including CrgA that forms a large octamer[143]. Although given the relatively uncommon occurrence was suspicious.

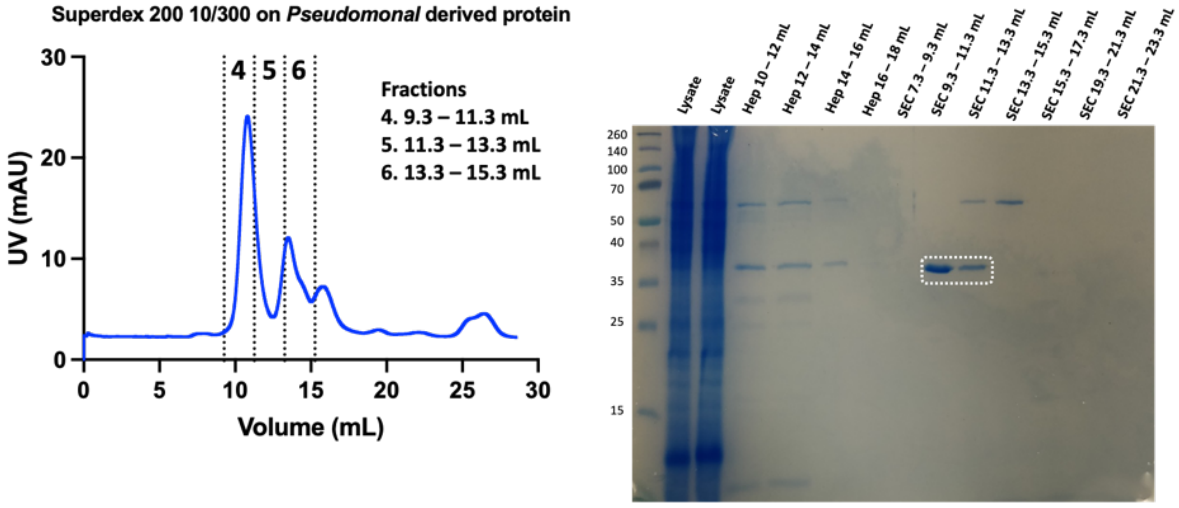

Figure 6.8. Elution of native *P. aeruginosa* sample from Superdex 10/300 column. Most of the 40 kDa species is contained within fraction 4 (9.3 – 11.3 mL) with an apparent M_r of 353 kDa. Contaminating band ~60 kDa is partially separated and eluted in the proceeding fractions 5 and 6.

6.4.2 Mass spectrometry and crystallisation

The presumed PqsR protein, contained in fraction 4, and the contaminating protein from fractions 5 and 6 were analysed for composition using mass spectrometry (University of York). This unfortunately revealed the 40 kDa protein to be IlvC, a Ketol-acid reductoisomerase, responsible for the biosynthesis of branched amino acids. The contaminating protein was shown to be a biosynthetic enzyme carbamoyl transferase. IlvC crystallised under multiple conditions from MIDAS, LMB and Nucleix giving rise to several different crystal habits as shown in Figure 6.9. These diffracted to 2.38 Å and were structurally identical to the published model 1N3P except for disulphide linkages observed between Cys 9 and 169 and the presence of bound magnesium. These differences are detailed in Appendix 9.8. The affinity to the initial IMAC column could be accounted for by a dyad of histidine residues His29 and His59, not present in the *E. coli* homolog, that could weakly chelate Nickel[277].

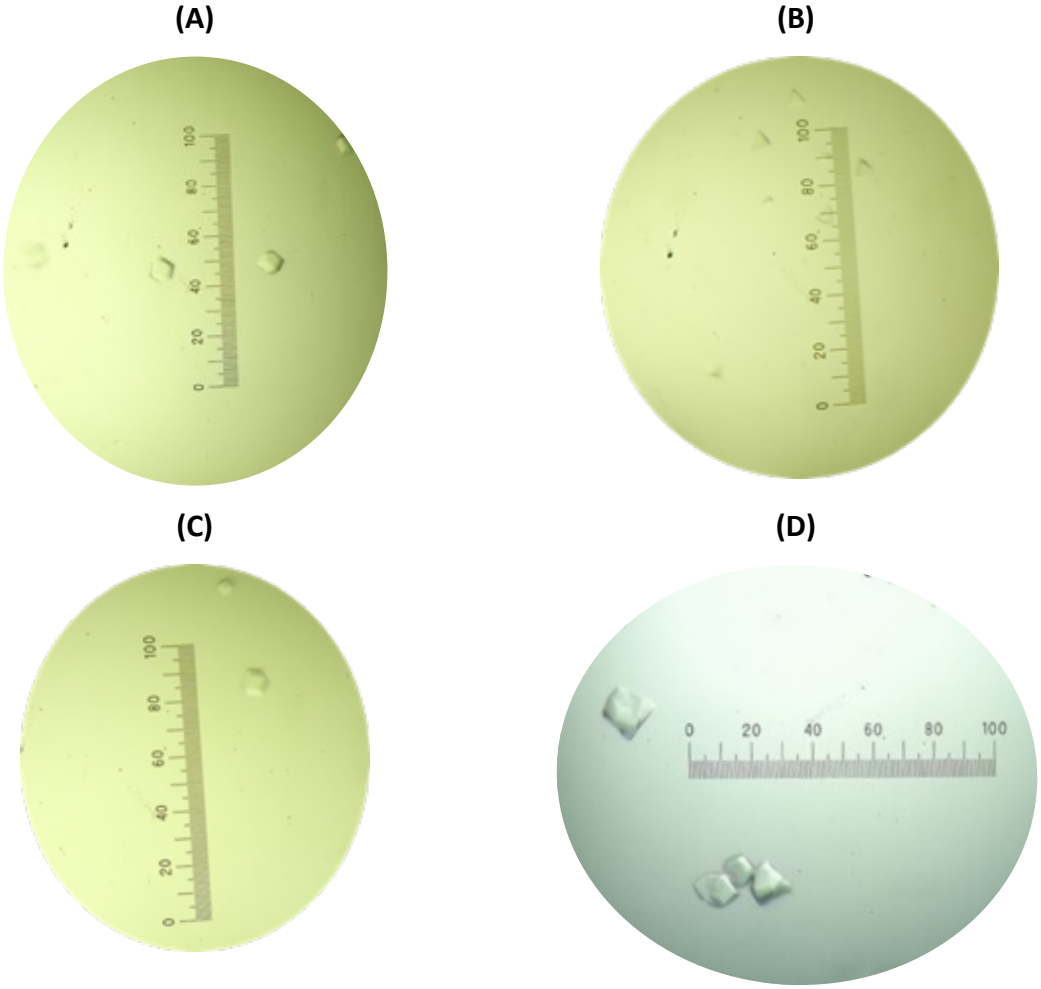

Figure 6.9. Crystal habits displayed by *P. aeruginosa* IlvC contaminating protein. **(A)** Hexagonal habit grown in 20% w/v PEG6000, 0.1 M sodium citrate pH = 4, 0.2 M LiCl (LMB) **(B)** Pyramidal crystal habit grown in 50 mM cacodylate pH = 6, 15 mM magnesium acetate, 1.7 M ammonium sulphate (Nucleix) **(C)** Cubic crystals grown in 0.1 M sodium chloride, 0.1 M Tris pH = 8, 35% v/v jeffamine SD-2001, 30% jeffamine M-600, 10% dimethyl sulfoxide (MIDAS) and **(D)** Diamond shaped crystals grown from 0.2 M potassium acetate, 0.1 M MES pH = 6, 15 % v/v pentaerythritol ethoxylate (15/4 EO/OH) 3 % v/v jeffamine® T-403 (MIDAS). All crystal forms grown at 20°C and appeared within a week of crystallisation set up.

6.5 Carrier-driven solubilisation of PqsR

As used for other LysR protein solubilisation can be achieved with addition of a fusion protein[278]. Several fusion proteins such as MBP, Thioredoxin (Trx) and GST have already been extensively characterised for use in protein solubilisation but can also aid in crystallisation. As such *pqsR* was cloned into MBP and Trx vectors by restriction and SOEing PCR (Methods 2.4.4) respectively. GST was not attempted as it had previously been found to produce insoluble protein (personal communication Dr. Aravindan Ilangovan). The MBP construct chosen was a pMAL derivative that had been optimised through a SER campaign

to increase crystallisability[215]. Novel in-house tags developed by the Dreveny group (University of Nottingham) were also employed including 1BKR (Calponin Homology Domain Human) and 2GKG (Receiver domain from *Myxococcus xanthus*).

6.5.1 Expression of MBP-PqsR

PqsR was cloned into pMAL(X)E, harbouring 5 alanine SER mutations (82/83/172/173/239), with a short rigid linker expected to form a helical structure. Expression in BL21(DE3)CP produced a band between 58 and 80 kDa consistent with the theoretical mass of 77.5 kDa. To further optimise expression the conditions were altered to exploit sorbitol as a chemical chaperone[279]. Although growth rate was retarded in the presence of high sorbitol concentration the final OD of each culture was not significantly different. Comparison of soluble fractions liberated from each culture showed that the amount of solubilised protein increased at sorbitol concentrations >250 mM (Figure 6.10). A similar effect was observed for a variant of the construct containing a longer linker (AAAAS).

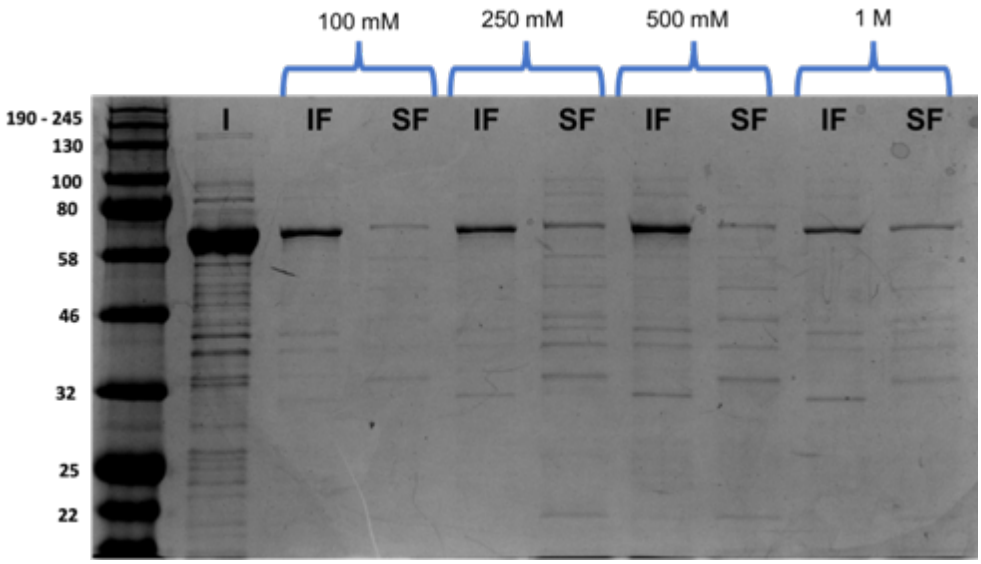

Figure 6.10. Effect of sorbitol media concentration on MBP-PqsR solubility. BL21 (DE3) CP pMAL::*pqsR* grown in 50 mLs media and induced at OD_{600} 0.7 with 1 mM IPTG. Cultures lysed by sonication and insoluble fraction attained by boiling the insoluble pellet in 10% SDS. Lanes are identified as follows: I = induced, IF = insoluble fraction and SF = soluble fraction. An increase in soluble material is observed at sorbitol concentrations above 250 mM.

Expression was further optimised by examining induction temperature. Cultures of BL21 (DE3) grown at higher (22°C) and lower temperature (17°C) showed that temperature had relatively little impact on protein expression however, the amount of insoluble material

significantly decreased. In the case of the shorter linker a commitment decrease was observed in the soluble fraction but suggests that the ratio of soluble:insoluble material is more favourable at lower temperature and as such a high protein quality may be attained.

A similar effect was observed for the protein containing the longer linker except that the soluble band became more intense. These observations suggest that PqsR favours low temperature for expression likely taking advantage of reduced protein synthesis.

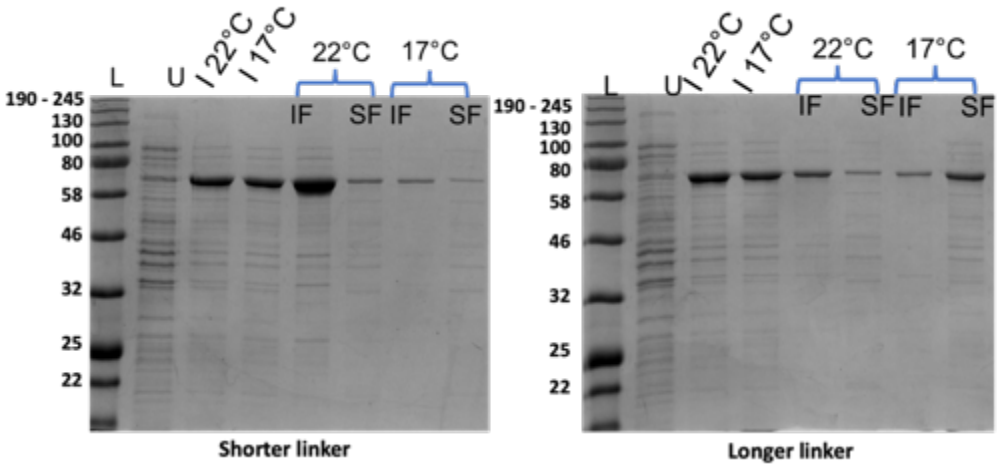

Figure 6.11. Effect of temperature on MBP-PqsR solubility. Comparison of temperature expression conditions for short (right) and long linker (left). Samples induced at 0.5 mM IPTG for 20 hours in 50 mL TB media. Lanes are identified as follows: U = Induced, I(temperature)= induced, IF = insoluble fraction and SF = soluble fraction. Lower temperature expression decreased the insoluble fraction in the shorter linker construct and increased soluble material in the longer linker construct.

To further optimise construct enrichment both salt concentration and buffer pH for extraction were examined. Modification of these variables is usually recommended to increase product yield and purity[280]. As shown in Figure 6.12 the two pMAL constructs were tested against a pH screen from 5 to 9. No significant changes could be observed in solubilisation however for the longer construct solubilisation was poorest below the predicted isoelectric point (pI) of 5.81. This highlights that the constructs were sensitive to surface charge changes so pH should be kept above the pI for purification procedures. The longer linker construct appeared to have greater instability at the highest and lowest pH values tested as apparent soluble recovery was distinctly lower. This indicated the shorter linker was a more stable construct for further work.

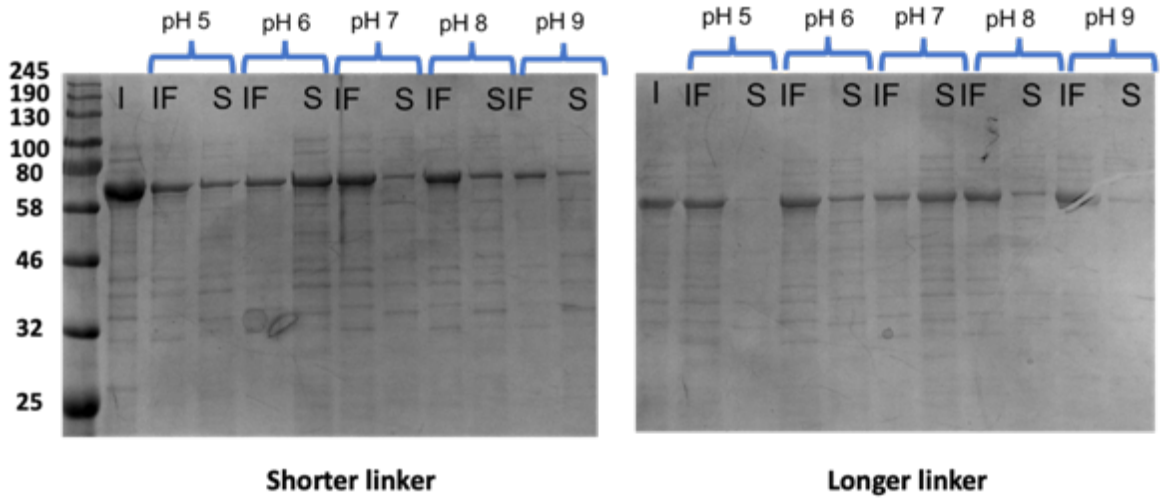

Figure 6.12. pH buffer optimisation of MBP-PqsR. Lysis of MBP-PqsR with a gradient of different pH buffers. Cell pellets were resuspended in 1 mL of each test buffer and lysed by sonication. Soluble and insoluble fractions were separated by centrifugation and insoluble pellet dissolved in 10% SDS. Buffering solution for pH's 5, 6 and 7-9 were sodium acetate-acetic acid, MES-NaOH and Tris-HCl respectively. Each buffer was supplemented with 250 mM NaCl, 1 mM EDTA and 1 mM DTT. The longer linker construct shows less soluble recovery at pH 5, 8 and 9 showing greater instability.

A screen was also performed on varying salt concentration to determine suitable extraction conditions (Figure 6.13). A small gradient of salt concentration from 0.1 – 1 M was tested. The amount of liberated material appeared unaffected by varying salt concentration however, less insoluble material remained after usage of 1 M NaCl suggesting that salt concentration should remain relatively high. Replacement of KCl for NaCl was also tested and appeared to be less successful at solubilisation compared to an equivalent concentration of NaCl.

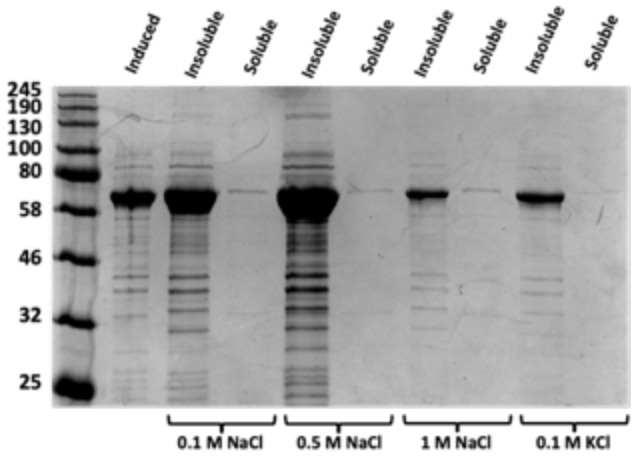

Figure 6.13. **Salt extraction optimisation of MBP-PqsR.** Cell pellets containing MBP-PqsR were resuspended in the presence of varying salt concentration showing a preference towards NaCl. Less insoluble material was present at the highest NaCl concentration. Each buffer also contained 50 mM Tris-HCl (pH 7.4), 1 mM EDTA and 1 mM DTT.

Given that high salt concentrations and a pH above pI gave the most abundance post-lysis a buffer containing 500 mM NaCl and physiological pH (7.4) were chosen for purification using dextrin affinity chromatography (MBPTrap) which successfully enriched the protein. However, a significant number of contaminating bands were observed both above and below the desired material (between 58 – 80 kDa markers) (Figure 6.14). Unlike other affinity tags, such as His, binding to the dextrin requires the protein to be correctly folded. The fusion was pooled and concentrated prior to loading onto gel filtration however it was observed that the sample began to go cloudy soon after elution suggesting that it was prone to aggregation. Although the same effect was often present in the ligand binding domain and could be due to the high protein concentration.

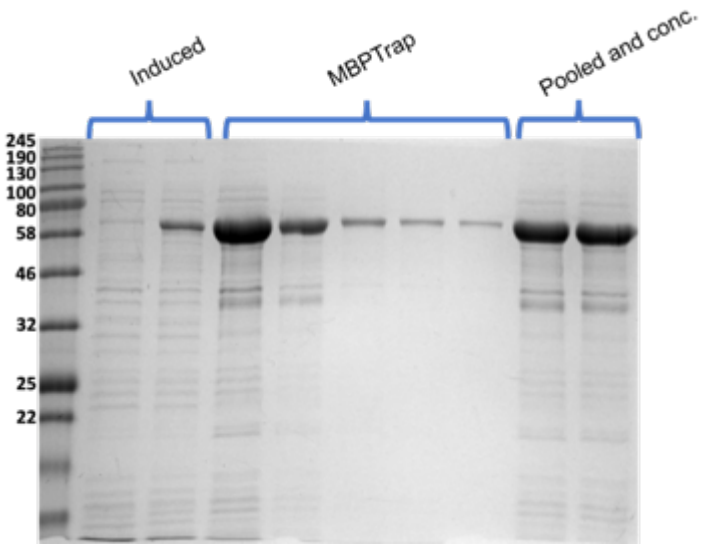

Figure 6.14. MBP-PqsR purification. Extraction and enrichment of MBP-PqsR using a 5 mL MBPTrap column eluted with 10 mM D-Maltose. 5 fractions eluted from the MBPTrap with most of the material eluting in the first two 5 mL fractions. Pooled and concentrated protein shows several contaminating bands. The most abundant contaminant is between 32 and 46 kDa and may represent cleaved MBP.

However, subsequent gel filtration of the pooled material showed that the sample was heavily aggregated as evident by the elution at the column's void volume (45 mL). The expected elution volume, assuming a tetrameric assembly would be 55 mL (310 kDa). However, the tailing peak from the void suggested that some material could maintain the correct quaternary structure.

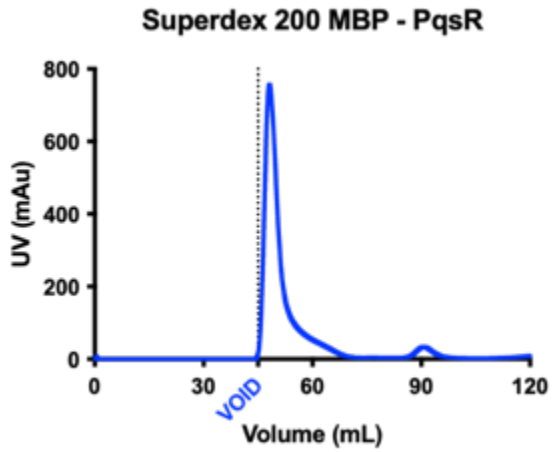

Figure 6.15. Chromatogram of MBP-PqsR elution from a Superdex 200 16/60 column. Column was connected to an AKTA PURE system with a flow rate of 0.8 mL/min maintained during a 120 mL run. Void volume of the column is marked with a dashed line. MBP-PqsR eluted as an aggregate in the tailing peak starting at 45 mL.

The material eluting in the tailing peak (50-65 mL) was recovered and re-loaded onto the same column to ascertain whether it contained correctly folded protein. However, the aggregated material was still not entirely separated from another species that eluted at 59 mL, which corresponds to an apparent M_r of 226 kDa, corresponding to a trimer or significantly extended dimer. Given that trimeric arrangements have not been observed in LTTRs it is likely that the resultant complex is representative of the latter. Examination of the resultant SDS PAGE gel showed a band around 130 kDa that may be representative of a non-fully denatured dimer. This phenomenon is observed in proteins that contain large hydrophobic patches or proteins with some degree of membrane interaction[281]. Alternatively, the band may be representative of an *E. coli* contaminant from dextrin affinity that has thus far been unreported.

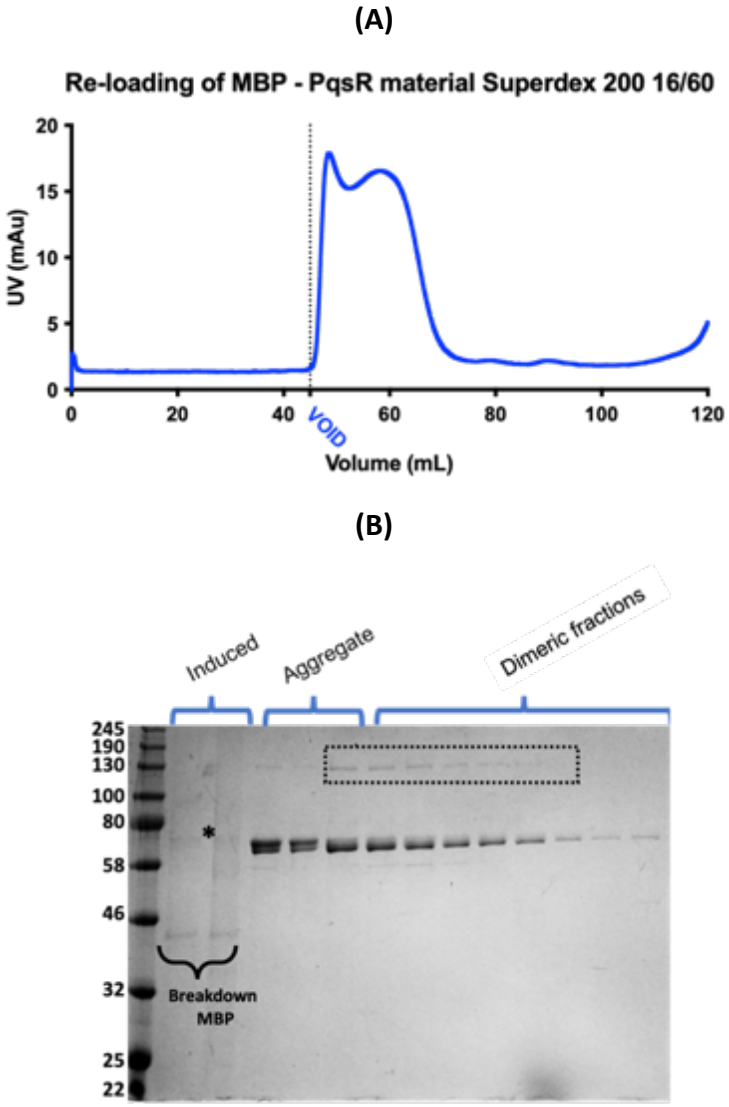

Figure 6.16. Re-elution of MBP-PqsR from Superdex 200 16/60 (A) Chromatogram of MBP-PqsR to separate aggregated HMW material from properly folded species. Aggregated material and suspected dimer eluting at 45 and 59 mL respectively. **(B)** SDS PAGE of MBP-PqsR showing a good degree of homogeneity after gel filtration. * Indicates induced band from diluted cell lysate and apparent breakdown MBP product is highlighted. Suspected undissociated dimer visible and shown in a dashed box and is contained in each fraction with band intensity related to MBP-PqsR concentration thereby implying a species relationship.

Extended dimer, partially separated by gel filtration, was entered into crystallisation trials. The protein was concentrated to 3 mg/mL and screened using Morpheus, PACT premiere, JCSG+ and the MPD suite. No condition gave rise to crystalline material with most conditions producing light or heavy amorphous precipitate. The sample seemed particularly sensitive to PEG conditions shown by the vast majority (96.9%) of conditions yielded dark, amorphous precipitate. The MPD suite yielded the greatest number of clear drops and light

precipitate, perhaps due to MPD acting to stabilise the protein as it binds to the pocket in the C-terminal domain. To improve crystallisation, the sample was buffer exchanged into a phosphate buffer (50 mM, pH = 7.5) based on the rationale that phosphate ion would stabilise the highly charged DNA binding domain. However, this had no effect on protein crystallisation as most conditions still yielded precipitate with a low incidence of salt crystals arising from metal containing conditions.

6.5.2 Screening for additional crystallisation tags

As MBP produced soluble aggregates, three other tags were fused to N-terminally to PqsR including Thioredoxin TRX (provided by Thomas Warwick) and two novel tags developed by the Dreveny lab 2GKG and 1BKR. The latter two were mined from the PDB based upon favourable characteristics including size, compact globular shape and that they were solved to high resolutions of 1.1 and 1 Å respectively. Initial solubility testing after a short induction of 4 hours at 37°C showed sparingly little soluble material post lysis. However, as shown in Figure 6.17, after the temperature was lowered to 20°C the 1BKR-PqsR construct yielded soluble material.

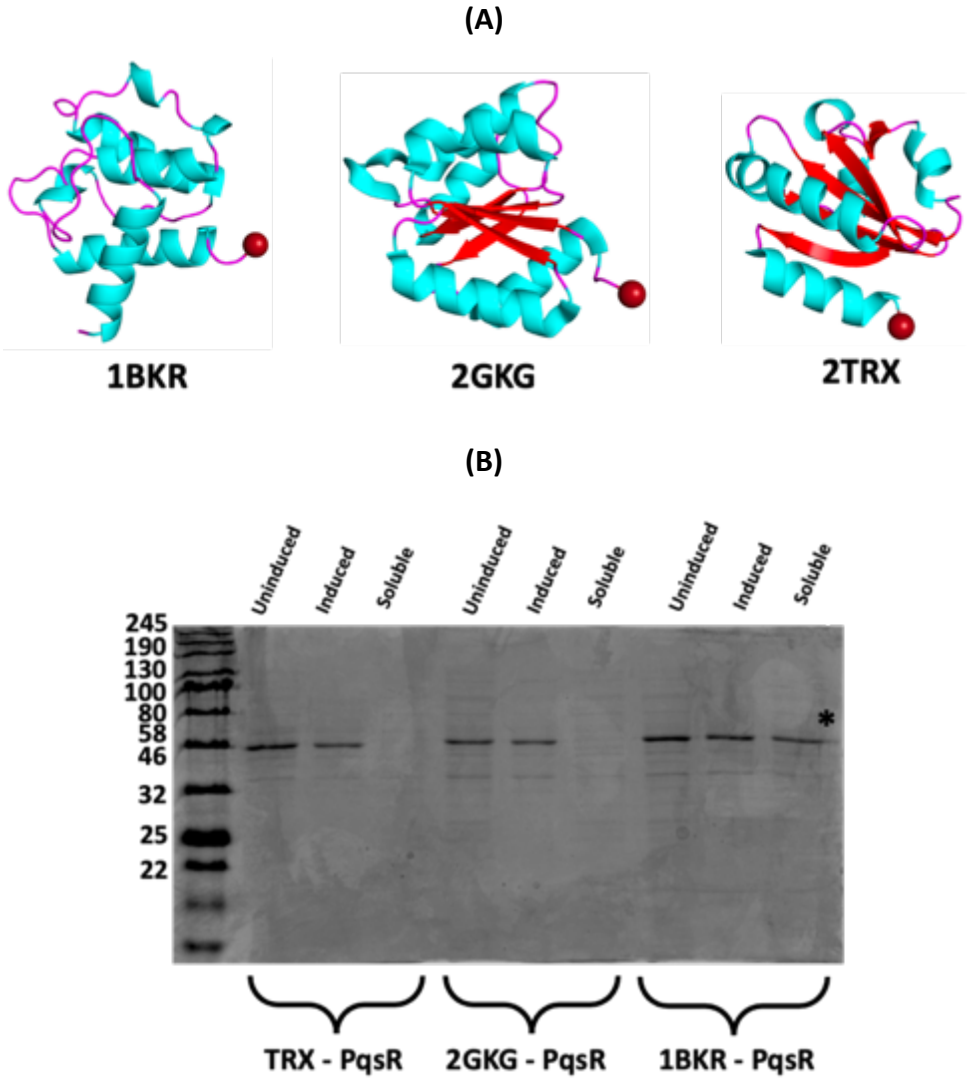

Figure 6.17. Solubility testing with additional carrier proteins. (A) Models of carrier proteins with C – termini marked by red spheres. Colouring set to secondary structure features – light blue helices, red beta sheets and pink loops. PDB codes for each model stated below cartoon structure. **(B)** SDS PAGE to assess solubility of the carrier proteins with PqsR. Uninduced and induced are derived from cell pellets, normalised to the same density. Soluble fraction attained by micro-sonication of the induced sample. "*" indicates the presence of soluble material post-lysis. Proteins expressed at 20°C overnight in 50 mL TB media induced with IPTG. Target proteins expected M_r for Trx-PqsR, 2GKG-PqsR and 1BKR-PqsR are 50.2, 50.7 and 51.4 kDa respectively and as such migrate towards a similar position on SDS PAGE.

6.5.3 Purification of 1BKR-PqsR

Given the observations made with respect to MBP, a similarly high sorbitol concentration of 500 mM was used in expression media to bolster yield. Capture was successful using tandem HisTrap HP columns eluting at an imidazole concentration of 150 mM. The resultant material was dialysed overnight into a lower salt buffer (175 mM). Salt concentration could

not be further reduced, and precipitation was observed at lower concentrations. The sample was further purified and concentrated using Heparin chromatography using a gradient elution with 1BKR-PqsR eluting at a low concentration of 300 mM NaCl. Due to the Heparin column having a lower binding capacity compared to HisTrap the column was loaded and eluted twice. Subsequent material was pooled and concentrated for gel filtration (Figure 6.18).

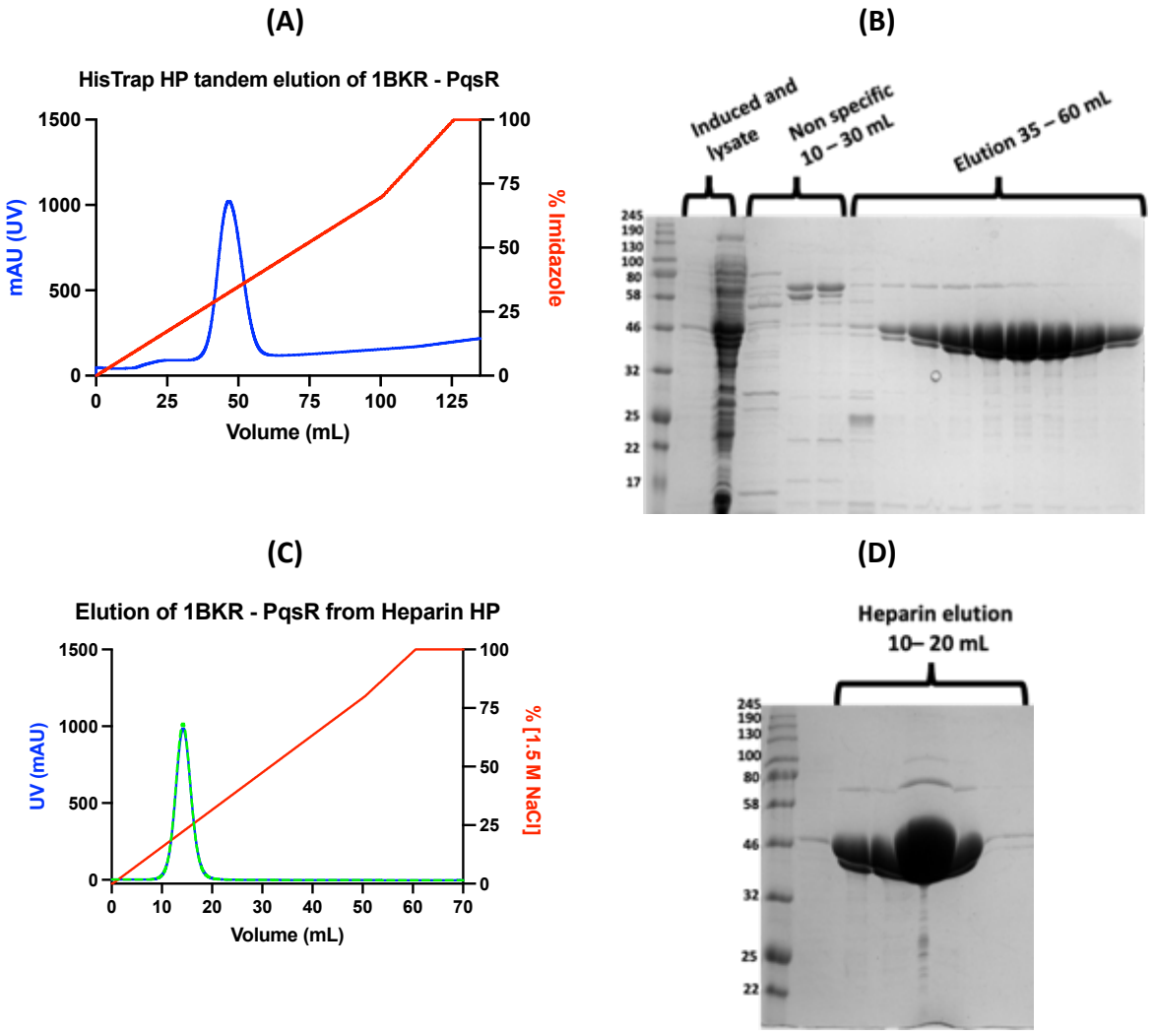

Figure 6.18. Capture and concentration of 1BKR-PqsR. (A) Elution chromatogram of 1BKR-PqsR from 2 HisTrap HP columns connected in tandem. Maximum imidazole concentration of 500 mM. **(B)** SDS PAGE showing purification from HisTrap HP column. Material observed to have a M_r between 46 and 58 kDa which is consistent for the predicted mass of the construct (51.4 kDa). **(C)** Concentration by Heparin chromatography running a gradient from 175 mM (Dialysis buffer concentration) to 1.5 M. Separate elutions shown as blue and green dashed lines. **(D)** Subsequent SDS PAGE showing less HMW contaminant.

The protein eluted isocratically at an elution volume of 60.4 mL which according to calibration standards suggests the M_r is 203.2 kDa corresponding to a tetrameric assembly. This is in good agreement with previously reported LTTRs that either adopt dimers or tetramers. The 58 – 80 kDa contaminant was observed to elute in the HMW shoulder. Given the size and recombinant origin it is likely an *E. coli* chaperone bound to a small portion of the sample. Interestingly, the band of interest came off as a doublet suggesting minor breakdown at the protein terminal.

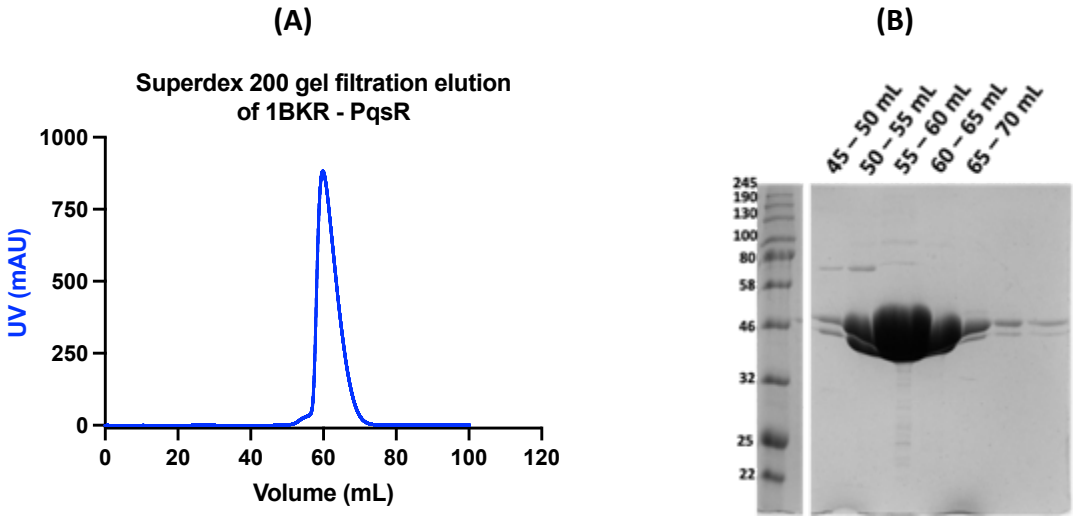

Figure 6.19. Gel filtration of 1BKR-PqsR using a Superdex 200 16/60. (A) Chromatogram of protein elution injecting 5 mL concentrated sample from pooled heparin eluate using a flow rate of 0.8 mL/min in a buffer containing 200 mM NaCl to maintain solubility. **(B)** SDS PAGE showing purification of 1BKR-PqsR. High molecular weight contaminants partially separated by gel filtration and is most prevalent in the earlier fractions (50 – 55 mL). The gel image is from the same figure 6.18d.

The sample's identity was confirmed by mass spectrometry (University of York) derived from two excised SDS PAGE samples. As the sample displayed a doublet band pattern on PAGE these samples corresponded to the upper and lower band. Both bands returned fragments that matched with PqsR giving a combined coverage of 32.5%. The matched fragments are highlighted below in blue:

MPIHNLNHVNMFLQVIASGSISSAARILRKSHTAVSSAVSNLEIDLCVELVRRDGYKVEPTEQALRLIPYM
R**SLLNYQQLIGDIAFNLNKGPR**NLRVLLDTAIPPSFCDTVSS**VLLDDFNMVSLIR**TSPADSLATIKQDNAEI
DIAITIDEELKISRFNQCVLGYTK**AFVVAHPQHPLCNASLHSIASLANYR**QISLGSRSGQHSNLLRPVSDK**V
LFVENFDDMLRLVEAGVGWGIAPHYFVEER**LRNGTLAVLSELYEPGGIDTKVYCYYNTALESERSFLRFLE
SARQRLRELGRQRFDDAPAWQPSIVETAQRRSGPKALAYRQRAAPE

Due to the apparent salt sensitivity of the sample and observation made with other LTTRs suggesting that salt concentration can influence oligomeric state[282]. A series of gel filtration experiments were conducted at different NaCl concentrations of 200, 300, 400 and 500 mM. However, no significant change in elution volume was observed nor were additional peaks conferring to higher or lower M_r species.

6.5.4 Crystal trials for full length PqsR

PqsR was successfully concentrated to 16 mg/mL using a Vivaspin 20 and entered into crystal trials. Initial screening was conducted using Nucleix, MPD suite, PACT premier and JCSG+ commercial screens. PEG conditions, such as those contained in the PACT premier screen produced heavy precipitate with the Nucleix suite producing the widest range of conditions including heavy and light precipitate as well as clear drops. The only conditions giving rise to crystals were B6 and G1 (Nucleix) consisting of a common buffer and primary precipitate of 50 mM sodium cacodylate (pH = 6.5) and 1.3 M lithium sulphate supplemented with either 10 mM magnesium acetate or 30 mM magnesium chloride & 1 mM spermine respectively. The commonality of the cacodylate is interesting as it can act as a phosphate mimic that in some cases has been essential to crystal formation with other phosphate binders such as dUTP pyrophosphatase[283]. Further experimentation with protein concentration showed that crystals could be reproduced at lower concentrations of 4 and 8 mg/mL (pictured below in Figure 6.20) adopting thin rods and plates habits respectively. At these concentrations some amorphous precipitate also formed congruently.

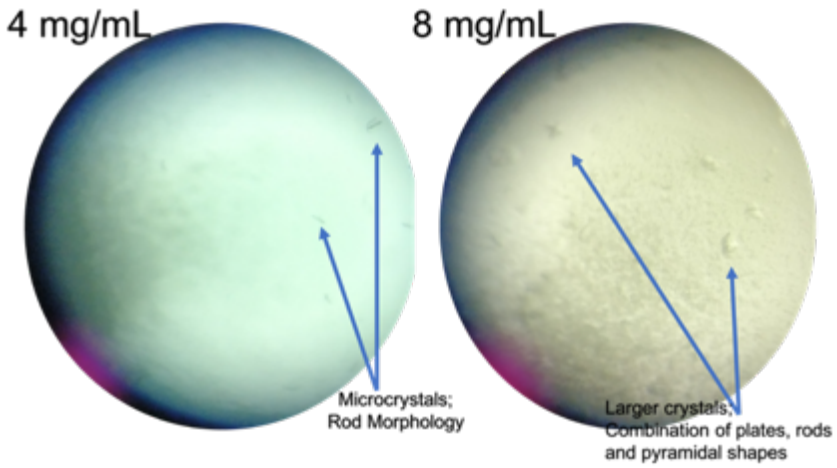

Figure 6.20. Initial crystals observed from Nucleix suite. Crystals generated from condition B6 with concentrations shown in each drop. Crystals grown in Swissci 96 well plates incubated at 20°C. Nucleation was observed within 2 days.

To improve crystal growth additive screening was attempted using two commercial suites Morpheus and Hampton. Initially, the crystal growth could not be reproduced in conjunction with additive. However, this was remedied by increasing the concentration of the primary precipitant salt lithium sulphate to 1.6 M (from 1.3 M) showing that condition dilution needed to be accounted for. The Morpheus additive screen produced a higher number of reproduced crystal conditions (18.75% of screen) compared to the Hampton additive screen (< 10%). The best improvement in crystallisation came from adding ethylene glycol to the base condition. However, when used in a gradient appeared to form spherulites (Figure 4.21). Morphology appeared to deteriorate at higher concentrations of ethylene glycol with the crystal form transitioning from small plates to spherulites. These forms were testing for diffraction, but the resultant pattern was not analysable due the presence of multiple overlapping lattices and were of low resolution.

The rod and plate habits were difficult to reproduce reliable. As such microseeding was employed to successfully reproduce crystallisation. Using the MMS methodology (detailed in chapter 2.8.4) crystals could be readily reproduced using two incomplete factorial screens (detailed in Appendix 9.2) with less amorphous precipitate observed within the drops. MMS screening into other screens failed to yield improvement with several conditions forming large salt crystals.

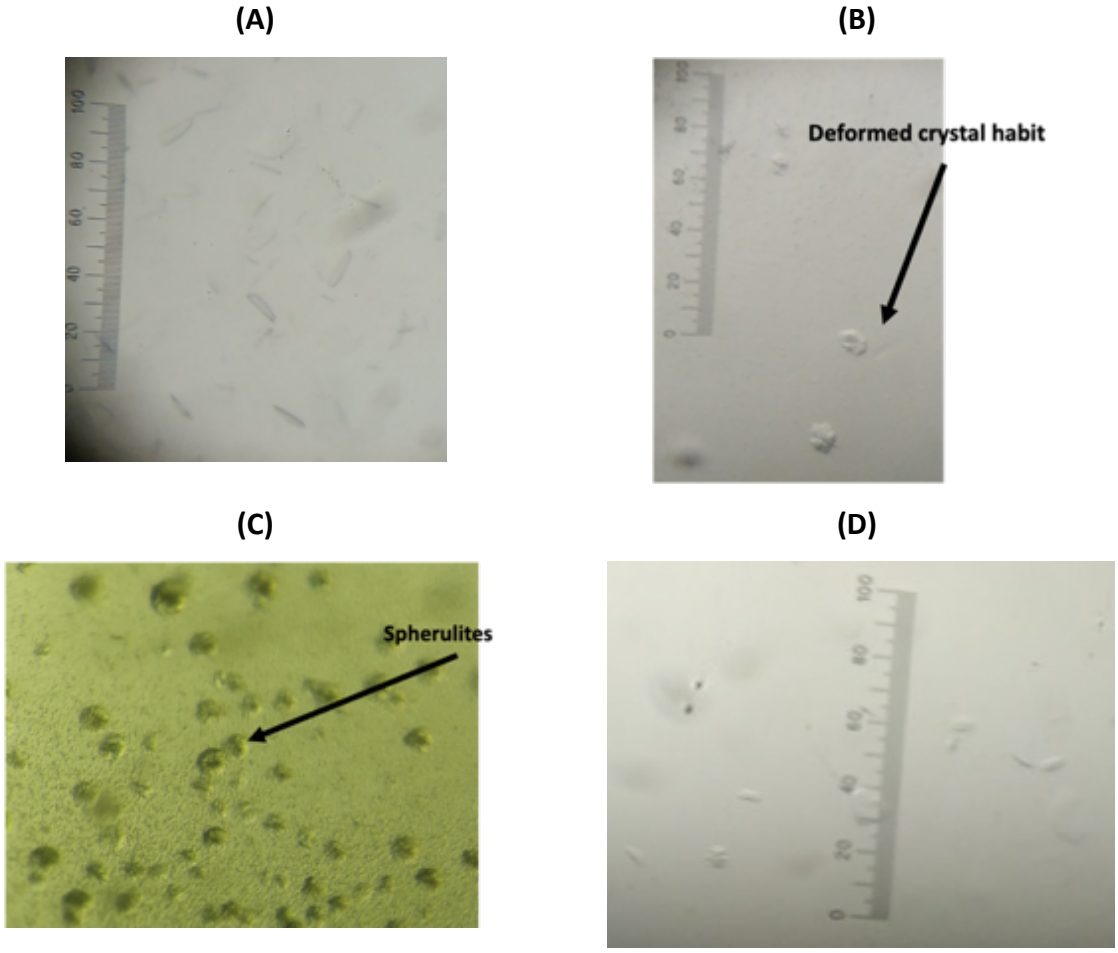

Figure 6.21. Optimisation of 1BKR-PqsR crystals. (A – C) Effect of ethylene glycol on crystal growth with concentrations of 2.5%, 5% and 7.5% respectively. **(D-E)** Microseeding in combination with INFAC screening condition consisting of 1.4 M lithium sulphate, 50 mM cacodylate, 20 mM magnesium acetate, 50 mM ammonium acetate, drop size 600 nL with 100 nL seed stock addition. Crystals grown in 96 well plates at a temperature of 20°C.

To improve crystal morphology and control nucleation the crystals were reproduced in a gel phase condition consisting of low molecule weight agarose (0.1-0.2%) (Figure 4.22). Previous studies have reported gel phase growth to improve crystal properties including 3D growth by providing a support network[222]. In conjunction with microseeding crystals successfully were produced. However, removing the crystals from agarose proved difficult as the surface tension usually permitting crystal adsorption to loops was negated. Larger chunks of excised agarose were grid scanned for diffraction properties at DLS i24 but yielded poor diffraction.

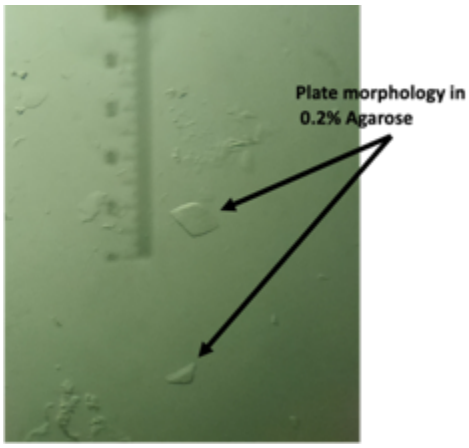

Figure 6.22. **PqsR crystals grown in low melting temperature agarose.** Plate morphology reproduced in gelated 0.2% w/v agarose supplementing the primary condition of 1.3M lithium sulphate, 20 mM magnesium acetate, 5% ethylene glycol and 50 mM sodium cacodylate. Crystal nucleation bypassed using the addition of microseeds.

Other optimisations not described in the text are detailed below giving strategy, rationale, and outcome:

Optimisation strategy	Rationale	Outcome
Mined 24 JBScreen (Jena) conditions with lithium sulphate. Screened at 20°C and 10°C.	Assumption that lithium sulphate was essential was crystallisation. Finding condition variants would broaden scope of optimisation.	No crystals grew in 24 conditions with protein concentration of 5 mg/mL.
Substitution of sodium cacodylate trihydrate with MES – NaOH	Substitution would reduce radiation absorption from the large arsenic atom	No crystal formation
Removing cacodylate by using MES based cryo-protectant	‘’	No improvement in diffraction
Screening for additives from Morpheus, JCSG+ and Stura screens	Primary screens contain a wider array of ligands compared to additive screens	Adding 25% primary screen to drop volume prevent crystal reproduction
Addition of 5% dioxane	Nucleation poison to reduce/prevent *de novo* nucleation.	Crystal growth abolished even in the presence of seeds.
Fine Protein concentration gradient from 2 to 4.2 mg/mL	Find an ideal concentration to avoid over-nucleation	Nucleation evident from 2 mg/mL onwards
Addition of malonate to cryoprotectant	Malonate has been shown to improve diffraction of salt grown crystals [284]	No effect on diffraction
Varying cryo-protectant conditions to include sugars and small organics	Testing a variety of cryo conditions and combinations thereof can improve diffraction characteristics	No significant improvements observed
Streak seeding	Common methodology to improve crystallisation. Large seeds transferred to fresh drop	Morphology inferior to crystals grown by microseeding

6.6 Modification to 1BKR-PqsR construct to improve crystallisation

6.6.1 Addition of cleavage site to remove 1BKR

A common rescue strategy for crystallisation is to cleave flexible regions or additional domains. To allow for specific cleavage a Tobacco Etch Virus (TEV) cleavage site was added after the triple alanine rigid linker – 1BKR-AAA**ENLYFQ/S**PIHN -PqsR. As shown in Figure 6.23a induction, under the same conditions as the non-cleavable fusion (high sorbitol TB media), yielded a product of the correct size (between 46-58 kDa) with a small amount of material present in the soluble fraction. However, this appeared less prominently than in the non-cleavable construct. Initial purification yielded incredibly little material after Ni-NTA suggesting the construct was unstable. To abate sample instability the lysis was repeated in the presence of a stabilising additive trehalose that had already been characterised for its solubilising properties[285]. As shown by Figure 6.23b, this improved solubilisation and permitted a slight increase in apparent yield (as judged by the area under the curve). However, the resultant material was heavily contaminated with smaller M_r products. Further purification by Heparin chromatography reduced the number of contaminants, including an intense band at ~25 kDa. The contaminants could include breakdown products from the fusion construct such as the solubility tag and DNA binding domain of approximately 25.3 kDa. This would have DNA binding affinity and as such would be expected to elute at a similar NaCl concentration. LMW contaminants were removed by an ultrafiltration Vivaspin 20 concentrator (20 kDa MWCO).

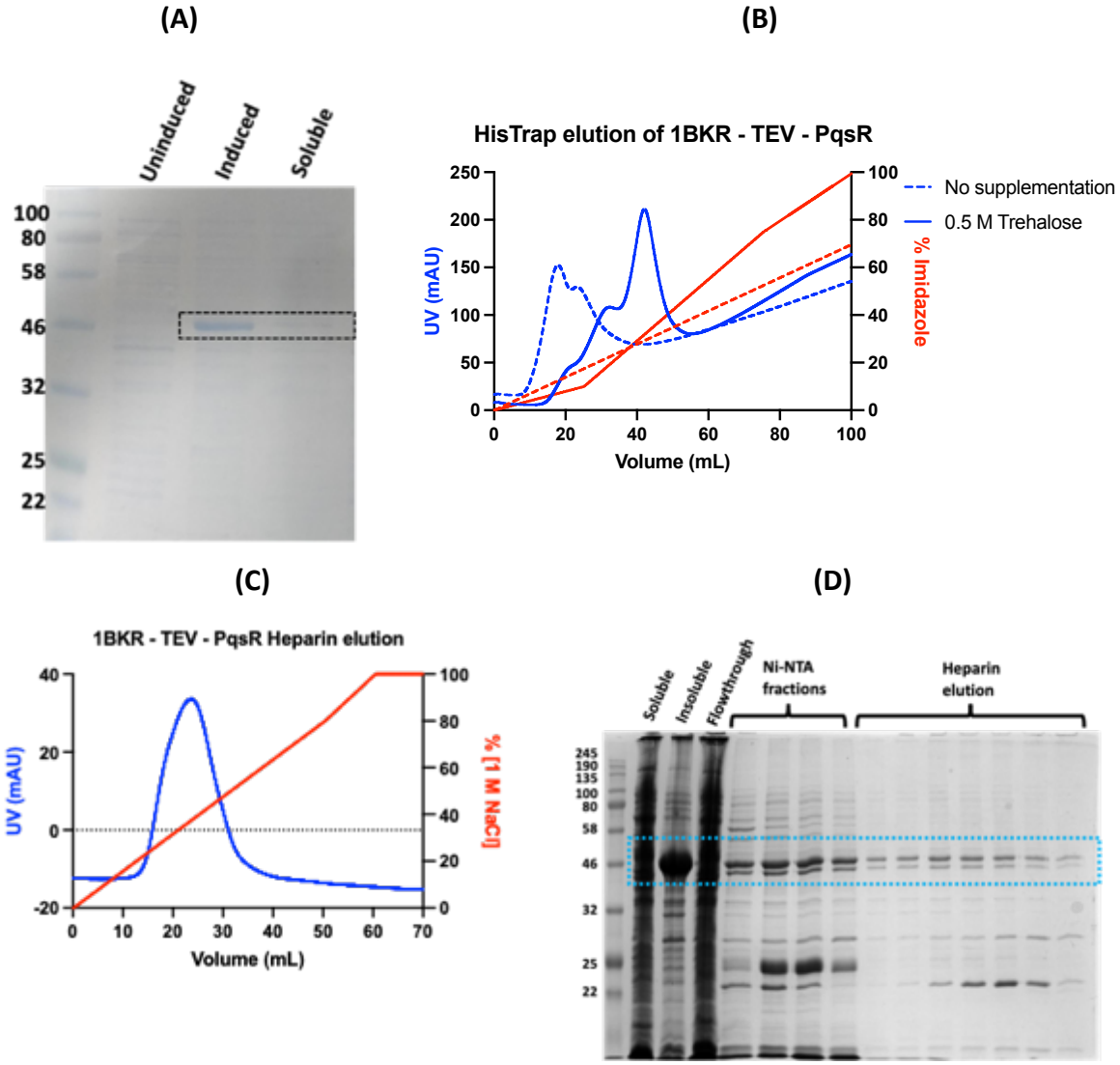

Figure 6.23. Purification of 1BKR-TEV-PqsR. (A) SDS PAGE gel showing induced and soluble band after induction in TB media supplemented with 500 mM sorbitol. **(B)** Ni-NTA purification from lysate in the presence/absence of trehalose supplementation marked by a solid and dashed line respectively. Addition of trehalose to the suspension buffer has improved separation. **(C)** Elution of 1BKR-TEV-PqsR from a 5 mL Heparin HP column. **(D)** SDS PAGE of Ni-NTA and Heparin fractions, target protein marked with blue box. Considerable amounts of protein was still contained within the insoluble fraction and the heparin fractions are contaminated with purity below 50% (judged by PAGE). Contaminants species below the target protein could include breakdown products from the fusion protein including the tag and DNA binding domain (20.1 kDa) and ligand binding domain (29 kDa).

Initial attempts to cleave 1BKR using purified TEV protease (construct kindly provided by Prof. Hyojung Kim) failed to produce a cleaved 37 kDa product after a short (hours) and long (overnight) incubation at room temperature. As a similar result was produced in a paper using a SUMO tag for PqsR solubilisation it was determined the cleaved product was likely unstable. To ameliorate the instability a small screen was designed for testing cleavage

conditions (detailed in Appendix 9.9). However, no condition yielded the expected 37 kDa product suggesting that either the cleavage site was inaccessible or that the protein was liable to aggregate. Given the instability observed during purification the latter explanation is more likely.

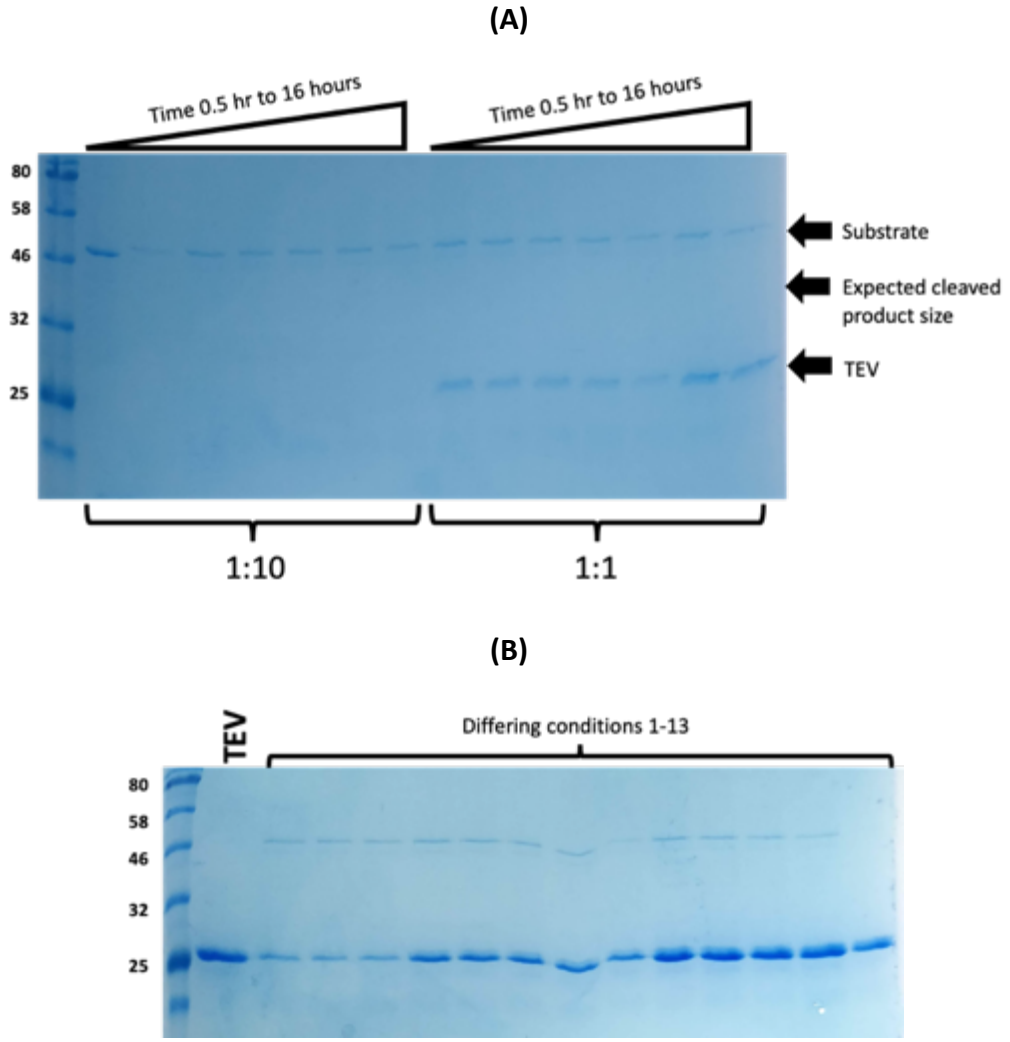

Figure 6.24. Trial cleavage conditions (A) 100 µL cleavage reaction with two different ratios of substrate to TEV enzyme. Samples taken at timepoints between 0.5 to 16 hours. **(B)** Cleavage with 1:5 ratio substrate to TEV with different conditions. Reaction performed at room temperature overnight. No cleaved product was observed under any reaction condition.

6.6.2 Truncation of PqsR C-terminal residues to reduce disorder

Removing flexible regions of a protein can often improve crystallisation. Terminal residues often exhibit a greater degree of flexibility and disorder as shown by Figure 6.2. This was also highlighted by lack of C-terminal electron density in the PqsR$^{94\text{-}309}$ construct used for

antagonist determination. To this end two C-terminal truncations were constructed creating boundaries at residues 310 and 296. As shown in Figure 6.25b expression was successful with both constructs showing an apparent M_r between 40-50 kDa that satisfied the expected 47.3 and 49 kDa sizes.

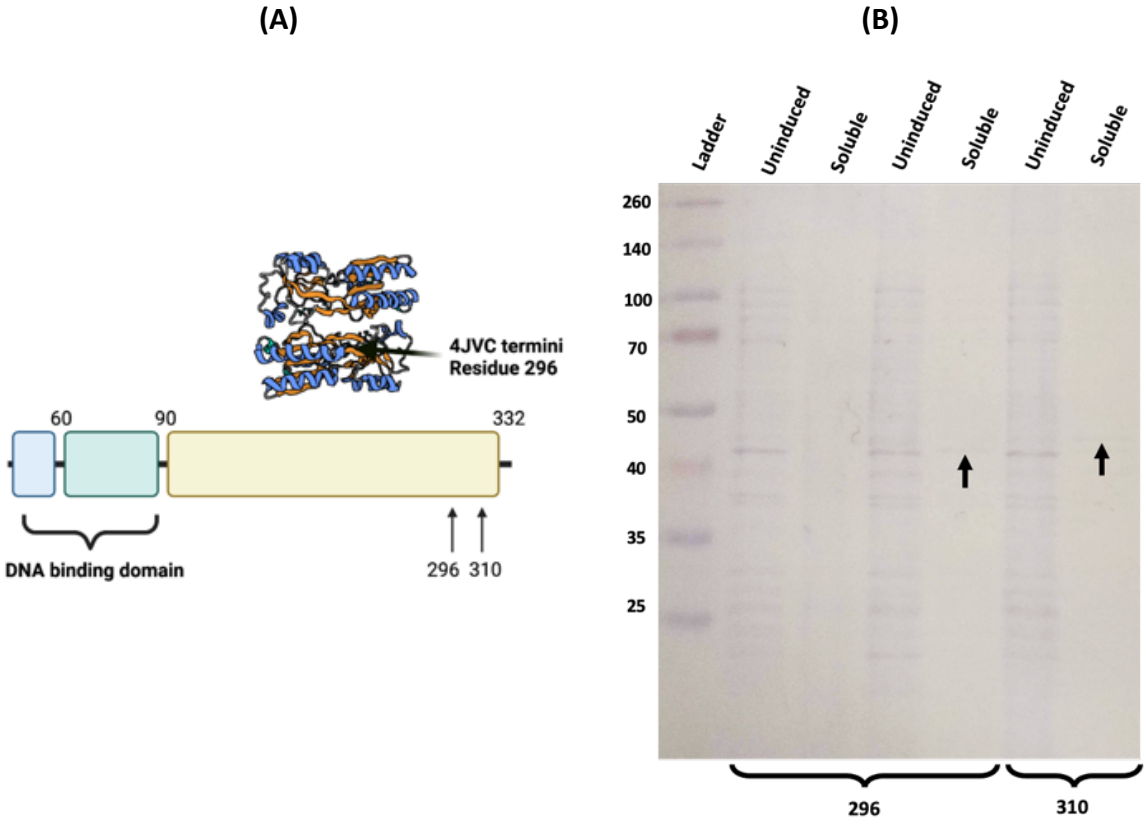

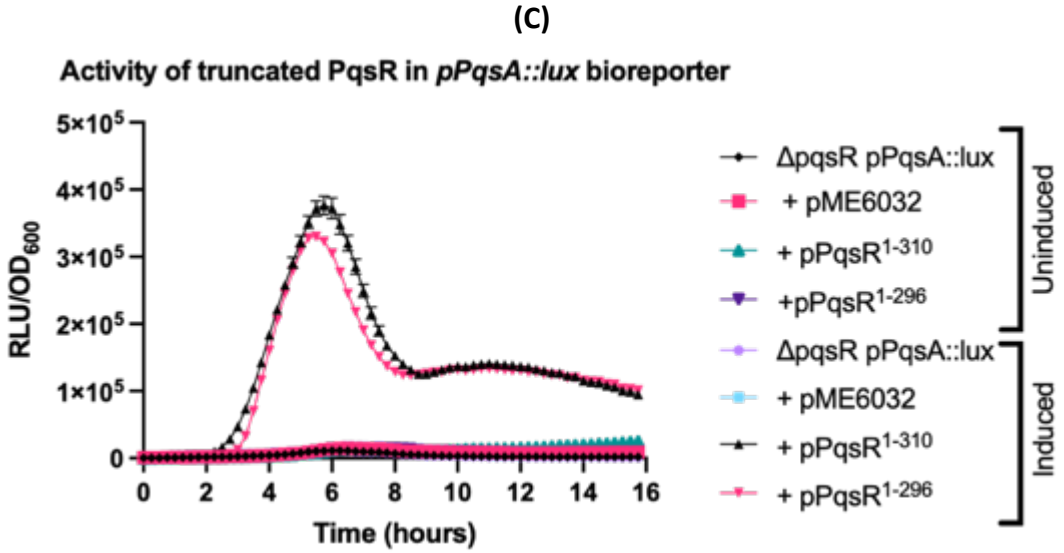

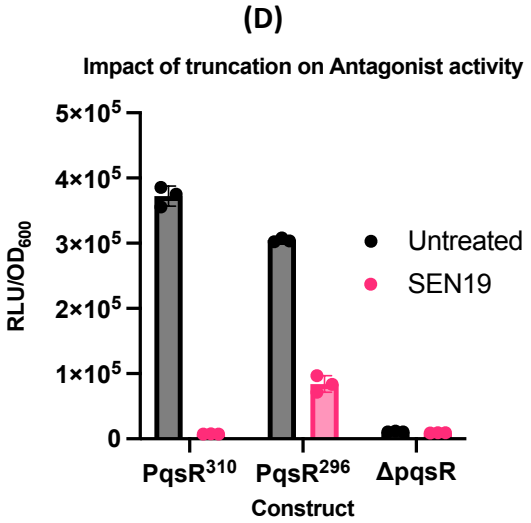

Figure 6.25. Truncated PqsR constructs (A) Schematic indicating regions of truncation **(B)** SDS PAGE gel showing faint bands in the soluble fraction with the correct approximate sizes for 1BKR-PqsR^{310} and 1BKR-PqsR^{296} truncations. **(C) Functional analysis of truncated PqsR.** PqsR functionality monitored by a CTX::P$_{pqsA}$-*lux* promoter fusion. All conditions were prepared in 200 µL volumes with LB broth and monitored with a TECAN plate reader over 16 hours. pME6032 plasmid and derivatives induced with 1 mM IPTG (Induced in legend). **(D)** Maximum expression of promoter fusion determined at 6 hours either untreated or with 10 µM SEN19.

Prior to purification, the effect of the truncations were examined using the complementation construct transformed into PAO1 – L *ΔpqsR* CTX::P$_{pqsA}$-*lux* which showed that the C-terminal was dispensable with respect to pqsA promoter activation. However, it should be noted that PqsR^{296} retained slightly less activity compared to PqsR^{310}. Additionally, a similar experiment testing the effect of antagonist activity with truncations was performed. As shown in Figure 6.25d, activity was entirely supressed with PqsR^{310} whereas PqsR^{296} was not fully attenuated. This suggests that the binding site may have become deformed in the absence of the full terminal.

6.6.3 Purification and crystallisation of 1BKR-PqsR^{296}

Despite its apparent solubility 1BKR-PqsR^{296} showed poor yield upon elution from two tandem connected HisTrap HP columns. The sample eluted at an imidazole concentration of 75 mM as a part of a shallow peak and smaller peak around 50 mL. To retain more material onto the column the imidazole concentration in buffer A was reduced from 50 mM to 20 mM. Although more material came off the column the desired truncated material did not enrich further suggesting that poor column retention was not the limiting factor. A likely

explanation was that the material was less stable due to the truncation. This partially agrees with the purification efforts of the ligand binding domain that showed that truncates to 296 were unable to form crystals and 291 precipitated upon initial purification[228]. The first preparation could be further purified by Heparin chromatography and eluted at a NaCl concentration of 116 mM, but the resultant yield was very poor. Furthermore, the baseline on the chromatogram shows a declining slope that may be evident of aggregation and non-specific sample adsorption (Figure 6.26c). The resultant protein was estimated to be >95% pure and was subsequently used for crystal trials (Figure 6.26d).

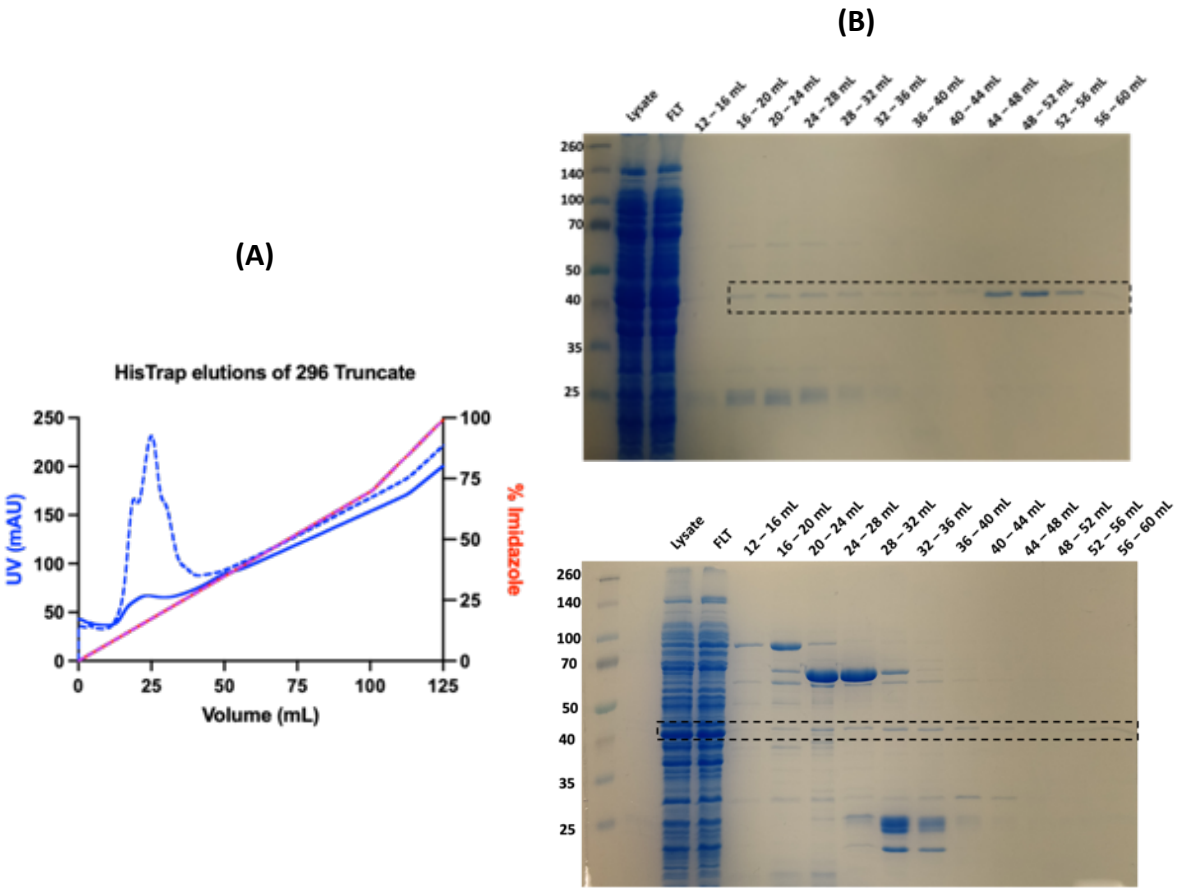

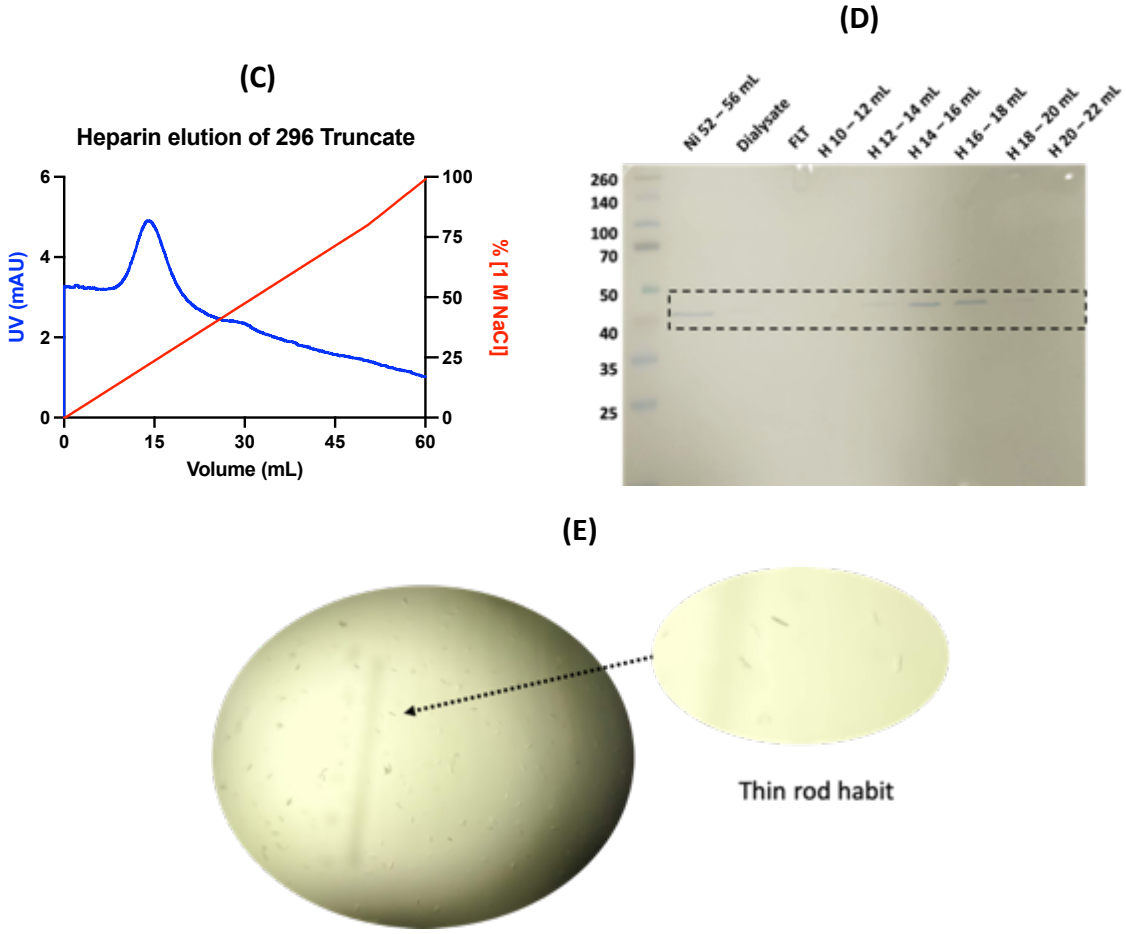

Figure 6.26. 1BKR-PqsR^{296} purification via HisTrap HP and Heparin HP column (A) HisTrap HP elution chromatogram with first and second trial shown as a solid and dashed line respectively **(B)** SDS PAGE gels comparing first and second trial. Protein of interest (judged by size) is marked with a dashed box. **(C)** Heparin elution of truncate from first trial **(D)** SDS PAGE of Heparin column elution showing a single band with a slight difference in migration due to NaCl concentration differences between IMAC fractions and Heparin gradient **(E) Microcrystals of 1BKR-PqsR^{296}.** Representative images of the microcrystals formed from 0.35 mg/mL in the absence of seeds in INFAC screens 1 & 2 at 20°C.

Due to the poor yield crystal trays could only be put down at 0.35 mg/mL in INFAC 1 and INFAC 2 with and without seeds. However, the plate-like morphology seen with the full-length construct did not form. The protein did show microcrystal showers in several INFAC wells in the absence of seeds suggesting that *de novo* nucleation was possible. Due to the relatively poor yields and inferior crystal quality this variant was not explored further.

6.6.4 Purification and crystallisation of 1BKR-PqsR^{310}

Purification of 1BKR-PqsR^{310} gave substantially better yield compared to the smaller truncate. Elution from HisTrap HP gave rise to two large and isolated peaks. The first larger

peak eluted between 80 – 195 mM imidazole and the second peak eluted later at 260 mM imidazole. Unexpectantly the first, larger peak did not contain a band corresponding to the truncate and appeared to contain a heavy abundance of two unknown proteins with apparent sizes of 70 and 25 kDa which may represent *E. coli* chaperones DnaK and GrpE respectively. Material from the second peak was dialysed overnight and loaded onto a Heparin column eluting at a similar salt concentration as the full length protein (280 mM). It should be further noted that unlike the full length, a doublet banding pattern is not observed, suggesting the minor breakdown product is occurring at the C-terminal. As shown by Figure 6.27e the protein eluted at 63.8 mL corresponding to an apparent M_r of 156 kDa which represents a smaller than expected volume (tetramer weight of 196 kDa). This suggests that without most of the disordered C-terminal the protein adopts a more compact arrangement.

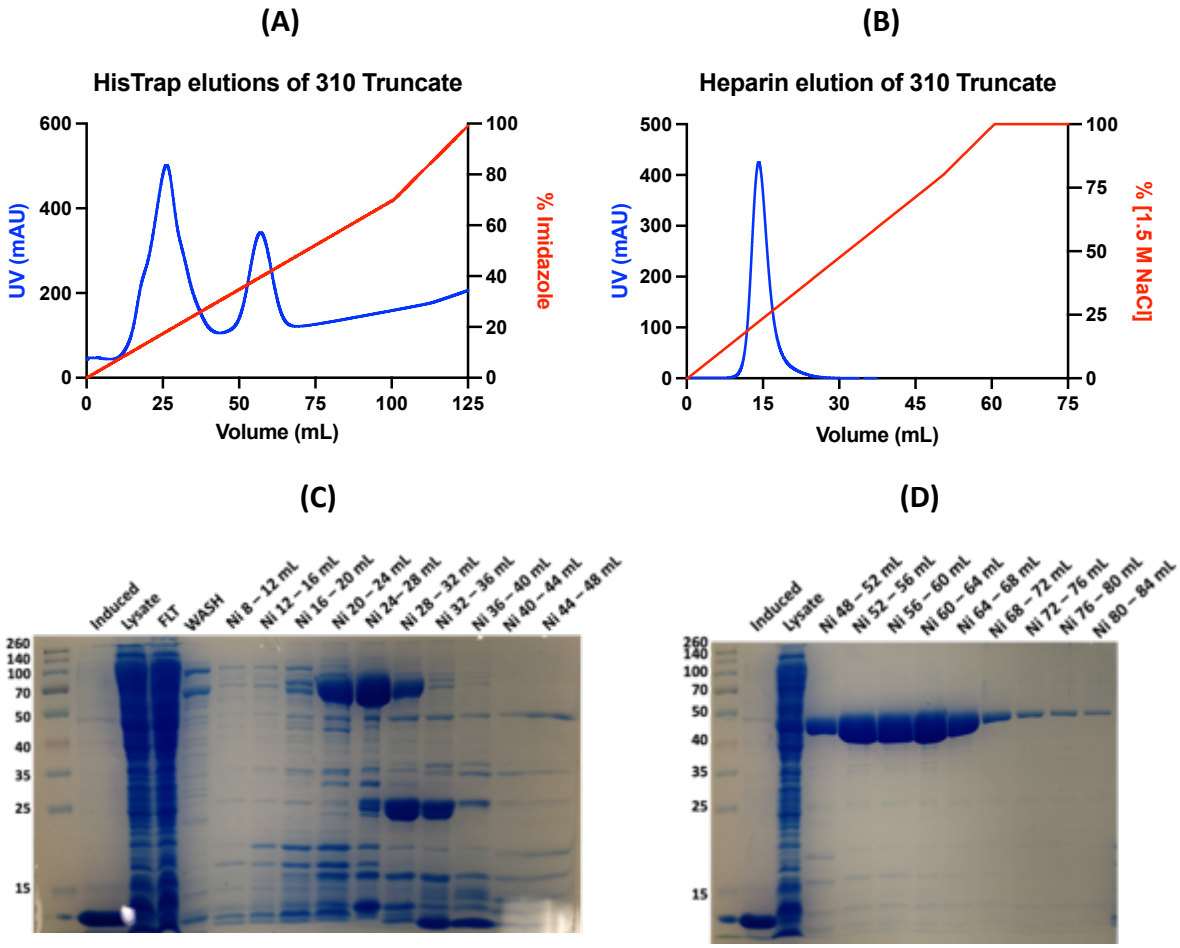

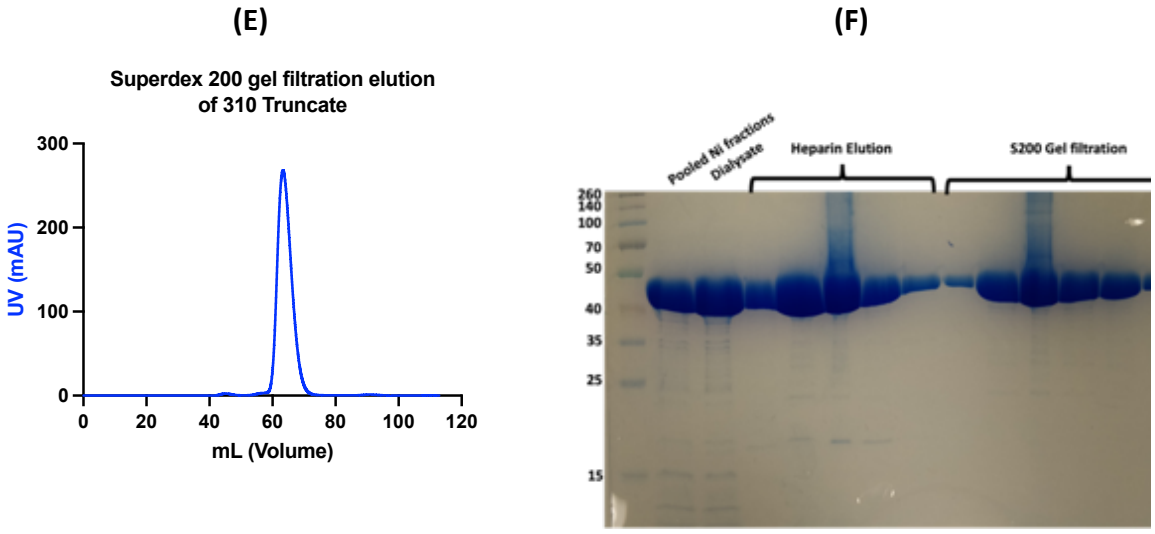

Figure 6.27. 1BKR-PqsR^{310} purification (A) Tandem HisTrap (10 mL) elution with two distinctive peaks **(B)** Chromatogram of truncate eluting from a 5 mL Heparin HP column **(C)** SDS PAGE showing earlier HisTrap fractions corresponding to first peak. Strong band in the induced lane ~10 kDa is Lysozyme used to digest cells during lysate preparation. **(D)** SDS PAGE showing later peak composition with an intense band of the same size as the induced control lane **(E)** Gel filtration of truncate using a Superdex 200 16/60 column. **(F)** SDS PAGE showing final sample purity (>95%). Some smearing is observed due to high concentration.

Interestingly, this truncation showed no *de novo* crystal formation in any of the tested crystal screens including Nucleix, Morpheus, LMB and INFAC screens. However, in combination with seeds (generated from full length crystals) crystal formation occurred in both custom INFAC screens with similar appearance to the full length (plate-like habit) (Figure 6.28). As shown in Figure 6.28C & D the diffraction was of resolution lower than 10 Å with axis B enlarged compared to the non-truncated protein.

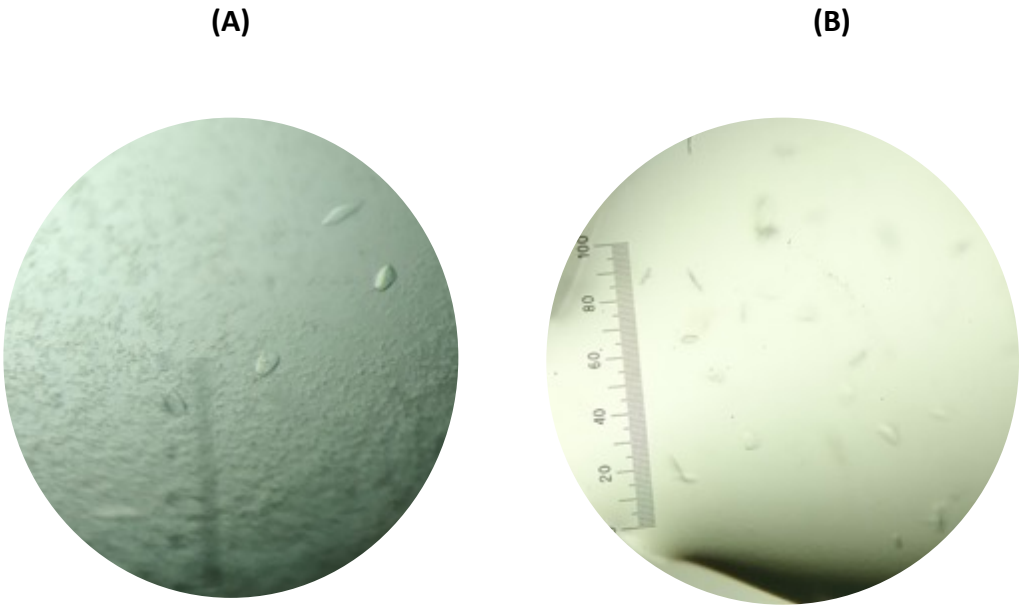

(C)

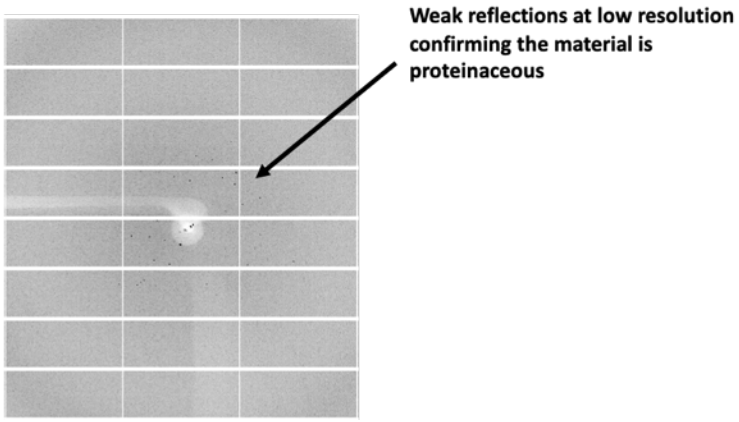

(D)

Space group	C 2 2 2_1
a ,b, c (Å)	131.77, 590.82, 185.22
α, β, ɣ (°)	90, 90. 90
Volume ($Å^3$)	1.44 x 10^7

Figure 6.28. Representative crystals produced from $PqsR^{310}$ MMS screening. **(A)** Crystals grown from 1.4M lithium sulphate, 0.05M cacodylate (pH 6) and 0.1M ammonium acetate. **(B)** Condition containing 1.2M lithium sulphate, 0.05M cacodylate (pH 6.5) and 0.1M potassium chloride. Drop conditions for both are 600 nL containing 100 nL seed stock with a protein concentration of 1.6 mg/mL. **(C)** Low resolution diffraction image observed on DLS i24 **(D)** Table of crystal parameters determined by ISPyB plug-in.

6.7 1BKR-PqsR SER variants

In chapter 6 a SER campaign was undertaken to generate new crystal forms and improve resolution for antagonist determination. The most successful of these variants included S123C which displayed the highest number of hit conditions and 180-185 loop variant (DR variant hereafter) producing a new crystal form with superior resolution. Given the success of these variants they were both applied to the full-length receptor to improve crystal quality. Both variants were successfully expressed as judged by SDS PAGE (data not shown).

6.7.1 S123C variant purification

The S123C 1BKR-PqsR was successfully captured from a HisTrap HP column but at a lesser yield (judged by UV AUC) compared to the progenitor construct. The protein eluted largely in a single peak starting at 145 mM imidazole. The resultant product was pure except for a minor HMW contaminant with a size on SDS PAGE of ~70 kDa. Furthermore, PAGE shows a doublet banding pattern resembling the wildtype construct. The material was further purified by Heparin chromatography with the desired protein contained within the second larger peak eluting at 480 mM NaCl. Purification by gel filtration gave an elution volume of 62.84 mL corresponding to an apparent M_r of 169.8 kDa (Figure 6.29d). This is smaller than

the progenitor construct suggesting that disulphide formation allows for a more compact quaternary arrangement.

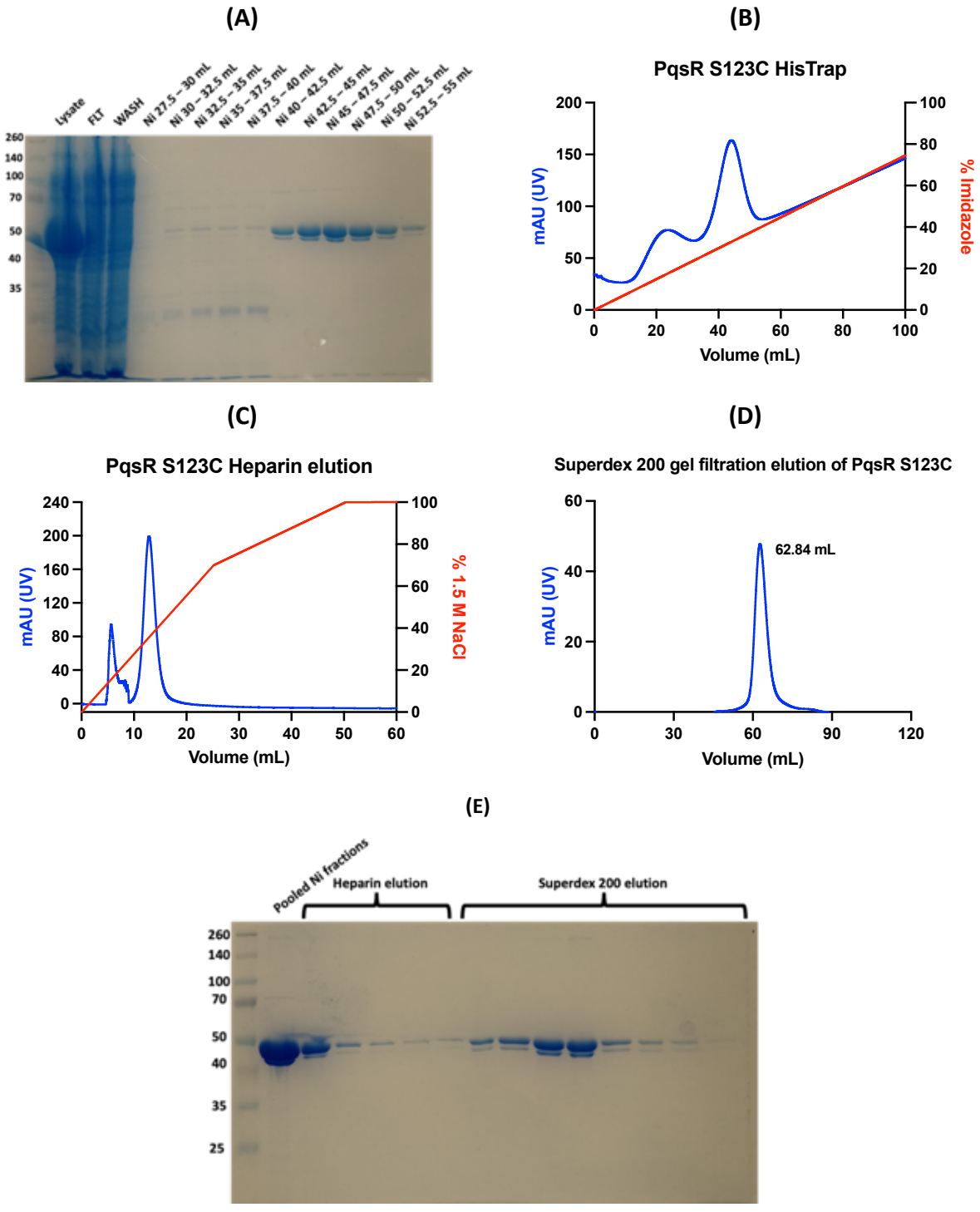

Figure 6.29. Purification of PqsR S123C (A) SDS PAGE showing HisTrap elution. Doublet banding pattern from SDS PAGE is visible. **(B)** HisTrap elution with a first non-specific peak followed by the desired material contained in the second larger peak. **(C)** Heparin chromatogram showing elution using 1.5 M NaCl. Desired material was contained in the second peak. **(D)** Gel filtration using a Superdex 200 column with an elution volume corresponding to a more compact tetramer **(E)** SDS PAGE showing final purity of the sample is >95%.

The protein was entered into crystallisation trials, biased towards the original cacodylate and lithium sulphate crystal conditions (INFAC, Nucleix & MIDAS) with and without the 488 antagonist. No screen produced any crystalline material and upon incubation with 488 amorphous precipitate was observed.

6.7.2 Loop mutant (180 – 185) insolubility

Purification of the loop mutant proved difficult yielding no enrichment from a HisTrap column (data not shown). This differs from the LBD which could tolerate this mutation and demonstrated superior stability with respect to the wildtype sequence. Given this variant favoured a different dimeric arrangement (described further chapter 6) it is likely this is not the arrangement favoured by the full-length receptor.

6.8 Binding to PQS

To determine the feasibility in using PQS as a ligand for co-crystallisation, an ITC experiment was conducted to derive thermodynamic binding parameters. Other studies have indicated that PQS binds to PqsR with an affinity of 1.2 ± 0.3 μM (as determined by FRET titrations at 450 nm). For titration 200 μM PQS was injected into a sample cell containing 20 μM 1BKR – PqsR supplemented with 4% DMSO co-solvent to maintain AQ solubility. The resultant isotherm, shown below in Figure 6.30 show an exothermic release of heat but upon integration showed no indication of a sigmoidal relationship (very low C – number). As such stoichiometry and binding parameters are unreliable. A similar observation was made when PQS was titrated into the ligand binding domain[286]. Non-saturation could be accounted for by a very low K_D that requires much higher concentrations of sample and titrant to accurately determine binding or that the protein is unstable in the presence of AQ ligand.

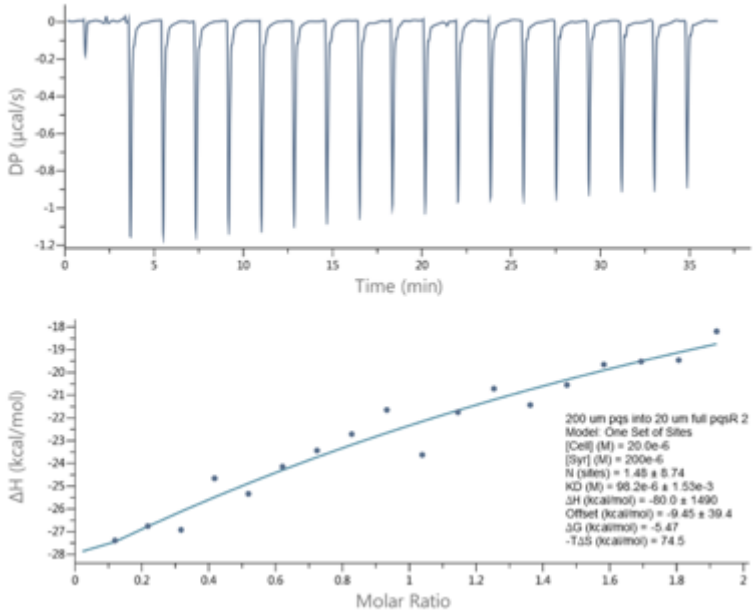

Figure 6.30. ITC data for titration of PQS (200 µM) into 1BKR-PqsR (20 µM). Top panel shows raw ITC showing exothermic release of heat upon injection. Bottom panel shows the isotherm produced by the integration of heats. Data shows very low C value and as such is not reliable.

6.9 1BKR-PqsR – DNA complex characterisation

Regulatory proteins can crystallise in isolation or as a larger complex with their corresponding DNA. Recommended strategies to generate complexes are to choose a minimum required binding sequence and increase length to find an optimal sequence[287]. For PqsR, the 13 bp LysR-box palindromic sequence, present in the *pqsA* promoter was chosen due to previous studies highlighting it to be essential for binding[158]. To determine if the sequence bound effectively to the protein a series of gel filtration experiments were run to determine if a complex would readily form. Injections of 50 µL containing 29 µM 1BKR-PqsR with differing concentrations of LysR box duplex showed that the construct had no apparent affinity for the sequence due to a lack of comigration (Figure 6.31). Considering earlier studies suggested that binding required PQS the same experiments were carried out in its presence. However, after 1 hour of incubation and subsequent clarification no PqsR had remained in an unaggregated state as shown by its absence in the UV trace. This explains the poor ITC result as clearly the presence of PQS is inducing aggregation that would mask the signal from binding. Additionally, a lack of DNA binding may be due to steric hindrance from the 1BKR tag as it is fused to the DNA binding domain.

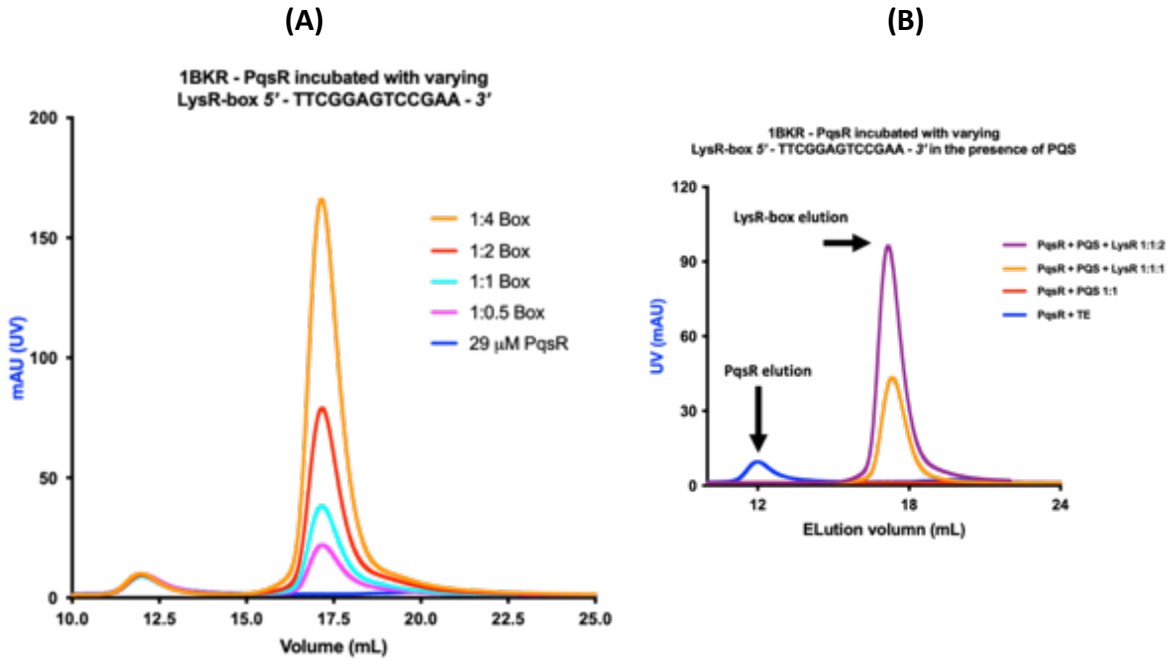

Figure 6.31. Analytical gel filtration with different ratios of PqsR and LysR-box (A) 29 µM 1BKR-PqsR was injected onto a Superdex 200 10/300 column (24 bed volume) with a flow rate of 0.5 ml/min. Varying concentrations of LysR box were incubated with PqsR for 1 hour prior to loading. Binding would be expected to cause an increase in absorbance for the PqsR sample at 12 mL. At all concentration ratios tested the migration and area under the curve for PqsR elution remains unchanged. Absorbance was monitored at A280 corresponding to the absorption maxima for proteins with overlap for DNA detection. **(B)** Gel filtration experiments with PQS pre-incubation. In the presence of PQS the protein does not elute at the expected 12 mL volume suggesting that the sample had been entirely precipitated by PQS prior to centrifugation and sample injection. Controls for both A and B are PqsR sample loaded without additional components and is shown on both plots by a blue line.

6.10 Assessing sample folding by SAXS

To assess the folding of 1BKR-PqsR, solution scattering SAXS was performed. A sample of PqsR was buffer exchanged by SEC on a Superdex 200 10/30 into a buffer consisting of 50 mM Tris – HCl (pH = 8), 200 mM NaCl and 1 mM TCEP. The additional TCEP supplementation was to abrogate radiation damage using data collection. At a relatively low sample concentration of 0.4 mg/mL, to inhibit aggregation, scattering data was collected. Examination of the Guinier plot showed the sample, despite low concentration, was still prone to aggregation as the plot gave a poor linear fit across a wide range from low to high q. To ameliorate the poor fit only data from low q was used to determine values such as R_g using the expected <1.3 cutoff for a globular protein. The R_g was determined to be 151.12 Å and Dmax 327.8 Å. Examination of the Kratky plot showed the protein possessed a globular arrangement but given the shallow gradient back to baseline is indicative of flexibility. Attempts to calculate molecular weight gave a value of 445 kDa, significantly larger than

that determined by gel filtration. A potential explanation is that the analysis has been affected by a larger than expected Porod volume likely due to PqsR possessing domains with a high degree of uncorrelated flexibility. Attempts to generate an *ab initio* reconstruction yielded a relatively flat, elongated surface (not shown). Additionally, negative stain data collected by Dr Maurer showed globular particles that was consistent with the globular folding indicated by the Kratky plot (detailed in Appendix 9.11).

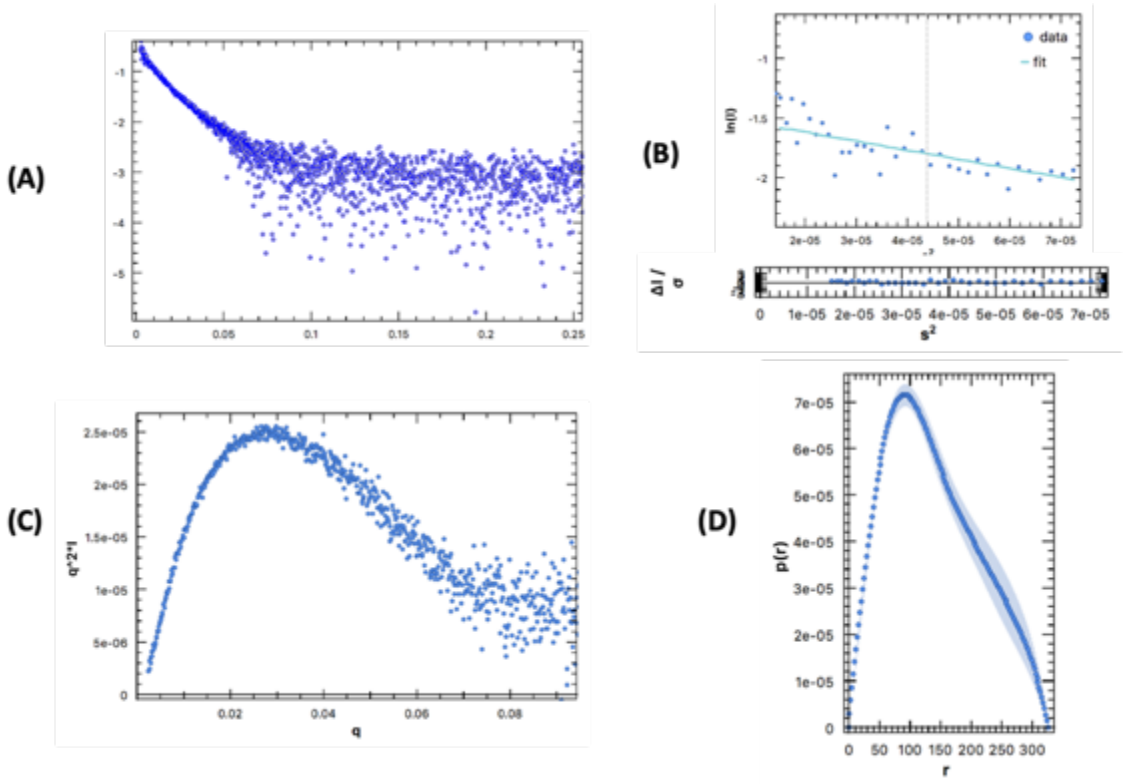

Figure 6.32. SAXS analysis of PqsR (A) SAXS profile of FL-PqsR as a function of scattering intensity against angle ($Å^{-1}$) **(B)** Guinier fit with residuals shown underneath. **(C)** Dimensionless Kratky plot showing sample has a globular fold **(D)** P(r) plot with skew towards the low r suggestive of an elongated arrangement.

6.11 Identification of alternative ligands for co-crystallisation

Crystallisation can often be aided by the presence of bound ligands that can induce favourable conformation changes. This has been reported to improve crystallisation with respect to resolution and has been shown to improve protein stability[287]. The latter is often observed in other classes of DNA binders including LuxR type regulators such as *P. aeruginosa* LasR that can only be stabilised upon addition of a suitable AHL[288]. As Pseudomonal ligands PQS and HHQ were incompatible with purified protein, causing heavy precipitation, and in the case of PQS entirely aggregating the sample. Examination of the literature suggested that Burkholderia spp. AQ ligands may be a suitable alternative.

Burkholderia favours methylation at C3 position and in a previous investigation was found not to influence phenazine production – purportedly controlled by PqsR[289]. Analysis of the top three methylated Burkholderia products (pictured in Figure 6.32a) with a *P. aeruginosa* biosensor highlighted that Me-HHQ did possess PqsR agonism and activated the *pqsA* promoter. Curiously *Burkholderia* ligands possessing an unsaturated C2-C3 linkage failed to produce a response which suggests the AQ ligand selectivity is influenced by the rigidity of the alkyl chain. To test if virulence could be controlled by Me-HHQ a pyocyanin assay was performed showing that although an agonist the molecule was unable to stimulate pyocyanin production suggesting the molecule acted more in a HHQ manner than PQS. Upon addition of equimolar Me-HHQ ligand to 1 mg/mL of purified 1BKR-PqsR the protein precipitated rapidly and after clarification by centrifugation the resultant protein concentration, measured by UV absorption (with the same volume of ligand added to a blank), had been depleted to < 0.1 mg/mL and was therefore unsuitable for further work.

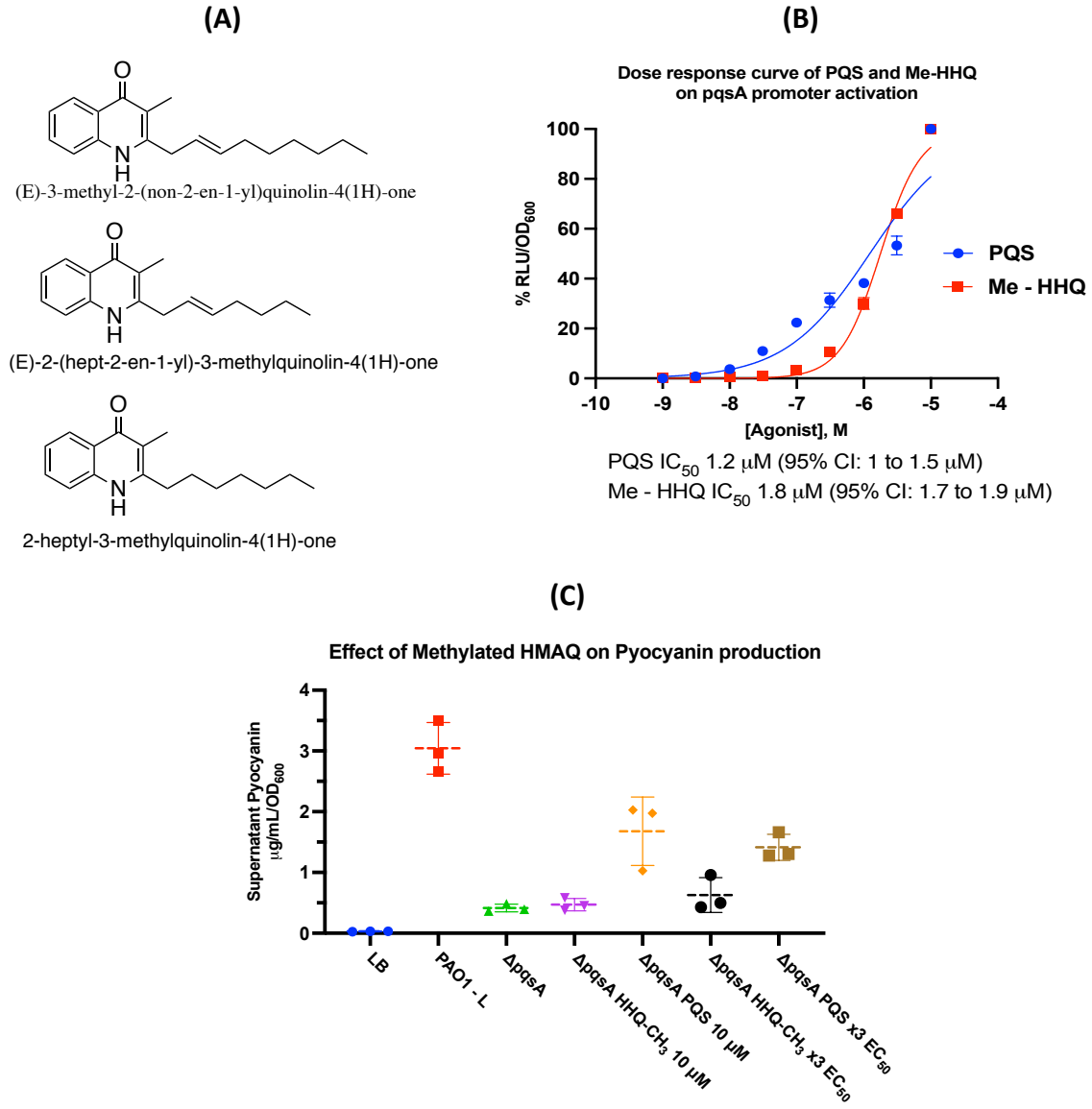

Figure 6.33. Effect of *Burkholderia* spp. AQs on *P. aeruginosa* (A) Molecular structure of three Burkholderia ligands tested. 2-heptyl-3-methylquinolin-4(1H)-one referred to as Me – HHQ. **(B)** EC_{50} determination using PAO1 – L *ΔpqsA* CTX::P_{pqsA}-*lux*. AQs added to 200 µL cultures monitored over 16 hours. EC_{50} fitted to a variable slope of response (normalised to maximum observed for each AQ) using PRISM with 95% confidence intervals given. Neither 3-methy-2-(non-2-en-1-yl)quinoline-4-one or 2-(hept-2-en-1-yl)-3-methylquinolin-4-one acted as agonists. **(C)** Pyocyanin quantification from 10 mL cultures grown for 16 hours supplemented with AQ or DMSO solvent to a concentration of 0.1%. Data is representative of biological triplicate cultures. PAO1-L and the isogenic Δ*pqsA* mutant were used as controls.

6.12 Stabilisation of the protein by thermal shift assays

To further stabilise the receptor a series of thermal shift assays were conducted to ascertain whether buffer conditions and additives could be successfully applied to optimise the sample for crystallisation. T_m determination was complicated by the presence of two distinct

peaks observed in the melt curve (biphasic). It was surmised that the higher and lower melting temperature peaks corresponded to the tag and PqsR respectively. In some instances, the peaks were too close to fully resolve the melting temperature of the more stable tag. T_m increases linearly with respect to salt concentration with ammonium sulphate giving the steepest gradient (Figure 6.34a). This could be due to the sulphate anion possessing similar chemical features to phosphate with respect to polarity and geometry. The hypothesis was further supported by observations that other sulphate containing salts including lithium and magnesium gave similar positive linear relationships. Greater stability was observed towards lower pH's irrespective of salt concentration (either physiological 150 mM or high 250 mM) suggesting that the protein was most stable with a positive surface charge. Sugars were effective in increasing stability whereas conventionally used cryoprotectants glycerol and ethylene glycol destabilised the protein. Solvents (typically used for ligand addition) and reducing agents were destabilising. Addition of ligand 488 caused significant destabilisation and addition of Me-HHQ gave a distorted melt curve (data not shown). Triton X-100 and tween 20 were attempted but these gave spurious signals due to the hydrophobic nature of the detergent.

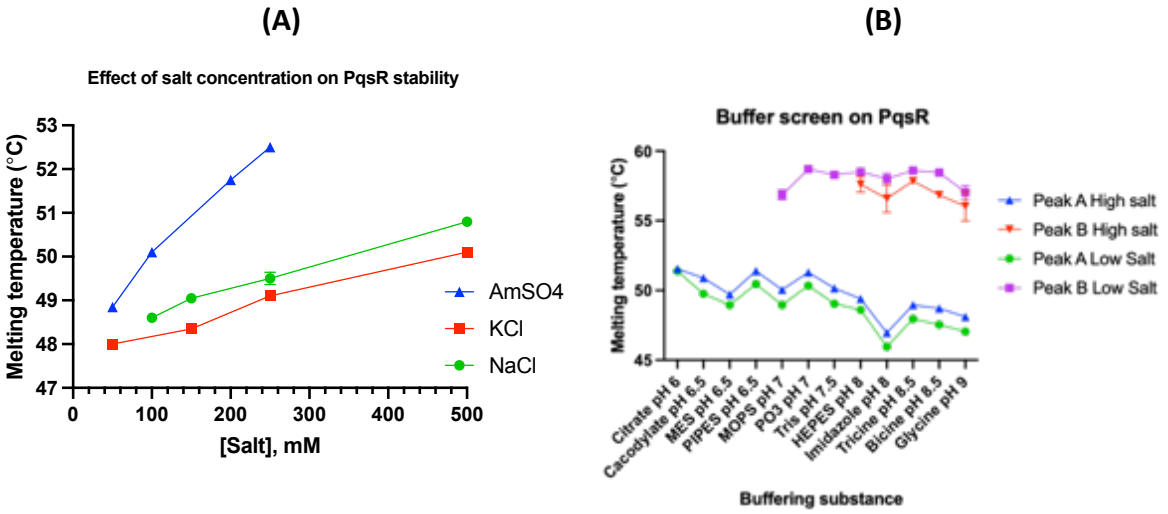

(C)

Regent	Effect (+/-/)	Conc. dependent
Trehalose	+	✓
Glucose	+	✓
Ethylene Glycol	-	✓
Glycerol	-	✓
Gua-HCl	-	✓
Urea	-	✓
DMSO	-	✓
Ethanol	-	✓
TCEP	-	ns
DTT	-	ns
Na_2SO_4	+	✓
Am Acetate	+	✓
Na Acetate	NA	NA
K Acetate	NA	NA

Figure 6.34. Thermal shift melting analysis on PqsR with respect to buffer composition (A) Melting T_m attained from NAMI analysis of melt curve data from Biosystems 7500 instrument with different salt gradients. **(B)** Effect of buffer pH on T_m . Peaks A and B refer to lower and higher melting points respectively. **(C)** Table summarising the effect of additives on PqsR stability. For concentration dependency ✓ indicates a relationship was observed, NA = no affect observed, and ns shows the concentration dependency was not examined.

Despite a higher stability, exchanging the protein into an optimised buffer consisting of 50 mM sodium citrate (pH = 6), 200 mM ammonium sulphate and putting down trays with the INFAC screen failed to reproduce the plate-like habit.

6.13 Attempts to phase diffraction data

6.13.1 Analysis of diffraction data for 1BKR-PqsR

The highest diffracting crystal (pictured in Figure 6.35) adopting the plate habit was examined on i24. Diffraction limits were extended by applying ellipsoidal data cut offs (STARANISO) with axis limits determined as 3.85, 8.03, 4.15 Å for a*, b* and c* respectively. The plots showing intensity distributions for these axes can be found in the Table 6.1.

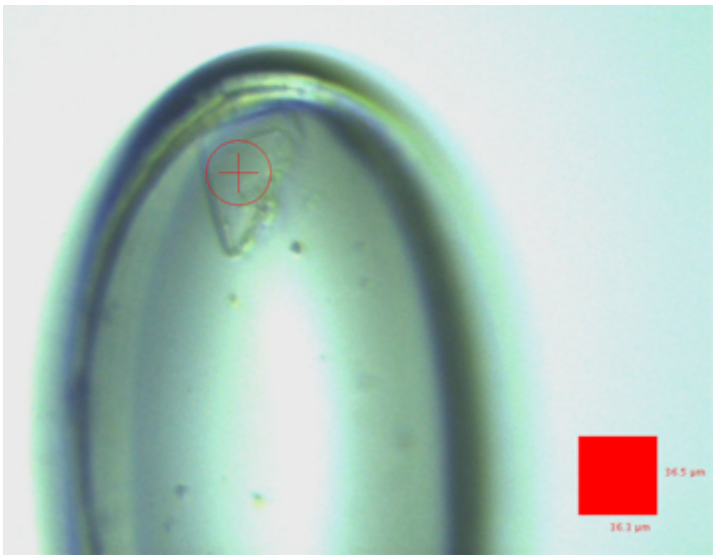

Figure 6.35. Image of 1BKR-PqsR crystal in cryoloop. Stacked-plate crystal morphology from drop seeded with microcrystals. Photo captured on beamline i24. Crystal is approximately 50 µm x 50 µm. An accurate determination of depth is not possible.

Data collection		Reciprocal plane plots
Beamline	I24	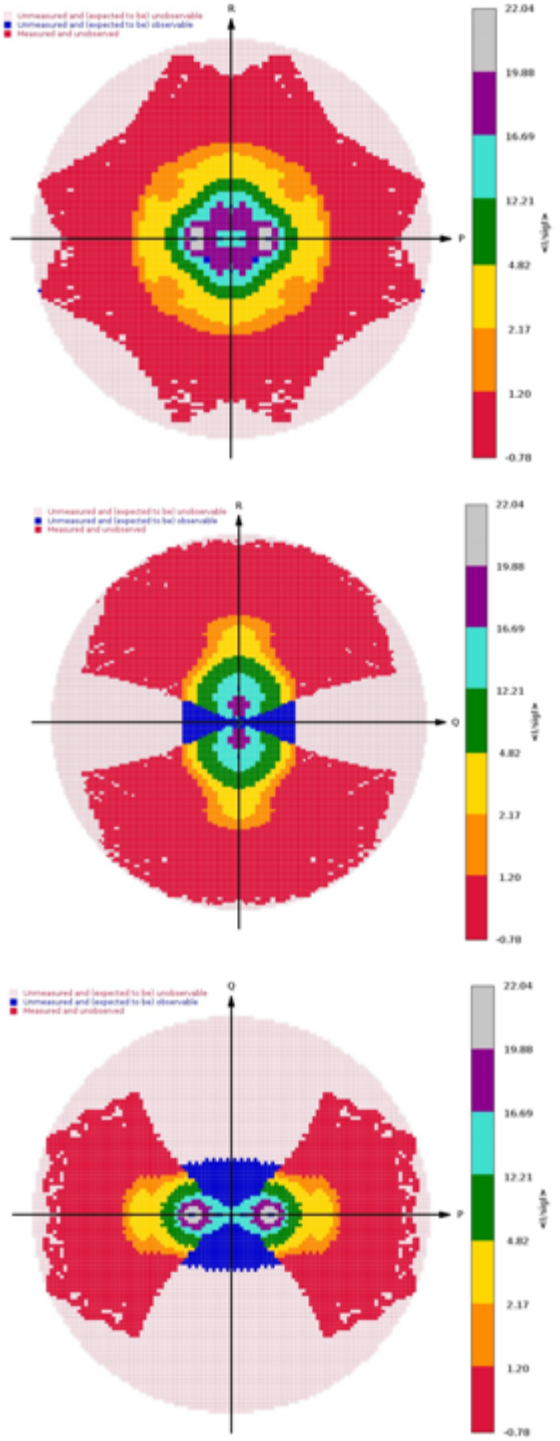
Wavelength (Å)	0.9686	
Space group	$C222_1$	
a ,b, c (Å)	129.6, 191, 185.3	
α, β, γ (°)	90, 90, 90	
Resolution	107.22 – 4.1	
No. of unique reflections	8510 (426)	
I/Sig(I)	4.8 (1.4)	
CC1/2	0.983 (0.552)	
Completeness (spherical)	46.2 (13.5)	
Completeness (elliposoidal)	84.9 (63.4)	

Table 6.1. Data collection statistics for 1BKR-PqsR crystal diffracted on i24. Right column shows reciprocal plane lots describing intensity with respect to direction. Table statistics were outputted by STARANISO.

The space group was identified as C 2 2 2_1 with unit cell dimensions determined as: A = 129.6 Å, B = 191 Å, C = 185.3 Å and all angles at 90°. As shown by the plot below the unit cell

volume accounts for a likely 4 - 5 copies of the protein with associated solvent contents of 56.38 and 45.47% respectively. Given the relatively poor diffraction quality (a pathology of high solvent content crystals) the former is more likely.

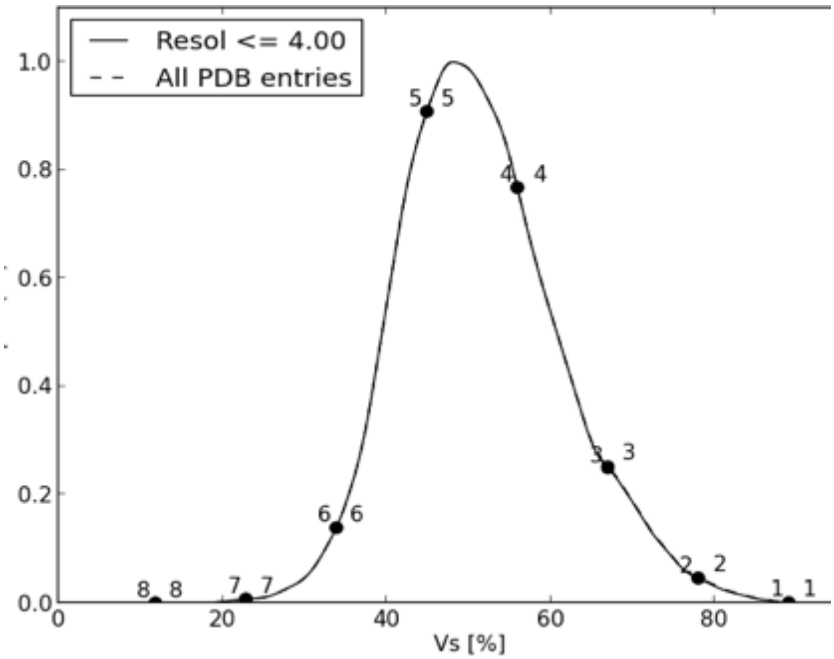

Figure 6.36. Matthews probability distribution. Probability of a given number of macromolecules by solvent content (%). Figure produced by the Rupp web server calculator [290].

6.14 Molecular replacement trials for diffraction data

6.14.1 Phasing 1BKR-PqsR by molecular replacement

A series of phasing trials were conducted using MolRep and Phaser[248] using the ligand binding domain (4JVC), 1BKR (tag) and linker helices from other receptors. No phasing attempt yielded a solution with sufficiently interpretable phases. A wider search using MrBump was attempted but also failed to find a convincing solution. To ensure the sample was not the product of a contaminant protein sequence independent phasing was attempted using SIMBAD[291] to search through known contaminant and lattice databases. No solution was identified (results detailed in Appendix 9.10).

6.14.2 Phasing with *de novo* model

As homology models identified by MrBUMP and manual phasing failed to identify a suitable model a series of *ab initio* models were generated using the Robetta server implementing the RoseTTAFold methodology[292]. Given that the method is informed from the PDB only the

sequence of PqsR was provided and not the fusion as the linker and restrains would likely give a less accurate prediction. 5 models were generated with a confidence score of 0.76. The models were aligned which highlighted the predicted solutions were highly convergent with only the C-terminal region possessing substantially diverged positions. In models 1 and 2 the termini were predicted to fold over the LBD whilst in the rest of the models the termini fold against the long linker helix. Subsequent phasing attempts however failed to find a reasonable solution with the calculated LLGs falling below 100 (ranging from 31-83) and the signal-to-noise TFZ score less than 7. Additionally, neither solutions produced by Phaser or Molrep possessed a LBD dimeric arrangement nor was any additional density, which should the protein N-terminal was observed. Truncating the variable C-terminal to residue 292 also failed to produce an acceptable solution.

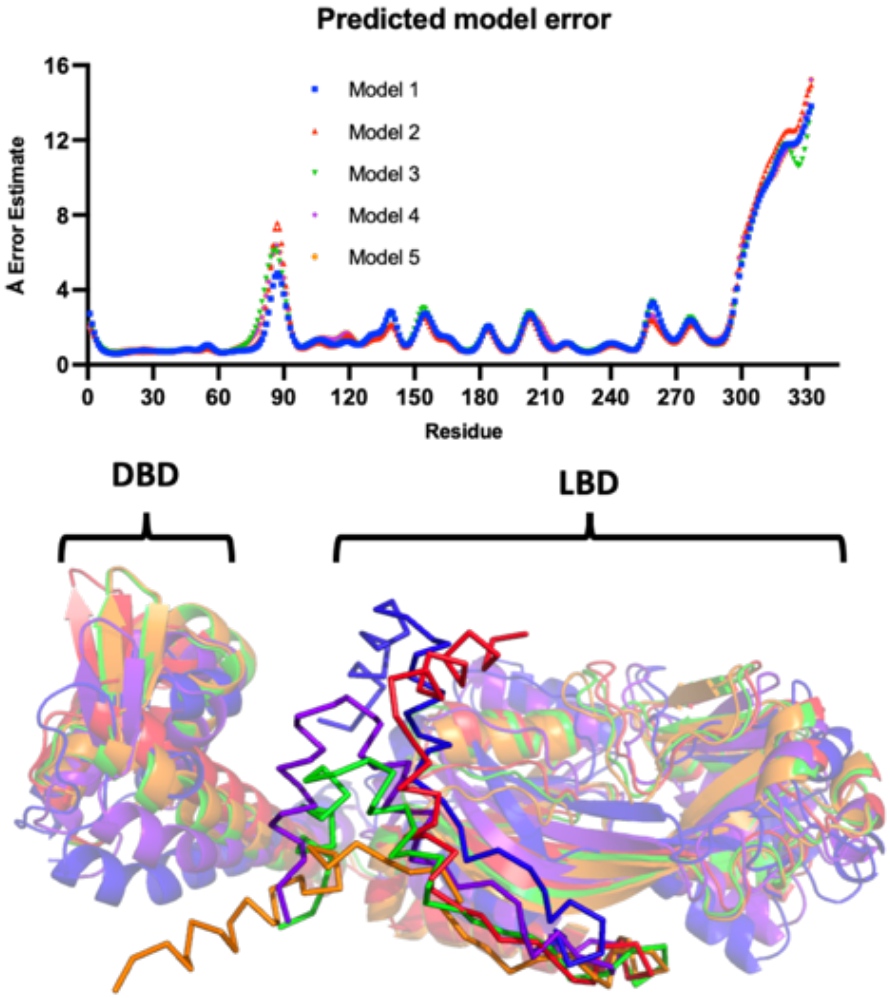

Figure 6.37. Models for phasing predicted by Robetta server. Predicted model error given above and 5 models aligned in PyMOL shown below with the same colouring regime. Converged regions depicted as a cartoon whilst diverged C-termini shown as thick ribbons.

6.15 *In vivo* complementation with 1BKR-PqsR protein

Given the observation that the protein does not bind strongly to the expected LysR-box and binding to PQS could not be established due to sample aggregation it was decided to determine if the 1BKR fusion protein could successfully complement a *pqsR* mutant. The sequence encoding the entire fusion was cloned into the complementation vector pME6032. Using a gradient of IPTG inducer it was apparent that the fusion construct retained no ability to complement the deletion and as such was deemed inactive (Figure 6.38). This was in contrast with the wildtype sequence in which increased inducer concentration corresponded to increased promoter activity. As shown in previous experimentation (Figure 6.25c) the truncations engaged less with the *pqsA* promoter compared to wildtype. The lack of promoter engagement is not surprisingly given the lack of LysR-box binding observed through analytical gel filtration experiments.

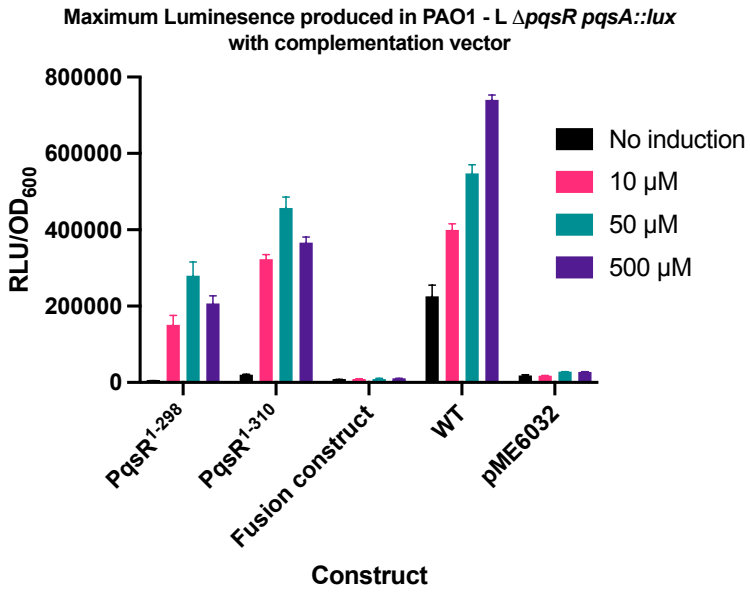

Figure 6.38. Complementation experiment on fusion construct. PAO1-L *ΔpqsR* CTX::P_{pqsA}-*lux* transformed with complementation constructs with empty vector pME6032 as a control. Data represents response at 10 hours (peak) monitored in a 200 µL volume of LB in a TECAN microplate reader. Wildtype sequence (WT) includes a C – terminal hexahistidine tag without linker sequence. 1BKR-PqsR fusion sequence is unable to active the pqsA promoter highlighting the protein is likely inactive. The truncations are less active compared to the wildtype sequence. IPTG inducer concentration given in the key on the right.

6.16 Discussion

When expressed without a solubility tag PqsR remains highly insoluble and other studies have found the protein to be recalcitrant to refolding efforts[133]. Analysis of N-terminal

residues suggest a significant degree of hydrophobicity which is likely to play a role in the insolubility. Additionally, a distinct lack of enrichment was observed when attempting to purify the protein from its native *P. aeruginosa*. Other studies, using AQ-based probes, have also reported a lack of PqsR enrichment from *Pseudomonal* lysate[293 133]. The authors surmised either a lack of abundance in the lysate, sequestration by DNA binding or instability was responsible. As we observed a band for PqsR after induction and lysis the latter explanation is supported. Future studies could attempt to increase stability using detergents or chaotropic agents. Other methods of lysis could also be experimented with in relation to both heterologous and homologous purification. Sonication and bead bashing both sheer DNA, albeit to different extents, which may disrupt DNA-protein interaction leading to protein insolubility. Preserving these interactions could improve solubility during the early stages of purification and was used on full length CbnR to stabilise the protein during His-tag cleavage[294].

Large N-terminal MBP LTTRs fusions have been shown to retain DNA binding in several studies including *X. axonopodis* LcrX, *Vibrio cholerae* LeuO and a single study used *in vivo* complementation to show activity of N-terminal fusions[259 295 296 297]. However, our study showed that an MBP fusion to PqsR produced aggregated material. This is not an uncommon occurrence for MBP solubilised proteins that can form 'micelle-like' aggregates with misfolded passenger protein[298]. In contrast the use of 1BKR as a fusion partner could produce monodispersed protein with the expected tetrameric arrangement but was unable to bind the expected DNA nor could complement the *in vivo* bioreporter[134]. The most likely explanation for this is steric hindrance from 1BKR impeding DNA interaction. If so, this could be optimised using more flexible linker sequences or varying linker length. However, as protein stability was compromised with a TEV sequence inserted care must be taken to ensure linker modification does not impede solubility.

Using the 1BKR fusion, crystals diffracting to 4 Å were grown but proved recalcitrant to several optimisation strategies. The SER strategy used in chapter 6 was successful in generating new crystal forms, but these mutants did not have the desired effect on the fusion. This suggests the premise that the LBD and full length crystal forms share crystal interfaces is likely false. A more extensive SER campaign with the receptor could be

productive in improving crystal resolution. In a similar vein other strategies could be employed to reduce flexibility including limited proteolysis of the sample. This has been reported to improve diffraction markedly and analysis of a large testing pool showed proteolysis was more effective on samples giving poorly diffracting crystals compared to proteins not producing any crystals [299].

Despite acquiring a crystal that diffracted to 4 Å phasing through molecular replacement failed to identify a suitable solution. Phasing was attempted with many homologs from the PDB as well as *ab initio* structures. The composition of the crystallisation drop may aid structural solution as the Arsenic from the cacodylate buffer can be used as an anomalous scatterer in SAD phasing possessing a K-edge (~1.04 Å) slightly higher than the commonly used selenium (~0.98 Å)[300]. Although the presence of arsenic carries the undesirable effect of increasing the crystals absorbed dose compared to lighter components[301].

6.17 Conclusions

- PqsR could be successfully solubilised using an N-terminally fused novel crystallisation chaperone 1BKR. Solubilised protein could be purified by a three step chromatography procedure yielding a monodispersed sample with an apparent M_r corresponding to a tetrameric arrangement.
- Basic shape determination using SAXS highlights the macromolecule is likely in an extended conformation but whether this is a function of the tag is not known.
- The fusion protein, although soluble was unable to form a complex with its cognate LysR-box sequence or PQS. The construct was also unable to complement a *pqsR* mutant in PAO1-L suggesting it was inactive.
- As intended the crystallisation chaperone permitted formation of crystals with a plate habit crystals that diffracted anisotropically to 4.1 Å. Diffraction analysis showed crystals to be orthorhombic with a $C222_1$ space group and cell dimensions A = 129.6 Å, B = 191 Å, C = 185.3 Å (volume of 4.5 x 10^6 Å^3).
- The disordered C-terminal, not observed in the LBD structures, contributes weakly to function. Observations made in purifying the truncation variants suggests the terminal residues contribute to protein stability.

- The most common *Burkholderia* spp. AQ, possessing a bioisosteric replacement of the C3 hydroxyl group with a methyl acts as a PqsR agonist with EC_{50} weaker than PQS and acting in a similar manner to HHQ i.e. pqsA promoter activating but does not impact virulence.
- Attempts to extract PqsR from *P. aeruginosa* lysate indicates the native protein is unstable out of the cellular environment.

7 Disruption of the PQS system via PqsA inhibition

7.1 Introduction

As demonstrated in chapter 3 PqsR antagonists have been examined extensively with several lead candidates found to significantly reduce virulence factor production such as pyocyanin and AQ biosynthesis. However, as demonstrated by several studies antagonists that are effective in bioreporters do not necessarily have concomitant activity with respect to virulence phenotypes and some antagonists are known to undergo inversion at high concentration[342]. Moreover, studies performed by colleagues have shown that successful PqsR antagonists that perform well in established lab strains including PAO1 – L and PA14 do not have as much efficacy in clinical isolates[235 205]. Exploitation of additional targets would therefore proof advantageous in combatting PQS mediated virulence.

PqsA, the first enzyme encoded in the Pqs biosynthetic operon, represents a good target for inhibitor development. A *ΔpqsA* mutant exhibits reduced virulence in a *C. elegans* infection model and murine immunological studies[343]. Several inhibitors of PqsA have been reported in the literature with various potencies. Methyl anthranilate was first assumed to be a PqsA inhibitor and reduced not only extracellular PQS levels but also the production of virulence factors such as elastase in a dose dependent manner[344]. Additional anthranilic acid derivatives were also identified as PqsA inhibitors, able to inhibit PqsA competitively and could reduce PQS levels in culture supernatant when used at substantially high concentration (1 mM)[314]. Further studies showed that high concentration of these derivatives were able to reduce virulence in mice but these were also treated with mM concentrations[345]. Rationally designed inhibitors were generated with the aim of creating a suitable non-hydrolysable mimetic of anthraniloyl-AMP, the product from the first half reaction performed by PqsA. This series built upon the previously reported success of similar sulfonyladenosine inhibitors used on other proteins in the ANL superfamily including MenE from *M. tuberculosis*[346]. However, despite very tight *in vitro* inhibition the inhibitors proved to have poor efficacy in cell-based assays and could only reduce AQ production when used at mM concentrations. This was attributed to poor cell penetration due to the highly charged adenosine moiety[347]. Attempts to improve cell penetration abated activity in most

instances highlighting that improving the anthraniloyl-AMP scaffold will be challenging. The chemical structures from each inhibitor generation are shown below is Figure 7.1.

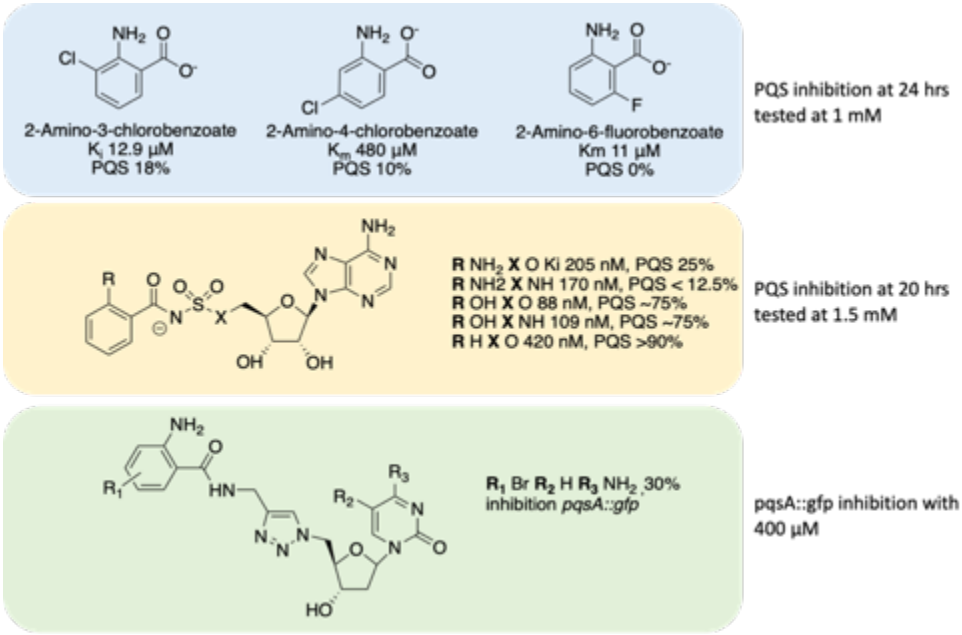

Figure 7.1. PqsA inhibitors described in the literature. Previous development of PqsA inhibitors tested on purified enzyme or against a bioreporter system. Inhibitors grouped according to study with overall impact given on the right.

7.2 Aims of this chapter

The goal of this chapter was to identify a PqsA inhibitor with a novel scaffold that possessed inhibitory activity in both enzymatic assays using purified enzyme and in whole cell assays (*in vivo*) to seed future medicinal chemistry development. To facilitate the work with purified PqsA, three constructs were created using His and Strep-II tags with the full length enzyme and a truncated form excluding the thioester domain shown in the literature to form crystals[219]. These are shown in Figure 7.2 below:

Figure 7.2. Constructs for PqsA protein purification. Constructs tagged at the C-terminal as described in the literature[314].

7.3 Results

7.3.1 Screening and hit compound identification

7.3.1.1 Purification of PqsA via a three step method

Full length PqsA was purified to >95% purity using a three step method utilising Streptavidin affinity chromatography followed by anionic exchange and gel filtration (Superdex 75). The protein was well expressed in BL21 (DE3) CP and eluted from a StrepTrap column with most of the sample eluting in the first 10 mL. Due to capacity limitations significant amount of the desired protein was found in the flowthrough which in some instances was reloaded and successfully eluted. Due to the amount of material (>25 mL) anionic exchange was used to concentrate the sample prior to loading onto gel filtration and eluted isocratically as a single peak. Gel filtration suggested the protein adopts a tight globular arrangement with the gel filtration volume corresponding to 33.1 kDa whereas the theoretical mass is 57.8 kDa. PqsA was previously highlighted to have significant hydrophobicity which may account for this discrepancy as column media interactions will retard migration (Figure 7.3a). This was further observed in the SDS PAGE showing the protein migrating faster than the expected 57.8 kDa likely due to suboptimal SDS binding. As shown in Figure 7.3c the gel filtration highlighted some ‘void’ volume showing that PqsA had propensity towards a small degree of aggregation.

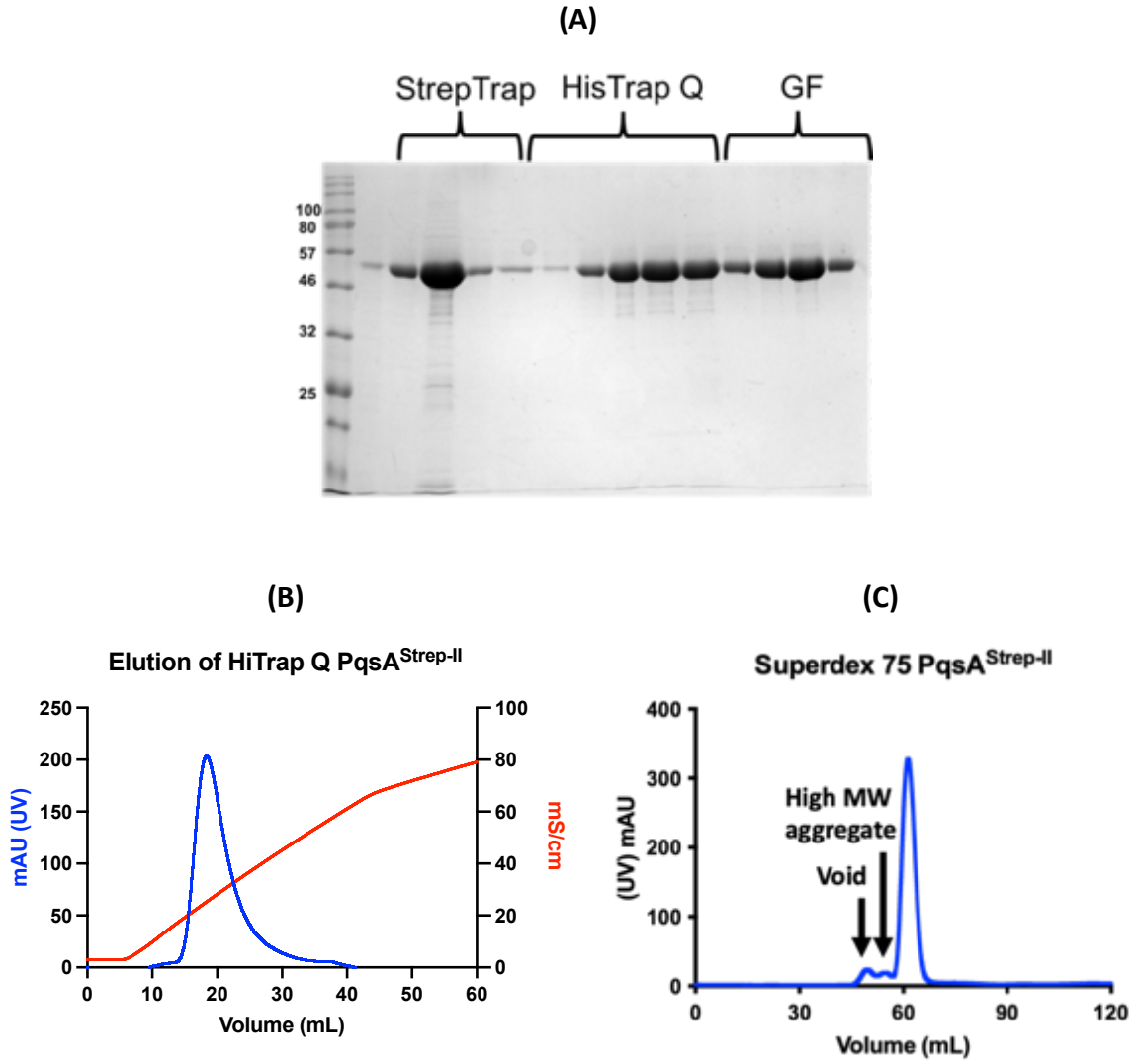

Figure 7.3. Purification of PqsA anthranilate ligase. (A) SDS PAGE showing purification process of the 57.8 kDa PqsA^{Strep} product. StrepTrap elution possesses some minor contaminants which are removed via anionic exchange and further purified by gel filtration. **(B)** Elution from HisTrap Q with a salt concentration of 22-34 mS/cm. Lack of asymmetry due to relatively high flow rate and large loading volume **(C)** Gel filtration chromatograph of PqsA^{Strep} showing separation of undesired aggregated material and HMW oligomer.

7.3.1.2 Activity measurements by absorbance

PqsA activity was tested by monitoring anthraniloyl-CoA product formation by absorbance at its known maxima of 365 nm[314]. As shown in Figure 7.4 the Km attained for PqsA^{Strep} was higher than that attained in previous studies although this was attributed to the different assay set up. It suggests that measurements taken in a microplate reader may not be as sensitivity compared to the larger pathlength found in a quartz curvette. Vmax could not be

calculated in terms of molarity over time due to a lack of a suitable synthetic standard for concentration interpolation.

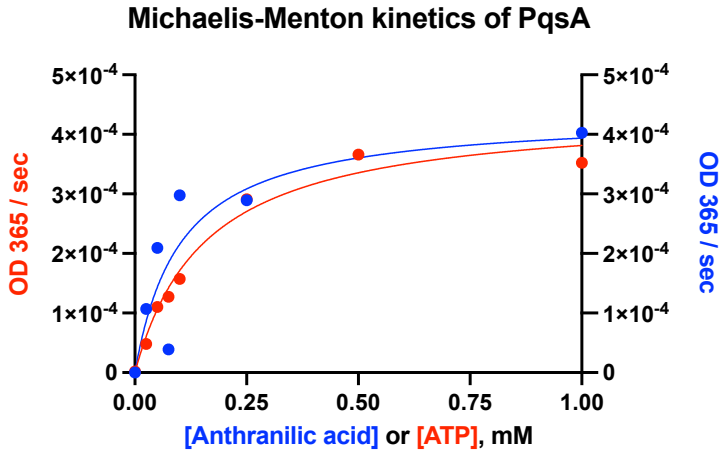

	K_m (µM)	V_{max} (ΔOD_{365}/min)
Anthranilic acid	101.6	0.026022
ATP	158	0.026502

Figure 7.4. Enzyme kinetic parameters from absorbance assay. PqsA Michaelis-Menton enzyme kinetics calculated in PRISM. Points are representative of n = 3 reactions averaged.

7.3.1.3 Screening with purified PqsA enzyme

Compound screening and additional experiments (7.3.1.3 & 7.3.2) were conducted by Chawan Kritsanaviparkporn and Siddharth Tyagi (BMedSci students University of Nottingham, School of Medicine) under my supervision and that of Dr Soukarieh. Dr Soukarieh performed initial docking and compound withdrawal from the NCC (detailed in Appendix 9.13).

Screening was conducted in 200 µL volume with a final DMSO concentration of 0.5% and inhibitor concentration tested at 50 µM. Anthraniloyl-sulfamoyladenosine (AMS) was used as a control inhibitor (re-synthesised by Sunny Wong. Molecular structure shown in Figure 7.1). In accordance with the literature this was confirmed to be a competitive inhibitor with respect to ATP with an apparent K_i of 1.093 µM (95% CI 0.72 – 1.64 µM). This is higher than previously reported (0.2 µM) which, again reflects the different assay set-up[347]. To confirm

previous observations that anthraniloyl-AMS was insufficient to inhibit PQS synthesis *in vivo* dose-dependency was tested on the PAO1 – L CTX::P_{pqsA}-*lux* bioreporter strain which showed no significant inhibition up to 10 µM (Figure 7.5b).

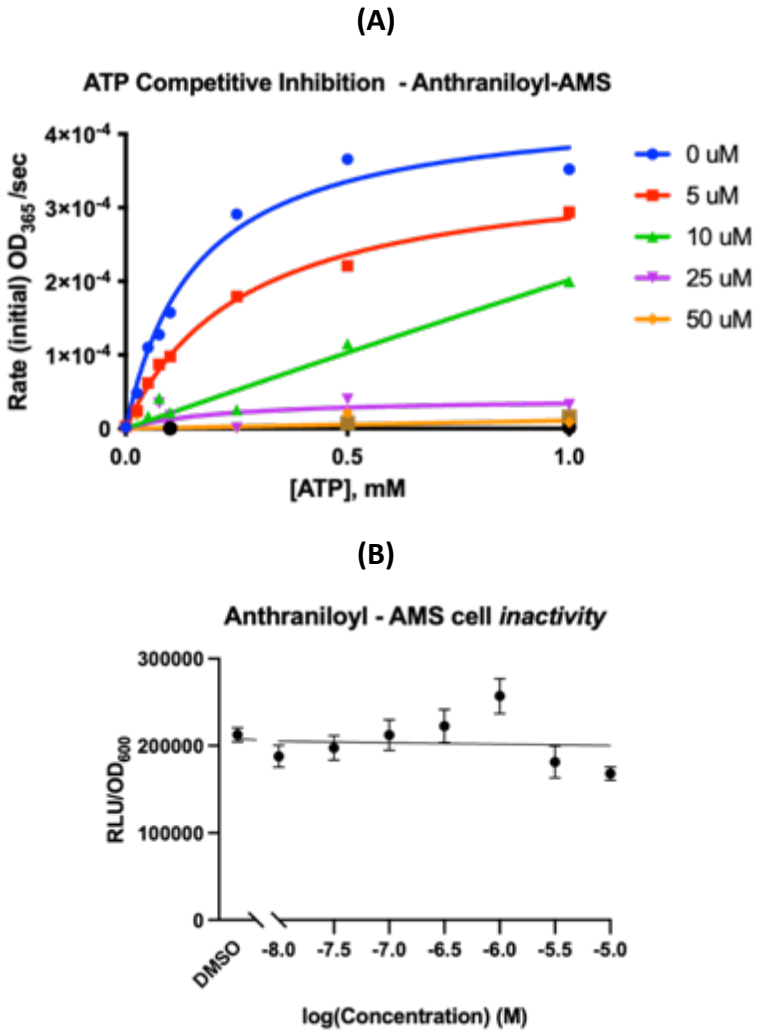

Figure 7.5. Anthraniloyl – AMS control compound testing. (A) Competitive inhibition mode confirmation by absorbance-based assay providing a Ki of 1.093 µM. Assay conducted in 200 µL in n = 3. **(B)** Lack of cellular potency observed in bioreporter assay. Results are representative of n = 3 technical repeats produced from the same starter culture.

A total of 496 inhibitor candidates were screened using an absorbance-based assay showing a total of 24 compounds that possessed activity below the 50% threshold. Of these 24, 9 showed significant inhibition by T-testing. This constitutes an overall hit rate of 1.8%. It was noted the assay had considerable variability which was likely due to a relatively low concentration of co-solvent used and the lack of detergent to abate compound driven aggregation[348]. The approximate Z factor[349] per screening plate was defined in the equation

below whereby σ_p & σ_n are the positive and negative control standard deviation and μ_p and μ_n the mean of positive and negative controls respectively.

$$Z\ Factor = 1 - \frac{3(\sigma_p + \sigma_n)}{\mu_p - \mu_n}$$

It was observed the apparent Z-factor between screening plates changed considerably ranging from negative values close to zero to 0.32. This suggested significant crossover between positive and negative controls. Z factor deterioration appeared to affect latter assays more suggesting the positive inhibitor degradation over time. This is plotted against reaction number in Appendix 9.14.

7.3.1.4 Re-screening by orthogonal PAO1-L CTX::P*pqsA*-*lux* bioreporter

Testing through the absorbance-based assay was insufficient due to reported variability so compounds that exhibited inhibition near the 50% threshold were spot screened against the PAO1-L CTX::P*pqsA*-*lux* bioreporter to determine if the *in vitro* "hits" were able to affect the pqs system. Re-screening showed that out of the 24 compounds tested at 10 µM only one, ZN8751275, was able to reduce *pqsA* expression to 50% (the original criterion set in the SENBIOTAR project detailed in chapter 3).

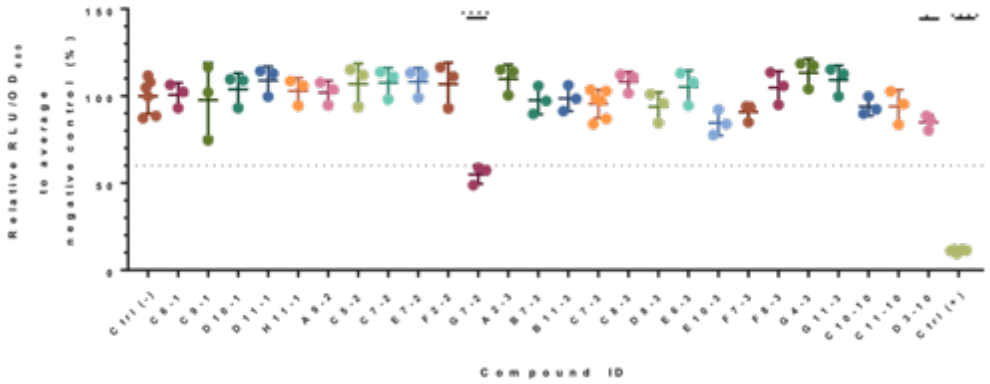

Figure 7.6. Re-screening of *in vitro* hits against PAO1-L CTX::P*pqsA*-*lux*. Summarised results of screening *in vitro* 'hit' compounds against the bioreporter strain at 7.5 hours growth. Negative control represents vehicle DMSO at 0.1% and positive is 10 µM AM204-004 previously characterised in chapter 3 as a SEN89 derivative. The NCC screening plate ID G7-2 is compound ZN8751275 from the ZINC database.

7.3.2 Discounting false positives through potential inhibition of the bioreporter *lux* gene products

The lux bioreporter can be susceptible to false positives in which the inhibitor of interest interferes with luminescence output. This possibility was discounted using a constitutively expressed *lux* (*luxCDABE*) cassette inserted into the chromosome of PAO1-L. As shown in Figure 7.7 no significant difference could be observed when cells were treated with 10 µM ZN8751275 compared to DMSO control. This shows the inhibitor does not directly influence the luciferase-based reporter system.

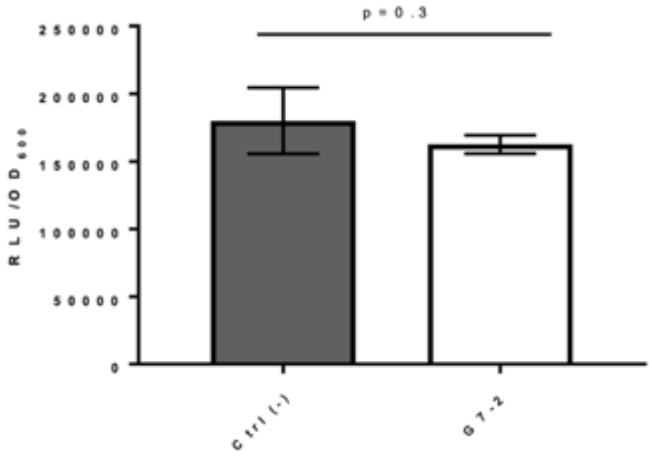

Figure 7.7. ZN8751275 does not influence luminescence. Luminescence produced by PAO1-L CTX::P_{km}-*lux* normalised by cell density (at 7 hours) when treated with 10 µM ZN8751275 or 0.1% DMSO vehicle. No significant difference is observed between test conditions.

7.3.3 Validation of ZN8751275 as a PqsA inhibitor

7.3.3.1 Enzyme Kinetics

To optimise signal to noise the plate microtitre volume was increased to 350 µL from 200 µL as used for screening. Response with inhibitor concentrations ranging from 0 to 75 µM with respect to anthranilate highlighted that ZN8751275 was non-competitive although due to inaccuracies at low concentration of anthranilate changes in K_m could not be fully determined. As shown in Figure 7.8 analysis varying ATP also showed non-competitive inhibition and due to lower affinity of ATP the K_m could be determined with greater accuracy.

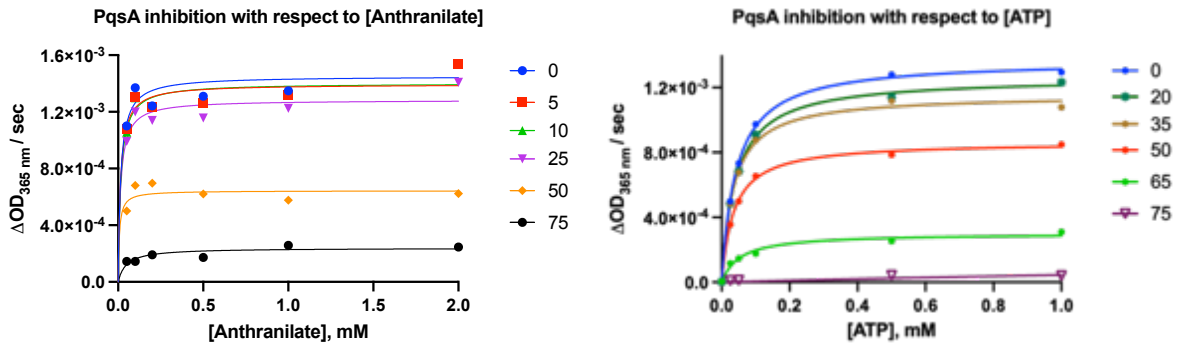

Figure 7.8. Non-competitive inhibition with respect to anthranilate and ATP. Each datapoint represents the mean of 3 reactions. 350 µL reactions containing 100 nM PqsA. Data plotted in PRISM and lines are fits to Michaelis-menton kinetics. Data points and lines are coloured according to [ZN8751275]. ZN8751275 acted non-competitively with respect to anthranilate and ATP.

7.3.3.2 IC_{50} determination

As kinetic analysis proved difficult to attain suitable parameters a simple dose dependency experiment was performed. Reaction velocity upon incubation with varying concentration of inhibitor up to 100 µM showed an IC_{50} of 16.57 µM, but the confidence interval was relatively wide, further underlining limitations with the absorbance based microtitre assay.

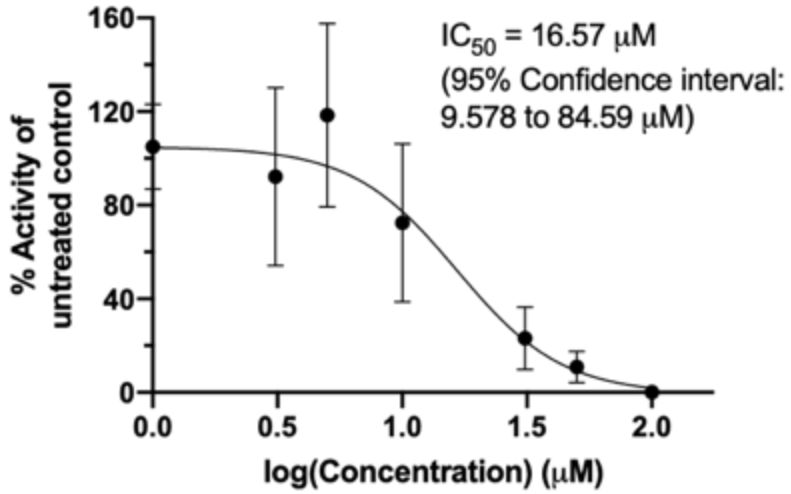

Figure 7.9. IC_{50} determination for ZN8751275 on PqsA activity. Enzymatic reaction of PqsA with ZN8751275 monitored by Δ absorbance over time in a 350 µL reaction volume. Data is representative of 3 independent enzyme reactions for each inhibitor concentration.

7.3.4 IC_{50} determination by LCMS/MS product analysis

To improve the certainty interval LC-MS/MS product quantification was employed which has the added advantage of isolating the product prior to measurement. The linearity of

uninhibited reaction was assessed by absorbance and shown to be well correlated for at least 10 minutes (Appendix 9.17). As such samples were incubated for 5 minutes after reaction initiation and resultant anthraniloyl-CoA quantified. As shown in Figure 7.10 the apparent IC_{50} derived from this experiment was poorer, at 47.92 µM, but the confidence interval was improved.

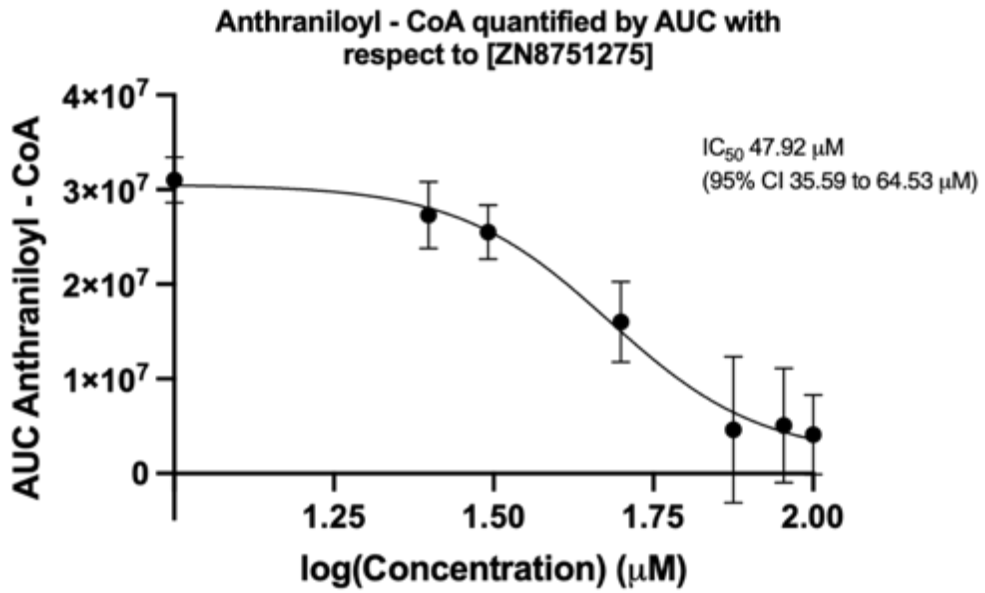

Figure 7.10. Enzymatic reaction of PqsA with ZN8751275 quantified by LC-MS/MS. Reaction stopped by denaturing organic solvent after 5 minutes. Data is representative of 3 independent reaction series with errors shown. Final co-solvent DMSO concentration at 7%.

7.3.5 Detecting binding by thermal shift

To determine if the inhibitor bound directly to PqsA a thermal shift assay was conducted. However, as noted in chapter 5, PqsA was not as amenable to thermal shift as PqsR and required high concentrations of ligand to invoke a response. At 250 µM ZN8751275 a 1°C shift in melting temperature was observed compared to the DMSO control. This was weaker than the change invoked by the same concentration of anthranilic acid. it should also be noted the melting curve shape was altered slightly suggesting the protein conformation changed or became locked into a different position.

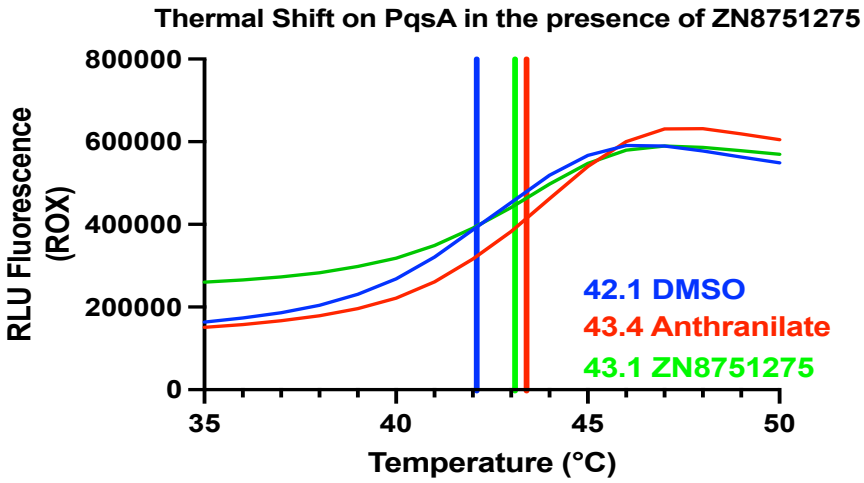

Figure 7.11. Thermal shift assay for PqsA in the presence of anthranilic acid and ZN8751275. Data is the result of three melting curves plotted in PRISM. Melting temperature, marked with on the x axis, and given as a colour coded line, determined in NAMI and in agreement with a Boltzmann sigmoid calculated in Prism. Addition of inhibitor increased melting temperature by 1°C compared to solvent-only sample.

7.3.6 Crystallisation attempts for PqsA

7.3.6.1 Failure to purify PqsA$^{1-399}$

Previous studies for PqsA gave suitable construct boundaries and crystallisation conditions. As shown in Figure 7.12 the construct expressed well but replicating the purification for the specified PqsA$^{1-399}$ construct proved difficult as it had very poor affinity for nickel and did not elute as a single peak. This required the use of anionic exchange to concentrate the fractions, but the resultant yield was extremely poor (< 0.5 mg) suggesting that the His tag was not accessible for efficient extraction from lysate and warranted modification.

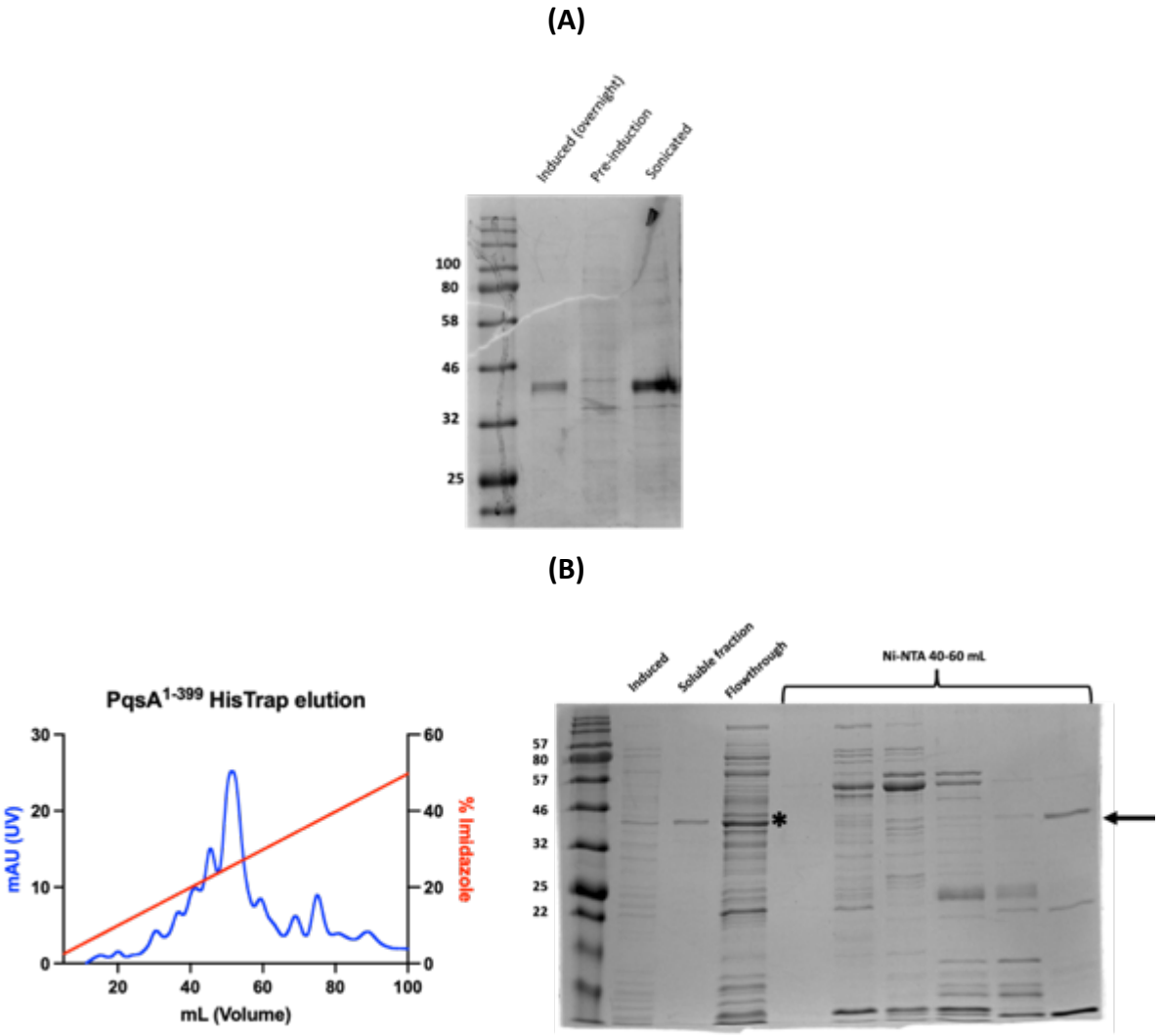

Figure. 7.12. Expression of PqsA$^{1-399}$ and purification trial (A) SDS PAGE showing successful expression of PqsA$^{1-399}$ **(B)** Poor binding to HisTrap HP column with several unresolved peaks seen on elution chromatogram. Most of the protein was found within the flowthrough as marked by an asterisk on the SDS PAGE. Isolated band for the construct is observed around ~60 mL but was in low abundance.

7.3.7 Use of a StrepTrap for PqsA$^{1-399}$ purification

As with the full-length enzyme a StrepTag (WSHPGFEK) was used as an alternative to the His tag. This gave reasonable yield from the StrepTrap column and was further purified and concentrated by anionic exchange on a HiTrap Q. The subsequent concentrated material was eluted from a Superdex 75 16/60 with an elution volume of 63.2 mL suggesting the protein was monomeric in agreement with the full length enzyme.

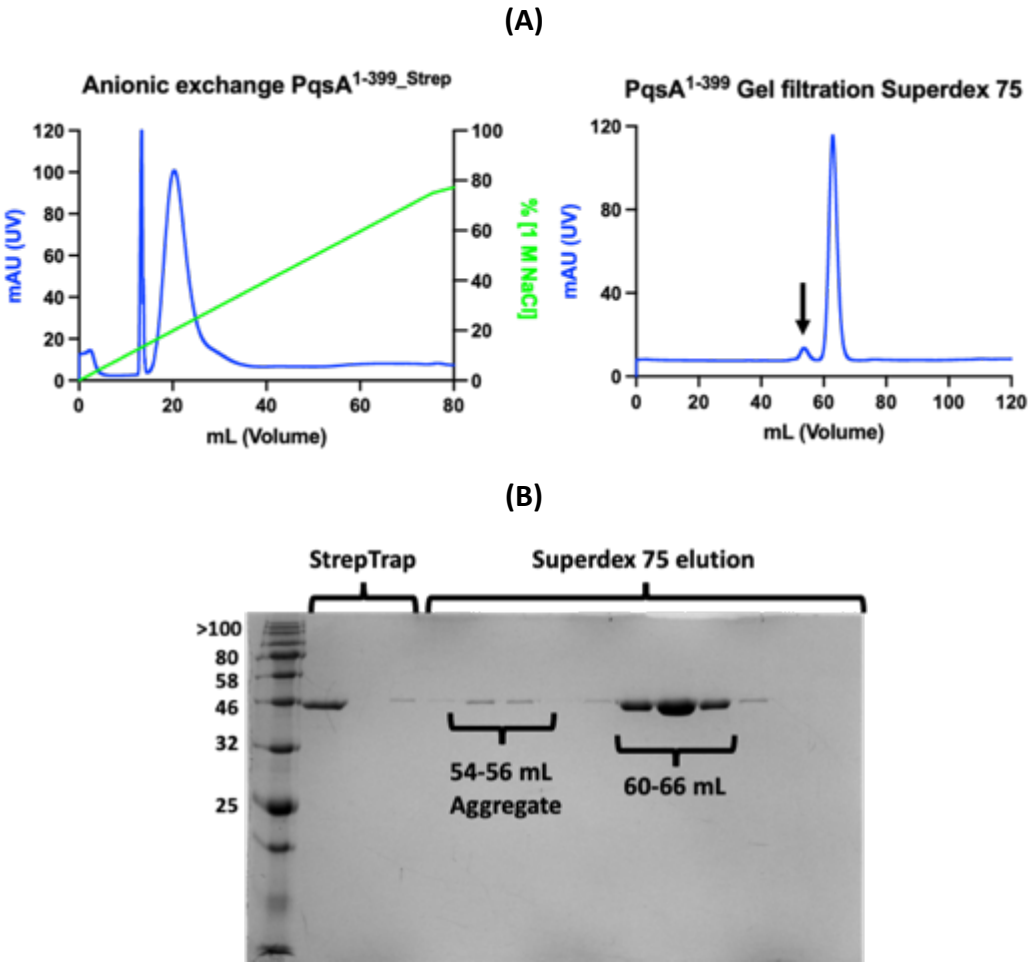

Figure 7.13. Purification of PqsA$^{1-399}$strep (A) Chromatographs of material concentration by anionic exchange and subsequent gel filtration to separate aggregated material from monomer. **(B)** SDS PAGE PqsA$^{1-399}$ construct after gel filtration with an estimated purity of >95%.

7.3.8 Crystallisation of PqsA$^{1-399}$Strep

The PqsA$^{1-399}$strep construct was concentrated by ultrafiltration to >15 mg/mL and supplemented with excess anthranilic acid and ATP[219]. To ensure complex formation the substrates and enzyme were incubated for 1 hour at room temperature. To bias the crystallisation towards success an optimisation plate of known PqsA crystallisation conditions based upon PEG3350 as the primary precipitant was set up alongside PACT and Morpheus. As shown in Figure 7.14 small crystals formed within 1 week in a 25% PEG 3350 condition, although they were too small for data collection. Subsequent attempts to reproduce the morphology were unsuccessful.

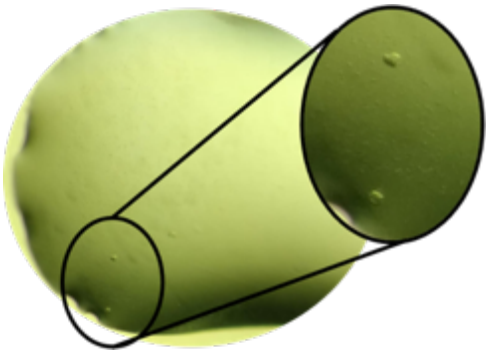

Figure 7.14. Quasi-crystals of PqsA$^{1-399}$ 15 mg/mL grown in 22-27% PEG 3350, 100 mM sodium citrate (pH 5.8-6.1), 200 mM ammonium acetate in a 2 µL drop.

7.3.9 Determining the binding mode of ZN8751275 in PqsA by molecular docking

As crystallisation attempts for PqsA$^{1-399}$ did not generate crystals viable for soaking studies/ligand displacement molecular docking using previously elucidated structures was performed instead.

7.3.9.1 Blind docking

To characterise the likely binding position of the ZN8751275 blinding docking was performed using the online SwissDock tool. The PDB chosen for docking was 5OE5 (crystal form 3) based upon model quality indicators generated by wwPDB Validation. The ligand dictionary was downloaded from the ZINC database. For blinding docking no search box was specified to allow for potential ligand placement throughout the domain. In total 45 ligand position clusters were identified, and these clusters were individually curated, removing duplicate clusters or implausible binding poses. Clusters were grouped into five potential binding sites termed S1-S5.

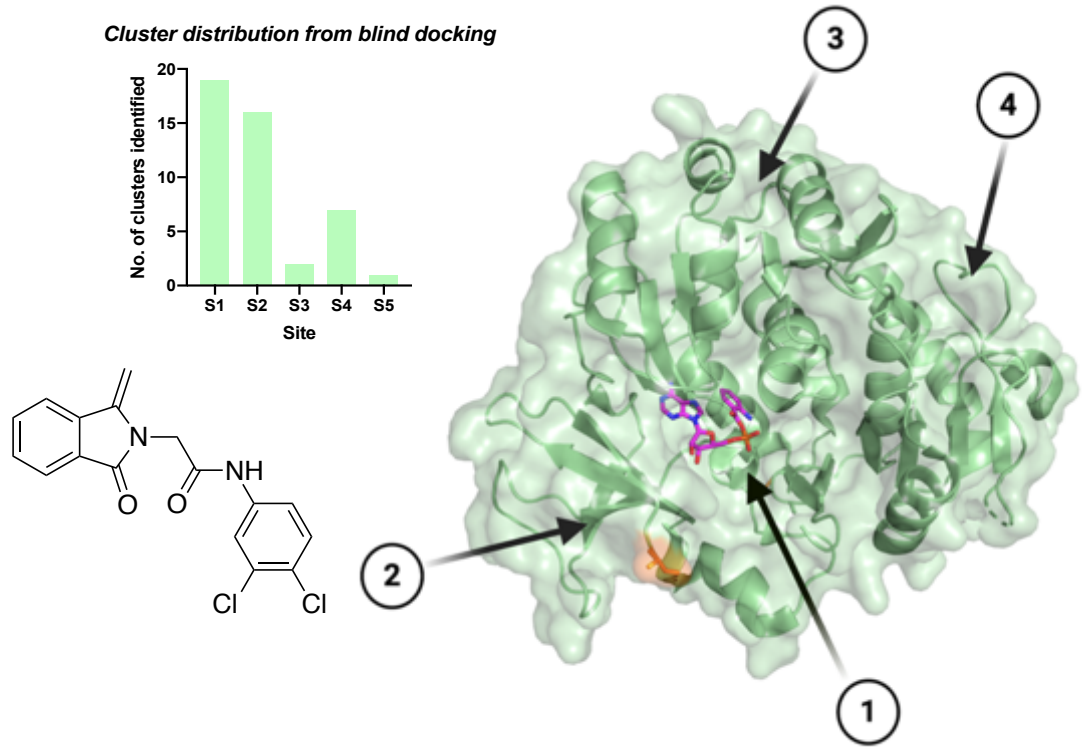

Figure 7.15. **Blind docking with ZN8751275 performed with SwissDock**. Distribution of potential binding sites on PqsA (PDB ID: 5OE5) for ZN8751275 as determined via SwissDock. Site 5 is located on the opposite face of the structure and as such is not marked. Co-crystallised ligand anthraniloyl-AMP is highlighted in pink. C-terminal of the crystallisation construct is highlighted by orange colouring.

The most populated cluster, S1, is in the active site pocket with binding modes showing either the isoindoline ring or the dichlorophenyl occupying the compact anthranilic acid binding pocket. Interestingly, S2 is located at the construct boundary which constitutes the hinge region on which the C – terminal domain rotates. Preventing hinge movement could impair domain conformation changes needed for catalysis. S3 and S4 are both located distally from the active site pockets in small cavities. As S1 and 2 were most prominent in the blinding docking run these were explored further using AutoDock Vina.

7.3.9.2 Docking ZN8751275 to the active site (S1)

To investigate the binding pose within the active site pocket, another round of docking was performed using AutoDock Vina. Anthranilic acid and anthraniloyl – AMP were used as controls with the docking solution closely matching the published crystallographic experimental model (Appendix 9.16). Docking runs performed with ZN8751275 did not

highlight a single outcome with significantly higher binding energy. However, 3 poses within the active site were most prominent; their respective binding energies and interacting residues are detailed in the table below:

Compound	Binding energy ΔG (kcal/mol)	Interacting residues
ZN8751275 Pose 1	- 7.3	**His 394**, **Asp 382**, Ala 303, Ile 301, *HOH 1184*
,, Pose 2	- 6.8	**Thr 304, Gly 279**, Thr 323, Asp 299, Ser 280, Ile 301, Pro 281, Gly 300, His 394, Gly 302, Ala 303, *HOH 1184*
,, Pose 3	- 6.8	**Asp 299, Gly 279**, Tyr 211, Gly 302, Gly 210, Ala 303, Ile 301, His 394, Ser 280, *HOH 1184*
Anthranilic acid	- 7	**Thr 304**, **Tyr 221**, **Gly 307**, His 308, Gly302, Ala 278, Val 309, Ala 303, *HOH 1184*
Anthraniloyl – AMP	-10.6	**Thr 304, Tyr 221, Gly 307, Tyr 378, Thr 380, Asp 382, Arg 397, Gly 302, Asp 299, Gly 300, Gly 278**, Ser 280, Pro 281, Ala 278, Ala 303, His 394, Ile 301, *HOH 1180, HOH 1090, HOH 1184, HOH 1081*

Table 7.1. Docking poses of ZN8751275 in the PqsA active site. Docking results showing binding energy and interacting residues. Residues interacting through a significantly electrostatic interaction are listed in bold. Interactions facilitated by hydrophobic interactions are written in plain text and water listed in italics. Residues determined by LigPlot^{+} and PyMOL.

Pose 1 with the highest binding energy shows ZN8751275 does not interact with the anthranilic acid binding pocket. Instead the inhibitor exploits a weak hydrogen bond from the amide carbonyl to the carboxylate group of Asp (3.5 Å) and an electrostatic interaction between water 1184 and the amide nitrogen. The dichlorophenyl group rests upon Ile 301 and the *para* chlorine atom shares an Cl–π interaction with His 394 (3.9 Å). The isoindoline is

orientated outside of the binding pocket and as such would interact with the unmodelled thioesterase domain (Figure 7.16a).

Poses 2 and 3 occupy the same position but adopt opposite orientations. Pose 2 has the dichlorophenyl group occupying the anthranilate binding pocket and the isoindoline positioned in place of the Adenine moiety of AMP. Additionally, the *para* chlorine atom forms a halogen bond with the hydroxyl of Thr 304 with a measured distance of 4 Å. The inhibitor shares hydrogen bonds with between the backbone amide of Gly 279 and the isoindoline carbonyl (2.9 Å). Gly 279 participates further in binding via another hydrogen bond to the NH of ZN8751275 amide linker (Figure 7.16b). The inverse orientation, pose 3, shares the same hydrogen bonding to Gly 279 with comparable bond distances. Unlike pose 2 the *meta* chlorine atom participates in halogen bonding to the carboxylate of Asp 299 (Figure 7.16c).

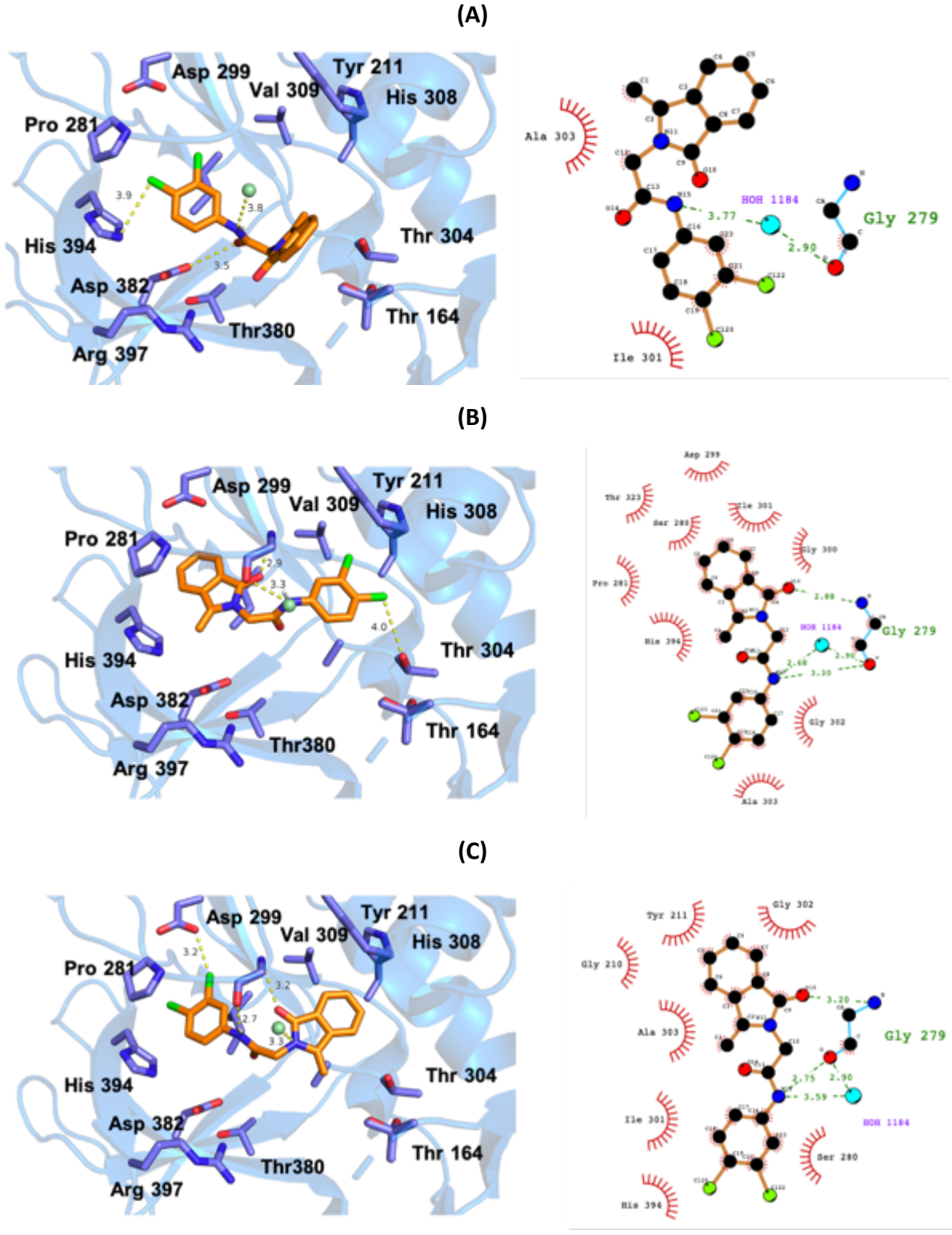

Figure 7.16. Potential binding poses at the PqsA active site determine by AutoDock Vina. A-C representing poses 1-3 respectively. Left, 3D representation of ligand coloured in orange, receptor coloured in blue and interacting residues coloured in light purple. Corresponding ligplot+ diagram for each potential pose is shown on the right. In pose 1 a π -halogen interaction is observed between the *para* chlorine atom at His 394 whilst the isoindoline is orientated outside of the active site. Poses 2 & 3 share the same position but are in opposite orientations. In each pose a hydrogen bond between the amide NH and Gly 279 backbone is observed.

As the anthranilic acid binding pocket of PqsA can accept a broad range of aromatics we hypothesised that pose 2 would be the likely pose and that its bulkier chlorine atoms were sterically hindering the inhibitor from binding to the pocket[314]. To test if the addition of the disubstituted chlorine was detrimental to binding we reproduced our docking run with ZN8772630 – that possessed a phenyl group. Docking highlighted a slight shift moving the aromatic ring closer to the predicted position of anthranilic acid. Additionally, a more favourable binding energy -7.2 kcal/mol compared to the 3,4-dichlorophenyl was observed suggesting that in this pose the chlorine atoms are unfavourable to binding.

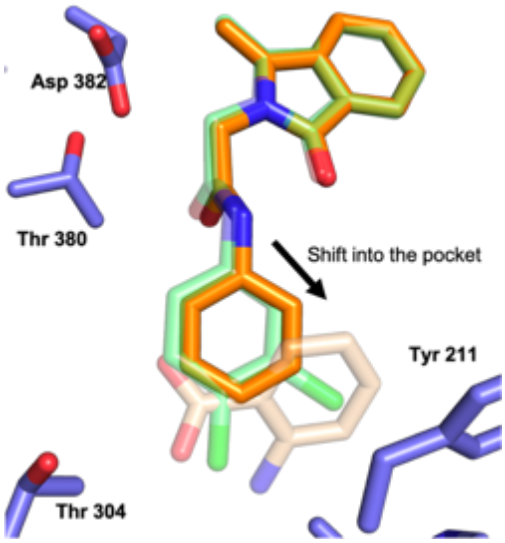

Figure 7.17. Replacement of 3,4-dichlorophenyl with a phenyl group shifts binding pose. Orange sticks represent ZN8772630 (phenyl); green and cream representing the original hit (ZN8751275) in pose 2 and predicted position of anthranilic acid respectively. Movement not observed in the position of the 3-methyleneisoindol-1-one.

7.3.9.3 Hinge region

The re-docking on the S2 site revealed that the inhibitor bound within a narrow cavity adjacent to the hinge region of PqsA. The 3,4-dichlorophenyl is sandwiched between Arg 337 and Arg 379 residues permitting strong cation- π interactions. Additionally, the amide bond of the compound permits hydrogen bonding from both Arg 337 and Glu 398 on opposing sites of the cavity. Despite the significant bonding the calculated binding energy for the pose was determined to be weaker than poses from site 1 (~6 kcal/mol). However, the location of the site next to the hinge may play a more significant role in binding. Enzymes of the ANL superfamily have been characterised to use a domain alternation

mechanism for function that requires a 140° rotation of the C – terminal domain. To gauge the impact of inhibitor binding on domain alternation, two structures of the related 4-chlorobenzoyl-CoA ligase (3CW8 & 3CW9) in alternative conformations were superimposed onto the 5OE5 structure. This highlighted a strong likelihood of clashes when the C-terminal adopts the position for thioesterification (Figure 7.18c).

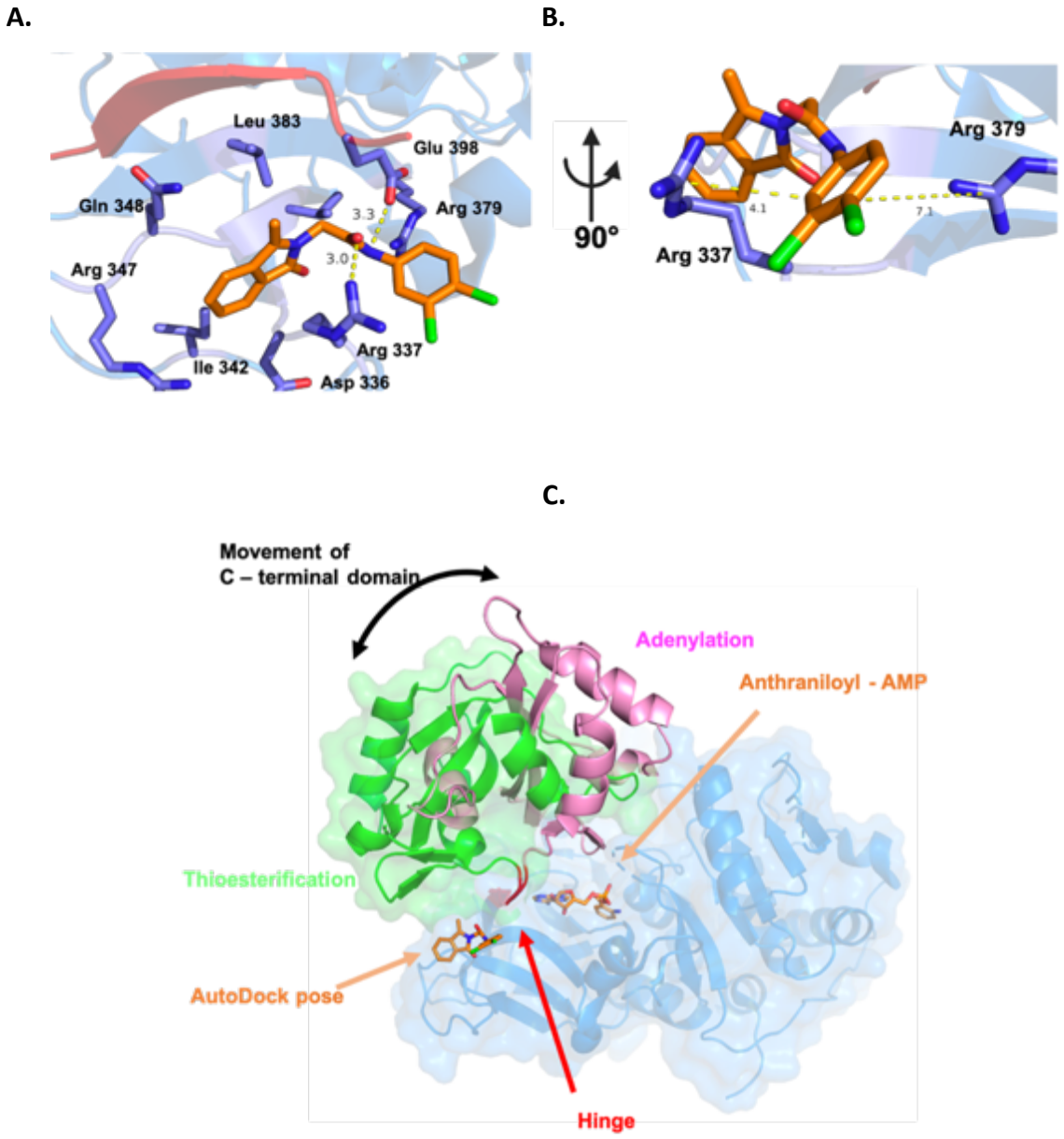

Figure 7.18. Docking poses of ZN8751275 on PqsA hinge loop. **(A)** Proposed binding mode of hit compound within the hinge cavity. **(B)** 90° vertical turn showing the two strong cation-pi interactions from opposite facing arginine residues. **(C)** Superposition of C-terminal domains of benzoate ligase homolog PDB IDs 3CW8 and 3CW9 coloured pink and green respectively.

7.3.10 Biological analysis of ZN8751275 on *P. aeruginosa*

To better understand if the inhibitor ZN8751275 is capable of being an effective biological agent for PQS inhibition the compound was evaluated for biological activity relating to or under the control of the PQS system. Biological validation is often required due to an observed lack of activity of hits identified exclusively using *in vitro* assays.

7.3.10.1 Impact of ZN8751275 on *P. aeruginosa* growth

Ideal anti-virulence agents should not impact bacterial growth that would lead to increased selection pressure. To assess this, PAO1 – L was grown in the presence inhibitor at varying concentrations from 2 – 60 µM. Growth data, shown in Figure 7.19, was plotted to a logistic growth model highlighting that the peak culture OD (maximum population) was unaffected. However, analysis did show that the lag phase was slightly extended at inhibitor concentration >10 µM (by approximately 0.5 hours). A similar result was apparent for a *ΔpqsA* mutant (data not shown).

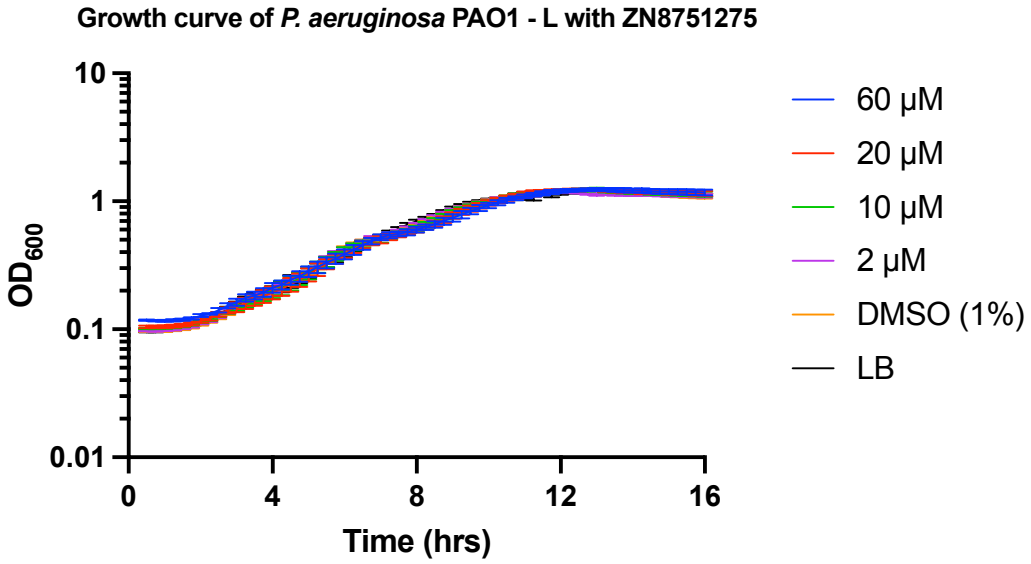

Figure 7.19. Impact of ZN8751275 on *P. aeruginosa* growth. PAO1 – L growth curve with varying concentrations of ZN8751275 with a final DMSO concentration of 1%. Data representative of mean and SD from 2 biologically independent cultures prepared in triplicate.

7.3.10.2 Effect of ZN8751275 on the P_{pqsA} promoter IC_{50}

The ZN8751275 inhibitor demonstrated antagonist activity when tested against the PAO1-L CTX::P_{pqsA}-*lux* bioreporter. This is presumably due to decreased concentration of the AQ

activators upon treatment. Potency determination from the assay suggested the inhibitor has favourable characteristics and gave a higher than expected potency of 0.68 µM given the IC_{50} determined in the LC-MS/MS enzyme assay. Disappointingly the efficacy of the inhibitor was decidedly poor with a reduction in activity observed to 50% compared to the untreated control. Lack of complete inhibition could be attributed to a reduced cell permeability which has affected other PqsA inhibitors[347].

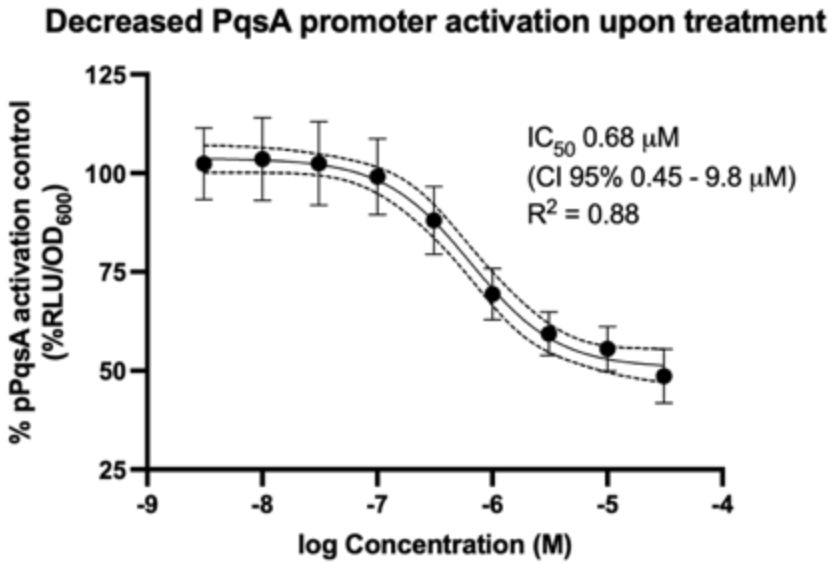

Figure 7.20. Decrease in *pqsA* promoter activation in PAO1 – L upon addition of ZN8751275. Half-log concentrations of inhibitor tested in 200 µL with a final DMSO concentration of 0.1%. Peak taken at 7 hours with y axis representing the activation compared to the untreated control. Results are representative of n = 9 (biological and technical triplicate). Confidence interval plotted alongside the dose-response curve.

7.3.10.3 Effect of ZN8751275 on AQ production

An expected effect of a PqsA inhibitor should be a reduction in exported AQs into the extracellular environment. A non-AQ producing *ΔpqsA* strain was used as control which would represent the phenotype of an efficacious PqsA inhibitor. Three concentrations of inhibitor were added to 10 mL cultures prior to incubation at 37°C. However, no significant inhibition in PQS, HHQ or HQNO was observed even at 60 µM. A very negligible reduction was observed in HHQ at the highest concentration of inhibitor 60 µM (Figure 7.21). Given the relatively weak efficacy observed in the bioreporter assay it is likely that changes in AQ production would only be apparent at a much earlier timepoint to those tested in this assay.

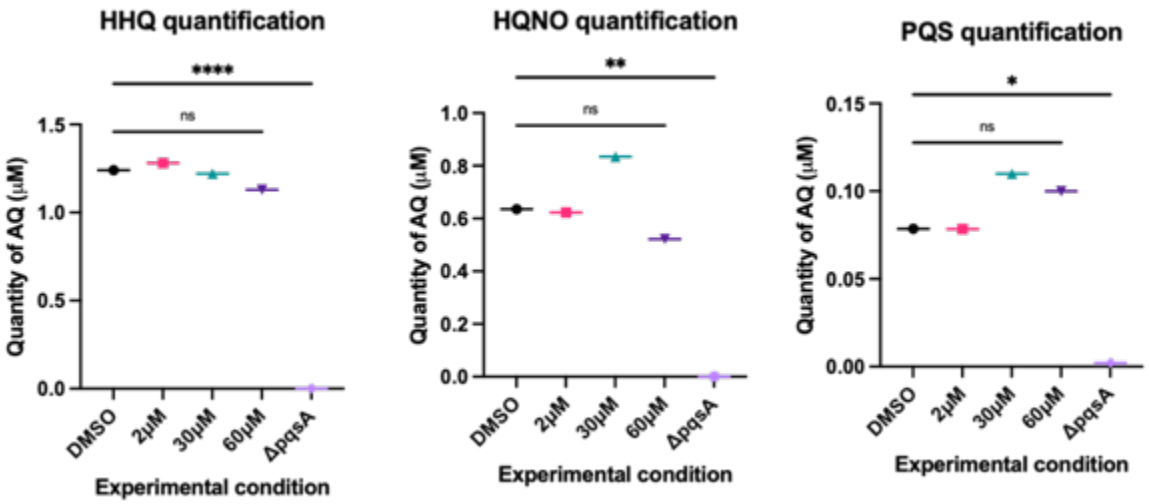

Figure 7.21. Effects of ZN8751275 on AQ biosynthesis. Varying concentrations of inhibitors added to a freshly diluted 10 mL cultures prior to incubation. After 18 hours incubation at 37°C culture supernatant was collected after centrifugation and AQs extracted with acidified ethyl acetate solvent. Quantification performed by LC-MS/MS using internal deuterated standards as described in methods 2.12.6. Results are representative of biological triplicates. Statistical testing performed using one-way ANOVA and Tukey's multiple comparison testing. As expected, the Δ*pqsA* mutant control produced no detectable AQs and ZN8751275 had no apparent effect on AQ output.

7.3.10.4 Promotion of bacterial aggregation by ZN8751275

Interestingly, whilst growing cells for supernatant analysis it was observed that cells treated with inhibitor compound appeared to have a greater degree of bacterial aggregation compared to non-treated controls. This appeared to follow a dose dependent pattern suggesting the compound was inducing the aggregation. To discount compound precipitation as the reason for aggregation the compound was incubated alone in LB under similar conditions and showed no aggregation (Appendix 9.18). This observation suggests that the compound likely induces *P. aeruginosa* self-association which is not exclusively controlled by the PQS system[126 350 351].

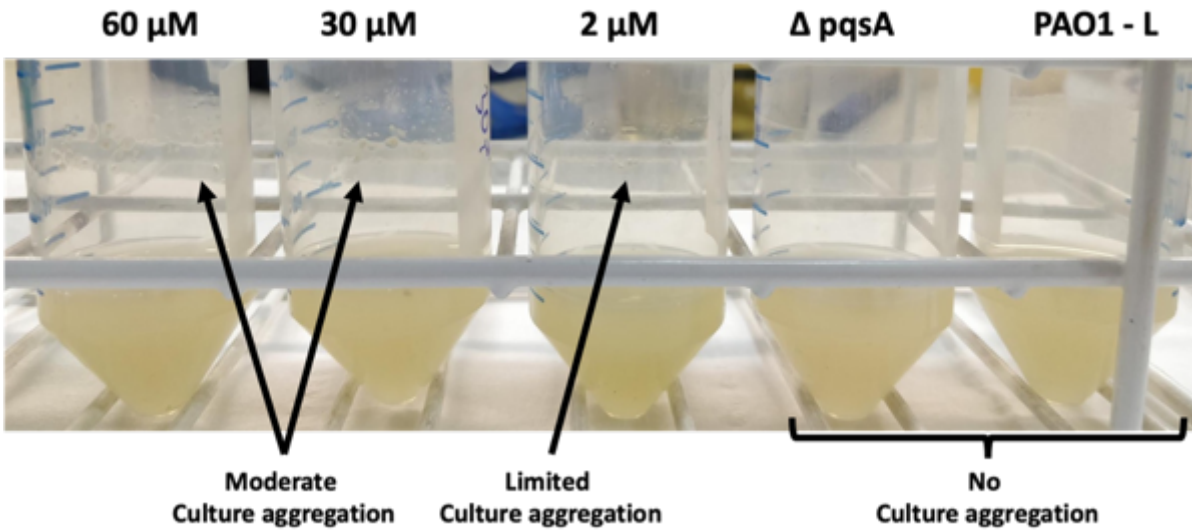

Figure 7.22. Effect of ZN8751275 on *P. aeruginosa* aggregation. Examination of cultures grown for 18 hours in the presence of either 1% DMSO or inhibitor (representative photos taken for n = 3 biological replicates. Aggregation is not observed in the *pqsA* knockout & wild type PAO1 – L. Aggregation was qualitatively observed in the form of bacterial material located on the plastic tube, outside of the liquid broth and likely deposited during shaking incubation at 200 rpm.

7.3.10.5 Synergism of ZN8751275 with a potent PqsR antagonist

Apparent antagonism using the ZN8751275 inhibitor alone and the unexpected negative results with respect to AQ reduction suggests the efficacy of the inhibitor is too weak to be an effective anti-virulence agent. However, its ability to potentiate an existing agent may prove equally as useful as phenotypical analysis of known PqsR antagonists have demonstrated that the desired virulence phenotypes are not always abated. Upon testing the inhibitor in combination with a known PqsR antagonist – SEN19 (the binding characterised in chapter 3) – the activity was improved. The synergy score of 5.553 classifies the relationship as primarily additive rather than truly synergistic. The ZIP model's boundary for a synergistic relationship is a score >10 whilst a score between -10 and 10 represents an additive relationship. Examination of the 3D topology model (Figure 7.23b) showed that at higher concentrations of PqsR antagonist greater synergy (ZIP score 10.69) was observed, likely due to depletion of PqsA protein. However, it should be noted that this area had greater variability likely due to biological variation.

(A)

SEN19 (μM) & ZN8751275 (μM)

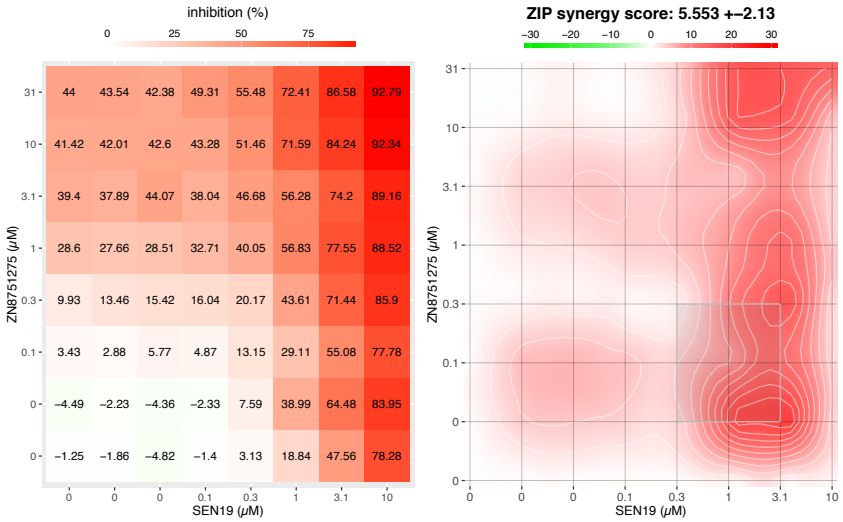

(B)

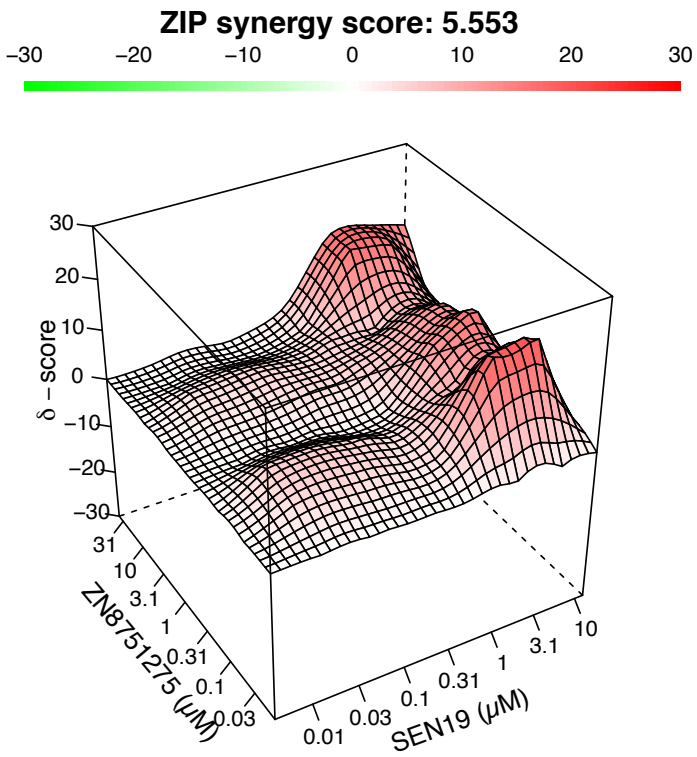

Drug combinations:

Drug combination	Synergy score	Most synergistic area score	Method
SEN19 - ZN8751275	5.553 +-2.13	10.69	ZIP

(C)

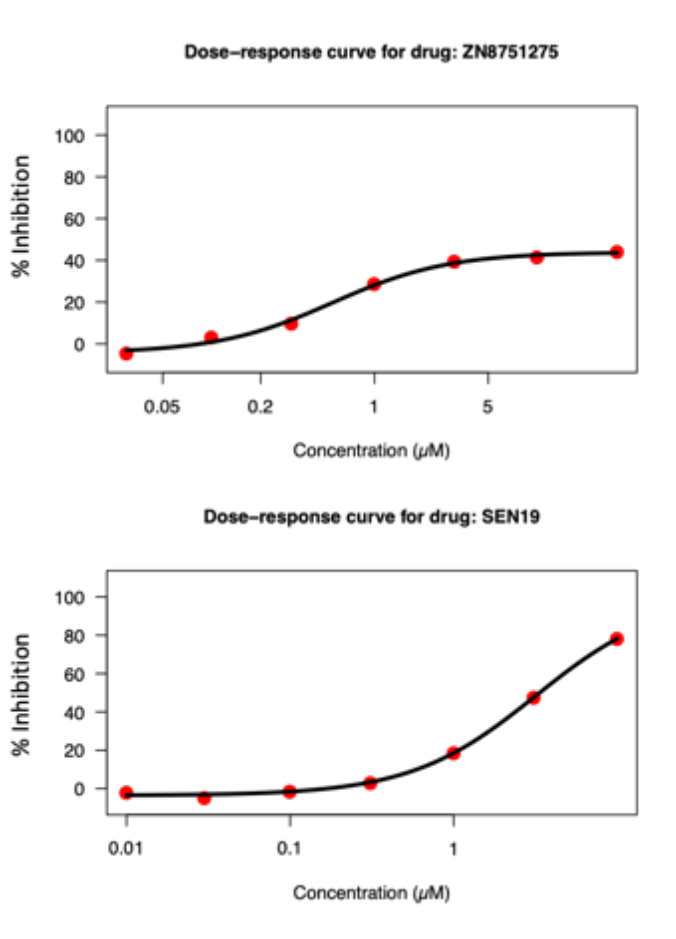

Figure 7.23. Synergism analysis with SEN19 and ZN8751275 on PAO1-L CTX::P*pqsA*-*lux* bioreporter. Synergy analysis of ZN8751275 functioning with SEN19 produced using SynergyFinder by input of a formatted csv file providing pqsA promoter activity with different concentrations of both compounds (n = 3 for each combination) **(A)** Left 8 x 8 Grid of concentrations showing % inhibition. Right Synergy topology diagram highlighting areas of interaction **(B)** 3D topology diagram for easier visualisation of areas of interaction **(C)** Independently generated dose-response curves for each antagonist/inhibitor whilst the other was at 0 µM. Y-axis percentage inhibition compared to untreated control. Points are representative of three replicates. ZIP model used for calculating degree of synergy.

7.3.10.6 Impact of ZN8751275 and SEN19 on virulence phenotypes

To examine the additive relationship further several virulence factors were further examined to determine if the inhibitor was able to aid anti-virulence effects of an existing agent (SEN19).

7.3.10.7 Pyocyanin

Pyocyanin is a secondary metabolite produced by *P. aeruginosa* and is under control of the PqsR[213] and to some extent PqsE through a uncharacterised mechanism[352]. Using a *pqsA* mutant, expected to produce substantially less pyocyanin, as a control strain the effect of single compounds and their combination was tested. As shown in Figure 7.24, a *pqsA* mutant produced very small amounts of pyocyanin compared to the wildtype PAO1-L. ZN8751275, added at the start of culture incubation to 5 µM, failed to reduce pyocyanin biosynthesis and appeared to cause a slight increase even if not significant. SEN19 alone was able to reduce pyocyanin to ~25%. Co-dosing appeared to cause no significant change although the variability in replicates was greater than the single dose SEN19.

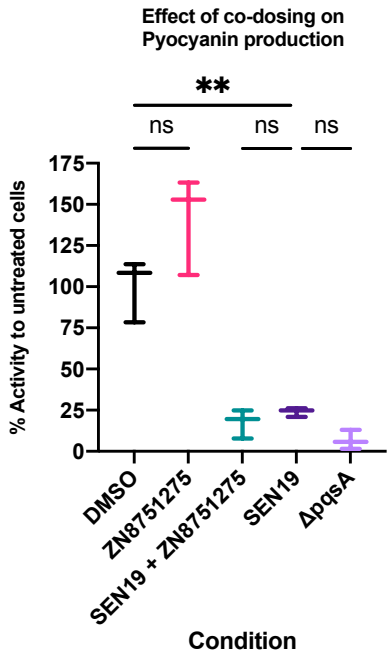

Figure 7.24. Impact of ZN8751275 and SEN19 on pyocyanin production. ZN8751275 and SEN19 were added to PAO1-L cultures at 0 hours at 5 and 3 µM respectively. These were added separately or in combination with a final DMSO concentration of 0.2%. After incubation at 37°C for 18 hours pyocyanin was extracted by organic phase extraction and acidification. As negative and positive controls DMSO at 0.2% and the *pqsA* isogenic mutants were used. Data is derived from three biological repeats with graph showing minimum, maximum, and average. (**, P ≤ 0.01).

7.3.10.8 eDNA release

PQS has been implicated in eDNA release in response to prophage-mediated lysis with previous research finding that this is prevalent in planktonic culture[353]. However, using a simple precipitation methodology this phenotype was not observable. This suggests the lysis phenotype is only weakly associated with a *pqsA* mutant. It is also likely that the presence of different UV absorbing components may have been co-purified with DNA that interferes with accurate determination.

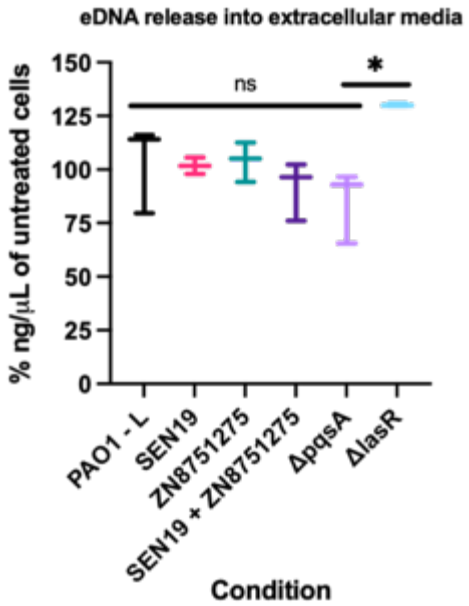

Figure 7.25. Impact of ZN8751275 and SEN19 on eDNA release. ZN8751275 and SEN19 were added to PAO1-L cultures at 0 hours at 5 and 3 µM respectively. These were added separately or in combination with a final DMSO concentration of 0.2%. After incubation at 37°C for 18 hours 450 µL of supernatant was collected and DNA precipitated with sodium acetate. After washing with ice-cold ethanol the precipitated DNA was resuspended in distilled water and quantified by Nanodrop ND-1000 using absorbance at A_{260}. As negative and positive controls DMSO at 0.2% and the *pqsA* isogenic mutants were used. Data is representative of 3 biological repeats with minimum, maximum and average shown. (*, $P \leq 0.1$).

7.3.10.9 Elastase

P. aeruginosa releases several proteases during an infection including LasB, a 52 kDa protease, that has been shown to interfere with immune responses and is regulated in part by PQS[50 354]. A *lasR* mutant was used as a control strain given its known low protease release phenotype. Additionally, the ZN8751275 PqsA inhibitor possessed some structural similarities to known LasB inhibitors (common dichlorophenyl group)[52 355]. However, despite the structural similarity no apparent effect on LasB activity was observed. Unexpectedly the

PqsR antagonist SEN19 did not show any apparent effect on LasB release and no difference was observed when used in combination with ZN8751275.

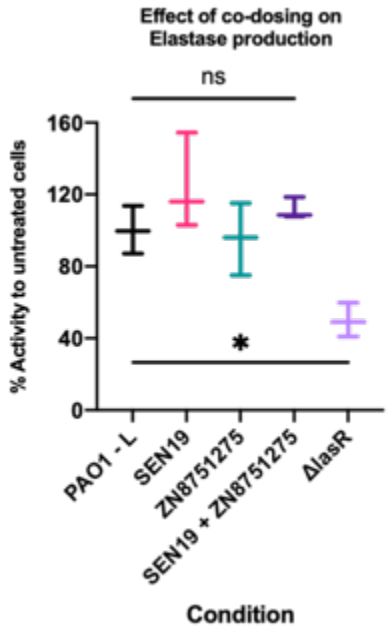

Figure 7.26. Impact of ZN8751275 and SEN19 on supernatant LasB activity. ZN8751275 and SEN19 were added to PAO1-L cultures at 0 hours at 5 and 3 µM respectively. These were added separately or in combination with a final DMSO concentration of 0.2%. After incubation at 37°C for 18 hours 100 µL of culture supernatant was added to a 20 mg/mL Congo-Red solution and incubated for 4 hours. Cleaved product was quantified using a spectrophotometer. As negative and positive controls 0.2% DMSO and an isogenic *lasR* mutant were used. Data is representative of 3 biological repeats with minimum, maximum and average shown. (*, P ≤ 0.1).

7.3.10.10 Pyoverdine

PqsA has been shown to influence pyoverdine release through iron depletion and induced aggregation from PQS[356]. Given the previous observation that the inhibitor induced aggregation a concomitant effect on pyoverdine would be expected. A literature study also showed a *pqsA* mutant to have impaired pyoverdine release[356]. However, as shown in Figure 7.27c, there was no difference between wildtype and *pqsA* after 10 hours. This could be due to subline variation as observations by Francis Smith (personal communication) found that in the Denmark subline of PAO1 the *pqsA* mutant also produced less pyoverdine compared to the wildtype. Repetition in RPMI showed attenuated pyoverdine release in a *pqsR* mutant but not *pqsA* suggesting the regulatory activity of *pqsR* plays a role in pyoverdine regulation under nutrient starvation conditions. Neither SEN19 or ZN8751275 were able to affect

pyoverdine output even when used in combination. Given that products such as pyoverdine release is significantly affected by media it is difficult to draw significant conclusions[357].

(A)

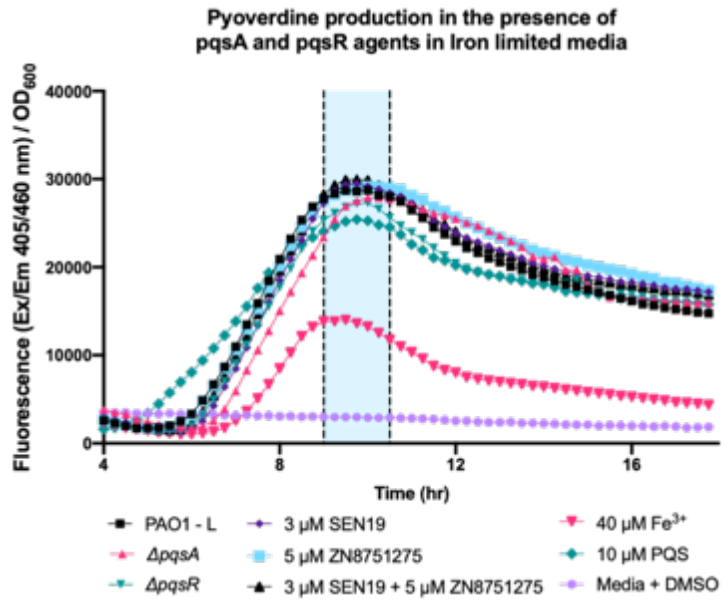

(B)

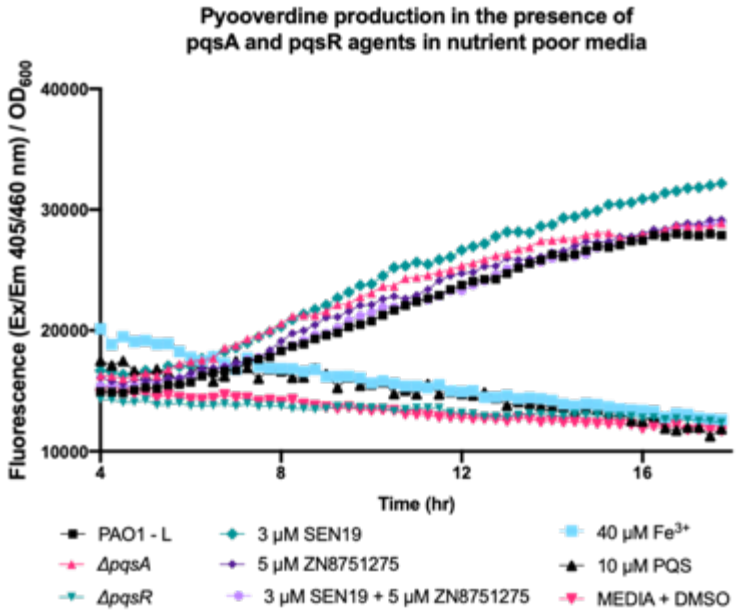

(C)

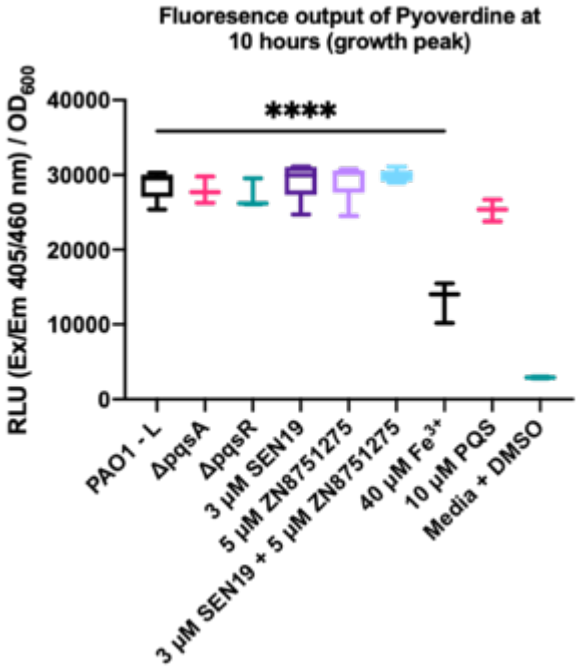

Figure 7.27. Impact of ZN8751275 and SEN19 on pyoverdine production in PAO1 – L. ZN8751275 and SEN19 were added to PAO1-L cultures in 96 well plates at 0 hours at concentrations of 5 and 3 µM respectively. These were added separately or in combination with a final DMSO concentration of 0.2%. Pyoverdine was monitored by means of fluorescence emission at 460 nm. Free iron was used as a low pyoverdine production control. Both *pqsR* and *pqsA* mutants were used to show the effect of a deficient PQS system. (A) Experiment performed in CAA media with peak marked in blue (B) Experiment performed in RPMI (C) Maximum fluorescence produced by P*. aeruginosa* in CAA media at 10 hours. Data is representative of 3 biological repeats with mean, minimum and maximum shown. (****, P ≤ 0.0001).

7.3.11 Effect of ZN8751275 on *Burkholderia* PqsA Homologs

7.3.11.1 Selection of homologs and conservation analysis

The PQS system is not exclusive to *P. aeruginosa* but is also found in *Burkholderia spp*. The *Burkholderia cepacia* complex (BCC), a classification referring to over 20 species, has a similar pathology to *P. aeruginosa* in that it is environmentally ubiquitous and an opportunistic pathogen of the lungs in cystic fibrosis patients. Other *Burkholderia spp*, not included in the complex, such as *B. pseudomallei* is able to cause severe infection. Studies have shown that Burkholderia spp produce a variety of AQs excluding PQS. Two Burkholderia homologs of PqsA were selected for inhibitor cross-validation including HmqA

from *Burkholderia ambifaria* and HhqA from *Burkholderia pseudomallei*. Despite being homologous the proteins share low sequence identity. Alignment of primary sequence against PqsA shows HmqA and HhqA share 28.32 and 27.71% identity respectively. As shown in Figure 7.28, despite poor overall conservation the active site residues are well conserved.

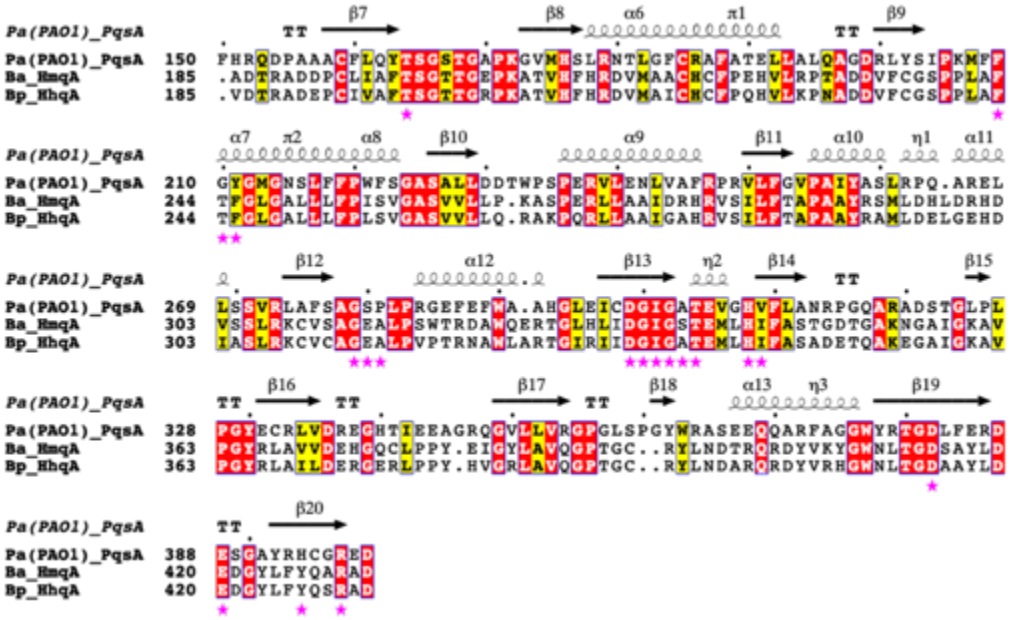

Figure 7.28. Alignment of PqsA and Burkholderia spp. homologs. Clustal alignment of *P. aeruginosa* PqsA (PA0996), *B. ambifaria* HmqA (Bamb_5763) and *B. pseudomallei* HhqA (BPSS0481) rendered in ESPript3. Residues within 3 Å of the anthraniloyl-AMP that constitute the active site in the N-terminal are marked with a pink stars. Residues sharing sequence identity are shown in red and weaker conservation shown in yellow.

7.3.11.2 Purification of homologs from *B. ambifaria* and *B. pseudomallei*

Given the success using the Strep-II-tag for PqsA purification the same tag was applied to HmqA and HhqA. The expression vectors were produced by amplification of genes synthesised by GeneScript with primers listed in Table 2.8. As shown by SDS PAGE in Figure 7.29 both constructs expressed well in *E. coli* BL21(DE3) CP grown in TB media with 0.2 mM IPTG induction. Bands were detectable post-lysis by sonication suggesting a high degree of solubility.

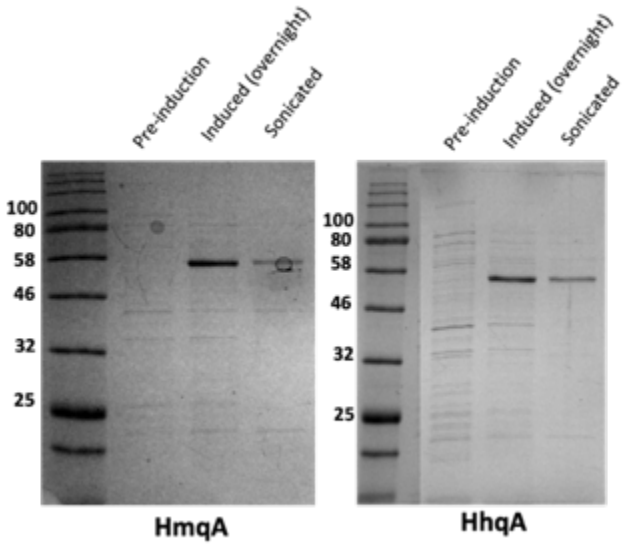

Figure 7.29. Solubility assessment of HmqA and HhqA prior to protein purification. pET24b::HmqA^{Strep} and pET24b::HhqA^{Strep} grown in TB media for 18 hours with 0.2 mM IPTG induction at 18°C. Cells normalised to 0.7 OD_{600} prior to lysis and/or SDS PAGE. Pre-induction and induced lanes contain whole cell. Sonicated sample was clarified by centrifugation prior to loading on SDS PAGE and as such contains 'soluble' protein. HmqA and HhqA bands clearly observable between 46 and 58 kDa.

7.3.11.3 HmqA^{Strep} purification

HmqA was successfully purified using the same methodology as for PqsA. The StrepTrap elution contained the presence of several contaminants but at low concentration. These were effectively removed by anionic exchange chromatography (Materials and methods section 2.5.5). Unexpectedly despite the higher pI compared to PqsA the protein eluted off the anionic exchange column later than PqsA suggesting greater surface charge properties. During purification it was further observed that the preparation contained a greater degree of aggregated material compared to PqsA. As shown by SDS PAGE in Figure 7.30a a light band can be observed above the intense HmqA band. This was suspected to be co-purified GroEL that was subsequently removed by gel filtration. Copurification may suggest the homologue is not as stable as PqsA and co-expression of a chaperone could be useful in future preparations to increase yield[358].

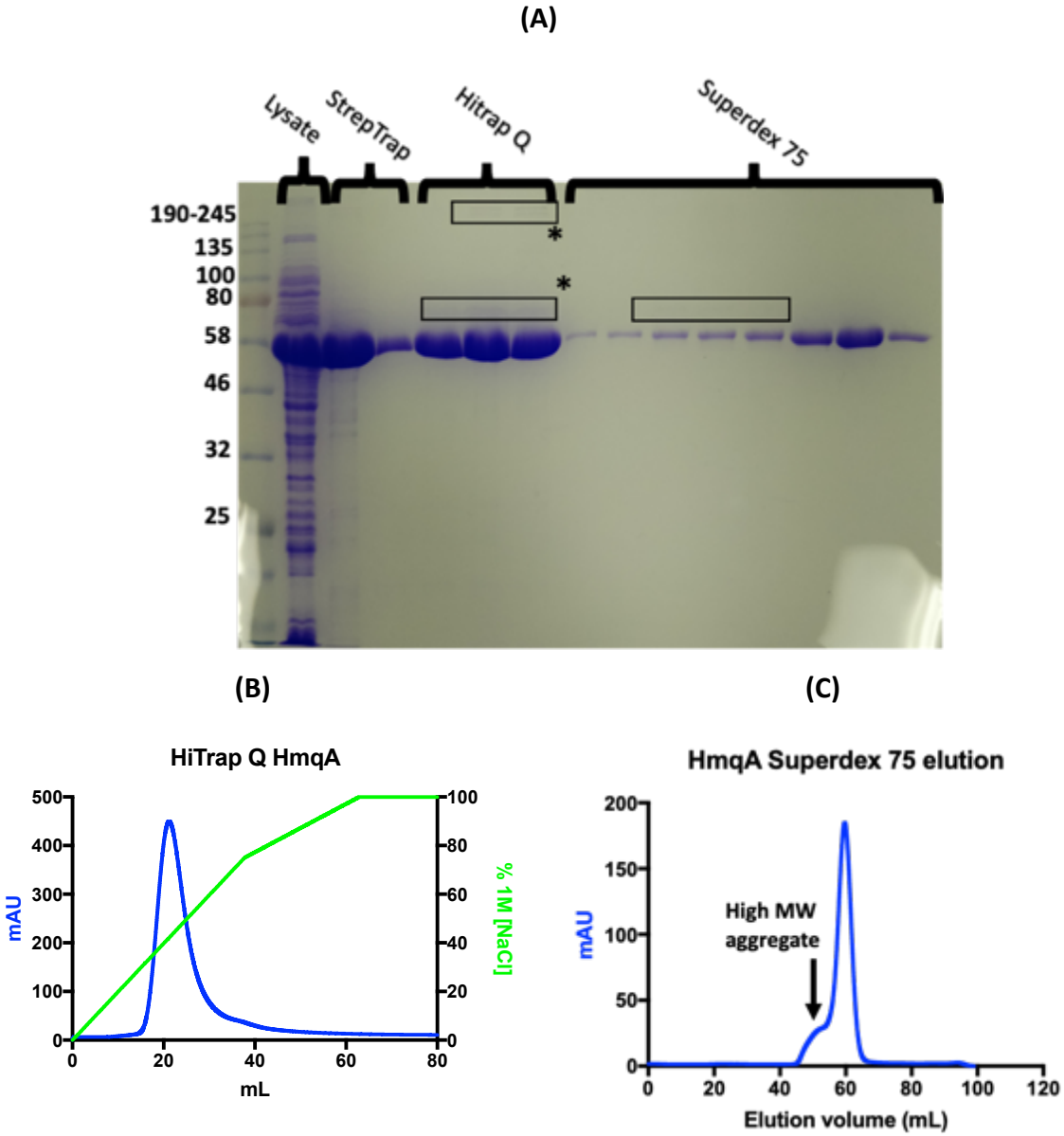

Figure 7.30. Purification of HmqA anthranilate ligase. (A) SDS PAGE showing purification of 61.1 kDa product. Prevalence of many contaminants after StrepTrap elution which are readily removed by anionic exchange. Final polishing achieved with gel filtration to remove aggregated material and small band above HmqA$^{Strep-II}$ (marked by box and star). **(B)** Elution of HmqA$^{Strep-II}$ from HiTrap Q with a salt concentration of >400 mM. **(C)** Gel filtration on S75 required to separate aggregate from correctly folded sample.

7.3.11.4 HhqA ^{Strep} purification

HhqA from *B. pseudomallei* proved that, despite being prevalent after sonication, was recalcitrant to purification. Enrichment from the StrepTrap column was significantly lower compared to PqsA and HmqA. Attempts to concentrate the protein by anionic exchange failed as the protein seemed to readily adsorb onto surfaces. As an alternative means to

concentrate the sample ultrafiltration (vivaspin) was used but sample was lost to the membrane and concentration did not increase past 0.5 mg/mL.

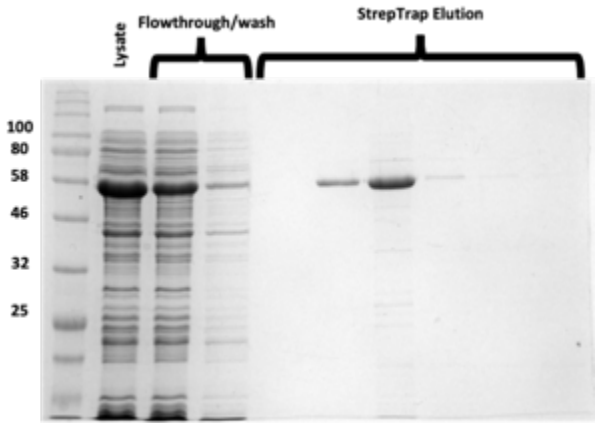

Figure 7.31. Purification of HhqA using StrepTrap HP column. Protein eluted with 6 CV (30 mL) of desthiobiotin containing buffer as described in Materials and Methods 2.5.3. Band of interest observed between 46 and 58 kDa. Lysate contained large amount of material but was unable to bind to the column effectively. Most of the protein eluted in the second and third 5 mL CVs.

7.3.11.5 Confirmation of HhqA and HmqA Anthraniloyl – CoA product synthesis by LC MS/MS

Despite bioinformatic analysis showing sequence conservation the identity of the enzymes as anthranilate ligases was further confirmed by LC MS/MS analysis using PqsA as a control with respect to column retention time and m/z fragmentation (Appendix 9.15). As shown in Figure 7.32, anthraniloyl – CoA was detectable in reactions from both purified homologs, but the quantity produced varied significantly with both homologs producing significantly less product. It should be noted that HhqA activity seemed to decrease very quickly after purification likely due to further aggregation over time.

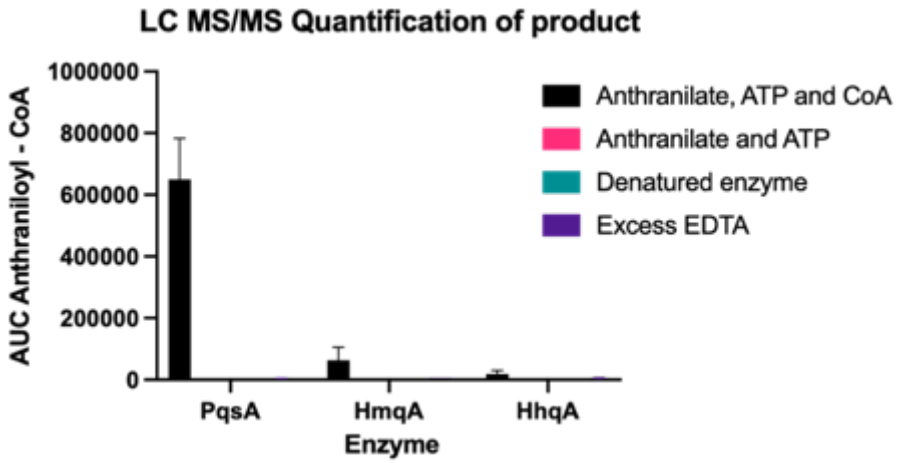

Figure 7.32. Semi-quantification of methanol extracted anthraniloyl-CoA by LC MS/MS. Enzyme reactions prepared as described in 2.6.7. As negative controls heat denatured enzyme samples as well as reactions lacking coenzyme A were used and show no product formation. Reactions containing enzyme and all three substrates produced the expected anthraniloyl-CoA. As an inhibitor proxy >5 mM EDTA was used which reduced activity significantly. Due to low residual activity these are not apparent on the axis but when represented as a percentage of uninhibited activity are 0.6, 9.7 and 25.9% for PqsA, HmqA and HhqA respectively.

7.3.11.6 Effect of ZN8751275 on HmqA enzymatic activity

To attempt to confirm the binding site of ZN8751275 the LC-MS/MS assay was conducted using the HmqA homolog. Rationally, similar potency would suggest the inhibitor bound to a conserved region in both enzymes. In agreement with this hypothesis, we found that ZN8751275 produced a similar IC_{50} of 43.72 µM. Our attempts to generate a concentration-dependent response for HhqA failed as the enzyme produced too little material, in the assay timescale for accurate quantification.

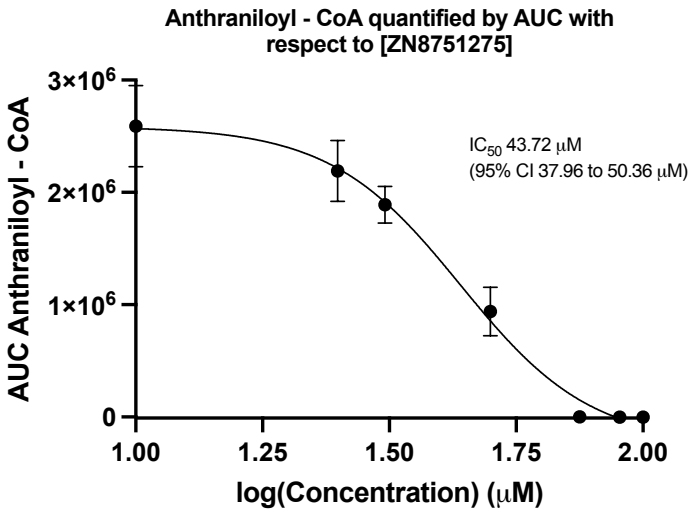

Figure 7.33. Enzymatic reaction of HmqA with ZN8751275 quantified by LC-MS/MS. Reaction stopped by denaturing organic solvent after 5 minutes. Data is representative of 3 independent reaction series with errors shown. Final co-solvent DMSO concentration at 7%.

7.3.11.7 Crystal trials for HmqA and HhqA

Given that PqsA crystals could not be reproduced using the same PqsA$^{1\text{-}399}$ construct the homolog proteins were assessed for crystallisability. Analysis of proteins from the ANL superfamily in the PDB shows the majority are crystallised as full length constructs but around 20% possessed a disordered C-termini due to the inherent flexibility in the thioesters domains[359 360 361 362]. To remedy disorder of the accessory domain a common strategy is to omit the domain for crystallisation. Disorder prediction using PsiPred on both HmqA and HhqA suggest the C-terminal domain is at least partially disordered. Using Pfam the domain boundaries for HmqA and HhqA were assessed which showed the Burkholderia homologs possessed additional sequence at their respective N-termini ahead of the AMP binding domain (represented in Figure 7.33a). As such to design a suitable truncation the known structure of PqsA was superimposed with one generated using I-TASSER showing that residue 430 held the same likely position as D399 (C-terminal of PqsA 5OE5). Given the use of His-tag for PqsA crystallisation the same tag was applied to these expression constructs.

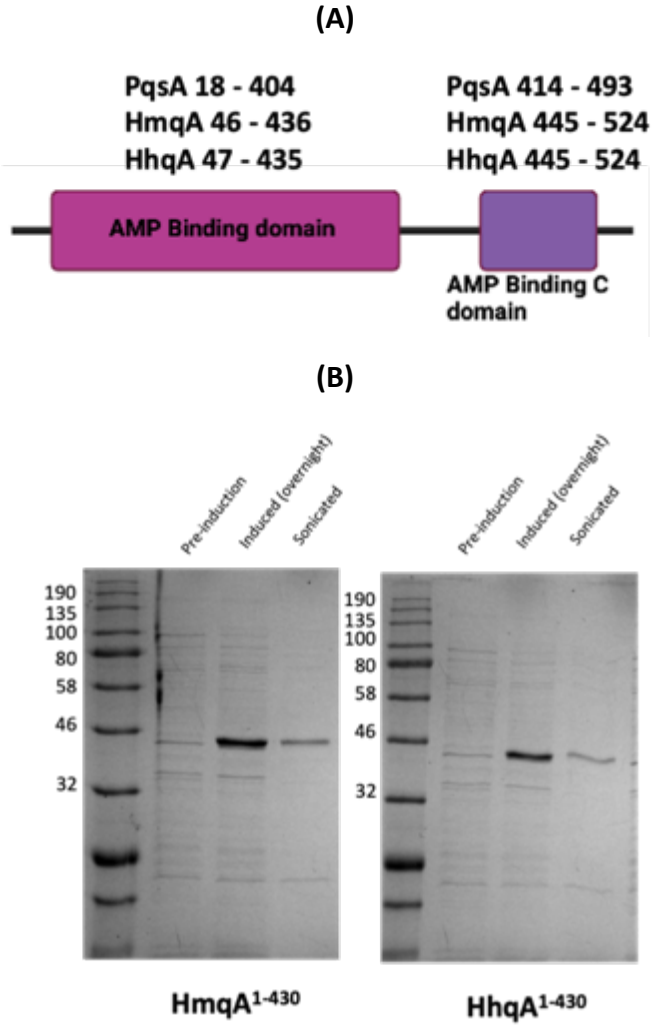

Figure 7.34. Construct design and solubility of HmqA$^{1-430}$ and HhqA$^{1-430}$ (A) Cartoon representation of Pfam domain recognition showing boundary markers. AMP binding domain and C-terminal thioesterase domain coloured in pink and purple respectively. **(B)** Successful expression of HmqA$^{1-430}$ and HhqA$^{1-430}$ grown in TB media for 18 hours with 0.2 mM IPTG induction at 18°C. Induced overnight cultures normalised to pre-induction OD_{600} 0.7 prior to SDS PAGE. Band of interest is observed between 32 and 46 kDa molecular weight markers on both SDS PAGE gels.

Expression of the two homologs under the same conditions as the full-length variants yielded soluble protein after sonication as shown in Figure 7.33b. The migration was slightly quicker than expected for the theoretical size of 47 kDa but this was likely due to the high degree of hydrophobicity observed with PqsA.

7.3.11.8 HmqA$^{1-430}$ purification

HmqA was successfully purified using a modified protocol as used for the full-length constructs with the key exception that affinity capture was performed on a HisTrap HP.

HmqA$^{1-430}$ was eluted at an imidazole concentration >200 mM in a volume of ~20 mL. As shown by SDS PAGE some HMW bands were observed (Figure 7.35a) which were subsequently removed with a HiTrap Q in which the protein eluted at 400 mM NaCl. To separate aggregated material the protein was further purified by gel filtration eluting at 66.4 mL as a single sharp peak representative of a monomer. Comparison of gel filtration from the full length and truncate showed the full length was more prone to aggregation as more material eluted in the void volume (Figure 7.35b).

(A)

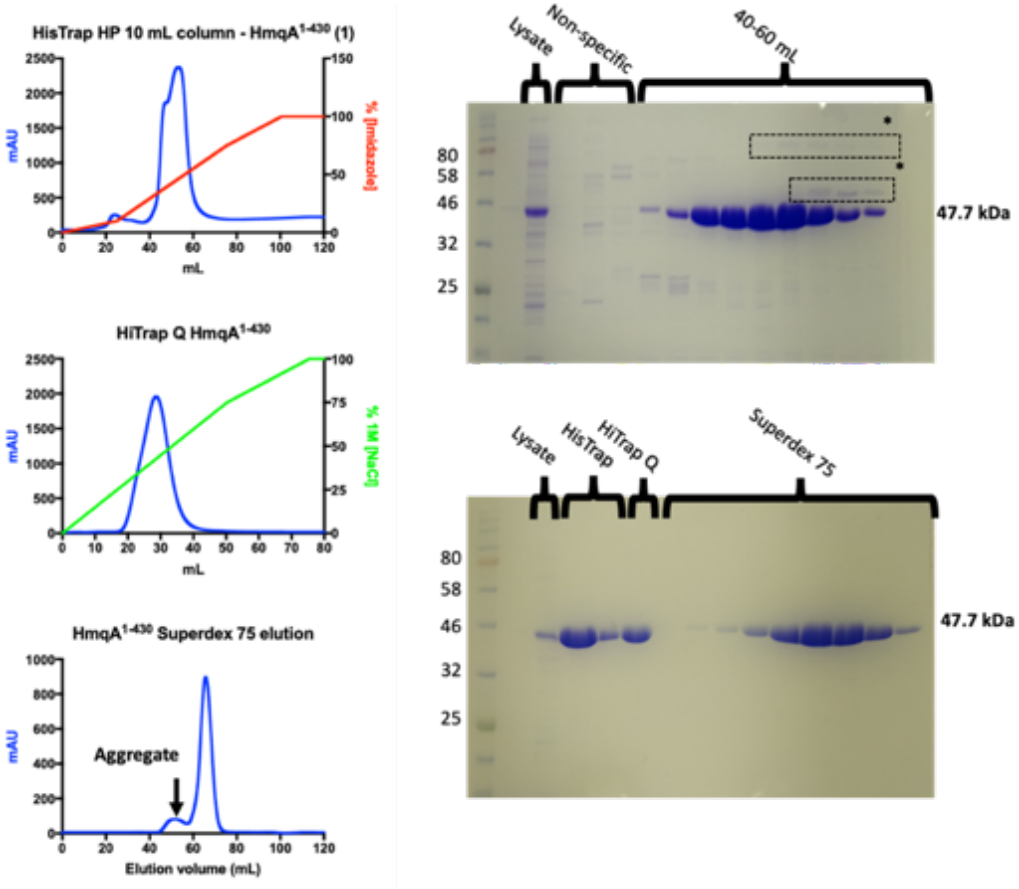

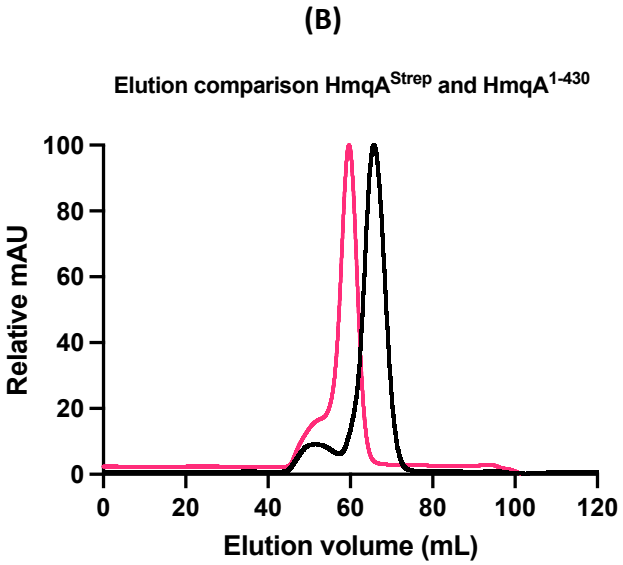

Figure 7.35. Purification of HmqA$^{1-430}$ for crystallisation trials. **(A)** Purification chromatograms of HisTrap HP elution (10 mL resin), HiTrap Q anionic exchange and final gel filtration for polishing. Contaminants from the HisTrap HP column are marked by a rectangular box. These are subsequently removed after HiTrap Q and not visible in the final product. Aggregated material from gel filtration is marked by an arrow. **(B)** Comparison of HmqA$^{1-430}$ (black) and HmqA^{strep} (pink) gel filtration showing a greater degree of aggregation in the full length enzyme.

7.3.11.9 Crystallisation HmqA$^{1-430}$

In accordance with ANL superfamily crystallisation the protein was concentrated to 30 mg/mL and diluted with anthranilate, $MgCl_2$ and ATP. After 1 hour of incubation, (to form the intermediate product) the protein was screened for crystallisation with MORPHEUS, JCSG+, PACT and MIDAS as described in Materials and Methods 2.8.1. The only conditions to yield crystals were Morpheus conditions containing 0.3 M sodium nitrate, 0.3 M phosphate dibasic and 0.3 M ammonium sulphate with different organic components. The crystals displayed an asymmetric bipyramidal habit. Additionally, the crystals were soft and easily broken when handled suggesting the presence of proteinaceous material. However, diffraction analysis highlighted a very small unit cell confirming these crystals to be small molecule likely derived from the anthranilic acid or magnesium salt.

7.3.11.10 HhqA$^{1-430}$ purification

Similar instability was observed with HhqA$^{1-430}$ as with the full-length version with the initial HisTrap elution containing poor yield (Figure 7.37a). To permit solubilisation and to expose the HisTag for affinity purification the lysis buffer was supplemented with 10 mM anthranilic acid, 10 mM ATP and 20 mM $MgCl_2$. The rationale being that greater stability would be maintained in the presence of the anthraniloyl-AMP intermediate. An unanticipated drawback was that the presence of anthranilic acid caused column nickel leeching thereby lowering effective binding capacity. Furthermore, buffers were supplemented with 5% ethylene glycol that have been shown to stabilise protein structure[363 364]. This seemingly liberated a large amount of protein from the lysate with 10 - 14.9 mg attained from 1 L (Figure 7.37b). However, eluted protein quickly precipitated and formed thick white precipitate. After clarification the protein continued to precipitate over time and adsorbed onto dialysis membrane during buffer exchange. To further remedy instability the protein was prepared in the same manner but immediately diluted upon elution into a low salt buffer supplemented with additional ligand. Unfortunately, this did not prevent precipitation and sample adsorption and as such the construct was deemed too unstable for crystallisation.

(A) No ligand

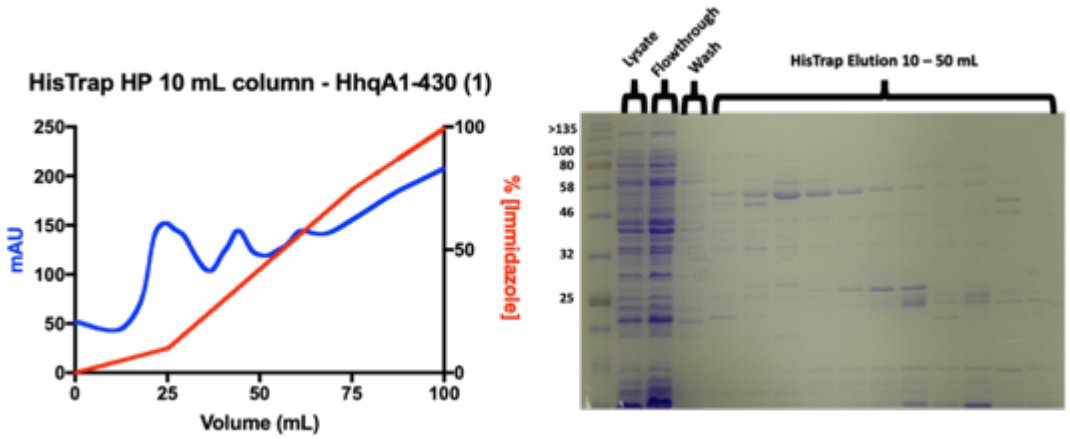

(B) Anthranilate + Mg^{2+}ATP

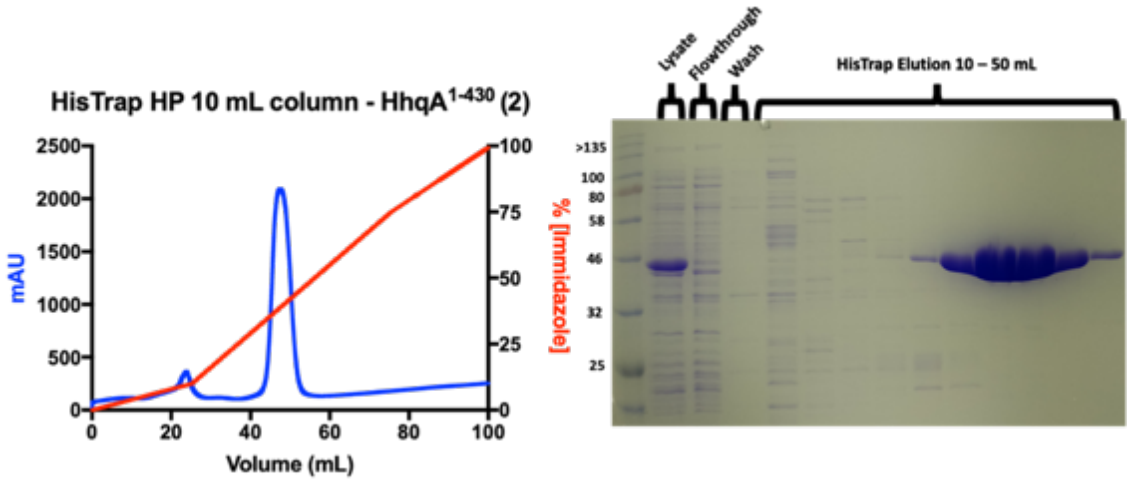

Figure 7.37. Extraction and purification of $HhqA^{1-430}$ with and without ligand. HisTrap HP elution (10 mL resin) of $HhqA^{1-430}$ with a linear gradient of imidazole with or without prior supplementation with anthranilate & ATP. **(A)** Low yield, un-supplemented purification in which no distinct band can be identified in either lysate, flowthrough, or elution. **(B)** Supplemented $HhqA^{1-430}$ preparation with lysate showing an intense band between 32 and 46 kDa. Chromatogram showing sample elution at ~50 mL and SDS PAGE showing >95% purity.

7.4 Discussion

The development of PqsR antagonists, as described in chapter 3, represent an effective way to abrogate PQS mediated quorum sensing. However, this is limited to *P. aeruginosa* as no PqsR homologs have been identified in AQ producing *Burkholderia spp*[365 123]. Subsequently supplementing PqsR antagonists with additional agents to suppress signal synthesis would represent a viable adjuvant to improve activity. Whilst such agents have been identified for

PqsD and to a limited extend PqsE only a few published attempts to identify a PqsA inhibitor are available[366 170 113 367].

Regrettably the inhibitor ZN8751275, despite showing reasonable biochemical potency was unable to lower AQ production in *P. aeruginosa*. As the CTX::P_{pqsA}-*lux* bioreporter only showed a reduction of ~50% it is likely that this is too poor to prevent PQS autoregulation. Optimisation of the ligand may negate this as other PqsA inhibitors such as methyl-anthranilate have been reported to reduce AQ production albeit at high concentration[344]. An investigation into cell permeability and target affinity would be useful in guiding further optimisation. Additionally, synergistic affects between ZN8751275 and a known PqsR antagonist are encouraging as a basis for further work. Inhibitory activity observed in *B. ambifaria* HmqA is encouraging as it demonstrates that PqsA inhibitors may have additional utility. Little work has been undertaken to show cross-species inhibition although a series of covalent HmqD inhibitors were recently described and shown to reduce AQ production in *B. ambifaria* AMMD[368].

Interesting, the inhibitor ZN8751275 does share some structural similarities with a series of PqsD inhibitors, likely due to shape complementarity in having to accommodate the same active site ligand anthraniloyl-CoA[369]. This suggests a route for SAR optimisation by modification to the linker region between the isoindoline and dichlorophenyl moieties to increase flexibility. An alternative means of optimisation may be examining the activity of simpler scaffolds. Assuming the dichlorophenyl occupies the small anthranilate binding pocket removal of bulky halogen constituents should increase the binding affinity (as shown by docking) and improve potency. Furthermore, SAR should be examined to provide evidence that the docked binding poses are correct.

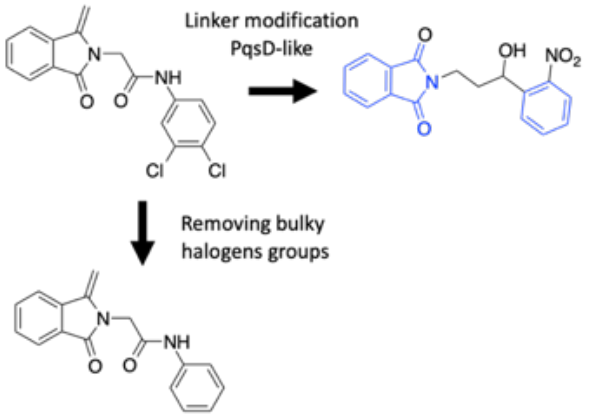

In silico analysis of the inhibitor excludes the possibility that the compound is a PAIN (**P**an **A**ssay **In**terference)[370]. However, structural similarity searching shows similar compounds (below) possessing inhibitory activity to several human and bacterial targets. This should be assessed further by measuring toxicity in a human cell line.

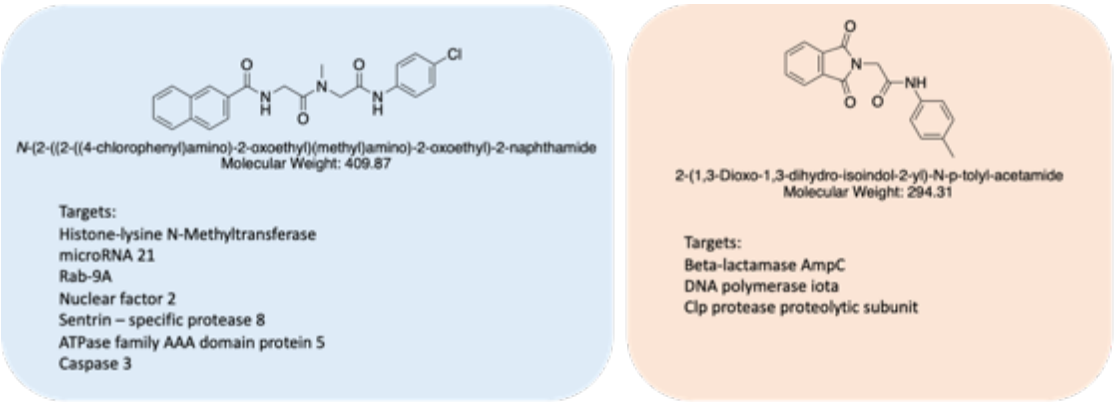

7.5 Conclusions

- From a library of 496 compounds a single inhibitor, ZN8751275, was shown to possess *in vitro* and *in vivo* activity.
- ZN8751275 effectively reduced CTX::P_{pqsA}-*lux* activity to under 50% which seems to explain a lack of virulence inhibition. This can serve as a benchmark for future medicinal chemistry optimisation
- ZN8751275 produced an additive effect when used in combination with PqsR antagonist SEN19
- The inhibitor gave a similar IC_{50} in *B. ambifaria* homolog HmqA suggesting a common binding site.

8 Outlook

This thesis has examined several aspects of PqsR's structure and basis of antagonism. The necessity to create new therapeutic options to successfully treat and manage *P. aeruginosa* infection is undeniable. The most recent English surveillance programme for antimicrobial utilisation and resistance (ESPAUR) report highlights that 10% of patient *P. aeruginosa* isolates exhibit resistance to at least one clinical agent.

In terms of translating the antagonists described in chapter 3 into viable anti-virulence therapeutics significant attention should focus on pulmonary drug delivery and penetration of the *P. aeruginosa* biofilm. Nanoparticle encapsulation for anti-biofilm applications has already been described for the sesquiterpene alcohol Farnesol. Previous studies have shown that pH-responding polymers can selectively release agents into the biofilm as they possess an acidic microenvironment[371]. Additionally, nanoparticles containing QSI have already given encouraging results in biofilm-associated murine pyelonephritis models further highlighting the appropriateness of this delivery method[372].

Our experiments on PqsA elucidated a single inhibitor for future development that could act in an additive fashion with a known PqsR antagonist SEN19. Given that inhibitors for most of the pqsABCDE biosynthetic cluster are available further experiments could focus on screening pairs to determine if synergy can be achieved with multiple targets. We could also examine the possibility of creating dual targeting agents, as similarly observed with PqsR/BC and PqsR/D[184 202]. Studies in our lab have focused on antibiotic synergism with Tobromycin - an antibiotic used in the treatment of respiratory *P. aeruginosa* infection. However, as PqsR upregulates several efflux pumps further screening for antibiotic synergy should be performed on clinically used agents such as meropenem and ciprofloxacin.

In a search to find superior diffracting $PqsR^{LBD}$ crystals a new dimer interface was determined. This new form adopted an arrangement characteristic of other LTTRs but was not prevalent in solution. The prevailing theory of LTTR activation is the sliding dimer hypothesis whereby subtle interfaces changes influences DNA interaction[138]. Our new models suggests that a substantial conformational change could occur upon ligand binding.

However, our understanding of LTTR structural changes is limited as receptors are often solved in a single state. PqsR possesses a substantially larger binding pocket compared to most LTTRs[155]. This leads us to theorise that the activation mechanism may be distinct to accommodate this. A wider structural study of LTTRs that bind high M_r ligands would be required to determine if this is the case.

Our study on the full length receptor failed to yield active protein, as determined by a lack of complex formation and inability to complement a *ΔpqsR* strain. Although activity is dispensable for further structural studies. To acquire active protein other rescue strategies could be attempted. Recently the first full length LTTR-DNA complex was solved – CbnR – that was also reported to have low solubility. However, upon forming a complex with DNA the protein was stable to 7.0 mg/mL[294]. A similar strategy could be used with PqsR with DNA introduced during cell lysis. In some instances, as with LuxR based transcriptional regulators, ligand are strictly required for solubility and *in vitro* activity[102]. Attaining both active and soluble PqsR will allow for more complex *in vitro* investigation such as determining binding site requirements.

9 Appendix

9.1 PqsR^{LBD} MPD crystal screen

pH						
5	0.1 M Trisodium sodium citrate 0.2 M Ammonium acetate 3 % MPD	0.1 M Trisodium sodium citrate 0.2 M Ammonium acetate 4 % MPD	0.1 M Trisodium sodium citrate 0.2 M Ammonium acetate 5 % MPD	0.1 M Trisodium sodium citrate 0.2 M Ammonium acetate 6 % MPD	0.1 M Trisodium sodium citrate 0.2 M Ammonium acetate 7 % MPD	0.1 M Trisodium sodium citrate 0.2 M Ammonium acetate 8 % MPD
5.5						
6						
6.5						

9.2 INFAC screening plates

INFAC Lithium Sulphate no 1 (broad) 1-48

1	1.7M Lithium sulphate + 0.02M Potassium acetate + 0.05M Cacodylate pH 6 + 0.025M Imidazole	13	1.5M Lithium sulphate + 0.01M Magnesium Acetate + 0.05M MES pH 6 + 0.025M Imidazole	25	1.3M Lithium sulphate + 0.01M Magnesium Acetate + 0.05M Cacodylate pH 6.5 + 2% Ethylene glycol	37	1.3M Lithium sulphate + 0.01M Potassium acetate + 0.05M Cacodylate pH 6 + 0.05M Ammonium acetate
2	1.6M Lithium sulphate + 0.02M Potassium acetate + 0.05M Cacodylate pH 6 + 0.05M Ammonium acetate	14	1.4M Lithium sulphate + 0.02M Magnesium chloride + 0.05M Cacodylate pH 6 + 2% Ethylene glycol	26	1.4M Lithium sulphate + 0.01M Magnesium Acetate + 0.05M MES pH 6 + 0.1M Ammonium acetate	38	1.7M Lithium sulphate + 0.01M Potassium acetate + 0.05M Cacodylate pH 6.5 + 5% MPD
3	1.5M Lithium sulphate + 0.02M Magnesium chloride + 0.05M Cacodylate pH 6.5 + 0.1M Imidazole	15	1.3M Lithium sulphate + 0.01M Magnesium chloride + 0.05M MES pH 6.5 + 0.1M Imidazole	27	1.2M Lithium sulphate + 0.01M Magnesium chloride + 0.05M Cacodylate pH 6.5 + 2% Ethylene glycol	39	1.5M Lithium sulphate + 0.01M Magnesium Acetate + 0.05M Cacodylate pH 6 + 5% Ethylene glycol
4	1.4M Lithium sulphate + 0.02M Magnesium Acetate + 0.05M MES pH 6 + 2% MPD	16	1.6M Lithium sulphate + 0.01M Magnesium Acetate + 0.05M MES pH 6.5 + 5% MPD	28	1.5M Lithium sulphate + 0.02M Potassium acetate + 0.05M Cacodylate pH 6.5 + 2% Ethylene glycol	40	1.4M Lithium sulphate + 0.02M Potassium acetate + 0.05M Cacodylate pH 6.5 + 0.1M Imidazole
5	1.2M Lithium sulphate + 0.01M Magnesium chloride + 0.05M MES pH 6 + 0.025M Imidazole	17	1.7M Lithium sulphate + 0.02M Magnesium chloride + 0.05M MES pH 6 + 5% Ethylene glycol	29	1.6M Lithium sulphate + 0.02M Potassium acetate + 0.05M MES pH 6 + 0.025M Imidazole	41	1.2M Lithium sulphate + 0.01M Potassium acetate + 0.05M MES pH 6 + 0.05M Ammonium acetate
6	1.3M Lithium sulphate + 0.01M Potassium acetate + 0.05M Cacodylate pH 6 + 5% Ethylene glycol	18	1.2M Lithium sulphate + 0.02M Magnesium chloride + 0.05M Cacodylate pH 6.5 + 0.1M Ammonium acetate	30	1.7M Lithium sulphate + 0.01M Magnesium chloride + 0.05M Cacodylate pH 6 + 0.1M Ammonium acetate	42	1.6M Lithium sulphate + 0.02M Magnesium Acetate + 0.05M MES pH 6.5 + 0.1M Imidazole
7	1.2M Lithium sulphate + 0.02M Potassium acetate + 0.05M Cacodylate pH 6 + 0.1M Imidazole	19	1.5M Lithium sulphate + 0.02M Magnesium Acetate + 0.05M Cacodylate pH 6 + 2% MPD	31	1.6M Lithium sulphate + 0.01M Magnesium chloride + 0.05M Cacodylate pH 6.5 + 2% Ethylene glycol	43	1.6M Lithium sulphate + 0.02M Magnesium chloride + 0.05M Cacodylate pH 6 + 0.1M Ammonium acetate
8	1.5M Lithium sulphate + 0.01M Potassium acetate + 0.05M MES pH 6.5 + 0.1M Ammonium acetate	20	1.7M Lithium sulphate + 0.01M Potassium acetate + 0.05M Cacodylate pH 6.5 + 2% MPD	32	1.7M Lithium sulphate + 0.02M Potassium acetate + 0.05M MES pH 6.5 + 2% Ethylene glycol	44	1.7M Lithium sulphate + 0.01M Magnesium Acetate + 0.05M MES pH 6 + 0.1M Imidazole
9	1.6M Lithium sulphate + 0.01M Magnesium chloride + 0.05M Cacodylate pH 6.5 + 5% Ethylene glycol	21	1.4M Lithium sulphate + 0.01M Magnesium chloride + 0.05M Cacodylate pH 6.5 + 0.025M Imidazole	33	1.2M Lithium sulphate + 0.02M Potassium acetate + 0.05M MES pH 6.5 + 5% Ethylene glycol	45	1.2M Lithium sulphate + 0.02M Magnesium chloride + 0.05M Cacodylate pH 6 + 2% MPD
10	1.3M Lithium sulphate + 0.02M Magnesium Acetate + 0.05M MES pH 6 + 0.025M Imidazole	22	1.3M Lithium sulphate + 0.02M Potassium acetate + 0.05M Cacodylate pH 6.5 + 5% MPD	34	1.3M Lithium sulphate + 0.02M Magnesium chloride + 0.05M MES pH 6.5 + 0.1M Ammonium acetate	46	1.3M Lithium sulphate + 0.02M Magnesium Acetate + 0.05M MES pH 6 + 2% MPD
11	1.4M Lithium sulphate + 0.01M Magnesium Acetate + 0.05M MES pH 6.5 + 5% Ethylene glycol	23	1.2M Lithium sulphate + 0.02M Magnesium Acetate + 0.05M MES pH 6.5 + 5% MPD	35	1.4M Lithium sulphate + 0.02M Magnesium Acetate + 0.05M MES pH 6.5 + 0.05M Ammonium acetate	47	1.4M Lithium sulphate + 0.01M Magnesium chloride + 0.05M Cacodylate pH 6 + 5% MPD
12	1.7M Lithium sulphate + 0.01M Magnesium Acetate + 0.05M MES pH 6.5 + 0.05M Ammonium acetate	24	1.6M Lithium sulphate + 0.01M Potassium acetate + 0.05M MES pH 6 + 2% MPD	36	1.5M Lithium sulphate + 0.01M Potassium acetate + 0.05M MES pH 6.5 + 0.05M Ammonium acetate	48	1.5M Lithium sulphate + 0.01M Magnesium chloride + 0.05M MES pH 6 + 5% MPD

INFAC Lithium Sulphate no 1 (broad) 49-96

49	1.2M Lithium sulphate + 0.02M Magnesium Acetate + 0.05M Cacodylate pH 6.5 + 5% Ethylene glycol	61	1.4M Lithium sulphate + 0.01M Magnesium Acetate + 0.05M MES pH 6 + 2% MPD	73	1.4M Lithium sulphate + 0.01M Potassium acetate + 0.05M Cacodylate pH 6.5 + 5% MPD	85	1.2M Lithium sulphate + 0.02M Magnesium Acetate + 0.05M Cacodylate pH 6.5 + 0.1M Ammonium acetate
50	1.3M Lithium sulphate + 0.01M Magnesium chloride + 0.05M Cacodylate pH 6 + 2% Ethylene glycol	62	1.3M Lithium sulphate + 0.02M Magnesium chloride + 0.05M MES pH 6.5 + 0.05M Ammonium acetate	74	1.7M Lithium sulphate + 0.02M Magnesium chloride + 0.05M MES pH 6 + 5% MPD	86	1.4M Lithium sulphate + 0.02M Potassium acetate + 0.05M MES pH 6 + 0.05M Ammonium acetate
51	1.7M Lithium sulphate + 0.02M Magnesium Acetate + 0.05M MES pH 6 + 0.025M Imidazole	63	1.2M Lithium sulphate + 0.01M Potassium acetate + 0.05M MES pH 6 + 2% Ethylene glycol	75	1.3M Lithium sulphate + 0.02M Magnesium Acetate + 0.05M MES pH 6 + 0.1M Imidazole	87	1.6M Lithium sulphate + 0.01M Magnesium chloride + 0.05M MES pH 6 + 2% Ethylene glycol
52	1.4M Lithium sulphate + 0.01M Potassium acetate + 0.05M Cacodylate pH 6.5 + 0.1M Imidazole	64	1.5M Lithium sulphate + 0.01M Magnesium chloride + 0.05M Cacodylate pH 6.5 + 0.05M Ammonium acetate	76	1.6M Lithium sulphate + 0.02M Potassium acetate + 0.05M Cacodylate pH 6 + 2% MPD	88	1.5M Lithium sulphate + 0.02M Magnesium chloride + 0.05M MES pH 6.5 + 0.1M Ammonium acetate
53	1.6M Lithium sulphate + 0.01M Magnesium Acetate + 0.05M Cacodylate pH 6 + 0.025M Imidazole	65	1.6M Lithium sulphate + 0.02M Magnesium chloride + 0.05M Cacodylate pH 6.5 + 5% Ethylene glycol	77	1.2M Lithium sulphate + 0.01M Magnesium chloride + 0.05M MES pH 6 + 0.05M Ammonium acetate	89	1.7M Lithium sulphate + 0.01M Magnesium chloride + 0.05M Cacodylate pH 6 + 0.1M Imidazole
54	1.5M Lithium sulphate + 0.02M Magnesium Acetate + 0.05M Cacodylate pH 6 + 5% Ethylene glycol	66	1.7M Lithium sulphate + 0.02M Potassium acetate + 0.05M MES pH 6.5 + 5% Ethylene glycol	78	1.5M Lithium sulphate + 0.02M Magnesium Acetate + 0.05M Cacodylate pH 6 + 0.025M Imidazole	90	1.3M Lithium sulphate + 0.01M Magnesium chloride + 0.05M Cacodylate pH 6 + 0.1M Ammonium acetate
55	1.4M Lithium sulphate + 0.02M Magnesium chloride + 0.05M Cacodylate pH 6 + 5% Ethylene glycol	67	1.2M Lithium sulphate + 0.02M Magnesium chloride + 0.05M Cacodylate pH 6 + 0.1M Imidazole	79	1.6M Lithium sulphate + 0.01M Magnesium Acetate + 0.05M Cacodylate pH 6.5 + 0.05M Ammonium acetate	91	1.6M Lithium sulphate + 0.02M Magnesium Acetate + 0.05M MES pH 6.5 + 5% MPD
56	1.2M Lithium sulphate + 0.01M Magnesium Acetate + 0.05M MES pH 6.5 + 2% MPD	68	1.5M Lithium sulphate + 0.02M Potassium acetate + 0.05M MES pH 6 + 2% Ethylene glycol	80	1.3M Lithium sulphate + 0.01M Potassium acetate + 0.05M MES pH 6.5 + 5% Ethylene glycol	92	1.4M Lithium sulphate + 0.02M Magnesium chloride + 0.05M MES pH 6.5 + 0.025M Imidazole
57	1.5M Lithium sulphate + 0.02M Magnesium chloride + 0.05M MES pH 6.5 + 5% MPD	69	1.3M Lithium sulphate + 0.02M Potassium acetate + 0.05M MES pH 6 + 2% MPD	81	1.2M Lithium sulphate + 0.02M Potassium acetate + 0.05M Cacodylate pH 6 + 0.025M Imidazole	93	1.2M Lithium sulphate + 0.01M Magnesium Acetate + 0.05M MES pH 6.5 + 5% MPD
58	1.6M Lithium sulphate + 0.01M Potassium acetate + 0.05M MES pH 6.5 + 0.1M Ammonium acetate	70	1.4M Lithium sulphate + 0.02M Magnesium Acetate + 0.05M MES pH 6.5 + 2% Ethylene glycol	82	1.4M Lithium sulphate + 0.01M Magnesium chloride + 0.05M Cacodylate pH 6 + 0.1M Ammonium acetate	94	1.3M Lithium sulphate + 0.01M Magnesium Acetate + 0.05M Cacodylate pH 6.5 + 5% MPD
59	1.7M Lithium sulphate + 0.02M Magnesium chloride + 0.05M Cacodylate pH 6.5 + 2% MPD	71	1.7M Lithium sulphate + 0.01M Potassium acetate + 0.05M Cacodylate pH 6 + 0.05M Ammonium acetate	83	1.5M Lithium sulphate + 0.01M Potassium acetate + 0.05M MES pH 6 + 2% MPD	95	1.5M Lithium sulphate + 0.01M Magnesium Acetate + 0.05M Cacodylate pH 6.5 + 0.1M Imidazole
60	1.3M Lithium sulphate + 0.02M Potassium acetate + 0.05M Cacodylate pH 6.5 + 0.025M Imidazole	72	1.6M Lithium sulphate + 0.01M Potassium acetate + 0.05M MES pH 6 + 0.1M Imidazole	84	1.7M Lithium sulphate + 0.01M Magnesium Acetate + 0.05M MES pH 6.5 + 0.1M Ammonium acetate	96	1.7M Lithium sulphate + 0.02M Magnesium Acetate + 0.05M Cacodylate pH 6.5 + 2% Ethylene glycol

INFAC Lithium Sulphate no 2 Conditions 1-48 (narrow)

1	1.5M Lithium sulphate + 0.1M Cacodylate pH 6 + 0.1M Potassium Chloride	13	1.2M Lithium sulphate + 0.1M Cacodylate pH 6 + 0.1M Magnesium Sulphate	25	1.7M Lithium sulphate + 0.1M Cacodylate pH 6 + 0.05M Ammonium Acetate	37	1.7M Lithium sulphate + 0.1M Cacodylate pH 6.5 + 0.1M Magnesium Sulphate
2	1.4M Lithium sulphate + 0.1M Cacodylate pH 6.5 + 0.05M Ammonium Acetate	14	1.7M Lithium sulphate + 0.05M Cacodylate pH 6.5 + 0.1M Magnesium Chloride	26	1.6M Lithium sulphate + 0.05M Cacodylate pH 6.5 + 0.05M Ammonium Acetate	38	1.5M Lithium sulphate + 0.1M Cacodylate pH 6 + 0.1M Potassium Acetate
3	1.6M Lithium sulphate + 0.1M Cacodylate pH 6.5 + 0.05M Magnesium Sulphate	15	1.3M Lithium sulphate + 0.1M Cacodylate pH 6 + 0.01M Magnesium Chloride	27	1.5M Lithium sulphate + 0.05M Cacodylate pH 6 + 0.01M Potassium Chloride	39	1.6M Lithium sulphate + 0.1M Cacodylate pH 6 + 0.1M Ammonium Sulphate
4	1.7M Lithium sulphate + 0.1M Cacodylate pH 6 + 0.05M Ammonium Sulphate	16	1.4M Lithium sulphate + 0.05M Cacodylate pH 6.5 + 0.05M Magnesium Chloride	28	1.2M Lithium sulphate + 0.1M Cacodylate pH 6 + 0.01M Potassium Acetate	40	1.2M Lithium sulphate + 0.05M Cacodylate pH 6.5 + 0.1M Ammonium Sulphate
5	1.2M Lithium sulphate + 0.1M Cacodylate pH 6.5 + 0.1M Potassium Acetate	17	1.6M Lithium sulphate + 0.05M Cacodylate pH 6.5 + 0.05M Potassium Acetate	29	1.3M Lithium sulphate + 0.1M Cacodylate pH 6 + 0.01M Potassium Chloride	41	1.3M Lithium sulphate + 0.1M Cacodylate pH 6.5 + 0.1M Ammonium Sulphate
6	1.3M Lithium sulphate + 0.1M Cacodylate pH 6.5 + 0.05M Magnesium Chloride	18	1.5M Lithium sulphate + 0.1M Cacodylate pH 6.5 + 0.01M Magnesium Chloride	30	1.4M Lithium sulphate + 0.1M Cacodylate pH 6 + 0.1M Magnesium Acetate	42	1.4M Lithium sulphate + 0.1M Cacodylate pH 6.5 + 0.01M Magnesium Chloride
7	1.5M Lithium sulphate + 0.05M Cacodylate pH 6 + 0.1M Ammonium Sulphate	19	1.2M Lithium sulphate + 0.05M Cacodylate pH 6 + 0.05M Potassium Chloride	31	1.5M Lithium sulphate + 0.1M Cacodylate pH 6.5 + 0.1M Ammonium Acetate	43	1.5M Lithium sulphate + 0.05M Cacodylate pH 6.5 + 0.01M Potassium Acetate
8	1.2M Lithium sulphate + 0.05M Cacodylate pH 6.5 + 0.05M Ammonium Sulphate	20	1.3M Lithium sulphate + 0.05M Cacodylate pH 6 + 0.1M Magnesium Acetate	32	1.4M Lithium sulphate + 0.05M Cacodylate pH 6.5 + 0.01M Magnesium Sulphate	44	1.7M Lithium sulphate + 0.05M Cacodylate pH 6.5 + 0.01M Potassium Acetate
9	1.3M Lithium sulphate + 0.05M Cacodylate pH 6.5 + 0.1M Magnesium Sulphate	21	1.7M Lithium sulphate + 0.1M Cacodylate pH 6.5 + 0.05M Magnesium Acetate	33	1.7M Lithium sulphate + 0.05M Cacodylate pH 6 + 0.1M Potassium Acetate	45	1.3M Lithium sulphate + 0.05M Cacodylate pH 6.5 + 0.01M Magnesium Acetate
10	1.7M Lithium sulphate + 0.05M Cacodylate pH 6 + 0.01M Potassium Chloride	22	1.6M Lithium sulphate + 0.1M Cacodylate pH 6 + 0.05M Ammonium Sulphate	34	1.6M Lithium sulphate + 0.05M Cacodylate pH 6 + 0.05M Potassium Chloride	46	1.2M Lithium sulphate + 0.1M Cacodylate pH 6.5 + 0.1M Magnesium Acetate
11	1.4M Lithium sulphate + 0.05M Cacodylate pH 6 + 0.1M Magnesium Sulphate	23	1.4M Lithium sulphate + 0.1M Cacodylate pH 6 + 0.05M Ammonium Sulphate	35	1.2M Lithium sulphate + 0.05M Cacodylate pH 6 + 0.01M Magnesium Chloride	47	1.4M Lithium sulphate + 0.05M Cacodylate pH 6 + 0.1M Ammonium Acetate
12	1.6M Lithium sulphate + 0.05M Cacodylate pH 6 + 0.1M Magnesium Acetate	24	1.5M Lithium sulphate + 0.05M Cacodylate pH 6.5 + 0.05M Magnesium Acetate	36	1.3M Lithium sulphate + 0.05M Cacodylate pH 6 + 0.1M Potassium Acetate	48	1.6M Lithium sulphate + 0.1M Cacodylate pH 6.5 + 0.01M Magnesium Acetate

INFAC Lithium Sulphate no 2 Conditions 49-96 (narrow)

49	1.7M Lithium sulphate + 0.05M Cacodylate pH 6 + 0.01M Magnesium Acetate	61	1.7M Lithium sulphate + 0.1M Cacodylate pH 6 + 0.1M Potassium Chloride	73	1.6M Lithium sulphate + 0.05M Cacodylate pH 6 + 0.01M Magnesium Chloride	85	1.3M Lithium sulphate + 0.1M Cacodylate pH 6 + 0.1M Ammonium Acetate
50	1.4M Lithium sulphate + 0.1M Cacodylate pH 6.5 + 0.1M Magnesium Chloride	62	1.2M Lithium sulphate + 0.05M Cacodylate pH 6 + 0.05M Ammonium Acetate	74	1.5M Lithium sulphate + 0.05M Cacodylate pH 6.5 + 0.05M Ammonium Acetate	86	1.4M Lithium sulphate + 0.05M Cacodylate pH 6.5 + 0.05M Magnesium Sulphate
51	1.3M Lithium sulphate + 0.05M Cacodylate pH 6 + 0.01M Potassium Acetate	63	1.4M Lithium sulphate + 0.05M Cacodylate pH 6.5 + 0.05M Potassium Chloride	75	1.7M Lithium sulphate + 0.1M Cacodylate pH 6 + 0.1M Ammonium Acetate	87	1.6M Lithium sulphate + 0.05M Cacodylate pH 6.5 + 0.1M Potassium Acetate
52	1.5M Lithium sulphate + 0.1M Cacodylate pH 6 + 0.05M Magnesium Sulphate	64	1.5M Lithium sulphate + 0.05M Cacodylate pH 6.5 + 0.1M Magnesium Acetate	76	1.2M Lithium sulphate + 0.05M Cacodylate pH 6 + 0.05M Potassium Acetate	88	1.7M Lithium sulphate + 0.05M Cacodylate pH 6.5 + 0.05M Potassium Acetate
53	1.2M Lithium sulphate + 0.1M Cacodylate pH 6.5 + 0.1M Magnesium Chloride	65	1.6M Lithium sulphate + 0.05M Cacodylate pH 6 + 0.1M Magnesium Chloride	77	1.3M Lithium sulphate + 0.1M Cacodylate pH 6.5 + 0.1M Magnesium Chloride	89	1.5M Lithium sulphate + 0.1M Cacodylate pH 6 + 0.05M Potassium Chloride
54	1.6M Lithium sulphate + 0.1M Cacodylate pH 6.5 + 0.05M Magnesium Acetate	66	1.3M Lithium sulphate + 0.1M Cacodylate pH 6.5 + 0.1M Potassium Chloride	78	1.4M Lithium sulphate + 0.1M Cacodylate pH 6.5 + 0.1M Ammonium Sulphate	90	1.2M Lithium sulphate + 0.1M Cacodylate pH 6 + 0.05M Magnesium Chloride
55	1.7M Lithium sulphate + 0.05M Cacodylate pH 6.5 + 0.05M Magnesium Sulphate	67	1.3M Lithium sulphate + 0.1M Cacodylate pH 6 + 0.01M Magnesium Sulphate	79	1.6M Lithium sulphate + 0.1M Cacodylate pH 6.5 + 0.01M Potassium Acetate	91	1.7M Lithium sulphate + 0.1M Cacodylate pH 6.5 + 0.05M Potassium Chloride
56	1.5M Lithium sulphate + 0.05M Cacodylate pH 6 + 0.1M Magnesium Sulphate	68	1.2M Lithium sulphate + 0.1M Cacodylate pH 6 + 0.05M Magnesium Sulphate	80	1.2M Lithium sulphate + 0.1M Cacodylate pH 6.5 + 0.01M Potassium Chloride	92	1.6M Lithium sulphate + 0.1M Cacodylate pH 6 + 0.1M Ammonium Acetate
57	1.2M Lithium sulphate + 0.05M Cacodylate pH 6.5 + 0.01M Magnesium Acetate	69	1.5M Lithium sulphate + 0.1M Cacodylate pH 6.5 + 0.01M Magnesium Sulphate	81	1.7M Lithium sulphate + 0.05M Cacodylate pH 6 + 0.01M Magnesium Sulphate	93	1.5M Lithium sulphate + 0.05M Cacodylate pH 6 + 0.05M Magnesium Chloride
58	1.4M Lithium sulphate + 0.05M Cacodylate pH 6 + 0.05M Magnesium Acetate	70	1.7M Lithium sulphate + 0.1M Cacodylate pH 6.5 + 0.05M Magnesium Chloride	82	1.5M Lithium sulphate + 0.1M Cacodylate pH 6.5 + 0.05M Ammonium Sulphate	94	1.3M Lithium sulphate + 0.05M Cacodylate pH 6.5 + 0.05M Potassium Chloride
59	1.6M Lithium sulphate + 0.1M Cacodylate pH 6 + 0.01M Magnesium Sulphate	71	1.6M Lithium sulphate + 0.05M Cacodylate pH 6.5 + 0.01M Potassium Chloride	83	1.3M Lithium sulphate + 0.05M Cacodylate pH 6 + 0.05M Potassium Acetate	95	1.2M Lithium sulphate + 0.05M Cacodylate pH 6.5 + 0.1M Potassium Chloride
60	1.3M Lithium sulphate + 0.05M Cacodylate pH 6.5 + 0.05M Magnesium Acetate	72	1.4M Lithium sulphate + 0.1M Cacodylate pH 6 + 0.05M Potassium Acetate	84	1.4M Lithium sulphate + 0.1M Cacodylate pH 6 + 0.01M Magnesium Acetate	96	1.4M Lithium sulphate + 0.05M Cacodylate pH 6 + 0.1M Potassium Chloride

9.3 Strains possessing PqsR mined from Pseudomonas Genome Database

List of strains, taken from Pseudomonas Genome Database, used for conservational analysis of PqsR. Only strains with a complete genome were selected for analysis.

	Strains	Origin	Source		Strains	Origin	Source		Strains	Origin	Source		Strains	Origin	Source
1	PAO1	Australia	Wound	**51**	DN1	China	Environmental	**101**	LES431	UK	Clinical (non-CF)	**151**	PA_D1	China	Respiratory
2	PA14	USA	Burn	**52**	DSM 50071	Unknown	Unknown	**102**	LW	China	Respiratory	**152**	PA_D16	China	Respiratory
3	LESB58	UK	Respiratory	**53**	E6130952	Canada	Respiratory	**103**	M1608	USA	Clinical (non-CF)	**153**	PA_D2	China	Respiratory
4	PAK	USA	Unknown	**54**	E80	Unknown	Respiratory	**104**	M18	China	Environmental	**154**	PA_D21	China	Respiratory
5	12-4-4(59)	USA	Burn	**55**	F22031	USA	Clinical (non-CF)	**105**	MRSN12280	USA	Wound	**155**	PA_D22	China	Respiratory
6	12939	China	Unknown	**56**	F23197	USA	Clinical (non-CF)	**106**	MTB-1	India	Environmental	**156**	PA_D25	China	Respiratory
7	1334/14	Poland	Eye infection	**57**	F5677	USA	Clinical (non-CF)	**107**	N15-01092	Canada	Unknown	**157**	PA_D5	China	Respiratory
8	19BR	Brazil	Unknown	**58**	F63912	USA	Clinical (non-CF)	**108**	N17-1	China	Environmental	**158**	PA_D9	China	Respiratory
9	213BR	Brazil	Unknown	**59**	F9676	China	Environmental	**109**	NCGM1900	Japan	Catheter	**159**	PB350	USA	Respiratory
10	24Pae112	Colombia	Blood	**60**	FA-HZ1	China	Environmental	**110**	NCGM1984	Japan	Catheter	**160**	PB353	USA	UTI
11	268	USA	Clinical (non-CF)	**61**	FDAARGOS_501	USA	Clinical (non-CF)	**111**	NCGM2.S1	Japan	UTI	**161**	PB354	USA	UTI
12	8380	Japan	Clinical (non-CF)	**62**	FDAARGOS_505	USA	Respiratory	**112**	NCGM257	Japan	UTI	**162**	PB367	USA	Respiratory
13	97	Ghana	UTI	**63**	FDAARGOS_532	USA	Respiratory	**113**	NCTC10332	Czech Republic	Unknown	**163**	PB368	USA	Clinical (non-CF)
14	AES1M	Australia	Respiratory	**64**	FDAARGOS_570	USA	Clinical (non-CF)	**114**	NCTC10728	UK	Unknown	**164**	PB369	USA	Clinical (non-CF)
15	AES1R	Australia	Respiratory	**65**	FDAARGOS_571	USA	Clinical (non-CF)	**115**	NCTC11445	Unknown	Unknown	**165**	PPF-1	Canada	Environmental

16	AR439	USA	Unknown	**66**	FDAARGOS_610	USA	Environmental	**116**	NCTC12903	Unknown	Blood	**166**	RIVM-EMC2982	Netherlands	Clinical (non-CF)
17	AR441	USA	Unknown	**67**	FDAARGOS_767	USA	Clinical (non-CF)	**117**	NCTC13359	Unknown	Environmental	**167**	RP73	Germany	Respiratory
18	AR442	USA	Unknown	**68**	FRD1	USA	Respiratory	**118**	NCTC13618	Unknown	Clinical (non-CF)	**168**	S86968	USA	Clinical (non-CF)
19	AR444	USA	Unknown	**69**	GIMC5015:PAKB6	Russia	Respiratory	**119**	NCTC13715	UK	UTI	**169**	SCV20265	Germany	Respiratory
20	AR445	USA	Unknown	**70**	H25883	Switzerland	Burn	**120**	Nhmuc	Germany	Clinical (non-CF)	**170**	SCVFeb	UK	Animal
21	AR_0095	USA	Unknown	**71**	H26023	Switzerland	Respiratory	**121**	Ocean-1155	Japan	Environmental	**171**	SCVJan	UK	Animal
22	AR_0110	USA	Unknown	**72**	H26027	Switzerland	Burn	**122**	Ocean-1175	Japan	Environmental	**172**	SP2230	India	Respiratory
23	AR_0111	USA	Unknown	**73**	H27930	USA	Clinical (non-CF)	**123**	PA1	China	Respiratory	**173**	SP4371	India	Respiratory
24	AR_0230	USA	Unknown	**74**	H5708	USA	Clinical (non-CF)	**124**	PA1088	Brazil	UTI	**174**	SP4527	India	Respiratory
25	AR_0353	USA	Unknown	**75**	HS9	China	Environmental	**125**	PA11803	Brazil	Blood	**175**	SP4528	India	Respiratory
26	AR_0354	USA	Unknown	**76**	IMP-13	Belgium	UTI	**126**	Pa1207	Mexico	Blood	**176**	T38079	USA	Clinical (non-CF)
27	AR_0356	USA	Unknown	**77**	IOMTU 133	Nepal	Catheter	**127**	PA121617	China	Respiratory	**177**	USDA-ARS-USMARC-41639	USA	Animal
28	AR_0357	USA	Unknown	**78**	isolate 1	Germany	Unknown	**128**	Pa124	Mexico	Respiratory	**178**	VA-134	Unknown	Burn
29	AR_0360	USA	Unknown	**79**	isolate B10W	Hawaii	Environmental	**129**	Pa1242	Mexico	Blood	**179**	VRFPA04	India	Wound
30	AR_0446	USA	Unknown	**80**	F30658	USA	Clinical (non-CF)	**130**	Pa127	Mexico	Respiratory	**180**	W16407	USA	Clinical (non-CF)
31	AR_455	USA	Unknown	**81**	F9670	USA	Clinical (non-CF)	**131**	PA1R	Unknown	Unknown	**181**	W36662	USA	Clinical (non-CF)
32	AR_458	USA	Unknown	**82**	H47921	USA	Clinical (non-CF)	**132**	PA1RG	China	Environmental	**182**	W45909	USA	Clinical (non-CF)
33	AR_460	USA	Unknown	**83**	M37351	USA	Clinical (non-CF)	**133**	PA298	China	Feces	**183**	W60856	USA	Clinical (non-CF)
34	ATCC 15692	Unknown	Wound	**84**	PA14Or	France	Environmental	**134**	PA34	India	Eye infection	**184**	WCHPA075019	China	Clinical (non-CF)

35	ATCC 27853	China	Respiratory	**85**	paerg000	Switzerland	Clinical (non-CF)	**135**	Pa58	Mexico	Respiratory	**185**	X78812	USA	Clinical (non-CF)
36	ATCC 27853	Netherlands	Unknown	**86**	paerg002	Switzerland	Clinical (non-CF)	**136**	PA7790	Brazil	Respiratory	**186**	Y31	USA	Clinical (non-CF)
37	B136-33	China	Clinical (non-CF)	**87**	paerg003	Switzerland	Clinical (non-CF)	**137**	PA8281	Brazil	Respiratory	**187**	Y71	South Korea	Respiratory
38	B14130	India	Blood	**88**	paerg004	Switzerland	Clinical (non-CF)	**138**	PA83	Germany	Blood	**188**	Y82	South Korea	Respiratory
39	B17932	India	Blood	**89**	paerg005	Switzerland	Clinical (non-CF)	**139**	Pa84	Mexico	Respiratory	**189**	Y89	South Korea	Respiratory
40	B41226	India	Blood	**90**	paerg009	Switzerland	Clinical (non-CF)	**140**	PABL012	USA	Blood	**190**	YL84	Malaysia	Environmental
41	BA15561	India	Blood	**91**	paerg010	Switzerland	Clinical (non-CF)	**141**	PABL017	USA	Blood				
42	BA7823	India	Blood	**92**	paerg011	Switzerland	Clinical (non-CF)	**142**	PABL048	USA	Blood				
43	BAMC 07-48	USA	Wound	**93**	paerg012	Switzerland	Clinical (non-CF)	**143**	PACS2	Unknown	Respiratory				
44	C-NN2 isolate	Germany	Respiratory	**94**	PcyII-10	France	Clinical (non-CF)	**144**	PAER4_119	Poland	Unknown				
45	Carb01 63	Netherlands	Clinical (non-CF)	**95**	RW109	Unknown	Environmental	**145**	PAO1161	Poland	Wound				
46	CCUG 70744	Sweden	Respiratory	**96**	T52373	USA	Clinical (non-CF)	**146**	PAO1_Orsay	Unknown	Unknown				
47	CR1	India	Environmental	**97**	T63266	USA	Clinical (non-CF)	**147**	PASGNDM345	Singapore	Respiratory				
48	DHS01	France	Assymptomatic	**98**	JB2	USA	Environmental	**148**	PASGNDM699	Singapore	Respiratory				
49	DK1 NH57388A	Denmark	Respiratory	**99**	K34-7	Norway	Respiratory	**149**	PA_150577	China	Unknown				
50	DK2	Denmark	Respiratory	**100**	L10	China	Environmental	**150**	PA_154197	China	Unknown				

9.4 Origin of each isolate from the Pseudomonas Genome Database

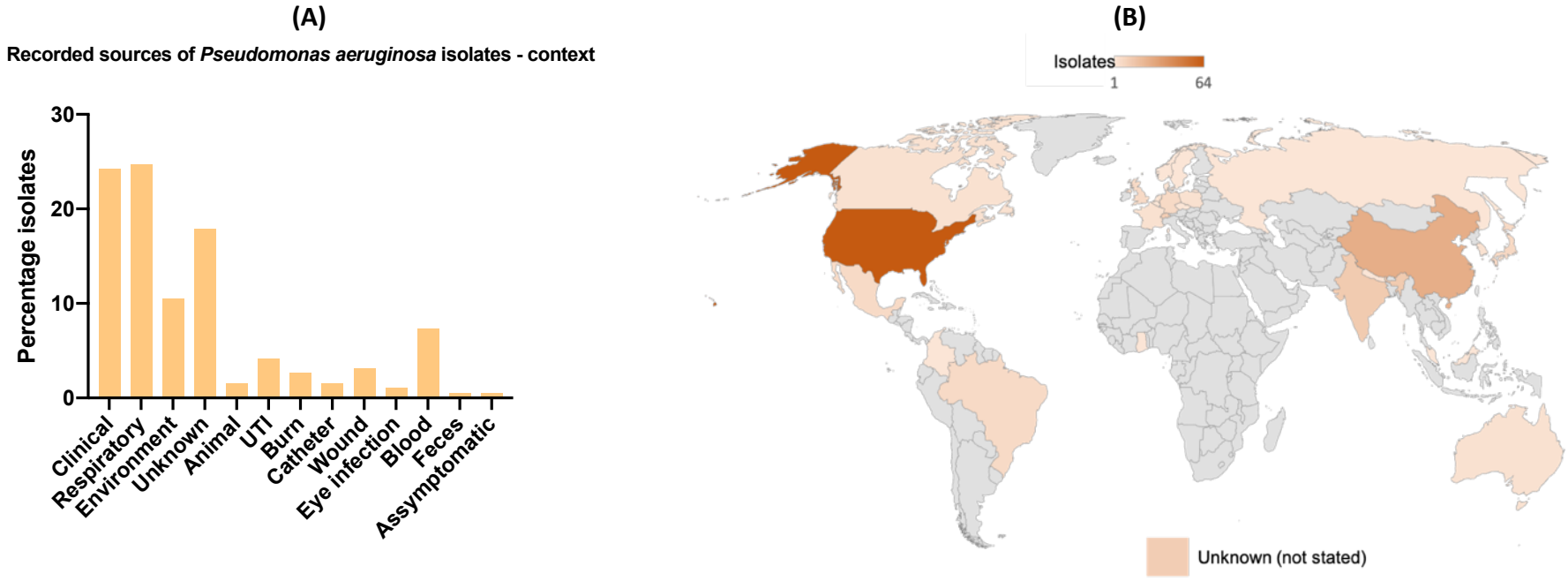

Sequence information - Isolate distribution with respect to source type **(A)** and location **(B)** attained from information provided with the relevant BioSample (NCBI) ID code. In some instances, information was not provided in these records and have been indicated as “unknown (not stated)”. Most isolates originate from clinical sources in the United States.

9.5 Frequency of missense, deletions, and insertions across PqsR

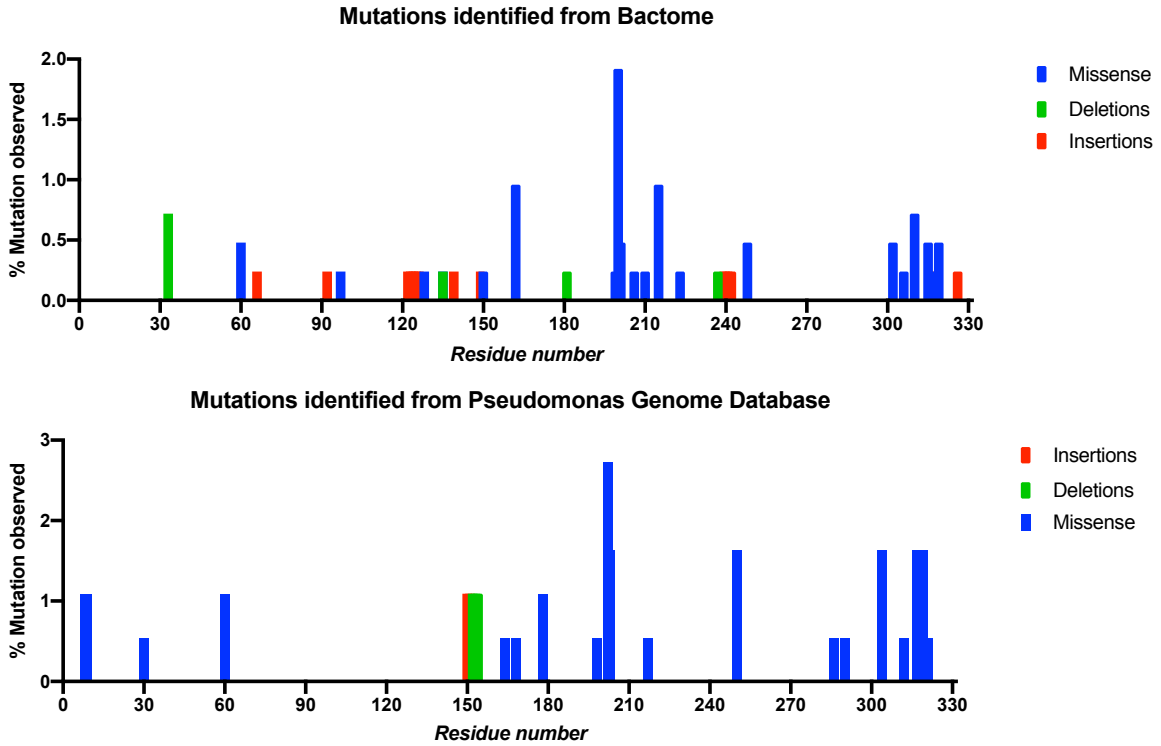

Distribution of mutations represented as a portion of isolates identified in each sequence dataset: Bactome (top) and PGD (bottom). Mutations are represented by colour. The very common 314 A/V mutation is not shown. The ligand binding domain from residues 94-332 possesses a greater proportion of mutations compared to the DNA binding domain. Missense mutations are most often observed in each dataset.

9.6 Predicted impact of missense mutations on protein stability

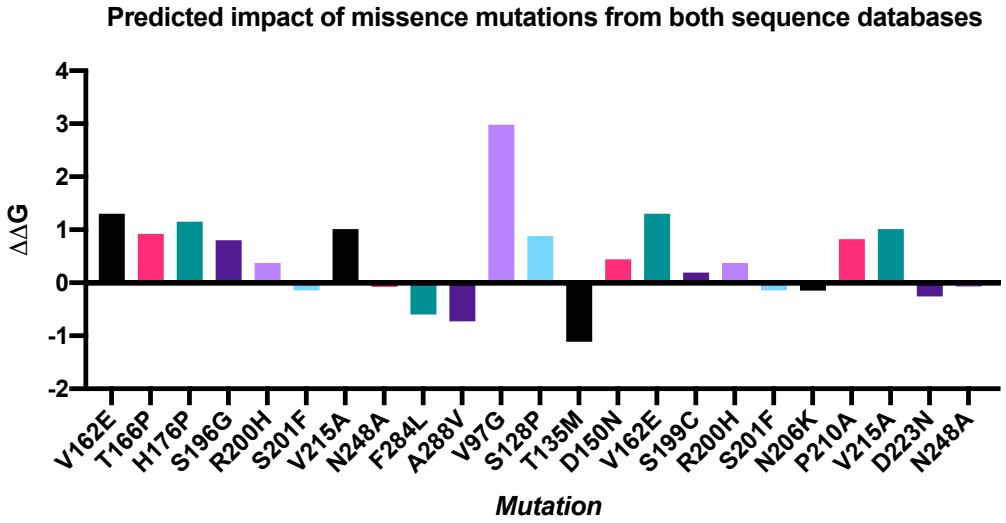

Predicted impact of each missense mutation on protein stability, represented as *ΔΔG* kcal mol^{-1}, calculated by PremPS server. Positive values and negative values corresponding to stabilising and destabilising mutations respectively. Most missense mutations have little impact on predicted protein stability.

9.7 Boltzmann melting temperature analysis from change in Molar Ellipticity

Melting of $PqsR^{94-332}$ (& mutants) conducted on a Chirascan instrument. Change in molar ellipticity showed as a function of temperature. Data plotted in PRISM and data fitted using a Boltzmann model. Legend showing samples differentiated by colour. 488 ligand added in a 1:3 ratio of protein:ligand. T_m calculation given in Figure 3.36 with T265N giving the largest increase in temperature upon ligand addition.

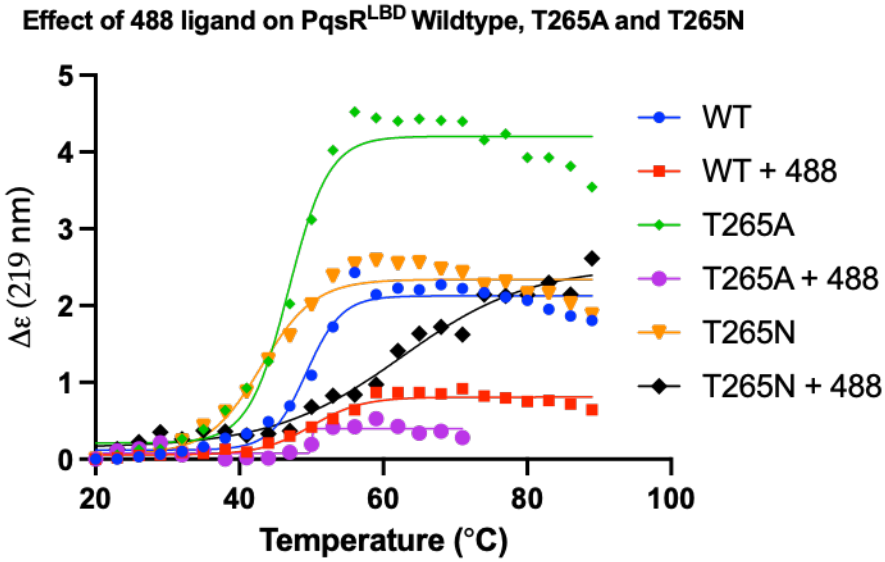

9.8 IlvC data collection statistics and figures

The unique purification contaminant IlvC diffracted to 2.38 Å on i24. Crystal space group and unit cell parameters are the same as contained in PDB 1N3P. The collection and refinement details are given below:

Data collection	*P. aeruginosa* IlvC
Wavelength (Å)/beamline	I24
Space group	P 2_1 3
a, b, c (Å)	185.2, 185.2, 185.2
α, β, γ (°)	90, 90, 90
Resolution (Å)	53.44 – 2.38
No. of unique reflections	84205
Rmerge (%)	0.239 (1.95)
Mean I/Sig(I)	4 (0.5)
Completeness	99.7 (100)
Redundnacy	3.8 (3.9)
CC½	1 (0.3)
Refinement	
Resolution range (Å)	53.50 - 2.38
R/Rfree (%)	0.216 / 0.263
Mean B-factor (Å)	58.23
r.m.s.d. bond lengths (Å)	0.0091
r.m.s.d. bond angles (°)	1.641
Ramachandran plot statistics (%)	
Preferred regions	91.70
Outliers	1.08
PDB ID	N/A

*Structure not deposited in PDB

Model differences compared to the published model 1N3P:

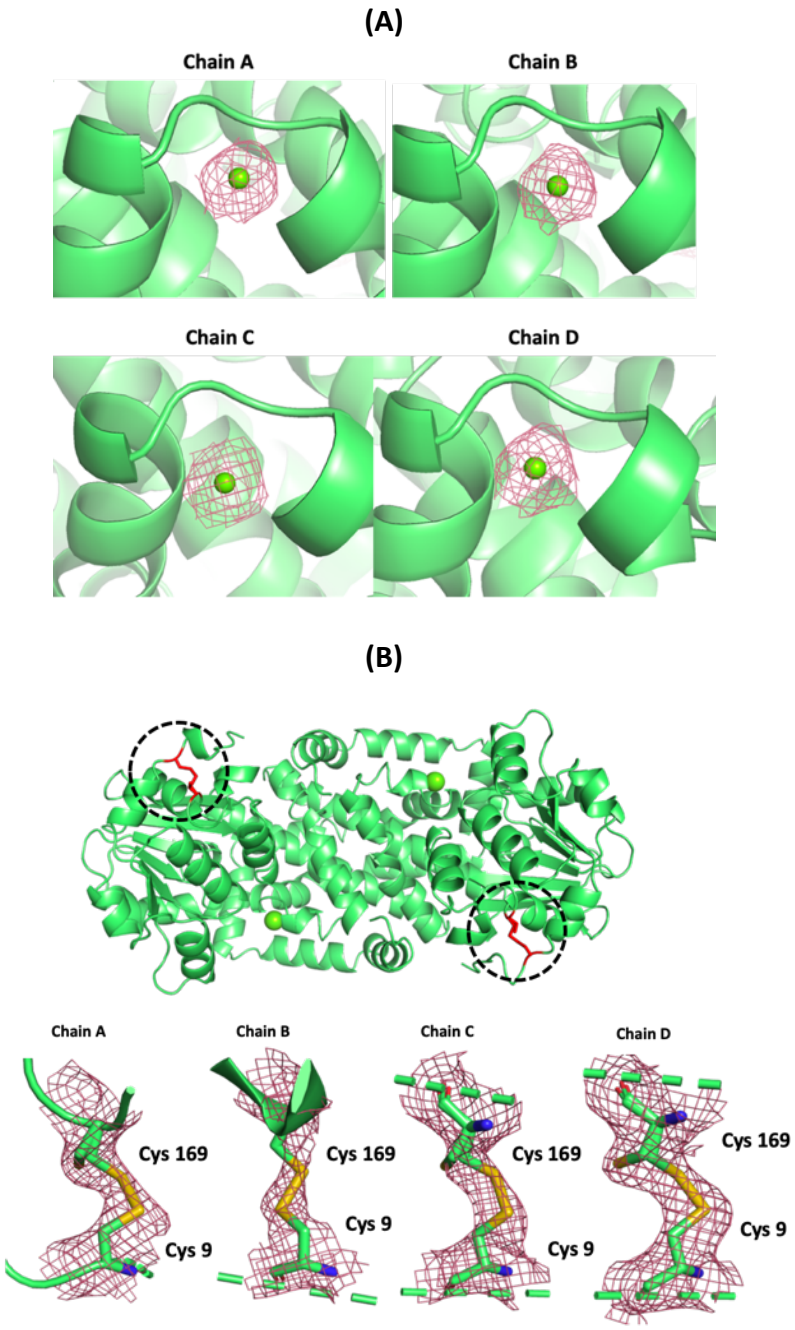

Overview of IlvC model differences to published 1N3P (A) Cartoon representation of IlvC magnesium binding site. Electron density of magnesium ions showed as a 2Fo-Fc map contoured at 1 σ. As expected the ions, with interactions to protein backbone, side chains and water adopt a hexadentate geometry. **(B)** Protein dimer modelled as a green cartoon with new disulphide bonds marked in red and circled. Model with bonds represented as stick and backbone loop as a cartoon (green). 2Fo-Fc map coloured in red and contoured to 1 σ.

9.9 Cleavage conditions

Cleavage conditions, set up in a 100 µL digestion volume, used to screen for stable PqsR conditions.

No.	Additive	Concentration
1.	Glycerol	10%
2.	KCl	0.5 M
3.	Urea	100 mM
4.	$MgSO_4$	25 mM
5.	Ammonium sulphate	50 mM
6.	Ethylene Glycol	5%
7.	MES	25 mM
8.	Trehalose	0.5 M
9.	Citrate	10 mM
10.	Tween 20/80 (either)	0.1%
11.	Triton X100	0.1%
12.	Lithium Sulphate	100 mM
13.	CH_3 - HHQ	50 µM
14.	gDNA	1:1 (based on mass of fusion protein)

9.10 Lattice and contaminant screening of FL PqsR crystals

Using SIMBAD (**S**equence-**I**ndependent **M**olecular replacement **B**ased on **A**vailable **D**atabases) the highest resolution dataset, processed using Staraniso to 4.06 Å, attained from FL PqsR plate morphology was examined for potential solutions through lattice and common crystal contaminant searches. The following table highlights the output from the runs showing that no satisfactory solution could be identified from these databases suggesting the crystal was not derived from a purification artefact of *E. coli* expression. Search was performed with likely spacegroup $C222_1$ and repeated omitting the screw axis (C222). No model yielded a solution with R/Rfree below 0.45 suggesting no solution was identified. TFZ score (signal-to-noise ratio) of greater than 6 would highlight a possible solution with greater score correlating with certainty. LLG score for a successful phaser run is >120. Lattice search was conducted but failed to find any suitably similar models.

C 2 2 2_1

No.	PDB code	Phaser TFZ score	LLG	R/Rfree (2 dp)
1.	4r0f	4.4	32	0.51/0.51
2.	2z19	5.4	26	0.53/0.51
3.	2hgg (A)	6.1	31	0.54/0.51
4.	4p2e	5.3	30	0.52/0.52
5.	5uxz	5.1	26	0.51/0.52
6.	2vf4	4.4	31	0.51/0.52
7.	2hgg (A)	4.6	22	0.55/0.53
8.	4zjl (A)	4.4	23	0.54/0.53
9.	1dc5	5.3	28	0.53/0.53
10.	2psg	3.8	31	0.5/0.53
11.	4tun	3.9	31	0.52/0.53
12.	2d4j	5.4	27	0.51/0.53
13.	4bap	4.4	29	0.52/0.54
14.	5c7r	3.6	27	0.46/0.54
15.	1dc6	4.0	26	0.49/0.54

16.	1q31	3.7	28	0.51/0.54
17.	2hrt (A)	5.4	29	0.53/0.56
18.	4ki8 (F)	4.6	12	0.56/0.56
19.	3sev	4.0	23	0.5/0.57
20.	3klb	(-)*	(-)*	0.41/0.58

C 2 2 2

No.	PDB code	Phaser TFZ score	LLG	R/Rfree (2 dp)
1.	3lgl (A)	4.1	30	0.51/0.5
2.	2hgg (A)	4.2	21	0.52/0.51
3.	2hrt (A)	4.7	27	0.51/0.51
4.	1u2k	3.7	28	0.49/0.51
5.	1z7e (B)	3.7	28	0.49/0.52
6.	4kl8 (F)	5.9	12	0.54/0.52
7.	1mly	4.8	28	0.49/0.52
8.	1dc5	4.5	23	0.47/0.53
9.	2vf4	4.7	31	0.50/0.52
10.	1dc6	4.4	21	0.46/0.53
11.	3hy1	5	21	0.49/0.54
12.	2vf4 (X)	4	28	0.5/0.54
13.	3sev	(-)*	(-)*	0.46/0.54
14.	3k1b	(-)*	(-)*	0.49/0.54
15.	5c7r	4.2	20	0.48/0.55
16.	4kl8 (C)	5.3	12	0.55/0.55
17.	2hrt (D)	5.3	23	0.53/0.56
18.	4zjl (A)	4	20	0.53/0.55
19.	3sey	(-)*	(-)*	0.49/0.56

*(-) TFZ performed using the MOLREP pipeline and therefore TFZ and LLG score is not applied.

9.11 Negative stain images of PqsR

Negative stain images, taken on a Gatan Ultrascan camera, of FL PqsR prepared at a concentration of 1-2 µg/mL.

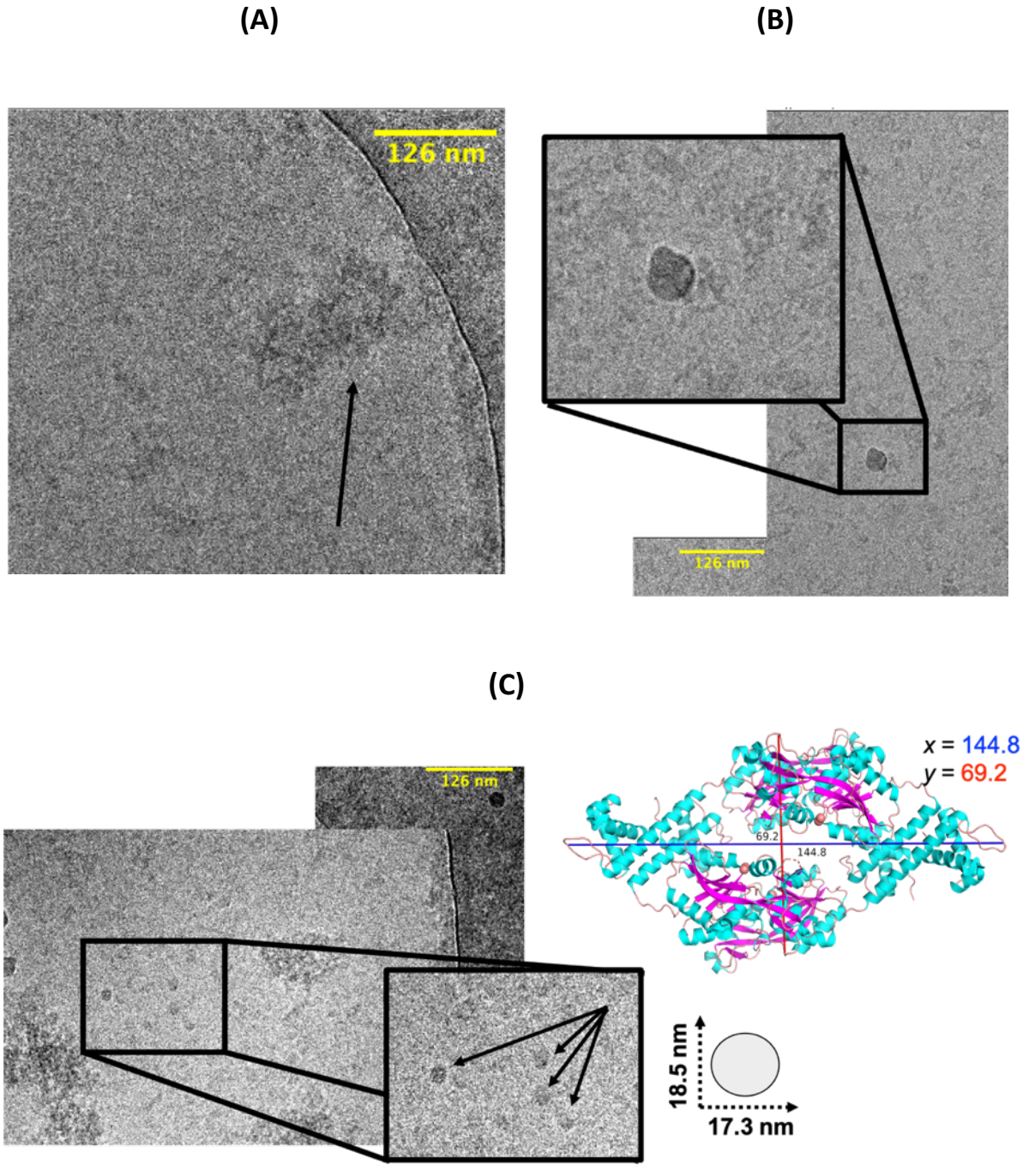

(A) Sample aggregation by the grid hole perimeter observed on an image taken at 20,000 x magnification at 200 kV. **(B)** Irregular contaminant with relatively high contrast – Ethane contaminant. **(C)** Small circular discrete objects which do not have the same high contrast as the larger irregular objects. Contrast enhanced using ImageJ 2.5% pixel saturation. Circular object measurements are given in nm weight and length and the dimensions of a typical LysR regulator (OxyR) is given above in Angstroms Å (PyMOL).

9.12 Surface Entropy reduction screen

Screening conditions for SER mutant crystals are given below:

	1	2	3	4	5	6
A	0%	2%	5%	7.5%	10%	12.5%
B	15%	20%	25%	30%	35%	40%
C	0%	2%	5%	7.5%	10%	12.5%
D	15%	20%	25%	30%	35%	40%
E	5%	10%	12.5%	15%	20%	25%
F	30%	35%	40%	45%	50%	55%
G	5%	10%	12.5%	15%	20%	25%
H	30%	35%	40%	45%	50%	55%

	7	8	9	10	11	12
A	2%	2%	2	2	5% EG/5%	5% M/5%
B	5%	5%	2.1	2.1	15% EG/5%	10% M/5%
C	7.5%	7.5%	2.2	2.2	25% EG/5%	15% M/5%
D	10%	10%	2.3	2.3	40% EG/5%	30% M/5%
E	12.5%	12.5%	2.4	2.4	5% EG/10%	5% M/10%
F	15%	15%	2.5	2.5	15% EG/10%	10% M/10%
G	20%	20%	2.6	2.6	25% EG/10%	15% M/10%
H	25%	25%	2.7	2.7	40% EG/10%	30% M/10%

Formulation key:

- Green - MPD: Varying precipitant concentrations buffered with 0.1 M sodium citrate tribasic dihydrate (pH 5.5 & 6) supplemented with 0.2 M ammonium acetate.
- Yellow - Ethylene Glycol: Varying ethylene glycol concentrations buffered with 0.1 M Tris-HCl (pH 8.25 – 8.5) supplemented with 0.2 M magnesium chloride hexahydrate.
- Red - Ethanol: Increasing concentrations of ethanol with 0.2 M lithium chloride buffered with sodium citrate tribasic dihydrate (pH 5.5 & 6)
- Blue – NaCl: >2M NaCl with 0.1 M MES buffered with phosphate (pH 5.5 – 6)
- Grey - Glycerol/MPD/EG (mixture) – composition either the same as green or yellow.

9.13 SDS PAGE gels for SER constructs

Uncropped SDS PAGE gels of PqsR$^{94-309}$ K154A K214Y (A) and K154A E278A (B) showing pooled fraction from Ni-NTA followed by thrombin digestions to remove the N-terminal His-tag and “reverse IMAC” to remove uncleaved material.

(A)

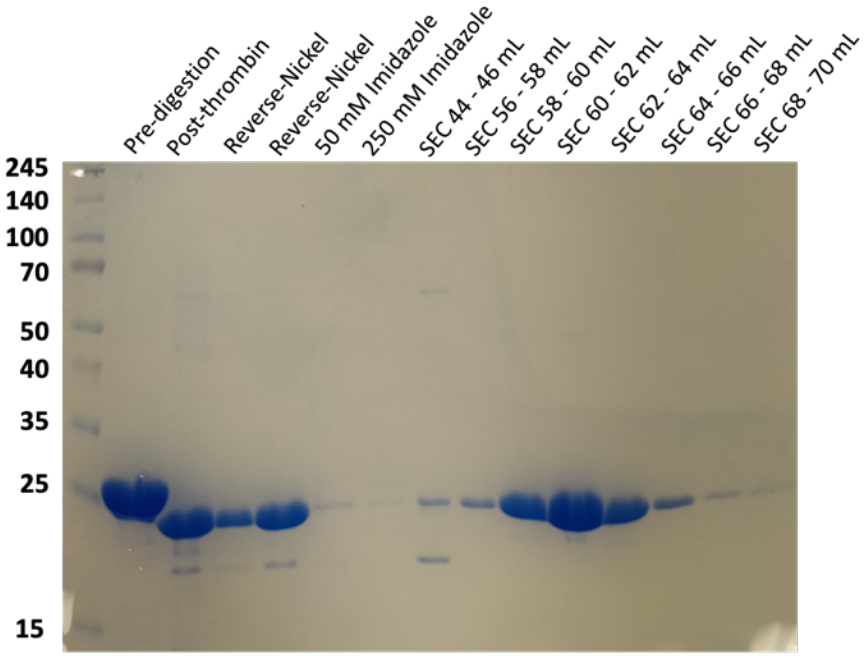

(B)

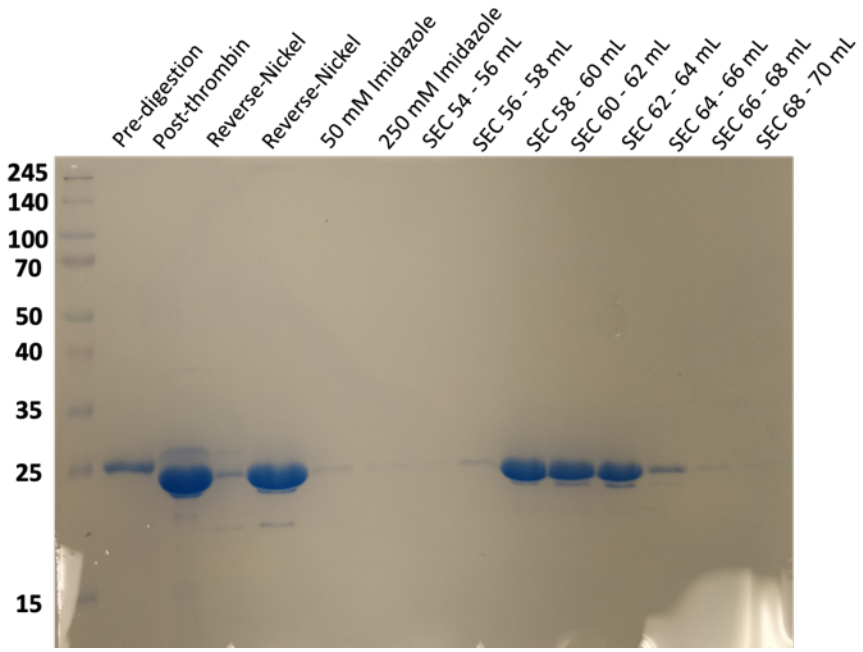

9.14 Screening method for PqsA used for NCC library search

Initial docking and selection of inhibitor candidates was performed by Dr Soukarieh using a licenced Schrödinger package (University of Nottingham, School of Pharmacy). The method, a provided by Dr Soukarieh, is given below:

Preparation of Protein and Receptor Grid Generation

The X-ray crystal structure of PqsA (PDB ID: **5OE5**) was used as a protein template. The protein was prepared using the protein preparation wizard (Small-Molecule Drug Discovery Suite 2017-4, Schrödinger, LLC, New York, NY, USA), where hydrogen atoms were added, water molecules were removed, and the correct bond order was assigned to the amino acid residues.

Ligand Preparation

The chemical structures of the inhibitors were sketched using ChemDraw (Version 16.0.1.4, PerkinElmer informatics) via an SDF file. LigPrep module (Small-Molecule Drug Discovery Suite 2017-4, Schrödinger, LLC, New York, NY, USA) was then used for final preparation of ligands into their lowest energy 3D conformations. The partial atomic charges were assigned to the molecular structures, using the 2005 implementation of the OPLS-AA force field. These energy-minimized structures were used for Glide) docking.

Molecular Docking

The “Extra Precision” (XP) mode of Glide docking (Small-Molecule Drug Discovery Suite 2017-4, Schrödinger, LLC, New York, NY, USA) was used to perform all docking calculations, using the OPLS-AA 2005 force field. The scale factor of 1.0 for van der Waals radii was applied to atoms of protein with absolute partial charges of less than or equal to 0.25. The number of position per ligand was set to five, after energy minimization. The best docked structures were chosen using an XP Glide Score (XP Gscore) function as well as visual observations.

9.15 Screening method for PqsA used for NCC library search

The screening conditions using anthraniloyl-AMS and DMSO only as positive and negative controls respectively. The earlier screening reaction runs have a tighter deviation suggesting deteriorating reproducibility over time.

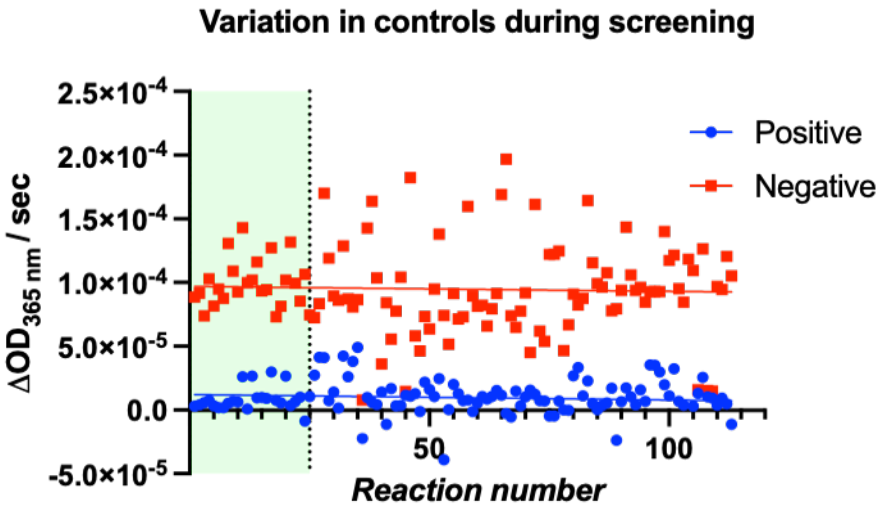

Variation in assay controls used for inhibitor screening BMedSci project. Controls including with each screening reaction set up. Earlier runs with better Z-Factor highlighted in green.

9.16 LC – MS identification of Anthraniloyl Coenzyme A: PqsA

(A)

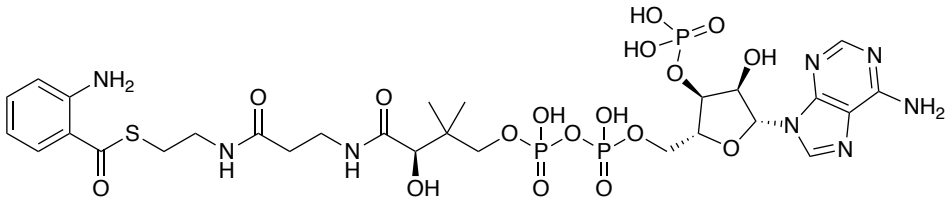

Exact Mass: 886.15
Molecular Weight: 886.66
m/z: 886.15 (100.0%), 887.16 (31.4%), 888.16 (8.5%), 888.15 (5.5%), 887.15 (3.8%), 889.16 (1.7%), 889.15 (1.7%)

Anthraniloyl-CoA

(B)

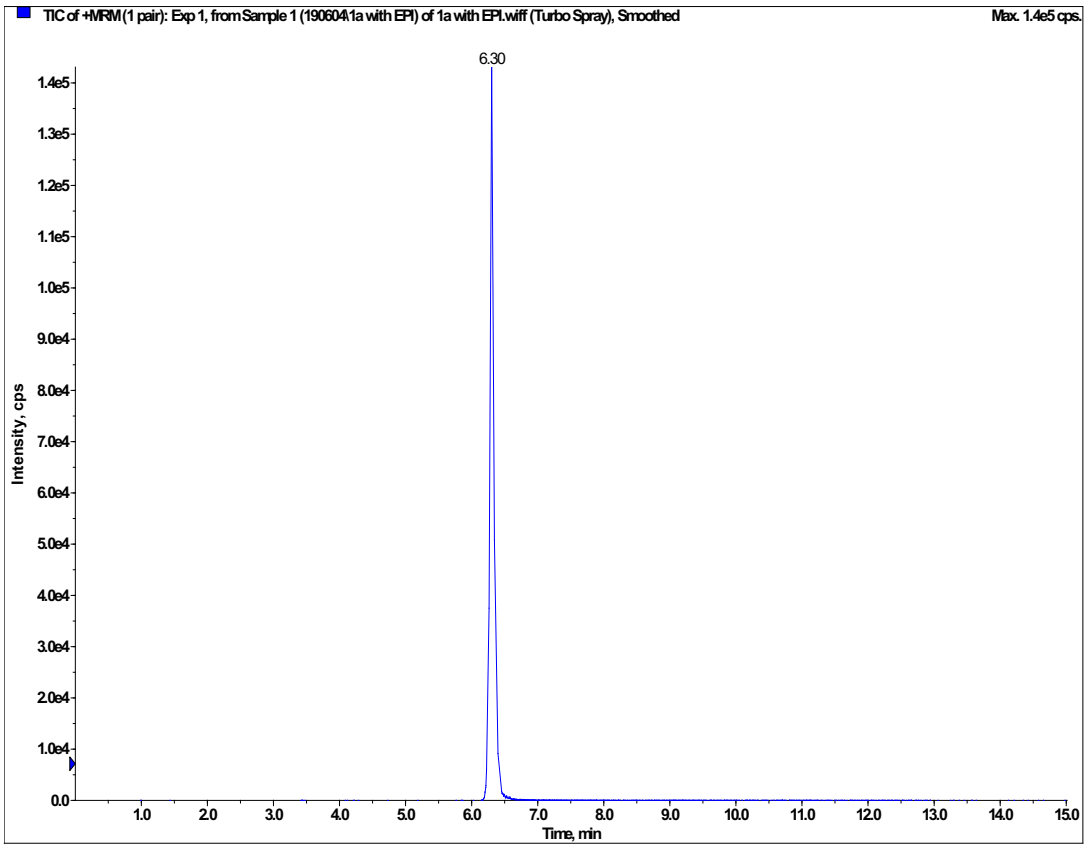

(C)

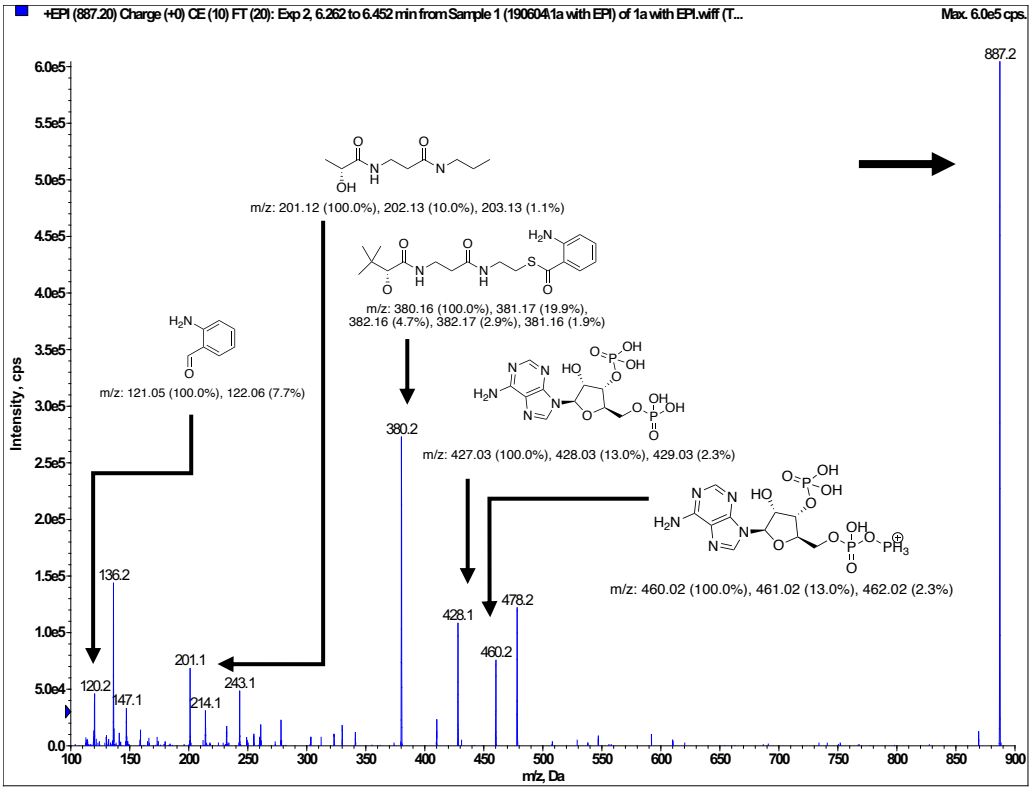

LC MS/MS Analysis of PqsA enzymatic reaction with anthranilic acid. **A.** Diagram of anthraniloyl-CoA with M/Z ion prediction (ChemDraw) **B.** Liquid Chromatogram of enzyme reaction to isolate anthraniloyl-CoA product. **C.** MS/MS output with arrow denoting parent ion (m/z: 887.2) and additional abundant ion marked for product identification derived from coenzyme A and anthranilic acid.

LC – MS identification of Anthraniloyl Coenzyme A: Burkholderia homologs

Product identification was performed using the same parameters as the experiment above. In the case of HmqA, a LC MS/MS run was completed but in the case of HhqA the relatively low amount of material did not meet the required abundance threshold for M/S data acquisition but the retention time on the HPLC column remains concordant. (6.3 min PqsA, HmqA vs 6.31 min HhqA).

(A)

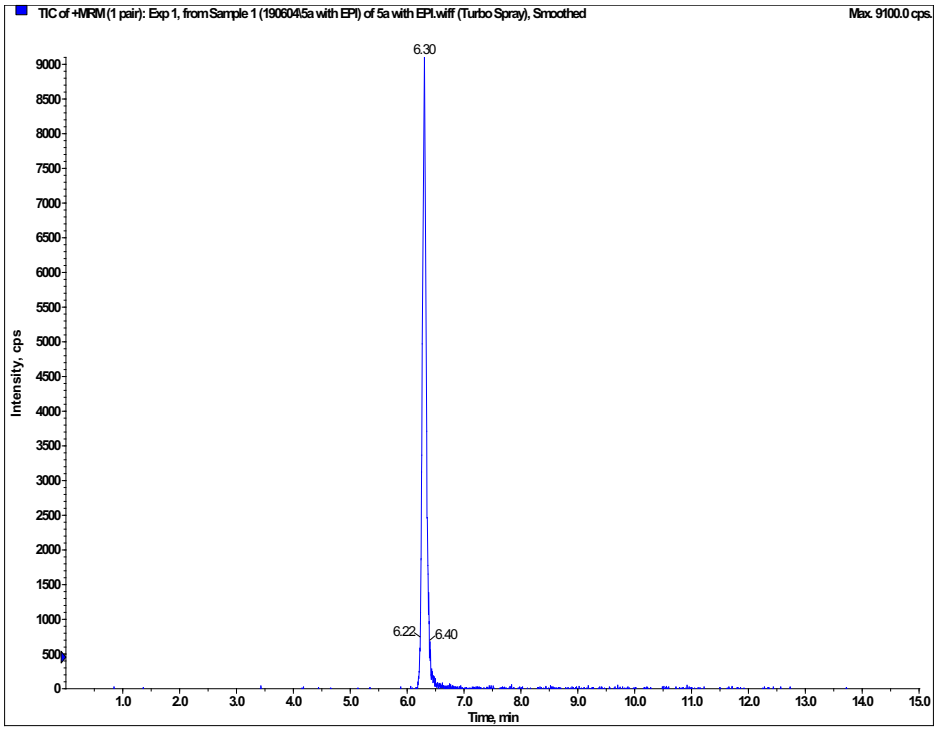
TIC of +MRM (1 pair): Exp 1, from Sample 1 (190604\5a with EPI) of 5a with EPI.wiff (Turbo Spray), Smoothed
Max. 9100.0 cps.
6.30
6.22
6.40
Intensity, cps
Time, min

(B)

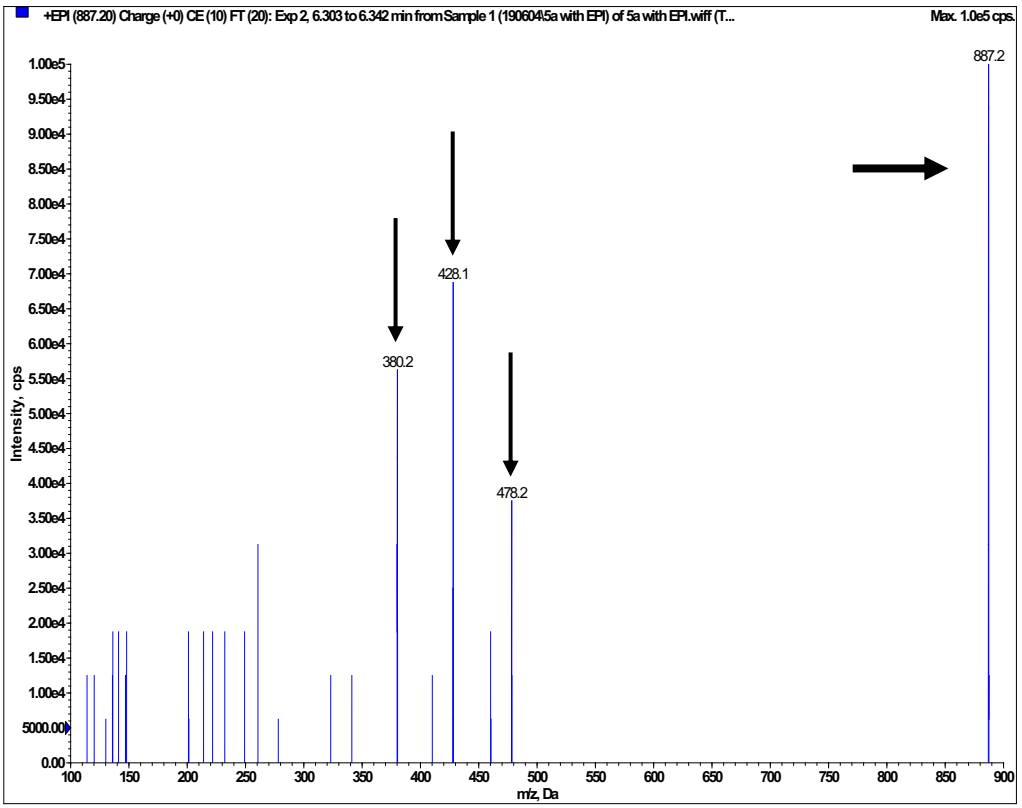
+EPI (887.20) Charge (+0) CE (10) FT (20): Exp 2, 6.303 to 6.342 min from Sample 1 (190604\5a with EPI) of 5a with EPI.wiff (T...
Max. 1.0e5 cps.
887.2
428.1
380.2
478.2
Intensity, cps
m/z, Da

(C)

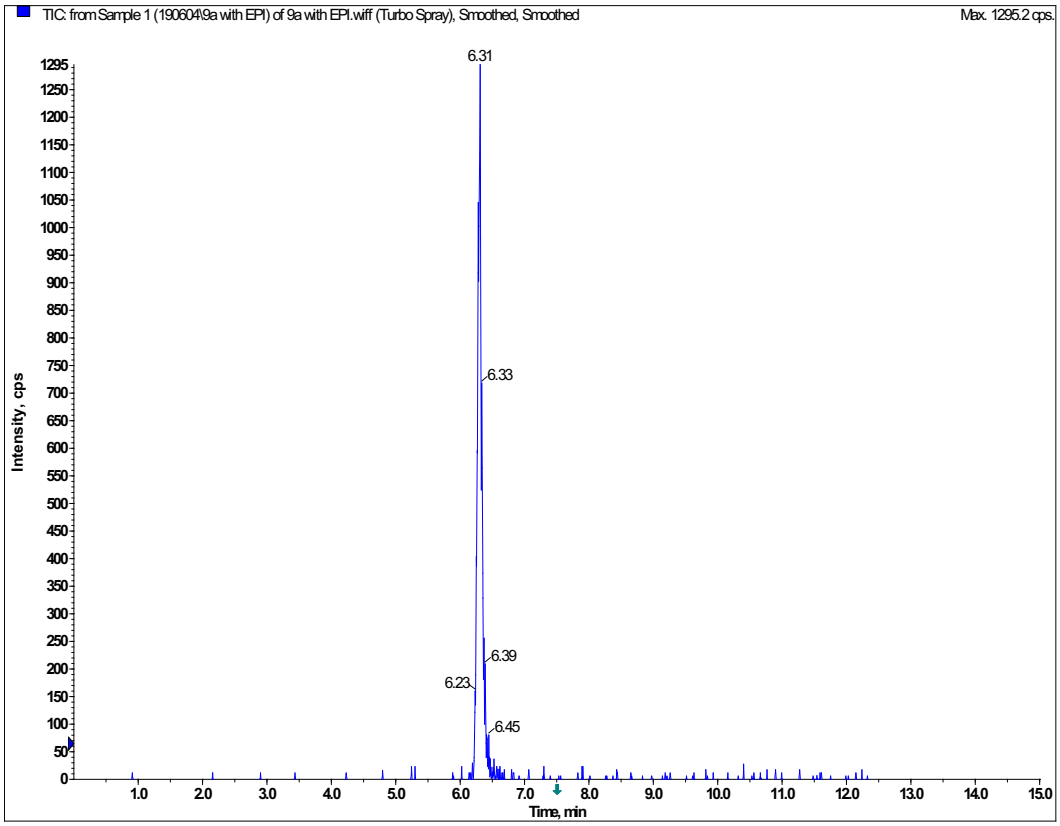

LC MS/MS Analysis of HmqA and HhqA enzymatic reaction with anthranilic acid. **A.** Liquid Chromatogram of HmqA enzyme reaction with retention of a product at 6.3 mins. **B.** MS/MS output showing similar fragmentation as PqsA product (arrows marking the same ions) and the same parent ion (m/z: 887.2) **C.** Liquid Chromatogram of HhqA enzyme reaction with retention of a product at 6.31 mins.

9.17 Reproduction of Anthraniloyl-AMP and anthranilic acid using Autodock vina

Autodock vina was run using parameters stated in the chapter 2.7 with anthraniloyl-CoA and anthranilic acid ligands. These were compared to the experimentally determined PqsA complex (PDB 5OE5 with ligand identifier 3UK) to determine if the binding positions had been accurately predicted. In the case of 3UK the position was reproduced accurately with the key discrepancy in the position of the carbonyl (flipped 180°) preceding the ester bond. This has influenced the angle of the anthraniloyl ring in the pocket causing deviation of the whole molecule compared to the experimentally determined position. The anthranilic acid ring position was correctly predicted but the ring is rotated by 66.7 degrees compared to the anthraniloyl moiety in 3UK.

(A)

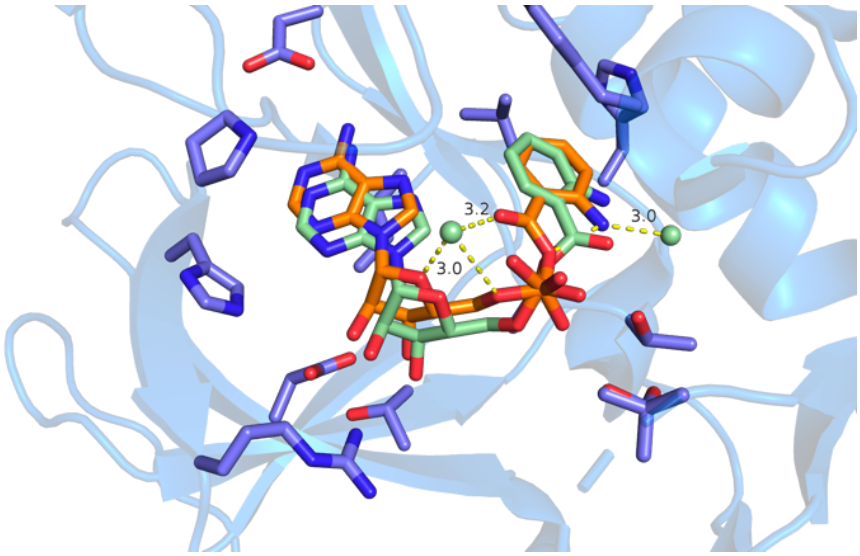

(B)

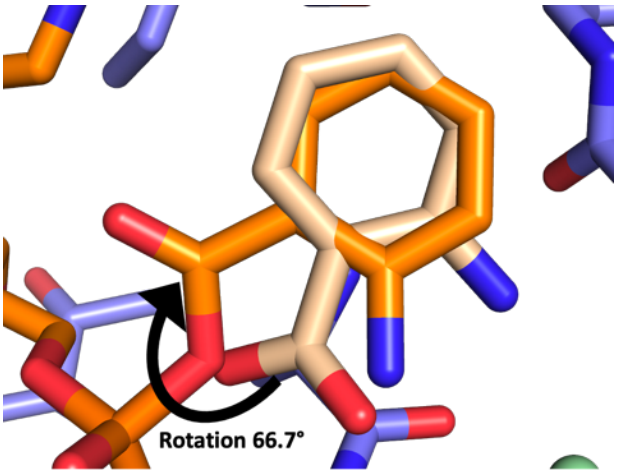

Reproduction of binding pose using AutoDock vina. (A) 3UK determined in 5OE5 (orange) and docking pose (light green). Adenosine and ribose ring are correctly positioned with key discrepancy phosphoester bond. **(B)** Anthranilic acid docking pose (cream) and 3UK (orange). Ring is rotated by 66.7° compared to 3UK ligand. Vina docking scores are given in Table 7.1.

9.18 Linearity test for PqsA enzymatic activity

For IC_{50} determination by LC MS/MS linearity was pre-tested by absorbance based assay showing that an initial starting reactant concentration of 0.5 mM anthranilic would have a linear reaction rate for at least 10 minutes.

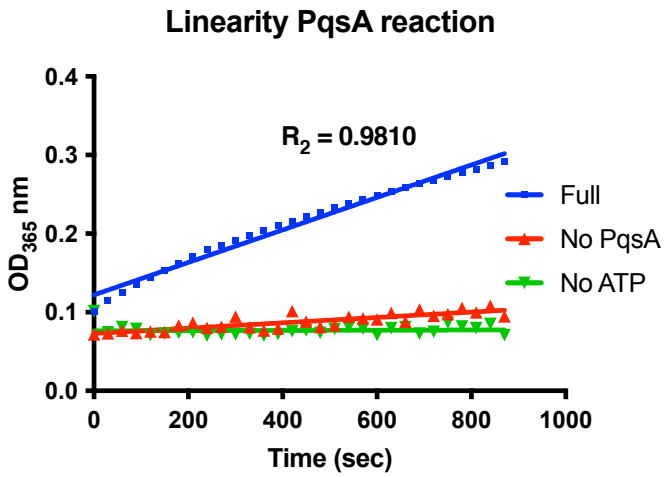

Simple reaction linearity test for IC_{50} determination examined by monitoring change in absorbance over time. Linearity confidence highlighted by an R^2 of 0.9810.

9.19 Control incubations for ZN8751275

To conclude whether the aggregation observed was due to compound precipitation over time or *P. aeruginosa* an incubation experiment without bacterial inoculation was conducted. As a solvent control, a water sample was also prepared. Interestingly, no precipitation was observed in the LB sample compared to the water suggesting the aggregated material observed in 18-hour cultures were bacterial. Differences in compound solubility will likely be due to LB components such as increased salt concentration and presence of organic components.

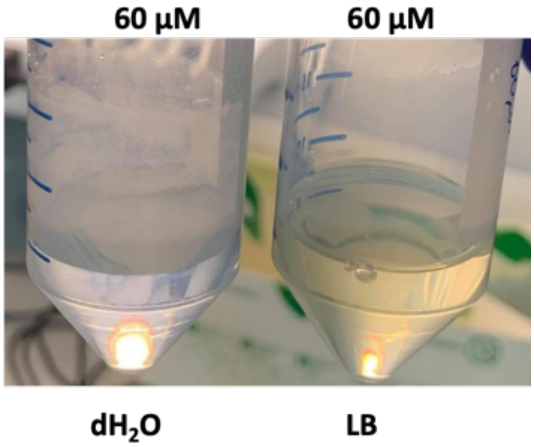

Incubation of ZN8751275 in water and LB. Incubation in water alone was insufficient to solubilise the inhibitor at the desired concentration of 60 µM but LB was able to solubilise the ligand more effectively with 1% DMSO.

9.20 Disorder prediction on PqsA homolog and alignment

Disorder profiles for HmqA and HhqA showing partial C-termini disorder (highlighted in red):

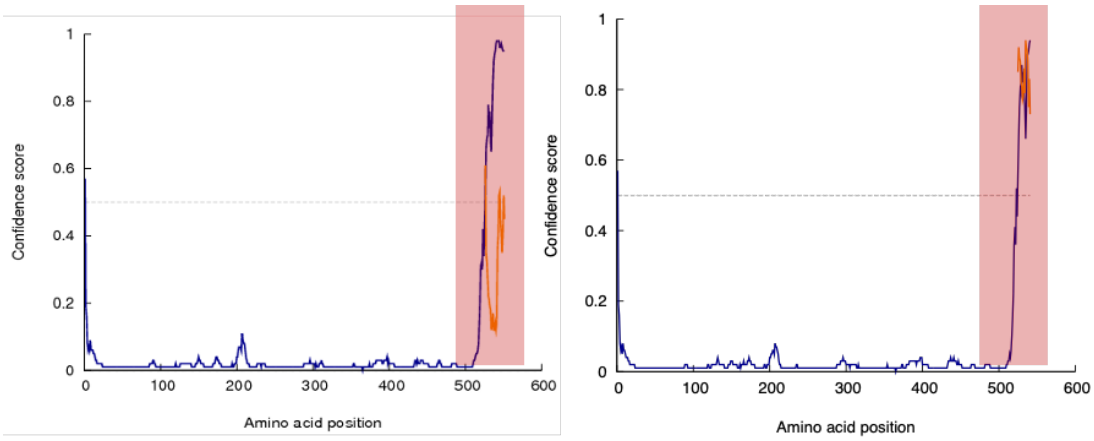

HmqA **HhqA**

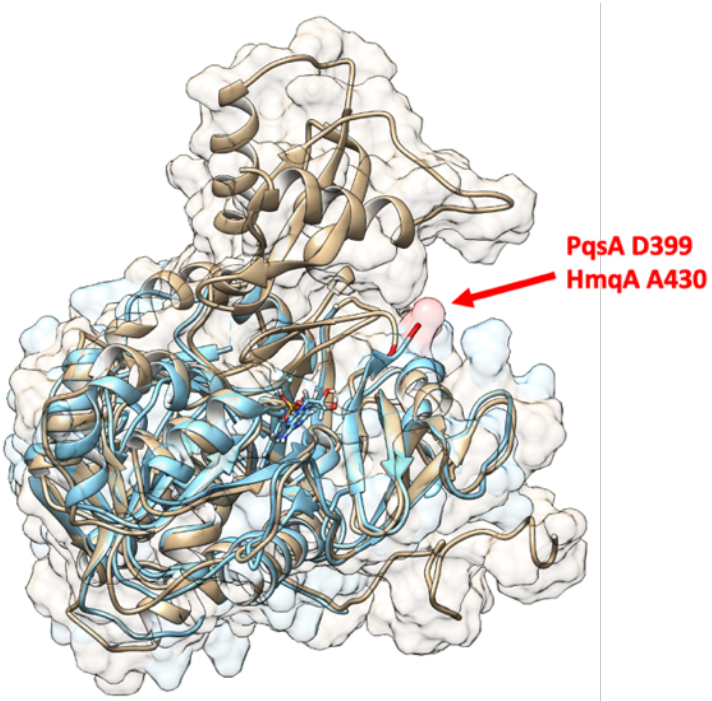

Superposition of PqsA crystal structure with I-TASSER homology models of HmqA highlighting the congruent position of D399 and A430. Additional N-terminal sequence is shown on the bottom right and is predicted to form a long loop.

9.21 Gel filtration standards

Gel filtration standards (GE Healthcare) were injected onto Superdex 75 16/60, Superdex 200 16/60 and Superdex 200 10/300 under the same flow rates as used for protein preparation and analysis. Elution of standards were monitored on an AKTA PURE instrument. Molecular weights for protein could be approximated by gel filtration using the following equation:

$$\log 10[MW, kDa] = (slope) * K_{av} + intercept$$

Whereby **K_{av}** *(gel-phase distribution coefficient)* is defined as **(Elution volume – Void volume)/(Column volume-void volume). K_{av}** is defined by the proportion of pores available for the protein of interest to migrate and discriminated by relative pore size. Deviation from expected size can be attributed to shape, disorder and interactions with the column media.

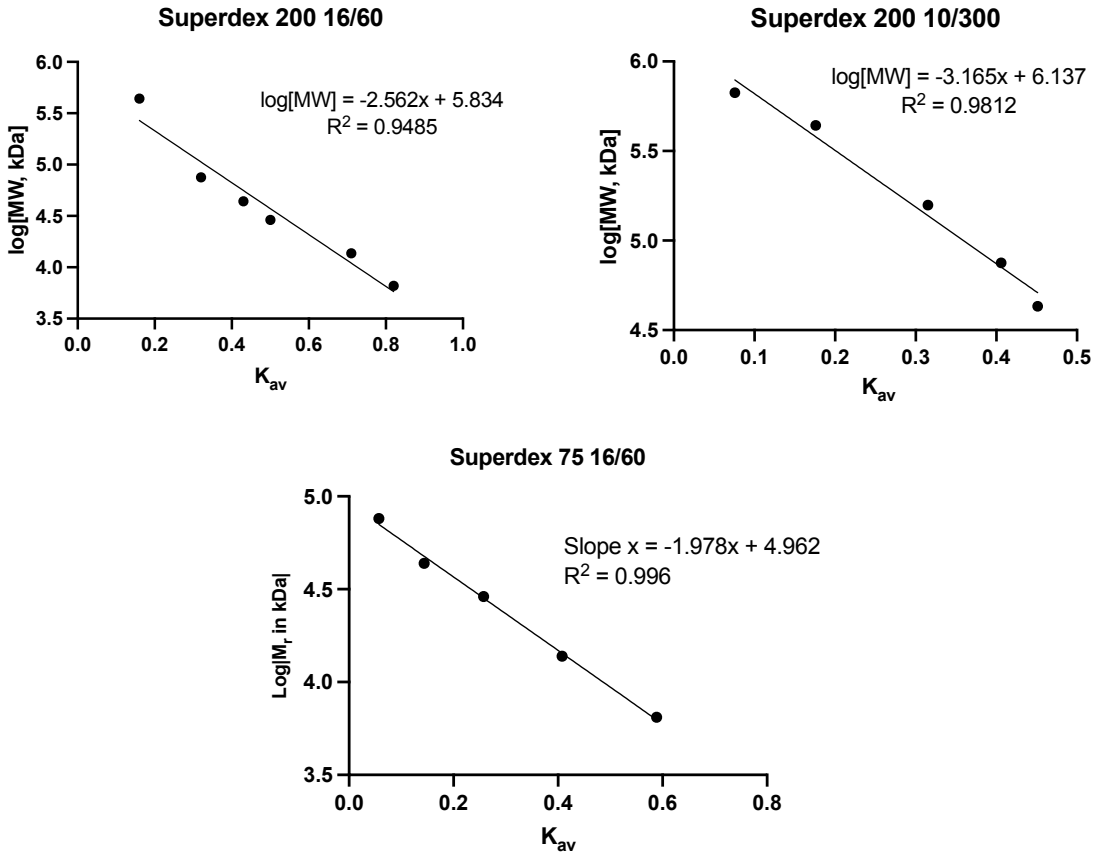

Gel filtration standards with linear regression slope and y intercept given for each column. Goodness of fit given as R^2. Superdex 200 column information generated by William Richardson. Superdex 75 16/60 calibration kindly provided by Dr Thomas Warwick.

10 Bibliography

1. O'Neill, J. TACKLING DRUG-RESISTANT INFECTIONS GLOBALLY: FINAL REPORT AND RECOMMENDATIONS. (2016).
2. Kåhrström, C. T. Entering a post-antibiotic era? *Nat. Rev. Microbiol.* **11**, 146–146 (2013).
3. Dadgostar, P. Antimicrobial Resistance: Implications and Costs. *Infect. Drug Resist.* **Volume 12**, 3903–3910 (2019).
4. Hutchings, M. I., Truman, A. W. & Wilkinson, B. Antibiotics: past, present and future. *Curr. Opin. Microbiol.* **51**, 72–80 (2019).
5. Payne, D. J., Gwynn, M. N., Holmes, D. J. & Pompliano, D. L. Drugs for bad bugs: confronting the challenges of antibacterial discovery. *Nat. Rev. Drug Discov.* **6**, 29–40 (2007).
6. Collignon, P. & Beggs, J. J. Socioeconomic Enablers for Contagion: Factors Impelling the Antimicrobial Resistance Epidemic. *Antibiotics* **8**, 86 (2019).
7. Roberts, S. C. & Zembower, T. R. Global increases in antibiotic consumption: a concerning trend for WHO targets. *Lancet Infect. Dis.* **21**, 10–11 (2021).
8. Llor, C. & Bjerrum, L. Antimicrobial resistance: risk associated with antibiotic overuse and initiatives to reduce the problem. *Ther. Adv. Drug Saf.* **5**, 229–241 (2014).
9. Doernberg, S. B. *et al.* Essential Resources and Strategies for Antibiotic Stewardship Programs in the Acute Care Setting. *Clin. Infect. Dis.* **67**, 1168–1174 (2018).
10. Lu, J. *et al.* Non-antibiotic antimicrobial triclosan induces multiple antibiotic resistance through genetic mutation. *Environ. Int.* **118**, 257–265 (2018).
11. D'Arezzo, S., Lanini, S., Puro, V., Ippolito, G. & Visca, P. High-level tolerance to triclosan may play a role in Pseudomonas aeruginosa antibiotic resistance in immunocompromised hosts: evidence from outbreak investigation. *BMC Res. Notes* **5**, 43 (2012).
12. Westfall, C. *et al.* The Widely Used Antimicrobial Triclosan Induces High Levels of Antibiotic Tolerance In Vitro and Reduces Antibiotic Efficacy up to 100-Fold In Vivo. *Antimicrob. Agents Chemother.* **63**, (2019).
13. Landers, T. F., Cohen, B., Wittum, T. E. & Larson, E. L. A Review of Antibiotic Use in Food Animals: Perspective, Policy, and Potential. *Public Health Rep.* **127**, 4–22 (2012).
14. Alcock, B. P. *et al.* CARD 2020: antibiotic resistome surveillance with the comprehensive antibiotic resistance database. *Nucleic Acids Res.* (2019) doi:10.1093/nar/gkz935.
15. Partridge, S. R., Kwong, S. M., Firth, N. & Jensen, S. O. Mobile Genetic Elements Associated with Antimicrobial Resistance. *Clin. Microbiol. Rev.* **31**, (2018).
16. Blair, J. M. A., Webber, M. A., Baylay, A. J., Ogbolu, D. O. & Piddock, L. J. V. Molecular

mechanisms of antibiotic resistance. *Nat. Rev. Microbiol.* **13**, 42–51 (2015).

17. Olesen, S. W., Lipsitch, M. & Grad, Y. H. The role of "spillover" in antibiotic resistance. *Proc. Natl. Acad. Sci.* **117**, 29063–29068 (2020).
18. Zurawski, D. V. & McLendon, M. K. Monoclonal Antibodies as an Antibacterial Approach Against Bacterial Pathogens. *Antibiotics* **9**, 155 (2020).
19. Dickey, S. W., Cheung, G. Y. C. & Otto, M. Different drugs for bad bugs: antivirulence strategies in the age of antibiotic resistance. *Nat. Rev. Drug Discov.* **16**, 457–471 (2017).
20. Leonard, H., Colodner, R., Halachmi, S. & Segal, E. Recent Advances in the Race to Design a Rapid Diagnostic Test for Antimicrobial Resistance. *ACS Sensors* **3**, 2202–2217 (2018).
21. Butini, M. E., Abbandonato, G., Di Rienzo, C., Trampuz, A. & Di Luca, M. Isothermal Microcalorimetry Detects the Presence of Persister Cells in a Staphylococcus aureus Biofilm After Vancomycin Treatment. *Front. Microbiol.* **10**, (2019).
22. Ho, C.-S. *et al.* Rapid identification of pathogenic bacteria using Raman spectroscopy and deep learning. *Nat. Commun.* **10**, 4927 (2019).
23. Glupczynski, Y., Evrard, S., Huang, T.-D. & Bogaerts, P. Evaluation of the RESIST-4 K-SeT assay, a multiplex immunochromatographic assay for the rapid detection of OXA-48-like, KPC, VIM and NDM carbapenemases. *J. Antimicrob. Chemother.* **74**, 1284–1287 (2019).
24. Tsuji, A., Kaneko, Y., Takahashi, K., Ogawa, M. & Goto, S. The Effects of Temperature and pH on the Growth of Eight Enteric and Nine Glucose Non-Fermenting Species of Gram-Negative Rods. *Microbiol. Immunol.* **26**, 15–24 (1982).
25. Klockgether, J., Cramer, N., Wiehlmann, L., Davenport, C. F. & Tümmler, B. Pseudomonas aeruginosa Genomic Structure and Diversity. *Front. Microbiol.* **2**, (2011).
26. Stover, C. K. *et al.* Complete genome sequence of Pseudomonas aeruginosa PAO1, an opportunistic pathogen. *Nature* **406**, 959–964 (2000).
27. Lambiase, A. *et al.* Microbiology of airway disease in a cohort of patients with Cystic Fibrosis. *BMC Infect. Dis.* **6**, 4 (2006).
28. Courtney, J. M. *et al.* Predictors of mortality in adults with cystic fibrosis. *Pediatr. Pulmonol.* **42**, 525–532 (2007).
29. Maliniak, M. L., Stecenko, A. A. & McCarty, N. A. A longitudinal analysis of chronic MRSA and Pseudomonas aeruginosa co-infection in cystic fibrosis: A single-center study. *J. Cyst. Fibros.* **15**, 350–356 (2016).
30. Yin, C. *et al.* Co-infection of Pseudomonas aeruginosa and Stenotrophomonas maltophilia in hospitalised pneumonia patients has a synergic and significant impact on clinical outcomes. *Eur. J. Clin. Microbiol. Infect. Dis.* **36**, 2231–2235 (2017).

31. Whiteford, M. L. *et al.* Outcome of Burkholderia (Pseudomonas) cepacia colonisation in children with cystic fibrosis following a hospital outbreak. *Thorax* **50**, 1194–1198 (1995).
32. Decraene, V. *et al.* An outbreak of multidrug-resistant Pseudomonas aeruginosa in a burns service in the North of England: challenges of infection prevention and control in a complex setting. *J. Hosp. Infect.* **100**, e239–e245 (2018).
33. Rello, J. *et al.* Risk Factors for Ventilator-associated Pneumonia by Pseudomonas aeruginosa in Presence of Recent Antibiotic Exposure. *Anesthesiology* **105**, 709–714 (2006).
34. Hamed, K. & Debonnett, L. Tobramycin inhalation powder for the treatment of pulmonary Pseudomonas aeruginosa infection in patients with cystic fibrosis: a review based on clinical evidence. *Ther. Adv. Respir. Dis.* **11**, 193–209 (2017).
35. Moore, J. E. & Mastoridis, P. Clinical implications of Pseudomonas aeruginosa location in the lungs of patients with cystic fibrosis. *J. Clin. Pharm. Ther.* **42**, 259–267 (2017).
36. Mantero, M. *et al.* Once daily aerosolised tobramycin in adult patients with cystic fibrosis in the management of Pseudomonas aeruginosa chronic infection. *Multidiscip. Respir. Med.* **12**, 2 (2017).
37. Lucena, A. *et al.* Nosocomial infections with metallo-beta-lactamase-producing Pseudomonas aeruginosa: molecular epidemiology, risk factors, clinical features and outcomes. *J. Hosp. Infect.* **87**, 234–240 (2014).
38. Bellido, F., Martin, N. L., Siehnel, R. J. & Hancock, R. E. Reevaluation, using intact cells, of the exclusion limit and role of porin OprF in Pseudomonas aeruginosa outer membrane permeability. *J. Bacteriol.* **174**, 5196–5203 (1992).
39. Ude, J. *et al.* Outer membrane permeability: Antimicrobials and diverse nutrients bypass porins in Pseudomonas aeruginosa. *Proc. Natl. Acad. Sci.* **118**, e2107644118 (2021).
40. Shigemura, K. *et al.* Association of overexpression of efflux pump genes with antibiotic resistance in Pseudomonas aeruginosa strains clinically isolated from urinary tract infection patients. *J. Antibiot. (Tokyo).* **68**, 568–572 (2015).
41. Zahedi bialvaei, A. *et al.* Expression of RND efflux pumps mediated antibiotic resistance in Pseudomonas aeruginosa clinical strains. *Microb. Pathog.* **153**, 104789 (2021).
42. Ferrer-Espada, R. *et al.* A permeability-increasing drug synergizes with bacterial efflux pump inhibitors and restores susceptibility to antibiotics in multi-drug resistant Pseudomonas aeruginosa strains. *Sci. Rep.* **9**, 3452 (2019).
43. Wright, L. L., Turton, J. F., Livermore, D. M., Hopkins, K. L. & Woodford, N. Dominance of international 'high-risk clones' among metallo- -lactamase-producing Pseudomonas aeruginosa in the UK. *J. Antimicrob. Chemother.* **70**, 103–110 (2015).

44. Ma, Z. *et al.* A MexR Mutation Which Confers Aztreonam Resistance to Pseudomonas aeruginosa. *Front. Microbiol.* **12**, (2021).
45. Cazares, A. *et al.* A megaplasmid family driving dissemination of multidrug resistance in Pseudomonas. *Nat. Commun.* **11**, 1370 (2020).
46. Upritchard, H. G., Cordwell, S. J. & Lamont, I. L. Immunoproteomics To Examine Cystic Fibrosis Host Interactions with Extracellular Pseudomonas aeruginosa Proteins. *Infect. Immun.* **76**, 4624–4632 (2008).
47. Horvat, R. T. & Parmely, M. J. Pseudomonas aeruginosa alkaline protease degrades human gamma interferon and inhibits its bioactivity. *Infect. Immun.* **56**, 2925–2932 (1988).
48. Prasad, A. S. B. *et al.* Pseudomonas aeruginosa virulence proteins pseudolysin and protease IV impede cutaneous wound healing. *Lab. Investig.* **100**, 1532–1550 (2020).
49. Gonzalez, M. R. *et al.* Effect of Human Burn Wound Exudate on Pseudomonas aeruginosa Virulence. *mSphere* **1**, (2016).
50. Saint-Criq, V. *et al.* Pseudomonas aeruginosa LasB protease impairs innate immunity in mice and humans by targeting a lung epithelial cystic fibrosis transmembrane regulator–IL-6–antimicrobial–repair pathway. *Thorax* **73**, 49–61 (2018).
51. Sun, J. *et al.* The Pseudomonas aeruginosa protease LasB directly activates IL-1β. *EBioMedicine* **60**, 102984 (2020).
52. Kany, A. M. *et al.* Binding Mode Characterization and Early in Vivo Evaluation of Fragment-Like Thiols as Inhibitors of the Virulence Factor LasB from Pseudomonas aeruginosa. *ACS Infect. Dis.* **4**, 988–997 (2018).
53. Tang, A., Caballero, A. R., Marquart, M. E. & O'Callaghan, R. J. Pseudomonas aeruginosa Small Protease (PASP), a Keratitis Virulence Factor. *Investig. Opthalmology Vis. Sci.* **54**, 2821 (2013).
54. Tang, A., Caballero, A. R., Marquart, M. E., Bierdeman, M. A. & O'Callaghan, R. J. Mechanism of Pseudomonas aeruginosa Small Protease (PASP), a Corneal Virulence Factor. *Investig. Opthalmology Vis. Sci.* **59**, 5993 (2018).
55. Basta, D. W., Angeles-Albores, D., Spero, M. A., Ciemniecki, J. A. & Newman, D. K. Heat-shock proteases promote survival of Pseudomonas aeruginosa during growth arrest. *Proc. Natl. Acad. Sci.* **117**, 4358–4367 (2020).
56. Wilson, R. *et al.* Measurement of Pseudomonas aeruginosa phenazine pigments in sputum and assessment of their contribution to sputum sol toxicity for respiratory epithelium. *Infect. Immun.* **56**, 2515–7 (1988).
57. Higgins, S. *et al.* Differential Regulation of the Phenazine Biosynthetic Operons by Quorum Sensing in Pseudomonas aeruginosa PAO1-N. *Front. Cell. Infect. Microbiol.* **8**, (2018).

58. Gupte, A., Jyot, J., Ravi, M. & Ramphal, R. High pyocyanin production and non-motility of Pseudomonas aeruginosa isolates are correlated with septic shock or death in bacteremic patients. *PLoS One* **16**, e0253259 (2021).
59. Muller, M., Li, Z. & Maitz, P. K. M. Pseudomonas pyocyanin inhibits wound repair by inducing premature cellular senescence: Role for p38 mitogen-activated protein kinase. *Burns* **35**, 500–508 (2009).
60. Muller, M. Pyocyanin induces oxidative stress in human endothelial cells and modulates the glutathione redox cycle. *Free Radic. Biol. Med.* **33**, 1527–1533 (2002).
61. Kang, D. *et al.* Pyoverdine-Dependent Virulence of Pseudomonas aeruginosa Isolates From Cystic Fibrosis Patients. *Front. Microbiol.* **10**, (2019).
62. Reid, D. W., Carroll, V., O'May, C., Champion, A. & Kirov, S. M. Increased airway iron as a potential factor in the persistence of Pseudomonas aeruginosa infection in cystic fibrosis. *Eur. Respir. J.* **30**, 286–292 (2007).
63. Caiazza, N. C., Shanks, R. M. Q. & O'Toole, G. A. Rhamnolipids Modulate Swarming Motility Patterns of Pseudomonas aeruginosa. *J. Bacteriol.* **187**, 7351–7361 (2005).
64. Zulianello, L. *et al.* Rhamnolipids Are Virulence Factors That Promote Early Infiltration of Primary Human Airway Epithelia by Pseudomonas aeruginosa. *Infect. Immun.* **74**, 3134–3147 (2006).
65. VAN GENNIP, M. *et al.* Inactivation of the rhlA gene in Pseudomonas aeruginosa prevents rhamnolipid production, disabling the protection against polymorphonuclear leukocytes. *APMIS* **117**, 537–546 (2009).
66. Waite, R. D., Papakonstantinopoulou, A., Littler, E. & Curtis, M. A. Transcriptome Analysis of Pseudomonas aeruginosa Growth: Comparison of Gene Expression in Planktonic Cultures and Developing and Mature Biofilms. *J. Bacteriol.* **187**, 6571–6576 (2005).
67. Thi, M. T. T., Wibowo, D. & Rehm, B. H. A. Pseudomonas aeruginosa Biofilms. *Int. J. Mol. Sci.* **21**, 8671 (2020).
68. Mann, E. E. & Wozniak, D. J. Pseudomonas biofilm matrix composition and niche biology. *FEMS Microbiol. Rev.* **36**, 893–916 (2012).
69. Seviour, T. *et al.* The biofilm matrix scaffold of Pseudomonas aeruginosa contains G-quadruplex extracellular DNA structures. *npj Biofilms Microbiomes* **7**, 27 (2021).
70. Turnbull, L. *et al.* Explosive cell lysis as a mechanism for the biogenesis of bacterial membrane vesicles and biofilms. *Nat. Commun.* **7**, 11220 (2016).
71. Oluyombo, O., Penfold, C. N. & Diggle, S. P. Competition in Biofilms between Cystic Fibrosis Isolates of Pseudomonas aeruginosa Is Shaped by R-Pyocins. *MBio* **10**, (2019).

72. Fricks-Lima, J. *et al.* Differences in biofilm formation and antimicrobial resistance of Pseudomonas aeruginosa isolated from airways of mechanically ventilated patients and cystic fibrosis patients. *Int. J. Antimicrob. Agents* **37**, 309–315 (2011).
73. Mulcahy, L. R., Burns, J. L., Lory, S. & Lewis, K. Emergence of Pseudomonas aeruginosa Strains Producing High Levels of Persister Cells in Patients with Cystic Fibrosis. *J. Bacteriol.* **192**, 6191–6199 (2010).
74. Milivojevic, D. *et al.* Biofilm-forming ability and infection potential of Pseudomonas aeruginosa strains isolated from animals and humans. *Pathog. Dis.* **76**, (2018).
75. Albuquerque, P. & Casadevall, A. Quorum sensing in fungi – a review. *Med. Mycol.* **50**, 337–345 (2012).
76. Shrestha, A., Grimm, M., Ojiro, I., Krumwiede, J. & Schikora, A. Impact of Quorum Sensing Molecules on Plant Growth and Immune System. *Front. Microbiol.* **11**, (2020).
77. Whiteley, M., Diggle, S. P. & Greenberg, E. P. Progress in and promise of bacterial quorum sensing research. *Nature* **551**, 313–320 (2017).
78. Rajput, A. & Kumar, M. In silico analyses of conservational, functional and phylogenetic distribution of the LuxI and LuxR homologs in Gram-positive bacteria. *Sci. Rep.* **7**, 6969 (2017).
79. Papenfort, K. & Bassler, B. L. Quorum sensing signal–response systems in Gram-negative bacteria. *Nat. Rev. Microbiol.* **14**, 576–588 (2016).
80. Schuster, M., Joseph Sexton, D., Diggle, S. P. & Peter Greenberg, E. Acyl-Homoserine Lactone Quorum Sensing: From Evolution to Application. *Annu. Rev. Microbiol.* **67**, 43–63 (2013).
81. Verbeke, F. *et al.* Peptides as Quorum Sensing Molecules: Measurement Techniques and Obtained Levels In vitro and In vivo. *Front. Neurosci.* **11**, (2017).
82. Mukherjee, S. & Bassler, B. L. Bacterial quorum sensing in complex and dynamically changing environments. *Nat. Rev. Microbiol.* **17**, 371–382 (2019).
83. Thoendel, M. & Horswill, A. R. Biosynthesis of Peptide Signals in Gram-Positive Bacteria. in 91–112 (2010). doi:10.1016/S0065-2164(10)71004-2.
84. Zhang, L. *et al.* Sensing of autoinducer-2 by functionally distinct receptors in prokaryotes. *Nat. Commun.* **11**, 5371 (2020).
85. Winzer, K. Bacterial cell-to-cell communication: sorry, can't talk now — gone to lunch! *Curr. Opin. Microbiol.* **5**, 216–222 (2002).
86. Gambello, M. J. & Iglewski, B. H. Cloning and characterization of the Pseudomonas aeruginosa lasR gene, a transcriptional activator of elastase expression. *J. Bacteriol.* **173**, 3000–3009 (1991).
87. Pearson, J. P. *et al.* Structure of the autoinducer required for expression of Pseudomonas

aeruginosa virulence genes. *Proc. Natl. Acad. Sci.* **91**, 197–201 (1994).

88. Pearson, J. P., Passador, L., Iglewski, B. H. & Greenberg, E. P. A second N-acylhomoserine lactone signal produced by Pseudomonas aeruginosa. *Proc. Natl. Acad. Sci.* **92**, 1490–1494 (1995).
89. Pesci, E. C. *et al.* Quinolone signaling in the cell-to-cell communication system of Pseudomonas aeruginosa. *Proc. Natl. Acad. Sci.* **96**, 11229–11234 (1999).
90. Cao, H. *et al.* A quorum sensing-associated virulence gene of Pseudomonas aeruginosa encodes a LysR-like transcription regulator with a unique self-regulatory mechanism. *Proc. Natl. Acad. Sci.* **98**, 14613–14618 (2001).
91. Lee, J. *et al.* A cell-cell communication signal integrates quorum sensing and stress response. *Nat. Chem. Biol.* **9**, 339–343 (2013).
92. Cornelis, P. Putting an end to the Pseudomonas aeruginosa IQS controversy. *Microbiologyopen* **9**, (2020).
93. Mukherjee, S., Jemielita, M., Stergioula, V., Tikhonov, M. & Bassler, B. L. Photosensing and quorum sensing are integrated to control Pseudomonas aeruginosa collective behaviors. *PLOS Biol.* **17**, e3000579 (2019).
94. Papaioannou, E., Utari, P. & Quax, W. Choosing an Appropriate Infection Model to Study Quorum Sensing Inhibition in Pseudomonas Infections. *Int. J. Mol. Sci.* **14**, 19309–19340 (2013).
95. Albus, A. M., Pesci, E. C., Runyen-Janecky, L. J., West, S. E. & Iglewski, B. H. Vfr controls quorum sensing in Pseudomonas aeruginosa. *J. Bacteriol.* **179**, 3928–3935 (1997).
96. Juhas, M. Global regulation of quorum sensing and virulence by VqsR in Pseudomonas aeruginosa. *Microbiology* **150**, 831–841 (2004).
97. Chugani, S. A. *et al.* QscR, a modulator of quorum-sensing signal synthesis and virulence in Pseudomonas aeruginosa. *Proc. Natl. Acad. Sci.* **98**, 2752–2757 (2001).
98. Siehnel, R. *et al.* A unique regulator controls the activation threshold of quorum-regulated genes in Pseudomonas aeruginosa. *Proc. Natl. Acad. Sci.* **107**, 7916–7921 (2010).
99. Gilbert, K. B., Kim, T. H., Gupta, R., Greenberg, E. P. & Schuster, M. Global position analysis of the Pseudomonas aeruginosa quorum-sensing transcription factor LasR. *Mol. Microbiol.* **73**, 1072–1085 (2009).
100. Heurlier, K., Dénervaud, V., Pessi, G., Reimmann, C. & Haas, D. Negative Control of Quorum Sensing by RpoN (σ 54) in Pseudomonas aeruginosa PAO1. *J. Bacteriol.* **185**, 2227–2235 (2003).
101. Rumbaugh, kendra P., Griswold, J. A. & Hamood, A. N. Contribution of the Regulatory Gene

lasR to the Pathogenesis of Pseudomonas aeruginosa Infection of Burned Mice. *J. Burn Care Rehabil.* **20**, 42–49 (1999).

102. Schuster, M., Urbanowski, M. L. & Greenberg, E. P. Promoter specificity in Pseudomonas aeruginosa quorum sensing revealed by DNA binding of purified LasR. *Proc. Natl. Acad. Sci.* **101**, 15833–15839 (2004).
103. Bottomley, M. J., Muraglia, E., Bazzo, R. & Carfì, A. Molecular Insights into Quorum Sensing in the Human Pathogen Pseudomonas aeruginosa from the Structure of the Virulence Regulator LasR Bound to Its Autoinducer. *J. Biol. Chem.* **282**, 13592–13600 (2007).
104. Corral-Lugo, A., Daddaoua, A., Ortega, A., Espinosa-Urgel, M. & Krell, T. Rosmarinic acid is a homoserine lactone mimic produced by plants that activates a bacterial quorum-sensing regulator. *Sci. Signal.* **9**, ra1–ra1 (2016).
105. Kiratisin, P., Tucker, K. D. & Passador, L. LasR, a Transcriptional Activator of Pseudomonas aeruginosa Virulence Genes, Functions as a Multimer. *J. Bacteriol.* **184**, 4912–4919 (2002).
106. Ochsner, U. A. & Reiser, J. Autoinducer-mediated regulation of rhamnolipid biosurfactant synthesis in Pseudomonas aeruginosa. *Proc. Natl. Acad. Sci.* **92**, 6424–6428 (1995).
107. Medina, G., Juárez, K., Valderrama, B. & Soberón-Chávez, G. Mechanism of Pseudomonas aeruginosa RhlR Transcriptional Regulation of the rhlAB Promoter. *J. Bacteriol.* **185**, 5976–5983 (2003).
108. Cruz, R. L. *et al.* RhlR-Regulated Acyl-Homoserine Lactone Quorum Sensing in a Cystic Fibrosis Isolate of Pseudomonas aeruginosa. *MBio* **11**, (2020).
109. Limmer, S. *et al.* Pseudomonas aeruginosa RhlR is required to neutralize the cellular immune response in a Drosophila melanogaster oral infection model. *Proc. Natl. Acad. Sci.* **108**, 17378–17383 (2011).
110. McCready, A. R., Paczkowski, J. E., Cong, J.-P. & Bassler, B. L. An autoinducer-independent RhlR quorum-sensing receptor enables analysis of RhlR regulation. *PLOS Pathog.* **15**, e1007820 (2019).
111. Mukherjee, S. *et al.* The PqsE and RhlR proteins are an autoinducer synthase–receptor pair that control virulence and biofilm development in Pseudomonas aeruginosa. *Proc. Natl. Acad. Sci.* **115**, E9411–E9418 (2018).
112. Groleau, M.-C., de Oliveira Pereira, T., Dekimpe, V. & Déziel, E. PqsE Is Essential for RhlR-Dependent Quorum Sensing Regulation in Pseudomonas aeruginosa. *mSystems* **5**, (2020).
113. Taylor, I. R. *et al.* Inhibitor Mimetic Mutations in the Pseudomonas aeruginosa PqsE Enzyme Reveal a Protein–Protein Interaction with the Quorum-Sensing Receptor RhlR That Is Vital for Virulence Factor Production. *ACS Chem. Biol.* **16**, 740–752 (2021).

114. Lépine, F., Milot, S., Déziel, E., He, J. & Rahme, L. G. Electrospray/mass spectrometric identification and analysis of 4-hydroxy-2-alkylquinolines (HAQs) produced by Pseudomonas aeruginosa. *J. Am. Soc. Mass Spectrom.* **15**, 862–869 (2004).

115. Hodgkinson, J., Bowden, S. D., Galloway, W. R. J. D., Spring, D. R. & Welch, M. Structure-Activity Analysis of the Pseudomonas Quinolone Signal Molecule. *J. Bacteriol.* **192**, 3833–3837 (2010).

116. Gallagher, L. A., McKnight, S. L., Kuznetsova, M. S., Pesci, E. C. & Manoil, C. Functions Required for Extracellular Quinolone Signaling by Pseudomonas aeruginosa. *J. Bacteriol.* **184**, 6472–6480 (2002).

117. Knoten, C. A., Wells, G., Coleman, J. P. & Pesci, E. C. A Conserved Suppressor Mutation in a Tryptophan Auxotroph Results in Dysregulation of Pseudomonas Quinolone Signal Synthesis. *J. Bacteriol.* **196**, 2413–2422 (2014).

118. Gruber, J. D. *et al.* The role of 2,4-dihydroxyquinoline (DHQ) in Pseudomonas aeruginosa pathogenicity. *PeerJ* **4**, e1495 (2016).

119. Lin, J., Cheng, J., Wang, Y. & Shen, X. The Pseudomonas Quinolone Signal (PQS): Not Just for Quorum Sensing Anymore. *Front. Cell. Infect. Microbiol.* **8**, (2018).

120. Schertzer, J. W., Brown, S. A. & Whiteley, M. Oxygen levels rapidly modulate Pseudomonas aeruginosa social behaviours via substrate limitation of PqsH. *Mol. Microbiol.* **77**, 1527–1538 (2010).

121. Drees, S. L. & Fetzner, S. PqsE of Pseudomonas aeruginosa Acts as Pathway-Specific Thioesterase in the Biosynthesis of Alkylquinolone Signaling Molecules. *Chem. Biol.* **22**, 611–618 (2015).

122. Que, Y.-A. *et al.* A Quorum Sensing Small Volatile Molecule Promotes Antibiotic Tolerance in Bacteria. *PLoS One* **8**, e80140 (2013).

123. Vial, L. *et al.* Burkholderia pseudomallei , B. thailandensis , and B. ambifaria Produce 4-Hydroxy-2-Alkylquinoline Analogues with a Methyl Group at the 3 Position That Is Required for Quorum-Sensing Regulation. *J. Bacteriol.* **190**, 5339–5352 (2008).

124. Szamosvári, D., Prothiwa, M., Dieterich, C. L. & Böttcher, T. Profiling structural diversity and activity of 2-alkyl-4(1 H)-quinolone N -oxides of Pseudomonas and Burkholderia. *Chem. Commun.* **56**, 6328–6331 (2020).

125. Diggle, S. P. *et al.* The Pseudomonas aeruginosa 4-Quinolone Signal Molecules HHQ and PQS Play Multifunctional Roles in Quorum Sensing and Iron Entrapment. *Chem. Biol.* **14**, 87–96 (2007).

126. Häussler, S. & Becker, T. The Pseudomonas Quinolone Signal (PQS) Balances Life and Death in

Pseudomonas aeruginosa Populations. *PLoS Pathog.* **4**, e1000166 (2008).

127. Abdalla, M. Y. *et al.* Pseudomonas Quinolone Signal Induces Oxidative Stress and Inhibits Heme Oxygenase-1 Expression in Lung Epithelial Cells. *Infect. Immun.* **85**, (2017).
128. Pezzoni, M., Meichtry, M., Pizarro, R. A. & Costa, C. S. Role of the Pseudomonas quinolone signal (PQS) in sensitising Pseudomonas aeruginosa to UVA radiation. *J. Photochem. Photobiol. B Biol.* **142**, 129–140 (2015).
129. Rieger, B. *et al.* Pseudomonas Quinolone Signal molecule PQS behaves like a B Class inhibitor at the I Q site of mitochondrial complex I. *FASEB BioAdvances* **2**, 188–202 (2020).
130. Kim, K. *et al.* HHQ and PQS, two Pseudomonas aeruginosa quorum-sensing molecules, down-regulate the innate immune responses through the nuclear factor-κB pathway. *Immunology* **129**, 578–588 (2010).
131. Mashburn-Warren, L. *et al.* Interaction of quorum signals with outer membrane lipids: insights into prokaryotic membrane vesicle formation. *Mol. Microbiol.* **69**, 491–502 (2008).
132. Cooke, A. C. *et al.* Pseudomonas Quinolone Signal-Induced Outer Membrane Vesicles Enhance Biofilm Dispersion in Pseudomonas aeruginosa. *mSphere* **5**, (2020).
133. Hodgkinson, J. T., Gross, J., Baker, Y. R., Spring, D. R. & Welch, M. A new Pseudomonas quinolone signal (PQS) binding partner: MexG. *Chem. Sci.* **7**, 2553–2562 (2016).
134. Maddocks, S. E. & Oyston, P. C. F. Structure and function of the LysR-type transcriptional regulator (LTTR) family proteins. *Microbiology* **154**, 3609–3623 (2008).
135. Celis, R. T. . Repression and activation of arginine transport genes in Escherichia coli K 12 by the ArgP protein. *J. Mol. Biol.* **294**, 1087–1095 (1999).
136. Gong, W., Xiong, G. & Maser, E. Identification and Characterization of the LysR-Type Transcriptional Regulator HsdR for Steroid-Inducible Expression of the 3α-Hydroxysteroid Dehydrogenase/Carbonyl Reductase Gene in Comamonas testosteroni. *Appl. Environ. Microbiol.* **78**, 941–950 (2012).
137. Aravind, L., Anantharaman, V., Balaji, S., Babu, M. M. & Iyer, L. M. The many faces of the helix-turn-helix domain: Transcription regulation and beyond. *FEMS Microbiol. Rev.* **29**, 231–262 (2005).
138. Monferrer, D. *et al.* Structural studies on the full-length LysR- type regulator TsaR from Comamonas testosteroni T-2 reveal a novel open conformation of the tetrameric LTTR fold. *Mol. Microbiol.* **75**, 1199–1214 (2010).
139. Berntsson, R. P.-A., Smits, S. H. J., Schmitt, L., Slotboom, D.-J. & Poolman, B. A structural classification of substrate-binding proteins. *FEBS Lett.* **584**, 2606–2617 (2010).
140. Santiago, A. S. *et al.* Characterization of the LysR-type transcriptional regulator YcjZ-like from

Xylella fastidiosa overexpressed in Escherichia coli. *Protein Expr. Purif.* **113**, 72–78 (2015).

141. Guadarrama, C., Medrano-López, A., Oropeza, R., Hernández-Lucas, I. & Calva, E. The Salmonella enterica Serovar Typhi LeuO Global Regulator Forms Tetramers: Residues Involved in Oligomerization, DNA Binding, and Transcriptional Regulation. *J. Bacteriol.* **196**, 2143–2154 (2014).
142. Zhang, M. *et al.* Regulation of Glutarate Catabolism by GntR Family Regulator CsiR and LysR Family Regulator GcdR in Pseudomonas putida KT2440. *MBio* **10**, (2019).
143. Sainsbury, S. *et al.* The structure of CrgA from Neisseria meningitidis reveals a new octameric assembly state for LysR transcriptional regulators. *Nucleic Acids Res.* **37**, 4545–4558 (2009).
144. Zhou, X. *et al.* Crystal Structure of ArgP from Mycobacterium tuberculosis Confirms Two Distinct Conformations of Full-length LysR Transcriptional Regulators and Reveals Its Function in DNA Binding and Transcriptional Regulation. *J. Mol. Biol.* **396**, 1012–1024 (2010).
145. Taylor, J. L. *et al.* The crystal structure of AphB, a virulence gene activator from Vibrio cholerae, reveals residues that influence its response to oxygen and pH. *Mol. Microbiol.* **83**, 457–470 (2012).
146. Lerche, M. *et al.* The solution configurations of inactive and activated DntR have implications for the sliding dimer mechanism of LysR transcription factors. *Sci. Rep.* **6**, 19988 (2016).
147. Kim, Y. *et al.* Crystal structure of the ligand-binding domain of a LysR-type transcriptional regulator: transcriptional activation via a rotary switch. *Mol. Microbiol.* **110**, 550–561 (2018).
148. Goodsell, D. S., Autin, L. & Olson, A. J. Illustrate: Software for Biomolecular Illustration. *Structure* **27**, 1716-1720.e1 (2019).
149. Rahme, L. G. *et al.* Use of model plant hosts to identify Pseudomonas aeruginosa virulence factors. *Proc. Natl. Acad. Sci.* **94**, 13245–13250 (1997).
150. Brouwer, S. *et al.* The PqsR and RhlR Transcriptional Regulators Determine the Level of Pseudomonas Quinolone Signal Synthesis in Pseudomonas aeruginosa by Producing Two Different pqsABCDE mRNA Isoforms. *J. Bacteriol.* **196**, 4163–4171 (2014).
151. Déziel, E. *et al.* The contribution of MvfR to Pseudomonas aeruginosa pathogenesis and quorum sensing circuitry regulation: multiple quorum sensing-regulated genes are modulated without affecting lasRI, rhlRI or the production of N-acyl- l-homoserine lactones. *Mol. Microbiol.* **55**, 998–1014 (2004).
152. Maura, D., Hazan, R., Kitao, T., Ballok, A. E. & Rahme, L. G. Evidence for Direct Control of Virulence and Defense Gene Circuits by the Pseudomonas aeruginosa Quorum Sensing Regulator, MvfR. *Sci. Rep.* **6**, 34083 (2016).
153. Kitao, T. *et al.* Molecular insights into function and competitive inhibition of pseudomonas

aeruginosa multiple virulence factor regulator. *MBio* **9**, 1–13 (2018).

154. Fang, Y.-L. *et al.* The Anti-activator QslA Negatively Regulates Phenazine-1-Carboxylic Acid Biosynthesis by Interacting With the Quorum Sensing Regulator MvfR in the Rhizobacterium Pseudomonas aeruginosa Strain PA1201. *Front. Microbiol.* **9**, (2018).
155. Ilangovan, A. *et al.* Structural Basis for Native Agonist and Synthetic Inhibitor Recognition by the Pseudomonas aeruginosa Quorum Sensing Regulator PqsR (MvfR). *PLoS Pathog.* **9**, e1003508 (2013).
156. Xiao, G. *et al.* MvfR, a key Pseudomonas aeruginosa pathogenicity LTTR-class regulatory protein, has dual ligands. *Mol. Microbiol.* **62**, 1689–1699 (2006).
157. Welch, M., Hodgkinson, J. T., Gross, J., Spring, D. R. & Sams, T. Ligand binding kinetics of the quorum sensing regulator PqsR. *Biochemistry* **52**, 4433–4438 (2013).
158. Xiao, G., He, J. & Rahme, L. G. Mutation analysis of the Pseudomonas aeruginosa mvfR and pqsABCDE gene promoters demonstrates complex quorum-sensing circuitry. *Microbiology* **152**, 1679–1686 (2006).
159. Farrow, J. M., Hudson, L. L., Wells, G., Coleman, J. P. & Pesci, E. C. CysB Negatively Affects the Transcription of pqsR and Pseudomonas Quinolone Signal Production in Pseudomonas aeruginosa. *J. Bacteriol.* **197**, 1988–2002 (2015).
160. Guo, Y. *et al.* Antitoxin HigA inhibits virulence gene mvfR expression in Pseudomonas aeruginosa. *Environ. Microbiol.* **21**, 2707–2723 (2019).
161. Maura, D., Ballok, A. E. & Rahme, L. G. Considerations and caveats in anti-virulence drug development. *Curr. Opin. Microbiol.* **33**, 41–46 (2016).
162. Wang, L.-H., Weng, L.-X., Dong, Y.-H. & Zhang, L.-H. Specificity and Enzyme Kinetics of the Quorum-quenching N-Acyl Homoserine Lactone Lactonase (AHL-lactonase). *J. Biol. Chem.* **279**, 13645–13651 (2004).
163. Billot, R. *et al.* Engineering acyl-homoserine lactone-interfering enzymes toward bacterial control. *J. Biol. Chem.* **295**, 12993–13007 (2020).
164. Tettmann, B. *et al.* Enzyme-Mediated Quenching of the Pseudomonas Quinolone Signal (PQS) Promotes Biofilm Formation of Pseudomonas aeruginosa by Increasing Iron Availability. *Front. Microbiol.* **7**, (2016).
165. Ibacache-Quiroga, C. *et al.* The hydrocarbon-degrading marine bacterium Cobetia sp. strain MM1IDA2H-1 produces a biosurfactant that interferes with quorum sensing of fish pathogens by signal hijacking. *Microb. Biotechnol.* **6**, 394–405 (2013).
166. Xue, X. *et al.* Synthetic Polymers for Simultaneous Bacterial Sequestration and Quorum Sense Interference. *Angew. Chemie Int. Ed.* **50**, 9852–9856 (2011).

167. O'Loughlin, C. T. *et al.* A quorum-sensing inhibitor blocks Pseudomonas aeruginosa virulence and biofilm formation. *Proc. Natl. Acad. Sci.* **110**, 17981–17986 (2013).
168. Paczkowski, J. E. *et al.* Flavonoids Suppress Pseudomonas aeruginosa Virulence through Allosteric Inhibition of Quorum-sensing Receptors. *J. Biol. Chem.* **292**, 4064–4076 (2017).
169. Srinivasarao, S. *et al.* Design, synthesis and biological evaluation of 1,2,3-triazole based 2-aminobenzimidazoles as novel inhibitors of LasR dependent quorum sensing in Pseudomonas aeruginosa. *RSC Adv.* **9**, 29273–29292 (2019).
170. Valastyan, J. S. *et al.* Discovery of PqsE Thioesterase Inhibitors for Pseudomonas aeruginosa Using DNA-Encoded Small Molecule Library Screening. *ACS Chem. Biol.* **15**, 446–456 (2020).
171. Weidel, E. *et al.* Structure Optimization of 2-Benzamidobenzoic Acids as PqsD Inhibitors for Pseudomonas aeruginosa Infections and Elucidation of Binding Mode by SPR, STD NMR, and Molecular Docking. *J. Med. Chem.* **56**, 6146–6155 (2013).
172. Sahner, J. H. *et al.* Combining in Silico and Biophysical Methods for the Development of Pseudomonas aeruginosa Quorum Sensing Inhibitors: An Alternative Approach for Structure-Based Drug Design. *J. Med. Chem.* **56**, 8656–8664 (2013).
173. Sahner, J. H. *et al.* Exploring the chemical space of ureidothiophene-2-carboxylic acids as inhibitors of the quorum sensing enzyme PqsD from Pseudomonas aeruginosa. *Eur. J. Med. Chem.* **96**, 14–21 (2015).
174. Allegretta, G., Weidel, E., Empting, M. & Hartmann, R. W. Catechol-based substrates of chalcone synthase as a scaffold for novel inhibitors of PqsD. *Eur. J. Med. Chem.* **90**, 351–359 (2015).
175. Drees, S. L. *et al.* PqsBC, a Condensing Enzyme in the Biosynthesis of the Pseudomonas aeruginosa Quinolone Signal. *J. Biol. Chem.* **291**, 6610–6624 (2016).
176. Maura, D. *et al.* Polypharmacology Approaches against the Pseudomonas aeruginosa MvfR Regulon and Their Application in Blocking Virulence and Antibiotic Tolerance. *ACS Chem. Biol.* **12**, 1435–1443 (2017).
177. Allegretta, G. *et al.* In-depth Profiling of MvfR-Regulated Small Molecules in Pseudomonas aeruginosa after Quorum Sensing Inhibitor Treatment. *Front. Microbiol.* **8**, (2017).
178. Maura, D. & Rahme, L. G. Pharmacological Inhibition of the Pseudomonas aeruginosa MvfR Quorum-Sensing System Interferes with Biofilm Formation and Potentiates Antibiotic-Mediated Biofilm Disruption. *Antimicrob. Agents Chemother.* **61**, (2017).
179. Li, W.-R., Zeng, T.-H., Xie, X.-B., Shi, Q.-S. & Li, C.-L. Inhibition of the pqsABCDE and pqsH in the pqs quorum sensing system and related virulence factors of the Pseudomonas aeruginosa PAO1 strain by farnesol. *Int. Biodeterior. Biodegradation* **151**, 104956 (2020).

180. Mok, N., Chan, S. Y., Liu, S. Y. & Chua, S. L. Vanillin inhibits PqsR-mediated virulence in Pseudomonas aeruginosa. *Food Funct.* **11**, 6496–6508 (2020).
181. Wang, M. *et al.* Cladodionen Is a Potential Quorum Sensing Inhibitor Against Pseudomonas aeruginosa. *Mar. Drugs* **18**, 205 (2020).
182. Lu, C. *et al.* Discovery of Antagonists of PqsR, a Key Player in 2-Alkyl-4-quinolone-Dependent Quorum Sensing in Pseudomonas aeruginosa. *Chem. Biol.* **19**, 381–390 (2012).
183. Soukarieh, F. *et al.* In silico and in vitro-guided identification of inhibitors of alkylquinolone-dependent quorum sensing in pseudomonas aeruginosa. *Molecules* **23**, (2018).
184. Starkey, M. *et al.* Identification of Anti-virulence Compounds That Disrupt Quorum-Sensing Regulated Acute and Persistent Pathogenicity. *PLoS Pathog.* **10**, (2014).
185. Schütz, C. *et al.* A New PqsR Inverse Agonist Potentiates Tobramycin Efficacy to Eradicate Pseudomonas aeruginosa Biofilms. *Adv. Sci.* **8**, 2004369 (2021).
186. Cugini, C. *et al.* Farnesol, a common sesquiterpene, inhibits PQS production in Pseudomonas aeruginosa. *Mol. Microbiol.* **65**, 896–906 (2007).
187. Jacquemard, C. & Kellenberger, E. A bright future for fragment-based drug discovery: what does it hold? *Expert Opin. Drug Discov.* **14**, 413–416 (2019).
188. Giordanetto, F., Jin, C., Willmore, L., Feher, M. & Shaw, D. E. Fragment Hits: What do They Look Like and How do They Bind? *J. Med. Chem.* **62**, 3381–3394 (2019).
189. Robson-Tull, J. Biophysical screening in fragment-based drug design: a brief overview. *Biosci. Horizons Int. J. Student Res.* **11**, (2018).
190. Folmer, R. H. A. Integrating biophysics with HTS-driven drug discovery projects. *Drug Discov. Today* **21**, 491–498 (2016).
191. Lamoree, B. & Hubbard, R. E. Current perspectives in fragment-based lead discovery (FBLD). *Essays Biochem.* **61**, 453–464 (2017).
192. Murray, C. W. & Rees, D. C. The rise of fragment-based drug discovery. *Nat. Chem.* **1**, 187–192 (2009).
193. Ferenczy, G. G. & Keserű, G. M. Thermodynamic profiling for fragment-based lead discovery and optimization. *Expert Opin. Drug Discov.* **15**, 117–129 (2020).
194. Murray, C. W. & Blundell, T. L. Structural biology in fragment-based drug design. *Curr. Opin. Struct. Biol.* **20**, 497–507 (2010).
195. Storz, M. P. *et al.* Validation of PqsD as an Anti-biofilm Target in Pseudomonas aeruginosa by Development of Small-Molecule Inhibitors. *J. Am. Chem. Soc.* **134**, 16143–16146 (2012).
196. Storz, M. P. *et al.* Biochemical and Biophysical Analysis of a Chiral PqsD Inhibitor Revealing Tight-binding Behavior and Enantiomers with Contrary Thermodynamic Signatures. *ACS*

Chem. Biol. **8**, 2794–2801 (2013).

197. Zender, M. *et al.* Dissecting the Multiple Roles of PqsE in Pseudomonas aeruginosa Virulence by Discovery of Small Tool Compounds. *ACS Chem. Biol.* **11**, 1755–1763 (2016).
198. Seetoh, W.-G. & Abell, C. Disrupting the Constitutive, Homodimeric Protein–Protein Interface in CK2β Using a Biophysical Fragment-Based Approach. *J. Am. Chem. Soc.* **138**, 14303–14311 (2016).
199. Klein, T. *et al.* Identification of Small-Molecule Antagonists of the Pseudomonas aeruginosa Transcriptional Regulator PqsR: Biophysically Guided Hit Discovery and Optimization. *ACS Chem. Biol.* **7**, 1496–1501 (2012).
200. Zender, M. *et al.* Discovery and Biophysical Characterization of 2-Amino-oxadiazoles as Novel Antagonists of PqsR, an Important Regulator of Pseudomonas aeruginosa Virulence. *J. Med. Chem.* **56**, 6761–6774 (2013).
201. Zender, M. *et al.* Flexible Fragment Growing Boosts Potency of Quorum-Sensing Inhibitors against Pseudomonas aeruginosa Virulence. *ChemMedChem* **15**, 188–194 (2020).
202. Thomann, A., de Mello Martins, A. G. G., Brengel, C., Empting, M. & Hartmann, R. W. Application of Dual Inhibition Concept within Looped Autoregulatory Systems toward Antivirulence Agents against Pseudomonas aeruginosa Infections. *ACS Chem. Biol.* **11**, 1279–1286 (2016).
203. Soto-Aceves, M. P. *et al.* Inactivation of the quorum-sensing transcriptional regulators LasR or RhlR does not suppress the expression of virulence factors and the virulence of Pseudomonas aeruginosa PAO1. *Microbiology* **165**, 425–432 (2019).
204. Bru, J.-L. *et al.* PQS Produced by the Pseudomonas aeruginosa Stress Response Repels Swarms Away from Bacteriophage and Antibiotics. *J. Bacteriol.* **201**, (2019).
205. Oton, E. V. Pseudomonas aeruginosa PQS mediated virulence regulation and interference. (2019).
206. Maestro. (2021).
207. Bryant, F. R. Construction of a recombinase-deficient mutant recA protein that retains single-stranded DNA-dependent ATPase activity. *J. Biol. Chem.* **263**, 8716–23 (1988).
208. William Studier, F., Rosenberg, A. H., Dunn, J. J. & Dubendorff, J. W. [6] Use of T7 RNA polymerase to direct expression of cloned genes. in 60–89 (1990). doi:10.1016/0076-6879(90)85008-C.
209. Simon, R., Priefer, U. & Pühler, A. A Broad Host Range Mobilization System for In Vivo Genetic Engineering: Transposon Mutagenesis in Gram Negative Bacteria. *Bio/Technology* **1**, 784–791 (1983).

210. Klockgether, J. *et al.* Genome Diversity of Pseudomonas aeruginosa PAO1 Laboratory Strains. *J. Bacteriol.* **192**, 1113–1121 (2010).
211. Liu, Y.-C. Understanding chronic inflammatory diseases in the human lung: the cystic fibrosis and idiopathic pulmonary fibrosis paradigms. (2014).
212. Heeb, S., Blumer, C. & Haas, D. Regulatory RNA as Mediator in GacA/RsmA-Dependent Global Control of Exoproduct Formation in Pseudomonas fluorescens CHA0. *J. Bacteriol.* **184**, 1046–1056 (2002).
213. Diggle, S. P. *et al.* The Pseudomonas aeruginosa 4-Quinolone Signal Molecules HHQ and PQS Play Multifunctional Roles in Quorum Sensing and Iron Entrapment. *Chem. Biol.* **14**, 87–96 (2007).
214. Gasteiger, E. *et al.* Protein Identification and Analysis Tools on the ExPASy Server. in *The Proteomics Protocols Handbook* 571–607 (Humana Press, 2005). doi:10.1385/1-59259-890-0:571.
215. Moon, A. F., Mueller, G. A., Zhong, X. & Pedersen, L. C. A synergistic approach to protein crystallization: Combination of a fixed-arm carrier with surface entropy reduction. *Protein Sci.* **19**, 901–913 (2010).
216. Manalastas-Cantos, K. *et al.* ATSAS 3.0 : expanded functionality and new tools for small-angle scattering data analysis. *J. Appl. Crystallogr.* **54**, 343–355 (2021).
217. Neubauer, S. *et al.* LC-MS/MS-based analysis of coenzyme A and short-chain acyl-coenzyme A thioesters. *Anal. Bioanal. Chem.* **407**, 6681–6688 (2015).
218. Trott, O. & Olson, A. J. AutoDock Vina: Improving the speed and accuracy of docking with a new scoring function, efficient optimization, and multithreading. *J. Comput. Chem.* NA-NA (2009) doi:10.1002/jcc.21334.
219. Witzgall, F., Ewert, W. & Blankenfeldt, W. Structures of the N-Terminal Domain of PqsA in Complex with Anthraniloyl- and 6-Fluoroanthraniloyl-AMP: Substrate Activation in Pseudomonas Quinolone Signal (PQS) Biosynthesis. *Chembiochem* **18**, 2045–2055 (2017).
220. Morris, G. M. *et al.* AutoDock4 and AutoDockTools4: Automated docking with selective receptor flexibility. *J. Comput. Chem.* **30**, 2785–2791 (2009).
221. Brodersen, D. E., Andersen, G. R. & Andersen, C. B. F. Mimer : an automated spreadsheet-based crystallization screening system. *Acta Crystallogr. Sect. F Struct. Biol. Cryst. Commun.* **69**, 815–820 (2013).
222. Lorber, B. *et al.* Crystal growth of proteins, nucleic acids, and viruses in gels. *Prog. Biophys. Mol. Biol.* **101**, 13–25 (2009).
223. Murshudov, G. N. *et al.* REFMAC 5 for the refinement of macromolecular crystal structures.

Acta Crystallogr. Sect. D Biol. Crystallogr. **67**, 355–367 (2011).

224. Long, F. *et al.* AceDRG : a stereochemical description generator for ligands. *Acta Crystallogr. Sect. D Struct. Biol.* **73**, 112–122 (2017).
225. Emsley, P., Lohkamp, B., Scott, W. G. & Cowtan, K. Features and development of Coot. *Acta Crystallogr. Sect. D Biol. Crystallogr.* **66**, 486–501 (2010).
226. Ianevski, A., Giri, A. K. & Aittokallio, T. SynergyFinder 2.0: visual analytics of multi-drug combination synergies. *Nucleic Acids Res.* **48**, W488–W493 (2020).
227. Yadav, B., Wennerberg, K., Aittokallio, T. & Tang, J. Searching for Drug Synergy in Complex Dose–Response Landscapes Using an Interaction Potency Model. *Comput. Struct. Biotechnol. J.* **13**, 504–513 (2015).
228. Ilangovan, A. Structural studies of Pseudomonas quoinolone signal regulator PqsR. (University of Nottingham, 2011).
229. Xu, N., Yu, S., Moniot, S., Weyand, M. & Blankenfeldt, W. Crystallization and preliminary crystal structure analysis of the ligand-binding domain of PqsR (MvfR), the Pseudomonas quinolone signal (PQS) responsive quorum-sensing transcription factor of Pseudomonas aeruginosa. *Acta Crystallogr. Sect. F Struct. Biol. Cryst. Commun.* **68**, 1034–1039 (2012).
230. Liebschner, D. *et al.* Polder maps: improving OMIT maps by excluding bulk solvent. *Acta Crystallogr. Sect. D Struct. Biol.* **73**, 148–157 (2017).
231. Zhou, P., Tian, F., Lv, F. & Shang, Z. Geometric characteristics of hydrogen bonds involving sulfur atoms in proteins. *Proteins Struct. Funct. Bioinforma.* **76**, 151–163 (2009).
232. Bai, N., Roder, H., Dickson, A. & Karanicolas, J. Isothermal Analysis of ThermoFluor Data can readily provide Quantitative Binding Affinities. *Sci. Rep.* **9**, 2650 (2019).
233. Parry, N. J., Pantalone, P. & Williams, P. LACTAMS FOR USE IN THE TREATMENT OF SKIN LESIONS. (2017).
234. Sabir, S. *et al.* Thioether-linked dihydropyrrol-2-one analogues as PqsR antagonists against antibiotic resistant Pseudomonas aeruginosa. *Bioorg. Med. Chem.* **31**, 115967 (2021).
235. Pantalone, P. Elucidating the mechanism of action of novel lactams on Pseudomonas aeruginosa. (2019).
236. Dai, R., Wilson, D. J., Geders, T. W., Aldrich, C. C. & Finzel, B. C. Inhibition of Mycobacterium tuberculosis Transaminase BioA by Aryl Hydrazines and Hydrazides. *ChemBioChem* **15**, 575–586 (2014).
237. Dai, R. *et al.* Fragment-Based Exploration of Binding Site Flexibility in Mycobacterium tuberculosis BioA. *J. Med. Chem.* **58**, 5208–5217 (2015).
238. Krasavin, M. *et al.* Screening of benzenesulfonamide in combination with chemically diverse

fragments against carbonic anhydrase by differential scanning fluorimetry. *J. Enzyme Inhib. Med. Chem.* **35**, 306–310 (2020).

239. Klose, D. P., Wallace, B. A. & Janes, R. W. 2Struc: the secondary structure server. *Bioinformatics* **26**, 2624–2625 (2010).
240. Micsonai, A. *et al.* BeStSel: a web server for accurate protein secondary structure prediction and fold recognition from the circular dichroism spectra. *Nucleic Acids Res.* **46**, W315–W322 (2018).
241. Mahootchi, E. *et al.* Structure and substrate specificity determinants of the taurine biosynthetic enzyme cysteine sulphinic acid decarboxylase. *J. Struct. Biol.* **213**, 107674 (2021).
242. Ainsworth, N. M. Developing Methods to Assess Enzyme Stability in Liquid Laundry Detergents. (University of Durham, 2018).
243. Tedesco, D. & Bertucci, C. Induced circular dichroism as a tool to investigate the binding of drugs to carrier proteins: Classic approaches and new trends. *J. Pharm. Biomed. Anal.* **113**, 34–42 (2015).
244. Cagan, R. Drug screening using model systems: some basics. *Dis. Model. Mech.* **9**, 1241–1244 (2016).
245. Jin, G. & Wong, S. T. C. Toward better drug repositioning: prioritizing and integrating existing methods into efficient pipelines. *Drug Discov. Today* **19**, 637–644 (2014).
246. D'Angelo, F. *et al.* Identification of FDA-Approved Drugs as Antivirulence Agents Targeting the pqs Quorum-Sensing System of Pseudomonas aeruginosa. *Antimicrob. Agents Chemother.* **62**, (2018).
247. Wojdyr, M., Keegan, R., Winter, G. & Ashton, A. DIMPLE - a pipeline for the rapid generation of difference maps from protein crystals with putatively bound ligands. *Acta Crystallogr. Sect. A Found. Crystallogr.* **69**, s299–s299 (2013).
248. McCoy, A. J. *et al.* Phaser crystallographic software. *J. Appl. Crystallogr.* **40**, 658–674 (2007).
249. Winsor, G. L. *et al.* Enhanced annotations and features for comparing thousands of Pseudomonas genomes in the Pseudomonas genome database. *Nucleic Acids Res.* **44**, D646–D653 (2016).
250. Hornischer, K. *et al.* BACTOME—a reference database to explore the sequence- and gene expression-variation landscape of Pseudomonas aeruginosa clinical isolates. *Nucleic Acids Res.* **47**, D716–D720 (2019).
251. Sievers, F. *et al.* Fast, scalable generation of high-quality protein multiple sequence alignments using Clustal Omega. *Mol. Syst. Biol.* **7**, 539 (2011).
252. Ritter, B. *et al.* Two WXXF-based motifs in NECAPs define the specificity of accessory protein

binding to AP-1 and AP-2. *EMBO J.* **23**, 3701–3710 (2004).

253. Lee, J. & Kim, S.-H. PDB Editor : a user-friendly Java-based Protein Data Bank file editor with a GUI. *Acta Crystallogr. Sect. D Biol. Crystallogr.* **65**, 399–402 (2009).
254. Chen, Y. *et al.* PremPS: Predicting the impact of missense mutations on protein stability. *PLOS Comput. Biol.* **16**, e1008543 (2020).
255. Aleksić, I. *et al.* Long-Chain 4-Aminoquinolines as Quorum Sensing Inhibitors in Serratia marcescens and Pseudomonas aeruginosa. *ACS Chem. Biol.* **12**, 1425–1434 (2017).
256. Ehrmann, F. R. *et al.* Soaking suggests “alternative facts”: Only co-crystallization discloses major ligand-induced interface rearrangements of a homodimeric tRNA-binding protein indicating a novel mode-of-inhibition. *PLoS One* **12**, e0175723 (2017).
257. Momany, C. & Neidle, E. L. Defying stereotypes: the elusive search for a universal model of LysR-type regulation. *Mol. Microbiol.* **83**, 453–456 (2012).
258. Ezezika, O. C., Haddad, S., Neidle, E. L. & Momany, C. Oligomerization of BenM, a LysR-type transcriptional regulator: structural basis for the aggregation of proteins in this family. *Acta Crystallogr. Sect. F Struct. Biol. Cryst. Commun.* **63**, 361–368 (2007).
259. Park, H. *et al.* A LysR-Type Transcriptional Regulator LcrX Is Involved in Virulence, Biofilm Formation, Swimming Motility, Siderophore Secretion, and Growth in Sugar Sources in Xanthomonas axonopodis Pv. glycines. *Front. Plant Sci.* **10**, (2020).
260. Tumen-Velasquez, M. P., Laniohan, N. S., Momany, C. & Neidle, E. L. Engineering CatM, a LysR-Type Transcriptional Regulator, to Respond Synergistically to Two Effectors. *Genes (Basel).* **10**, 421 (2019).
261. Jaiyen, Y. Novel inhibitors of the Staphylococcus aureus quorum sensing system. (2017).
262. Yang, J. *et al.* Improved protein structure prediction using predicted interresidue orientations. *Proc. Natl. Acad. Sci.* **117**, 1496–1503 (2020).
263. Ishida, T. & Kinoshita, K. PrDOS: prediction of disordered protein regions from amino acid sequence. *Nucleic Acids Res.* **35**, W460–W464 (2007).
264. Buchan, D. W. A. & Jones, D. T. The PSIPRED Protein Analysis Workbench: 20 years on. *Nucleic Acids Res.* **47**, W402–W407 (2019).
265. Qing, G. *et al.* Cold-shock induced high-yield protein production in Escherichia coli. *Nat. Biotechnol.* **22**, 877–882 (2004).
266. Sugiki, T., Fujiwara, T. & Kojima, C. Cold-Shock Expression System in E. coli for Protein NMR Studies. in 345–357 (2017). doi:10.1007/978-1-4939-6887-9_23.
267. Vasina, J. A. & Baneyx, F. Recombinant protein expression at low temperatures under the transcriptional control of the major Escherichia coli cold shock promoter cspA. *Appl. Environ.*

Microbiol. **62**, 1444–1447 (1996).

268. Fragel, S. M. *et al.* Characterization of the pleiotropic LysR-type transcription regulator LeuO of Escherichia coli. *Nucleic Acids Res.* **47**, 7363–7379 (2019).

269. Song, Y. *et al.* Molecular insights into the master regulator CysB-mediated bacterial virulence in Pseudomonas aeruginosa. *Mol. Microbiol.* **111**, 1195–1210 (2019).

270. Truan, D., Vasil, A., Stonehouse, M., Vasil, M. L. & Pohl, E. High-level over-expression, purification, and crystallization of a novel phospholipase C/sphingomyelinase from Pseudomonas aeruginosa. *Protein Expr. Purif.* **90**, 40–46 (2013).

271. Brillet, K. *et al.* A β Strand Lock Exchange for Signal Transduction in TonB-Dependent Transducers on the Basis of a Common Structural Motif. *Structure* **15**, 1383–1391 (2007).

272. Poh, W.-H. *et al.* The SiaABC threonine phosphorylation pathway controls biofilm formation in response to carbon availability in Pseudomonas aeruginosa. *PLoS One* **15**, e0241019 (2020).

273. Bleffert, F. *et al.* Pseudomonas aeruginosa esterase PA2949, a bacterial homolog of the human membrane esterase ABHD6: expression, purification and crystallization. *Acta Crystallogr. Sect. F Struct. Biol. Commun.* **75**, 270–277 (2019).

274. Schweizer, H. P. Escherichia-Pseudomonas shuttle vectors derived from pUC18/19. *Gene* **97**, 109–112 (1991).

275. Frimmersdorf, E., Horatzek, S., Pelnikevich, A., Wiehlmann, L. & Schomburg, D. How Pseudomonas aeruginosa adapts to various environments: a metabolomic approach. *Environ. Microbiol.* **12**, 1734–1747 (2010).

276. Retallack, D. M., Jin, H. & Chew, L. Reliable protein production in a Pseudomonas fluorescens expression system. *Protein Expr. Purif.* **81**, 157–165 (2012).

277. Bolanos-Garcia, V. M. & Davies, O. R. Structural analysis and classification of native proteins from E. coli commonly co-purified by immobilised metal affinity chromatography. *Biochim. Biophys. Acta - Gen. Subj.* **1760**, 1304–1313 (2006).

278. Riggs, P., Vallie, E. R. & McCoy, J. M. Introduction to Expression by Fusion Protein Vectors. *Curr. Protoc. Mol. Biol.* **28**, (1994).

279. Prasad, S., Khadatare, P. B. & Roy, I. Effect of Chemical Chaperones in Improving the Solubility of Recombinant Proteins in Escherichia coli. *Appl. Environ. Microbiol.* **77**, 4603–4609 (2011).

280. Protein production and purification. *Nat. Methods* **5**, 135–146 (2008).

281. Jiang, S. *et al.* Diverse supramolecular structures formed by self-assembling proteins of the *Bacillus subtilis* spore coat. *Mol. Microbiol.* **97**, 347–359 (2015).

282. Drazic, A. *et al.* Tetramers Are the Activation-competent Species of the HOCl-specific

Transcription Factor HypT. *J. Biol. Chem.* **289**, 977–986 (2014).

283. Prasad, G. S. *et al.* Crystal structure of dUTP pyrophosphatase from feline immunodeficiency virus. *Protein Sci.* **5**, 2429–2437 (1996).
284. Holyoak, T. *et al.* Malonate: a versatile cryoprotectant and stabilizing solution for salt-grown macromolecular crystals. *Acta Crystallogr. Sect. D Biol. Crystallogr.* **59**, 2356–2358 (2003).
285. Leibly, D. J. *et al.* Stabilizing Additives Added during Cell Lysis Aid in the Solubilization of Recombinant Proteins. *PLoS One* **7**, e52482 (2012).
286. Richardson, W. K. Antimicrobials and antimicrobial resistance (MRes). (University of Nottingham, 2017).
287. Hassell, A. M. *et al.* Crystallization of protein–ligand complexes. *Acta Crystallogr. Sect. D Biol. Crystallogr.* **63**, 72–79 (2007).
288. You, Z. *et al.* Purification and characterization of LasR as a DNA-binding protein. *FEMS Microbiol. Lett.* **142**, 301–307 (1996).
289. Reen, F. J. *et al.* Structure–function analysis of the C-3 position in analogues of microbial behavioural modulators HHQ and PQS. *Org. Biomol. Chem.* **10**, 8903 (2012).
290. Weichenberger, C. X. & Rupp, B. Ten years of probabilistic estimates of biocrystal solvent content: new insights via nonparametric kernel density estimate. *Acta Crystallogr. Sect. D Biol. Crystallogr.* **70**, 1579–1588 (2014).
291. Simpkin, A. J. *et al.* SIMBAD : a sequence-independent molecular-replacement pipeline. *Acta Crystallogr. Sect. D Struct. Biol.* **74**, 595–605 (2018).
292. Baek, M. *et al.* Accurate prediction of protein structures and interactions using a three-track neural network. *Science (80-.).* eabj8754 (2021) doi:10.1126/science.abj8754.
293. Baker, Y. R. *et al.* Identification of new quorum sensing autoinducer binding partners in Pseudomonas aeruginosa using photoaffinity probes. *Chem. Sci.* **8**, 7403–7411 (2017).
294. Giannopoulou, E. *et al.* Crystal structure of the full-length LysR-type transcription regulator CbnR in complex with promoter DNA. *FEBS J.* **288**, 4560–4575 (2021).
295. Bina, X. R., Bina, J. E. & Ante, V. M. The LysR-type regulator LeuO regulates the acid tolerance response in Vibrio cholerae. *Microbiology* **161**, 2434–2443 (2015).
296. Grob, P. & Guiney, D. G. In vitro binding of the Salmonella dublin virulence plasmid regulatory protein SpvR to the promoter regions of spvA and spvR. *J. Bacteriol.* **178**, 1813–1820 (1996).
297. A. Stella, N., E. Fender, J., M. Lahr, R., J. Kalivoda, E. & M. Q. Shanks, R. The LysR Transcription Factor, HexS, Is Required for Glucose Inhibition of Prodigiosin Production by <i>Serratia marcescens</i> *Adv. Microbiol.* **02**, 511–517 (2012).

298. Lebendiker, M. & Danieli, T. Purification of Proteins Fused to Maltose-Binding Protein. in 281–293 (2011). doi:10.1007/978-1-60761-913-0_15.
299. Wernimont, A. & Edwards, A. In Situ Proteolysis to Generate Crystals for Structure Determination: An Update. *PLoS One* **4**, e5094 (2009).
300. Liu, X., Zhang, H., Wang, X.-J., Li, L.-F. & Su, X.-D. Get Phases from Arsenic Anomalous Scattering: de novo SAD Phasing of Two Protein Structures Crystallized in Cacodylate Buffer. *PLoS One* **6**, e24227 (2011).
301. Garman, E. F. Radiation damage in macromolecular crystallography: what is it and why should we care? *Acta Crystallogr. Sect. D Biol. Crystallogr.* **66**, 339–351 (2010).
302. Ó Muimhneacháin, E., Reen, F. J., O'Gara, F. & McGlacken, G. P. Analogues of Pseudomonas aeruginosa signalling molecules to tackle infections. *Org. Biomol. Chem.* **16**, 169–179 (2018).
303. Nepali, K., Lee, H.-Y. & Liou, J.-P. Nitro-Group-Containing Drugs. *J. Med. Chem.* **62**, 2851–2893 (2019).
304. Huang, D. & Caflisch, A. Library screening by fragment-based docking. *J. Mol. Recognit.* n/a-n/a (2009) doi:10.1002/jmr.981.
305. Good, A. C. *et al.* Implications of Promiscuous Pim-1 Kinase Fragment Inhibitor Hydrophobic Interactions for Fragment-Based Drug Design. *J. Med. Chem.* **55**, 2641–2648 (2012).
306. Teotico, D. G. *et al.* Docking for fragment inhibitors of AmpC -lactamase. *Proc. Natl. Acad. Sci.* **106**, 7455–7460 (2009).
307. Silvestre, H. L., Blundell, T. L., Abell, C. & Ciulli, A. Integrated biophysical approach to fragment screening and validation for fragment-based lead discovery. *Proc. Natl. Acad. Sci.* **110**, 12984–12989 (2013).
308. Harder, E. *et al.* OPLS3: A Force Field Providing Broad Coverage of Drug-like Small Molecules and Proteins. *J. Chem. Theory Comput.* **12**, 281–296 (2016).
309. Lovering, F., Bikker, J. & Humblet, C. Escape from Flatland: Increasing Saturation as an Approach to Improving Clinical Success. *J. Med. Chem.* **52**, 6752–6756 (2009).
310. Enamine. Fragment Libraries. 1 https://enamine.net/compound-libraries/fragment-libraries (2021).
311. Huynh, K. & Partch, C. L. Analysis of Protein Stability and Ligand Interactions by Thermal Shift Assay. *Curr. Protoc. Protein Sci.* **79**, (2015).
312. Yu, H. S. *et al.* General Theory of Fragment Linking in Molecular Design: Why Fragment Linking Rarely Succeeds and How to Improve Outcomes. *J. Chem. Theory Comput.* **17**, 450–462 (2021).
313. Gupta, P. *et al.* A fragment-based approach to assess the ligandability of ArgB, ArgC, ArgD and

ArgF in the L-arginine biosynthetic pathway of Mycobacterium tuberculosis. *Comput. Struct. Biotechnol. J.* **19**, 3491–3506 (2021).

314. Coleman, J. P. *et al.* Pseudomonas aeruginosa PqsA is an anthranilate-coenzyme A ligase. *J. Bacteriol.* **190**, 1247–1255 (2008).
315. Pollock, K. *et al.* Fragment-based screening identifies molecules targeting the substrate-binding ankyrin repeat domains of tankyrase. *Sci. Rep.* **9**, 19130 (2019).
316. Douse, C. H., Vrielink, N., Wenlin, Z., Cota, E. & Tate, E. W. Targeting a Dynamic Protein-Protein Interaction: Fragment Screening against the Malaria Myosin A Motor Complex. *ChemMedChem* **10**, 134–143 (2015).
317. Munshi, S., Hall, D. L., Kornienko, M., Darke, P. L. & Kuo, L. C. Structure of apo, unactivated insulin-like growth factor-1 receptor kinase at 1.5 Å resolution. *Acta Crystallogr. Sect. D Biol. Crystallogr.* **59**, 1725–1730 (2003).
318. Cooper, D. R. *et al.* Protein crystallization by surface entropy reduction: optimization of the SER strategy. *Acta Crystallogr. Sect. D Biol. Crystallogr.* **63**, 636–645 (2007).
319. Bauman, J. D. *et al.* Crystal engineering of HIV-1 reverse transcriptase for structure-based drug design. *Nucleic Acids Res.* **36**, 5083–5092 (2008).
320. Pearce, N. M. *et al.* A multi-crystal method for extracting obscured crystallographic states from conventionally uninterpretable electron density. *Nat. Commun.* **8**, 15123 (2017).
321. Goldschmidt, L., Cooper, D. R., Derewenda, Z. S. & Eisenberg, D. Toward rational protein crystallization: A Web server for the design of crystallizable protein variants. *Protein Sci.* **16**, 1569–1576 (2007).
322. Krissinel, E. & Henrick, K. Inference of Macromolecular Assemblies from Crystalline State. *J. Mol. Biol.* **372**, 774–797 (2007).
323. Bogan, A. A. & Thorn, K. S. Anatomy of hot spots in protein interfaces. *J. Mol. Biol.* **280**, 1–9 (1998).
324. Conte, L. Lo, Chothia, C. & Janin, J. The atomic structure of protein-protein recognition sites 1 1Edited by A. R. Fersht. *J. Mol. Biol.* **285**, 2177–2198 (1999).
325. Liu, Y. & Kuhlman, B. RosettaDesign server for protein design. *Nucleic Acids Res.* **34**, W235–W238 (2006).
326. Pu, M. *et al.* Protein crystal quality oriented disulfide bond engineering. *Protein Cell* **9**, 659–663 (2018).
327. Craig, D. B. & Dombkowski, A. A. Disulfide by Design 2.0: a web-based tool for disulfide engineering in proteins. *BMC Bioinformatics* **14**, 346 (2013).
328. Gao, X., Dong, X., Li, X., Liu, Z. & Liu, H. Prediction of disulfide bond engineering sites using a

machine learning method. *Sci. Rep.* **10**, 10330 (2020).

329. Jin, T. *et al.* Design of an expression system to enhance MBP-mediated crystallization. *Sci. Rep.* **7**, 40991 (2017).
330. Sauter, C. *et al.* Agarose gel facilitates enzyme crystal soaking with a ligand analog. *J. Appl. Crystallogr.* **42**, 279–283 (2009).
331. Blackburn, A. *et al.* A Simple Technique to Improve Microcrystals Using Gel Exclusion of Nucleation Inducing Elements. *Crystals* **8**, 464 (2018).
332. Leslie, A. G. W. & Powell, H. R. Processing diffraction data with mosflm. in 41–51 (2007). doi:10.1007/978-1-4020-6316-9_4.
333. Incardona, M.-F. *et al.* EDNA : a framework for plugin-based applications applied to X-ray experiment online data analysis. *J. Synchrotron Radiat.* **16**, 872–879 (2009).
334. Svergun, D., Barberato, C. & Koch, M. H. J. CRYSOL – a Program to Evaluate X-ray Solution Scattering of Biological Macromolecules from Atomic Coordinates. *J. Appl. Crystallogr.* **28**, 768–773 (1995).
335. Ekimoto, T. & Ikeguchi, M. Hybrid Methods for Modeling Protein Structures Using Molecular Dynamics Simulations and Small-Angle X-Ray Scattering Data. in 237–258 (2018). doi:10.1007/978-981-13-2200-6_15.
336. Sainsbury, S., Ren, J., Saunders, N. J., Stuart, D. I. & Owens, R. J. Structure of the regulatory domain of the LysR family regulator NMB2055 (MetR-like protein) from Neisseria meningitidis. *Acta Crystallogr. Sect. F Struct. Biol. Cryst. Commun.* **68**, 730–737 (2012).
337. Choi, H.-J. *et al.* Structural Basis of the Redox Switch in the OxyR Transcription Factor. *Cell* **105**, 103–113 (2001).
338. Li, Y. & He, Z.-G. The Mycobacterial LysR-Type Regulator OxyS Responds to Oxidative Stress and Negatively Regulates Expression of the Catalase-Peroxidase Gene. *PLoS One* **7**, e30186 (2012).
339. Jo, I. *et al.* Structural basis for HOCl recognition and regulation mechanisms of HypT, a hypochlorite-specific transcriptional regulator. *Proc. Natl. Acad. Sci.* **116**, 3740–3745 (2019).
340. Kim, S. O. *et al.* OxyR - a molecular code for redox-related signaling. *Cell* **109**, 383–396 (2002).
341. Chang, W., Small, D. A., Toghrol, F. & Bentley, W. E. Microarray analysis of Pseudomonas aeruginosa reveals induction of pyocin genes in response to hydrogen peroxide. *BMC Genomics* **6**, 115 (2005).
342. Lu, C., Maurer, C. K., Kirsch, B., Steinbach, A. & Hartmann, R. W. Overcoming the Unexpected Functional Inversion of a PqsR Antagonist in Pseudomonas aeruginosa : An In Vivo Potent Antivirulence Agent Targeting pqs Quorum Sensing. *Angew. Chemie Int. Ed.* **53**, 1109–1112

(2014).

343. Bala, A., Chhibber, S. & Harjai, K. Pseudomonas quinolone signalling system: A component of quorum sensing cascade is a crucial player in the acute urinary tract infection caused by Pseudomonas aeruginosa. *Int. J. Med. Microbiol.* **304**, 1199–1208 (2014).
344. Calfee, M. W., Coleman, J. P. & Pesci, E. C. Interference with Pseudomonas quinolone signal synthesis inhibits virulence factor expression by Pseudomonas aeruginosa. *Proc. Natl. Acad. Sci.* **98**, 11633–11637 (2001).
345. Lesic, B. *et al.* Inhibitors of Pathogen Intercellular Signals as Selective Anti-Infective Compounds. *PLoS Pathog.* **3**, e126 (2007).
346. Lux, M. C., Standke, L. C. & Tan, D. S. Targeting adenylate-forming enzymes with designed sulfonyladenosine inhibitors. *J. Antibiot. (Tokyo).* **72**, 325–349 (2019).
347. Ji, C. *et al.* Designed small-molecule inhibitors of the anthranilyl-CoA synthetase PqsA block quinolone biosynthesis in pseudomonas aeruginosa. *ACS Chem. Biol.* **11**, 3061–3067 (2016).
348. Acker, M. G. & Auld, D. S. Considerations for the design and reporting of enzyme assays in high-throughput screening applications. *Perspect. Sci.* **1**, 56–73 (2014).
349. Zhang, J.-H., Chung, T. D. Y. & Oldenburg, K. R. A Simple Statistical Parameter for Use in Evaluation and Validation of High Throughput Screening Assays. *J. Biomol. Screen.* **4**, 67–73 (1999).
350. Chen, G. *et al.* The SiaA/B/C/D signaling network regulates biofilm formation in Pseudomonas aeruginosa. *EMBO J.* **39**, (2020).
351. Berlutti, F. *et al.* Iron Availability Influences Aggregation, Biofilm, Adhesion and Invasion of Pseudomonas Aeruginosa and Burkholderia Cenocepacia. *Int. J. Immunopathol. Pharmacol.* **18**, 661–670 (2005).
352. Rampioni, G. *et al.* Unravelling the Genome-Wide Contributions of Specific 2-Alkyl-4-Quinolones and PqsE to Quorum Sensing in Pseudomonas aeruginosa. *PLOS Pathog.* **12**, e1006029 (2016).
353. Allesen-Holm, M. *et al.* A characterization of DNA release in Pseudomonas aeruginosa cultures and biofilms. *Mol. Microbiol.* **59**, 1114–1128 (2006).
354. Diggle, S. P. *et al.* The Pseudomonas aeruginosa quinolone signal molecule overcomes the cell density-dependency of the quorum sensing hierarchy, regulates rhl-dependent genes at the onset of stationary phase and can be produced in the absence of LasR. *Mol. Microbiol.* **50**, 29–43 (2003).
355. Kany, A. M. *et al.* Tackling Pseudomonas aeruginosa Virulence by a Hydroxamic Acid-Based LasB Inhibitor. *ACS Chem. Biol.* **13**, 2449–2455 (2018).

356. Kang, D., Turner, K. E. & Kirienko, N. V. PqsA promotes pyoverdine production via biofilm formation. *Pathogens* **7**, (2018).

357. Neve, R. & Phelan, V. Artificial Sputum Medium Formulation Impacts Pseudomonas aeruginosa Phenotype and Chemotype. *BioRXiv* (2021) doi:https://doi.org/10.1101/2021.01.25.428197.

358. Yan, X., Hu, S., Guan, Y.-X. & Yao, S.-J. Coexpression of chaperonin GroEL/GroES markedly enhanced soluble and functional expression of recombinant human interferon-gamma in Escherichia coli. *Appl. Microbiol. Biotechnol.* **93**, 1065–1074 (2012).

359. Lee, T. V. *et al.* Structure of a Eukaryotic Nonribosomal Peptide Synthetase Adenylation Domain That Activates a Large Hydroxamate Amino Acid in Siderophore Biosynthesis. *J. Biol. Chem.* **285**, 2415–2427 (2010).

360. Tan, X.-F. *et al.* Structure of the adenylation–peptidyl carrier protein didomain of the Microcystis aeruginosa microcystin synthetase McyG. *Acta Crystallogr. Sect. D Biol. Crystallogr.* **71**, 873–881 (2015).

361. Drake, E. J., Duckworth, B. P., Neres, J., Aldrich, C. C. & Gulick, A. M. Biochemical and Structural Characterization of Bisubstrate Inhibitors of BasE, the Self-Standing Nonribosomal Peptide Synthetase Adenylate-Forming Enzyme of Acinetobactin Synthesis,. *Biochemistry* **49**, 9292–9305 (2010).

362. Cieślak, J. *et al.* Biochemical characterization and structural insight into aliphatic β-amino acid adenylation enzymes IdnL1 and CmiS6. *Proteins Struct. Funct. Bioinforma.* **85**, 1238–1247 (2017).

363. Lebendiker, M. & Danieli, T. Production of prone-to-aggregate proteins. *FEBS Lett.* **588**, 236–246 (2014).

364. Murray, G. J., Youle, R. J., Gandy, S. E., Zirzow, G. C. & Barranger, J. A. Purification of β-glucocerebrosidase by preparative-scale high-performance liquid chromatography: The use of ethylene glycol-containing buffers for chromatography of hydrophobic glycoprotein enzymes. *Anal. Biochem.* **147**, 301–310 (1985).

365. Coulon, P. M. L., Groleau, M.-C. & Déziel, E. Potential of the Burkholderia cepacia Complex to Produce 4-Hydroxy-3-Methyl-2-Alkyquinolines. *Front. Cell. Infect. Microbiol.* **9**, (2019).

366. Hinsberger, S., de Jong, J. C., Groh, M., Haupenthal, J. & Hartmann, R. W. Benzamidobenzoic acids as potent PqsD inhibitors for the treatment of Pseudomonas aeruginosa infections. *Eur. J. Med. Chem.* **76**, 343–351 (2014).

367. Baldelli, V. *et al.* Identification of FDA-approved antivirulence drugs targeting the Pseudomonas aeruginosa quorum sensing effector protein PqsE. *Virulence* **11**, 652–668

(2020).

368. Prothiwa, M., Filz, V., Oehler, S. & Böttcher, T. Inhibiting quinolone biosynthesis of Burkholderia. *Chem. Sci.* **12**, 6908–6912 (2021).

369. Storz, M. P., Allegretta, G., Kirsch, B., Empting, M. & Hartmann, R. W. From in vitro to in cellulo : structure–activity relationship of (2-nitrophenyl)methanol derivatives as inhibitors of PqsD in Pseudomonas aeruginosa. *Org. Biomol. Chem.* **12**, 6094–6104 (2014).

370. Baell, J. B. & Holloway, G. A. New Substructure Filters for Removal of Pan Assay Interference Compounds (PAINS) from Screening Libraries and for Their Exclusion in Bioassays. *J. Med. Chem.* **53**, 2719–2740 (2010).

371. Sims, K. R. *et al.* Enhanced design and formulation of nanoparticles for anti-biofilm drug delivery. *Nanoscale* **11**, 219–236 (2019).

372. Vadekeetil, A., Chhibber, S. & Harjai, K. Efficacy of intravesical targeting of novel quorum sensing inhibitor nanoparticles against Pseudomonas aeruginosa biofilm-associated murine pyelonephritis. *J. Drug Target.* **27**, 995–1003 (2019).